Selectie, experimentele bepaling en evaluatie
van een wiskundig model voor scheepsmanoeuvres in ondiep water

Selection, Experimental Determination and Evaluation
of a Mathematical Model for Ship Manoeuvring in Shallow Water

Katrien Eloot

UNIVERSITEIT
GENT

Selectie, experimentele bepaling en evaluatie
van een wiskundig model voor scheepsmanoeuvres in ondiep water

Selection, Experimental Determination and Evaluation
of a Mathematical Model for Ship Manoeuvring in Shallow Water

Katrien Eloot

UNIVERSITEIT
GENT

Dankwoord

Het uitvoeren van het doctoraatsonderzoek en het neerschrijven van alle bevindingen in dit proefschrift was meer dan eens een eenzame activiteit, hoewel ik nauwelijks kan inschatten hoe groot de inbreng wel degelijk was van zovele mensen. Ik wil niemand in het bijzonder bedanken maar ik wil heel graag iedereen bedanken die dagelijks, wekelijks, maandelijks of zelfs jaarlijks, rechtstreeks of onrechtstreeks, bij dit proefschrift betrokken is geweest.

Ik hoop bovendien dat de samenwerking wat het maritiem onderzoek betreft, mag bestendigd worden en dat deze samenwerking op nationaal of internationaal vlak nog heel veel vruchten mag afwerpen zodat niet alleen de maritieme wereld maar elke samenleving er beter kan van worden.

Word of thanks

The realization of this research and the writing of this doctoral thesis has rather been a lonesome activity, although I probably cannot estimate how important the contribution has been of so many people. I do not want to thank somebody in particular but I want to thank anybody who has been involved daily, weekly, monthly or yearly, directly or indirectly, in this thesis.

Moreover, I hope that the co-operation concerning maritime research can be continued and that this co-operation on a national or international scale can still yield rich rewards so that not only the maritime world but each society can benefit from this progress.

English summary

The worldwide development towards larger ships seems to be a never ending story. Although the lock dimensions of the Panama Canal have long been used as reference dimensions for the so-called Panamax-sized ships with a beam of 32.3 m, ship's dimensions for e.g. the container traffic are constantly growing with existing maximum ratios nowadays of 9000 TEU (Twenty feet Equivalent Units) and an expected ratio of 11000 to 12000 TEU for the new designed locks in Panama. Taking into account the limited water depth available in the North Sea and the tidal dependent entrance of ships to the Flemish harbours, ship manoeuvring in shallow water has become an important topic for the public authorities. With the installation of a ship manoeuvring simulator in 1989 and a towing tank in 1992 at Flanders Hydraulics Research (FHR), Flemish authorities have definitely chosen for an experimental investigation of ship manoeuvring in environmental conditions which differ largely from the design conditions of a ship.

The aim of this research is threefold:
1. The selection of a mathematical model for the prediction of ship manoeuvres in especially shallow and laterally unrestricted water conditions will be based on experiments executed in the Towing Tank for Manoeuvres in Shallow Water (co-operation Flanders Hydraulics Research – Ghent University).
2. The test programs, executed on a slender ship (fourth generation containership) and a full ship (tanker Esso Osaka), will be evaluated and some guidelines and recommendations will be given.
3. The derived manoeuvring simulation models will be evaluated comparing full scale and prediction: a difficult task due to a lack of reference data to perform an objective validation.

The prediction of ship manoeuvrability based on mathematical models started in the middle of last century at several institutes all over the world. Considering the historical overview of mathematical models in chapter 1, a physical model or *modular model* referring to the physical components hull, propeller and rudder of a manoeuvring ship will be selected. Compared to the formal regression models (e.g. Taylor series expansions) this model guarantees a large adjustability, an indispensable requirement for prediction models of harbour manoeuvres characterized by speed limitations, and even reversed speed, *four quadrants of operation* and limited water depth. Although time dependent or 'memory' effects will play a part in low speed manoeuvring, a *quasi-steady approach* will be adopted. In addition, only the three degrees of freedom linked to the ship motions in a horizontal plane (surge, sway and yaw) will be considered.

Three mathematical models which provide some interesting features like physical background (the MMG model), four-quadrant operation (the Oltmann & Sharma model or HSVA model) or tabular model forms (the DEN-Mark 1 model) will be discussed in detail in chapter 2 and will be used as a guideline for the development of a manoeuvring model.

Although a great progress has been made in using CFD methods (Computational Fluid Dynamics) for the prediction of unsteady ship motions and manoeuvring, difficulties still remain e.g. concerning the inclusion of environmental effects as shallow water. The selected

determination method for this research, EFD or experimental fluid dynamics, makes use of scale models and is divided into captive model tests and free sailing tests. During a captive model test a fully appended ship model follows a prescribed motion. Forces are measured on each module together with the kinematical (velocities and accelerations) and control parameters (propeller rate and rudder angle). A description of stationary and non-stationary captive PMM (Planar Motion Mechanism) tests, executed in the towing tank of FHR, is given in chapter 3. Non-conventional tests, i.e. alternative, non-harmonic PMM sway tests and multi-modal tests, have been introduced to overcome some disadvantages of a conventional PMM sway test on the one hand or to enlarge the amount of parameters that can be varied during one test run on the other. These tests provide promising opportunities although test parameters will have to be selected with care to avoid undesirable flow phenomena in the tank.

The development of the mathematical model for ship manoeuvres in shallow water is subdivided into three chapters according to the three modules: hull, propeller and rudder.

❑ Chapter 4: The most important acceleration derivatives, the added mass due to sway and the added moment of inertia due to yaw, are affected by the test parameters of the harmonic captive tests. The velocity dependent terms are presented as tabular models of drift angle, yaw rate angle and a cross-coupling angle for sway and yaw.

❑ Chapter 5: Wake and thrust deduction factors, which determine the propeller thrust and the propeller induced longitudinal force, depend on the propeller loading and the inflow angle into the propeller. In addition, the wake factor decreases with increasing water depth to draught ratio. The propeller induced lateral force and yawing moment are expected to be small in deep water and only induce an asymmetry effect at reversed propeller; in shallow water, on the other hand, they increase with increasing inflow angle if the flow due to the ship motion and the propeller flow have the same sense, and are oscillating and suffer from unstable phenomena if both flows at the stern are opposite.

❑ Chapter 6: A rudder deflection does not only cause forces on the rudder itself, but in shallow water, rudder action is characterized by an important correlation between hull, propeller and rudder, modelled through the correlation parameters. A four quadrant model for the flow velocity V_R at the rudder, induced by the wake flow and the propeller slipstream, is developed based on the evaluation of generally accepted models. This model is based on an alternative concept where flow straightening at the rudder due to hull-propeller-rudder interaction is realized by a combination of wake factor at the rudder and the coefficient K_m depending on the propeller effect; both coefficients are function of the rudder angle and the inflow angle into the rudder.

During the validation process, reported in chapter 7, the flexibility of the developed mathematical model is highly appreciated. A good correspondence between the predicted and real manoeuvres for the tanker Esso Osaka can only be obtained considering a sensitivity analysis of some isolated force components related to the modules hull, propeller and rudder. This sensitivity analysis can be justified taking into account the limited knowledge about scale effects and the influence of selected test parameters on the mathematical model.

These difficulties accompanying the prediction of ship manoeuvrability have also been recognized by international organizations as the ITTC (International Towing Tank Conference) and the IMO (International Maritime Organization), two organizations involved with safe navigation through the ITTC procedures for prediction or the IMO criteria for evaluation of ship manoeuvring characteristics. The hope is expressed that this detailed research concerning ship manoeuvring in shallow water could serve their objectives.

Nederlandstalige samenvatting

De wereldwijde ontwikkeling naar steeds grotere schepen lijkt een verhaal zonder einde. Hoewel de afmetingen van het sluizencomplex in Panama lang richtinggevend geweest zijn voor de zogenaamde schepen van het Panamax type met een scheepsbreedte van 32.3 m, nemen de scheepsafmetingen van bijvoorbeeld het containerverkeer voortdurend toe. Het maximale aantal vervoerde containereenheden per schip bedraagt momenteel 9000 TEU (Twenty feet Equivalent Units) terwijl de nieuwe sluizen in Panama ontworpen worden voor 11000 tot 12000 TEU containerschepen. Rekening houdend met de beperkte waterdiepte in de Noordzee en de getij-afhankelijke scheepvaart naar de Vlaamse havens, is de manoeuvreerbaarheid van schepen in ondiep water een belangrijk onderzoeksdomein geworden voor waterwegbeheerders en havenautoriteiten. Met de installatie van een scheepsmanoeuvreersimulator in 1989 en een sleeptank in 1992 in het Waterbouwkundig Laboratorium (WL), hebben de Vlaamse autoriteiten duidelijk gekozen voor het experimenteel onderzoek van scheepsmanoeuvres in omgevingsomstandigheden die sterk verschillen van de ontwerpcondities.

Het doel van dit onderzoek is drieledig:
1. De selectie van een wiskundig model voor de voorspelling van scheepsmanoeuvres in ondiep maar open water (i.e. geen beperkingen door oevers) wordt gebaseerd op modelproeven uitgevoerd in de Sleeptank voor Manoeuvres in Ondiep Water (samenwerkingsverband WL – Universiteit Gent).
2. De proevenprogramma's, uitgevoerd op een slank schip (een vierde generatie containerschip) en een vol schip (de tanker Esso Osaka), worden geëvalueerd en een aantal richtlijnen en aanbevelingen worden gegeven.
3. De afgeleide manoeuvreermodellen worden vervolgens vergeleken met proeven op ware grootte: een moeilijke opdracht aangezien de gegevens ontbreken om een objectieve validatie te kunnen uitvoeren.

Midden vorige eeuw werd bij verschillende instituten gestart met het onderzoek naar wiskundige modellen voor de voorspelling van scheepsmanoeuvres. Na een historische analyse van bestaande wiskundige modellen die opgenomen is in hoofdstuk 1, werd besloten een modulair model te gebruiken. Dit modeltype refereert maximaal naar de fysische componenten waaruit een manoeuvrerend schip is samengesteld: namelijk, romp, schroef en roer. In vergelijking met de regressie-modellen (bijv. Taylorreeks-ontwikkelingen) biedt dit model de garantie van een grote aanpasbaarheid: een essentiële vereiste voor het voorspellen van havenmanoeuvres die gekenmerkt worden door lage snelheden en zelfs achteruitvaren, een variatie in de vier kwadranten (d.w.z. alle tekencombinaties van voorwaartse snelheid en schroeftoerental) en beperkte waterdiepte. Hoewel tijdsafhankelijke of 'geheugen'effecten een belangrijke rol blijken te spelen voor het manoeuvreren bij lage snelheden, wordt een quasi-stationaire aanpak vooropgesteld. Bovendien worden alleen de scheepsbewegingen in het horizontale vlak beschouwd: schrikken, verzetten en gieren.

Drie wiskundige modellen die een aantal interessante elementen aanbrengen zoals de fysische achtergrond van het MMG model, de vier-kwadrantenvoorstelling van het Oltmann & Sharma model (of HSVA model) en de tabulaire modellen van het DEN-Mark 1 model, worden in detail

besproken in hoofdstuk 2. Deze worden ook gebruikt als leidraad voor de ontwikkeling van een manoeuvreermodel.

Het gebruik van CFD technieken (Computational Fluid Dynamics) voor de voorspelling van scheepsbewegingen en manoeuvres heeft een grote vooruitgang gemaakt, maar moeilijkheden bij bijvoorbeeld het in rekening brengen van omgevingscondities zoals ondiep water, blijven bestaan. De methode voor de bepaling van het wiskundige model die hier toegepast wordt, EFD of experimental fluid dynamics, maakt gebruik van schaalmodellen; hierbij wordt een onderscheid gemaakt tussen gedwongen modelproeven en vrijvarende proeven. Tijdens een gedwongen modelproef volgt het volledig uitgeruste scheepsmodel een voorgeschreven traject. De krachten die aangrijpen op elke module, worden opgemeten samen met de kinematische (snelheden en versnellingen) en controle (schroeftoerental en roerhoek) veranderlijken. Een beschrijving van stationaire en niet-stationaire gedwongen PMM (Planar Motion Mechanism) proeven, zoals zij uitgevoerd worden in de sleeptank van het WL, wordt gegeven in hoofdstuk 3. Niet-conventionele proeven, zoals alternatieve niet-harmonische PMM verzetproeven en multi-modale proeven, werden geïntroduceerd om de nadelen van conventionele verzetproeven te niet te doen enerzijds of het aantal parameters dat kan variëren tijdens een proef te vergroten anderzijds. Deze proeftypes bieden belangrijke mogelijkheden hoewel de proefparameters nauwkeurig moeten gekozen worden om ongewenste stromingen in de sleeptank te vermijden.

De ontwikkeling van een wiskundig model voor scheepsmanoeuvres in ondiep water is onderverdeeld in drie hoofdstukken, die overeenkomen met krachtwerkingen op de romp, de schroef en het roer.

❑ Hoofdstuk 4: De belangrijkste versnellingsafgeleiden, i.e. de toegevoegde massa ten gevolge van verzetten en het toegevoegde traagheidsmoment ten gevolge van gieren, worden beïnvloed door de gekozen proefparameters voor de harmonische proeven. De snelheidsafhankelijke termen worden voorgesteld als tabellen, functie van de drifthoek, de gierhoek en een hoek die de koppeling tussen verzetten en gieren voorstelt.

❑ Hoofdstuk 5: Het volgstroomgetal en het zoggetal, die gebruikt worden bij de modellering van de stuwkracht en de langskracht ten gevolge van schroefwerking, zijn afhankelijk van de schroefbelasting en de instroomhoek in de schroef. Bovendien neemt het volgstroomgetal af wanneer de waterdiepte toeneemt. In diep water zijn de dwarskracht en het giermoment, opgewekt door schroefwerking, klein en induceren zij een asymmetrie-effect bij het achteruitslaan van de schroef. In ondiep water echter, nemen dwarskracht en giermoment toe bij toenemende instroomhoek wanneer de aanstroming ten gevolge van de scheepsbewegingen en de stroom geïnduceerd door de schroef een zelfde zin hebben. Indien deze beide stromingen tegengesteld zijn aan elkaar, treden onstabiele effecten op en geven de oscillerende stromingen aanleiding tot een oscillerende kracht en moment.

❑ Hoofdstuk 6: Een roeruitslag veroorzaakt niet alleen krachten op het roer zelf, maar vooral in ondiep water treedt een aanzienlijke interactie op tussen romp, schroef en roer, waarvoor correlatiecoëfficiënten worden gebruikt. Het model voor de stroomsnelheid V_R ter plaatse van het roer, houdt rekening met de vier werkingstoestanden van een schip en is gebaseerd op een evaluatie van bestaande modellen. Deze stroomsnelheid wordt enerzijds veroorzaakt door de volgstroom en anderzijds door de slipstream van de schroef. Het begrip 'flow straightening', waarbij de stromingsrichting ter plaatse van het roer beïnvloed wordt door romp-schroef-roer interactie, wordt op een andere manier toegepast: het volgstroomgetal ter plaatse van het roer en de coëfficiënt K_m die bepaald wordt door de schroefwerking, worden voorgesteld als functies van de roerhoek en de instroomhoek in het roer.

Op basis van de validatie die beschreven staat in hoofdstuk 7, kan men de flexibiliteit van het ontwikkelde manoeuvreermodel inderdaad onderschrijven. Een goede overeenkomst tussen voorspelling en ware grootte proeven voor de Esso Osaka kan alleen bekomen worden indien een onderzoek wordt uitgevoerd naar de sensitiviteit van sommige geïsoleerde componenten in het model die betrekking hebben op de modules romp, schroef en roer. Dit

sensitiviteitsonderzoek is gerechtvaardigd indien men rekening houdt met de beperkte kennis over schaaleffecten en de invloed van gekozen proefparameters op het wiskundige model.

Deze moeilijkheden bij het opzetten van een voorspellingsmodel van scheepsmanoeuvres, worden ook erkend door internationale organisaties zoals de ITTC (International Towing Tank Conference) en de IMO (International Maritime Organization), twee instellingen die veilige scheepvaart hoog in het vaandel dragen door de invoering van enerzijds de ITTC procedures voor de voorspelling en anderzijds de IMO criteria voor de evaluatie van scheepsmanoeuvreerkarakteristieken. De hoop wordt daarom uitgesproken dat dit gedetailleerd onderzoek naar scheepsmanoeuvres in ondiep water, tot deze doelstelling kan bijdragen.

Contents

Nomenclature

The nomenclature gives only the frequently used symbols in this thesis. The symbols related to the literature study which are not consequently used in the following chapters, are not repeated in this list.

A_0, A	propeller area	(m²)
A_E	expanded propeller area	(m²)
A_R	rudder area	(m²)
A_{RP}	rudder area effected by the propeller	(m²)
a_H	hull coefficient due to rudder action	(-)
B	ship's beam	(m)
C_B	block coefficient	(-)
C_{DR}	drag coefficient	(-)
C_{LR}	lift coefficient	(-)
C_{FT}	tangential rudder coefficient	(-)
C_{FN}	normal rudder coefficient	(-)
C_Q	torque coefficient	(-)
C_T	thrust coefficient	(-)
C_F	frictional resistance coefficient	(-)
C_R	residuary resistance coefficient	(-)
C_W	wave resistance coefficient	(-)
d	ship's draught	(m)
D_P	propeller diameter	(-)
F_n	Froude number	(-)
F_{RT}	tangential rudder force	(N)
F_{RN}	normal rudder force	(N)
F_X	longitudinal rudder force	(N)
F_Y	lateral rudder force	(N)
G	centre of gravity	(-)
h	water depth	(m)
I_{zz}	moment of inertia about z-axis	(kgm²)
J_{zz}	added moment of inertia due to yaw	(kgm²)
J', J_S	apparent advance coefficient	(-)
J	advance coefficient	(-)
K_Q	torque coefficient	(-)
K_T	thrust coefficient	(-)
$K_{1,2}$	parameter for selecting quadrants	(-)
K_m	coefficient for the contribution of the propeller to the rudder velocity	(-)
k	form factor	(-)
k_{HPR}, k_{HR}	straightening coefficient	(-)
L, L_{PP}	ship's length (between perpendiculars)	(m)

N	yawing moment	(Nm)
N_i	hydrodynamic derivative (i = $\dot{v}$, $\dot{r}$,...)	(-)
N_{PT}	non-dimensional average yaw moment due to propeller action: $N^{(0)}/(L_{PP}T)$	(-)
N_{PTA}	non-dimensional amplitude of oscillations of yaw moment due to propeller action	(-)
m	ship's mass	(kg)
m_y	added mass due to sway	(kg)
n	propeller rpm	(s^{-1})
n_0	maximum propeller rpm	(s^{-1})
$\dot{n}$	propeller acceleration	(s^{-2})
P	propeller pitch	(m)
Q_P	propeller torque	(Nm)
Q_E	engine torque	(Nm)
r	yaw rate	(rad/s)
$\dot{r}$	yaw acceleration	(rad/s²)
s	slip ratio	(-)
T, T_P	propeller thrust	(N)
t	time	(s)
t_P	thrust deduction factor	(-)
t_R	deduction factor for X_R	(-)
u	longitudinal velocity	(m/s)
$u_{A\infty}$	u due to the propeller slipstream at infinity	(m/s)
u_P	u near propeller	(m/s)
U_P	total ship velocity near propeller	(m/s)
u_R	u near rudder	(m/s)
u_{R0}	u near rudder induced by the wake	(m/s)
u_{RP}	u near rudder induced by the propeller	(m/s)
$\dot{u}$	longitudinal acceleration	(m/s²)
V	ship velocity	(m/s)
v	lateral velocity	(m/s)
v_R	v near rudder	(m/s)
$\dot{v}$	lateral acceleration	(m/s²)
w_i	wake factor (i = P, Q, RX, RY)	(-)
X	longitudinal force	(N)
X_i	hydrodynamic derivative (i = $\dot{u}$,...)	(-)
x	longitudinal coordinate	(m)
x_G	longitudinal position center of gravity	(m)
x_H	application point of $a_H F_Y$	(m)
x_R	longitudinal position rudder axis	(m)
Y	sway force	(N)
Y_i	hydrodynamic derivative (i = $\dot{v}$, $\dot{r}$,...)	(-)
Y_{PT}	non-dimensional average lateral force due to propeller action: $Y^{(0)}/T$	(-)
Y_{PTA}	non-dimensional amplitude of oscillations of lateral force due to propeller	(-)

action

y, y_{0A}	lateral coordinate, sway amplitude	(m)
Z	number of propeller blades	(-)
α_R, α	angle of attack of flow	(deg)
β	drift angle	(deg)
β_P	inflow angle at the propeller	(deg)
β_R^*	apparent inflow angle at the rudder	(deg)
β_R	inflow angle at the rudder	(deg)
γ	yaw angle	(deg)
ζ	ratio of wake factor ($1-w_{R0}$) to wake factor ($1-w_{P0}$)	(deg)
δ_R, δ	rudder angle	(deg)
δ_0	rudder asymmetry correction	(deg)
ε	hydrodynamic angle or advance angle	(deg)
ε^*	apparent hydrodynamic angle or apparent advance angle	(deg)
ρ	density	(kg/m³)
ϕ	phase angle of oscillations	(deg)
χ	correlation angle	(deg)
ψ_A	yaw amplitude	(deg)
ω	frequency of oscillations	(rad/s)

CFD	Computational Fluid Dynamics
CPMC	Computerized Planar Motion Carriage
EFD	Experimental Fluid Dynamics
FHR	Flanders Hydraulics Research
IMO	International Maritime Organization
ITTC	International Towing Tank Conference
PMM	Planar Motion Mechanism
WL	Waterbouwkundig Laboratorium

1 Prediction of ship manoeuvrability: introduction

The environmental conditions and their consequences for sea-going vessels to the Flemish ports are described in section 1.1 and the need for maritime research on local and international scale is motivated. For the prediction of ship manoeuvrability mathematical models will be used and a historical overview of formal and modular models is given in 1.2. Restrictions in both vertical and lateral direction are a common difficulty for ships entering Flemish harbours. In 1.3 some modifications made to the mathematical manoeuvring models are discussed and even low speed manoeuvring is introduced in 1.4 with the occurrence of so called "memory effects". Finally, some choices will be made for the development of a mathematical model in the following chapters.

1.1 Belgian and international needs for maritime research

1.1.1 Maritime activity in Belgium

Belgian maritime activity is concentrated around four major ports which are accessible for sea-going vessels. Two of them, the Port of Zeebrugge and the Port of Oostende, are situated at the coastline while the Port of Ghent (Gent) and the Port of Antwerp (Antwerpen) are connected to the North Sea by the Canal Ghent-Terneuzen on the one hand and the River Scheldt or Western Scheldt on the other (Figure 1.1).

While entering one of these ports, specific difficulties must be overcome:

❑ The port of Antwerp, one of the most important European ports in the Hamburg-Le Havre range, is accessible through the Western Scheldt, a tidal estuary requiring significant dredging efforts to deepen and maintain the navigation channel. In 1998, a second deepening program 38'-43'-48' was completed which guarantees a tide independent access for ships with draughts up to 11.60 m (38 ft). During the next years a new deepening program will be executed to increase this value to 13.10 m (43 ft). Taking into account that the design draught of very large tankers and bulkcarriers is much larger and that even the design draught of the last generation of containerships is 14.5 m, the tidal range has to be used to guarantee the required water depth.

❑ The port of Ghent is linked to the North Sea via the Western Scheldt, the artificially dug Seacanal Ghent-Terneuzen and the lock complex of Terneuzen. The port can accommodate vessels up to 80000 tons deadweight. The maximum admitted vessel's dimensions in the Westsluis lock are a length over all of 265 m, a breadth of 34 m and a draught of 12.3 m. The water depth in the canal is 13.5 m so that an under keel clearance of almost 10% of the draught must be available. Nowadays, a pilot project is running for an increase of the draught up to 12.5 m, so that only 1 m keel clearance is provided.

❑ The port of Zeebrugge has several terminals which can handle nearly all types of cargo and corresponding traffic lines (LNG, containers, cars, roro, passengers). Container traffic is of increasing importance; since recently new shipping lines call at Zeebrugge with vessels up to 8500 TEU. Since its major extension in the 1970s, the outer harbour is nevertheless subject to sedimentation so that permanent maintenance dredging is necessary to keep the port accessible for deep-drafted vessels. If the bottom is covered with soft mud layers, the boundary between water and bottom is hard to define and the ship's behaviour above this "nautical bottom" will change remarkably.

❑ The port of Oostende is a typical port accessible for ro-ro traffic which dimensions are restricted compared to the ship's dimensions for the other Belgian harbours. Nevertheless, the aim of the port authority has always been to receive the largest ships operating for the ro-ro traffic lines.

Maritime activity plays an important part in Flanders, both on an economical and governmental scene. During the last two decades scientific research projects concerning the maritime accessibility of Flemish harbours are especially executed by two Flemish institutes, Flanders

Hydraulics Research and Ghent University – Maritime Technology division, who started a co-operation in 1986. For the port of Antwerp and the port of Ghent, of which the access channels are partially situated on the Dutch territory, a co-operation with the Dutch government and research institutes is necessary, so that maritime activities are extended to an international scale.

1.1.2 Belgian and international maritime research facilities

In the 1970s and 1980s the former Ministry of Public Works ordered nautical studies for some maritime related problems, like the entrance manoeuvre of the West lock in Terneuzen, which have all been executed on ship manoeuvring simulators abroad. In 1987, the decision was made to build a ship manoeuvring simulator in Flanders Hydraulics Research (FHR) [1]. Nowadays, the laboratory has two ship manoeuvring simulators (SIM360+ installed in 2004 with a view of 360 deg and SIM225 with a view of 225 deg) which differ extremely from the one installed in 1989. Manoeuvres cannot only be tested in real-time with sea-going and inland navigation vessels but even a tug boat can be simulated during its towing activities. Ship simulators for training can also be found at the Antwerp Maritime Academy.

The prediction of ship's behaviour is based on mathematical models which describe the relationship between force components on the one hand and kinematical and control parameters on the other. Force components can be of different origin: related to the ship motions through the water (hydrodynamic forces) or related to external disturbances (like wind, current, waves). The kinematical parameters are ship velocities and accelerations while ship's behaviour can be controlled by the propeller (rate) and the rudder (angle). A historical overview of different types of mathematical models is given in section 1.2.

After the installation of the ship manoeuvring simulator at FHR, a lack of information grew about ship manoeuvrability in shallow and restricted water, conditions which are for the Belgian waterways more the rule than the exception. Therefore, with the co-operation of Ghent University [2] a towing tank was installed in 1992 which provided a test facility for the study of ship manoeuvring behaviour on model scale. This towing tank is described in detail in chapter 3 and gave from that moment the possibility of determining the coefficients of a mathematical manoeuvring model based on experimental data. Many test programs have run and thousands of test runs have been executed in the mean time. In this research the large amount of test data derived from different test types for two ship models (a containership and a tanker) have been examined and evaluated based on their use. It concerns a detailed and hopefully well documented analysis which is still seldom found in literature as can be confirmed by the International Towing Tank Conference considering the difficulties they have to overcome while executing comparative studies. A towing tank is also available in Belgium at the International University of Liège.

Since the installation of the ship manoeuvring simulator and the towing tank at Flanders Hydraulics Research many studies have been executed to examine the feasibility of new buildings or new shipping traffic and to ensure safe navigation. Two projects, fulfilled by the author in 2003, describe each of them some important aspects concerning ship manoeuvrability prediction for Belgian maritime situations.

❑ *Mod689: Accessibility of S-class containerships to the port of Antwerp* (Figure 1.2)
In 2003 S-class containerships of Maersk Sealand with an overall length of 352 m and a beam of 42.8 m (17 containers wide) had to travel along the Western Scheldt during their trip to the port of Antwerp. According to a regulation which was based on some arbitrary chosen limitations from the past, the maximum overall length of ships travelling on the Scheldt was not expected to be greater than 340 m. In addition, the draught of containerships which travel from the port to the North Sea in one tide may until now not exceed 14.0 m at departure and must be restricted for ships longer than 300 m according to the assumption of 1 dm less draught for each 10 m more length compared to the 300 m limit. For the S-class containerships this means a maximum draught of 13.5 m at departure while the scantling

draught is 14.5 m.

To map out this problem and offer a research platform for Dutch and Belgian authorities it was decided to execute some real-time manoeuvres using the ship manoeuvring simulator of the laboratory. Due to a lack of experimental data according to the manoeuvring behaviour of these large containerships, especially in shallow water, a mathematical manoeuvring model was developed based on a scaling process of a smaller containership. The scope was not to have a ship which really behaves as an S-class containership but to be sure that it is not better than this ship type. Therefore, the mathematical model was validated by two captains of Maersk Sealand on shore while the ship was steered by Belgian and Dutch pilots. For both of them it concerns a subjective validation (see chapter 7) in the course of which the pilots steer an (until now) unknown ship in a known area while the captains validate a known ship in an unknown area.

❏ *Mod670: Port of Antwerp: Tidal dock Saeftinge*
In 2005 the tidal dock Deurganckdok along the Western Scheldt is brought into use. In 2003 a research started to examine the position and lay-out of another tidal dock which has to increase the area for transhipment at the left bank. Several arrival and departure manoeuvres have been tested with an 8000 TEU containership at some important combinations of wind and current influences. During this project it was clear that a harbour manoeuvre is composed of a diversity of working conditions concerning the hull-propeller-rudder combination (Figure 1.3). All combinations of propeller working direction and ship movement have to be considered. As a ship is in the first place designed to travel as easy and as quick as possible from point A to B these typical harbour manoeuvres have to be modelled in a proper way. Several questions arise about for example the rudder effectiveness during an astern motion with reversed propeller or propeller ahead and the hull effect during a swinging manoeuvre with small ship velocity.

The need for a general standardized prediction model describing ship manoeuvres in a wide area of application is a topic which also occupies two international organizations involved with maritime safety and the prediction of hydrodynamic performance of all kind of vessels:

❏ the International Maritime Organization (IMO) [3]:
"*The International Maritime Organization is a specialized agency of the United Nations which is responsible for measures to improve the safety and security of international shipping and to prevent marine pollution from ships. It is also involved in legal matters, including liability and compensation issues and the facilitation of international maritime traffic. It was established by means of a Convention adopted under the auspices of the United Nations in Geneva on 17 March 1948 and met for the first time in January 1959. It currently has 166 Member States. ... The main technical work is carried out by the Maritime Safety, Marine Environment Protection, Legal, Technical Co-operation and Facilitation Committees and a number of sub-committees.*"

The IMO, and more particularly the Maritime Safety Committee, plays an important part in the evaluation of ship manoeuvrability by the introduction of the IMO "Standards for ship manoeuvrability" which standards will be discussed in chapter 7.

❏ the International Towing Tank Conference (ITTC) [4]:

"*The International Towing Tank Conference is a voluntary association of worldwide organizations that have responsibility for the prediction of hydrodynamic performance of ships and marine installations based on the results of physical and numerical modelling. ...*

The primary task of the International Towing Tank Conference is to stimulate progress in solving the technical problems that are of importance to towing tank Directors and Superintendents who are regularly responsible for giving advice and information regarding

full-scale performance to designers, builders and operators of ships and marine installations based on the results of physical and numerical modelling. The Conference also aims at stimulating research in all fields in which a better knowledge of the hydrodynamics of ships and marine installations is needed to improve methods of model experiments, numerical modelling and full-scale measurements; at recommending procedures for general use in carrying out physical model experiments and numerical modelling of ships and marine installations; in validating the accuracy of such full-scale predictions and measurements for quality assurance; at formulating collective policy on matters of common interest; and at providing an effective organisation for the interchange of information on such matters."

The triennial reports of the ITTC's subcommittees and specialist committees give a clear overview of the research developed in some sub-domains which are listed in [4] and have often been used as reference work for this research.

1.2 Mathematical modelling of ship manoeuvres: a historical overview

1.2.1 Mathematical modelling: introduction

The prediction of ship manoeuvrability based on mathematical models started in the middle of last century at several institutes all over the world. At that time decades of research work had been carried out to understand the resistance and propulsive characteristics of existing and new building ships. Proceeding from this subject a need was growing not only to examine the straight ahead motion of a ship but especially to have tools to predict the manoeuvring performance.

A historical overview of mathematical models will be given starting with a more general paragraph 1.2.2 describing the theory of mathematical models for horizontal ship motions. Formal mathematical models which were based on Taylor-series developments of the hydrodynamic forces are summarized in paragraph 1.2.3. Disadvantages related to formal mathematical models (1.2.4) led to the introduction of modular models which are presented in 1.2.5. A classification into formal and modular models could be passed by the introduction of properties of mathematical models so that new features like CFD (computational fluid dynamics) can be brought together with existing methods (1.2.6). In 1.2.7 a unified mathematical model is presented combining manoeuvring and seakeeping making use of impulse response functions.

1.2.2 General assumptions, conventions and symbols

Mathematical models describing ship manoeuvrability and seakeeping are based on six equations of motion according to the six degrees of freedom of a ship (three translations and three rotations, Figure 1.4) and an equation of equilibrium for ship propulsion. When the emphasis lays on ship manoeuvrability the equations linked to the horizontal motions (surge, sway and yaw) have to be considered, although in case of containerships the roll motion will also be important but neglected in this research.

In manoeuvring theory, a set of axes Gxyz fixed to the rigid body is considered (axes Gxyz are not shown on Figure 1.5). The origin is fixed at the centre of mass G and this frame moves relative to the space fixed system $OX_0Y_0Z_0$ and is such that Gxz is the plane of port and starboard symmetry. The Gz and OZ_0 axes are chosen to point downwards. In the theory of body axes, a vessel is brought to its actual orientation by imposing the sequence of Euler angle orientations.

The equations of motion in a ship fixed system with the origin at the centre of gravity G are:

$$m(\dot{u}_G - v_G r_G) = X_G(\dot{u}_G, \dot{v}_G, \dot{r}_G, u_G, v_G, r_G, n, \delta_R)$$

$$m(\dot{v}_G + u_G r_G) = Y_G(\dot{u}_G, \dot{v}_G, \dot{r}_G, u_G, v_G, r_G, n, \delta_R) \qquad (1.1)$$

$$I_{zG} \dot{r}_G = N_G(\dot{u}_G, \dot{v}_G, \dot{r}_G, u_G, v_G, r_G, n, \delta_R)$$

whereas the parameters denote:

4

$\dot{u}_G, \dot{v}_G, \dot{r}_G$ the accelerations related to the centre of gravity G

u_G, v_G, r_G the velocities related to the centre of gravity G

X_G, Y_G, N_G components of hydrodynamic forces and moment related to the centre of gravity G

I_{zG} the moment of inertia around the Gz-axis

n   the propeller rate of turn

δ_R the rudder angle

For an axis system with the origin at the midship point O (different from the origin of the space fixed system $OX_0Y_0Z_0$, see Figure 1.5) equations (1.1) become:

$$
\begin{aligned}
m\left(\dot{u} - vr - x_G r^2\right) &= X = X_G \\
m\left(\dot{v} + ur + x_G \dot{r}\right) &= Y = Y_G \\
I_{zz}\dot{r} + mx_G\left(\dot{v} + ur\right) &= N = N_G + Y_G x_G
\end{aligned}
$$

(1.2)

with a relationship between ship velocities

$$
\begin{aligned}
u &= u_G \\
v &= v_G - x_G r_G \\
r &= r_G
\end{aligned}
$$

(1.3)

and x_G the longitudinal distance between the centre of gravity G and the midship point O. I_{zz} is the moment of inertia around the Oz-axis and the relationship between I_{zG} and I_{zz} is:

$$
I_{zG} = I_{zz} - mx_G^2
$$

(1.4)

A reference system with the origin at the midship point is preferred as the position of the centre of gravity changes with the loading condition.

The equations of motion can be summarized as:

$$
\begin{aligned}
X &= m\left(\dot{u} - vr - x_G r^2\right) \\
Y &= m\left(\dot{v} + ur + x_G \dot{r}\right) \\
N &= I_{zz}\dot{r} + mx_G\left(\dot{v} + ur\right)
\end{aligned}
$$

(1.5)

$$
2\pi I_{pp}\dot{n} = Q_E - Q_P
$$

with Q_E the engine torque and Q_P the propeller torque.

1.2.3 Formal mathematical models

The equations of motion in the horizontal plane, introduced by Abkowitz [5] in the 1960s, are based on a third order Taylor-series development of the hydrodynamic forces. The theory of Abkowitz in mathematical modelling is based on the assumption that forces at any instant are determined by the prevailing instantaneous motions of the ship. Just small perturbations are performed while the forces exerted on the ship do not remember the previous fluid flow surrounding the ship model. These forces are functions of the ship form, the characteristics of the surrounding fluid, the kinematical and the control parameter δ (= δ_R).

$$
\begin{aligned}
\left(m - X_{\dot{u}}\right)\dot{u} &= f_1\left(u, v, r, \delta\right) \\
\left(m - Y_{\dot{v}}\right)\dot{v} + \left(mx_G - Y_{\dot{r}}\right)\dot{r} &= f_2\left(u, v, r, \delta\right) \\
\left(mx_G - N_{\dot{v}}\right)\dot{v} + \left(I_{zz} - N_{\dot{r}}\right)\dot{r} &= f_3\left(u, v, r, \delta\right)
\end{aligned}
$$

(1.6)

$$f_1(u,v,r,\delta) = X^0 + X_u\Delta u + \frac{1}{2}X_{uu}(\Delta u)^2 + \frac{1}{6}X_{uuu}(\Delta u)^3$$

$$+ \frac{1}{2}X_{vv}v^2 + \left(\frac{1}{2}X_{rr} + mx_G\right)r^2 + \frac{1}{2}X_{\delta\delta}\delta^2$$

$$+ \frac{1}{2}X_{vvu}v^2\Delta u + \frac{1}{2}X_{rru}r^2\Delta u + \frac{1}{2}X_{\delta\delta u}\delta^2\Delta u$$

$$+ (X_{vr} + m)vr + X_{v\delta}v\delta + X_{r\delta}r\delta + X_{vru}vr\Delta u$$

$$+ X_{v\delta u}v\delta\Delta u + X_{r\delta u}r\delta\Delta u$$

(1.7)

$$f_2(u,v,r,\delta) = Y^0 + Y_u^0\Delta u + Y_{uu}^0(\Delta u)^2 + Y_v v + \frac{1}{6}Y_{vvv}v^3$$

$$+ \frac{1}{2}Y_{vrr}vr^2 + \frac{1}{2}Y_{v\delta\delta}v\delta^2 + Y_{vu}v\Delta u + \frac{1}{2}Y_{vuu}v(\Delta u)^2$$

$$+ (Y_r - mu_1)r + \frac{1}{6}Y_{rrr}r^3$$

$$+ \frac{1}{2}Y_{rvv}rv^2 + \frac{1}{2}Y_{r\delta\delta}r\delta^2 + Y_{ru}r\Delta u + \frac{1}{2}Y_{ruu}r(\Delta u)^2$$

$$+ Y_\delta\delta + \frac{1}{6}Y_{\delta\delta\delta}\delta^3 + \frac{1}{2}Y_{\delta vv}\delta v^2 + \frac{1}{2}Y_{\delta rr}\delta r^2$$

$$+ Y_{\delta u}\delta\Delta u + \frac{1}{2}Y_{\delta uu}\delta(\Delta u)^2 + Y_{\delta rv}\delta rv$$

(1.8)

$$f_3(u,v,r,\delta) = N^0 + N_u^0\Delta u + N_{uu}^0(\Delta u)^2 + N_v v + \frac{1}{6}N_{vvv}v^3$$

$$+ \frac{1}{2}N_{vrr}vr^2 + \frac{1}{2}N_{v\delta\delta}v\delta^2 + N_{vu}v\Delta u + \frac{1}{2}N_{vuu}v(\Delta u)^2$$

$$+ (N_r - mx_G u_1)r + \frac{1}{6}N_{rrr}r^3$$

$$+ \frac{1}{2}N_{rvv}rv^2 + \frac{1}{2}N_{r\delta\delta}r\delta^2 + N_{ru}r\Delta u + \frac{1}{2}N_{ruu}r(\Delta u)^2$$

$$+ N_\delta\delta + \frac{1}{6}N_{\delta\delta\delta}\delta^3 + \frac{1}{2}N_{\delta vv}\delta v^2 + \frac{1}{2}N_{\delta rr}\delta r^2$$

$$+ N_{\delta u}\delta\Delta u + \frac{1}{2}N_{\delta uu}\delta(\Delta u)^2 + N_{\delta rv}\delta rv$$

(1.9)

The propeller rate of turn is not explicitly included in these functions but is incorporated in the terms depending on the variation of the longitudinal velocity component Δu.

Due to the port-starboard symmetry of a ship's hull all odd powers in v, r and δ are missing in the equation of the longitudinal hydrodynamic force X and all even powers of these variables are missing in the equations of the lateral force Y and the yawing moment N.

The hydrodynamic coefficients must be read as the following derivatives:

$$N_v = \frac{\partial N}{\partial v}, \quad X_{\delta\delta} = \frac{\partial^2 X}{\partial\delta^2}, \quad Y_{\delta rv} = \frac{\partial^3 Y}{\partial\delta\partial r\partial v} \dots$$

(1.10)

This mathematical model is one of the first so-called *formal* or regression models "*which treats ship/fluid interaction phenomenon as a black box and are based on series expansion around equilibrium state*" [6]. These mathematical models had been produced "*to be used in simulators*"

with a predominantly didactic role in mind" [7]. Later on *"it became apparent that the mathematical simulation model could be used for tasks which were much more varied than those required in a purely training or teaching environment"*. The requirements of mathematical simulation models alter if they have to be useful for e.g. assessment studies concerning the design of waterways and fairways or the prediction of the manoeuvring performance of ships at the design stage.

In 1971 Norrbin [8] presented a mathematical manoeuvring model at SSPA (Statens Skeppsprovningsanstalt, Göteborg, Sweden) in which he tries to show in a modest way the physical background of the different hydrodynamic forces. This model can be considered as a link between the pure regression models and the now popular so-called modular mathematical models.

Functions are introduced for the propeller thrust T, the propeller torque Q and the inflow velocity to the rudder c, whereas the wake fraction and the thrust deduction are considered to be independent of the propeller loading. μ is the position of the telegraph ("engine output ratio", "engine setting"). For deep water the equations are:

$$T = T(u,n)$$
$$Q = Q(u,n) \qquad\qquad (1.11)$$
$$c = c(u,n)$$

$$\begin{aligned}
(m - X_{\dot{u}})\dot{u} &= X_{uu}u^2 + (m + X_{vr})vr + X_{vv}v^2 \\
&\quad + X_{c|c|\delta\delta}c|c|\delta^2 + X_{c|c|\beta\delta}c|c|\beta\delta \\
&\quad + (1-t)T \\
(m - Y_{\dot{v}})\dot{v} &= (Y_{ur} - m)ur + Y_{uv}uv + Y_{v|v|}v|v| \\
&\quad + Y_{c|c|\delta\delta}c|c|\delta^2 + Y_{c|c|\beta|\beta||\delta|}c|c|\beta|\beta||\delta| \\
&\quad + Y_T T \\
(I_{zz} - N_{\dot{r}})\dot{r} &= (N_{ur} - mx_G)ur + N_{uv}uv + N_{v|r|}v|r| \\
&\quad + N_{c|c|\delta}c|c|\delta + N_{c|c|\beta|\beta||\delta|}c|c|\beta|\beta||\delta| \\
&\quad + N_T T
\end{aligned}$$

$$\begin{aligned}
T &= T_{uu}u^2 + T_{un}un + T_{n|n|}n|n| \\
(I_P - Q_{\dot{n}})\dot{n} &= Q_F + Q_{uu}u^2 + Q_{un}un + Q_{n|n|}n|n| \\
&\quad + Q_n n + Q_\mu \mu
\end{aligned}$$

$$\begin{aligned}
c &= c_{un}un + c_{nn}n^2, \, n > 0 \qquad\qquad (1.12) \\
c &= 0 \qquad\qquad , n < 0
\end{aligned}$$

These expressions are characterized by terms of the form a|b| which lead to a better modelling of the physical phenomena. Other institutes developed comparable mathematical models adapted to their specific needs.

1.2.4 Disadvantages of formal mathematical models

Disadvantages of formal mathematical models were mentioned by several authors in an attempt to summarize the requirements of a new and flexible mathematical model with applicability in a wide range of environmental and operational conditions.

☐ The contributions of the hull, propeller and rudder to the hydrodynamic forces and moment are determined only by *global regression coefficients* and do not directly allow for separate hull, propeller and rudder characteristics. Changes in the individual elements during for example the design process of a ship can not be incorporated easily. This so-called *combined approach* [9] leads to a model which only performs satisfactorily when taken as a whole.

☐ The regression model is often directly related to the data coming from experiments with the fully appended model. The fitting of the data to predefined functions can lead to a poor physical background of the mathematical models.

☐ Due to the large non-uniformity of the regression models of different institutes this model type makes a meaningful model or data exchange impossible.

☐ The description of propeller and rudder action at various combinations of ship speed and propeller loading can lead to functions with enormous higher order terms which do not contribute to an easy understanding of the underlying physics.

1.2.5 Modular mathematical models

In the 1980s the "*concept of modularity based on a separate representation of elements of the manoeuvring model*" [6] has been fully recognized among the world. The ship's hull, propeller and rudder are considered as interacting modules and the mathematical models are based on an examination of the established hydrodynamic principles.

The principal structural form of a modular manoeuvring model neglecting the external forces is based on Newton's equations:

$$m(\dot{u} - vr - x_G r^2) = X_H + X_P + X_R$$
$$m(\dot{v} + ur + x_G \dot{r}) = Y_H + Y_P + Y_R \tag{1.13}$$
$$I_{zz}\dot{r} + mx_G(\dot{v} + ur) = N_H + N_P + N_R$$

where the terms with subscripts H, P and R represent the hull forces, the propeller forces and the rudder forces. These force components do not only incorporate the characteristic influence of the individual modules but even express the interacting effects occurring at the fully equipped ship (Figure 1.6).

Long before the publication of references belonging to the differential approach of mathematical modelling in the 1980s, the basic idea was launched by A. Basin [10] and K. Fediaevsky [11] in the 1960s. Nevertheless, the functional presentations of the hydrodynamic characteristics and the equations of motions of these authors differ from the widespread accepted modular manoeuvring models belonging to the following authors and institutes:

☐ Group-MMG, Mathematical Model Workgroup organized in the Manoeuvrability Subcommittee of the Japan Towing Tank Committee (JTTC), [12] "*... a new mathematical model is proposed. The model consists of the individual open-water characteristics of hull, propeller, and rudder, and the interaction effect between them. The insistence of the model is put on that it has physical meaning as much as possible and is constructed as simple as possible.*"

☐ Oltmann & Sharma, Germany, HSVA, Hamburgische Schiffbau-Versuchsanstalt, Institut für Schiffbau der Universität Hamburg, [13] "*The principal purpose ... is to present an alternative mathematical model suitable for the digital simulation of combined engine and rudder maneuvers for a wide range of surface ships. The core of this model is a rather new scheme for the mathematical approximation of the complex hydrodynamic forces generated in response to the motion of a maneuvering hull and to the operation of its primary control organs (rudder and screw propeller). ... The main advantages claimed for the new model are*

applicability to forward and backward motion, explicit accounting of the three-way hull-propeller-rudder interaction, ... and the modelling of engine characteristics up to and even beyond speed reversal."

☐ Dand, United Kingdom, British Maritime Technology Ltd. [7], "... *The demand was therefore for a mathematical model which was more flexible than the pure regression model, could be tailored to a specific ship rather than a more general ship type and which could cater for a wider range of environmental conditions. Thus was the Modular Simulation Model born. ... In such a model any hull can be combined with any rudder, propeller, or engine and the effect on manoeuvring behaviour determined. The modular model therefore has the potential to become a flexible design tool, allowing the effect of design changes to be assessed rapidly and effectively.*"

☐ Asinovsky, USA [9], "*The differential approach is based on the separate determination and analysis of the hydrodynamic characteristics for the hull, rudder(s) and propeller(s), and on the hydrodynamic interactions in the hull/propeller/rudder system. ... It is concluded that the consideration of the separate hydrodynamic characteristics of the bare hull and rudder(s) and the characteristics of interaction in the hull/propulsion/rudder system (differential approach) provides the most nearly universal and flexible technique for maneuverability studies.*"

☐ Ankudinov, USA [6], "... *The basic concept is to keep the mathematical model as general and as modular as possible so that each module can be modified or replaced by a module of a higher or lower accuracy as required by a specific user or task.*"

The research work published by these authors during the last and this century is of great value for the prediction of ship manoeuvrability. However, none of the existing methods is sufficiently broad and accurate at present to be raised up to a *general, standardized manoeuvring model* [14]. Some of these models will be described in detail in chapter 2 as they form the basis of the on-going research on mathematical modelling and captive model testing in shallow water.

For an extensive description of the formal and modular models a reference is made to the introductory chapters of [15].

1.2.6 Properties of hydrodynamic models

In 1996 Pawlowski presented "*an analysis of properties required of hydrodynamic models for ship manoeuvring simulation*" [16]. Due to the significant improvement of the CFD (Computational Fluid Dynamics) methodology for ship manoeuvring during the last few decades one of the most important disadvantages of a modular mathematical model, the inadequate knowledge of complicated flow phenomena, is expected to be gradually overcome in the future.

The formal and modular models described above are classified as formal and rational hydrodynamic models according to Pawlowski (Table 1.1).

Table 1.1 Classification of hydrodynamic mathematical models according to [16]

Hydrodynamic models			
Rational models		Formal models	
Superposition models	CFD models		
Semi-empirical formulae	Boundary value problems	Taylor's series	Other polynomials

"*The rational models are distinguished from the formal models by displaying a mathematical structure which is compatible with the physical structure of modelled flow phenomena. This is achieved by superposing hydrodynamic forces and moments determined from semi-empirical formulae, in superposition models* (compare with modular manoeuvring models), *or by determining the forces and moments from solutions to the corresponding boundary value*

9

problems, in CFD models".

The understanding of the physical processes occurring around a manoeuvring ship is still insufficient for many environmental and operational conditions during the life-time of a ship, approaching and entering harbours, like:
- □ manoeuvring with a small under keel clearance
- □ manoeuvring in harbours and at low speeds
- □ manoeuvring strongly affected by hull-propeller-rudder interactions
- □ passing near banks, approaching banks
- □ passing and approaching other ships

To meet these complicated situations during mathematical modelling "*a framework must be developed for a consistent, complementary and cross-reference use of different types of hydrodynamic models*" so that the feasibilities of every mathematical model and every modelling methodology can be brought together. The development of a general, standardized manoeuvring model is in the light of this philosophy not desirable and rather utopian but a classification of hydrodynamic models could nevertheless be of great help to everyone involved with mathematical modelling and marine simulation.

In addition Pawlowski list the requirements which have to be satisfied by hydrodynamic models and which help to categorize all existing models. These requirements are:

- □ **functionality**: The functionality of a hydrodynamic model is determined by the range of modelling functions covered by the model. Manoeuvring simulation is a "*task oriented activity*" and the functions describing the manoeuvring behaviour of a ship may differ according to the situations they have to predict.
- □ **validity**: A model and more in detail a function is characterized by its validity. Different ranges and levels of validity may be achieved according to, for instance, their method of validation and the availability of input data to determine the function parameters.
- □ **expandability**: The expandability of a hydrodynamic model determines the possibility of adding new functionalities to a given model.
- □ **adjustability**: The model adjustability characterizes the possibility of increasing the range or improving the level of validity of existing functionalities of the model.

Keeping these properties definitions in mind, each hydrodynamic model can be judged to what extent it can be adapted to solve a well-defined ship manoeuvrability prediction problem.

In [16] a new dimension is added to the modelling problem as "*the basic boundary value problem for a flow around a body submerged in an ambient flow is reduced to an approximate modal form, which expresses the flow velocity field and pressure field, and the resulting hydrodynamic forces and moments exerted on the body, in terms of the velocities of the body and a finite set of time dependent amplitudes characterizing the ambient flow.*

Although a quasi-steady approach is adopted for almost all existing manoeuvring mathematical models the basic philosophy of bringing together flow and force models in [16] makes it possible to tackle the problem of memory effects in the flow during complex manoeuvres in harbours.

1.2.7 Unified mathematical model describing manoeuvring and seakeeping

In agreement with the combined flow-force model in the previous section a unified mathematical model described in [17] brings together the theories of manoeuvring and seakeeping whilst retaining the fundamental characteristics associated with each theory. Although manoeuvring in this research is restricted to horizontal motions, manoeuvring of a ship in a seaway requires a solution to the 6 degrees of freedom problem with the symmetric motions of surge, heave and pitch and the anti-symmetric motions of sway, roll and yaw.

A reference axis system will be adopted other than the traditional body fixed axis system for

manoeuvring theory and the equilibrium axis system for seakeeping. In [17] the unified theory is simplified to a linear theory although this choice could be open to criticism. Nevertheless, based on first order derivatives manoeuvring and seakeeping theory will be linked thanks to a combination of components associated with slow motion derivatives or zero frequency measured data on the one hand (manoeuvring) and frequency dependent hydrodynamic coefficients on the other (seakeeping).

Frequency dependent oscillatory derivatives $Y_v(\omega_e)$ and $Y_{\dot{v}}(\omega_e)$ with ω_e the frequency of encounter determined from a manoeuvring based PMM experiment are compared to frequency dependent hydrodynamic coefficients derived from a corresponding seakeeping experiment. These derivatives and coefficients are specific to sinusoidal motions. A ship motion can nevertheless not be considered simply sinusoidal so that the mathematical model must account for transient and even random motions. Volterra convolution integral series are introduced to express any fluid action:

$$\int_0^t h(\tau)q(t-\tau)d\tau \qquad (1.14)$$

where the impulse response function

$$\begin{aligned} h(\tau) &= 0 & \tau < 0 \\ h(\tau)q(t-\tau) &= 0 & \tau > t \end{aligned} \qquad (1.15)$$

is the fundamental building block describing the fluid-structure interaction mechanisms and contains the inherent dynamic characteristics of the interacting system. This method of combining manoeuvring and seakeeping will not be discussed further on as it is out of the scope of this research, but this short description should make clear how the 6 degrees of freedom problem could be solved theoretically.

1.3 From deep to shallow water manoeuvring

1.3.1 Description of the shallow water problem

Scientific research is often characterised by a division of a research problem in several elemental whether or not simplified questions. Manoeuvring models were firstly developed to cope with the prediction problem in deep water. Due to the growth in ship size and the expansion of harbours to at first sight unsuitable areas the shallow water problem had to be solved.

In [18] a rather arbitrary distinction is made between:
- deep water   h/d>3.0
- medium deep water   1.5<h/d<3.0
- shallow water   1.2<h/d<1.5
- very shallow water   h/d<1.2

The effect of depth restrictions based on the ratio h/d can be noticed in medium deep water, is very significant in shallow water and dominates the ship motion in very shallow water.

In general, hydrodynamic forces increase with decreasing water depth as the flow around the hull is hindered by the restricted clearance between the keel and the bottom. A three-dimensional flow in deep water is turned into a flow which is more concentrated at the ends (bow and stern) of the ship and influences the hydrodynamic forces remarkably. In Figure 1.7 the increase of measured lateral force during oblique towing with decreasing under keel clearance (UKC) is clearly seen for both a slender and a full body. These measurements show that the shallow water effect can not be neglected.

One of the aspects which must be considered while moving in areas with restricted under keel clearances is the change of pressure field around the hull, causing trim and sinkage of the body. The size of sinkage increases considerably in shallow water due to the proximity of the sea bed. This phenomenon, known as *squat*, will not be examined in detail in this research but could be responsible for some aspects that will be discussed in the following chapters.

The shallow water effect on ship turning performance was examined by Yasukawa and Kobayashi in [19] based on free-running model tests for four different ship models. A classification was proposed dividing the shallow water effect into three different types:

❑ *Type-N (normal)*: the turning circle becomes larger monotonously with the decrease of water depth. This shallow water effect is found for slender ships like containerships with block coefficients C_B lower than 0.75.
❑ *Type-U (unstable)*: the turning circle becomes larger with the decrease of water depth, however course keeping instability appears in medium deep water (about h/d=1.5). This could be found for the tanker Esso Osaka and is generally adopted for full ship forms.
❑ *Type-S (small)*: the turning circle becomes smaller with the decrease of water depth. Thanks to the increase of the rudder normal force at decreasing water depth a wide beam and small draft ship (L_{PP}/B is lower than B/d) turns easier in shallow than in deep water.

This remarkable conclusion must be accounted for while examining the manoeuvring performance of different ship types. For conventional ships (type-N and type-U in [19]) the shallow water effect is especially expected to affect the hull forces while rudder forces are considered to remain invariable. Several authors have incorporated the shallow water effect on hydrodynamic forces acting on ship's hull by comparing values in deep and shallow water (see 1.3.2).

1.3.2 Adaptations to the mathematical models

The mathematical model introduced by Norrbin incorporated already the influence of water depth by adding equations depending on the parameter z:

$$z = \frac{T}{h-T} \tag{1.16}$$

with h the water depth and T (=d) the draught.

The right hand side of Norrbin's equations summarised in paragraph 1.2.3 are filled up with the following terms, dedicating "confined" waters [8]:

$$X_{conf} = X_{\dot{u}z}\dot{u}z + X_{uuz}u^2z + X_{vrz}vrz + X_{vvzz}v^2z^2$$

$$Y_{conf} = Y_{\dot{v}z}\dot{v}z + Y_{urz}urz + Y_{uvz}uvz + Y_{v|v|z}v|v|z + Y_{c|c|\beta|\beta\|\delta|z}c|c|\beta|\beta\|\delta|z \tag{1.17}$$

$$N_{conf} = N_{\dot{r}z}\dot{r}z + N_{urz}urz + N_{uvz}uvz + N_{r|v|z}r|v|z + N_{c|c|\beta|\beta\|\delta|z}c|c|\beta|\beta\|\delta|z$$

For the lateral force Y_{conf} and the yawing moment N_{conf} not only hull forces are adapted but even the contribution of the rudder is augmented with a term in the parameter z. The restriction of the shallow water effect to hull forces could be questioned.

The empirical formulae for the hydrodynamic derivatives, published by several authors, often incorporate the effect of water depth by introducing ratios of restricted to deep water values. The alteration of hydrodynamic coefficients f with decreasing water depth is for example modelled by Gronarz based on an exponential equation built up of a constant term c_0 indicating the deep water case and a term depending on the water depth or ratio (T/h):

$$f = c_0 + c_n(T/h)^n \tag{1.18}$$

Only hull dependent coefficients had been investigated with exponent values n varying between 1 and 11, while propeller and rudder induced forces are expected to be independent of water depth [20].

1.3.3 Examination of the shallow water effect

Shallow water manoeuvring is very important for Belgian maritime conditions. With minimum UKC's of 12.5% on the Dutch part of the Western Scheldt and 10% on the Flemish part very shallow water is more standard than one should expect. In this research the shallow water problem will consequently more be taken as a starting point than as an annex. Given that not only hull forces will be influenced by the restricted water depth, all exerted force components even at the propeller and the rudder will be investigated for changes due to the reduced water depth.

1.4 Ship manoeuvring performance at low speed

1.4.1 Service speed versus low speed

Mathematical models have initially been developed to have a valuable tool for the prediction of ship's performance at the design stage. To improve the accuracy and the adjustability of the mathematical models to for example new or modified control features the conversion from formal to modular models has been a step forward. Ship owners and shipyards with them are still especially interested in ship's performance at service speed and in deep water (see the IMO standard manoeuvres in chapter 7) as ship manoeuvring characteristics in shallow water and low speed are still uncommon on pilot cards. On the other hand, public authorities, more and more encouraged by the man in the street, are especially involved with questions about safe and fluent navigation within economical and operational limits. Taken the Belgian situation in mind, shallow water and even muddy area conditions have become a constant factor together with manoeuvring at low speeds and at a diversity of speed-propeller loading combinations.

The question arises whether a ship can be judged to manoeuvre satisfactory at its service speed using the IMO criteria while it appears to have poor manoeuvrability in areas like harbours where most of the manoeuvring takes place. Research will have to focus on:

❑   speed limitations and even reversed speed
❑   four quadrants of operation during harbour manoeuvres such as drifting and swinging
❑   due to the low ship velocities the ship motions become time dependent and memory effects
    may occur (see section 1.4.4).

At the International Conference on Marine simulation and Ship Manoeuvrability (MARSIM) in 2003 [21] two papers have been presented dealing with the issue of characterising ship manoeuvring performance at (s)low speed:

❑   In [22] Dand argues low speed manoeuvring through the IMO Guidelines for merchant ships
    and makes some suggestions as to the form the criteria might take.
❑   In [23] by Hwang W-Y et al. an extensive study is described, performed by the Technical and
    Research Program of the Society of Naval Architects and Marine Engineers (SNAME)
    through Panel H-10 (Ship Controllability). The objective of the project was to identify and
    develop slow speed manoeuvres within the philosophy of the IMO standard manoeuvres for
    deep water, which are considered to be *simple, relevant, comprehensive, measurable and
    practicable*.

These papers are of great value on international scale as they fix the attention of institutes and companies involved with ship manoeuvrability on the importance of classifying not only ship's performance in design conditions but also in more complex situations like navigation in waterways and canals near and in harbour areas. Some aspects of these papers will therefore be discussed later on in chapter 7 (validation).

1.4.2 Four quadrants of operation

Harvald's research work concerning *"wake and thrust deduction at extreme propeller loadings"*, published in 1967 at SSPA [24], is considered to be the groundwork for the modelling of propeller thrust at wide ranges of ship speed and propeller revolutions. The four possible combinations of ship velocity and propeller rate have led to the introduction of the four quadrants of operation definition. This definition relates to the combination of forward speed component u and propeller rate n, although a four quadrants definition can also be recognized for kinematical parameters like the drift angle β and the yaw rate angle γ.

The division into quadrants for the propeller loading will be based on a mathematical definition where angle α is defined as:

$$\alpha = \text{Arctan2}(y, x) \tag{1.19}$$

Arctan2(y,x) is a value in [$-\pi; \pi$], defined as:

$$
\begin{aligned}
\text{Arctan2}(y, x) &= \text{Arctan}(y/x) & \text{for } x > 0 \\
&= \text{Arctan}(y/x) + \pi & \text{for } x < 0,\ y > 0 \\
&= \text{Arctan}(y/x) - \pi & \text{for } x < 0,\ y < 0 \\
&= \pm \pi/2 & \text{for } x = 0
\end{aligned} \tag{1.20}
$$

or for the apparent advance angle ε^* for a straight ahead motion with velocity component u:

$$\varepsilon^* = \text{Arctan2}(u, 0.7\pi n D_P) \tag{1.21}$$

In [23] and [24] the division into quadrants is not based on this mathematical definition and the relationship between the different definitions can be found in Table 1.2.

Table 1.2 Comparison of the definitions for the four quadrants of operation

velocity u	propeller rate n	ε^*	mathematical definition	according to [23] and [24]
positive	positive	[0; 90 deg]	quadrant 1	quadrant 1
positive	negative	]90; 180 deg[	quadrant 2	quadrant 3
negative	negative	[-180 deg; -90 deg]	quadrant 3	quadrant 4
negative	positive	]-90 deg; 0 deg[	quadrant 4	quadrant 2

1.4.3 Mathematical models incorporating low speed manoeuvring

Running through the titles of papers dealing with ship manoeuvring, the term "low" or "slow" can mostly be interpreted in two ways:

❑ Reports dealing with modified expressions for the *hull forces* due to the existence of large drift angles and/or yaw rate angles when ships are for example laterally shifted or turned by tug boats. For example: [25] and [26]

❑ Reports dealing not only with wide ranges of kinematical parameters but also with all possible combinations of propeller operation and consequently rudder operation. For example: [13], [27], [28], [29] and [30].

The list of reports summarized above is not limitative and only indicates the attention different authors have paid during the last two decades to understand the specific needs of low speed manoeuvring.

1.4.3.1 Low speed manoeuvring based on hull force models for different speed ranges

In [29] the hydrodynamic forces acting on the ship hull are described by four mathematical expressions classified within the following speed ranges:

❑ *Ordinary advance speed model* for the speed range larger than that corresponding to the specified Froude number F_{nmin1}: $F_n \geq F_{nmin1}$

❑ *Low speed model* with three different speed ranges:
  ○ *Low advance speed model* for the speed range: $0 \leq F_n < F_{nmin2}$
  ○ *Averaged model* of the two mathematical models for the speed range between F_{nmin1} and that corresponding to the upper value of the low advance speed model F_{nmin2}: $F_{nmin2} \leq F_n \leq F_{nmin1}$
  ○ *Astern model* for backing condition: $F_n < 0$

In [29] very low values of $F_{nmin1} = 0.01$ and $F_{nmin2} = 0.005$ (corresponding to speed values of 0.54 m/s and 0.27 m/s for a ship with a length of 300 m) were adopted.

The averaged model is necessary to match the ordinary advance speed model and the low speed model. The following manner is used:

$$\begin{bmatrix} X_H \\ Y_H \\ N_H \end{bmatrix} = g_1 \begin{bmatrix} X_H \\ Y_H \\ N_H \end{bmatrix}_{ordinary} + g_2 \begin{bmatrix} X_H \\ Y_H \\ N_H \end{bmatrix}_{low} \tag{1.22}$$

where

$$g_1 = \frac{F_n - F_{nmin2}}{F_{nmin1} - F_{nmin2}}$$

$$g_2 = \frac{F_{nmin1} - F_n}{F_{nmin1} - F_{nmin2}} \tag{1.23}$$

Thanks to this subdivision based on the speed ranges the hull force model can be adjusted to the required level of detail.

1.4.3.2 Low speed manoeuvring according to Hydronautics Research Inc.

Goodman [31] and Roseman [32] introduced in the 1970s a formal mathematical model taking into account all possible manoeuvres characterised by varying propeller loading, positive or negative ship velocity and positive or negative propeller rate. This model has proven to be of great value and the only disadvantages are the formal character of the expressions and "*the need for matching and patching piecewise approximations*" (written discussion in [13]) due to the division based on the ratio of propeller loading.

The mathematical model summarized in this section is based on the modified equations according to the manoeuvring behaviour of the Esso Osaka tanker in deep and shallow water [33].

For the longitudinal force:

$$m(\dot{u} - vr - x_G r^2) = \frac{\rho}{2} L^3 \left[X'_{\dot{u}} \dot{u} + \left(X'_{vr} |\cos\beta| - X'_{\dot{u}} |\sin\beta| \right) vr \right] + \frac{\rho}{2} L^4 \left(X'_{rr} r^2 \right)$$

$$+ \frac{\rho}{2} L^2 \left(X'_{vv} v^2 \right) + \frac{\rho}{2} L^2 u^2 \left(a_i + b_i \eta + c_i \eta^2 \right) + \frac{\rho}{2} L^2 \left[X'_{vv\eta} v^2 (\eta - 1) \right] \tag{1.24}$$

$$+ \frac{\rho}{2} L^2 u_P^2 X'_{RUD} \delta^2$$

For the lateral force:

$$m(\dot{v} + ur + x_G\dot{r}) = \frac{\rho}{2}L^4\left(Y'_{\dot{r}}\,\dot{r} + Y'_{r|r|}\,r|r|\right) + \frac{\rho}{2}L^3\left(Y'_{\dot{v}}\,\dot{v}\right)$$

$$+ \frac{\rho}{2}L^3\left(Y'_r\,ur + Y'_{v|r|}\,v|r|\right) + \frac{\rho}{2}L^4\left(Y'_{vrr}\,\frac{vr^2}{U}\right)$$

$$+ \frac{\rho}{2}L^2\left[Y'_v\,uv + Y'_{v|v|}\,v|v| + \left(Y'_{v\eta}\,uv + Y'_{v|v|\eta}\,v|v|\right)(\eta-1)\right] \qquad (1.25)$$

$$+ \frac{\rho}{2}L^3 Y'_{r\eta}\,ur(\eta-1) + \frac{\rho}{2}L^2 u_P^2 Y'_{RUD}\,\delta + \frac{\rho}{2}L^2 w_P^2 Y'_*$$

For the yawing moment:

$$I_z\dot{r} + mx_G(\dot{v} - ur) = \frac{\rho}{2}L^5\left\{N'_{\dot{r}}\,\dot{r} + N'_{r|r|}\,r|r|\left[1 + 2\left(1 - \tanh\left|\frac{2u}{rL}\right|\right)\right]\right\} + \frac{\rho}{2}L^4\left(N'_{\dot{v}}\,\dot{v}\right)$$

$$+ \frac{\rho}{2}L^4\left(N'_r\,ur + N'_{v|r|}\,|v|r\right) + \frac{\rho}{2}L^5\left(N'_{vrr}\,\frac{vr^2}{U}\right)$$

$$+ \frac{\rho}{2}L^3\left[N'_v\,uv + N'_{v|v|}\,v|v| + \left(N'_{v\eta}\,uv + N'_{v|v|}\,v|v|\right)(\eta-1)\right] \qquad (1.26)$$

$$+ \frac{\rho}{2}L^5 N'_{r\eta}\,ur(\eta-1) + \frac{\rho}{2}L^3 u_P^2 N'_{RUD}\,\delta + \frac{\rho}{2}L^3 w_P^2 N'_*$$

with rudder induced derivatives X'$_{RUD}$, Y'$_{RUD}$, N'$_{RUD}$ defined as

$$X'_{RUD} = X'_{\delta\delta}\left(1 + \bar{v}_{RUD}\,\frac{Y'_{\delta|v|}}{Y'_\delta}\right)$$

$$Y'_{RUD} = Y'_\delta + \bar{v}_{RUD}\,Y'_{\delta|v|} \qquad (1.27)$$

$$N'_{RUD} = N'_\delta + \bar{v}_{RUD}\,N'_{\delta|v|}$$

with velocities at the rudder position $\bar{v}_{RUD}$ and U_{RUD} and the application point x_δ given by:

$$\bar{v}_{RUD} = |v + rx_\delta|\,\frac{u}{U_{RUD}^2}$$

$$U_{RUD}^2 = u^2 + (v + rx_\delta)^2 \qquad (1.28)$$

$$x_\delta = L\,\frac{N'_\delta}{Y'_\delta}$$

and velocities u_P and w_P denoting the hull-propeller-rudder combination

$$u_P^2 = \left(dU_{RUD}^2 + eDnU_{RUD} + fD^2n^2\right)$$

$$w_P^2 = \left(d_A U_{RUD}^2 + e_A DnU_{RUD} + f_A D^2n^2\right) \qquad (1.29)$$

Asymmetry from the propeller itself is incorporated through the terms Y'$_*$ and N'$_*$. η is the ship propulsion ratio and is defined as a function of the apparent advance coefficient J' and the advance coefficient at self propulsion J_c:

$$\eta = \frac{\left(n/u\right)}{\left(n_c/u_c\right)} = \frac{J_c}{J'} \qquad (1.30)$$

This propulsion ratio reaches specific values at the following situations:

16

- ❑ At self propulsion: $\eta = 1$
- ❑ At bollard pull: $\eta = \infty$
- ❑ At stopped propeller: $\eta = 0$

The coefficients a_i, b_i and c_i for the longitudinal force change depending on the propeller loading. Four regions are considered in Table 1.3. Although the expressions (1.24) to (1.26) are not formulated in this way, they are composed of pure hull components, hull-propeller components (combination of kinematical parameters and the ship propulsion ratio η) and hull-propeller-rudder components (index RUD). These formulations could be compared to modular models which will be summarized in chapter 2.

Table 1.3 Regions considered in (1.24) for the longitudinal force according to the propeller loading

i =		
1	$1 < \eta < \infty$	from self propulsion to bollard pull (positive propeller action) or from ordinary to low speed manoeuvring with propeller action; quadrant 1 (going ahead) and quadrant 3 (going astern)
2	$0 \leq \eta \leq 1$	from stopped propeller to self propulsion; quadrant 1 (going ahead) and quadrant 3 (going astern)
3	$-1 \leq \eta < 0$	from self propulsion to stopped propeller; quadrant 2 (stopping from headway) and quadrant 4 (stopping from sternway)
4	$-\infty < \eta < -1$	from bollard pull (negative propeller action) to self propulsion; quadrant 2 (stopping from headway) and quadrant 4 (stopping from sternway)

1.4.4 The introduction of memory effects

The concept of "*memory effects*" or "*time history effects*" has been introduced with the introduction of Planar Motion Mechanisms (see chapter 3) to determine and measure fluid forces. These forces and moments acting on a manoeuvring ship model can be greatly influenced by the previous motion so that a "memory effect" is the hydrodynamic effect on the local flow at some part of the ship due to the earlier flow at another part of the ship.

Bishop et al. have reported some experiments in [34] and [35] to demonstrate a "memory effect". A ship's hull is considered to be composed of lifting and non-lifting elements so that the behaviour of a hull is replaced by a simple craft with two vertical fins, one at the bow, the other at the stern (Figure 1.8). "*Tests were conducted in a circulating water channel. First of all, the leading foil was rotated about its vertical axis to a steady angle and measurements were taken of the change of side force on the after foil. The after foil was positioned at several stations downstream of the leading foil and also displaced laterally*". The results show a considerable amount of response directly downstream of the leading foil but opposite in direction. If the trailing foil is laterally displaced the force transfer falls off.

Another test was executed to expose time effects. The leading foil was rapidly brought to a certain angle of attack. The time delay was measured between this movement and the reactive force measured on the trailing foil. The time delay seemed to increase with the distance downstream and to decrease with the water speed. Translated to ship manoeuvring motions at slow speed a ship's hull could suffer from perturbed flows around it.

The two fin craft was also subjected to a steady sway motion (Figure 1.9). The lateral force arises from the drift angle β of both fins, plus the influence of the leading foil on the trailing foil. Taking into account the effect of a lateral displacement of the trailing foil compared to the position of the leading foil, the latter response influence will decrease at increasing drift angle. This non-linear effect in the Y-β curve could be explained by a kind of force transfer from the bow to the stern or a memory effect.

In chapter 3 some other flow effects induced during PMM sway and yaw tests executed at various frequencies and amplitudes will be visualized and discussed.

In this research a quasi-steady representation of fluid forces will be adopted so that no time dependent force components will be found in the mathematical model for hull forces. Nevertheless, some kind of memory effects, like the effect of the bow to the stern during oblique towing tests will be incorporated through the derived force models. This simplification concerning the mathematical model representation is supported by Hwang in [23], as it has still to be determined whether omitting the memory effects could have a meaningful impact on low speed simulation.

If memory effects have to be inserted explicitly, the unified mathematical model for manoeuvring and seakeeping in section 1.2.7 makes it possible to include the time history of the ship motion by expressing the fluid forces and moment in terms of functional analysis. Thanks to this functional representation of hydrodynamic forces the relationship between the time domain and frequency domain offer an important feature to the incorporation of all kind of memory effects in mathematical models.

1.5 Choices concerning mathematical modelling

The evolution in mathematical models described in section 1.2 learns a lot about the possibilities and limitations of these models. Some choices have consequently been made to develop a mathematical model which will meet the characteristics summed by Pawlowski. In addition, despite of the choices that will be made, everyone must be aware of the following conclusion from Gill found in the written discussion in [35]: *"No mathematical model can give an exact description of the complicated non-linear time dependent system exemplified by a manoeuvring ship; some simplifying assumptions must always be made in order to allow a manageable model to be developed. The nature of these assumptions should depend on the use to which the math model is to be put, and while some applications may require a linear model with fluid memory, for other uses a non-linear quasi-steady model may be more appropriate."*

❑ Although harbour manoeuvres will suffer from fluid memory effects, a **quasi-steady approach**[1] will be adopted. This supposes the development of a mathematical model depending on kinematical and control parameters where frequency and time dependence is ignored.
❑ A physical model or **modular model** referring to the physical components hull, propeller and rudder of a manoeuvring ship will be preferred. This choice is especially linked to the adjustability characteristic of mathematical models. It offers an important feature while validating a mathematical model in a given situation so that each of the model parts can be raised to a higher accuracy.
❑ The mathematical model will describe the manoeuvring behaviour of the ship in **medium deep to shallow water** which is unrestricted in lateral direction (no bank effects) and only restricted in available under keel clearance expressed as a percentage of the draught.

---

[1] The terms (quasi-)steady and (quasi-)stationary are frequently found in papers concerning mathematical modelling of ship manoeuvres where they are considered to be equivalent. This is in contrast with the use of these terms in general fluid mechanics ("stationary" means "not moving", "steady" means "not varying in time"). In this research the term "(quasi-)steady" will mainly be used for the mathematical model type while "(non-)stationary" will mainly be used for the model test type. A "stationary" test type is a test of which the test parameters (velocities, accelerations, rudder angle, propeller rate) do not vary in time during the useful part of the test run.

2 Mathematical models: background and formulations

The historical overview of mathematical models given in chapter 1 will be extended with a description of three distinctive models: the MMG model (section 2.2), the four-quadrant model of Oltmann & Sharma or the HSVA model (section 2.3) and the DEN-Mark 1 model (section 2.4). They provide some interesting features like physical background, four-quadrant operation or tabular model forms which will be used as a guideline for the development of a model describing ship manoeuvrability. This description will be preceded by a literature study of the physical phenomena acting on the system elements hull (section 2.1.1), propeller (section 2.1.2) and rudder (section 2.1.3). At the end, some advantages and disadvantages of the described mathematical models will be listed (section 2.5).

2.1 Physical phenomena

The physical phenomena acting on a manoeuvring ship will be divided in:
❏   the hydrodynamic forces and moment on the ship's hull;
❏   the forces and moment due to propeller action;
❏   and the rudder induced forces and moment.

Each of these force components forms the basis of an individual chapter:
❏   chapter 4: Modelling of hull forces and moment
❏   chapter 5: Modelling of propeller forces and moment
❏   chapter 6: Modelling of rudder forces and moment

For each contribution, modelling of the specific forces and moment starts with a description of some observations during captive model testing followed by the determination and evaluation of the mathematical model.

2.1.1 Hydrodynamic forces and moment on ship's hull

Hydrodynamic hull forces and moment acting on a manoeuvring vessel are mostly considered to originate from four main causes [15]:

❏   Effects linked with a **potential flow** and **ideal fluids**.

In the absence of free surface effects which can be ignored in low speed manoeuvres, the underwater body of a vessel is considered as the symmetric lower part of a double-body moving in an unbounded fluid with three degrees of freedom. Added masses for a manoeuvring vessel are reduced to the matrix:

$$\begin{bmatrix} -X_{\dot{u}} & -X_{\dot{v}} & -X_{\dot{r}} \\ -Y_{\dot{u}} & -Y_{\dot{v}} & -Y_{\dot{r}} \\ -N_{\dot{u}} & -N_{\dot{v}} & -N_{\dot{r}} \end{bmatrix} = \begin{bmatrix} m_x & -X_{\dot{v}} & -X_{\dot{r}} \\ -Y_{\dot{u}} & m_y & -Y_{\dot{r}} \\ -N_{\dot{u}} & -N_{\dot{v}} & J_{zz} \end{bmatrix} \qquad (2.1)$$

According to the potential theory this matrix is symmetrical. In addition, the asymmetry between fore and aft body is rather small so that

$$N_{\dot{v}} = Y_{\dot{r}} \ll X_{\dot{u}}, Y_{\dot{v}}, N_{\dot{r}}$$

and making use of the slender body theory (B, d << L_PP)

$$X_{\dot{u}} \ll Y_{\dot{v}}, N_{\dot{r}}$$

Thanks to the port-starboard symmetry of a vessel ($X_{\dot{v}} = X_{\dot{r}} = 0$), the equations of motion for a vessel in an ideal fluid are reduced to ([6] and [36]):

19

$$X_I = X_{\dot{u}}\dot{u} - Y_{\dot{v}}vr - Y_{\dot{r}}r^2$$
$$Y_I = Y_{\dot{v}}\dot{v} + X_{\dot{u}}ur + Y_{\dot{r}}\dot{r} \tag{2.2}$$
$$N_I = N_{\dot{r}}\dot{r} + N_{\dot{v}}\left(\dot{v} + ur\right) + \left(Y_{\dot{v}} - X_{\dot{u}}\right)uv$$

The last term of the ideal yawing moment N_I in (2.2) represents the Munk moment which increases the inflow angle (a positive drift angle during a motion ahead gives a positive moment) and destabilises the ship motion.

❑ *Lift* effects

At small drift angles the ship's hull can be considered as a lifting surface with the drift angle taking the role of the conventional angle of attack [6]. The ship's hull develops lift and circulation and shed trailing vortexes. The lift F_L works perpendicular to the inflow direction and is accompanied by an induced drag F_D which is proportional to the square of the lift and acts parallel to the inflow. The resulting lateral force generates a yawing moment due to the position of its point of application x_F.

❑ *Viscous cross flow* effects dominate a flow at larger inflow angles where a three-dimensional approach is required due to the transverse flow from the high to the low pressure side. It is an essentially non-linear phenomenon and simple strip theory is mostly used. Forces and moment are function of the local coefficient of cross-flow drag $C_{CFD}(x)$, local lateral velocity due to swaying and turning and the local lateral underwater area $d(x)dx$ so that total lateral force and yawing moment are written as:

$$Y_{HC} = -\frac{1}{2}\rho \int_{-\frac{1}{2}L}^{\frac{1}{2}L} (v + xr)|v + xr| C_{CFD}(x)d(x)dx$$

$$\tag{2.3}$$

$$N_{HC} = -\frac{1}{2}\rho \int_{-\frac{1}{2}L}^{\frac{1}{2}L} (v + xr)|v + xr| C_{CFD}(x)d(x)xdx$$

❑ *Resistance* acts in the longitudinal direction of the ship motion and is according to the ITTC written as a sum of a frictional resistance component C_F, function of the Reynolds number, and a wave resistance C_W, function of the Froude number.

$$C_T = \frac{R}{\frac{1}{2}\rho Su^2} = (1+k)C_F(R_n) + C_W(F_n) \tag{2.4}$$

The frictional resistance force can be estimated based on the ITTC 1957:

$$C_F = \frac{0.075}{\left(\log R_n - 2\right)^2} \tag{2.5}$$

These four main causes of hull forces and moment where extended to six "*elementary fluid forces*" by Karasuno in [26]. The proposed physical-mathematical model is based on one of the most detailed analyses of forces acting on a ship's hull during large drifting and turning motion at low forward speed. The model is reported in detail in [37] and other publications. The six elementary force components are shown in Figure 2.1 and five of them correspond to the four force contributions discussed above:

(1) Ideal fluid forces with only the Munk moment N_I are represented on Figure 2.1. In most mathematical models the ideal fluid forces related to ship velocities are incorporated in the

conventional lift equations combining viscous lift and ideal fluid terms.

(2) Viscous lift (L_v) according to Karasuno is one of the fluid forces which are concentrated on the trailing and − to a lesser degree - leading edges of the ship's hull. Viscous lift forces at both edges are assumed to depend on the geometrical inflow angle along each edge.

(3) Shedding vortices generate an induced drag (D_i) which is oriented by the bound vortices of the ship under the down wash flow. Contrary to the viscous lift, the main part of this induced drag is generated along the leading edge of the ship where the main portion of the bound vortices occurs.

(4) Cross flow drag (with lateral force component Y_C)

(5) accompanied by a cross flow lift along the longitudinal axis (X_C). The cross flow drag is perpendicular to the longitudinal ship axis. Although the cross flow drag coefficient C_D is independent of the drift angle of the ship according to the principle of cross flow theory (see also equation (2.3)), in [26] the coefficient is assumed to depend on the geometrical inflow angle β_x of the ship's section at position x. In [6] a similar postulation is made and the cross flow drag coefficient depends especially on section geometry and drift angles and possibly on Froude and Reynolds numbers. The cross flow lift is perpendicular to the direction of the cross flow (according to the definition of lift) and is asymmetrical along the fore and aft ends of the ship.

(6) Calculating the frictional resistant force (X_F) during low speed manoeuvres wave excitation can be ignored and the total longitudinal resistance is mainly composed of the frictional resistance.

In [26] and [37] a stall effect was introduced as a result of the analysis of forces and moment during an oblique motion. The force contributions listed above suffice to describe measured lateral force and yawing moment while an additional longitudinal force X_{ST}, composed of lift L_{ST} and drag D_{ST} must be incorporated to correct the influences of viscous lift and induced drag. This so called stall effect on the longitudinal force was not repeated in [38] and following publications. It could nevertheless explain some unusual phenomena observed at larger drift angles and discussed in chapter 4 as the stall effect hardly occurs in the range of small drift angles [26].

Hydrodynamic hull forces and moment can be summarized by the equations:

$$X = X_I + X_{Lv} + X_{Di} + (X_C + X_F + X_{ST})$$
$$Y = Y_I + Y_{Lv} + Y_{Di} + (Y_C)$$
$$N = N_I + N_{Lv} + N_{Di} + (N_C)$$

(2.6)

where detailed expressions for each elementary force component can be found in [37]. These elementary forces are illustrated for a pure car carrier model in oblique motion and pure turning motion in deep water (Figure 2.2 and Figure 2.3). The principle particulars of this ship model are $L_{PP} = 3.0$ m, B = 0.537 m, d = 0.137 m and $C_B = 0.547$. Due to the existence of a cross flow lift X'_C the total non-dimensional longitudinal force X' is non-zero at a drift angle of 90 degrees even in deep water. In shallow water this effect will be reinforced due to the reduced area between keel and bottom so that the measured longitudinal force at β = 90 deg can differ from zero. As a positive X'$_C$ value is found even for an oblique as well as for a pure turning motion, the relatively slender fore body of the ship compared to the aft body induces this positive flow towards the leading edge.

The analysis of fluid forces is a difficult task and additionally, fluid forces in shallow water will be affected by flow modifications due to the vicinity of the boundaries. Nevertheless, hull forces and moment measured during captive model tests can be analysed keeping in mind these elementary forces and their variation with characteristic inflow angles (drift angle β and yaw rate angle γ).

In [37] a modified mathematical model similar to the model described above is deduced from a simplified vortex model with the special feature of estimating rotatory coefficients and hydrodynamic forces in turning motion by analysed results of experiments in oblique motion.

Moreover, according to Karasuno in [38], hydrodynamic forces X, Y and N that occur at large drift angles can be estimated based on hydrodynamic forces measured during a small range of drift angles β, for example for a range from [0; 30 deg].

2.1.2 Propeller action

The publication of Harvald concerning *wake and thrust deduction at extreme propeller loadings* [24] deals with the modelling of propeller thrust at wide ranges of ship speed and propeller revolutions. Although the condition parameters (e.g. deep or shallow water) are not specified in [24], the model tests have probably been executed in deep water. In [39] the research of Harvald is extended to shallow water conditions for a bulk carrier.

Wake and thrust deduction have been determined in [24] by tests with models of a fishing trawler and a bulk carrier. Estimation of wake can be based on the *thrust identity* or *torque identity method*. The effective wake velocity is defined as the difference between the ship velocity V and the velocity V_A which in a homogeneous field would enable the propeller at the same number of revolutions to create a thrust or to absorb a torque equal to that measured. If the number of revolutions is kept constant, the advance numbers are written as:

$$J' = \frac{V}{nD_P} \quad , \quad J = \frac{V_A}{nD_P} = \frac{(1-w)V}{nD_P} \tag{2.7}$$

so that the wake factor is expressed by:

$$w = \frac{J'-J}{J'} \tag{2.8}$$

Consequently the wake can be determined by the use of a propeller diagram in which K_T and K_Q curves of the propeller behind the ship (i.e. as a function of J') are plotted together with the corresponding K_T and K_Q curves from the open water experiments (i.e. as a function of J).

In [24] thrust K_T and torque coefficient K_Q are not based on a four quadrants presentation so that these coefficients are defined by:

$$K_T = \frac{T}{\rho n^2 D_P^4} \quad , \quad K_Q = \frac{Q}{\rho n^2 D_P^5} \tag{2.9}$$

According to Harvald the wake factor is composed of the following contributions:

$$w = w_P + w_F + w_W + w_{COR} \tag{2.10}$$

❑ w_P: potential wake coefficient
❑ w_F: frictional wake coefficient
❑ w_W: wave wake coefficient
❑ w_{COR}: a correction which makes allowance for the apparent change of the wake coefficient, partly due to the change of the rotation of the propeller jet and partly due to other alterations in the inflow conditions. w_{COR} could be negative.

The thrust deduction coefficient is determined by

$$t = \frac{K_T - K_R}{K_T} \tag{2.11}$$

where K_R is defined by

$$K_R = \frac{R + F}{\rho n^2 D_P^4} \tag{2.12}$$

R is the ship resistance and F is the tow rope pull. For a model running freely F equals zero. The thrust deduction can easily be determined by inserting the K_R curves in the propeller diagrams.

Based on Figure 2.4 the test results (only straight ahead and astern motion, no oblique or yawing motion) show clearly that the thrust deduction as well as the wake vary considerably with the propeller load and consequently also with the advance number. Some of the variation is obviously due to the way the wake coefficient has been defined. For both models there is a rather large difference between the wake coefficient found by thrust identity and the one found by torque identity.

In addition, although both ship models are equipped with the same propeller P36, a different loss of thrust coefficient with increasing J' can be observed. This reduction is less for the bulk carrier than for the trawler which could be expected based on the form of the aft body. The effective inflow into the propeller, (1-w)V, is indeed lower for the bulk carrier than for the trawler.

There seems to be a difference in the variation of w with J', when the speed is varied and the number of revolutions is kept constant, and when the number of revolutions is varied and the speed is kept constant.

For quadrant 3 and 4 or a motion astern the wake factor is expected to be negligible as the inflow at the propeller is not obstructed by the ship and will approximate the flow of a freely rotating propeller. This is not really seen on Figure 2.5 where the fishing trawler is tested at a constant velocity and a small pitch ratio (P/D = 0.6) for propeller P36. At the third quadrant (mathematical definition) the wake factor is non-zero while for the fourth quadrant w is almost zero. In Figure 2.5 at the bottom the fishing trawler is tested at a constant velocity and a large pitch ratio (P/D = 1.2) for propeller P39. At the third quadrant a constant non-zero value for the wake factor can be found.

Quadrants with opposite flows related to the ship motion on one hand and propeller action on the other are characterized by unusual phenomena. When the propeller is going ahead (n positive) and the ship going astern (V negative) for example, the conditions are very unstable [24]. A wave train originates from the propeller and moves in the sailing direction, disappears at a certain distance ahead of the ship and another one is produced at the propeller. The distance depends on the velocity and the number of revolutions. Furthermore, it should be mentioned that there is a heavy eddy formation at the propeller. This phenomenon can be clearly seen on series of photographs (Figure 2.6 and Figure 2.7) taken during a stationary captive model test with ship model U (for the characteristics see chapter 3).

2.1.3 Rudder induced forces and moment

2.1.3.1 General overview of flow characteristics at the rudder

Rudder modelling technique is derived from aerodynamic theories of wing profiles in an air flow. A rudder profile in a uniform flow with velocity U_R and inflow angle α_R undergoes a lift F_L and drag force F_D. These forces are oriented respectively perpendicular and parallel to the direction of the flow and can be decomposed into a normal rudder force F_{RN} and a tangential rudder force F_{RT}, respectively perpendicular and parallel to the rudder chord (Figure 2.8, [40]).

Nevertheless, a rudder attached to a manoeuvring ship is acting in a non-uniform flow affected by the wake of the hull, the longitudinal, lateral and yaw motions of the ship and the propeller slipstream [6]. Depending on the quadrant of operation of the propeller compared to the ship motion, rudder forces can differ considerably and the transition from open water characteristics to a global rudder action is not made easily. Important effects are:

❑ A rudder deflection does not only result into forces on the rudder itself, but even induces lateral force (and yawing moment) on the hull.
❑ Lift characteristics of a rudder in a uniform flow differ from these characteristics in the propeller slipstream. The appearance of stall or an abrupt decrease of lift is delayed in a propeller stream and depends even on the propeller loading.
❑ The inflow velocity and direction at the position of the rudder are influenced by the rudder

angle, the velocity components of the ship, the wake and the propeller slipstream. The complex character of the rudder inflow is illustrated in Figure 2.9. Figure 2.10 gives a block diagram of the flow effects around a manoeuvring ship where the effect of miscellaneous external disturbances is neglected for the sake of simplicity. The rudder force generation in a typical single screw-rudder arrangement is regarded as an input/output relation where the rudder function is driven by the inflow stream related to hull forms, surface friction or propeller loading condition. Referring to Figure 2.10 the cause and effect relations of the rudder force can be symbolically expressed as in [12]:

$$
\begin{aligned}
[F_R] &= [F_R(U_R)] \\
&= [R] \cdot [U_R] \\
&= [R] \cdot [[P] \cdot [W_2] + [W_3]] \\
&= [R] \cdot [[P] \quad 1] \cdot \begin{bmatrix} [W_2] \\ [W_3] \end{bmatrix} \\
&= [R] \cdot [[P] \quad 1] \cdot \begin{bmatrix} [H(W_2)] \\ [H(W_3)] \end{bmatrix} \cdot [U]
\end{aligned}
\tag{2.13}
$$

A general impression of the axial flow field near the rudder is shown in Figure 2.9. Rudder inflow velocity is a result of a combination of propeller inflow velocity and slipstream velocity, where the first component can possibly be modified by a sway or turning motion of the vessel. The effective rudder inflow velocity can be detected based on the measured rudder normal force characteristic curve obtained for open water through a rudder force identity method.

The average acceleration of rudder inflow stream by a propeller in the axial direction is usually estimated by use of the axial momentum theory for an actuator disc (Figure 2.11) where u_P is the uniform propeller inflow velocity, Δu_S the additional velocity due to the propeller at the rudder position. The rudder is not necessarily affected by the propeller across the complete rudder height or rudder area so that a model will be constructed consisted of two separated rudder zones affected by different inflow velocities, for example A_{RP} the area affected by the propeller and $(A_R - A_{RP})$ the area only affected by the "non-disturbed" rudder inflow velocity u_R.

Sway and yaw velocity components of the ship generate a lateral inflow velocity v_R at the position of the rudder which is nevertheless influenced by the presence of the hull and the propeller, represented by the "flow rectification" or "flow-straightening" coefficient k_{HR}:

$$
v_R = k_{HR}(v + x_R r)
\tag{2.14}
$$

While turning or drifting the flow can enter the aft body with rudder attached more easily from port or starboard side and compared to a straight-line motion the flow is bend off. Additionally, propeller action can modify this inclined flow and straighten it so that the value of k_{HR} becomes lower than 1 in (2.14). In Figure 2.12 the definition of the flow-straightening coefficient k_{HR} (or γ) is illustrated for a turning motion and an oblique motion according to [12] and measured coefficients for two ship models are presented in Figure 2.13. At small drift angles the flow-straightening coefficient can take values greater than 1 while propeller action diminishes this ratio.

2.1.3.2 Description of a four-quadrant model for rudder forces

A new concept for the open water characteristics of a rudder is introduced by Molland and Turnock [41]. According to these authors there is a reasonable amount of information available for rudders working in a free stream but detailed information on the forces developed by the rudder in the presence of a propeller is sparse. Consequently, rudder and propeller are considered as a coupled system in isolation and in the absence of the hull. A detailed investigation of the interaction between these two control elements is executed through wind tunnel measurements to examine the parametric relationships suitable for predicting the lift and

drag of various rudder-propeller combinations.

The parameters which govern the interaction are grouped into four categories:
- Flow variables which control the magnitude of the forces developed. These include the free stream velocity, the propeller rate of revolution and the properties of the fluid.
- Rudder geometric variables which determine how the flow passes over the rudder (for example rudder span S and mean chord c)
- Propeller geometric variables which control how the propeller imparts energy into flow and generates thrust (for example propeller diameter D_P and propeller pitch P).
- Relative position and size of the rudder and propeller. Propeller and rudder are separated longitudinally (X), laterally (Y) and vertically (Z).

Rudder side force (lift C_L) is of primary importance in ship manoeuvring and can be expressed as a function of non-dimensional variables belonging to these four categories.

For a particular rudder-propeller combination the parameters reduce to:
$$C_L = f\{[J, R_n, \gamma][\alpha][P/D_P]\}$$
(2.15)

with γ defined as the *yaw angle* between the combination and the free stream and α the rudder incidence. For a fixed pitch propeller the two fundamental controlling parameters are the propeller advance ratio J and the rudder incidence α (Figure 2.14). The other parameters will be of less importance. Positive values for rudder lift and rudder incidence are, in accordance with Figure 2.14, defined opposite to positive values of rudder normal force F_{RN} and rudder angle δ_R in this research.

Qualitative results of open water characteristics for the complete system and a free stream velocity of 10m/s are shown in Figure 2.15 for the lift coefficient and in Figure 2.16 for the drag coefficient. The positive direction of rotation of the propeller is anti-clockwise when viewed from the rudder. The rudder has a chord of 667 mm, a NACA0020 section and span of 1000 mm.

- A decrease in advance ratio J (or an increase in propeller thrust K_T) gives an increase in lift-curve slope.
- The lift varies almost linearly with incidence until stall is approached for all investigated advance ratios. For the high advance ratio the lift-curve slope is almost identical to that for the free stream. However, there is a significant delay in stall compared with the free stream and the magnitude of this delay increases with increasing propulsion loading.
- Due to the influence of the propeller slipstream the stall angle is no longer the same for positive and negative incidence. Stall occurs later for positive incidence (or negative rudder angle, rudder to starboard) and therefore a greater value of maximum side force is measured at positive incidence.
- There is a rotational nature of the inflow from the propeller to the rudder.
- Only small changes in the rudder lift characteristics due to a change in longitudinal separation are observed.
- Rudder drag is a significant component of resistance at larger rudder angles.

In [42] rudder-propeller interaction is discussed for low and zero speed cases and four quadrants of operation. These cases are an important aspect of ship manoeuvring and are often treated in a step motherly way during modelling of harbour manoeuvres. Although various simulation models of low speed and backing manoeuvres have also been proposed by other authors, Molland and Turnock give a clear understanding of the flow physics which controls rudder-propeller interaction based on their wind tunnel experiments.

To incorporate the four quadrants and low speed manoeuvring near zero ship velocity two presentations of rudder forces due to propeller-rudder interaction are suggested:
- For forward and backward ship motion in the four quadrants of operation the rudder forces are turned into a non-dimensional representation using the wake (or free stream) velocity

which provides the best physical presentation, showing an increase in rudder forces with increasing propeller thrust loading, and tending to the free stream results as revolutions and propeller thrust loading tend to zero:

$$\frac{1}{2}\rho A V^2 \qquad (2.16)$$

❑ The case when the ship speed is at or near zero, where propeller induced velocities dominate, is treated as a separate domain and rudder forces are made non-dimensional using a function of the theoretical prediction of propeller induced velocities at zero J:

$$\frac{1}{2}\rho A K_T n^2 D_P^2 \qquad (2.17)$$

An advantage of presentations (2.16) and (2.17) is that they merge satisfactorily at low J values. In [43] a third method of data presentation is proposed in quadrants II, III and IV, allowing the cases of n=0 also to be included and combining presentations (2.16) and (2.17). A non-dimensional representation is based on:

$$\frac{1}{2}\rho A \left(V^2 + K_T n^2 D_P^2 \right) \qquad (2.18)$$

and rudder forces are presented in terms of propeller advance angle across the four quadrants for different fixed values of incidence α or rudder angle δ_R. The K_T value used across all four quadrants is that at zero J.

The parameter presenting the propeller thrust loading is generally based on K_T/J^2 but this parameter is not suitable for the transitions between Quadrants I and IV (positive propeller zone) and between Quadrants II and III (negative propeller zone) where the ship speed goes through zero (J=0). Using the zero and low speed presentation this problem can be overcome and the parameter K_T/J^2 can be derived from the four quadrants curves of the Wageningen B-series [44].

Conclusions for rudder forces measured in the four quadrants of operation are illustrated in [42] and some interesting features are quoted here, all for an absolute free stream velocity of 10m/s, which is rather high:

❑ In Quadrant I, although this is not really clear on the side force figure, for low propeller revolutions less than about 800rpm, the side force characteristic falls below free stream performance and keeps reducing as revolutions are further reduced. Based on the spanwise load distributions over the propeller shown in [42] it is clearly noticeable that the propeller is now extracting energy from the fluid and forces developed by the rudder are small.

❑ In Quadrant II at small negative propeller revolutions, no flow passes over the rudder in way of the propeller race. As propeller revolutions are increased, flow over the rudder is reversed, resulting into small rudder lift forces. This complicated situation with opposite flows from free stream flow and propeller action even causes vibrations of the test rig at higher thrust loading. Further on, it is interesting to note that the rudder profile is generating a kind of thrust force.

❑ For Quadrant III the rudder is now operating upstream of the propeller and is irrespective of propeller thrust loading working close to its astern free stream condition. The only major difference is the delay in stall for higher thrust loadings.

❑ In Quadrant IV at a backward free stream speed of −10m/s and even relatively high propeller revolutions the flow has still not reversed. The positive rotating propeller is slowing the flow passing over the rudder and rudder forces diminish. A decrease in speed or an increase in propeller thrust loading will be necessary to generate some rudder lift force.

The influence of positive revolutions is examined for low and zero advance ratio. Two remarks can be made concerning the stall angle of the rudder lift force and the lift curve slope. The stall angle at zero J occurs later than in the low advance ratio tests and the lift curve slope at zero incidence is a little lower at zero J. An important unusual observation is a lift and drag offset at zero speed and low propeller revolutions that can be explained, according to [42], due to a combination of small values of absolute rudder force and possible scale effects. For zero speed and negative revolutions the propeller is unlikely to develop any significant rudder force.

A universal model for calculating rudder side force for a given rudder-propeller geometry and flow regime follows the philosophy of considering the rudder as two separate areas, one in way of the propeller race and one only exposed to free stream flow.

$$C_L = (\alpha - \alpha_0)\left(\frac{dC_L}{d\alpha}\right)_v \left[q_f(1-\xi)+q_p\xi k_0\right] \qquad (2.19)$$

ξ is the fraction of the rudder covered by the propeller race, α_0 the rudder incidence of rudder angle for zero lift, $(dC_L/d\alpha)_v$ the free stream rudder lift-curve slope and k_0 is a function of the propeller thrust loading. Constants q_f (free stream) and q_p (propeller) are introduced to cover four quadrants and the signs depend on the particular quadrant (see Table 2.1).

Table 2.1 Values for q_f and q_p according to [42]

Quadrant	I	II	III	IV
q_f	+1	+1	-1	-1
q_p	+1	-1	-1	+1

An alternative formulation is given for the zero and low speed case

$$C_L{}^* = (\alpha - \alpha_0)\left(\frac{dC_L}{d\alpha}\right)_v \left[q_f\frac{J^2}{K_T}(1-\xi)+\xi k_1\right] \qquad (2.20)$$

where k_1 is expressed solely as a function of the propeller thrust coefficient K_T.

In [41] and [42] rudder-propeller performance is restricted to a straight ahead free stream flow. The influence of an effective angle of drift on the isolated rudder-propeller combination is also examined through wind tunnel experiments and reported in [45]. Due to the restrictions of the wind tunnel section nevertheless drift angles up to only ±15 degrees were achieved without significant tunnel blockage effects.

The effect of drift based on these test results can be summarised in the following issues:
❑ The overall shape of the rudder side force characteristic remains constant with changes in drift angle and simply results in a shift in rudder incidence for zero side force and for maximum and minimum side forces corresponding with positive and negative stall angles.
❑ The amount and sign of the offset vertically and horizontally depend on the magnitude and direction of the drift angle.
❑ The higher the thrust loading for a constant drift angle test the lower the value of rudder incidence for zero side force. This can be understood in terms of the stronger propeller race for higher thrust loadings aligning the local flow onto the rudder more closely with the propeller axis.
❑ Due to flow straightening, the magnitude of the zero side force incidence is always less than the applied drift angle
❑ The drag characteristic is affected by the drift angle.

The observations for an isolated rudder-propeller combination will be used in chapter 6 as background for the modelling of rudder performance and manoeuvring characteristics of a fully appended ship in shallow water. The presence of a hull and especially the environmental conditions (vertically and horizontally restricting bottom and wall) will nevertheless affect the final ship manoeuvrability so that slightly modified presentations can be developed.

2.1.3.3 Effect of hull on rudder performance

The extensive programme of experimental and theoretical work described in [41] and [42] and quoted above, has led to the development of an *enhanced rudder force prediction model* [43]. This model is noteworthy because of the underlying philosophy but it will not be used for the modelling of rudder forces in this research for lack of experimental data of an isolated propeller-rudder combination. The experiments that will be discussed in chapter 6 give indeed only

information about measurements on a rudder which is part of a fully appended ship model.

A traditional model of rudder-propeller interaction treats the rudder and the propeller separately, relying on the use of rudder free stream characteristics and using propeller actuator disc theory to model the rudder axial inflow velocity. According to Molland this model type is limited because it does not correctly model the basic physical behaviour and its use is generally restricted to the origins of the empiricism. A detailed flow chart for the enhanced rudder force prediction algorithm taken from [43] is shown in Figure 2.17. In [45] the influence of an upstream body on the rudder-propeller combination is clearly described based on experiments with three different configurations of a centre-board and a Mariner stern form.

The effect of hull on rudder performance, which will be developed in chapter 6, will be based on the model for hull-propeller-rudder interaction proposed by Ogawa and Kasai [12] and is schematically presented in Figure 2.18. A rudder deflection at the stern gives not only rise to rudder forces, but it also induces a lateral force $a_H F_Y$ acting on the hull with an application point x_H. A full description can be found in 2.2.5.

2.2 MMG mathematical model, Japan

2.2.1 Introduction

The 'Investigating Group of Mathematical Models of Manoeuvring Motion' (MMG-group) is established by the second section of the Japan Towing Tank Committee (JTTC) in March 1976. The MMG-group belongs to the Japan Manoeuvrability Prediction Working Group (JAMP Working group). The developed MMG theory was highly appreciated by the Manoeuvring Technical Committee of the 15th International Towing Tank Conference (ITTC), and almost all the organizations in Japan have now set up mathematical models of manoeuvring motion in accordance with this theory.

MMG mathematical models are characterized by a division of all hydrodynamic forces into elements which contribute to a hull, a propeller and a rudder. The description of each element is based on its individual open-water performance and the interactions between the three different parts of a ship can be taken into account using interaction coefficients.

Compared to formal mathematical models MMG models have proved to be very effective when scale-effects which appear due to the execution of captive or free running model tests, need to be treated.

The description of the MMG mathematical model is mainly based on:
  □ [12] Ogawa A. & Kasai H.;
  □ [46] Kose K.;
  □ [47] The prediction of ship manoeuvrability, MMG-group.

The mathematical model was initially developed to predict the manoeuvring behaviour of a ship in calm and deep water at rather high speed. Later, additional research made it possible to incorporate the shallow water effects and low speed manoeuvring by introducing correction formulae (e.g. [48]).

2.2.2 Co-ordinate system and equations of motion

The Japan Manoeuvrability Prediction Working Group (JAMP) uses a method where the centre of gravity is considered as an origin to describe manoeuvring motions, whereas the midship point is considered as an origin to express hydrodynamic forces. The equations of motion in a horizontal plane with the origin at the position of the centre of gravity G:

$$m(\dot{u}_G - v_G r_G) = X_G(\dot{u}_G, \dot{v}_G, \dot{r}_G, u_G, v_G, r_G, n, \delta_R)$$

$$m(\dot{v}_G + u_G r_G) = Y_G(\dot{u}_G, \dot{v}_G, \dot{r}_G, u_G, v_G, r_G, n, \delta_R) \qquad (2.21)$$

$$I_{zG} \dot{r}_G = N_G(\dot{u}_G, \dot{v}_G, \dot{r}_G, u_G, v_G, r_G, n, \delta_R)$$

are transformed to the equations of motion with the origin at the midship point O:

$$m\left(\dot{u} - vr - x_G r^2\right) = X = X_G$$
$$m\left(\dot{v} + ur + x_G \dot{r}\right) = Y = Y_G$$
$$I_{zz}\dot{r} + mx_G\left(\dot{v} + ur\right) = N = N_G + Y_G x_G$$

(2.22)

The basic modular form of the MMG model shows the different contributions of hull (H), propeller (P) and rudder (R) to the hydrodynamic horizontal forces and moment:

$$X = X_H + X_P + X_R$$
$$Y = Y_H + Y_P + Y_R$$
$$N = N_H + N_P + N_R$$

(2.23)

Propeller induced lateral force and yawing moment are often rather small and difficult to measure. Due to their dependence on the propeller loading these contributions must be considered within the scope of model-ship correlation. The lateral force and yawing moment acting on the hull-propeller system are therefore considered in common:

$$X = X_H + X_P + X_R$$
$$Y = Y_{HP} \qquad + Y_R$$
$$N = N_{HP} \qquad + N_R$$

(2.24)

Due to the elementary structural form of the MMG model external disturbances caused by for example wind, waves and tug boats can be easily added to the hydrodynamic manoeuvring model.

The non-dimensional representation of forces and moment in the MMG model is based on the prime system with the reference area Ld.

2.2.3 Hydrodynamic force contribution of a hull

Hull forces and moment are composed of acceleration (index a) and velocity (index v) dependent contributions. Added masses (m_x, m_y) and added moment of inertia (J_{zz}) are represented in the ideal fluid equations:

$$X_{Ha} = X_{\dot{u}}\dot{u} - Y_{\dot{v}}vr = -m_x\dot{u} + m_y vr$$
$$Y_{Ha} = Y_{\dot{v}}\dot{v} + Y_{\dot{r}}\dot{r} + X_{\dot{u}}ur = -m_y\dot{v} + Y_{\dot{r}}\dot{r} - m_x ur$$
$$N_{Ha} = N_{\dot{v}}\dot{v} + N_{\dot{r}}\dot{r} = N_{\dot{v}}\dot{v} - J_{zz}\dot{r}$$

(2.25)

Velocity dependent forces and moment have a polynomial form. The longitudinal force X_{Hv} is composed of the resistance force due to a straight ahead motion X(u) and the additional resistance forces due to yawing and swaying.

$$X_{Hv} = X(u) + X_{vv}v^2 + X_{vr}vr + X_{rr}r^2$$

(2.26)

During high and normal speed manoeuvring the forward speed component of a ship is relatively large compared to the lateral speed component due to yawing and swaying motions so that linear derivatives are dominant. Nevertheless, to find a wide application of the MMG model and bearing in mind the physical phenomena of lift and cross flow, lateral hull force and yawing moment are decomposed of linear and non-linear terms.

$$Y_{Hv} = Y_L + Y_{NL} = Y_v v + Y_r r + Y_{NL}$$
$$N_{Hv} = N_L + N_{NL} = N_v v + N_r r + N_{NL}$$

(2.27)

$$Y_{NL} = \int_{-1/2L}^{1/2L} C_D(x)|v+rx|(v+rx)dx$$

$$N_{NL} = \int_{-1/2L}^{1/2L} C_D(x)|v+rx|(v+rx)xdx$$

(2.28)

The cross flow drag coefficient $C_D(x)$ can be modelled as a constant or a polynomial of the longitudinal position x along the ship.

In spite of the physical background of formulation (2.28), in general a second and third order polynomial is chosen as a basis for the non-linear terms.

$$Y_{NL} = Y_{vv}v^2 + Y_{vr}vr + Y_{rr}r^2 + Y_{vvv}v^3 + Y_{rrr}r^3 + (Y_{vvr}v + Y_{vrr}r)vr$$

$$N_{NL} = N_{vv}v^2 + N_{vr}vr + N_{rr}r^2 + N_{vvv}v^3 + N_{rrr}r^3 + (N_{vvr}v + N_{vrr}r)vr$$

(2.29)

In [46] third order power polynomials are preferred to second power polynomials.

$$Y_{NL} = Y_{vvv}v^3 + Y_{rrr}r^3 + (Y_{vvr}v + Y_{vrr}r)vr$$

$$N_{NL} = N_{vvv}v^3 + N_{rrr}r^3 + (N_{vvr}v + N_{vrr}r)vr$$

(2.30)

Other expressions only use second order terms.

$$Y_{NL} = Y_{|v|v}|v|v + Y_{|v|r}|v|r + Y_{|r|v}|r|v + Y_{|r|r}|r|r$$

$$N_{NL} = N_{|v|v}|v|v + N_{|v|r}|v|r + N_{|r|v}|r|v + N_{|r|r}|r|r$$

(2.31)

2.2.4 Hydrodynamic force contribution of a propeller

The propeller thrust T_P is the moving force of a ship. Starting from the open-water characteristics of the propeller K_T, propeller thrust can be modelled and the interaction of hull and propeller can be expressed by the thrust deduction t_P. The non-dimensional propeller induced longitudinal force is written as:

$$X_P' = \frac{(1-t_P)T_P}{\frac{\rho}{2}Ldu^2}$$

$$= \frac{2(1-t_P)K_T(J)\left(\frac{D_P^2}{Ld}\right)}{J_S^2}$$

(2.32)

- J_S, the apparent advance coefficient, is inversely proportional to the propeller rate of turn n: $J_S = u/nD_P$ so that an increasing propeller loading gives a decreasing advance coefficient.

- The advance coefficient J incorporates the modifications in the flow due to the wake field behind the ship: $J = u_P/nD_P = u(1-w_P)/nD_P$.

- The thrust deduction t_P is usually considered constant, although for full ship forms the parameter t_P can vary according to the ship motion (yawing and swaying) and the propeller loading [47].

- The open-water characteristics of the propeller, the thrust coefficient K_T, can be modelled based on a quadratic polynomial expression for the first quadrant of operation (forward motion, thrusting ahead).

$$K_T(J) = a_0 + a_1 J + a_2 J^2 \tag{2.33}$$

- The wake factor at straight ahead motion w_{P0} is influenced by swaying and yawing. Two main expressions are used for $1-w_P$:

$$1 - w_P = (1 - w_{P0}) + f(v', r') \tag{2.34}$$

$$1 - w_P = (1 - w_{P0}).f(v', r') \tag{2.35}$$

Depending on the authors different functions are published for the wake factor $1-w_P$ at any manoeuvring motion [47].

$$1 - w_P = (1 - w_{P0}) + \tau \left\{ v_P' + C_P v_P' | v_P' | \right)^2 + C_{Pv} v' + C_{Pr} r' \right\} \tag{2.36}$$

$$1 - w_P = (1 - w_{P0}) \left[1 + \tau \left\{ v_P' + C_P v_P' | v_P' | \right)^2 + C_{Pv} v' + C_{Pr} r' \right\} \right] \tag{2.37}$$

$$1 - w_P = 1 - w_{P0} \cos^2(k_w v_P) + k_{w1} v_P \tag{2.38}$$

$$1 - w_P = 1 - w_{P0} \exp(- C v_P'^2) \tag{2.39}$$

$$1 - w_P = (1 - w_{P0}) + C_1 v' + C_2 r' + C_3 v'^2 + C_4 v' r' + C_5 r'^2 \tag{2.40}$$

with v'_P the non-dimensional lateral velocity component at the propeller defined as:

$$v'_P = v' + x'_P r' \tag{2.41}$$

and x'_P the non-dimensional longitudinal position of the propeller referred to the origin of the co-ordinate system. According to the MMG working group the wake factor is also influenced by the propeller loading which contribution is restricted to the wake factor at straight ahead motion:

$$(1 - w_{P0}) = b_0 + b_1 J_S \tag{2.42}$$

$$(1 - w_{P0}) = b_0' + b_1' J_S + b_2' J_S^2 \tag{2.43}$$

Propeller induced lateral force and yawing moment can be considered to be proportional to the square of the propeller rate [49]:

$$Y_P = \rho n^2 D_P^4 Y_P^*$$
$$N_P = \rho n^2 D_P^5 N_P^* \tag{2.44}$$

2.2.5 Hydrodynamic force contribution of a rudder

The hydrodynamic forces and moment generated by rudder action are expressed as:

$$X_R = -(1 - t_R) F_N \sin \delta_R$$
$$Y_R = -(1 + a_H) F_N \cos \delta_R \tag{2.45}$$
$$N_R = -(x_R + a_H x_H) F_N \cos \delta_R$$

These expressions are based on a positive rudder angle δ_R for a rudder deflection to starboard. The different elements in formula (2.45) are modelled using the following expressions and approximations:

- The total rudder force F_R is composed of a normal force F_N, perpendicular to the rudder chord, and a tangential force $F_{T,}$ parallel to the rudder chord. The contribution of the tangential force is considered to be negligible.

□ (1-t_R) is an experimental coefficient incorporating a reduction of resistance compared to the longitudinal force component acting on the rudder. Realistic values for this parameter are 0.7 to 0.8.

□ Rudder deflection not only generates a lateral force component on the rudder, but due to the disturbed flow around the hull a lateral hull force is induced proportional to the lateral rudder force (fraction a_H). The parameter x_H denotes the longitudinal position of the point of application of this additional hull force.

□ The parameter a_H depends on the distance between the aft body and the rudder, but is not clearly influenced by the ship motions. The influence of propeller loading and ship form are not fully examined but a decrease of a_H at increasing propeller loading is observed.

2.2.5.1 Rudder normal force F_N

The non-dimensional rudder normal force F'_N for the rudder in the propeller slipstream is:

$$F'_N = \frac{F_N}{\frac{\rho}{2}LdV^2}$$

$$= \frac{\frac{\rho}{2}A_R V_R^2 f_\alpha(\Lambda_R, \alpha_R)}{\frac{\rho}{2}LdV^2}$$

$$= \left(\frac{A_R}{Ld}\right)f_\alpha(\Lambda_R, \alpha_R)\left(\frac{V_R}{V}\right)^2$$

(2.46)

A_R and Λ_R are the rudder area and the aspect ratio of the rudder, respectively.

The gradient of the normal force coefficient f_α on a rudder moving separately in open water can be measured during open water rudder tests with the rudder submitted to a uniform flow with an inflow angle α_R or can be estimated based on Fujii's formula [50]:

$$f_\alpha(\Lambda_R, \alpha_R) = \frac{6.13\Lambda_R}{2.25 + \Lambda_R}\sin\alpha_R$$

(2.47)

For a rudder in a non-uniform flow behind the hull and the propeller the effective inflow velocity and inflow angle are:

$$V_R = \sqrt{u_R^2 + v_R^2}$$

(2.48)

$$\alpha_R = \delta_R - \text{Arctan}\left(\frac{-v_R}{u_R}\right)$$

(2.49)

2.2.5.2 Longitudinal component of the effective inflow velocity at the rudder: u_R

The rudder area is separated in two different flow areas:

□ At the upper and/or lower extremities of the rudder the flow velocity is not accelerated by a propeller. The flow is considered to be proportional to the flow velocity u_P behind the hull:

$$u_{R0} = \varepsilon u_P$$

(2.50)

According to [51] the wake factor at the rudder during a straight ahead motion w_{R0} differs from the wake factor at the propeller w_{P0} due to the interactions between hull, propeller and rudder. The coefficient ε is defined as:

$$\varepsilon = \frac{1 - w_{R0}}{1 - w_{P0}}$$ (2.51)

and is determined experimentally.

□ Depending on the rudder height to propeller diameter ratio, $\eta = H/D_P$, the inflow velocity into the rudder can be accelerated by a propeller. According to the momentum theory of an actuator disk the propeller induced rudder inflow velocity is:

$$u_{RP} = u_{R0} + k_x u_P \left(\sqrt{1 + \frac{8K_T}{\pi J^2}} - 1 \right)$$

$$= \varepsilon u_P + k_x u_P \left(\sqrt{1 + \frac{8K_T}{\pi J^2}} - 1 \right)$$ (2.52)

$$= u_P \left[\varepsilon + k_x \left(\sqrt{1 + \frac{8K_T}{\pi J^2}} - 1 \right) \right]$$

k_x is a function of the axial position of the rudder relative to the propeller (0.5 at the point of the propeller centre and 1 infinitely far downstream of the propeller). The effective rudder inflow velocity u_R can be expressed by a simple weighted average depending on the two flow areas:

$$u_R = \sqrt{\eta u_{RP}^2 + (1 - \eta) u_{R0}^2}$$ (2.53)

A simpler form for expression (2.53) based on (2.52)

$$u_R = \varepsilon u (1 - w_P) \sqrt{\eta \left\{ 1 + k \left(\sqrt{1 + \frac{8K_T}{\pi J^2}} - 1 \right) \right\}^2 + (1 - \eta)}$$ (2.54)

is

$$u_R = \varepsilon u_P \sqrt{1 + k \frac{8K_T}{\pi J^2}}$$ (2.55)

Some expressions reported on the MMG mathematical model use the propeller slip ratio instead of the thrust coefficient.

$$u_R = u_P \sqrt{1 + ks^{1.5}}$$ (2.56)

with the propeller slip ratio s

$$s = 1 - \frac{u_P}{nP}$$ (2.57)

2.2.5.3 Lateral component of the effective inflow velocity at the rudder: v_R

The flow at the rudder of single-screw ships is characterized by an asymmetry due to the propeller action even in a straight ahead motion. Consequently the rudder normal force F_N is non zero for a rudder in the neutral position. An offset rudder angle δ_0 is required to counteract the asymmetrical flow at the rudder which induces a lateral velocity component

$$v_R = \delta_0 u_R = k_P s u_R$$ (2.58)

The coefficient k_P has to be determined experimentally.

Due to swaying and yawing the lateral component of the effective inflow velocity at the rudder is increased by:

$$v_R = k_P s u_R + g(v', r')$$ (2.59)

Different expressions for the lateral velocity component and, consequently, for the effective

33

inflow angle α_R in the MMG model can be found in literature:

- In [12]

$$v'_R = v' + x'_R\, r' + C_R |v'| v'$$

(2.60)

The lateral velocity component is composed of the velocity at the rudder due to swaying and yawing and a component, the last term in equation (2.60) which is caused by the apparent down-wash effect due to the presence of the hull and the propeller.

$$\alpha_R = \delta_R - \alpha_0 = \delta_R - \text{Arctan}\left(\frac{-v'_R}{u'_R}\right) = \delta_R - \gamma\left(\frac{-v'_R}{u'_R}\right) = \delta_R + \gamma\left(\frac{v'_R}{u'_R}\right)$$

(2.61)

γ is a coefficient for flow-angle-correction or flow-straightening and is experimentally determined together with C_R. x'_R is the x-coordinate of the application point of the rudder normal force.

- In [46]

$$v'_R = v' + x'_R\, r'$$

(2.62)

$$\alpha_R = -(\delta_R - \delta_0) - \gamma\left(\frac{v'_R}{u'_R}\right)$$

(2.63)

The coefficient x'_R incorporates the contribution of the yaw velocity to the lateral rudder velocity compared to the lateral velocity v'. Although this coefficient is expected to coincide with the axial position of the rudder, experimentally determined values for x'_R can be twice as large as the geometrical co-ordinate x_R of the rudder.

- In [52] and [53]

$$v'_R = u'_R\,\beta_R = u'_R\,(\beta - 2x'_R\, r')$$

(2.64)

$$\alpha_R = \delta_R(+\delta_0) - \gamma\beta_R$$

(2.65)

In these expressions x'_R is approximated by -0.5.

- In [29]

$$v_R = k_P s u_R + V g(v' + l_R' r')$$

(2.66)

l'_R is an experimental coefficient twice as large as the longitudinal position of the rudder.

2.3 HSVA four-quadrant mathematical model, Germany

2.3.1 Introduction

The MMG model described above was initially intended to deal with manoeuvres retaining considerable forward speed. To increase the range of application of the model new features such as stopping and manoeuvring in shallow water at lower speeds have been added to the basic structure of the mathematical model. Contrary to this, the improved model of hull-propeller-rudder interactions fully described by Oltmann and Sharma in 1985 [13] is implemented based on the four-quadrant concept which means that a mathematical model must cover wide ranges of manoeuvres and must be applicable in all quadrants of operations (speed and propeller reversal included).

2.3.2 Equations of motion

The equations of motion of a surface ship manoeuvring in the horizontal plane with three degrees of freedom are extended with a dynamic equation for the simulation of engine

manoeuvres:

$$m\left(\dot{u} - vr - x_G r^2\right) = X$$
$$m\left(\dot{v} + ur + x_G \dot{r}\right) = Y$$
$$I_{zz}\dot{r} + mx_G\left(\dot{v} + ur\right) = N \tag{2.67}$$
$$2\pi \dot{n} I_{EP} = Q_E - Q_P$$

The propeller torque Q_P depends mainly on the longitudinal velocity component u and the propeller rate n, while the engine torque Q_E depends essentially on the propeller rate n and some engine characteristics such as the fuel rate.

To ensure a wide range of applications the model is based on the introduction of the following four angles:

$$\beta = \text{Arctan2}\left(-v, u\right)$$
$$\gamma = \text{Arctan2}\left(rL_{PP}, 2u\right)$$
$$\delta_e = \delta_R + \beta_R = \delta_R + \text{Arctan2}\left(-v_R, \overline{u}_R\right) \tag{2.68}$$
$$\varepsilon = \text{Arctan2}\left(u_P, c_P\right) = \text{Arctan2}\left(u_P, 0.7\pi n D_P\right)$$

The force expressions in the mathematical model will remain valid for all four quadrants of these four angles incorporating the five dynamic variables u, v, r (velocity components), rudder angle δ_R and propeller rate n. The drift angle β and the yaw rate angle γ define all possible motions of ship's hull through the water. The angle δ_e is the effective rudder angle and the angle ε represents a four-quadrant notation of all possible combinations of propeller rate of turn (forward and backward propeller) and longitudinal velocity component u_P (ahead and backward motion).

The development of a four-quadrant model is based on the following assumptions:

☐ The force components are partly decomposed into contributions associated with the system elements of a manoeuvring ship (hull, propeller and rudder) and with the physical mechanisms such as ideal fluid (I), hull lifting (HL) and cross-flow effects (HC).

$$X = X_H + X_P + X_R = X_I + X_{HL} - R_T + X_P + X_R$$
$$Y = Y_H + Y_P + Y_R = Y_I + Y_{HL} + Y_{HC} + Y_P + Y_R \tag{2.69}$$
$$N = N_H + N_P + N_R = N_I + N_{HL} + N_{HC} + N_P + N_R$$

☐ Intermediate variables have been introduced to account for the interactions between hull, propeller and rudder such as wake factor, thrust deduction, slipstream, flow rectification.

☐ A wider set of physically motivated functions are used together with polynomial functions to achieve sufficient accuracy.

☐ The four-quadrant model is simplified based on the nearly perfect port-starboard symmetry of a ship. The only relevant asymmetry is caused by the slipstream of a single screw propeller and is modelled based on the terms Y_P and N_P. Due to this simplification the forces need only to be presented in the first two quadrants utilizing symmetric or anti-symmetric functions of the angles β, γ and δ_e.

2.3.3 Hydrodynamic force contribution of a hull

2.3.3.1 Ideal fluid effects

Based on experiments the forces related to the "ideal fluid" effects contain terms involving accelerations and velocities:

$$X_I = X_{\dot{u}}\dot{u} + X_{vr}vr + X_{rr}r^2 + X_{vv}v^2$$

$$Y_I = Y_{\dot{v}}\dot{v} + X_{\dot{u}}ur + Y_{\dot{r}}\dot{r}$$

(2.70)

$$N_I = N_{\dot{r}}\dot{r} + N_{\dot{v}}(\dot{v} + ur) + (Y_{\dot{v}} - X_{\dot{u}})uv$$

These expressions deviate from the strict potential theory as the latter would require:

$$X_{vr} = -Y_{\dot{v}}, X_{rr} = -Y_{\dot{r}} = -N_{\dot{v}}, X_{vv} = 0$$

However, the goal of the modelling was to simulate the real effects occurring during model experiments after the pattern of potential theory which revealed for example a significant inequality of the derivatives X_{vr} and $-Y_{\dot{v}}$.

2.3.3.2 Hull lifting effects

For a pure drift motion the displacement hull acts like a slender lifting body generating a lift force F_L and a drag force F_D. The projection of the resultant force on the y-axis gives a yawing moment:

$$X = F_L \sin\beta - F_D \cos\beta$$

$$Y = F_L \cos\beta + F_D \sin\beta$$

$$N = x_F Y = -\frac{b_3}{b_1}L_{pp}(sgn\,u)\,Y$$

(2.71)

$$F_L = b_1 Ld\frac{\rho}{2}\left(u^2 + v^2\right)\cos\beta\sin\beta$$

$$F_D = b_2 F_L \cos\beta\sin\beta$$

For pure yawing comparable expressions as (2.71) are used modifying the drift angle β by the angle:

$$\gamma^* = Arctan2(krl(sgn\,u),u) = Arctan2(v^*,u)$$

(2.72)

which differs from the yaw rate angle by introducing a constant k to average the locally variable transverse velocity.

A combination of drift and yaw motions gives rise to the hull lifting forces and yawing moment:

$$X_{HL} = \frac{\rho}{2}Ld\frac{u(b_1'v^* - b_1 v)}{\sqrt{u^2 + (v^* - v)^2}}\left[(v^* - v) - \frac{u^2(b_2'v^* - b_2 v)}{u^2 + (v^* - v)^2}\right]$$

$$Y_{HL} = \frac{\rho}{2}Ld\frac{u(b_1'v^* - b_1 v)}{\sqrt{u^2 + (v^* - v)^2}}\left[1 + \frac{(b_2'v^* - b_2 v)(v^* - v)}{u^2 + (v^* - v)^2}\right]$$

(2.73)

$$N_{HL} = -\frac{\rho}{2}L^2 d\frac{u(b_3'v^* - b_3 v)}{\sqrt{u^2 + (v^* - v)^2}}\left[1 + \frac{(b_2'v^* - b_2 v)(v^* - v)}{u^2 + (v^* - v)^2}\right]$$

Considering the notation, the coefficients b_1, b_2, b_3 and b'_1, b'_2, b'_3 differ from the coefficients used in [13] to account for the preferable ITTC symbols for the hull characteristics (for example draught d). These coefficients are experimentally determined and to obtain a favourable accuracy a distinction can be made for a positive or negative longitudinal velocity component u.

2.3.3.3 Cross-flow effects

Forces due to cross flow can not be ignored given that the hull is designed to have a low longitudinal and a high transverse resistance. According to the strip theory the non-linear lateral force and yawing moment can be written as:

$$Y_{HC} = -\frac{\rho}{2}\int_{-l_a}^{l_f} d(x)C_{CFD}(x)|v+rx|(v+rx)dx$$

$$\text{(2.74)}$$

$$N_{HC} = -\frac{\rho}{2}\int_{-l_a}^{l_f} d(x)C_{CFD}(x)|v+rx|(v+rx)xdx$$

Expression (2.74) can be transformed into expression (2.3) equalizing the length of the aft body l_a and the fore body l_f to the length l (half the ship length L_{pp}). The local cross flow drag coefficient $C_{CFD}(x)$ at the longitudinal position x is modelled by a polynomial of higher order:

$$C_{CFD}(x) = a_0 + a_7\left(\frac{x}{l}\right)^7 + a_8\left(\frac{x}{l}\right)^8 + a_9\left(\frac{x}{l}\right)^9 \qquad \text{(2.75)}$$

2.3.3.4 Hull resistance

The longitudinal resistance force acting on a hull during a straight ahead or backward motion is modelled based on a third order polynomial:

$$R_T(u) = R_{Tu}u + R_{Tu|u|}u|u| + R_{Tuuu}u^3 \qquad \text{(2.76)}$$

Different coefficients can be introduced for forward or backward motion to increase the model accuracy.

2.3.4 Hydrodynamic force contribution of a propeller

The conventional representation of propeller characteristics in terms of advance coefficient J and thrust and torque coefficient K_T and K_Q is not favourable while developing a four quadrants of operation model. Therefore, to cover all possible combinations of axial and rotational motion a four quadrants representation is based on the advance angle ε and the coefficient C_T and C_Q:

$$C_T = \frac{T_P}{\frac{\rho}{2}A_0\left(u_P^2 + c_P^2\right)}$$

$$\text{(2.77)}$$

$$C_Q = \frac{Q_P}{\frac{\rho}{2}A_0D_P\left(u_P^2 + c_P^2\right)}$$

The axial velocity u_P is defined as in section 2.2.4, while the circumferential blade velocity is $c_P=0.7\pi nD_P$. The advance angle ε is defined in (2.68).

For the first quadrant of operation a good precision is essential within the range $[0,\varepsilon_0]$ for the advance angle with ε_0 the advance angle at zero propeller thrust. A tabular model is preferred within this range while expressions as (2.78) can be used for the remaining range of the first quadrant and the other quadrants.

$$C_T(\varepsilon) = A_T \cos\varepsilon|\cos\varepsilon| - B_T \sin\varepsilon|\sin\varepsilon|$$

$$\text{(2.78)}$$

$$C_Q(\varepsilon) = A_Q \cos\varepsilon|\cos\varepsilon| - B_Q \sin\varepsilon|\sin\varepsilon|$$

In [13] the interaction coefficients wake factor and thrust deduction are modelled as constant values depending on the motion direction, although complicated variations of wake factor and thrust deduction with the advance angle have been revealed.

The lateral force and yawing moment induced by propeller asymmetry of a single screw ship are rather small for a motion ahead with positive propeller rate while the influence increases for a propeller thrusting astern.

Horizontal forces and yawing moment are summarized as:

$$X_P = (1-t)T_P$$
$$Y_P = Y_{PT}T_P \tag{2.79}$$
$$N_P = N_{PT}T_P$$

2.3.5 Hydrodynamic force contribution of a rudder

The mathematical model of the rudder contribution to the horizontal forces and yawing moment is based on two assumptions:

□ For a rudder outside the propeller slipstream the interaction between hull and rudder is represented by the wake factor at the position of the rudder w_R and the flow rectification factor k_{HR}. The longitudinal and transverse flow velocity components into the rudder are:

$$u_R = (1-w_R)u$$
$$v_R = k_{HR}(v+rx_R) \tag{2.80}$$

The effective rudder inflow angle δ_e defined in (2.68) is based on the rudder angle δ_R and the local drift angle β_R. Hydrodynamic forces and moment induced by a rudder are:

$$X_R = \frac{\rho}{2}A_R(u_R^2 + v_R^2)(C_{LR}\sin\beta_R - C_{DR}\cos\beta_R)$$

$$Y_R = \frac{\rho}{2}A_R(u_R^2 + v_R^2)(C_{LR}\cos\beta_R + C_{DR}\sin\beta_R) \tag{2.81}$$

$$N_R = Y_R x_R$$

□ The inflow velocity into a rudder, located in the propeller slipstream, u_{RP} is increased compared to velocity u_R and can be modelled based on the elementary momentum theory. According to [13] the additional influence of the propeller on the inflow velocity at the rudder requires a tedious procedure involving several steps, of which only a simplified version is presented in [13]. The axial velocity increment in the slipstream at infinity is:

$$u_{A\infty} = (\text{sgn}\,u)\sqrt{u_P^2 + (\text{sgn}\,u)\frac{2T_P}{\rho A_0}} - u_P \tag{2.82}$$

The axial velocity at the position of the rudder becomes:

$$u_{RP} = u_P + \left[\left(k_{PR} - \frac{1}{2}\right)(\text{sgn}\,u) + \frac{1}{2}\right]u_{A\infty} \tag{2.83}$$

The coefficient k_{PR} has the same meaning as coefficient k_X in (2.52) and depends on the relative distance between the propeller and the rudder and takes a value within the range [0.5,1].

The rudder area A_{RP} influenced by the velocity u_{RP} can be estimated based on the diameter of the propeller slipstream D_{RP} at the position of the rudder given by the condition of continuity:

$$D_{RP}^2 u_{RP} = D^2\left(u_P + \frac{1}{2}u_{A\infty}\right) \tag{2.84}$$

Considering a rudder partially immersed in the slipstream the average axial velocity can be defined by:

$$\overline{u_R^2} = \frac{1}{A_R}\left[A_{RP}u_{RP}^2 + (A_R - A_{RP})u_R^2\right] \tag{2.85}$$

The horizontal force components and yawing moment X_R, Y_R and N_R represent the total system response to rudder application and not merely the forces acting on the rudder itself. Therefore,

the lift and drag characteristics of a rudder in the behind ship condition are not only based on the open water characteristics C_{LR}^0 and C_{DR}^0 but take into account the effect of propeller loading and hull-propeller-rudder interaction:

$$C_{LR} = \left(1 + k_{LR} \frac{u_P}{u_R}\right) C_{LR}^0$$

$$C_{DR} = \left(1 + k_{DR} \frac{u_P}{u_R}\right) C_{DR}^0$$

(2.86)

The equations for the horizontal force components and yawing moment (2.81) are transformed into:

$$X_R = \frac{\rho}{2} A_R \left(\overline{u}_R^2 + v_R^2\right)\left(C_{LR} \sin\beta_R - C_{DR} \cos\beta_R\right)$$

$$Y_R = \frac{\rho}{2} A_R \left(\overline{u}_R^2 + v_R^2\right)\left(C_{LR} \cos\beta_R + C_{DR} \sin\beta_R\right)$$

$$N_R = \left(1 - k_{NR} \frac{u_P}{u_R}\right) Y_R x_R$$

(2.87)

Equivalent expressions for the coefficients t_R, a_H and x_H which were introduced in the MMG model, are here incorporated in the modified characteristics C_{LR} and C_{DR} and the coefficient k_{NR} which are function of or multiplied with the ratio of inflow velocity into the propeller u_P to the average flow velocity at the rudder $\overline{u}_R$.

2.4 DEN-Mark 1 model, Denmark

2.4.1 Introduction

DEN-Mark 1 was the 5th generation of software for surface ship manoeuvring simulation developed and programmed at DMI (Danish Maritime Institute, now Force Technology) and reported by Jensen [54] and Chislett [55]. DEN-Mark 1 is an acronym for DMI Eclectic Nomenclature Mark 1. The model is innovative thanks to the use of look-up tables, the so-called tabulated shape coefficients, instead of hydrodynamic derivatives. This change of representation was finally made in 1990 and resulted in a total re-formulation and re-programming of the available manoeuvring simulation software.

The global design objectives and the strategies used to implement them in DEN-Mark 1 can be summarized as:

- □ Objectives:
  Simulation of arbitrary objects in 6 DOF
  Real-, fast-time, interactive and batch modes
  Training and research capability
  Optional degree of detail and cost at user-level
  User and future friendliness

- □ Strategies:
  Strictly physically motivated mathematical models
  Full utilisation of specialist-field knowledge
  Data in non-dimensional form
  Data in cubic-splined tabular form
  Compatibility with traditional data forms
  Model building via symbolic data
  Modular and separable data structure
  Structured software development methods

The objectives and strategies of the DEN-Mark 1 model coincide well with the four requirements of mathematical manoeuvring models listed in section 1.2.6. They meet in to the required functionality, validity, expandability and adjustability of mathematical manoeuvring models and they could definitely be used as basic assumptions of the mathematical model developed and described in the following chapters.

2.4.2 The equations of motion

The equations of motion based on Newton's second law are implemented in a general form with 6 DOF, but the actual number of DOF is user defined to be 3 (surge, sway, yaw), 4 (includes also roll) or 6.

The concept of shape coefficients is linked with the non-dimensional representation of the hydrodynamic force contributions acting on a manoeuvring vessel. In the DEN-Mark 1 model all fluid dynamic forces are made non-dimensional using a stagnation pressure, $1/2\rho AV^2$, in which A is a characteristic area and V is a characteristic flow velocity. Corresponding moments are written in non-dimensional form adding a physically motivated lever. *"When choosing a characteristic velocity, it is convenient to ensure that the related dimensional force is zero when the velocity is zero. Coefficients are then defined to be zero, to avoid numerical problems"* [55]. The resulting non-dimensional force coefficients can be referred to as shape coefficients the values of which are solely dependent on the flow pattern or shape and independent of size (A), speed (V) and density (ρ).

The non-dimensional independent variables of the different mathematical modules are divided into two sets of variables according to the shape characteristics of the flow patterns: the *boundary shape* and the *trajectory shape* variables. A few examples for the boundary shape variables are the depth to draught ratio, the rudder angle, the length to beam ratio, the block coefficient; typical trajectory shape variables are the drift angle, the yaw rate angle and the trim and heel angle. In the DEN-Mark 1 model all fluid dynamic force data are expressed as functions of physically motivated, non-dimensional parameters of these types.

2.4.3 Tabular functions

Hydrodynamic forces and moments are expressed in generalised, non-dimensional, tabulated form. The tables consist of one, or at most two independent variables. More complicated functions can therefore be built by optionally adding and/or multiplying any number of one or two dimensional tabulated functions together.

2.4.4 Hydrodynamic contributions of a hull

Although most data are in tabular form, the use of a derivative representation for acceleration dependent coefficients is recommended due to the nature of this hydrodynamic influence. Further on, the tabular representation of drift angle and yaw rate hydrodynamics are mentioned in [55].

Horizontal force components and yawing moment due to drift motion are made non-dimensional based on the lateral hull area $L_{PP}d$ and the total ship speed and are defined as functions of the drift angle β. The only real difference with other four-quadrant representations of this contribution is the use of tabulated functions instead of a polynomial expression.

Horizontal force components and yawing moment due to yawing are made non-dimensional based on the lateral hull area and the total velocity of the FP (forward perpendicular) V_C:

$$V_C^2 = u^2 + v^2 + (rL_{PP}/2)^2 = U^2 + (rL_{PP}/2)^2 \tag{2.88}$$

These force contributions are defined as functions of a newer yaw rate angle γ based on the total velocity U instead of the longitudinal velocity component u:

$$\gamma = \text{Arctan2}(rL_{PP}, 2U) \tag{2.89}$$

Compared to the yaw rate angle introduced by Oltmann and Sharma in [13] which is a function of the drift angle β as:

$$\tan\gamma = \frac{rL_{PP}}{2u} = \frac{rL_{PP}}{2U\cos\beta} \tag{2.90}$$

both yaw rate angles do not differ for small drift angles, contrary to large drift angles [55].

2.4.5 Hydrodynamic contributions due to a propeller and a rudder

Analogous to propeller loading a *Rudder Loading* concept is introduced where the rudder loading depends on slipstream velocity and speed of advance at the rudder. A non-dimensional representation of rudder forces can be based on water density, rudder area and average speed squared at the rudder which is usually calculated on propeller thrust according to [56] (discussion by Thulin S.A.R.) or equation (2.85). The introduction of a rudder loading angle in [55], defined by:

$$\xi = \text{Arctan}\left(\frac{u_A}{u_S}\right) = \text{Arctan}\left(\frac{u_R}{u_S}\right) \tag{2.91}$$

is proven to be indispensable to express the different combinations of speed of advance at the rudder u_A or u_R and slipstream speed at the rudder u_S. The same value of the averaged velocity at the rudder ($\overline{u}_R$ according to Oltmann and Sharma) can be obtained with a wide range of different combinations of u_A and u_S.

The ratio of two in-line velocities in (2.91) to define a four-quadrant angle is an artificial method in this case but provides relevant measures of the characteristic variations in flow geometry.

2.5 Pros and cons of described mathematical models

The mathematical models described in this chapter will form the basis for the modelling in the chapters 4 to 6. Some model partitions will be evaluated on their explicit usefulness judging the proposed expressions while for other modules only the general philosophy will be followed. Although pros and cons especially reveal during the modelling process, the main advantages and disadvantages can be summarized as:

Pros

❑ All these models have a modular character which contributes to the requirements of adjustability and expandability of a flexible mathematical model describing ship manoeuvrability.

❑ The models are based on a physical background for each module, namely hull, propeller and rudder, so that the horizontal force components and yawing moment are related to existing phenomena described through open water characteristics of the propeller and the rudder and the kinematical and control variables.

❑ The DEN Mark 1 model uses explicitly tabular forms so that the restrictions of polynomial expressions can be avoided.

Cons

❑ The four quadrants of operation are not fully applied in the MMG model, while for the HSVA model some derived coefficients like thrust deduction are only represented by constant values. The description of the DEN Mark 1 model is rather vague and although the ideas are promising the implementation of a concept like Rudder loading seems to be difficult in practice [57].

❑ Low speed manoeuvring or the availability of wide ranges of hydrodynamic inflow angles into the hull, the propeller and the rudder can be consequently found in the HSVA model but the detailed impact of speed-propeller rate combinations differing from self-propulsion on coefficients related to the propeller and the rudder module are not fully described and sometimes only expected.

- The advantage of a modular character for the mathematical manoeuvring model is also linked with the use of the open-water characteristics of for example propeller and rudder. In the HSVA model these characteristics are found judging the Wageningen B-series values for the propeller thrust and torque and the coefficients C_{LR}^0 and C_{DR}^0 for the rudder open-water characteristics. For the DEN Mark 1 model the exchange of rudder profiles will be much more difficult as rather specific measured lift coefficients C_L are considered in the rudder loading concept.

3 Determination of mathematical manoeuvring models

Different methods which can be used to determine the mathematical manoeuvring models or to predict the manoeuvring characteristics of a ship, are summarized in 3.1 with an emphasis on experimental fluid dynamics (EFD). The historical overview of EFD and the widespread accepted guidelines give some insight into captive model testing. A description of the Towing Tank for Manoeuvres in Shallow Water at Flanders Hydraulics Research (FHR) is given in 3.2, accompanied by an outline of the testing apparatus and the ship models. The harmonic sway and yaw test, generally accepted test types, are described in detail in 3.3. The alternative non-harmonic PMM sway test and the multi-modal test are test types which have been introduced to overcome some disadvantages of a conventional PMM sway test on the one hand or to enlarge the amount of parameters that can be varied during one test run on the other.

According to the concept of the four quadrants of operation, the test programs for a tanker and a containership are tabulated in 3.4, denoting important information about test type, Froude number, drift angle, propeller rate and rudder angle for the determination of the mathematical models. Some inaccuracies detected during specified test runs are discussed in 3.5 and the results could be used for the development of a physical test program for quality control. Analyzing the measurements, different methods will be used in 3.6: i.e. a Fourier analysis and a regression analysis.

3.1 Determination methods

The determination of mathematical manoeuvring models or the prediction of manoeuvring characteristics of a ship can be based on different methods [58]:

❑ The *database method*, an empirical method, can be considered if a database is provided of the manoeuvring characteristics from full scale ship trials and free-sailing model tests, characterized by a freely moving ship model driven by its own propeller and rudder. The manoeuvring characteristics of a new design can be estimated making use of the database results *without any simulation*. Variations in dimensions and sections are only justified if they lie within the range of available geometrical data of the ships.

❑ If the dimensions and ship form are far from those of the database, a mathematical manoeuvring model will be determined and a *simulation* will be executed to evaluate the manoeuvring characteristics. This mathematical manoeuvring model can be based on different determination methods which are classified in system based manoeuvring simulation and computational fluid dynamics (CFD) based manoeuvring simulation.
   o The *database method* can also be applied to the database of hydrodynamic forces and derivatives, a semi-empirical method where the hydrodynamic derivatives are determined as function of e.g. ship's dimensions, frame lines or the shape of the aft body, trim, environmental parameters like water depth.
   o *System identification* based on e.g. neural networks, will be used for the determination of the simulation models based on the measured ship motion and applied rudder angle during free-sailing model tests or full scale ship trials. In [58] this method is defined as "*a systematic approach to find a model of unknown system from the given input-output data. For the successful system identification three items should be properly selected or designed; mathematical model of a system, input-output data and parameter estimation scheme.*"
   o The coefficients of the mathematical model can also be determined based on captive model tests, the most traditional method. Both methods which make use of model tests can be summarized as methods of *experimental fluid dynamics (EFD)*.
   o This method is in contrast with the *computational fluid dynamics (CFD)*, computational methods like inviscid flow and RANS (Reynolds Averaged Navier-Stokes) methods which nowadays are also used for the prediction of unsteady ship motions and manoeuvring. A great progress has been made but difficulties

still remain e.g. concerning the inclusion of environmental effects as shallow water. Therefore, to increase the credibility of simulations based on CFD, verification and validation are still necessary and could be based on EFD validation data.

Considering this summary, model experiments still represent one of the most important techniques for the prediction of ship manoeuvring using mathematical models. With the installation of the Towing Tank for Manoeuvres in Shallow Water (co-operation Flanders Hydraulics Research – Ghent University) in 1992, Flanders has chosen for a determination of ship manoeuvring related problems using captive model tests.

3.1.1 Historical overview of EFD for the prediction of ship manoeuvrability

After the experience in the prediction of ship resistance and ship propulsion based on experiments in a tank, the prediction of ship manoeuvrability required a further step in the development of experimental techniques. A mathematical model of the hydrodynamic forces on a manoeuvring ship was first of all based on a linear analysis (see section 3.6.1) where a distinction was made between the components of hydrodynamic forces in phase and in quadrature with the imposed displacement of the model.

The simplest test is the steady-state oblique tow test in which the model is towed at a constant velocity and at various drift angles to the direction of motion [34] (Figure 3.1). Velocity dependent forces and moment or velocity derivatives could be determined although a lack of information about the acceleration derivatives still remained.

To obtain the derivatives due to an angular velocity of yaw attempts had been made to employ curved models in a straight towing tank. This method of towing a curved model along a straight path instead of towing a straight model along a circular path is taken from aerodynamic theory. In practice, this experiment was too complicated as a new model had to be constructed for each curvature. A rotating arm facility (Figure 3.2) by means of which a ship model can be towed along circular paths offered a solution to the problem of deriving velocity derivatives due to yawing although the need of a large tank and the limited flexibility of this facility proved to be important drawbacks.

The introduction in the early 1960s of the Planar Motion Mechanism (PMM, the history of PMM and PMM systems is outlined in Table 1 of [34]), pioneered by Gertler and Goodman by first using this mechanism in the 1950s for aircrafts and submarines, was a major step forward in the development of the experimental technique. This facility allowed the determination of sway acceleration and yaw dependent forces and moments in a relatively narrow tank. Due to mechanical constraints and limitations of available post-processing techniques, PMM systems of the first generation were only able to perform sinusoidal motions of sway and yaw. Some disadvantages can be recognised:

❏ although manoeuvring behaviour is generally considered as a quasi-steady problem, non-stationary effects are introduced due to the experimental technique
❏ moreover, the applied motions can hardly be considered as realistic.

Later on, a large amplitude planar motion mechanism has been designed which operates in the same way as the first generation PMM but which offers an increased range of prescribed motions thanks to the increased number of parameters that can be imposed. Some frequency effects which are inextricably linked with oscillatory testing can be overcome (see section 3.2).

Thanks to the development of computerised planar motion carriages (CPMC, [59]), the harmonic character of the trajectories implied to the ship models can no longer be considered as a restriction. However, the traditional techniques of performing captive manoeuvring tests with ship models were not fundamentally modified by the introduction of the CPMC.

The technique of EFD which uses scale models can be subdivided into two main groups [35]:

free-sailing models and constrained (or captive) models. The first group was especially invoked for the determination of the characteristics of a new design of ship. Standard manoeuvres should reveal the improvements thanks to modifications made to the design. For constrained models model testing is performed to provide data on forces and moments acting on the ship model subjected to a prescribed motion. The potential of this so-called captive model testing compared to free model testing, is the possibility to predict ship's behaviour under circumstances which differ from self propulsion or a condition where the model is running freely.

3.1.2 Existing guidelines for PMM testing [60]

Compared with stationary tests (e.g. oblique towing, rotating arm), the number of parameters determining a PMM test is rather large. Furthermore, the parameters cannot always be chosen independently, or the choice may be restricted by the concept of the mechanism or the tank dimensions. The guidelines for PMM testing which will be discussed in this section are based on some publications of the International Towing Tank Conference:

- ❑ [61] ITTC 1999, Seoul and Shanghai
- ❑ [62] ITTC 2002, Venice
- ❑ [63] ITTC Quality Systems Manual
- ❑ [64] ITTC Questionnaire discussed in MARSIM2000

If the model length L and the forward speed u are chosen, following parameters have to be determined (see also Figure 3.3 and Figure 3.4):

- ❑ oscillation frequency ω or period $T=2\pi/\omega$;
- ❑ number of cycles c;
- ❑ amplitudes of sway/yaw velocity and acceleration;
- ❑ static drift angle β (for PMM yawing tests);
- ❑ control variables: rudder angle δ_R, propeller rate n.

Ranges for β, δ_R, n have to be selected according to the application area of the mathematical manoeuvring model. This is in principle also the case for the range of acceleration and velocity amplitudes, but frequency and motion amplitude cannot be combined without restrictions. The obtained combinations of accelerations and velocities should be realistic, which can e.g. be found by considering low frequency rudder actions, as was recommended by Van Leeuwen [65], although this author admitted that such an approach leads to impractically low test frequencies. Moreover, such a criterion cannot always be applied to harbour manoeuvres, where yawing motions are not only determined by rudder action, but also by tugs, bow and stern thrusters, etc.

Other restrictions for test frequency are related to:

- ❑ the non-stationary character of PMM testing: as most mathematical manoeuvring models are quasi-steady, memory effects in the experimental results should be avoided;
- ❑ the tank dimensions.

3.1.2.1 Restrictions due to tank length.

The fraction ℓ of the tank length covered during one oscillation cycle can be expressed non-dimensionally:

$$\ell' = \frac{\ell}{L} = \frac{uT}{L} = \frac{2\pi u}{L\omega} = \frac{2\pi}{\omega'} \tag{3.1}$$

with $\omega'=\omega L/u$. Denoting the useful tank length by ℓ_T, the number of oscillation cycles c is limited to:

$$c \le \frac{\ell_T}{\ell} = \frac{1}{2\pi} \ell'_T \omega' \tag{3.2}$$

Accuracy improves with increasing c, but this effect is rather restricted if c>3 [66].

3.1.2.2 Restriction due to limitations of lateral motion

Harmonic sway tests

In a non-dimensional notation, sway velocity and acceleration amplitudes depend on frequency ω' and lateral amplitude $y'_{0A} = y_{0A}/L$:

$$v'_A = \frac{v_A}{u} = y'_{0A}\,\omega'$$

$$\dot{v}'_A = \frac{\dot{v}_A L}{u^2} = y'_{0A}\,\omega'^2 \tag{3.3}$$

y'_{0A} is restricted due to limitations of the mechanism, or in order to avoid wall effects; with respect to the latter, van Leeuwen considers half the tank width as an upper limit for the trajectory width. As a result, velocity and acceleration amplitudes can only be controlled by variation of the oscillation frequency.

Harmonic yaw tests

Yaw velocity and acceleration amplitudes can be written in a non-dimensional way:

$$r'_A = \psi_A\omega'$$

$$\dot{r}'_A = \psi_A\omega'^2 \tag{3.4}$$

For small yaw amplitudes, the non-dimensional amplitude of the lateral motion of the ship model can be approximated by $y'_{0A} \approx \psi_A/\omega'$, which yields:

$$r'_A = \psi_A\omega' \approx y'_{0A}\,\omega'^2$$

$$\dot{r}'_A = \psi_A\omega'^2 \approx y'_{0A}\,\omega'^3 \tag{3.5}$$

so that, in a non-dimensional notation, yaw velocity and acceleration amplitudes also depend on the frequency ω' and the lateral amplitude y'_{0A}, as is the case for PMM sway tests.

3.1.2.3 Restrictions due to non-stationary effects

Tank resonance

If the PMM frequency equals a natural frequency of the water in the tank, a standing wave system may interfere with the tests [56]. This occurs if the wave length λ of the waves induced by oscillatory ship motions takes one of following values:

$$\lambda = 2W, W, \tfrac{2}{3}W, \tfrac{2}{4}W,... \tag{3.6}$$

W being the tank width. $\lambda = 2\pi/k$ depends on the water depth h, as $gk\,\tanh kh = \omega^2$; the critical frequency according to $\lambda = 2W$ decreases with decreasing water depth. Frequencies higher than this critical value result into unacceptable scatter.

Waves due to combined pulsation and translation

A pulsating source with frequency ω moving at speed u in a free surface induces a wave system with a pattern depending on $\Gamma = \omega u/g$ [67]. If Γ is small, the waves are located in a sector of 2x19°28'16" behind the source. The sector grows with increasing Γ, reaches 2x90° at $\Gamma = 0.25$ and decreases again at higher Γ. During PMM tests, Γ should be considerably less than 0.25 [68], [56].

Non-stationary lift and memory effects

Taking account of the quasi-steady nature of mathematical manoeuvring models, experimental data should not be affected by memory effects due to the application of non-stationary techniques. This requirement is generally formulated by a maximum value for ω'. Van Leeuwen's [65] philosophy leads to optimal ω' for PMM yaw tests depending on the non-dimensional yaw velocity amplitude. Most authors, however, recommend semi-empirical values for ω':

❑ $\omega' \leq 2\text{-}2.5$, according to Nomoto [69].

❑ Smitt and Chislett [56] recommend ω'=3 as a maximum. In a comment, Glansdorp states that for some derivatives (Y_v', N_r') ω' should be limited to 1-1.5. The authors reply that ω'=3 is applied to yaw tests; a safer upper limit for sway tests, which are more sensitive to frequency, is ω'=2.

❑ Milanov [70] formulated, more qualitatively, a similar conclusion.

Memory effects at larger ω' can be explained by interference between the model's swept path and its own (lateral) wake, leading to unrealistic flow phenomena. The interference pattern depends on ω', y_{0A}' or ψ_A, B/L.

Especially for harmonic sway tests, ℓ should not be too small, in order to avoid the model to move in its own wake Figure 3.5. A minimum value of 2.5 for ℓ', corresponding with $\omega'<2.5$, seems reasonable, but may cause practical problems at very low and zero speed y_{0A}/B should be sufficiently large, allowing the model to move laterally in 'unaffected' water.

For harmonic yaw tests, swept paths covered during successive half cycles interfere with each other if ω' exceeds a value which depends on ψ_A and B/L; $\omega'<$ 4 appears to be a realistic guideline.

3.1.2.4 Influence of trajectory errors

Vantorre's theoretical developments yield following conclusions [66]:

PMM sway tests

❑ With increasing frequency, the relative error on the damping component and, therefore, on Y_{uv}, increases, while the relative error on the inertia terms decreases. At following optimal frequency, an equal accuracy is reached for both components:

$$\omega'_{opt} = \frac{Y'_{uv}}{Y'_{\dot{v}} - m'} \tag{3.7}$$

as the components in phase with sway velocity and with sway acceleration are of the same magnitude. ω'_{opt} takes very low values: 0.25 to 2.0 depending on hull shape and water depth. It therefore seems recommended to derive numerical values for the velocity derivatives from results of oblique towing tests, so that the accuracy of the inertia terms can be improved by increasing ω', at least to some extent.

❑ Similar conclusions can be drawn for the yawing moment. In this case, an 'optimum' is only reached at very large ω' (=10-20), so that an accurate determination of $N_{\dot{v}}$ might cause problems.

❑ Theoretically, $Y_{v|v|}$ and $N_{v|v|}$ can be derived from the third harmonic of lateral force and yawing moment. However, very large errors are expected.

PMM yaw tests

The following was concluded:

❑ The effect of heading angle fluctuations on the inertia terms of the yawing moment decreases with increasing ω'; the effect on the damping terms appears to be minimized at an 'optimal frequency':

$$\omega'_{opt} = \sqrt{\left| \frac{N'_{uv} - N'_{\dot{v}}}{N'_{ur} - m'x'_G} \right|} \tag{3.8}$$

taking values 2-4. The acceleration derivative in (3.8) is introduced during a PMM yaw test due to the occurrence of errors on steering and tuning of the mechanism. However, the choice of ω' is not very critical but should not be too small.

❑ An accurate determination of Y_{ur} and $Y_{\dot{r}}$ may be problematic due to the effect of heading angle fluctuations; for this reason, the yawing angle amplitude should not be taken too small.

3.2 Towing tank, CPMC and ship model information

3.2.1 Towing tank and CPMC at Flanders Hydraulics Research

Test facilities at Flanders Hydraulics Research for the research of ship manoeuvrability presently consist of a shallow water towing tank, equipped with a planar motion carriage, a wave generator and an auxiliary carriage for ship-ship interaction tests. Thanks to full computer control, the facilities are operated in an unmanned way, so that experimental programs are running day and night, 7 days a week (Figure 3.6). This *Towing Tank for Manoeuvres in Shallow Water (co-operation Flanders Hydraulics Research – Ghent University)* was accepted as a member organisation of the International Towing Tank Conference in 1993 [71].

The main dimensions of the towing tank are shown in Table 3.1 and are rather modest compared to other towing tank facilities although they were obtained while accommodating the requirement of an experimental facility for shallow water manoeuvring and the available space in the existing halls at the laboratory.

Table 3.1 Main dimensions of shallow water towing tank at Flanders Hydraulics Research

Length over all	88.0 m
Useful length	67.0 m
Width	7.0 m
Maximum water depth	0.5 m
Ship model length	3.5 - 4.5 m

The main carriage is a rectangular frame, composed of two wheel girders, connected by two box girders. A lateral carriage is guided between the transversal girders and carries a slide in which a yawing table is incorporated. This slide can be positioned in vertical sense over 0.4 m to take account of the water level. The ship model is connected to the carriage by means of a mechanism, the so-called beam, which allows free heave and pitch; roll can be restrained or free. In the horizontal plane, a rigid connection is provided. The rails on which the carriage moves are aligned with high accuracy: the level difference of both rails and the lateral deflection of the guiding rail are less than 0.5 mm.

Since the installation of the towing tank in 1992 two different beam types have been used. The first one is shown on the upper photograph of Figure 3.6 and is replaced by a new one in 1999 shown on the lower photograph. The captive model tests that will be used for the determination and validation of the mathematical manoeuvring models are executed with both beams as the experimental period is situated from 1996 until 2000. Some small differences in measured forces and derived models could probably be explained based on the use of these two different mechanisms.

The wave generator and auxiliary carriage for ship-ship interaction have not been used for the execution of captive manoeuvring tests in shallow and laterally unrestricted water, but will be shortly described here for completeness. The piston type wave maker, allowing generation of both regular and irregular waves, is driven by an electro-hydraulic unit with following kinematic characteristics: a stroke of 0.3m, velocity of 0.6 m/s and an acceleration of 4.4 m/s^2. The auxiliary carriage for ship-ship interaction allows a second ship model to perform a prescribed speed history along a straight trajectory, with a maximum speed of 1.2 m/s.

The three motion modes, the wave generator, rudder, propulsion, the auxiliary carriage and other external devices are controlled by a PC and six DIOCs (Direct Input Output Control). The DIOCs also assure the sampling of the analogue input signals. The number of channels is 6 x 8, the resolution is 12 bit and the maximum sampling frequency is 40 Hz. The instrumentation consists of (Figure 3.7):

❑ 4 x 2 dynamometers for longitudinal and lateral forces (20, 50, 100, 200 N)
❑ dynamometers for roll moment;
❑ measurement of propeller rpm;

- ❏ 2 propeller thrust and torque dynamometers (30 N, 0.5 Nm);
- ❏ measurement of vertical motion (due to squat or wave action) at 4 measuring posts;
- ❏ measurement of rudder angle;
- ❏ 2 rudder force and moment dynamometers (50 N, 2 Nm);
- ❏ wave height measurement devices.

This towing tank facility is especially useful for:

- ❏ Determination of manoeuvring simulation models by means of captive model tests, with special emphasis on harbour manoeuvres: large range of ship speeds (ahead and astern), large drift angles, rudder action, large range of propeller rates (ahead and astern), very shallow water (typical under keel clearance: 10 to 20% of draught);
- ❏ Manoeuvring behaviour in restricted waters: bank effects, navigation in canals, berthing;
- ❏ Ship-ship interaction tests;
- ❏ Captive seakeeping tests, for investigating vertical ship motions caused by waves in shallow water.

3.2.2 Ship model characteristics

Mathematical manoeuvring models will be developed for a 270 000 DWT tanker (model E) at the design draught of 21.79 m and a fourth generation container carrier (model D) at a draught of 15.0 m. This draught is rather high compared to the available scantling draught of most post-panamax containerships which is 14.5 m, although the design containership for the new locks in Panama has a prescribed draught of 15.0 m [72]. The characteristics of these ship models for the hull, propeller and rudder modules are shown in Table 3.2. The sections are represented in Figure 3.8 and the rudder profiles for both ship types in Figure 3.9.

Table 3.2 Characteristics of hull, propeller and rudder for model E and model D

Tanker E				Container carrier D		
	Model scale	Full scale	Full scale [73]		Model scale	Full scale
Hull				**Hull**		
L_{OA}	4.035 m	343.0 m	343.0 m	L_{OA}	4.020 m	301.5 m
L_{PP}	3.824 m	325.0 m	325.0 m	L_{PP}	3.864 m	289.8 m
B	0.623 m	53.0 m	53.0 m	B	0.537 m	40.3 m
d	0.256 m	21.8 m	21.8 m	d	0.200 m	15.0 m
C_B	0.83	0.83	0.83	C_B	0.61	0.61
Propeller				**Propeller**		
Z	4	4	5	Z	5	5
D_P	0.1031 m	8.763 m	9.1 m	D_P	0.1086 m	8.145 m
P/D_P	0.65	0.65	0.715	P/D_P	0.97	0.97
A_E/A_0	0.62	0.62	0.682	A_E/A_0	0.8	0.8
Rudder				**Rudder**		
A_R	174.83 cm^2	126.32 m^2	119.82 m^2	A_R	108 cm²	61 m²
Scale	1:85			Scale	1:75	

Model E is based on the tanker Esso Osaka which is one of the rare ships which are tested at full scale in a deep and shallow water area. Although the hull profile corresponds to the one of the full scale ship, the propeller and rudder characteristics differ in some aspects (Table 3.2). In accordance with the full scale trials reported by Crane [73], the shallow water conditions during the captive tests with the Esso Osaka model correspond to under keel clearances of 20% (condition EG) and 50% (condition EH). No model tests were carried out in deep water. The container carrier D at a draught of 15.0 m is tested at under keel clearance values of 20% (condition DA or D1) and 7% (condition DC or D3) of the draught.

These ship models have also been tested at other draughts and also other ship models have been used to examine some parts of the global mathematical model or some difficulties which arise while executing model tests. The characteristics of these models will be summarized in Table 3.3. All tests have been executed with the fully appended ship models.

49

Table 3.3 Characteristics of hull, propeller and rudder for some other ship models

	Model E (intermediate draught)		Model A		Model C		Model U	
	Model	Ship	Model	Ship	Model	Ship	Model	Ship
Hull								
L_{OA} (m)	4.035	343.0	3.533	265.0	3.594	230.0	4.356	352.0
L_{PP} (m)	3.824	325.0	3.456	259.2	3.438	220.0	4.106	331.8
B (m)	0.623	53.0	0.573	43.0	0.504	32.24	0.530	42.8
d (m)	0.207	17.6	0.195	14.6	0.191	12.25	0.179	14.5
C_B	0.797	0.797	0.844	0.844	0.811	0.811	0.65	0.65
Propeller								
D_P (m)	0.1031	8.763	0.0926	6.950	0.1038	6.64	0.1047	8.46
P/D_P	0.65	0.65	0.66	0.66	0.65	0.65	1.0	1.0
A_E/A_0	0.62	0.62	0.63	0.63	0.62	0.62	0.96	0.96
Rudder								
A_R (m²)	174.8E-04	126.32	116.8E-04	65.7	105.2E-04	43.1	127.3E-04	83.13
Scale	1:85		1:75		1:64		1:81	

3.3 Captive model test types at Flanders Hydraulics Research

3.3.1 Overview of captive model test types at FHR

The classical test types used during captive model testing like oblique towing tests or conventional PMM sway or yaw tests have been transformed at Flanders Hydraulics Research into a more extensive classification using the computerized planar motion carriage. A division is made according to the variation of kinematical (ship velocities and accelerations) and control (propeller rpm and rudder angle) parameters and the following classes are specified:

❑ **stationary** captive model **tests** where kinematical and control parameters are kept constant during the test run. Only ship velocities can be evoked and no information about acceleration derivatives will be found. Bollard pull tests, oblique towing tests (Figure 3.1) or circular motion tests (Figure 3.2, however no test facility is available at Flanders Hydraulics Research) can be considered. Depending on the imposed speed of the ship model, a test run can be composed of an arbitrary number of sub-runs, each with a chosen combination of constant kinematical and control parameters.

❑ **oscillatory** captive model tests where the kinematical parameters are harmonically varied in only one mode (a translation along the x-axis or the y-axis or a rotation around the z-axis, Figure 3.10) following an oscillatory motion. In the considered mode velocities and accelerations are varied, while the motions in the other modes and the control parameters are zero.

❑ **PMM sway and yaw tests** where the longitudinal velocity component u is kept constant and the lateral velocity component v (sway, Figure 3.3) or the yaw velocity r (yaw, Figure 3.4) are harmonically varied. Velocities and accelerations are generated and can be combined with constant values for the control parameters.

❑ **multi-modal tests** where kinematical and control parameters can be harmonically varied all at once.

Al these test types have a typical nomenclature which is presented in Table 3.4. PMM sway and yaw tests and multi-modal tests will be discussed in detail in the following sections as test parameters characterising these harmonic test types should be selected with care. This description is partially based on [74].

Table 3.4 Nomenclature of selected test types

stationary tests	STATX	stationary test with constant velocity V
	PAAL	bollard pull test with zero velocity
oscillatory tests	OSCX	oscillation along the x-axis
	OSCY	oscillation along the y-axis
	OSCPSI	oscillation around the z-axis
PMM sway test	PMMY and PMMY0 PMMY2 PMMY_L PMMYL2	see section 3.3.2.1 see section 3.3.2.2 see section 3.3.3.1 see section 3.3.3.2
PMM yaw test	PMMPSI and PMMPSI0 PMMPS2	see section 3.3.5.1 see section 3.3.5.2
multi-modal test	MULTI0 MULTI1	see section 3.3.6.1 see section 3.3.6.2

3.3.2 Conventional harmonic sway test

3.3.2.1 Description of test type PMMY or PMMY0

The active axes are the x_0 and the y_0 axis. The ψ axis is inactive. Different phases can be considered:

(a)   Waiting time ($0<t<t_1$) which gives the operator the opportunity to leave the main carriage
    ❏   The carriage is positioned in the starting position:

$$x_0 = x_{0,start}$$
$$y_0 = y_{0,mean} + y_{0A} \tag{3.9}$$

    ❏   Analogue and digital outputs are 0.

(b)   Calibration ($t_1<t<t_2$) during which phase averaged reference values are determined for all measured quantities.
    ❏   The carriage stays at his starting point.
    ❏   Analogue and digital outputs are 0.

(c)   Acceleration phase ($t_2<t<t_3$)
    ❏   The longitudinal carriage executes a uniformly accelerated movement starting from rest to a uniform velocity u_0. This velocity corresponds to:

$$PMMY0: \quad u_0 = sign * VX$$
$$PMMY : \quad u_0 = sign * \frac{VX}{\cos\psi} \tag{3.10}$$

The acceleration phase is accompanied with a constant acceleration a_{acc}:

$$x_0 = x_{0,start} + \frac{1}{2}a_{acc}(t - t_2)^2 \tag{3.11}$$

where a_{acc} is given, or derived from the acceleration time t_{acc} or the acceleration distance x_{acc}:

$$a_{acc} = \frac{u_0}{t_{acc}} = \frac{u_0^2}{2x_{acc}} \tag{3.12}$$

The lateral carriage remains at his starting position.
    ❏   Analogue outputs are driven. The rudder is positioned on its desired value, propellers stand still.

(d)   Oscillation phase ($t_3<t<t_4$)
    ❏   The longitudinal carriage moves with a constant velocity u_0:

$$x_0 = x_{0,3} + u_0(t - t_3) \tag{3.13}$$

    while the lateral carriage is executing a harmonically oscillating movement for c periods with amplitude y_{0A} and period T ($t_4=t_3+cT$):

$$y_0 = y_{0,mean} + y_{0A} \cos\frac{2\pi(t - t_3)}{T}$$ (3.14)

    ❏ Analogue outputs take their desired values and digital outputs are on.

(e)   Deceleration phase ($t_4 < t < t_5$)

    ❏ The longitudinal carriage executes a uniformly decelerated movement from constant velocity u_0 to standstill. Deceleration is accompanied with a constant deceleration a_{dec}:

$$x_0 = x_{0,4} + u_0(t - t_4) - \frac{1}{2}a_{dec}(t - t_4)^2$$ (3.15)

    where a_{dec} is given, or derived from the deceleration time t_{dec} or the deceleration distance x_{dec}:

$$a_{dec} = \frac{u_0}{t_{dec}} = \frac{u_0^2}{2x_{dec}}$$ (3.16)

    The lateral carriage is at his end point.

    ❏ Analogue and digital outputs are zero.

(f)   Additional measuring time ($t_5 < t < t_6$)

    ❏ The longitudinal carriage is at his end point: $x_0 = x_{0,5}$.

    ❏ Analogue and digital outputs are zero.

3.3.2.2 Description of test type PMMY2

Harmonic PMM sway tests described in section 3.3.2.1 have been modified in 1999 by the author so that the oscillation phase (d) with c oscillation cycles is subdivided in two phases, namely c_1 cycles with a harmonic sway motion and c_2 cycles with a straight-line motion without swaying ($c = c_1 + c_2$). The aim of this modified classical sway test was to visualize possible memory effects. Only oscillation phase (d) will be described.

(d)   Oscillation phase ($t_3 < t < t_4$)

    (d1) Harmonic sway motion ($t_3 < t < t_{4,1}$)

    ❏ The longitudinal carriage has a constant advance velocity u_0:

$$x_0 = x_{0,3} + u_0(t - t_3)$$

    while the lateral carriage executes a harmonically oscillating movement for c_1 cycles with amplitude y_{0A} and period T ($t_{4,1} = t_3 + c_1 T$):

$$y_0 = y_{0,mean} + y_{0A} \cos\frac{2\pi(t - t_3)}{T}$$

    ❏ Analogue outputs take their desired values and digital outputs are on.

    (d2) Run-out time ($t_{4,1} < t < t_4$)

    ❏ The longitudinal carriage moves during c_2 cycles with a constant velocity ($t_4 = t_{4,1} + c_2 T$):

$$x_0 = x_{0,4,1} + u_0(t - t_{4,1})$$ (3.17)

    while the lateral carriage is at his end point:

$$y_0 = y_{0,mean} + y_{0A}$$ (3.18)

    ❏ Analogue and digital outputs are zero.

3.3.2.3 Disadvantages of conventional harmonic sway tests (type PMMY, PMMY0, PMMY2)

Outline of disadvantages

❏ The transition from acceleration phase (c) to oscillation phase (d) is characterized by a discontinuity in the sway acceleration. A similar discontinuity, although less disturbing, occurs at the transition from phase (d) to the deceleration phase (e).

$$y = y_{0,mean} + y_{0A} \cos\omega t$$

$$v = -v_A \sin\omega t = -y_{0A}\omega \sin\omega t$$ (3.19)

$$\dot{v} = -\dot{v}_A \cos\omega t = -y_{0A}\omega^2 \cos\omega t$$

This abrupt change of sway acceleration from zero to maximum value, depending on test frequency and amplitude, will affect the oscillation phase during an unknown time span. Analysing measured forces, this will be accounted for by skipping half a period at the beginning and the end of the oscillation phase (d). The influence of this discontinuity can be illustrated based on tests of type PMMY2 (for example Figure 3.11).

❑ Skipping half a period at the beginning of the test run gives also the opportunity to minimize the influence of the acceleration phase on the useful test results. The longitudinal acceleration determined by the acceleration distance or acceleration time, is not always chosen judiciously so that fluctuations in the longitudinal force can be observed. The lateral force and yawing moment are fortunately hardly affected by this shortcoming.

❑ Due to the pure harmonic sway motion of the lateral carriage sway acceleration reaches a maximum at zero sway velocity. At low oscillation frequency, this may lead to control inaccuracies, especially in the case of a CPMC with independent control of the three degrees of freedom. Sway velocity and sway acceleration may reach values of v=0 and dv/dt=0 near maximum lateral displacement although a maximum sway acceleration is expected.

❑ The execution of tests at low frequencies requires a large useful tank length, otherwise the analysis is restricted to just one or two oscillation cycles. In general, a number of minimum three oscillation cycles is proposed to increase the accuracy.

❑ Depending on the imposed (non-dimensional) oscillation frequency, interference may occur between the trajectories described by the fore and aft body of the model. High frequencies ω' impose interference over a relatively substantial fraction of the oscillation period, as is illustrated in Figure 3.5. As this kind of interference takes place at maximum sway acceleration, the determination of the acceleration derivative may be affected. These so-called 'memory effects' occurring during captive model testing are illustrated in chapter 1 for an idealised two fin craft based on [35].

❑ The motion imposed to the ship model may be considered as rather unrealistic.

Non-stationary effects introduced during conventional harmonic sway tests

The introduction of classical PMM sway tests of type PMMY2 gives the opportunity to examine non-stationary effects linked with the harmonic character of these tests. Tests of type PMMY2 have been executed with the containership D at full load condition and tanker E at an intermediate draught of 17.6m and both at an under keel clearance of 20% of the draught.

Figure 3.11 shows lateral force and yawing moment measured during the oscillation phase (d) of a harmonic sway test with a test period of 16s, a sway amplitude of 0.35m and a Froude number F_n=0.041 (4.5knots) for model E. The sub-phase harmonic sway motion takes a length of 8 cycles (128s) and the run-out phase is equivalent to 7 cycles (112s). The harmonic motion during phase (d1) generates an oscillating lateral force and yawing moment measured during phase (d2) which is characterized by a constant lateral position. Lateral force and yawing moment are roughly composed of a function which dies out in time and a permanent oscillating contribution.

This decreasing time function can probably be explained based on the discontinuity in the sway acceleration from maximum to zero value at the transition from phase (d1) to (d2). It takes approximately two time periods of 16s before this influence has died out for the lateral force.

The oscillation period of the second component does not correspond to the period of 16 seconds of the imposed harmonic motion. Additionally, a variation of the test frequency ω while other test parameters (sway amplitude and forward velocity) are kept constant, seems not to affect the period of the oscillating rest function during the run-out phase (Figure 3.12). This period can be properly determined at higher test frequencies (ω'=6 or 4) and is approximately 10 seconds.

Harmonic sway tests at lower frequencies (ω'=2 or 3) generate no significant oscillating contributions in the towing tank.

These effects confirm the assumption that tank resonance occurs during oscillatory tests, such as harmonic sway tests, even though the test frequency does not equal a natural frequency of the water in the towing tank for this condition. A lateral wave system is induced by the oscillation and the wave length λ of this system equals 2W/n (n=1,2,...), W being the tank width. Natural frequencies of the water in the tank depend also on the water depth h. For model E at intermediate draught and 20% UKC these frequencies are:

$$\omega^2 = gk \tanh(kh) = g\frac{2\pi}{\lambda}\tanh\left(\frac{2\pi}{\lambda}h\right) = g\frac{2\pi n}{2W}\tanh\left(\frac{2\pi n}{2W}(1+UKC)d\right) \qquad (3.20)$$

The largest natural period for this particular case corresponds to 9 seconds or the dominating period of the oscillating forces during the run-out phase.

Maximum sway acceleration and sway velocity depend on test frequency and test amplitude, see equation (3.14), and determine not only the amplitude of oscillating lateral force Y during phase (d1) ($Y_{max(d1)}$) but also during the stationary part of phase (d2) ($Y_{max(d2)}$) so that the ratio $Y_{max(d2)}/Y_{max(d1)}$ is almost similar for all tests independent of test frequency.

The influence of test amplitude on harmonic sway tests with constant non-dimensional frequency (ω'=2.9) is illustrated in Figure 3.13. Comparable contributions arise due to fluctuations in the towing tank.

Based on equation (3.20) a contradiction has to be overcome: the natural period of the water in the towing tank decreases with decreasing tank width. This tendency could be used to increase the test frequency of oscillatory tests as acceleration derivatives are determined with more accuracy at higher test frequency or lower test period. A towing tank with a small tank width seems to be preferable for oscillatory tests although interaction with tank walls has to be avoided.

Test results, described above, are nevertheless not affected by interference effects with tank walls as can be seen on Figure 3.14. The only test parameter that has been changed is the mean lateral position $y_{0,mean}$, a zero value in the centreline of the tank or 0.75m out of the centre. If sway amplitude and sway period are kept constant, lateral force and yawing moment are identical and do not suffer from interference effects. According to Van Leeuwen [68] half the tank width may be considered as an upper limit for the trajectory width.

For a more slender ship shape similar tendencies can be observed, although this slenderness results into low lateral forces and yawing moments compared to the values measured for model E. Figure 3.15 shows lateral force and yawing moment measured during a harmonic sway test of type PMMY2 with a test period of 30 sec. Contributions measured during the run-out phase are small and the influence of decreasing the test frequency is negligible. The highest natural period of the water in the tank equals 9 seconds in this case, taken into account different scale ratios for model D and model E.

Maximum sway acceleration occurs at maximum lateral displacement and zero sway velocity. According to Figure 3.15 there is almost no contribution of an acceleration dependent moment to the total measured yawing moment as the latter reaches a zero value near maximum sway acceleration. The sway acceleration derivative for the yawing moment will be consequently negligible while the sway velocity component N_v will probably be important.

Residual oscillating forces and moments have not to be considered and only the discontinuity in sway acceleration at the transition from phase (d1) to (d2) gives a clear disturbance which vanishes after a time period of less than one oscillation cycle (60 seconds for the test runs on Figure 3.16 and 30 seconds in Figure 3.15). Skipping half a period at the beginning and the end

of the oscillation phase to determine acceleration and velocity derivatives is an acceptable assumption but half a period could perhaps be too small at higher frequencies.

3.3.3 Non-conventional sway test: type PMMY_L or PMMYL2

Non-conventional sway tests have been introduced to overcome some disadvantages related to traditional harmonic sway tests and have first been reported in [60].

A constant forward speed is combined with alternating sway motions to starboard (phase I) and port (phase III, path width $\Delta y = \Delta y_0$). Both phases are separated by a so-called link period with length ΔL (phase II), during which the model is kept in its maximum lateral position y_0, allowing the aft body to leave the fore body's 'lateral wake' (Figure 3.17).

Important modifications compared to classical sway test are:

❑ Variation of sway acceleration and sway velocity is characterized by a non-zero velocity at maximum sway acceleration. Additionally, at the beginning and the end of phase I or III acceleration and velocity are zero so that discontinuities are eliminated.

❑ Interference between fore and aft body during tests with high frequencies can be avoided thanks to the introduction of a link phase without sway motion.

Test type PMMYL2 is an amelioration to type PMMY_L.

3.3.3.1 Description of non-conventional sway test: type PMMY_L

The active axes are the x_0 and y_0 axis. The ψ axis is inactive. An alternative sway test is characterized by the distances Δy_0, Δx_0 and ΔL (Figure 3.17). Following phases are considered during a test run.

(a) Waiting time ($0 < t < t_1$)
    ❑ The carriage is positioned in the starting point:

$$x_0 = x_{0,start}$$

$$y_0 = y_{0,mean} - \frac{\Delta y_0}{2}$$

(3.21)

    ❑ Analogue and digital outputs are 0.

(b) Calibration ($t_1 < t < t_2$)
    ❑ The carriage stays at his starting point.
    ❑ Analogue and digital outputs are 0.

(c) Acceleration phase ($t_2 < t < t_3$)
    ❑ The longitudinal carriage executes a uniformly accelerated movement starting from rest to a uniform velocity u_0. This velocity corresponds to:

$$PMMY\_L \ : \quad u_0 = zin * \frac{VX}{\cos \psi}$$

(3.22)

The acceleration phase is accompanied with a constant acceleration a_{acc}:

$$x_0 = x_{0,start} + \frac{1}{2} a_{acc} (t - t_2)^2$$

(3.23)

where a_{acc} is given, or derived from the acceleration time t_{acc} or the acceleration distance x_{acc}:

$$a_{acc} = \frac{u_0}{t_{acc}} = \frac{u_0^2}{2 x_{acc}}$$

(3.24)

The lateral carriage remains at his starting point.
    ❑ Analogue outputs are driven. The rudder is positioned on its desired value, propellers stand still.

(d) Sway motion ($t_3 < t < t_4$)

This phase starts with a link period of $\Delta L = 5m$ (This length is chosen in accordance with a minimum of one mean model ship length).

Subsequently a sway motion from port side of the tank to the starboard side is executed (positive sway velocity), followed by a link phase of 5m and a sway motion from starboard side to port side (negative sway velocity). This series is ended once again by a link phase of 5m. This succession of phases may be repeated several times depending on the useful tank length and is indicated by a number of block distance $\Delta L + \Delta x_0$.

❑ The longitudinal carriage has a constant forward velocity u_0 both during the link phase and the sway motion:

$$x_0 = x_{0,i} + u_0(t - t_{i0}) \tag{3.25}$$

with i=1, ... and

$$t_{i0} = t_3 + (i-1)\frac{\Delta L + \Delta x_0}{u_0} \tag{3.26}$$

$$x_{0,i} = x_{0,3} + (i-1)(\Delta L + \Delta x_0)$$

During the link phase (duration $\Delta L/u_0$) the lateral carriage remains in its extreme position:

$$y_0 = y_{0,mean} + (-1)^i \frac{\Delta y_0}{2} \tag{3.27}$$

During the following phase, characterized by a sway motion (duration $\Delta x_0/u_0$), the lateral carriage executes a lateral movement based on the function:

$$y_0 = y_{0,mean} + (-1)^i \left(\frac{\Delta y_0}{2} - \frac{\Delta y_0}{\Delta x_0} u_0(t - t'_{i0}) + \frac{\Delta y_0}{2\pi} \sin\omega^* (t - t'_{i0}) \right) \tag{3.28}$$

with

$$t'_{i0} = t_{i0} + \frac{\Delta L}{u_0}$$

$$\omega^* = \frac{2\pi}{T^*} = \frac{2\pi u_0}{\Delta x_0} \tag{3.29}$$

Sway velocity and sway acceleration are determined by:

$$v_0 = (-1)^{i+1} \frac{\omega^* \Delta y_0}{2\pi} \left[1 - \cos\omega(t - t'_{i0}) \right]$$

$$\dot{v}_0 = (-1)^{i+1} \frac{\omega^{*2} \Delta y_0}{2\pi} \sin\omega(t - t'_{i0}) \tag{3.30}$$

with:

$$v_{0,max} = \frac{\omega^* \Delta y_0}{2\pi} = 2u_0 \frac{\Delta y_0}{\Delta x_0}$$

$$\dot{v}_{0,max} = \frac{\omega^{*2} \Delta y_0}{2\pi} = 2\pi u_0^2 \frac{\Delta y_0}{\Delta x_0^2} \tag{3.31}$$

❑ Analogue outputs take their desired values and digital outputs are on.

(e) Deceleration phase ($t_4 < t < t_5$)

❑ The longitudinal carriage executes a uniformly decelerated movement from constant velocity u_0 to standstill. Deceleration is accompanied with a constant deceleration a_{dec}:

$$x_0 = x_{0,4} + u_0(t - t_4) - \frac{1}{2}a_{dec}(t - t_4)^2 \tag{3.32}$$

where a_{dec} is given, or derived from the deceleration time t_{dec} or the deceleration distance x_{dec}:

$$a_{dec} = \frac{u_0}{t_{dec}} = \frac{u_0^2}{2x_{dec}}$$ (3.33)

The lateral carriage is at his end position.

❏ Analogue and digital outputs are zero.

(f)   Additional measuring time ($t_5 < t < t_6$)

❏ The longitudinal carriage is at his end point: $x_0 = x_{0,5}$.

❏ Analogue and digital outputs are zero.

3.3.3.2 Description of non-conventional sway test: type PMMYL2

Shortcomings of test type PMMY_L have been overcome by the introduction of the derived test type PMMYL2 with following additional features:

❏ During test type PMMY_L the link phase has a fixed length, while this length can be chosen for type PMMYL2. A minimum of 4 or 5m is recommended and a longer link phase gives the opportunity to examine non-stationary effects.

❏ The first link phase, immediately after the acceleration phase (c), has a fixed length of 4m, long enough to eliminate the influences of the acceleration phase out of the effective sway motion.

3.3.3.3 Non-stationary effects introduced during non-conventional sway tests

Conventional sway tests described in section 3.3.2 are affected by non-stationary effects which can be clearly detected during the run-out phase of an individual test. Although some disadvantages related to harmonic sway tests are overcome, even non-conventional sway tests make use of a harmonically created sway motion in a towing tank.

Compared to conventional sway tests, sway motion during alternative sway tests is obtained with higher frequencies as sway acceleration and sway velocity are zero at start and end of a particular movement to port or starboard. Measured lateral forces during the complete test run are shown for model D in Figure 3.18 and model E in Figure 3.19. Comparing the test runs at $\omega^{*'}=6$ for both ship models especially full bodied models like tanker E suffer from non-stationary effects with increasing test frequency.

At the two largest frequencies for model E at design draught lateral oscillating forces are observed during the link periods which differ from each other. Comparing the variation of lateral force Y during the first link period with lateral force measured during the following links a superposition of non-stationary effects generated in the tank due to the sway motion affect definitely not only the link phase but even the useful sway motion to port or starboard.

The largest natural frequency of the towing tank for model E at design draught and 20% UKC corresponds to a period of 8 seconds. Sway acceleration during the test with $\omega^{*'}=12$ varies with a period of 10 seconds. A standing wave system is probably generated in the tank and it can be seen that the period of the lateral forces during the link phases equals almost the largest natural period of the water. Even at the test run with $\omega^{*'}=6$ non-stationary effects are reinforced during consecutive link phases, although the test period T=13.3s differs from the highest natural period of the water in the tank. An explanation can hardly be given, but this behaviour is probably a result of a combination of inadequately chosen parameters, such as the length of the link phase and the non-dimensional frequency $\omega^{*'}$.

The consecutive cycles, indicated as motion 1, 2, ... on Figure 3.20 are to a certain extent reproducible, although a large difference between measured lateral force can be observed at the beginning of lateral motion 1 to starboard compared to the following motions. As sway acceleration increases quicker than sway velocity during this test run, acceleration derivatives will be especially affected by these non-stationary effects and will be discussed in chapter 4.

In conclusion non-conventional sway tests have to be executed with great caution as higher frequencies can be used compared to conventional sway tests and the length of the link phase

which is inserted to eliminate non-stationary effects can introduce totally unexpected disturbances. Tests at higher frequencies are affected by large oscillations of the lateral forces observed during consecutive link periods. At lower frequencies lateral forces during the link phases are still oscillating but smaller so that at the end of the link phase the interfering lateral force is almost damped.

3.3.4 Criteria for comparing conventional and non-conventional sway tests

Non-conventional sway tests have been designed to overcome some disadvantages of conventional PMM sway tests so that the acceleration derivatives derived from these tests are expected to alter. Two criteria have been proposed so that a comparison of both test types can be made.

❑ Criterion 1:

For a first series of non-conventional sway tests parameters Δx_0 and Δy_0 have been chosen so that maximum sway acceleration and maximum sway velocity are identical for both test types.

$$\Delta x_0 = \pi u_0 \frac{v_{max}}{\dot{v}_{max}}$$

$$\Delta y_0 = \frac{\Delta x_0 v_{max}}{2u_0}$$

(3.34)

with

$$\left| v_{max} \right| = \omega y_{0A}$$

$$\left| \dot{v}_{max} \right| = \omega^2 y_{0A}$$

(3.35)

so that

$$\Delta x_0 = \frac{1}{2} u_0 T$$

$$\Delta y_0 = \frac{1}{2} \pi y_{0A}$$

(3.36)

v_{max} and $\dot{v}_{max}$ are maximum sway velocity and sway acceleration of a conventional harmonic sway test. ω is the oscillation frequency of the conventional sway test.

Although maximum values are identical, sway acceleration is not created with an identical frequency for both test types. Based on equality of acceleration amplitudes the relationship between ω and ω^* is given by:

$$\omega^2 = \frac{\Delta y_0}{2\pi y_{0A}} \omega^{*2}$$

(3.37)

so that

$$\omega = \frac{1}{2} \omega^*$$

(3.38)

❑ Criterion 2:

As test frequency ω^* has an important influence on lateral forces measured during both test types, it is more obvious to choose test parameters Δx_0 and Δy_0 so that generation of sway acceleration for conventional and non-conventional tests are identical:

$$\omega = \omega^*$$

$$\dot{v}_{0,max}(PMMY\_L) = \dot{v}_{0,max}(PMMY)$$

(3.39)

58

These conditions reduce to:

$$\Delta x_0 = u_0 T$$

$$\Delta y_0 = 2\pi y_{0A}$$

(3.40)

with T and y_{0A} period and sway amplitude of a conventional sway test, respectively.

Meeting condition (3.40) for the lateral displacement $\Delta y_0/2$ a non-conventional sway test gives a higher value (factor π) compared to a conventional harmonic sway test, namely y_{0A}.

These criteria will be used in chapter 4.

3.3.5 Harmonic yaw test

3.3.5.1 Description of test type PMMPSI or PMMPSI0

A harmonic yaw test is characterized by amplitude ψ_A and frequency ω combined with a constant velocity in a ship fixed axis system. The active axes are consequently: x_0, y_0 and ψ axis. Longitudinal and lateral components of this velocity do not change during the oscillation phase of each test run and are determined by mean yaw angle ψ_{mean} and total velocity U (PMMPSI0) or longitudinal velocity component u (PMMPSI):

$$u = U\cos\psi_{mean}$$

$$v = U\sin\psi_{mean} = u\tan\psi_{mean}$$

(3.41)

Longitudinal and lateral carriages execute synchronous movements described by the functions:

$$x_0(t) = x_0(t_0) + U\int_{t_0}^{t} \cos(\psi - \psi_{mean})\, dt$$

$$y_0(t) = y_0(t_0) + U\int_{t_0}^{t} \sin(\psi - \psi_{mean})\, dt$$

(3.42)

with ψ given by a harmonic function around a mean value ψ_{mean}:

$$\psi = \psi_{mean} + \psi_A \cos\omega(t - t_0)$$

(3.43)

Time functions (3.42) are calculated based on numerical integration:

$$\psi(t + \Delta t) = \psi(t) - \psi_A \omega\sin[\omega(t - t_0)]\Delta t$$

$$x_0(t + \Delta t) = x_0(t) + U\cos[\psi(t) - \psi_{mean}]\Delta t$$

$$y_0(t + \Delta t) = y_0(t) + U\sin[\psi(t) - \psi_{mean}]\Delta t$$

(3.44)

High accelerations at the transition from acceleration phase to oscillation phase or oscillation to deceleration phase can be avoided by the multiplication of right-hand side equations in (3.44) with a 'ramp' function. Due to the need of synchronization of different axes, the length of acceleration and deceleration phase are predetermined and chosen to be half a period. The yaw angle obtained during these phases corresponds to the yaw amplitude ψ_A.

(a)   Waiting time ($0<t<t_1$)

    ❑ The carriage is positioned in its starting point:

$$x_0 = x_{0,start}$$

$$y_0 = y_{0,mean} + y_{0,offset}$$

(3.45)

$$\psi = \psi_{mean}$$

$y_{0,offset}$ is determined during generation of test run PMMPSI(0) so that the starting position of the lateral carriage at the end of the acceleration phase is at the mean

lateral position $y_{0,mean}$.
- ❑ Analogue and digital outputs are 0.
(b) Calibration ($t_1<t<t_2$)
- ❑ The carriage stays at his starting point.
- ❑ Analogue and digital outputs are 0.
(c) Acceleration phase ($t_2<t<t_3$)
- ❑ The acceleration phase takes half a period, $t_3=t_2+\frac{1}{2}T$. The velocity increases linearly from zero to value U, while drift angle ψ_{mean} is kept constant during the complete acceleration phase. The trajectory is described by:

$$\psi(t+\Delta t) = \psi(t) - \psi_A \omega \sin[\omega(t-t_2)]\frac{t-t_2}{\frac{1}{2}T}\Delta t$$

$$x_0(t+\Delta t) = x_0(t) + U\cos[\psi(t) - \psi_{mean}]\frac{t-t_2}{\frac{1}{2}T}\Delta t \qquad (3.46)$$

$$y_0(t+\Delta t) = y_0(t) + U\sin[\psi(t) - \psi_{mean}]\frac{t-t_2}{\frac{1}{2}T}\Delta t$$

At the end of phase (c) lateral carriage and yawing table are at the following positions:

$$y_{0.3} = y_{0,mean}$$
$$\psi_3 = \psi_{mean} - \psi_A \qquad (3.47)$$

- ❑ Analogue outputs are driven. The rudder is positioned on its desired value, propellers stand still.
(d) Oscillation phase ($t_3<t<t_4$)
- ❑ A number of c periods will be executed, $t_4=t_3+cT$. The positions of the axes are calculated:

$$\psi(t+\Delta t) = \psi(t) - \psi_A \omega \sin[\omega(t-t_3)]\Delta t$$
$$= \psi_{mean} + \psi_A \cos[\omega(t-t_3)] - \psi_A \omega \sin[\omega(t-t_3)]\Delta t$$
$$x_0(t+\Delta t) = x_0(t) + U\cos[\psi(t) - \psi_{mean}]\Delta t$$
$$y_0(t+\Delta t) = y_0(t) + U\sin[\psi(t) - \psi_{mean}]\Delta t \qquad (3.48)$$

- ❑ Analogue outputs take their desired values and digital outputs are on.
(e) Deceleration phase ($t_4<t<t_5$)
- ❑ The deceleration phase takes half a period, $t_5=t_4+\frac{1}{2}T$. During this phase the velocity decreases linearly from value U to zero, while drift angle is kept constant during the complete duration. The trajectory is described as:

$$\psi(t+\Delta t) = \psi(t) - \psi_A \omega \sin[\omega(t-t_4)]\frac{t_5-t}{\frac{1}{2}T}\Delta t$$

$$x_0(t+\Delta t) = x_0(t) + U\cos[\psi(t) - \psi_{mean}]\frac{t_5-t}{\frac{1}{2}T}\Delta t \qquad (3.49)$$

$$y_0(t+\Delta t) = y_0(t) + U\sin[\psi(t) - \psi_{mean}]\frac{t_5-t}{\frac{1}{2}T}\Delta t$$

At the end of this deceleration phase lateral carriage and yawing table are positioned at:

$$y_0 = y_{0,mean} \pm y_{0,offset}$$
$$\psi = \psi_{mean} \qquad (3.50)$$

with a + sign if number c is an integer and a − sign if c is an odd multiple of ½.
- ❏ Analogue and digital outputs are zero.

(f)   Additional measuring time ($t_5 < t < t_6$)
- ❏ The longitudinal carriage is at his end point.
- ❏ Analogue and digital outputs are zero.

3.3.5.2 Description of test type PMMPS2

A similar test type composed of two sub-phases for the oscillation phase (d) as was considered for the harmonic sway tests, is introduced for harmonic yaw tests. This type PMMPS2 with a total of c oscillation cycles, is subdivided in a harmonic yaw motion and a run-out phase where the ship model is first brought from maximum yaw angle (combination of yaw amplitude and mean yaw angle) to the mean yaw angle or drift angle ψ_{mean}, followed by a run-out motion with constant velocity components u and v.

(d)   Oscillation phase ($t_3 < t < t_4$)

(d1) Harmonic yaw motion ($t_3 < t < t_{4,1}$)
- ❏ A number of c_1 periods will be executed, $t_{4,1} = t_3 + c_1 T$. The positions of the axes are calculated based on (3.48).
- ❏ Analogue outputs take their desired values and digital outputs are on.

(d2) Run-out time ($t_{4,1} < t < t_4$)
- ❏ The carriages are moved based on similar equations compared to (3.49) with a constant total velocity U. (3.49) is changed to (3.51) with $t_{4,2} = t_{4,1} + \frac{1}{2}T$.

$$\psi(t + \Delta t) = \psi(t) - \psi_A \omega \sin[\omega(t - t_{4,1})] \frac{t_{4,2} - t}{\frac{1}{2}T} \Delta t$$

$$x_0(t + \Delta t) = x_0(t) + U \cos[\psi(t) - \psi_{mean}] \frac{t_{4,2} - t}{\frac{1}{2}T} \Delta t \tag{3.51}$$

$$y_0(t + \Delta t) = y_0(t) + U \sin[\psi(t) - \psi_{mean}] \frac{t_{4,2} - t}{\frac{1}{2}T} \Delta t$$

- ❏ From time $t_{4,2}$ to t_4 the ship model is moving with a constant velocity U and a constant drift angle ψ_{mean}. Memory effects resulting from the oscillating yaw motion during phase (d1) can be visualized during phase (d2) after half a period of time.
- ❏ Analogue and digital outputs are zero.

3.3.5.3 Non-stationary effects introduced during conventional harmonic yaw tests

Comparable disadvantages as noticed during a harmonic sway test occur during an oscillating yaw motion of a ship model. Discontinuities in yaw acceleration are generated at the beginning and the end of the oscillation phase (d) affecting the flow around the yawing ship model:

$$\psi = \psi_{mean} + \psi_A \cos \omega t$$

$$r = -\omega \psi_A \sin \omega t \tag{3.52}$$

$$\dot{r} = -\omega^2 \psi_A \cos \omega t$$

In Figure 3.21 lateral force and yawing moment measured during phases (d1) and (d2) are shown as function of the test period T=27s for model E. A regime situation is hardly reached as maxima measured for the lateral force increase in time during the first three cycles. During the run-out phase an oscillating water flow in the tank is observed with a period corresponding to the largest natural period of the water in the tank (9 seconds). From time t=135s to t=148.5s (first half period of run-out phase) the yaw angle is gradually decreased from maximum yaw angle to mean yaw angle which is zero for this test run. The forces and moment generated during this phase appear to be rather limited.

Yawing moment measured during run-out phase (d2) is very small compared to the maximum value measured during the oscillation phase. In addition, when half a period has passed during phase (d1), variation of yawing moment with yaw velocity and yaw acceleration is rather in regime for the five consecutive oscillation cycles. This small effect on yawing moment can be explained when visualizing lateral forces measured on fore and aft body of the ship model (Figure 3.22). As measuring points x_F and x_A of fore and aft gauges are equidistant from midship point, oscillating forces Y_F and Y_A, mutually shifted with 180 degrees or working in opposite directions, contribute both in the same sense to the measured yawing moment.

At high frequencies (for example ω'=4.4) swept paths followed by fore and aft body of the ship cover a considerable part of the manoeuvring lane bounded by the maximum lateral positions (Figure 3.23). At small frequencies both swept paths are closer to each other (Figure 3.24). These swept paths with varying frequency and varying yaw amplitude correspond to the measurements for the lateral force and the yawing moment shown in Figure 3.25. Using a limited test frequency or yaw amplitude will restrict oscillations which are generated in the towing tank and which especially affect the lateral force. According to Figure 3.25 almost half an oscillation period or the real duration of the starting motion of phase (d2) is necessary to account for the effects related to the installation of a mean yaw angle.

Lateral force and yawing moment measured during the run-out phase of a harmonic yaw test are small or even negligible for a slender body (model D at 20% UKC, Figure 3.26). Non-dimensional frequency ω' is 3.3 during the harmonic yaw motion and although the yaw amplitude is high, 35 degrees, oscillating flows in the towing tank affect the lateral force with an oscillation period which is lower than the maximum natural period of the water in the tank.

3.3.6 Multi-modal test type

The aim of a multi-modal test type is the variation of several kinematical and control parameters during one test run. Each variation is composed of the superposition of a constant value and a harmonically varying value. Depending on the chosen test parameters none (for example a bollard pull test) or all the axes can be active so that conventional oblique towing or harmonic test types can be replaced by these so called multi-modal harmonic test types. Two different test types are considered, type MULTI0 and MULTI1, which differ based on the defined parameters.

Using these multi-modal tests the number of test runs can be diminished as kinematical and control parameters can be varied over a certain range during one test run. Forty four stationary oblique towing tests to determine induced forces within a prescribed range of drift angles [-180 deg; 180 deg] can theoretically be replaced by two multi-modal tests with harmonically varying velocity components u and v and a constant yaw velocity r (r>0 for the first run and r<0 for the second one, Figure 3.27).

3.3.6.1 Description of multi-modal test, type MULTI0

Following parameters can be harmonically varied:
- u_0: velocity of the longitudinal carriage
- v_0: velocity of the lateral carriage
- ψ_0: position of the yawing table
- n_1 and n_2: propeller rate of turn for a single screw (n_1) or a double screw ship (n_1 and n_2)
- δ_R: rudder angle

For each of these parameters f four values determine the harmonic behaviour:
- a mean value f_m
- an amplitude f_A
- a period T_f
- a phase angle ϕ_f

The variation of parameter f during the regime phase ($t_3 < t < t_4$) is given by:

62

$$f(t) = f_m + f_A \sin\left(\frac{2\pi}{T_f}(t - t_3) + \phi_f\right)$$ (3.53)

During the acceleration phase the accelerations of the three mechanisms are continuous functions of time. Discontinuities are avoided even for the analogue outputs. Deceleration of the CPMC is based on a uniformly decelerated movement.

(a)   Waiting time (0<t<t$_1$)

   ❑ The carriage is positioned in its starting point:

$$x_0(0) = x_{0,start}$$

$$y_0(0) = y_0(t_3) - \frac{1}{2}\frac{dy_0}{dt}(t_3)T_{acc} + \frac{1}{12}\frac{d^2y_0}{dt^2}(t_3)T_{acc}^2$$ (3.54)

$$\psi(0) = \psi(t_3) - \frac{1}{2}\frac{d\psi}{dt}(t_3)T_{acc} + \frac{1}{12}\frac{d^2\psi}{dt^2}(t_3)T_{acc}^2$$

   with positions, velocities and accelerations at starting time t$_3$ of the regime phase defined by (f = y$_0$, ψ):

$$f(t_3) = f_m + f_A \sin\phi_f$$

$$\frac{df}{dt}(t_3) \equiv \dot{f}(t_3) = \omega_f f_A \cos\phi_f$$ (3.55)

$$\frac{d^2f}{dt^f}(t_3) \equiv \ddot{f}(t_3) = -\omega_f^2 f_A \sin\phi_f$$

   with

$$\omega_f = \frac{2\pi}{T_f}$$ (3.56)

   ❑ Analogue and digital outputs are 0.

(b)   Calibration (t$_1$<t<t$_2$)

   ❑ The carriage stays at his starting point.

   ❑ Analogue and digital outputs are 0.

(c)   Acceleration phase (t$_2$<t<t$_3$)

   ❑ The three mechanisms of the carriage (f = x$_0$, y$_0$, ψ) executes the following trajectories:

$$f = f(0) + \frac{1}{3}\frac{3\dot{f}(t_3) - \ddot{f}(t_3)T_{acc}}{T_{acc}^2}(t - t_2)^3 + \frac{1}{4}\frac{-2\dot{f}(t_3) + \ddot{f}(t_3)T_{acc}}{T_{acc}^3}(t - t_2)^4$$ (3.57)

   At the end of the acceleration phase the lateral carriage and the yawing table are at the positions given by (3.55). The position of the longitudinal carriage is:

$$x_0(t_3) = x_{0,start} + \frac{1}{2}\dot{x}_0(t_3)T_{acc} - \frac{1}{12}\ddot{x}_0(t_3)T_{acc}^2$$ (3.58)

   ❑ Propeller rate of turn n$_i$ is increasing linearly from zero to the desired value at t=t$_3$ (i=1,2):

$$n_i(t) = \left(n_{i,m} + n_{i,A} \sin\phi_{n_i}\right)\frac{t - t_2}{T_{acc}}$$ (3.59)

   ❑ Rudder angle δ$_R$ is immediately brought to the starting position:

$$\delta(t) = \delta_m + \delta_A \sin\phi_\delta$$ (3.60)

(d)   Oscillation phase (t$_3$<t<t$_4$)

   The motion of the longitudinal carriage is given by:

$$x_0(t) = x_0(t_3) + U_{0,m}(t - t_3) - \frac{U_{0,A}}{\omega_{u_0}}\left[\cos\left(\omega_{u_0}(t - t_3) + \phi_{u_0}\right) - \cos\phi_{u_0}\right]$$ (3.61)

while lateral carriage, yawing table and analogue outputs (propeller rate and rudder angle) are driven based on (3.53).

(e)   Deceleration phase ($t_4 < t < t_5$)

❑ A uniformly decelerating motion is used to stop the three mechanisms of the carriage ($f = x_0, y_0, \psi$):

$$f(t) = f(t_4) + \dot{f}(t_4)(t - t_4)\left(1 - \frac{1}{2}\frac{t - t_4}{T_{dec}}\right) \tag{3.62}$$

with positions at $t = t_4$, given by:

$$x_0(t_4) = x_0(t_3) + u_{0,m}T_{regime} - \frac{U_{0,A}}{\omega_{u_0}}\left[\cos\left(\omega_{u_0}T_{regime+\phi_{u_0}}\right) - \cos\phi_{u_0}\right]$$

$$y_0(t_4) = y_{0,m} + y_{0,A}\,\sin\left(\omega_{y_0}T_{regime} + \phi_{y_0}\right) \tag{3.63}$$

$$\psi(t_4) = \psi_m + \psi_A\,\sin\left(\omega_\psi T_{regime} + \phi_\psi\right)$$

and velocities:

$$\dot{x}_0(t_4) = u_{0,m} + u_{0,A}\,\sin\left(\omega_{u_0}T_{regime} + \phi_{u_0}\right)$$

$$\dot{y}_0(t_4) = y_{0,A}\omega_{y_0}\,\cos\left(\omega_{y_0}T_{regime} + \phi_{y_0}\right) \tag{3.64}$$

$$\dot{\psi}(t_4) = \psi_A\omega_\psi\,\cos\left(\omega_\psi T_{regime} + \phi_\psi\right)$$

❑ Analogue and digital outputs are set to zero.

(f)   Additional measuring time ($t_5 < t < t_6$)

❑ The longitudinal carriage is at his end point.

❑ Analogue and digital outputs are zero.

While examining hull-propeller-rudder combination some special test types derived from this MULTI0 type will be considered:

❑ a multi-modal test of type A is stationary in all kinematical parameters and the propeller rpm but gives a harmonically varying rudder angle, e.g. between a range of [-40 deg; 40 deg];

❑ a multi-modal test of type B is stationary in all kinematical parameters while the control parameters, propeller rate and rudder angle, are varied harmonically. Mostly the propeller rate is restricted to positive or negative values so that a propeller ahead and a reversed propeller condition are not combined during one test run. As both control parameters are varied at the same time a large amount of combinations (n, δ_R) can be reached during this test run. On the other hand, positive and negative rudder angles will not be combined with the same propeller rates so that differences may exist between forces measured at the rudder during a port and a starboard turn (Figure 3.28).

3.3.6.2 Description of multi-modal test, type MULTI1

A multi-modal test op type MULTI1 has the same objectives as a test of type MULTI0, although the test parameters are imposed in another way. The kinematical parameters are defined in a ship-fixed axis system. Following parameters can be harmonically varied:

❑ u: longitudinal velocity component

❑ v: lateral velocity component

❑ r: yaw velocity

❑ n_1 and n_2: propeller rate of turn for a single screw (n_1) or a double screw ship (n_1 and n_2)

❑ δ_R: rudder angle

The harmonic behaviour of these parameters is based on equation (3.53).

(a)   Waiting time ($0 < t < t_1$)

❑ The carriage is positioned in its starting point:

$$x_0(0) = x_{0,start}$$

$$y_0(0) = y_m - \frac{1}{2}(u_m \sin\psi_m + v_m \cos\psi_m)T_{regime} - \int_{t_2}^{t_3}[u(t)\sin\psi(t) + v(t)\cos\psi(t)]dt \quad (3.65)$$

$$\psi(0) = \psi_m - \frac{1}{2}r_m(T_{regime} + T_{acc}) - \frac{1}{2}r_A T_{acc} \sin\phi_r + \frac{1}{12}\omega_r r_A T_{acc}^2 \cos\phi_r$$

❑ Analogue and digital outputs are 0.

(b) Calibration ($t_1 < t < t_2$)
  ❑ The carriage stays at his starting point.
  ❑ Analogue and digital outputs are 0.

(c) Acceleration phase ($t_2 < t < t_3$)
  ❑ In a ship-fixed axis system following velocity components are imposed (f=u,v,r):

$$f = \left[3f(t_3) - \dot{f}(t_3)T_{acc}\right]\left(\frac{t-t_2}{T_{acc}}\right)^2 + \left[-2f(t_3) + \dot{f}(t_3)T_{acc}\right]\left(\frac{t-t_2}{T_{acc}}\right)^3 \quad (3.66)$$

with

$$f(t_3) = f_m + f_A \sin\phi_f$$
$$\dot{f}(t_3) = \omega_f f_A \cos\phi_f \quad (3.67)$$

At the end of the acceleration phase the positions are:

$$x_0(t_3) = x_0(0) + \int_{t_2}^{t_3}[u(t)\cos\psi(t) - v(t)\sin\psi(t)]dt$$

$$y_0(t_3) = y_m - \frac{1}{2}(u_m \sin\psi_m + v_m \cos\psi_m)T_{regime} \quad (3.68)$$

$$\psi(t_3) = \psi_m - \frac{1}{2}r_m T_{regime}$$

  ❑ Propeller rate of turn n_i is increasing linearly from zero to the desired value at $t=t_3$, (3.59). Rudder angle δ_R is immediately brought to the starting position (3.60).

(d) Oscillation phase ($t_3 < t < t_4$)
  The velocity components are varied according to (3.53). Integration gives:

$$x_0(t) = x_0(t_3) + \int_{t_3}^{t}[u(t)\cos\psi(t) - v(t)\sin\psi(t)]dt$$

$$y_0(t) = y_0(t_3) + \int_{t_3}^{t}[u(t)\sin\psi(t) + v(t)\cos\psi(t)]dt \quad (3.69)$$

$$\psi(t) = \psi_m + r_m\left(t - t_3 - \frac{1}{2}T_{regime}\right) - \frac{r_A}{\omega_r}[\cos(\omega_r(t - t_3) + \phi_r) - \cos\phi_r]$$

  Propeller rate and rudder angle follow equation (3.53).

(e) Deceleration phase ($t_4 < t < t_5$)
  ❑ A uniformly decelerating motion is used to stop the three mechanisms of the carriage (f = x_0, y_0, ψ), see equation (3.62).
  ❑ Analogue and digital outputs are set to zero.

(f) Additional measuring time ($t_5 < t < t_6$)
  ❑ The longitudinal carriage is at his end point.
  ❑ Analogue and digital outputs are zero.

3.4 Captive model test program for model E and model D

Manoeuvring mathematical models will only be developed for model E at the scantling draught and for model D at the draught of 15.0m. Considering a four-quadrant operation for hull,

propeller and rudder forces, the availability of captive model data for each quadrant must be examined. In the following sections a summary is given of the test types that have been executed in each quadrant with some additional information about the Froude number (based on the total ship velocity $V = \sqrt{u^2 + v^2}$, the propeller rate n (compared to the reference propeller rate n_0 which is 100 rpm full scale), the drift angle β and the rudder angle δ_R. For model E at scale 85 and model D at scale 75 the relationship between Froude number and full scale velocity is presented in Table 3.5.

The following tables give a lot of data that will be important for the analysis in the chapters 4 to 6 for the mathematical modelling and chapter 7 for the validation:

❑ Table 3.6: available test types for model E at 20% UKC, going ahead
❑ Table 3.7: available test types for model E at 20% UKC, going astern
❑ Table 3.8: available test types for model E at 50% UKC, going ahead
❑ Table 3.9: available test types for model E at 50% UKC, going astern
❑ Table 3.10: available test types for model D at 20% UKC, going ahead
❑ Table 3.11: available test types for model D at 20% UKC, going astern

Tests executed in 1997 with model E and rudder deflection are not included in these tables due to errors while executing the rudder angle tests.

Table 3.5 Relationship between Froude number and full scale ship velocity for model E and model D

Model	F_n						
	0.016	0.032	0.049	0.065	0.077	0.116	
D	1.66	3.32	5.08	6.74	7.99	12.03	Speed (knots)
E	1.76	3.52	5.38	7.14	8.46	N.A.	

3.4.1 Test program for model E at 20% and 50% UKC

The maximum ship speed for the determination of hull-propeller-rudder interaction is 7.1 knots full scale (going ahead) and -3.5 knots full scale (going astern); for the hull-propeller interaction this speed is somewhat higher. For the rudder induced forces and moment for quadrant 1, stationary tests (STATX) with non-zero drift angle and PMM yaw tests (PMMPSI) have only been executed with the smallest Froude number ahead, $F_n=0.016$, so that multi-modal tests of type B will have to be used for the determination of the influence of drift angle on rudder induced coefficients (see chapter 6 and 7). Model E has not been tested in all four quadrants at medium deep water or 50% UKC.

Table 3.6 Schematic overview of available test types for model E at 20% UKC, going ahead

	Test type	Quadrant 1	Quadrant 2
Hull-propeller combination	PAAL	no tests available	no tests available
	STATX	straigth-line tests F_n = 0.065, 0.057, 0.049, 0.033, 0.024, 0.016 n = 35, 50, 75, 100, 110%n_0 oblique towing tests $\|\beta\|$ = 2.5, 5, 8, 10, 20, 30, 35, 40, 60, 90 deg F_n = 0.065, 0.033, 0.016 n = 60, 100%n_0	straigth-line tests F_n = 0.076, 0.065, 0.064, 0.057, 0.049, 0.033, 0.024, 0.016 n = -35, -50, -75, -100, -110%n_0 oblique towing tests $\|\beta\|$ = 2.5, 5, 10, 15, 20, 25, 30, 60, 90 deg F_n = 0.076, 0.065, 0.064, 0.057, 0.049, 0.033, 0.024, 0.016 n = -50, -75, -100%n_0
	PMMY et al	no tests available	no tests available
	PMMY_L et al	F_n = 0.065, 0.033 n = 75,100%n_0	no tests available
	PMMPSI et al	$\|\beta\|$ = 0 deg F_n = 0.065, 0.049, 0.033, 0.016 n = 50, 100%n_0	$\|\beta\|$ = 0, 5 deg F_n = 0.016 n = -100%n_0
	MULTI0	multi B $\|\beta\|$ = 0, 2.5, 5, 10, 15, 20, 25, 30, 60, 90 deg	no tests available

	Test type	Quadrant 1	Quadrant 2
		F_n = 0.065, 0.049, 0.033, 0.016 n = 0 → 110% n_0	
	MULTI1	no tests available	no tests available
Hull-propeller-rudder combination	PAAL	no tests available	no tests available
	STATX	straigth-line tests F_n = 0.065, 0.033, 0.016 n = 50, 60, 100%n_0 $|\delta_R|$ = 20, 30, 40 deg oblique towing tests $|\beta|$ = 2.5, 5, 10, 30, 60, 90 deg F_n = 0.016 n = 60, 100%n_0 $|\delta_R|$ = 20, 40 deg	straigth-line tests F_n = 0.065, 0.016 n = -50, -75, -100%n_0 $|\delta_R|$ = 20, 40 deg oblique towing tests $|\beta|$ = 2.5, 5, 10, 30, 60, 90 deg F_n = 0.065, 0.016 n = -50, -75, -100%n_0 $|\delta_R|$ = 20, 40 deg
	PMMY et al	no tests available	no tests available
	PMMY_L et al	no tests available	no tests available
	PMMPSI et al	$|\beta|$ = 0 deg F_n = 0.016 n = 100%n_0 $|\delta_R|$ = 20, 40 deg	$|\beta|$ = 0 deg F_n = 0.016 n = -100%n_0 $|\delta_R|$ = 20, 40 deg
	MULTI0	multi A $|\beta|$ = 0 deg F_n = 0.065, 0.049, 0.033, 0.016 n = 50, 75, 100%n_0 $|\delta_R|$ = 0→ 40 deg multi B $|\beta|$ = 0, 2.5, 5, 10, 15, 20, 25, 30, 60, 90 deg F_n = 0.065, 0.049, 0.033, 0.016 n = 0 → 110% n_0 $|\delta_R|$ = 0→ 40 deg	no tests available
	MULTI1	no tests available	no tests available

Table 3.7 Schematic overview of available test types for model E at 20% UKC, going astern

	Test type	Quadrant 3	Quadrant 4
Hull-propeller combination	PAAL	no tests available	no tests available
	STATX	straigth-line tests F_n = -0.057, -0.049, -0.016 n = -35, -50, -75, -100, -110%n_0 oblique towing tests $|\beta|$ = 177.5, 175, 170, 150, 120 deg F_n = -0.033, -0.016 n = -50, -75, -100%n_0	straigth-line tests F_n = -0.057, -0.049, -0.035, -0.031, -0.016 n = 35, 50, 75, 100, 110%n_0 oblique towing tests $|\beta|$ = 177.5, 175, 170, 160, 150, 145, 140, 120 deg F_n = -0.049, -0.035, -0.031, -0.016 n = 50, 60, 75, 100%n_0
	PMMY et al	no tests available	no tests available
	PMMY_L et al	no tests available	no tests available
	PMMPSI et al	$|\beta|$ = 180, 175 deg F_n = -0.016 n = -100%n_0	$|\beta|$ = 180, 175 deg F_n = -0.016 n = 100%n_0
	MULTI0	no tests available	multi B $|\beta|$ = 180, 177.6, 175, 170, 150, 120, 90 deg F_n = -0.016 n = 0 → 110% n_0
	MULTI1	no tests available	no tests available
Hull-propeller-rudder combination	PAAL	no tests available	no tests available
	STATX	straigth-line tests F_n = -0.033, -0.016 n = -50, -75, -100,%n_0 $|\delta_R|$ = 20, 40 deg oblique towing tests $|\beta|$ = 177.5, 175, 170, 150, 120 deg	straigth-line tests F_n = -0.033, -0.016 n = 50, 60, 100%n_0 $|\delta_R|$ = 20, 40 deg oblique towing tests $|\beta|$ = 177.5, 175, 170, 150, 120 deg

67

	Test type	Quadrant 3	Quadrant 4
		F_n = -0.033, -0.016 n = -50, -75, -100%n_0 $|\delta_R|$ = 20, 40 deg	F_n = -0.033, -0.016 n = 60, 100%n_0 $|\delta_R|$ = 20, 40 deg
	PMMY et al	no tests available	no tests available
	PMMY_L et al	no tests available	no tests available
	PMMPSI et al	$|\beta|$ = 180 deg F_n = -0.016 n = -100%n_0 $|\delta_R|$ = 20, 40 deg	$|\beta|$ = 180 deg F_n = -0.016 n = 100%n_0 $|\delta_R|$ = 20, 40 deg
	MULTI0	no tests available	multi A $|\beta|$ = 180 deg F_n = -0.016 n = 50, 75, 100%n_0 $|\delta_R|$ = 0→ 40 deg multi B $|\beta|$ = 180, 177.5, 175, 170, 150, 120 deg F_n = -0.016 n = 0 → 110% n_0 $|\delta_R|$ = 0→ 40 deg
	MULTI1	no tests available	no tests available

Table 3.8 Schematic overview of available test types for model E at 50% UKC, going ahead

	Test type	Quadrant 1	Quadrant 2
Hull-propeller combination	PAAL	no tests available	no tests available
	STATX	straigth-line tests F_n = 0.065, 0.057, 0.033, 0.024, 0.016 n = 35, 50, 75, 100, 110%n_0 oblique towing tests $|\beta|$ = 2.5, 5, 8, 10, 20, 30, 35, 40, 60, 90 deg F_n = 0.065, 0.033, 0.016 n = 60, 100%n_0	straigth-line tests F_n = 0.065, 0.057, 0.033, 0.024, 0.016 n = -35, -50, -75, -100, -110%n_0 oblique towing tests $|\beta|$ = 2.5, 5, 10, 15, 20, 25, 30, 60, 90 deg F_n = 0.065, 0.057, 0.033, 0.024, 0.016 n = -50, -75, -100%n_0
	PMMY et al	no tests available	no tests available
	PMMY_L et al	no tests available	no tests available
	PMMPSI et al	$|\beta|$ = 0 deg F_n = 0.065, 0.049, 0.033 n = 50, 100%n_0	no tests available
	MULTI0	multi B $|\beta|$ = 0, 2.5, 5, 10, 15, 20, 25, 30, 60, 90 deg F_n = 0.065, 0.049, 0.033, 0.016 n = 0 → 110% n_0	no tests available
	MULTI1	$|\beta|$ = 0 → 180 deg F_n = -0.016 → 0.016 n = 75, 100%n_0	no test available
Hull- propeller-rudder combination	PAAL	no tests available	no tests available
	STATX	straigth-line tests F_n = 0.065, 0.033, 0.016 n = 50, 60, 100%n_0 $|\delta_R|$ = 20, 30, 40 deg oblique towing tests $|\beta|$ = 2.5, 5, 10, 30, 60, 90 deg F_n = 0.016 n = 60, 100%n_0 $|\delta_R|$ = 20, 40 deg	no tests available
	PMMY et al	no tests available	no tests available
	PMMY_L et al	no tests available	no tests available
	PMMPSI et al	no tests available	no tests available
	MULTI0	multi A $|\beta|$ = 0 deg F_n = 0.065, 0.049, 0.016	no tests available

	Test type	Quadrant 1	Quadrant 2
		$n = 50, 75, 100\%n_0$ $\|\delta_R\| = 0 \rightarrow 40$ deg multi B $\|\beta\| = 0, 2.5, 5, 10, 15, 20, 25, 30, 60, 90$ deg $F_n = 0.065, 0.049, 0.016$ $n = 0 \rightarrow 110\% n_0$ $\|\delta_R\| = 0 \rightarrow 40$ deg	
	MULTI1	no test available	no test available

Table 3.9 Schematic overview of available test types for model E at 50% UKC, going astern

	Test type	Quadrant 3	Quadrant 4
Hull-propeller combination	PAAL	no tests available	no tests available
	STATX	no test available	straigth-line tests $F_n = -0.016$ $n = 35, 50, 75, 100, 110\%n_0$ oblique towing tests $\|\beta\| = 177.5, 175, 170, 160, 150, 145, 140, 120$ deg $F_n = -0.016$ $n = 50, 60, 75, 100\%n_0$
	PMMY et al	no tests available	no tests available
	PMMY_L et al	no tests available	no tests available
	PMMPSI et al	no tests available	no tests available
	MULTI0	no tests available	multi B $\|\beta\| = 180, 177.6, 175, 170, 150, 120, 90$ deg $F_n = -0.016$ $n = 0 \rightarrow 110\% n_0$
	MULTI1	no tests available	see quadrant 1
Hull- propeller-rudder combination	PAAL	no tests available	no tests available
	STATX	no tests available	straigth-line tests $F_n = -0.016$ $n = 50, 100\%n_0$ $\|\delta_R\| = 20, 40$ deg blique towing tests $\|\beta\| = 177.5, 175, 170, 150, 120$ deg $F_n = -0.016$ $n = 60, 100\%n_0$ $\|\delta_R\| = 20, 40$ deg
	PMMY et al	no tests available	no tests available
	PMMY_L et al	no tests available	no tests available
	PMMPSI et al	no tests available	no tests available
	MULTI0	no tests available	multi A $\|\beta\| = 180$ deg $F_n = -0.016$ $n = 50, 75, 100\%n_0$ $\|\delta_R\| = 0 \rightarrow 40$ deg multi B $\|\beta\| = 180, 177.5, 175, 170, 150, 120$ deg $F_n = -0.016$ $n = 0 \rightarrow 110\% n_0$ $\|\delta_R\| = 0 \rightarrow 40$ deg
	MULTI1	no tests available	no tests available

3.4.2 Test program for model D at 20% UKC

The maximum ship speed for model D is much higher than for model E: 16 knots ahead and -3.3 knots astern at full scale. For quadrant 1, stationary tests for the hull-propeller-rudder combination are restricted to a drift angle of 5 deg so that multi-modal tests of type B will be added to the input data for the determination of rudder induced coefficients.

Table 3.10 Schematic overview of available test types for model D at 20% UKC, going ahead

	Test type	Quadrant 1	Quadrant 2
Hull-propeller combination	PAAL	n = 35, 50, 75, 100, 110% n_0	see quadrant 3
	STATX	straigth-line tests F_n = 0.116, 0.077, 0.065, 0.049, 0.032, 0.016 n = 50, 75, 100, 110%n_0 oblique towing tests $\|\beta\|$ = 2.5, 5, 10, 15, 20, 30, 40, 50, (70, 90) deg F_n = 0.116, 0.077, 0.049, 0.032, 0.016 n = 50, 75, 100%n_0	straigth-line tests F_n = 0.116, 0.077, 0.065, 0.049, 0.032, 0.016 n = -35, -50, -75, -100, -110%n_0 oblique towing tests $\|\beta\|$ = 2.5, 5, 10, 15, 20, 30, 40, 50, (60, 90) deg F_n = 0.116, 0.077, 0.065, 0.049, 0.032, 0.016 n = -35, -50, -75, -100%n_0
	PMMY et al	no tests available	no tests available
	PMMY_L et al	F_n = 0.065, 0.032 n = 75,100%n_0	no tests available
	PMMPSI et al	$\|\beta\|$ = 0, 2.5, 5 deg F_n = 0.065, 0.049, 0.032, 0.016 n = 50, 75, 100%n_0	$\|\beta\|$ = 0, 5 deg F_n = 0.049, 0.016 n = -75, -100%n_0
	MULTI0	multi B $\|\beta\|$ = 0, 2.5, 5, 10, 30, 60, 90 deg F_n = 0.065, 0.016 n = 0 $\rightarrow$ 110% n_0	no tests available
	MULTI1	no tests available	no tests available
Hull- propeller-rudder combination	PAAL	n = 35, 50, 75, 100, 110% n_0 $\|\delta_R\|$ = 10, 20, 30, 40 deg	see quadrant 3
	STATX	straigth-line tests F_n = 0.116, 0.077, 0.049, 0.032, 0.016 n = 50, 100% n_0 $\|\delta_R\|$ = 5, 10, 20, 30, 40 deg oblique towing tests $\|\beta\|$ = 5 deg F_n = 0.116, 0.077, 0.049, 0.016 n = 50, 100%n_0 $\|\delta_R\|$ = 5, 10, 20, 30, 40 deg	straigth-line tests F_n = 0.116, 0.077, 0.049, 0.016 n = -35, -50, -100%n_0 $\|\delta_R\|$ = 5, 10, 20, 30, 40 deg oblique towing tests $\|\beta\|$ = 5, 15 deg F_n = 0.032, 0.016 n = -35, -50, -100%n_0 $\|\delta_R\|$ = 10, 20, 30, 40 deg
	PMMY et al	no tests available	no tests available
	PMMY_L et al	no tests available	no tests available
	PMMPSI et al	$\|\beta\|$ = 0, 2.5, 5 deg F_n = 0.065, 0.049, 0.032, 0.016 n = 50, 75, 100%n_0 $\|\delta_R\|$ = 10, 20, 30, 40 deg	$\|\beta\|$ = 0 deg F_n = 0.049, 0.016 n = -75, -100%n_0 $\|\delta_R\|$ = 10, 20, 30, 40 deg
	MULTI0	multi A $\|\beta\|$ = 0 deg F_n = 0.154, 0.122, 0.081, 0.077, 0.065, 0.049, 0.032, 0.016 n = 35 $\rightarrow$ 122% n_0 $\|\delta_R\|$ = 0$\rightarrow$ 40 deg multi B $\|\beta\|$ = 0, 2.5, 5, 10, 15, 20, 30, 40, 50, 60, 70, 80, 90 deg F_n = 0.154, 0.122, 0.081, 0.077, 0.065, 0.049, 0.032, 0.016 n = 0 $\rightarrow$ 122% n_0 $\|\delta_R\|$ = 0$\rightarrow$ 40 deg	multi A $\|\beta\|$ = 0 deg F_n = 0.154, 0.122, 0.081, 0.077, 0.065, 0.049, 0.032, 0.016 n = -35 $\rightarrow$ -122% n_0 $\|\delta_R\|$ = 0$\rightarrow$ 40 deg
	MULTI1	no tests available	no tests available

Table 3.11 Schematic overview of available test types for model D at 20% UKC, going astern

	Test type	Quadrant 3	Quadrant 4
Hull- propeller combinati	PAAL	n = -50, -100%n_0	see quadrant 1
	STATX	straigth-line tests F_n = -0.032, -0.016 n = -35, -50, -75, -100%n_0	straigth-line tests F_n = -0.032, -0.016 n = 50, 75, 100%n_0

	Test type	Quadrant 3	Quadrant 4
		oblique towing tests $\lvert\beta\rvert$ = 177.5, 175, 170, 160, 150, 140, 130, 110 deg F_n = -0.032, -0.016 n = -35, -50, -75, -100%n_0	oblique towing tests $\lvert\beta\rvert$ = 177.5, 175, 170, 160, 150, 140, 130, 110 deg F_n = -0.032, -0.016 n = 35, 50, 75, 100%n_0
	PMMY et al	no tests available	no tests available
	PMMY_L et al	no tests available	no tests available
	PMMPSI et al	$\lvert\beta\rvert$ = 180, 175 deg F_n = -0.032, -0.016 n = -75, -100%n_0	$\lvert\beta\rvert$ = 180, 175 deg F_n = -0.032, -0.016 n = 75, 100%n_0
	MULTI0	no tests available	multi B $\lvert\beta\rvert$ = 180, 177.5, 175, 170, 150, 120 deg F_n = -0.016 n = 0 $\rightarrow$ 110% n_0
	MULTI1	no tests available	no tests available
Hull- propeller-rudder combination	PAAL	no tests available	see quadrant 1
	STATX	straigth-line tests F_n = -0.032, -0.016 n = -100%n_0 $\lvert\delta_R\rvert$ = 20, 40 deg oblique towing tests $\lvert\beta\rvert$ = 170, 150, 120 deg F_n = -0.032, -0.016 n = -50, -100%n_0 $\lvert\delta_R\rvert$ = 20, 40 deg	straigth-line tests F_n = -0.032, -0.016 n = 75, 100%n_0 $\lvert\delta_R\rvert$ = 10, 20, 30 deg oblique towing tests $\lvert\beta\rvert$ = 175, 170 deg F_n = -0.032, -0.016 n = 100%n_0 $\lvert\delta_R\rvert$ = 10, 30 deg
	PMMY et al	no tests available	no tests available
	PMMY_L et al	no tests available	no tests available
	PMMPSI et al	$\lvert\beta\rvert$ = 180 deg F_n = -0.032, -0.016 n = -75, -100%n_0 $\lvert\delta_R\rvert$ = 10, 20, 30, 40 deg	$\lvert\beta\rvert$ = 180 deg F_n = -0.032, -0.016 n = 75, 100%n_0 $\lvert\delta_R\rvert$ = 10, 20, 30, 40 deg
	MULTI0	multi A $\lvert\beta\rvert$ = 180 deg F_n = -0.032, -0.016 n = -35 $\rightarrow$ -122% n_0 $\lvert\delta_R\rvert$ = 0$\rightarrow$ 40 deg	multi A $\lvert\beta\rvert$ = 180 deg F_n = -0.032, -0.016 n = 35 $\rightarrow$ 122% n_0 $\lvert\delta_R\rvert$ = 0$\rightarrow$ 40 deg multi B $\lvert\beta\rvert$ = 180, 177.5, 175, 170, 160, 150, 140, 130, 120, 110, 100 deg F_n = -0.032, -0.016 n = 0 $\rightarrow$ 110% n_0 $\lvert\delta_R\rvert$ = 0$\rightarrow$ 40 deg
	MULTI1	no tests available	no tests available

3.5 Quality control: description of observed inaccuracies

Since the installation of the towing tank captive model tests described in section 3.3 have been executed following the philosophy stated in [66] and the ITTC Recommended Procedures (http://ittc.sname.org/documents.htm). Due to shortcomings of varied natures of which some of them will be discussed in this section, the modelling process in chapters 4 to 6 must be executed with care. This discussion could help in setting up an experimental platform which is based on international accepted procedures applied in such a way that shortcomings detected in the past will be avoided in the future. In the following discussions can be found according to:

❏ occurrence of interference between measured longitudinal and lateral force components during straight-line resistance tests: section 3.5.1;

❏ unrealistic measurements of propeller thrust due to mounting problems or measurements inaccuracies and unusual effects during propulsion tests: section 3.5.2;

- ❑ measurement errors on tangential rudder force F_T during rudder angle tests: section 3.5.3;
- ❑ the development of a test program for quality control of the modules hull, propeller and rudder of a ship model combination: section 3.5.4;
- ❑ the influence of an increasing waiting time between test runs: section 3.5.5.

3.5.1 Interference at straight-line resistance tests

Straight-line tests in open and calm water without rudder deflection and with low propeller loading only induce longitudinal forces. At high speed important sinkage and trim of the ship model will occur due to squat. Calibration tests could be executed to verify the existence of interference on lateral force measurement devices during these pure straight-line tests.

An example of measurement inaccuracies or unexpected physical phenomena generated in the towing tank during straight-line resistance tests with low propeller loading is given in Table 3.12. Resistance tests have been executed with model D at 7% UKC at different Froude numbers (series DC: low Froude numbers and series D3: higher Froude numbers). At 12 knots problems occur during test run D3_12100 and D3_12200 where mean values for the longitudinal and the lateral force measured during conditions 1 and 2 (italic form in Table 3.12) differ from values measured during condition 3 (end of the test run). Positive lateral forces (2 to 3.5N) are measured with lower absolute values for the resistance force X (6N instead of 7.5N). As only important longitudinal forces are expected, time series can be considered to evaluate this phenomenon which does not appear during test runs at lower Froude numbers.

Table 3.12 Straight-line resistance tests with model D at 7% UKC

Run name	u	position x in tank	X force	Y force	N moment	sinkage	trim	n	T thrust	Q torque
	(m/s)	(m)	(N)	(N)	(Nm)	(mm)	(mm/m)	(rpm)	(N)	(Nmm)
D3_10101	0.594	2.9997	-4.376	0.627	0.033	5.2	-0.68	10	0.202	-16.21
D3_10101	0.594	22.9878	-4.399	-0.118	-0.028	5.07	-0.71	10	0.186	-15.29
D3_10101	0.594	42.9759	-4.318	0.655	0.292	5.03	-0.64	9	0.208	-14.52
D3_10200	0.594	2.9997	-4.346	0.461	0.222	5.19	-0.65	10	-0.043	-10.52
D3_10200	0.594	22.9878	-4.292	0.561	0.181	5.05	-0.7	62	-0.074	-12.47
D3_10200	0.594	42.9759	-3.99	0.07	0.402	5.03	-0.64	149	-0.133	-16.34
D3_12100	*0.713*	*2.9946*	*-6.138*	*3.076*	*-0.013*	*8.08*	*-0.75*	*10*	*-0.221*	*-16.55*
D3_12100	*0.713*	*22.9943*	*-6.075*	*3.631*	*0.544*	*7.84*	*-0.79*	*10*	*-0.211*	*-16.37*
D3_12100	0.713	42.9939	-7.672	-0.38	0.085	7.52	-0.6	10	-0.204	-15.54
D3_12200	*0.713*	*2.9946*	*-6.216*	*2.089*	*-0.753*	*8.16*	*-0.76*	*10*	*0.025*	*-7.27*
D3_12200	*0.713*	*22.9943*	*-5.954*	*3.106*	*0.297*	*7.88*	*-0.8*	*61*	*0.011*	*-8.51*
D3_12200	0.713	42.9939	-7.31	-0.139	0.067	7.62	-0.62	149	-0.12	-13
D3_8102	0.475	2.9925	-2.764	-0.419	-0.273	2.96	-0.3	10	-0.515	-18.2
D3_8102	0.475	22.99	-2.723	-0.4	-0.125	2.84	-0.33	10	-0.508	-17.9
D3_8102	0.475	42.9875	-2.783	-0.085	0.104	2.91	-0.31	10	-0.492	-17.24
D3_8200	0.475	2.9925	-2.79	-0.015	0.196	2.95	-0.3	10	0.137	-12.22
D3_8200	0.475	22.99	-2.725	-0.174	0.046	2.84	-0.33	61	0.137	-13.14
D3_8200	0.475	42.9875	-2.449	0.034	0.109	2.98	-0.31	149	0.014	-18.39
DCCA01	0.4	5	1.411	0.242	-0.032	2.38	-0.36	433	3.045	46.08
DCCA01	0.4	23	-1.531	-0.225	0.231	2.01	-0.25	-1	-0.193	-50.41
DCCC01	0.2	5	2.624	-0.196	-0.134	0.52	-0.14	432	2.932	63.44
DCCC01	0.2	23	-0.3	-0.561	-0.494	0.37	-0.02	-1	-0.226	-7.69

Figure 3.29 and Figure 3.30 are connected with run D3_12100, while Figure 3.31 and Figure 3.32 summarize measurements for run D3_12200. Black full lines denote longitudinal force or lateral force and dotted lines denote propeller thrust or yawing moment. The analysis of each test run is based on a division of the complete time variation in three conditions with identical duration. At the end of test run D3_12100 the scatter increases with a generally more negative value for the longitudinal force while the variation in the lateral force is diminished during this phase. The reason of this phenomenon is hardly found as sinkage of the ship model and wave

heights at different positions along the tank do not change notably during the complete test run. The same conclusions can be drawn for run D3_12200 where the propeller rate varies from zero to almost 20% of the reference propeller rate comparing condition 1 to 3.

As hydrodynamic forces increase considerably with decreasing UKC flow disturbances in the towing tank should be avoided while executing tests at high speed in very shallow water conditions.

3.5.2 Mounting or measurement errors and unusual effects during propulsion tests

Analysing measured propeller thrust and torque the propeller model is supposed to run freely so that negligible thrust and torque values are measured at stopped propeller and low or zero forward speed. Test inaccuracies have nevertheless been noticed during propulsion tests with different ship models.

An example is given for model D at 20% UKC tested at two different moments in time. Two series can be distinguished based on the propeller thrust measurements (Figure 3.33):

❑ series 1 with tests executed at Froude numbers: 0.0, 0.016, 0.049, 0.077, 0.116;
❑ series 2 with tests executed at Froude numbers: 0.032, 0.065. These Froude numbers lie within the range of series 1.

With the exception of the propeller thrust measured at a combination of stopped propeller and $F_n=0.049$ (see Figure 3.33), measurements of thrust T_P for series 1 are physically realistic as negligible values are found around zero propeller rate and at higher propeller revolutions measured propeller thrust correspond to the open water value of an isolated propeller in a uniform flow. For series 2 a positive propeller thrust is measured at zero propeller revolutions, while at maximum model propeller rate measured propeller thrust is too low compared to the available open water curves. While the propeller thrust is lower at non-zero propeller rate for series 2, the propeller torque is much higher compared to the values of series 1. These inaccuracies are only related to measurement errors and not to any unexpected phenomenon in the flow around the aft body of the hull as increasing forward velocities, linked with test runs of series 1 and 2, give decreasing longitudinal forces for an identical propeller rate of turn (Figure 3.33 right).

A possible explanation of this unusual situation could be the mounting of the model propeller on the propeller shaft, where the propeller model is put under strain. The effect of this tension can disappear while increasing the propeller rate, but sometimes (see series 2) mounting problems can not be undone. Although measurement errors are relatively more important when forces are small, unusual phenomena which affect the propeller thrust over the complete range of propeller rate must be avoided.

The preceding figures are based on stationary propulsion tests. Multi-modal tests of type B (harmonically varying rudder angle and propeller rate of turn) can suffer from other remarkable phenomena:

❑ Due to a harmonically variation of the propeller rate transient effects are dominating during these test types resulting into lower thrust values during the increasing phase (development of the propeller slipstream, see Figure 3.34) compared to the decreasing phase (run-down of the propeller slipstream). This distinction which can be physically motivated, is especially seen for low ship velocities ($F_n=0.016$) and is negligible for higher Froude numbers ($F_n=0.081$). Instead, at low ship velocity a small positive propeller thrust is measured at very low propeller revolutions during the second phase while these values are almost zero at the start. A selection of measured propeller torque at start and end of each run is shown in Figure 3.35. Small but non-zero torque values are measured for both runs. In accordance with these test results at low speed, bollard pull tests suffer from circulating flows induced in the towing tank due to the propeller action. This observation could probably also explain the

difference between start and end at low ship velocities. Thrust measurements should be evaluated in detail, both quantitatively and visually, during tests at low speed and in shallow water.

❑ A second problem which can occur is the accordance between the desired and the measured value of the propeller rate of turn. Figure 3.36 is based on the same test run with F_n=0.016 as Figure 3.34 and Figure 3.35. A minimum force at the beginning and the end of the run is necessary to make the model propeller turn. Furthermore, maximum available propeller revolutions are restricted and do not reach the desired value.

In conclusion, the mounting of a propeller model must be done very carefully, the measurement equipment must be checked and control test runs must be developed to minimize the occurrence of inaccuracies.

3.5.3 Measurement errors on tangential rudder force F_T during rudder angle tests

During rudder angle tests the tangential rudder force F_{RT} parallel to the rudder chord is small compared to the normal rudder force F_{RN}. Small forces can relatively more be affected by measurement inaccuracies. For model D at 20% UKC inaccuracies occur during stationary and some PMM yaw tests which made the measurements of tangential force F_{RT} to be doubtful. If rudder forces F_X and F_Y in a ship fixed axis system are defined and modelled as:

$$F_X = F_{RT} \cos \delta_R - F_{RN} \sin \delta_R$$
$$F_Y = F_{RT} \sin \delta_R + F_{RN} \cos \delta_R$$

(3.70)

the unreliable measurements of F_{RT} affect the longitudinal rudder force F_X especially at low rudder angles. Rudder force F_X represents generally an additional resistance force at increasing rudder angles to port or starboard but based on Figure 3.37 at very low propeller loading this force turns into a positive contribution (less negative forces F_X, even an offset must be recognized) due to measurement errors at low velocity. The influence of inaccuracies are rather small for the lateral rudder force F_Y but the effect also depends on the propeller loading as lower values F_{RN} are measured at low propeller thrust loading. These errors result into physically unrealistic rudder forces F_Y as negative values are found for rudder angles to port (positive δ_R).

Although rudder angle tests are preceded by a calibration, measurement errors and a dysfunction of the rudder equipment must be avoided. Interference between longitudinal and lateral rudder force components must also be eliminated.

3.5.4 A physical test program for quality control

Until now at Flanders Hydraulics Research, the use of quality control tests focus on the execution of a number of prescribed multi-modal tests where different test parameters are varied during each test run. These tests, executed at the beginning and the end of a test program, are compared to each other to detect any dysfunction of one of the modules of a manoeuvring ship model or one of the measuring devices.

For a better understanding of the relationships between measured forces and applied phenomena and a quicker detection of any dysfunction of a module, this program could be changed to a physically motivated program so that some test runs can be evaluated on their feasibility for a number of isolated physical phenomena. These phenomena could be subdivided following the assembly of a ship model: namely, hull, propeller and rudder and three distinctive test types, a resistance (or oblique towing or yawing test) test, a propulsion test and a rudder angle test could be developed to verify the good behaviour of the active ship model combination.

3.5.5 Influence of waiting time between runs

According to [75] sufficient time must be allowed to achieve similar conditions for each of the runs and to obtain consistency in results. The waiting time will depend on the type and size of

the model, model speed, the size of the test facility and its wave absorption equipment such as beaches.

The influence of waiting time between two consecutive runs has been examined as a result of the conversion to the new beam for the computerized planar motion carriage in 1999. A comparison was made between the forces and yawing moment measured in the horizontal plane during stationary test runs with the old beam and the new beam. Test conditions are summarized in Table 3.13.

On Figure 3.38 longitudinal force, lateral force and yawing moment are compared for reference run EGCJ08. A better correspondence can be found with a huge waiting time of 5400 seconds or 90 minutes, especially for the lateral force and the yawing moment. With a waiting time of 1500 seconds or 25 minutes lateral force measurement devices are very sensitive to fluctuations in the flow around the ship model. A comparison based on reference run EGCL06 gives lower discrepancies (Figure 3.39) but still a better agreement is obtained with a large waiting time between the runs.

A waiting time of 5400 seconds is extremely high and reduces the number of test runs a day remarkably. The waiting time is generally situated between 20 and 30 minutes. Although the waiting time was rather moderate for the CPMC equipped with the old beam, the new beam seams to be more sensitive for remaining water flows in the tank.

Table 3.13 Test conditions of run EGCJ08 (quadrant 4) and EGCL06 (quadrant 1) with model E at 20% UKC

run name	model speed (m/s)	angle of carriage (deg)	propeller rate (rpm)	rudder angle (deg)
EGCJ08 cond1	-0.1	30	0	0
EGCJ08 cond2	-0.1	30	553	0
EGCJ08 cond3	-0.1	30	922	0
EGCL06 cond1	0.4	0	0	40
EGCL06 cond2	0.4	0	553	40
EGCL06 cond3	0.4	0	922	40

3.6 Analysis techniques

Depending on the test type, measurements of forces at fore and aft gauges, sinkage, propeller thrust and torque, propeller rate, rudder angle, rudder forces and rudder torque are analyzed using different methods. Mean values will be calculated for the stationary tests (STATX and PAAL) while a Fourier analysis will be adopted to the harmonic PMM sway and yaw test in 3.6.2. Multi-modal tests are preferably evaluated using a regression analysis, described in 3.6.3. In addition, these descriptions will be preceded by a literature study of linear theory for mathematical modelling based on PMM testing.

3.6.1 Linear theory for mathematical modelling based on PMM testing

3.6.1.1 General outline of linear theory

The determination of acceleration derivatives (added masses and added moment of inertia for horizontal motions) is made possible with the introduction of the PMM system. A PMM imposes an unsteady, sinusoidal motion to the ship model. Frequency, amplitude and model velocity can be changed during different test runs to provide data concerning the effect of acceleration on the hull forces to be described by mathematical manoeuvring models. It has always been of main concern whether the application of the theory of quasi-steady flow could be justified to the unsteady flow that is inescapably associated with PMM testing.

In a linear theory of a PMM sway test the lateral force ΔY due to the sinusoidal lateral motion y is written as ([34] and [35]):

$y = y_0 \sin\omega t$ and $y_{max} = y_0$

$v = y_0\omega \cos\omega t$ and $v_{max} = y_0\omega$

$\dot{v} = -y_0\omega^2 \sin\omega t$ and $\dot{v}_{max} = -y_0\omega^2$

$$\Delta Y = Y_v v + Y_{\dot{v}} \dot{v} \qquad (3.71)$$

$$= Y_v y_0\omega \cos\omega t - Y_{\dot{v}} y_0\omega^2 \sin\omega t$$

$$= Y_v v_{max} \cos\omega t + Y_{\dot{v}} \dot{v}_{max} \sin\omega t$$

$$= \Delta Y_{QUAD} \cos\omega t + \Delta Y_{IN} \sin\omega t$$

Although some authors deny the influence of frequency during PMM testing, measured force contributions ΔY_{IN} and ΔY_{QUAD} depend on frequency ω so that in a quasi-steady approach the derivatives Y_v and $Y_{\dot{v}}$ will be considered as the 'slow motion derivatives':

$$Y_v = \lim_{\omega \to 0}\left(\frac{\Delta Y_{QUAD}}{v_{max}}\right)$$

$$Y_{\dot{v}} = \lim_{\omega \to 0}\left(\frac{\Delta Y_{IN}}{\dot{v}_{max}}\right) \qquad (3.72)$$

The determination of these zero frequency values from PMM results is sometimes problematic as an extrapolation to zero frequency is needed based on tests executed at non-zero frequency. The true added mass of a ship in sway motion is $Y_{\dot{v}}(\infty)$ by definition:

$$Y_{\dot{v}}(\infty) = \lim_{\omega \to \infty}\left(\frac{\Delta Y_{IN}}{-y_0\omega^2}\right) \qquad (3.73)$$

Both derivatives depending on sway acceleration would only be the same if there were no 'memory' effects. In [34] tests have been executed with a Mariner model at scale λ=70 at high velocities (V=0.922 m/s and V=1.23 m/s) and frequencies ω varying between 1 and 13 rad/s. The results are therefore more related to small amplitude and high frequency testing. In the written discussion in [35] Gill denotes that thanks to the development of large amplitude PMM the problem of memory effects could be overcome by limiting the frequency. A non-dimensional frequency $\omega L_{PP}/u$ of 2 or 3 is often quoted as a maximum below which memory effects are negligible.

In [76] an analysis technique is introduced to determine acceleration derivatives and linear velocity derivatives because the previous method suffers from large scatter in the in-phase side force results in the low-frequency range of $\omega L_{PP}/u$. For a sinusoidal sway motion equation (3.71) for the lateral force is changed to:

$$Y(t) = Y_{IN} \sin\omega t + Y_{QUAD} \cos\omega t \qquad (3.74)$$

with

$$Y_{IN} = F\cos\varepsilon_F + A\cos\varepsilon_A$$
$$Y_{QUAD} = -F\sin\varepsilon_F - A\sin\varepsilon_A \qquad (3.75)$$

F and A being the magnitude of the forces measured at the fore and aft gauges, respectively; the corresponding phase angles are denoted ε_F and ε_A.

Slow motion derivatives at zero frequency can be determined based on

$$-Y_v = \lim_{\omega \to 0} \left\{ \frac{(F-A)}{y_0 \omega} \right\}$$

$$m - Y_{\dot{v}} = -\frac{d\varepsilon_F}{d\omega} \lim_{\omega \to 0} \left(\frac{F}{y_0 \omega} \right) + \frac{d\varepsilon_A}{d\omega} \lim_{\omega \to 0} \left(\frac{A}{y_0 \omega} \right)$$

$$-N_v = \bar{x} \lim_{\omega \to 0} \left\{ \frac{F+A}{y_0 \omega} \right\}$$

$$-N_{\dot{v}} = -\bar{x} \frac{d\varepsilon_F}{d\omega} \lim_{\omega \to 0} \left(\frac{F}{y_0 \omega} \right) - \bar{x} \frac{d\varepsilon_A}{d\omega} \lim_{\omega \to 0} \left(\frac{A}{y_0 \omega} \right)$$

(3.76)

with $\bar{x}$ distance of force gauges from amidships.

Equation (3.76) shows that the knowledge of the zero frequency limit of the ratios ($F/y_0\omega$, $A/y_0\omega$) of the forces F and A to the maximum sway velocity $y_0\omega$ and of the derivative of phase angles ε_F and ε_A to frequency makes it possible to determine the derivatives associated with sway motion.

According to Gill analysing the experimental data in this way reduces the scatter in the results at low frequencies compared with the conventional way of analysing PMM results in which the in phase and quadrature components are calculated. The expected values of phase angles ε_F and ε_A at zero frequency or steady state are known and equal 90 deg at the fore gauge and -90 deg at the aft gauge so that only measured forces F and A have to be extrapolated to zero frequency. Comparable expressions can be found for a sinusoidal yaw motion.

The tests reported in [76] have been conducted in a circulating water channel (CWC) so that the duration of the test run (especially at low frequencies) is not limited by the overall length of the towing tank. Indeed, the ship model has a zero forward speed while the water travels with the imposed test velocity (rather high values of 0.77 m/s or 0.85 m/s). Two tanker models and a fine model were oscillated in deep water at frequencies within the range of 0.06 to 1.6 rad/s and at various amplitudes within the philosophy that the larger the amplitude of oscillation the lower the frequency whereas the smaller the amplitude the higher the frequency.

Some problems nevertheless still arise (see written discussion in [76]):
- ❑ The gradient of the phase angle especially of the aft gauge can not be determined easily as the angle changes abruptly near zero frequency.
- ❑ Using a CWC in shallow water conditions could reveal some difficulties concerning the uniformity of the velocity distribution in transverse direction. This uniformity is essential as modified boundary layers in a CWC compared to a towing tank will affect the manoeuvring behaviour of the model.
- ❑ The question arises if there is a lower limit on the imposed test frequency below which no practical and realistic values can be obtained.
- ❑ Tests have been executed with constant motion amplitude so that the velocity amplitude decreases to zero with decreasing frequency.

The main conclusion is that steady state or 'slow motion' derivatives cannot be estimated with sufficient accuracy from oscillating experiments even if low frequencies have been used. In addition the use of 'slow motion' or zero frequency derivatives is questioned as transient motions always accompany ship manoeuvres.

In [77] this research is extended to small depth to draught ratios or shallow water conditions (a minimum of 1.21 for the tanker and 1.6 for the fine form). The effect of the boundary layer can be accounted for by defining an effective water depth which is the measured water depth less the displacement thickness of the boundary layer. The maximum amplitudes during the oscillatory tests were y_0=0.4 m for the sway tests and ψ_0=0.105 rad or 6 degrees for the yaw tests. These

limited values are chosen to minimize the wall effects of the CWC with a channel width of 3.66 m.

An attempt was made to visualize the speed dependence of non-dimensional lateral force and yawing moment as function of drift angle during oblique tow test with the tanker in shallow water. Although the speed was corrected for the additional blockage due to the drift angle no clear relationship is found between measured forces and Froude numbers. Only for the acceleration derivatives some tendency towards lower absolute values at decreasing velocity can be recognized. The results of the pure sway test with the tanker model at h/d=1.21 and F_n=0.066 will be compared in chapter 4 with the results of the Esso Osaka model. Another important observation during the pure sway tests was that at the higher speeds and large amplitudes the model was observed to heave and pitch at twice the frequency of the sway motion. Gill concludes by advising to clearly state the test parameters imposed during oscillatory tests if a comparison will be made between results published by several authors.

According to Mikelis and Price in [78] the validity of a strip wise theoretical calculation of hydrodynamic derivatives is questionable for ship manoeuvring in shallow or restricted waters. For small clearances between hull and the enclosed boundary, the flow becomes less two-dimensional and therefore the coefficients determined by considering only two-dimensional flows are of little physical relevance. Thus the only satisfactory method of determining the required hydrodynamic coefficients is by a three-dimensional analysis, modelling the flow around the arbitrary shaped body and the confining geometry. A 3D approach or an approach based on boundary element methods is necessary as using strip-theory resultant acceleration derivatives do not account for any longitudinal deviation in the fluid flow and thus results into an overestimation of the true value.

Although experimental results in this research are not compared to results of theoretical calculations, Bailey et al. [79] supposes that hybrid data bases could be created involving information from different types of experiment in conjunction with theoretical predictions to produce effective and efficient procedures allowing easier assessment of the behaviour of the vessel in different modes of operation. An extension of the research of these authors is also found in [80].

3.6.1.2 Comparison of results from stationary and oscillatory tests

In this research a comparison of velocity dependent tabular models from stationary and oscillatory tests can only be made for a sway motion, as no stationary yawing tests or circular motion tests have been executed. Some results can be found in chapter 4.

Even in earlier research a comparison of derivatives from stationary and oscillatory tests has been made. In [34] a reference can be found to the work of Gertler, reported in the 12th ITTC Proceedings, where the results of co-operative tests on the Mariner form were presented and the conclusion was that the values of the derivatives vary quite widely. A comparison in [34] made between results of deep water tests carried out at high velocities of 15 and 20 knots reveals that the steady state test and the planar motion mechanism tests are complementary if tests are executed and test results are analysed under certain controlled conditions.

Karasuno compares in [81] the results for quasi-steady hull forces obtained from a planar motion mechanism test with low frequencies to the results from stationary straight-line and circular test with test parameters within the range of exerted kinematical variables in the PMM test. For a deep water case the agreement is good while an extrapolation of PMM results to a wider range could also be justified.

Although these conclusions could be hopeful no results are found concerning shallow and very shallow water conditions where the influence of the applied test parameters during different test types is quite more important and hydrodynamic forces are considerably larger.

3.6.2 Fourier analysis

Programs have been developed to calculate hydrodynamic derivatives directly resulting from PMM tests based on a simplified version of a mathematical manoeuvring model for the hull forces and a Fourier analysis. This model for the horizontal forces and yawing moment is [74]:

$$X = \left(X_{\dot{u}} - m\right)\dot{u} + X_{u|u|} u|u| + X_{vv} v^2 + \left(X_{rr} + mx_G\right)r^2 + \left(X_{vr} + m\right)vr$$

$$Y = \left(Y_{\dot{v}} - m\right)\dot{v} + \left(Y_{\dot{r}} - mx_G\right)\dot{r} + Y_{uv} uv + \left(Y_{ur} - m\right)ur + Y_{v|v|} v|v| + Y_{r|r|} r|r| + Y_{v|r|} v|r| + Y_{r|v|} r|v|$$

$$N = \left(N_{\dot{v}} - mx_G\right)\dot{v} + \left(N_{\dot{r}} - I_{zz}\right)\dot{r} + N_{uv} uv + \left(N_{ur} - mx_G\right)ur + N_{v|v|} v|v| + N_{r|r|} r|r| + N_{v|r|} v|r| + N_{r|v|} r|v|$$

<div align="right">(3.77)</div>

The division in harmonic components is based on:

$$[X] = \begin{bmatrix} X \\ Y \\ N \end{bmatrix} = [X]^0 + \sum_{j=1}^{\infty} \left([X]_c^{[j]} \cos j\omega t + [X]_s^{[j]} \sin j\omega t\right)$$

<div align="right">(3.78)</div>

and mostly restricted to the third order components. The relationship between the acceleration derivatives and linear and non-linear velocity dependent derivatives is summarized in [74]. The acceleration derivatives can be determined based on the first harmonic cosine components:

❑ for sway

$$Yv'(1) \equiv -\frac{Y_c^{[1]}}{\omega^2 y_{0A}} \approx Y_{\dot{v}} - m$$

<div align="right">(3.79)</div>

$$Nv'(1) \equiv -\frac{N_c^{[1]}}{\omega^2 y_{0A}} \approx N_{\dot{v}} - mx_G$$

<div align="right">(3.80)</div>

❑ for yaw

$$Yr'(1) \equiv -\frac{Y_c^{[1]}}{\omega^2 \psi_A} \approx Y_{\dot{r}} - mx_G$$

<div align="right">(3.81)</div>

$$Nr'(1) \equiv -\frac{N_c^{[1]}}{\omega^2 \psi_A} \approx N_{\dot{r}} - I_{zz}$$

<div align="right">(3.82)</div>

3.6.3 Regression analysis

The regression analysis that will be widely used for the determination of the different modules of the mathematical model is based on the free "ODRPACK Software for Weighted Orthogonal Distance Regression" described in [82]. "*ODRPACK is a software package for weighted orthogonal distance regression, i.e., for finding the parameters that minimize the sum of the squared weighted orthogonal distances from a set of observations to the curve or surface determined by the parameters. It can also be used to solve the nonlinear ordinary least squares problem.*"

ODRPACK is a collection of Fortran subroutines for fitting a model to data and it has especially been used in this research for the determination of tabular models (see chapter 2). While using tabular models the sequence between the consecutive table values is based on a linear interpolation; no B-spline or other interpolation functions have been used.

The selection of the tabular input parameters has an important influence on modelled resultant or output parameters. This selection is mostly performed arbitrarily within the range of available input data. In Figure 3.40 an example is given of a tabular regression analysis for the longitudinal force due to pure yaw measured during an individual test run with model D. Tabular model 1 is based on a model with a step of 10 deg within the range of yaw rate angles [-60 deg; 60 deg]. Due to a lack of data at yaw rate angles near zero and the selection of tabular input parameters near these γ angles tabular output parameters will be determined which have

unrealistic high values near zero yaw rate angle. A second model with less input parameters near $\gamma=0$ gives better results.

The standard deviations that will be presented in the following chapters as error bars on the derived table values are "*the square roots of the diagonal elements of the covariance matrix for the estimators*". This means that if a 95% confidence interval is computed for each estimator or output parameter the standard deviations have to be multiplied with approximately 2. This remark could be important for the evaluation of the accuracy of some tabular models.

4 Modelling of hull forces and moment

Hull forces and moment acting on a manoeuvring ship are subdivided into acceleration dependent terms (section 4.1) and velocity dependent terms (section 4.2). Acceleration derivatives are determined based on non-stationary PMM tests and will depend on the test parameters applied during the PMM tests for surge (section 4.1.1), sway (section 4.1.2) and yaw motion (section 4.1.3). Velocity dependent forces and moment will be presented as tabular models and are examined considering the same elementary motions as for the acceleration derivatives:

❑ section 4.2.2: velocity dependent hull forces and moment due to a pure sway motion
❑ section 4.2.3: velocity dependent hull forces and moment due to a pure yaw motion
❑ section 4.2.4: combination of sway and yaw additional forces

Finally, a comparison is made for model E in section 4.2.5 between the medium deep water and shallow water condition which can be used for the validation of hull forces in chapter 7.

4.1 Acceleration dependent forces and moment

Acceleration dependent forces and moment can be summarized:

$$X_{Ha} = X_{\dot{u}}\dot{u} = m_x\dot{u}$$

$$Y_{Ha} = Y_{\dot{v}}\dot{v} + Y_{\dot{r}}\dot{r} = -m_y\dot{v} + Y_{\dot{r}}\dot{r} \tag{4.1}$$

$$N_{Ha} = N_{\dot{v}}\dot{v} + N_{\dot{r}}\dot{r} = N_{\dot{v}}\dot{v} - J_{zz}\dot{r}$$

The added masses m_x and m_y, the added moment of inertia J_{zz} and the acceleration derivatives $Y_{\dot{r}}$ and $N_{\dot{v}}$ will be discussed considering a surge (4.1.1), a sway (4.1.2) and a yaw (4.1.3) motion.

4.1.1 Surge motion

A ship's hull can be regarded as a slender body resulting into a low added mass m_x compared to the added mass due to sway m_y or the added moment due to yaw J_{zz}. In general, the added mass due to surge is just a fraction of the ship's mass m, so that this hydrodynamic coefficient is less important. The added mass m_x can be derived from oscillatory tests. Two different test types have been considered:

❑ oscillatory tests in x-direction (OSCX) with varying surge amplitude x_A (1 and 2 metres) and varying test frequency ω (from 0. 078 to 0.157rad/s)
❑ multi-modal tests (MULTI0) with harmonically varying longitudinal velocity (forward *or* backward motion) and harmonically varying longitudinal acceleration (acceleration *and* deceleration during one test run). In Figure 4.1 an example is given of variation of velocity and acceleration during a forward motion with model E at fully laden draught and 20% UKC. Measured sinkage and trim are especially dependent on velocity as maximum values are reached near maximum velocity. This means that in accordance with the observation reported by Gill in [77] the sinkage varies with a frequency of twice the test frequency.

Multi-modal tests offer advantages compared to oscillatory tests as no discontinuities in longitudinal velocity or acceleration occur at the start. Velocity and acceleration are built up gradually from zero value at the beginning and end at zero value. Additionally, positive and negative velocities are not combined during one test run contrary to oscillatory tests where measured longitudinal force will suffer from memory effects due to ship motion through its own wake.

Oscillatory tests are analysed based on a Fourier analysis up to the third order. To visualize the influence of wake, two calculations are made, one with a stop and start percentage of half a period which means an analysis for different oscillation cycles (method 1), and one with an

analysis of just the first cycle (method 2). The analysis of multi-modal tests makes use of a regression analysis over the complete test range. A summary of added masses is shown in Table 4.1.

Table 4.1. Ratio of added mass for surge to ship's mass (m_x/m)

m_x/m	Model D 20% UKC	Model D 7% UKC	Model E 50% UKC	Model E 20% UKC
OSCX, method 1	0.0628	0.0887	0.1139	0.1421
OSCX, method 2	0.0541	0.0830	0.1088	0.1396
MULTI			0.1120	0.2469

The influence of test frequency and surge amplitude during oscillatory tests appears to be small, even in very shallow water. The added mass based on the first oscillation cycle is lower than the value according to method 1. The influence of memory effects is nevertheless negligible. For model E a comparison can be made of added masses measured during multi-modal and oscillatory tests. At 50% UKC similar values are obtained. Although maximum acceleration values obtained during the two test types lie in the same range, the added mass at 20% UKC during a multi-modal test is almost 25% of the ship's mass compared to 14% during oscillatory tests. This tendency has to be confirmed in the future analysing multi-modal tests in very shallow water conditions for other full and slender ships.

Due to the streamlined design of model D the added mass due to surge is very small and does not increase remarkably with decreasing water depth.

4.1.2 Sway motion

The influence of sway acceleration on the lateral force appears to be more important than the influence on yawing moment. The influence of test parameters on lateral force acceleration derivatives based on conventional and non-conventional harmonic sway tests will be discussed in 4.1.2.1 and 4.1.2.2 while yawing moment derivatives will only be treated in section 4.1.2.3 where a comparison will be made between the results obtained for conventional and non-conventional sway tests.

4.1.2.1 Conventional harmonic sway test

Non-dimensional acceleration derivative $Y'_{\dot{v}}$ or added mass due to sway m'_y:

$$m'_y = -Y'_{\dot{v}} = \frac{-Y_{\dot{v}}}{\frac{1}{2}\rho L_{pp}^2 d} \qquad (4.2)$$

can be derived based on two different analysis techniques described in section 3.6, a Fourier analysis or a regression analysis. Differences are nevertheless limited to just a few percentages (for example for model D a maximum difference of 2.5% is reached). Model D has a non-dimensional own mass m' of 0.17 and model E a mass m' of 0.27. Values of m'_y according to (4.2) must be compared to these own masses m'.

Captive model tests have been executed with varying Froude number, sway amplitude and test frequency. Even oscillatory sway tests with zero forward speed are considered. A summary of test parameters of harmonic sway tests is given in Table 4.2.

Added mass due to sway is presented for model D (containership) in Figure 4.2 for water depth to draught ratios of 20% UKC, 13% UKC and 7% UKC. Similar figures can be found for model E (tanker) in Figure 4.3 (50% UKC and 20% UKC).

Added mass is shown as a function of non-dimensional frequency ω':

$$\omega' = \frac{\omega L_{PP}}{u} \qquad (4.3)$$

for different sway amplitudes y_{0A} or y_A.

Table 4.2 Test parameters during harmonic sway tests

	Froude number F_n	Frequency range ω'	Sway amplitude y_{0A} (m)
Model D, 20% UKC	0.032	1.2 – 4.1	0.15; 0.25; 0.5; 1.0
	0.049	1.4 – 2.0	0.25; 0.5; 1.0
	0.065	1.0 – 2.0	0.15; 0.25; 0.5
Model D, 13% UKC	0.032	1.5 – 3.0	0.5; 1.0
	0.049	1.0 – 2.0	0.25; 0.5; 1.0
	0.065	1.0 – 2.0	0.25; 0.5
	0.077	0.9 – 1.3	0.25; 0.5
	0.116	0.85	0.25
	0.135	0.98	0.25
Model D, 7% UKC	0.032	1.5 – 3.0	0.5; 1.0
	0.049	1.0 – 2.0	0.25; 0.5; 1.0
	0.065	1.0 – 2.0	0.25; 0.5
	0.077	0.9 – 1.3	0.25; 0.5
	0.089	0.9 – 1.1	0.25
Model E, 50% UKC	0.033	1.5 – 6.0	0.25; 0.5; 1.0
	0.049	1.0 – 2.0	0.25; 0.5; 1.0
	0.065	1.0 – 2.0	0.25; 0.5
Model E, 20% UKC	0.033	1.5 – 6.0	0.25; 0.5; 1.0
	0.049	1.0 – 2.0	0.25; 0.5; 1.0
	0.065	1.0 – 2.0	0.25; 0.5

During oscillatory tests with zero forward speed u this frequency reaches infinity so that added mass at infinite frequency is displayed after the axis breaks in Figure 4.2 and Figure 4.3. These results are the added masses for all the oscillation cycles during an oscillatory test and may be affected by memory effects induced by the ship model moving through its own wake. In Figure 4.3 for the full ship model differences in oscillation period and/or amplitude can give high discrepancies in resulting added mass. Generally, this scatter can be reduced by only considering the first oscillation cycle. The influence of induced flows in the tank and memory effects are consequently limited resulting for model E at 50% UKC in a maximum value for m'_y of 0.47 instead of 0.56. This way of limiting the number of oscillation cycles is not in agreement with the fact that the accuracy improves with increasing number of cycles c (see section 3.1.2.1).

The effect of the under keel clearance on captive model test results is clearly illustrated by a comparison of the displayed figures. As the water depth decreases the influence of non-dimensional frequency ω' on the acceleration derivative increases considerably. At lower frequency the scatter becomes very important. This makes an extrapolation to zero frequency impossible. Roughly spoken, added mass m_y decreases with decreasing frequency. Additionally, although an identical analysis procedure is used for all frequency – amplitude – Froude number combinations, negative added masses are obtained in case of containership D at low under keel clearances ($h/d \leq 1.13$) and low frequencies. A negative added mass can physically not be motivated as an opposite hydrodynamic reaction is expected when the ship model is moved with positive sway acceleration. Additionally, extrapolation to zero frequency to determine the so-called slow motion derivatives of a quasi-steady mathematical model will be accompanied with great difficulties taking into account the large scatter at low frequencies.

This scatter and physically unexpected hydrodynamic behaviour can partly be explained as follows. At low oscillation frequency, the lateral force component due to sway acceleration becomes less important compared to the force component induced by sway velocity. In order to quantify the relative magnitude of the sway acceleration dependent terms, an angle ϕ is defined:

$$\phi = \text{Arctan}\left(\frac{Y_s^{[1]}}{Y_c^{[1]}}\right) \tag{4.4}$$

with $Y_s^{[1]}$ (related to sway velocity) and $Y_c^{[1]}$ (related to sway acceleration) the first harmonic sine

and cosine component obtained by Fourier analysis of the lateral force. If ϕ takes values near ±90 degrees, only a minor part of the total lateral force is caused by sway acceleration, so that some doubt may arise about the accuracy or the reliability of m_y. This can be illustrated applying following formulation for the lateral forces due to sway motion:

$$Y = \left(Y_{\dot{v}} - m\right)\dot{v} + Y_{uv} uv + Y_{v|v|} v|v|$$

$$= -\left(Y_{\dot{v}} - m\right)\omega^2 y_{0A} \cos\omega t - Y_{uv} u\omega y_{0A} \sin\omega t - Y_{v|v|}\omega^2 y_{0A}^2 \sin\omega t|\sin\omega t| \quad (4.5)$$

$$\approx \left(m_y + m\right)\omega^2 y_{0A} \cos\omega t - \left(Y_{uv} u\omega y_{0A} + \frac{8}{3\pi} Y_{v|v|}\omega^2 y_{0A}^2\right)\sin\omega t + \frac{8}{15\pi} Y_{v|v|}\omega^2 y_{0A}^2 \sin3\omega t + \ldots$$

yielding following expression for ϕ:

$$\phi = \text{Arctan} \frac{-\left(Y_{uv} u\omega y_{0A} + \frac{8}{3\pi} Y_{v|v|}\omega^2 y_{0A}^2\right)}{-\left(Y_{\dot{v}} - m\right)\omega^2 y_{0A}} = \text{Arctan} \frac{-Y'_{uv}\left(1 + \frac{8}{3\pi}\frac{Y_{v|v|}}{Y_{uv}}\omega'\frac{y_{0A}}{L}\right)}{-\left(Y'_{\dot{v}} - m'\right)\omega'} \quad (4.6)$$

with

$$Y'_{uv} = \frac{Y_{uv}}{\frac{1}{2}\rho L_{pp} d} \quad ; \quad Y'_{v|v|} = \frac{Y_{v|v|}}{\frac{1}{2}\rho L_{pp} d} \quad ; \quad m' = \frac{m}{\frac{1}{2}\rho L_{pp}^2 d} \quad (4.7)$$

Based on (4.5) the added mass m_y is determined:

$$m_y = -Y_{\dot{v}} = \frac{Y_c^{[1]}}{\omega^2 y_{0A}} - m \quad (4.8)$$

Phase angle ϕ of first harmonic components of lateral force Y is measured based on a Fourier analysis for model D and model E and non-dimensional added mass m'_y is shown as function of this angle in Figure 4.4 and Figure 4.5. A comparison of the results for a slender or a full ship proves clearly that for slender ships the sway acceleration derivative is derived from smaller force components relative to the sway velocity dependent components. For model D the absolute value of angle ϕ is used so that negative added masses which give usually negative phase angles can be displayed within the range from 0 to 90 degrees.

Generally, smaller and negative values for the added mass m'_y coincide with $\phi \approx 90\text{deg}$, indicating less reliable measurements. Although identical test parameters have been applied for model E at 50 and 20% UKC, larger under keel clearances lead to more reliable derivatives. Frequency dependence of measured added mass is obviously a shallow water problem and is furthermore emphasized for slender vessels. In [60] a comparison is made of frequency dependence of added mass for full ships (model E and model A) at three different water depth to draught ratios: 150% UKC or deep water (model A), 50% UKC or medium to shallow water (model E), 20% UKC or shallow to very shallow water (model E). These results are repeated in Figure 4.6. In addition, the added mass increases considerably with decreasing under keel clearance. In deep water captive harmonic sway tests are usually executed at low frequencies nowadays (see for example test results reported in [81]) or frequency is considered as a non-affecting parameter. In shallow water and low speed manoeuvring, nevertheless, this common procedure need to be revised or to be executed with caution.

Values for the added mass m_y can be selected by introducing an arbitrarily chosen limit for ϕ. For model D two limits have been used to determine accurate results: ϕ_1 equals 60 degrees at 20% UKC and due to a lack of sufficient data a larger limit ϕ_2 of 70 degrees is chosen for under keel clearances of 13 and 7%. Results are shown in Figure 4.7. It is remarkable that the introduction of a limit for ϕ reduces the scatter according to the frequency considerably. At 20% UKC and lower frequency ($\omega'<2$) only tests carried out with small sway amplitude ($y_A=0.15$ or 0.25m) are

selected. It appears that increasing sway amplitude does not lead to a more reliable determination of the added mass. Nevertheless, this is in accordance with expression (4.6). For under keel clearances of 13 and 7% no tests have been executed with a sway amplitude of 0.15m so that introducing limit ϕ_2 eliminates all added masses determined with a test frequency ω' lower than 2.0. For this particular frequency added mass m_y lies within an identical range for 20% and 13% UKC while at 7% UKC or very shallow water added mass increases.

Two different limits ϕ are used for model E: 35 degrees at 50% UKC and 45 degrees at 20% UKC. Selected values within frequency range ω' [1.5; 2.0] correspond to sway amplitudes of 0.25m (Figure 4.8). The results for this model are compared with those of a tanker with comparable dimensions [77] tested at an under keel clearance of 21% and a Froude number of 0.066 which corresponds to the maximum Froude number of tests with model E. Sway amplitudes are somewhat smaller with values of 0.2 and 0.1m. A similar relationship between added mass and frequency can be observed.

4.1.2.2 Non-conventional sway tests

Non-conventional sway tests with alternating motion to port and starboard separated by a link phase are described in chapter 3 and have been analysed for model D at 20 and 7% UKC and model E at 50 and 20% UKC. Results of Model E at intermediate draught will not be entered in this report.

Non-dimensional frequency $\omega^{*'}$ (= $\omega^* L_{pp}/u$) varies between 2 and 12 (Table 4.3). Based on criterion 1 in chapter 3, this is double the frequency of conventional sway tests with a range of [1;6]. No alternative sway tests have been executed within the range [1;2] although an important variation of added mass with frequency is still recognized for conventional sway tests. Consequently, a conclusion that frequency dependence of added mass due to sway can be reduced executing non-conventional sway tests is hardly found.

Table 4.3 Test parameters during non-conventional sway tests

	Froude number F_n	Frequency range $\omega^{*'}$	Sway amplitude $\Delta y_0/2$ (m)
Model D, 20% UKC	0.032	3.0 – 12.0	0.2; 0.4
	0.065	2.0 – 3.0	0.2; 0.4
Model D, 7% UKC	0.032	3.0 – 12.0	0.2; 0.8
	0.065	2.0 – 4.0	0.2; 0.4
Model E, 50% UKC	0.033	3.0 – 12.0	0.2; 0.4; 0.8
	0.049	2.0 – 6.0	0.2; 0.4; 0.8
	0.065	2.0 – 4.0	0.2; 0.4
Model E, 20% UKC	0.033	3.0 – 12.0	0.2; 0.4; 0.8
	0.049	2.0 – 6.0	0.2; 0.4; 0.8
	0.065	2.0 – 4.0	0.2; 0.4

Determination of sway added mass m'_y is based on a regression analysis according to the mathematical model:

$$Y_H = Y_{Ha} + Y_{Hv} = \left(Y_{\dot{v}} - m\right)\dot{v} + Y_H^{(\beta)}(u,v,0) = -\left(m_y + m\right)\dot{v} + Y_H^{(\beta)}(u,v,0) \tag{4.9}$$

with $Y^{(\beta)}(u,v,0)$ a tabular model function of the drift angle β. Errors on determined added mass for the regression analysis will not be given, as these errors are too small.

As lateral force measured during consecutive sway motions is influenced by the generation of an oscillating flow in the towing tank, it could be useful to consider only the first sway motion from port to starboard to determine sway added mass m'_y. A comparison between the values of the added mass determined in this way and those based on the complete test run is made in Figure 4.9 for model D and Figure 4.10 for model E. On these figures the highest natural period of the water in the tank is also indicated $T^*_{natural}$. This period is an additional limitation to the execution of non-stationary tests as tank resonance will be generated.

For both slender and full form vessels and all examined under keel clearances the scatter on added mass values derived from the complete test run decreases if only the first motion is taken into account. For model D at 20% UKC at high oscillation frequencies near the highest natural period $T^*_{natural}$ the added mass m'_y diminishes (Figure 4.9). At 7% UKC or very shallow water the added masses at an oscillation period of 10 and 15 seconds increase if only the first sway motion is considered. A same tendency can be concluded for model E at respectively 50% and 20% UKC (Figure 4.10). This last figure contains the added mass of the test run shown in Figure 3.19 (reinforcement of oscillating lateral forces measured during consecutive link phases, test period of 13 seconds). The added mass derived from the first sway motion corresponds better to the surrounding values at 10 and 15 seconds.

An important conclusion based on this research is that although variation of added mass m'_y with test frequency can be diminished frequency dependence can not be avoided.

For model E at 50% UKC or moderate water depth the difference between the m'_y values derived from the complete test run and from the first motion becomes more important as the oscillation frequency increases. Scatter on the added mass coefficient can be reduced with about 50% if only the first sway motion is examined. In general, depending on forward velocity and tank length the number of oscillation cycles or consecutive sway motions is chosen as large as possible to improve the accuracy. Non-conventional sway tests executed at higher frequencies are characterized by important non-stationary effects which can partly be explained based on the occurrence of tank resonance as test period approximates a natural period of the water in the tank. At low under keel clearances (20% and 7%) other inexplicable disturbances play a part. Additionally, at high frequencies the link phase is not long enough to be able to determine the damping character of the oscillating hydrodynamic forces.

Although some disadvantages still remain, added masses m'_y measured during non-conventional sway tests do not suffer from inaccurate negative values at low frequencies. A decreasing water depth results into an increasing added mass m'_y for model D and all tested frequencies. A similar physically motivated increase with decreasing water depth can be found for full and slender ships. Values at 7% UKC are nevertheless larger than those measured during conventional sway tests (Figure 4.9).

A comparable angle ϕ can be defined for non-conventional sway tests. As lateral velocity is composed of a constant and a harmonic component and sway acceleration is a harmonic function, the sway acceleration derivative can be linked with a Fourier analysis based on the model:

$$Y_H = \left(Y_{\dot{v}} - m\right)\dot{v} + Y_{uv}uv + Y_{v|v|}v|v|$$ (4.10)

Substitution of equation (3.30) in (4.10) gives:

$$Y = Y_{uv}uv* + \frac{3}{2}Y_{v|v|}v*|v*| + \left(Y_{\dot{v}} - m\right)\omega* v* \sin\omega* t' - \left(Y_{uv}uv* + 2Y_{v|v|}v*|v*|\right)\cos\omega* t'$$

$$+ \frac{1}{2}Y_{v|v|}v*|v*|\cos 2\omega* t'$$ (4.11)

with

$$|v*| = \frac{\omega* \Delta y_0}{2\pi}$$ (4.12)

so that

$$\phi = \text{Arctan}\left(\frac{-\left(Y_{uv}u + 2Y_{v|v|}|v*|\right)}{\left(Y_{\dot{v}} - m\right)\omega*}\right) = \text{Arctan}\left(\frac{-\left(Y_{uv}u + 2Y_{v|v|}|v*|\right)}{-\left(m_y + m\right)\omega*}\right)$$ (4.13)

Following this criterion, the acceleration derivative can be determined more accurately compared to conventional sway tests (Figure 4.11 for model D and Figure 4.12 for model E). The evaluation of angle ϕ is based on all sway motions and values for ϕ lie farther away from 90 degrees.

4.1.2.3 Comparison between conventional and non-conventional sway tests

Lateral force acceleration derivative

On Figure 4.13 to Figure 4.16 a comparison is made between the added mass determined from conventional and non-conventional sway tests for model D at under keel clearances of 20% and 7% and for model E at 50% and 20% UKC. Criterion 1 with similar maximum sway velocities and accelerations described in chapter 3 is used to display added masses. Consequently, added masses for non-conventional sway tests are obtained with twice the frequency (see axis at the top of each figure) compared to conventional sway tests.

As was already noted in the preceding section, for slender ships and very shallow water (7% UKC, Figure 4.14) an important difference is seen between the results of both test types. Added mass is small at low frequencies and even negative values are found during conventional sway tests. For non-conventional tests a physically motivated increase of added mass with decreasing water depth is calculated (comparison of Figure 4.13 and Figure 4.14). Based on this analysis a preference for non-conventional tests can be concluded. Some doubt may arise about a possible overestimation of the added mass for 7% UKC as the maximum value of 2.1 is much higher than the other values. Probably there is some influence of forward velocity so that low speed manoeuvres (F_n=0.032) are more sensitive to variations in oscillation period. Time history of the test run with maximum added mass m'_y at 7% UKC is shown in Figure 3.18 and is rather smooth with low lateral forces during the link phases and comparable hydrodynamic effects during the consecutive sway motions.

For full ships at shallow (20% UKC) and medium (50% UKC) water depth added mass m'_y differs only slightly for the two test types with the same imposed oscillation frequency. No preference is made.

Yawing moment acceleration derivative

Yawing moment acceleration derivative N_{vdot} is made non-dimensional based on:

$$N'_{vdot} = N'_{\dot{v}} = \frac{N_{\dot{v}}}{\frac{1}{2}\rho L_{PP}^3 d} \tag{4.14}$$

For yawing moment acceleration derivative N'_{vdot} the scatter decreases considerably for the non-conventional sway tests and for both ship types if criterion 1 to compare test types is assumed (Figure 4.17 to Figure 4.20). Positive contributions N'_{vdot} are measured for model D and both under keel clearances. For model E N'_{vdot} is rather negative for the non-conventional sway tests.

A comparison of frequency dependence of N'_{vdot} for model E and for a tanker reported in [77] is shown in Figure 4.21. Derivatives are based on conventional harmonic sway tests. For the tanker at Froude number F_n=0.066 the acceleration derivative becomes positive as frequency decreases. A principally similar tendency can be seen for model E.

4.1.2.4 Frequency dependence of added mass due to squat?

In reply to the assumptions of other researchers reported in [83], the relationship between the acceleration derivative and the net under keel clearance during harmonic sway tests was studied.

During stationary straight ahead tests the net under keel clearance decreases approximately with the square of the ship velocity or the Froude number (Figure 4.22). At a full scale velocity of 12 knots the nominal UKC of 7% for the container carrier (model D) reduces to an UKC of 3% of

the draught.

During conventional harmonic sway tests sway acceleration is in phase with the lateral position of the ship model. As maximum sinkage occurs near maximum sway velocity (Figure 4.23, model E) high added masses at high frequencies cannot be explained by squat effects. In Figure 4.24 mean net UKC is shown for model D, tested at a nominal UKC of 7% and a Froude number F_n=0.065. A mean UKC of 5.8% corresponds to the net UKC during a straight ahead motion (see Figure 4.22). The net UKC is further diminished to 5.3% of the draught near maximum sway velocity or zero sway acceleration (zero lateral position). Sinkage measured during harmonic sway tests is in the first place caused by the forward velocity. At low speed manoeuvres and maximum sway velocity, a proportionally higher sinkage occurs compared to the net UKC at straight ahead motion, but the additional sinkage is all in all small (see Figure 4.23 at F_n=0.033).

The behaviour of the ship model during conventional sway tests at low forward velocity is in accordance with the findings of Gill in [77]. The maximum Froude number of 0.115 for the experimental results in [77] is much higher than the Froude numbers of oscillatory tests executed at Flanders Hydraulics Research. In the pure sway tests, at these higher speeds and large amplitudes, the model was observed to heave and pitch at twice the frequency of the sway motion resulting into a strong cross coupling between horizontal and vertical motions. At Froude numbers restricted to 0.065 nevertheless, net UKC decreases with only a few or a few tenth percentages for model E and D compared to the straight ahead motion.

For non-conventional sway tests the net UKC of fore body and aft body give a total other view than for conventional sway tests (model E, comparing Figure 4.23 and Figure 4.25). The sinkage of the aft body is smaller than obtained during a conventional test while the sinkage of the fore body still reaches a maximum at maximum lateral velocity v giving a minimum net UKC of 17,6%. A relationship between maximum sinkage and maximum velocity is still more accepted than an influence of squat on sway acceleration derivatives.

4.1.3 Yaw motion

Contrary to sway motion related acceleration coefficients the influence of yaw acceleration is especially important for the added moment of inertia J'_{zz}.

4.1.3.1 Pure yawing

Yawing moment acceleration derivative
Harmonic yaw tests have been executed with positive and negative forward speed. Unlike the added mass for sway m_y, determining the added moment of inertia, J_{zz}, does not cause specific problems. Non-dimensional acceleration derivative $N'_{\dot{r}}$ or added moment of inertia J'_{zz}:

$$J'_{zz} = -N'_{\dot{r}} = \frac{N_{\dot{r}}}{\frac{1}{2}\rho L_{pp}^4 d} \qquad (4.15)$$

can be derived from pure yawing tests or yawing tests with constant drift angle, utilizing a Fourier analysis or a regression analysis. In Figure 4.26 and Figure 4.27 resulting added moments of inertia are displayed for model E and model D based on pure yawing tests.

For full ships the added moment of inertia is rather insensitive to the selected test parameters (oscillation frequency, model speed, yaw amplitude) during harmonic yaw tests and oscillatory tests (F_n=0). At 20% UKC some test runs give outstanding values but the main part is concentrated around 0.025. At 50% UKC or medium water depth no scatter is seen within the range of selected test parameters. No conclusion can be made for under keel clearances lower than 20%.

For slender bodies, on the other hand, the influence is more pronounced. As pure yawing tests have been executed with varying yaw amplitude (see Table 4.4), scatter at a selected frequency

and model speed has to be explained based on this yaw amplitude. For test runs at a non-dimensional frequency of 2.25 variation of added moment of inertia with yaw amplitude is shown in Figure 4.28. There is no clear tendency and additionally, some tests have been applied with identical test parameters at different points in time revealing slight different values for J'_{zz}. The added moment of inertia for model D at 20% UKC is nevertheless small compared to values measured for a full ship. The determination of a mean value for all frequencies could be accepted.

In very shallow water (Figure 4.27, right) only a few tests have been executed at a Froude number greater than 0.07. Although a main part of the model tests give values within the range [0.03; 0.04], a much higher value is measured at a frequency of 1.5 and $F_n=0.096$. Due to a lack of efficient data at higher Froude numbers no conclusion can be drawn about the influence of frequency and yaw amplitude on J'_{zz} for slender ships.

Table 4.4 Test parameters during pure yaw tests

	Froude number F_n	Frequency range $|\omega'|$	Yaw amplitude Ψ_A (deg)
Model D, 20% UKC	-0.032	2.25 – 3.37	15; 25; 35
	-0.016	2.25 – 3.37	15; 25; 35
	0.016	2.25 – 6.74	15; 25; 35
	0.032	2.25 – 4.50	10; 15; 20; 25; 30; 35
	0.049	2.25 – 4.50	10; 15; 20; 25; 30; 35
	0.065	2.25 – 3.37	10; 15; 20; 25; 30; 35
Model D, 7% UKC	0.032	2.25 – 4.50	15; 20; 25; 30; 35
	0.049	2.25 – 2.70	20; 30
	0.065	2.25 – 2.71	15; 20; 25; 35
	0.077	1.89 – 2.28	15; 20
	0.096	1.51	20
Model E, 50% UKC	0.033	1.79 – 4.45	10; 15; 25; 35
	0.049	1.43 – 3.34	10; 15; 20; 25; 35
	0.065	1.43 – 2.86	10; 15; 20; 25
Model E, 20% UKC	-0.016	2.22 – 3.34	15; 35
	0.016	2.22 – 6.67	15; 25; 35
	0.033	1.79 – 4.45	10; 15; 25; 35
	0.049	1.43 – 3.34	10; 15; 20; 25; 35
	0.065	1.43 – 2.86	10; 15; 20; 25

Lateral force acceleration derivative

Determining the lateral force acceleration derivative is less straightforward, as the yaw amplitude ψ_A has a considerable influence on the acceleration derivative $Y'_{\dot{r}}$ (or Y'_{rdot} for the title of the figures):

$$Y'_{rdot} = Y'_{\dot{r}} = \frac{Y_{\dot{r}}}{\frac{1}{2}\rho L_{pp}^3 d} \qquad (4.16)$$

For model E tests executed at lower values for the yaw amplitude (10 and 15 degrees) give principally lower absolute values for the acceleration derivative compared to tests at higher yaw amplitude. This concerns both under keel clearances (Figure 4.29). One value of –0.09 for Y'_{rdot} at 15 degrees yaw amplitude and 20% UKC differs from this tendency. This particular test was executed at a Froude number of 0.016 or during low speed manoeuvring and is probably affected by non-stationary or destabilising effects around the yawing ship model. Oscillatory test results at zero forward speed are shown after the axis breaks and are small (in absolute value).

For slender ships and 20% UKC almost the same conclusions can be made as for tanker E, but in addition the great scatter at low frequencies due to varying yaw amplitude is extended to higher frequencies. At 7% UKC most values lie within the range [-0.14; -0.09] and a clear relationship between acceleration derivative and yaw amplitude can not be found. Due to a very limited water depth the influence of test parameters frequency, amplitude and forward speed is

not marked at all.

The variation of angle ϕ, defined as (4.4), explains just a part of this parameter dependence. If following simplified mathematical model is used:

$$Y = \left(Y_{\dot{r}} - mx_G\right)\dot{r} + \left(Y_{ur} - m\right)ur + Y_{r|r|}r|r|$$

$$= -\left(Y_{\dot{r}} - mx_G\right)\omega^2 \psi_A \cos\omega t - \left(Y_{ur} - m\right)u\omega \psi_A \sin\omega t - Y_{r|r|}\omega^2 \psi_A^2 \sin\omega t|\sin\omega t| \qquad (4.17)$$

$$\approx -\left(Y_{\dot{r}} - mx_G\right)\omega^2 \psi_A \cos\omega t - \left(\left(Y_{ur} - m\right)u\omega \psi_A + \frac{8}{3\pi}Y_{r|r|}\omega^2 \psi_A^2\right)\sin\omega t + ...$$

an expression for ϕ can be found:

$$\phi = \text{Arc}\tan\frac{-\left[\left(Y_{ur} - m\right)u\omega \psi_A + \frac{8}{3\pi}Y_{r|r|}\omega^2 \psi_A^2\right]}{-\left(Y_{\dot{r}} - mx_G\right)\omega^2 \psi_A} = \text{Arc}\tan\frac{-\left(Y'_{ur} - m'\right)\left(1 + \frac{8}{3\pi}\frac{Y'_{r|r|}}{Y'_{ur} - m'}\omega'\psi_A\right)}{-\left(Y'_{\dot{r}} - m'x'_G\right)\omega'} \qquad (4.18)$$

As the yaw amplitude increases, the acceleration derivative is determined with more accuracy, as – contrary to the sway induced lateral force – the numerator in (4.18) decreases, so that yaw acceleration dependent terms become relatively more important. At least, this is the case if $Y'_{r|r|}$ / $(Y'_{ur}-m')$ < 0. From this point of view, large amplitude and/or higher frequency yawing tests yield more reliable results. This is true for model E at both under keel clearances (Figure 4.32) and model D at 20% UKC (Figure 4.33), but not for very shallow water (model D at 7% UKC, Figure 4.34). In the case of the Esso Osaka (Figure 4.29), some modest convergence can indeed be noticed if frequency is increased – except for very large amplitude motions – but this is not the case for the container carrier model D at 20% UKC (Figure 4.30). At 7% UKC (Figure 4.31), nevertheless, forces are principally larger so that the scatter at a non-dimensional frequency of 4.5 is smaller than at 20% UKC.

The strong dependence of the lateral acceleration derivative for yawing on both frequency and yaw amplitude can qualitatively be explained by interference between the fore and aft body of the ship model occurring during yawing tests. The trajectories followed by the ship model generate complex flow patterns, which may affect the lateral force, and which appear to depend substantially on yaw amplitude as illustrated in chapter 3.

Although measured added moments of inertia for model tests at negative forward speed lie within the range of values at positive speed, this is not true for the lateral force acceleration derivative $Y'_{\dot{r}dot}$. First order harmonic force components measured on fore (F) and aft (A) body proportional to the yaw acceleration (cosine) change in magnitude if the ship is going astern compared to going ahead. If a ship is going ahead, the lateral force proportional to the acceleration is concentrated on the fore body during a yaw motion (Table 4.5).

Table 4.5 First harmonic force components (model E)

			cosine (N)		sine (N)	
run	F_n	$|\omega'|$	(F)	(A)	(F)	(A)
EGGH08	0.016	3.34	-4.4	1.4	-4.3	3.9
EGGI02	-0.016	3.34	-1.7	3.7	-1.8	5.0

Going astern, maximum forces are measured on the aft body. This results in a change of sign for the yaw acceleration derivative of lateral force. Discontinuities in hydrodynamic coefficients of a mathematical manoeuvring model have to be avoided but even small positive values for $Y'_{\dot{r}dot}$ have been measured during forward speed tests with model D at 20% UKC and low yaw amplitudes (10 degrees, Figure 4.30). At zero forward speed or oscillatory tests, the values obtained for the yaw acceleration derivative for the lateral force are indeed negligible so that a zero value for zero forward speed, a positive value for going astern and a negative value for going ahead could be adopted.

4.1.3.2 Yawing with drift angle

Compared to the results of pure yawing tests, the acceleration derivatives of the lateral force and yawing moment are affected by combining yaw and drift, depending on the hull form and the test parameters. Results are displayed for model E on Figure 4.35 to Figure 4.38 and for model D on Figure 4.39 to Figure 4.42.

At medium water depth (50% UKC, Figure 4.35) the absolute value of the lateral force acceleration derivative Y'_{rdot} increases considerably with increasing drift angle (positive or negative) for tests executed with low frequency (ω'=1.43 or 1.79) and/or low amplitude. The influence of drift angle on added moment of inertia is nevertheless negligible. Values lie within the range [0.015; 0.020].

At decreasing water depth (20% UKC, Figure 4.36 and Figure 4.37) a rough increase of the absolute value of Y'_{rdot} is also observed for model E with increasing drift angle $|\beta|$ but this tendency is more pronounced if the chosen yaw amplitude ψ_A and/or the non-dimensional frequency ω' are low. Values for the added moment of inertia are concentrated around 0.025 and 0.030 and somewhat outstanding values are only found for captive model tests at low frequency and/or low amplitude.

For the tanker going astern just a few tests have been executed at F_n=-0.016. The drift angle β has almost no influence on Y'_{rdot} derived from a test run with yaw amplitude 15 degrees and non-dimensional frequency 3.34. A test run with the same amplitude and a frequency of 2.22 gives an important difference for the acceleration derivative with or without a constant drift angle (Figure 4.38). For the added moment of inertia a few exceptions can be seen as well.

At 20% UKC similar conclusions can be drawn for the lateral force acceleration derivative for model D as for model E (Figure 4.39 and Figure 4.40). Test results are mainly influenced by the drift angle for runs carried out at low yaw amplitude and/or low frequency. For the added moment of inertia there is no clear influence of drift angle and the scatter at zero drift angle extends to non-zero values. The acceleration derivative values Y'_{rdot} for the containership when going astern lie within the same range as when going ahead but positive values are determined instead. An extreme influence of drift angle is seen for the captive model test with parameters F_n=-0.016, $|\omega'|$=2.25 and ψ_A=15 degrees (Figure 4.41).

Only a few tests have been executed at very shallow water or 7% UKC (model D, Figure 4.42). The lateral force acceleration derivative is not considerably influenced by the drift angle except for the test run with parameters F_n=0.065, ω'=2.25 and ψ_A=15 degrees. Both test runs at F_n=0.065 give an increasing added moment (from 0.03 to 0.05) for an increasing absolute drift angle. Although only a sensitivity analysis can reveal the importance of both acceleration derivatives for a yawing motion, some concluding remarks can be noted:

❑ The influence of a constant drift angle during a harmonic yawing test appears to be more significant for the acceleration derivative of lateral force both for slender and full ships and for the added moment of inertia of slender ships.
❑ The effect of drift is most important at low yaw amplitude ψ_A and/or low non-dimensional frequency ω'.
❑ Nevertheless, the increase of the derivatives is more or less symmetrical for positive and negative drift angles.

4.2 Velocity dependent forces and moments: four quadrants tabular models

4.2.1 The introduction of tabular models

In [84] a comparison was made of different mathematical models for the drift induced forces. These models are often subdivided in models with a physical background where force

components like lift, cross-flow and potential flow are formulated explicitly, and regression models which are based on a selection of polynomial terms resulting from assumptions regarding the mathematical representation of the force actions mentioned in chapter 2. In both cases, formulations are often based on the assumption that the drift angle β is small, which simplifies the expressions:

❑ goniometric functions can be approximated by means of a Taylor series;
❑ the lift force can be considered as a linear function of the angle of attack, as no stall occurs.

This assumption is justified for simulation of manoeuvres at medium or full speed, as the drift angle will always be limited in these conditions (for example $|\beta|<20$ degrees). For harbour manoeuvres at very low speed, however, such approximations are not always realistic.

The question was raised and answered whether formulations for drift induced hydrodynamic forces and moments which were originally developed for relatively small drift angles can be used for applications involving drift angles in four quadrants. It was concluded that a tabular representation of non-dimensional lateral force and yawing moment in function of drift angle β could be recommended as the most reliable way of modelling drift induced lateral forces and yawing moments.

The use of tabular models for simulation is still unusual as most researchers prefer regression models for formulating velocity dependent forces and moments. In the DEN-Mark1 model of the Danish Maritime Institute, described in section 2.4, so-called tabulated shape coefficients replace and represent the hydrodynamic coefficients and look-up tables are getting through to the whole mathematical model including not only hull forces, but propeller and rudder forces as well.

In this mathematical model hull forces and moment due to ship velocities will be defined as:

$$X_{Hv} = X^{(\beta)}(u,v,0) + X^{(\gamma)}(u,0,r) + X^{(\chi)}(0,v,r)$$

$$Y_{Hv} = Y^{(\beta)}(u,v,0) + Y^{(\gamma)}(u,0,r) + Y^{(\chi)}(0,v,r)$$

$$N_{Hv} = N^{(\beta)}(u,v,0) + N^{(\gamma)}(u,0,r) + N^{(\chi)}(0,v,r)$$

(4.19)

The velocity dependent forces in (4.19) are expressed as tabular models, the following angles varying over four quadrants from -180 deg to 180 deg:

$$\beta = \text{Arctan2}\,(-v, u)$$

(4.20)

$$\gamma = \text{Arctan2}\left(r\frac{L_{PP}}{2}, u\right)$$

(4.21)

$$\chi = \text{Arctan2}\left(r\frac{L_{PP}}{2}, v\right)$$

(4.22)

The expressions $f^{(\beta)}(u,v,0)$, $f^{(\gamma)}(u,0,r)$ and $f^{(\chi)}(0,v,r)$ with f=X, Y or N are respectively the forces or moment measured during pure sway, pure yaw or the additional forces measured during a combination of sway and yaw. β is the drift angle, γ is the yaw rate angle and the angle χ cannot be interpreted as an inflow angle as it is based on the ratio of two side velocities induced by yawing and swaying.

Non-dimensional expressions for the velocity dependent forces and yawing moment are formulated as follows:

❑ pure sway:

$$X' = \frac{X}{0.5\rho L_{PP} d(u^2 + v^2)}, \ Y' = \frac{Y}{0.5\rho L_{PP} d(u^2 + v^2)}, \ N' = \frac{N}{0.5\rho L_{PP}^2 d(u^2 + v^2)}$$

(4.23)

❑ pure yaw:

$$X' = \frac{X}{0.5\rho L_{PP} d \left(u^2 + \left(\frac{rL_{PP}}{2} \right)^2 \right)}, \quad Y' = \frac{Y}{0.5\rho L_{PP} d \left(u^2 + \left(\frac{rL_{PP}}{2} \right)^2 \right)}, \quad N' = \frac{N}{0.5\rho L_{PP}^2 d \left(u^2 + \left(\frac{rL_{PP}}{2} \right)^2 \right)}$$

(4.24)

❑ combination sway-yaw:

$$X' = \frac{X}{0.5\rho L_{PP} d \left(v^2 + \left(\frac{rL_{PP}}{2} \right)^2 \right)}, \quad Y' = \frac{Y}{0.5\rho L_{PP} d \left(v^2 + \left(\frac{rL_{PP}}{2} \right)^2 \right)}, \quad N' = \frac{N}{0.5\rho L_{PP}^2 d \left(v^2 + \left(\frac{rL_{PP}}{2} \right)^2 \right)}$$

(4.25)

The physical contribution of a manoeuvring ship to each of these force components is summarized in [26] (see chapter 2):

$$X = X_I + X_{Lv} + X_{Di} + (X_C + X_F + X_{ST})$$

$$Y = Y_I + Y_{Lv} + Y_{Di} + (Y_C)$$

$$N = N_I + N_{Lv} + N_{Di} + (N_C)$$

Each elementary motion (pure sway, pure yaw and combined sway-yaw) will fill in some parts of these components and will be discussed in the following sections.

4.2.2 Velocity dependent forces and moment due to a pure sway motion

As different test types can be used to determine the hull forces and moment due to sway velocity, test results will be compared for models D and E. Captive model tests have been executed on the fully equipped ship model and modelled hull forces and moment must be considered as resulting forces and moment of hull-propeller-rudder combination but without propeller action and with zero rudder deflection. Possible test types are:

❑ Oblique towing tests with or without propeller action but with zero rudder deflection: drift angle β varies within four quadrants [-180 deg; 180 deg]; if the propeller is running the effect of the propeller on total measured force or moment will be accounted for.
❑ Multi-modal tests with constant drift angle and harmonically varying propeller rate of turn without rudder deflection: drift angle β varies within four quadrants
❑ Multi-modal tests with constant drift angle and harmonically varying propeller rate of turn and rudder angle: drift angle β varies within four quadrants
❑ Conventional harmonic sway tests with a limited maximum drift angle
❑ Non-conventional or alternative sway tests with a limited maximum drift angle

The first three test types are stationary tests for the kinematical parameters as drift angle β does not change during one test run. The other test types are characterized by a continuous change of this angle and, consequently, the flow around the ship model.

4.2.2.1 Longitudinal force due to swaying

(a)   Tabular models based on stationary test types
Observations
Measured longitudinal forces at different drift angles have been analysed assuming:

❑ Oblique towing tests with negligible or very small propeller rates and zero rudder deflection will reveal the hull force on the fully equipped ship model.
❑ Oblique towing tests with propeller action will be analysed making use of a simplified formal mathematical model:

$$X = X_H + X_P$$

$$= X^{(\beta)}(u, v, 0) + X_{un}(\beta)un + X_{nn}(\beta)n^2 \qquad (4.26)$$

For both test types a separate regression analysis is made per Froude number and per drift angle. In this way the influence of ship velocity (low or ordinary speed) can be visualized. Subsequently a calculation of weighted averages over the total ship velocity is executed for each drift angle according to:

$$X'^{(\beta)} = \frac{\sum\limits_{i=1}^{n} X'^{(\beta)}_i V_i^2}{\sum\limits_{i=1}^{n} V_i^2} \qquad (4.27)$$

with V_i the total ship velocity of test run i.

For ship model D two series, series D1 and series DA, which have been executed at different points in time at 20% UKC and which differ somewhat in available test parameters, show the influence of Froude number on longitudinal hull force $X'^{(\beta)}$ (Figure 4.43). An asymmetrical behaviour for positive and negative drift angles can be observed with a quicker decrease to zero values for positive drift angles. Although some discrepancy between low and ordinary ship velocities can be noticed for very small drift angles ($|\beta| < 5$deg), series D1 and DA are globally in line. In addition, due to the small values measured for the longitudinal force compared to lateral force and yawing moment some influence of Froude number on calculated $X'^{(\beta)}$ can be recognized although there is no clear relationship. The calculation of weighted averages could be justified.

The results of conventional oblique towing tests can be compared to these of non-conventional multi-modal tests with constant drift angle per test run and harmonically varying propeller revolutions (multi-modal test type B). This test run is characterized by a variation of the propeller rate from zero to a maximum positive value (first half period) and back to zero (second half period). The total run time is one period. On Figure 4.44 and Figure 4.45 the following test types are defined:
❑   type 1: conventional oblique towing tests with zero rudder deflection
❑   type 2: non-conventional multi-modal tests type B with zero rudder deflection

The regression analysis is based on model (4.26) for both test types. As the longitudinal force measurement can be affected by the acceleration phase at the beginning of the test run, even for multi-modal tests with a gradual increase of the velocity, a transitional phase must be taken into account at low propeller rates during the first half period. Test results of type 2 are therefore restricted to the second half period.

Tabular models linked with these test types are shown in Figure 4.44 for low speed manoeuvring ($F_n=0.016$) and in Figure 4.45 for higher Froude numbers.

Some important remarks concerning these figures are:
❑   Although ship's hull D is symmetrical about the x-z plane, longitudinal forces differ comparing positive and negative drift angles (Figure 4.44, type 1). For positive drift angles the resistance force turns into a positive contribution within the range [15deg; 35deg]. Resistance force $X'^{(\beta)}$ increases with increasing negative drift angle and this tendency is extended from series D1 with $\beta > -50$ deg to series DA with -50 deg $< \beta <$ -90 deg for a motion ahead. A physical understanding is hard to be found and although the existence of a cross flow lift X_C can be motivated according to [26] this asymmetrical behaviour may be caused by measuring inaccuracies at very low speed ($F_n=0.016$). Cross talk could be a possible interpretation but in that case a correction should only be necessary for negative drift angles what is rather strange.

❑ Non-zero values for the non-dimensional longitudinal force at pure cross flow ($|\beta|$=90deg) can be expected as the water depth decreases. The mainly two-dimensional cross flow will be turned into a more three-dimensional flow around the ship model as the cross flow is hindered due to a very small under keel clearance. According to [26] a positive value for X_C is expected in deep water, while a negative value is found here at -90 degrees for all test types. The flow around the ship model should be deviated along the ship's stern, while its form is fuller and probably more obstructive than the ship's bow.

Test type 2 gives the most reliable model as asymmetry between positive and negative drift angles is restricted. Error bars for tabular models of test type 2 are also indicated. The level of error is rather high with larger error bars for the ship going astern (drift angles near 180 degrees). Error bars are limited for the ship moving laterally. This inaccuracy could be explained based on the large noise on measured longitudinal forces for these small ship models at low speed (model length of approximated 4 m).

The influence of decreasing UKC for ship model D (from 20% to 7% UKC) is shown on Figure 4.46 to Figure 4.48. At 7% UKC conventional oblique towing tests have only been executed with zero drift angle. The influence of Froude number on non-dimensional resistance force $X'^{(\beta)}$ for zero drift angle is shown on Figure 4.46. An increase of the resistance force with increasing ship velocity could be found for slender ships and is more pronounced as the under keel clearance decreases (below 20% UKC). This means that for very shallow water resistance force $X'^{(\beta)}$ must be modelled using higher orders (V^n, n>2).

A comparison is made of non-dimensional longitudinal force modelled based on equation (4.26) using measured values during multi-modal tests of type 2 (Figure 4.47 and Figure 4.48). At low speed and 7% UKC $X'^{(\beta)}$ is generally more negative than at 20% UKC for larger drift angles $|\beta|$. Measurements at low speed are nevertheless affected by inaccuracies as error bars can be considerable (Figure 4.48). At higher Froude numbers (F_n=0.065) longitudinal force $X'^{(\beta)}$ is modelled with more confidence and a decreasing water depth gives lower force magnitudes for drift angles $|\beta|$ greater than 2.5 degrees. During a straight ahead motion (or very small drift angles) a physically motivated increase of the resistance can still be observed.

The slenderness of ship model D raises some doubts about the accuracy of the determination of longitudinal force $X'^{(\beta)}$, as longitudinal forces are very small compared to lateral forces and yawing moments during low speed manoeuvres.

For tanker E some observations recognized for model D can also be found although the asymmetry between positive and negative drift angles is less striking. Results are shown for test types which can be compared with those for model D although small differences are available:

❑ type 1: conventional oblique towing tests *without propeller action* and with zero rudder deflection; the complete range of drift angles has been examined for F_n=0.016 (low speed manoeuvring) while higher values for F_n are only available at drift angles 0 and ±8 deg. Duplicate tests can be seen for drift angles 60 and 120 deg which only differ in the sense of execution of the test: with increasing or decreasing longitudinal position x_0 along the axis fixed to the towing tank.

❑ type 2: non-conventional multi-modal tests type B with propeller action and with zero rudder deflection; tests have been executed with Froude numbers from 0.016 to 0.065.

A comparison between results of type 1 and 2 for low speed manoeuvring is shown in Figure 4.49 for 50% UKC and Figure 4.51 for 20% UKC. For 20% UKC calculated values $X'^{(\beta)}$ for type 2 over the complete test run (one period) or for only decreasing propeller

rate (second half period) are compared. The calculation with only data of the second half period fits better with results of conventional oblique towing tests (e.g. drift angle of ±60 deg). For both under keel clearances and drift angles near going astern there is no accordance between type 1 and 2 and results of conventional test types are preferred, just like for model D. In medium deep water (50% UKC, Figure 4.50) the difference between both test types for F_n=0.016 is important, probably due to the magnitude of measured longitudinal forces when the propeller is not working. At drift angles ±8 deg the values are based on higher ship velocities and correspond to the surrounding values of test type 2. The values for low speed manoeuvring and conventional oblique towing tests without propeller action can therefore be considered to be outstanding. At decreasing UKC (20% UKC, Figure 4.52) the difference between both test types even for low speed manoeuvring is smaller.

Selected tabular model [85]

Due to the symmetry of a ship model about the x-z plane a symmetrical model for the longitudinal force $X'^{(\beta)}$ is preferred although this symmetry is not confirmed by the test results (Figure 4.53). A mean value will be calculated for each drift angle $|\beta|$ and the small influence of ship velocity will be accounted for using (4.27). Results of test types 1 and 2 will be combined:

- for slender ships (e.g. model D) results of non-conventional multi-modal tests (type 2) are chosen except for straight ahead and drift angles near going astern where results of conventional oblique towing tests are used. This choice is also motivated taking into account the occurrence of unstable flow patterns at the ship's stern during a motion astern with propeller working ahead (see chapter 5);
- for full ship forms (e.g. model E) both test types are equivalent except for low speed (F_n=0.016) so that non-conventional tests will be used for drift angles within the range [-30deg; 30deg] and stationary tests for higher drift angles and motion astern.

For full ships the longitudinal hull force turns from a resistance force acting aft into a component acting forward as the drift angle increases. The involved drift angle, at which this effect occurs, is decreasing with decreasing water depth (see also [47]). For slender ships this force component keeps on acting astern during a large range of drift angles and only becomes positive when the ship is moving astern.

(b) Tabular models based on harmonic test types

As measured longitudinal forces are affected by inaccuracies during stationary model tests, results of harmonic sway tests are expected not to contribute to a model for the longitudinal force so that these non-stationary tests will only be used for the lateral force Y and yawing moment N.

4.2.2.2 Lateral force and yawing moment due to swaying

These two contributions are examined together as lateral force and yawing moment are linked through the point of application. In addition, the hydrodynamic "resistance" during even small lateral movements of a ship causes a lateral force and yawing moment which increase rapidly with increasing drift angle so that difficulties as for the longitudinal force were not encountered to the same extent.

(a) Tabular models based on stationary test types
Observations
The influence of ship velocity or Froude number on non-dimensional lateral force and yawing moment is shown on Figure 4.54 for model D at 20% UKC. Only for drift angle $|\beta|$=10deg a slight increase of the absolute value of lateral force and yawing moment can be recognized as the ship velocity increases.

Using comparable test types as for the longitudinal force, with an additional test type 3

(multi-modal type B: harmonically varying propeller rate and rudder angle) the effect of an unusual phenomenon described in chapter 3 occurring during multi-modal tests of type B at the fourth quadrant of operation must be considered. Tabular models for the non-dimensional lateral force and yawing moment based on these tests will be compared using measurements for the complete test run on one hand and using results only measured during the first half period on the other (e.g. Figure 4.55 for type 2). Following mathematical models are used to determine lateral force $Y'^{(\beta)}$ and yawing moment $N'^{(\beta)}$ applied to the hull during hull-propeller combination tests:

$$Y = Y_0(u, v, n = 0) + Y_1(u, v, n)$$

$$= Y_0(u, v, n = 0)\left[1 + C(\beta)\left(\frac{n}{n_{max}}\right)^2\right] \tag{4.28}$$

$$= \frac{1}{2}\rho L_{PP} dV^2 Y'^{(\beta)}(u, v, n = 0)\left[1 + C(\beta)\left(\frac{n}{n_{max}}\right)^2\right]$$

$$N = N_0(u, v, n = 0) + N_1(u, v, n)$$

$$= N_0(u, v, n = 0) + x'_Y(\beta)Y_1(u, v, n)L_{PP} \tag{4.29}$$

$$= \frac{1}{2}\rho L_{PP}^2 dV^2\left[N'^{(\beta)}(u, v, n = 0) + x'_Y(\beta)Y'^{(\beta)}(u, v, n = 0)C(\beta)\left(\frac{n}{n_{max}}\right)^2\right]$$

$Y'^{(\beta)}$ and $N'^{(\beta)}$ are the lateral hull force and yawing moment for the fully equipped ship without propeller action and with zero rudder deflection. Lateral force Y is augmented with a part Y_1 proportional to the square of the propeller rate and varying with the drift angle $C(\beta)$. This lateral force Y_1 has a point of application $x'_Y L_{PP}$ and is responsible for the increase of $N'^{(\beta)}$ to N. Propeller induced mathematical models will be discussed in chapter 5. For tests of type 3 additional math models for the rudder induced force and yawing moment will be accounted for (see chapter 6).

For low speed manoeuvring differences between the three stationary test types especially manifest for drift angles near ±90 deg for the lateral force and drift angles near maximum moment for the yawing moment. Due to the harmonic oscillation of the rudder from port to starboard during test type 3 probably an unstable flow arises resulting into maxima for the yawing moment which may increase while lateral force is almost the same (Figure 4.55). During the test phase characterized by a decreasing propeller rate the flow is probably more developed so that the difference between the three test types is smaller. For higher Froude numbers results are shown in Figure 4.56 and Figure 4.57.

The observations for model E resemble these for model D and will not be discussed.

Selected tabular model [85]

Measured lateral force and yawing moment due to swaying are approximately anti-symmetrical due to small differences for positive and negative drift angles and the influence of ship velocity will be accounted for using weighted averages. Tabular models for the lateral force due to swaying for model D and model E are shown in Figure 4.58. As the under keel clearances decreases, cross flow induces important lateral forces around 90 deg drift angle. A part of this force must be attributed to the presence of the rudder. Due to a non-dimensional description of the lateral force based on the lateral underwater surface $L_{PP}d$, the tabular models for the tanker and the container carrier at 20% UKC differ hardly. Nevertheless, for the ship moving astern the application point of this lateral force is situated more aft in the case of the tanker, compared to the container carrier (Figure 4.59). Additionally, the influence of a decreasing water depth on the yawing moment due to pure sway is more significant for the tanker than for the container

carrier.

(b) **Tabular models based on harmonic test types**

Principally, velocity derivatives (e.g. $Y'_{uv}, Y'_{v|v|}, N'_{uv}, N'_{v|v|}$) or, in general, relations between the drift angle β and the non-dimensional lateral force and yawing moment can also be derived from PMM sway tests. Oblique towing (OT) tests as were examined in section (a), offer nevertheless the advantages of having a stationary character and allowing larger drift angles, which can only be realised by PMM tests with high oscillation frequencies and large lateral amplitudes.

PMM tests can yield velocity derivatives in two ways:

❑ by a regression analysis applied to the first harmonic component of Y or N in phase with sway velocity, measured during a series of tests executed at varying $v'_A = y'_{0A}\, \omega'$ (figure 2 in [60] for model E at 20% UKC);

❑ by means of a regression analysis applied to Y or N measured during individual PMM tests (Figure 4.60).

The first analysis can only be applied if a rather simple regression model is used for $Y'(\beta)$ or $N'(\beta)$, while the second also allows more complicated mathematical models, such as a tabular representation for a discrete number of drift angles. The latter appeared to be preferable to a regression model, as was pointed out by a detailed analysis of drift induced forces and moments resulting from oblique towing tests with model C at 10% UKC [84].

A comparison between damping forces and moments derived from oblique towing tests and from PMM sway tests carried out with constant sway amplitude ($y_A/B = 1$) with $1.35 <\omega'<3.6$ leads to following conclusions (Figure 4.60, values based on L_{PP}^2 instead of $L_{PP}d$):

❑ For $\omega'<2.7$, $Y'(\beta)$ and $N'(\beta)$ do not change significantly with increasing frequency. Compared to the stationary oblique towing tests, Y' and N' are underestimated for all drift angles; only at very small β, the fair agreement for Y' is observed.

❑ A significant difference is found between the $Y'(\beta)$ and $N'(\beta)$ curves obtained from PMM sway tests at relatively high frequency ($\omega'>2.7$) compared to tests performed in the lower frequency range.

❑ Even at low frequency it seems impossible to reproduce steady drift forces by one single PMM sway test.

There are indications that damping forces are affected by memory effects in the frequency range $\omega'>2.7$, which can be ascribed to wake interference. Besides, sway tests at higher ω' result into a relationship between measured drift induced force and moment and drift angle β which is not characterized by a single curve but by a loop.

Table 4.6 Characteristics of non-conventional harmonic sway test with model E at 20% UKC

Run	Δx_0 (m)	Δy_0 (m)	$\omega^{*'}$
EGLA0000	4	0.8	6
EGLA0100	6	0.8	4
EGLA0200	8	0.8	3
EGLA0300	6	1.6	4
EGLA0400	8	1.6	3
EGLA0700	2	0.4	12
EGLA0800	2	0.4	12

A comparison can also be made between stationary tests and non-conventional harmonic sway tests described in chapter 3 and already used while evaluating the acceleration derivatives. In Figure 4.61 non-dimensional lateral force and yawing moment are shown for the test runs summarized in Table 4.6 and a proposed tabular model based on stationary oblique towing and multi-modal tests. High non-dimensional frequencies $\omega^{*'}$ must be avoided as the discrepancies between both model test results are large. In addition,

although the difference in tabular form is less striking for Figure 4.61 compared to Figure 4.60 (probably due to the available under keel clearance), there still remain some differences if the individual stationary oblique towing tests should be replaced by one non-conventional sway test.

Although some papers concerning mathematical modelling in deep water quoted in section 3.6.1.2, proved some possibilities of replacing stationary tests by harmonic tests, this must be done carefully for shallow water conditions.

4.2.3 Velocity dependent forces and moment due to a pure yaw motion

As no rotating arm facility is available, all results for pure yawing are based on harmonic PMM yaw tests.

4.2.3.1 Longitudinal force due to yawing

The determination of the longitudinal force due to pure yawing can be based on model:

$$X_H = X^{(\beta)}(u,0,0) + X^{(\gamma)}(u,0,r)$$ (4.30)

and two representation methods:

1. the resistance force $X^{(\beta)}$ is not replaced by the value based on stationary straight-line tests but is calculated for each individual test run or for a group of test runs (for example per Froude number) and is compared to the resistance force from these stationary tests (see for example model D, Table 4.7 and Figure 4.62).
2. a reduced longitudinal force is calculated and represented:

$$X_{Hred} = X_H - X^{(\beta)}(u,0,0) = X^{(\gamma)}(u,0,r)$$ (4.31)

For this model the resistance force is expected to be completely included in value $X^{(\beta)}$, although a value $X^{(\gamma)}$ is found which differs from zero at zero yaw rate angle (model E, Figure 4.63, left).

Table 4.7 Model D, resistance force based on stationary straight-line tests (series D1)

Fn	0.016	0.049	0.077	0.116	astern
$X^{'(\beta)}(u,00)$	-0.0192	-0.0252	-0.0242	-0.0246	0.0331

Some conditions must be taken into account while executing a regression analysis:

❑ Both models $X^{(\beta)}$ and $X^{(\gamma)}$ can not be derived at the same time as mutually dependent variables must be avoided to obtain significant results.
❑ Depending on the maximum yaw rate angle during an individual test run tabular models are derived with an interval of 5 or 10 degrees. Small longitudinal forces are measured during low and even ordinary speed harmonic yaw tests so that the scatter can be important near zero yaw rate angle and some doubts may arise about the accuracy of the derived force at $\gamma=0$. In accordance with this observation, an increasing frequency gives the opportunity to increase the range of available yaw rate angles during an individual test although the accuracy at low yaw rate angles will be reduced. Determining the influence of γ on the longitudinal hull force can therefore not be based on only one test run.

For model D and all Froude numbers the sum $X^{(\beta)}+X^{(\gamma)}$ according to (4.30) at zero yaw rate angle differs from the values in Table 4.7, while for the motion astern ($\gamma=180$ deg) the values are nearby. The error bars for results of series DA in Figure 4.62 are considerable for $F_n=0.016$ and discrepancies can be observed near zero yaw rate angle comparing low and ordinary speed. For model E a global model for all Froude numbers is determined in medium deep and shallow water. Making use of a reduced hull force representation zero values for $X^{(\gamma)}$ are not found at $\gamma=0$. For both ship models a correction will be made mainly based on a displacement based on the residual hull force at $\gamma=0$ for a motion ahead and $\gamma=180$ deg for a motion astern. A

comparison is made in Figure 4.63 of a global model based on all available test runs and a model based on a selection of runs. This selection contains one ordinary speed test within the range $|\gamma| \leq 15$ deg and lower speed tests to obtain results for higher yaw rate angles.

4.2.3.2 Lateral force and yawing moment due to yawing [85]

Compared to the acceleration derivative of lateral force due to yawing, testing parameters frequency and yaw amplitude have a significant influence on the velocity dependent lateral force $Y'^{(\gamma)}$ both for full and slender ships.

In Figure 4.64 (left) the tabular models of individual test runs are compared for the tanker at the two available water depths. At 50% UKC the difference between the models based on runs at small frequency/small yaw amplitude or large frequency/large yaw amplitude is noticeable but small. At 20% UKC, on the other hand, the test parameters affect the resulting lateral force. The centrifugal force, -mur, proportional to the ship's mass m is added to the figures of $Y'^{(\gamma)}$.

The influence of the test parameters can partly be explained based on the sinkage measured during harmonic yaw tests. Maximum sinkage occurs at maximum yaw velocity or yaw rate angle and increases with decreasing water depth and increasing frequency and yaw amplitude (Figure 4.65).

Moreover, the involved test parameters during pure yaw tests with slender ships influence both the magnitude and the sign of the lateral force $Y'^{(\gamma)}$ at small yaw rate angles.

With increasing frequency ($\omega' > 3$) the centrifugal force –mur and the hydrodynamic lateral force $Y'^{(\gamma)}$ show the same dependence on yaw rate angle for yaw rate angles around zero (Figure 4.66). As the water depth to draught ratio decreases to very shallow water (UKC of 7%), hydrodynamic force $Y'^{(\gamma)}$ is opposite to the centrifugal force line so that hydrodynamic force and centrifugal force neutralize each other.

In Figure 4.67 global models are shown per Froude number for all available PMM runs. For series D1 (left figure) differences are small comparing the tabular models for the Froude numbers 0.032 through 0.065. During low speed PMM harmonic yaw tests (F_n=0.016) the scatter is large giving large error bars for series DA. A tabular model for model D at 20% UKC will be based on a selection of model tests with moderate frequency and speed around zero yaw rate angle and low speed at higher yaw rate angles.

Four quadrants tabular models for the tanker and the containership are illustrated in Figure 4.68. Values at 90 deg yaw rate angle are based on oscillating tests around ψ-axis (zero forward velocity) which are affected by memory effects caused by the ship going through its own wake. Therefore, 90 deg values were calculated based on the first cycle of oscillating tests during which memory effects are restricted. A totally different behaviour comparing model E and D can be recognized around 90 deg yaw rate angle. For a full body during pure turning (γ=90 deg) the lateral force acting on the ship's stern is dominant while the opposite is measured for the slender body. Only at small yaw rate angles ($|\gamma|$<30 deg) lateral force and yaw velocity have the same sign for the slender body.

Contrary to the lateral force, the yawing moment is scarcely influenced by the test parameters during pure yaw tests. Nevertheless, tabular models should be based on a selection of some test runs with varying model velocity and moderate frequency and amplitude as tabular models derived from individual test runs may differ somewhat as is presented for the tanker in Figure 4.69. Global models per Froude number are shown in Figure 4.70 for the container carrier. For the ship going ahead only the tabular model for the yawing moment at F_n=0.016 or low speed differs somewhat from the tabular models for higher speed. For the ship going astern both reduced velocities give comparable tabular models. These differences depending on the speed range are not taken into account while calculating the tabular models that will be used during validation (Figure 4.71). Although the tanker is a full body, the non-dimensional yawing moment

100

due to pure yawing is somewhat smaller than the yawing moment for the containership at an identical nominal under keel clearance of 20% of the draught.

4.2.4 Combination of sway and yaw additional forces

Cross flow effects are partly included in the lateral forces and yawing moments due to pure swaying and pure yawing. Additional forces and moment measured during harmonic yaw tests with constant drift angle are subject to errors as the values are small. A comparison of formal and tabular models for forces and yawing moment due to the combination of sway and yaw are presented in Figure 4.72 for model E at an UKC of 20%. The formal models are based on the equations:

$$X'^{(\chi)} = X'_{vr} \, v' r'$$

$$Y'^{(\chi)} = Y'_{v|r|} \, v' |r'| + Y'_{r|v|} \, r' |v'| \tag{4.32}$$

$$N'^{(\chi)} = N'_{v|r|} \, v' |r'| + N'_{r|v|} \, r' |v'|$$

For the longitudinal force both models are almost identical. For the lateral force and the yawing moment the formal and tabular model give the same results within a small range around $|\chi| = 90$ deg which could be explained based on the small drift angles used for the combination of sway and yaw. The scatter occurring at angles χ around 0° and 180° can only be reduced by executing tests at higher drift angles ($\beta \geq 5$ deg), possibly together with a small yaw amplitude and a moderate test frequency.

Tabular models for model E at 20% and 50% UKC are compared in Figure 4.73 where an increase of the water depth results into a decrease of forces and yawing moment due to the combination of sway and yaw. The scatter measured on a slender body is much larger as can be observed on Figure 4.74. The corrected model is rather arbitrarily chosen, taking into account the error bars and the assumption of a symmetrical behaviour according to the formal model in (4.32).

4.2.5 Comparison of velocity dependent hull forces

The validation of the mathematical manoeuvring model in which the hull forces play an important part, will be executed in chapter 7. For tanker E a comparative study of the velocity dependent hull forces at both water depths could help interpreting the results of this validation. Therefore, tabular models for horizontal forces and moment for pure sway, pure yaw and cross-coupling of sway and yaw will be represented in Figure 4.75. A comparison for model D will be presented in chapter 7.

5 Modelling of propeller forces and moment

An introduction to propeller induced forces is given in chapter 2 where propeller thrust T and propeller torque Q are discussed making use of the open water characteristics and the definition of wake at the ship's stern. The longitudinal force X_P acting on the ship's hull is proportional to the propeller thrust T and is reduced to a fraction (1-t_P) with t_P the thrust deduction factor.

$$X_P = (1 - t_P)T \tag{5.1}$$

Wake factor and thrust deduction express the interactive phenomena between the propeller and the ship's hull and are affected by each elementary manoeuvre (drifting, yawing). Propeller thrust and torque will be discussed in 5.2 where a tabular model for the wake factors w_P (thrust identity) and w_Q (torque identity) will be developed based on the observations summarized in 5.2.1. The dependence on model test type will be highlighted. The thrust deduction factor for the four quadrants of operation will be modelled in 5.3.

With regard to propeller induced lateral force Y_P and yawing moment N_P, usually only the effect of an asymmetrical flow due to a reversed propeller is considered. Both are then assumed to be proportional to the propeller thrust or the square of the propeller rate of turn. Another assumption is the execution of tests at model or ship self-propulsion point so that the influence of propeller action is included in the force and moment components Y_{HP} and N_{HP}. In section 5.4 the propeller effect is examined for each quadrant where a distinction is made according to the sense of the wake flow due to the ship motion and of the propeller slipstream. For the odd quadrants the observations are summarized in section 5.4.1.1 while the tabular models are presented in section 5.4.2.1. The observed flow patterns in quadrant 2 and 4 (section 5.4.1.2) are highly non-stationary and a time dependent model will be proposed (section 5.4.2.2).

5.1 General considerations for the propeller effect

Modelling the propeller effect on either longitudinal force X or lateral force and yawing moment some considerations have to be borne in mind which are shortly discussed here. These considerations will be used as a basis for the following sections.

5.1.1 Modelling of propeller thrust and propeller torque

Modelling of propeller thrust (propeller torque) measured during captive model tests is based on the propeller open water characteristics and the thrust (torque) identity method to determine the wake factor behind the ship.

Some disadvantages are attached to this modelling technique and the following remarks have to be borne in mind:

❑ Propeller open water characteristics are not always available so that these four quadrant characteristics of the thrust coefficient C_T and torque coefficient C_Q must be estimated based on standard series (e.g. Wageningen B-screw series).

$$C_T(\varepsilon) = \frac{T}{\frac{1}{2}\rho\left(u_P^2 + c_P^2\right)\frac{\pi}{4}D_P^2} = \frac{T}{\frac{1}{2}\rho\left(u_P^2 + (0.7\pi nD_P)^2\right)\frac{\pi}{4}D_P^2} \tag{5.2}$$

$$C_Q(\varepsilon) = \frac{Q}{\frac{1}{2}\rho\left(u_P^2 + c_P^2\right)\frac{\pi}{4}D_P^3} \tag{5.3}$$

In [44] thrust and torque coefficient are given as function of the propeller advance angle ε.

$$\varepsilon = \text{Arctan2}\left(u_P, 0.7\pi nD_P\right) = \text{Arctan2}\left((1 - w_P)u, 0.7\pi nD_P\right) \tag{5.4}$$

Determination of the wake factor at the propeller position depends strongly on the propeller open water characteristics applied during the analysis. This can be illustrated based on Figure 5.1. The K_T values measured during straight ahead captive model tests for the propeller behind the ship's hull are shown as symbols. A linear regression line for these values has a K_T value at zero advance ratio J'=0 which equals 0.466. Two estimation curves for the open water characteristics are based on the Wageningen B-screw series one without adaptation of the resulting curve (estimation 1) and one with adaptation of the K_T curve according to the regression value K_T(J'=0)=0.466. Thrust identity leads to lower values for the wake factor w_P based on estimation curve 1 compared to estimation curve 2. This disadvantage of the thrust and torque identity method can only be overcome by measuring the wake velocity behind the ship which is nevertheless expensive and must be executed very carefully. In addition, the wake varies over the propeller race and need to be averaged.

❑ In [86] wake distributions are measured behind ships travelling with a constant drift angle varying between 0 and 20 degrees. The ship models used are a mathematical Wigley hull, a cargo liner (Series 60) and a tanker. Velocities are measured on the cross section including the propeller plane and these measurements show clear differences of wake distributions and nominal wake factors among the three hulls. The experimental conditions are restricted to the ordinary speed range with Froude numbers of 0.18 for the slender hulls and 0.12 for the tanker. According to the international definition of positive values of drift angle only negative drift angles are tested and a symmetrical model for the influence of drifting on the nominal wake factor at propeller position w_P is adopted:

$$w_P = w_{P0} \exp\left(- 4.0\beta_P^4\right) \hspace{4cm} (5.5)$$

with w_{P0} the wake factor during straight ahead motion and β_P the inflow angle at the propeller. Compared to slender hulls larger nominal wake factors are measured for the tanker resulting in lower inflow velocities at the propeller position.

❑ Adaptation of the estimated K_T curve as described above is a pressing question. Some results of propeller contributions at low speed manoeuvring are mentioned by Kose in [27]. Thrust deduction and wake factor depend on propeller loading for the straight running conditions. When the longitudinal speed of the ship is zero, the propeller advance speed estimated by use of $(1-w_P)u$ is also zero. The actual thrust value K_T at J'=0, however, is somewhat different from the open water test result at J=0. Although further investigations are necessary, Kose proposes to estimate the thrust value at low speed by use of the propeller open water characteristics at J=0. From this line of remark an adaptation of the estimated K_T curve can be ignored.

❑ Modelling of propeller thrust T_P (or torque Q_P) based on the open water characteristics makes use of the non-dimensional propeller thrust (torque) coefficient K_T (K_Q). At lower propeller rates equation (2.9) can lead to K_T (K_Q) values affected by measurement errors due to the division by the square of the propeller rate.

5.1.2 Modelling of lateral force and yawing moment

The influence of propeller action on lateral force and yawing moment was first examined and reported by the author in [84] considering the combination drift-propeller action. Only a few mathematical models taking account of this influence had been found in literature. In most models the effect of propulsion on lateral force and yawing moment is ignored or incorporated in the pure drift formulation, assuming operation near the self-propulsion point. It is clear that for harbour manoeuvres this condition is not fulfilled. In [87] the influence of ship velocity, propeller rate and rudder angle on lateral force and yawing moment due to propeller action has been examined for the four quadrants of operation based on model tests. The lateral force acting on the propeller disk plane seems to depend strongly on the advance coefficient J'.

All mathematical manoeuvring models considered in [84] are based upon the assumption that the effects of drift without propulsion and of the modification of the flow field due to propeller

action can be formulated separately.

$$Y = Y_H + Y_P$$
$$= Y^{(\beta)}(u, v, n = 0) + Y_1(u, v, n)$$
$$N = N_H + N_P$$
$$= N^{(\beta)}(u, v, n = 0) + N_1(u, v, n)$$

(5.6)

Following expressions were proposed in [84] for positive propeller rates n (n_0 is the reference propeller rate):

$$Y = Y_H + Y_P$$
$$= Y^{(\beta)} + Y^{(\beta)} C_n(\beta) \left(\frac{n}{n_0} \right)^2$$
$$= \frac{1}{2} \rho L d V^2 \left[1 + C_n(\beta) \left(\frac{n}{n_0} \right)^2 \right] Y'^{(\beta)}$$

(5.7)

and

$$N = N_H + N_P = N_H + x_Y Y_P$$
$$= N^{(\beta)} + x_Y(\beta) Y^{(\beta)} C_n(\beta) \left(\frac{n}{n_0} \right)^2$$

(5.8)

Model (5.7) is based on the assumption that the flow circulation around the ship is apparently extended due to propeller action, which can be interpreted as an extension of the ship length L of the hull-propeller-rudder combination. This extended lateral force has a point of application $x_Y(\beta)$.

Discussing the hull-propeller combined forces and moment on a fully appended ship, an important remark must be borne in mind. At non-zero drift angle but zero rudder deflection the rudder profile will nevertheless be affected by the oblique flow resulting into forces measured on the rudder and consequently hull forces and moment induced by the rudder perturbation. In this report these forces at zero rudder deflection will be taken into account using models (5.7) and (5.8) and will not be based on a physically more accurate hull-propeller-rudder combination model for the lateral force and the yawing moment as described in chapter 6. Although the correspondence between cause (generated rudder forces) and model form (only hull-propeller combination with contributions Y_H and Y_P) is not really straightforward, this modular form will be developed.

Although the influence of propeller action on horizontal forces and moment was first examined for oblique towing, a yawing motion will also take part in this effect. The influence of drift angle and yaw rate angle will be examined further on in section 5.4.

In [84] some difficulties simulating hydrodynamic forces and moments due to drift and reversed propeller action have been illustrated. It is concluded that equations (5.7) and (5.8) cannot be used for this condition. The combination of forward ship motion with reversed propeller action for example causes an asymmetric flow pattern in the vicinity of the ship's stern, resulting into a lateral force to port and a positive yawing moment for a right handed propeller. Therefore, the effect of negative rpm is usually simulated by a lateral force formulated as $Y_{nn}n^2$ (equation (2.45)) or as a fraction of the propeller thrust (equation (2.80)), together with a corresponding term for the yawing moment.

In (very) shallow water, however, such an approach appears to be insufficient due to unsteady hydrodynamic phenomena which will be described in section 5.4.1.2. Although the sign of the average values for Y and N indeed confirm the behaviour described above, it was observed that

large eddies which are shed from the stern of the model result into slowly fluctuating lateral forces and yawing moments. Similar phenomena where reported by Ch'ng and Renilson in [88], who even observed amplitudes for the fluctuating forces of about 10 times the steady value.

5.2 Propeller thrust and torque

5.2.1 Wake factor: measurements

Only propeller thrust values T will be examined in the following sections. The modelling procedure that will be developed for this thrust component, is expected to be used for the propeller torque as well. For each quadrant the measurements of all available test types will be evaluated and compared so that differences can be recognized and estimated for the wake factor at the propeller.

5.2.1.1 First quadrant of operation: going ahead

Different test types have been executed to determine the propeller thrust and torque during a motion ahead due to the ship velocity (both longitudinal and lateral velocity, reflected by the Froude number and the drift angle), the yaw velocity, the propeller rate and the rudder deflection:

- ❑ During a *stationary test* run Froude number, propeller rate and rudder angle are kept constant so that a discrete value is measured for the thrust $T(F_n,n,\delta)$. According to the ship model's velocity propeller rate is varied below and above the model self propulsion point to cover a wide range of operation conditions.
- ❑ During a *PMM yaw test* with propeller action Froude number, propeller rate and rudder angle are kept constant while the influence of yaw rate angle on the propeller thrust is measured.
- ❑ During a *multi-modal test* two test types are considered:
  - ○ a run with constant propeller rate and harmonically varying rudder angle (test type A) or
  - ○ a run with harmonically varying propeller rate and rudder angle (test type B).

K_T values measured during *bollard pull tests* with rudder deflection are shown in Figure 5.2 as a function of the propeller rate. The propeller rate is generally expressed proportional to a reference propeller rate n_0 which is 100 rpm full scale for the containership D and the tanker E. The dependence of the thrust coefficient on propeller revolutions can be partially explained based on the expression (2.9):

$$K_T = \frac{T}{\rho n^2 D_P^4}$$

where low propeller rates could cause large errors for the thrust coefficient. Nevertheless, even at moderate and higher propeller revolutions different values are measured for K_T. At bollard pull condition the advance ratios J and J' are zero so that the K_T value is modelled based on the open water value $K_T(J=0)$ (Table 5.1). The open water values for the four quadrants of operation in Figure 5.3 are based on K_T instead of C_T.

Table 5.1 Thrust coefficient values $K_T(J=0)$ for model D and E at propeller ahead and astern

	$K_T(J=0)$	
	model D	model E
propeller ahead	0.488	0.263
propeller astern	-0.374	-0.183

Analysing the influence of drifting on the thrust coefficient K_T during *stationary tests* a distinction is made between low speed manoeuvring ($F_n=0.016$) and ordinary speed manoeuvring ($F_n \geq 0.049$) for model D (Table 5.2). This distinction in low and ordinary speed regions is based on observations for tests executed at $F_n=0.016$ and tests executed at Froude numbers of at least 0.049. The observations at ordinary speed correspond to the models summarized in the MMG-model (see chapter 2) for the influence of drift angle on propeller thrust.

The model tests at small drift angles ($|\beta| \leq 5$ deg) also reflect the influence of varying rudder deflection.

Table 5.2 Relationship between Froude numbers and ship velocity at full scale (knots) for model D

F_n	0.016	0.032	0.049	0.065	0.077	0.081	0.116	0.122	0.154
V (knots) at full scale	1.66	3.32	5.08	6.74	7.98	8.40	12.02	12.64	15.96

In Figure 5.4 (top) an increasing drift angle $|\beta|$ leads to an increase of the measured thrust coefficient for all test runs (including tests with varying rudder angle). Stationary tests have been executed at propeller rates of 50% (J'=0.13) and 100% (J'=0.06) of the reference propeller rate n_0 which values are far beyond the model self propulsion ratio for F_n=0.016. An increasing drift angle gives a decreasing value for the apparent advance ratio J' as the longitudinal velocity component diminishes. At higher propeller rates the dependence of the thrust coefficient on the drift angle is almost symmetrical. At lower propeller rates a small asymmetry is observed.

This relationship at low speed contrasts with the relationship shown in Figure 5.4 (bottom) for ordinary speed which can also be found in [47] and [86]. An increasing absolute value of the angle β leads now to a decreasing measured thrust coefficient K_T and consequently to a decreasing wake factor w_P. At straight ahead motion the wake factor is expected to be higher than at oblique motion as at non-zero drift angle the inflow into the propeller will be easier.

The influence of rudder action during low speed captive model tests (F_n=0.016) is clearer at moderate propeller revolutions and at zero drift angle (Figure 5.5). In this situation both positive and negative rudder angles give higher values for the thrust coefficient compared to zero rudder deflection. At very high overload conditions (n=100%n_0) or non-zero drift angle the influence of rudder action is rather small and not unequivocal which means that higher or lower values of K_T have been measured at non-zero rudder angles and drift angles compared to zero drift and zero rudder angle. At F_n=0.049 deviating K_T values are measured at zero drift angle compared to the overall results for higher Froude numbers. For ordinary speed and slender ships the influence of a rudder deflection is rather small. Therefore, the influence on thrust coefficient K_T and torque coefficient K_Q will not be modelled but will be incorporated in the specific model by evaluating the nominal wake factor based on all the available test results (including rudder deflection).

Multi-modal tests of type A (constant propeller rate and harmonically varying rudder angle) are expected to give a comparable relationship between the apparent advance ratio and the thrust coefficient K_T as stationary tests give. Related to the modelling of the propeller thrust based on measurements, another important issue is shown on Figure 5.6. The multi-modal tests have been executed at two time intervals: first Froude numbers F_n=0.016, 0.032, 0.049, 0.065, 0.081, immediately followed by model tests going astern (F_n= -0.016, -0.032) and once again tests ahead with F_n=0.077. Four days later tests have been executed at F_n= 0.122, 0.154. Propeller thrust generally decreases at constant propeller revolutions with increasing ship velocity. This is qualitatively true for almost all thrust values shown on Figure 5.6. Nevertheless, the thrust values measured at Froude number F_n=0.077 are rather too small compared to for example the values at F_n=0.081. Transforming the propeller thrust T into the propeller thrust coefficient K_T, this discrepancy leads to K_T values nearby the open water K_T curve resulting in nominal wake factors which are smaller than factors from stationary tests (Figure 5.7). Accurate measurements of thrust at low propeller revolutions are rather difficult due to the occurrence of test errors. In Figure 5.7 a selection is made of the multi-modal results based on propeller revolutions greater than 50% of the reference propeller rate. Thrust values K_T are equal or lower than stationary test results which are already restricted to propeller revolutions of minimum 50% of the reference propeller rate.

Multi-modal tests of type B (harmonically varying rudder angle and propeller rate) are characterised by some remarkable phenomena:

❑ At low ship velocity and straight ahead motion (F_n=0.016, Figure 5.8) a distinction can be made between thrust values measured during the increasing propeller rate phase and the decreasing propeller rate phase. Thrust measured during the increasing phase is lower compared to the thrust measured for the same propeller rate during the decreasing phase. This can be explained based on the lack of a stationary phase with a constant propeller rate. Transient effects are dominating resulting into lower thrust values during the increasing phase (development of the propeller slipstream) compared to the decreasing phase (run-down of the propeller slipstream). Furthermore, a small positive propeller thrust is measured at very low propeller revolutions during the second phase while these values are almost zero at the start. An explanation for this difference is hardly found or it should be a non-stationary effect due to for example circulation of the water in the tank. An examination of this phenomenon should be executed in the future by evaluating thrust measurements at low speed and in shallow water in detail.

❑ At ordinary ship velocity and straight ahead motion (F_n=0.081, Figure 5.8) the difference between the increasing and decreasing phase is rather small and negligible. Wake distributions at the propeller plane depend also on ship velocity and probably influence the delivered propeller thrust for low compared to ordinary speed manoeuvring during the two distinguished phases.

Figure 5.9 shows the relationship between measured thrust coefficient K_T and apparent advance coefficient J' for low speed manoeuvring and increasing and decreasing propeller rate. Compared to the stationary results following observations can be made:

❑ *Increasing propeller revolutions*:
At low ship velocity (F_n=0.016 and 0.032) measured K_T values are fluctuating around the resulting K_T values of stationary tests, even at low advance ratios or high propeller loading characterised by a strong propeller slipstream. This fluctuation can be partially explained based on the influence of the harmonically varying rudder angle but measured thrust values fluctuate far beyond stationary values measured at non-zero rudder deflection. As the ship velocity increases (F_n≥0.049) and the wake field at the propeller position becomes more pronounced, measured thrust values at moderate and high propeller loading (J'≤0.5) are not influenced by the harmonic character of the test type and only at low propeller loading (higher values of J') measured K_T values exceed the stationary ones.

❑ *Decreasing propeller revolutions*:
At all tested ship velocities multi-modal tests only approaches stationary measured thrust values nearby maximum propeller loading (or 100% of the reference propeller rate). Measured thrust coefficients at lower propeller revolutions overestimate the stationary ones and display the same tendency as thrust values measured during bollard pull tests at low propeller rate (n<50% n_0).

The same phenomena concerning the influence of ship velocity on measured propeller thrust during multi-modal tests of type B occur during an oblique motion with constant drift angle. The following figures are selected:

❑ Figure 5.10 shows the influence of positive and negative drift angles on thrust coefficient K_T for F_n=0.016. K_T values are considered as a function of an advance ratio depending on the total ship velocity V instead of the longitudinal velocity component u. This new dependency is linked with the different flows at the propeller during bollard pull condition (u=0, v=0) and pure sway motion (u=0, v≠0), both resulting in an apparent advance ratio J'=0 if this ratio is only based on the longitudinal velocity component. At bollard pull condition there is no wake at the propeller position, while a dominating cross flow at 90 degrees drift angle can be turned off in the vicinity of the propeller resulting in a non-zero inflow velocity into the propeller. This difference will be modelled by combining the total ship velocity at the propeller and the available drift angle.

The stationary results displayed on this figure and the following are restricted to straight ahead motion or zero drift angle with rudder deflection. For a detailed comparison with stationary drift angle tests Figure 5.10 and Figure 5.4 have to be put together taking into account the modified representation form.

Increasing and decreasing propeller revolutions give once again two curves for each drift angle. The increasing phase results into lower thrust coefficient values, whereas the decreasing phase gives thrust values lying more or less in the range of the measured stationary values. During multi-modal tests with a non-stationary character different dependencies on positive and negative drift angles occur. An evaluation can probably better be based on the modelled wake factor which will be described in section 5.2.2.

Compared to the execution of multi-modal tests type B at zero drift angle, imposing a drift angle (even small ones) gives a reduced increase of the measured thrust coefficient K_T during the second phase.

- Stationary results at $F_n=0.032$ are not available so that Figure 5.11 gives some additional information. Phenomena occurring during tests at $F_n=0.016$ can also be recognised but less pronounced at $F_n=0.032$. During the run-down of the propeller slipstream (decreasing phase) tests with non-zero drift angle give indeed higher thrust values compared to stationary straight run tests, but the mutual difference between the available drift angles is less clear than for the stationary drift angle tests.

- Asymmetry between positive and negative drift angles can be explained due to the induced asymmetry flow of a clockwise turning propeller and the non-stationary character of multi-modal captive model tests. As the ship velocity increases (Figure 5.12 and Figure 5.13) the difference between increasing and decreasing propeller revolutions diminishes. Based on the stationary test results a distinction was made between low and ordinary speed manoeuvring. From Froude number $F_n=0.049$ on, a similar distinction can be notified for multi-modal tests. Stationary results can be qualitatively approximated by multi-modal tests of type B, but a quantitative difference remains.

PMM yaw tests with or without constant drift angle have been executed to examine the influence of yaw velocity on thrust coefficient K_T. These non-stationary tests replace the stationary circular motion tests in the absence of a rotating arm facility. The dependence of the thrust coefficient K_T on the yaw velocity is not clear and rather negligible for Froude numbers $F_n=0.032$, 0.049 and 0.065. A decrease in the measured thrust can be notified for a yaw test with constant drift angle compared to a similar test with zero drift angle at ordinary speed. No conclusions can be drawn for higher Froude numbers or influences occurring during stationary circular motion tests.

5.2.1.2 Second quadrant of operation: stopping from headway

Depending on the characteristics of the propulsion mechanism and the geometry of the ship, at high forward ship velocities (e.g. varying between service speed and medium speed corresponding to a telegraph position of Full Sea to Slow Ahead) the reversed action of a propeller is counteracted due to the strong inflow at the propeller so that the efficiency of a reversed propeller can only be reached if the ship velocity has fallen down. Captive model tests with all combinations of forward velocity and propeller loading are nevertheless executed in the towing tank.

During *bollard pull tests* with model D two values of propeller rate (-50% and -100% of reference propeller rate) have been tested which do not reveal any influence and a mean value of –0.36 for the measured thrust coefficient can be compared with an estimated value of the open water characteristics (Table 5.1 and Figure 5.14).

The *stationary straight-line and oblique towing tests* (series D1, Figure 5.15) have been

executed with varying rudder deflection for the straight-line tests and with zero rudder angle for the oblique towing tests except for runs with $F_n=0.016$ and $|\beta|=5deg$. The propeller rate is varied with percentages of -35%, -50%, -100% of the reference propeller rate. Almost no influence of drift angle on thrust coefficient can be recognized for low speed manoeuvring (or $F_n=0.016$) while a clear influence of drift angle can be seen at lower propeller loading or higher J' values for higher ship velocities. Due to even a small drift angle the absolute value of thrust coefficient K_T is increased compared to a straight-line test and approaches the open water values of the propeller (Figure 5.15, J'<-0.75). In addition, the influence of rudder deflection on thrust coefficient K_T is negligible at ordinary speed manoeuvring and low speed manoeuvring with high propeller overload ($n=-100\%n_0$), clearly shown on Figure 5.16.

Multi-modal straight-line tests of type A are carried out with varying rudder deflection. Due to the disturbed inflow into the propeller during a stopping manoeuvre the measured propeller thrust is subject to fluctuations so that a mean value and standard deviation is calculated (Figure 5.17 and Figure 5.18). At low propeller loading some doubt may arise about the accuracy of measured propeller thrust. This inaccuracy or in other words inefficiency of the propeller could probably be explained due to a combination of higher forward velocity and lower propeller loading. Additionally, based on Figure 5.17 no clear tendency can be seen between forward velocity and measured propeller thrust, even at low and high propeller loading. A comparison of measured values for stationary and multi-modal straight-line tests gives similar results (Figure 5.19).

Almost no influence of yaw rate angle can be recognized on propeller thrust during *PMM yaw tests*. Probably this negligible influence could be explained based on the harmonic character of PMM yaw tests compared to the stationary character of sway velocity v or drift angle β during stationary and multi-modal captive model tests. An influence of yaw rate angle γ should be examined during circular motion tests where the yaw rate angle takes a constant value.

5.2.1.3 Third quadrant of operation: going astern

For *stationary straight-line and oblique towing tests* (series D1, Figure 5.20) at low propeller loading, the absolute K_T values are smaller than the open water results which means that a negative value for the wake factor w_P could be expected. The influence of an oblique motion is also not clear so that based on physical understandings a value of 0 for the wake factor w_P could be adopted for all drift angles during a motion astern. A zero wake factor means that the inflow into the propeller resembles the inflow for a propeller in a uniform flow during open water tests.

Similar results can be obtained based on straight-line *multi-modal tests of type A*. Figure 5.21 shows measured K_T values influenced by rudder deflection where the right figure is restricted to an absolute propeller rate higher than 50% of the reference propeller rate. A mean value is not calculated.

5.2.1.4 Fourth quadrant of operation: stopping from sternway

Stationary straight-line and oblique towing tests (series D1, with zero rudder deflection) show an increase of measured propeller thrust coefficient K_T with drift angle (Figure 5.22) which can be compared to the first quadrant of operation at low speed. Positive or negative drift angles give a symmetrical influence on propeller thrust. At a propeller rate of 50% of the reference rpm and oblique motion astern, measured propeller thrust values K_T are much higher than the open water values ($|\beta|\leq170deg$) at high propeller loading. These values can only be reached during open water tests at higher advance ratios.

Straight-line *multi-modal tests of type A* (with rudder deflection) suffer from a high scatter for propeller loadings lower than 50% of the reference propeller rate. The important influence of the rudder angle which can be seen on Figure 5.23, is not examined.

Only negative values for wake factor w_P can give a propeller thrust model based on the open water test results which correspond more or less to the measured values during a straight astern

110

motion at higher propeller loading. This means that the inflow velocity into the propeller should be higher. Taking account of measurement inaccuracies especially at lower propeller loading a model value of zero for the wake factor w_P could be physically motivated so that the inflow velocity into the propeller during a straight astern motion should be the same as during propeller open water tests. For an oblique motion and lower propeller loading, values of K_T higher than 0.5 can also only be reached if wake factor w_P is negative (and rather high in absolute value).

Small negative values for wake factor w_P have also been measured by Harvald and are shown in Figure 2.5 of chapter 2 (quadrant 2 according to Harvald's definition). A constant value was nevertheless proposed and if a constant value is adopted here, a zero value could be chosen.

5.2.2 Wake factor: model

5.2.2.1 Description of model for propeller thrust and torque

Modelling of propeller thrust T and torque Q is based on the open water K_T and K_Q curves (thrust and torque identity method) and a tabular model for the wake factor at the propeller position w_P respectively w_Q is obtained. These wake factors are function of the ship motion (velocity components u, v and r) and the propeller loading. General formulations are:

❑ For the propeller thrust T and torque Q based on the open water curve $K_T(\varepsilon)$ and $K_Q(\varepsilon)$:

$$T = \rho n^2 D_P^4 K_T(\varepsilon)$$
$$Q = \rho n^2 D_P^5 K_Q(\varepsilon)$$

(5.9)

❑ For the hydrodynamic pitch angle ε depending on w_P or w_Q:

$$\varepsilon = \text{Arctan2}\left(\left(1 - w_{P,Q}(\varepsilon^*,\beta_P)\right)U_P, 0.7\pi n D_P\right)$$

(5.10)

❑ For the wake factors at the propeller position $w_{P,Q}(\varepsilon^*,\beta_P)$:

$$\varepsilon^* = \text{Arctan2}\left(U_P, 0.7\pi n D_P\right)$$

(5.11)

$$\beta_P = \text{Arctan2}\left(-\left(C_v v + C_r x_P r\right), u\right)$$

(5.12)

with constants C_v and C_r which take values of 0 (false) or 1 (true) depending on the necessity to incorporate the influence of the lateral velocity and yaw velocity on the propeller thrust. x_P is the longitudinal position of the propeller.

❑ For the ship velocity at the propeller position U_P depending on the total ship motion:

$$U_P = \text{sgn}(u)\sqrt{u^2 + \left(C_v v + C_r x_P r\right)^2}$$

(5.13)

Judging on the measurements described above a distinction between low and ordinary speed manoeuvring could be proposed for the wake factor. This conclusion is nevertheless ship related and not generally found while examining different ship types and even different ship geometries within the same type. Two modelling techniques could be suggested:

❑ First of all, a tabular model can be determined for wake factor $w_{P,Q}(\varepsilon^*,\beta_P)$ for some well chosen Froude numbers, so that a clear distinction can be made between low and ordinary speed manoeuvring. This supposes the introduction of a "matching and patching" technique to link both elementary manoeuvring conditions. The averaged model method described by Kobayashi and quoted in chapter 1 can be used, defining two limits, an upper limit for the low speed manoeuvring case F_{nmin1} and a lower limit for the ordinary speed manoeuvring case F_{nmin2}. The averaged model gives the resulting wake factor between these two limits using:

$$w_P(\varepsilon^*,\beta_P) = g_1 w_P(\varepsilon^*,\beta_P)_{\text{ordinary}} + g_2 w_P(\varepsilon^*,\beta_P)_{\text{low}}$$

(5.14)

where coefficient g_1 and g_2 are defined as (1.22):

$$g_1 = \frac{F_n - F_{n\min 2}}{F_{n\min 1} - F_{n\min 2}}$$

$$g_2 = \frac{F_{n\min 1} - F_n}{F_{n\min 1} - F_{n\min 2}}$$

❑ The influence of low speed manoeuvring is partly included in the dependence of wake factor $w_{P,Q}(\varepsilon^*, \beta_P)$ from the propeller loading ε^* as low values (e.g. bollard pull or $\varepsilon^*=0$) can only be reached at low ship velocities. Based on this method a calculation is made for all Froude numbers at once. As angle ε^* is calculated from a combination of ship velocity and propeller rate moderate ε^* values within a short range could be obtained from a high speed – high propeller rate or a low speed – low propeller rate combination. In this case, as measured thrust and torque are more important for the high speed – high propeller rate combination, these test results will dominate so that if a clear distinction is necessary between low and high speeds separate calculations for several Froude numbers is preferred.

These two modelling techniques have been used for model D and for the first quadrant of operation. For the ship going astern (quadrant 3 or 4) ship speed is always limited and therefore low so that for the other quadrants no distinction will be made.

The influence of rudder deflection will be incorporated as tabular models are based on all test results with or without non-zero rudder angles.

A comparison of selected tabular models for a slender and a full ship is only justified if wake distributions are measured or if both ship models are equipped with the same propeller using the propeller thrust and torque identity method.

5.2.2.2 Positive ship velocity: first and second quadrant of operation

For ship model D and the first quadrant of operation tabular models for $1-w_P$ are calculated according to the various test types with a distinction on Froude number (*model per Froude number*):

❑ *Stationary drift angle tests*:
Bollard pull tests are not considered as wake factor $1-w_P$ has no influence on the velocity $(1-w_P)U_P$ at the propeller position $(u=0, v=0, r=0)$. The tabular value for $1- w_P$ at $\varepsilon^*=0$ and $\beta_P=0$ is arbitrary. Tabular results for Froude number $F_n=0.016$ at 100% and 50% of the reference rpm are shown on Figure 5.24. Error bars are indicated on the individual tabular coefficients. At 50% of the reference propeller rate or $\varepsilon^*=3.4$deg regression results are questionable as error bars are relatively large. Nevertheless, stationary tests with non-zero drift angle $(|\beta|\geq10$deg for $\varepsilon^*=1.6$deg) give negative values for $1-w_P$ which means that the inflow velocity into the propeller disc is negative or open water results of quadrant 4 are used (increase of the thrust coefficient compared to quadrant 1). This tendency is similar to the development of increasing K_T values for bollard pull conditions as the propeller rate decreases.

Figure 5.24 also displays tabular results for $1-w_P$ for ordinary speed $(F_n\geq0.049)$. As the absolute value of the drift angle increases, the wake factor $1-w_P$ increases as well resulting into lower thrust coefficients compared to a straight ahead motion. This is in accordance with the results published by other authors concerning ordinary speed manoeuvring.

❑ *Multi-modal tests of type A* (Figure 5.25):
A comparison is made between tabular models of stationary straight ahead tests (with a constant rudder angle) and of multi-modal tests of type A (with harmonically varying rudder angle). Both tests are evaluated incorporating all Froude numbers. Lower ε^* values correspond obviously to low speed manoeuvring. Various assumptions are made to calculate tabular models for $1-w_P$ based on multi-modal tests. All multi-modal test results give higher values for $1-w_P$ compared to stationary straight ahead tests which means that thrust

coefficient K_T is lower for an identical hydrodynamic angle ε^*.

❑ ***Multi-modal tests of type B*** (Figure 5.26, Figure 5.27, Figure 5.28 and Figure 5.29):
Multi-modal tests of type B with harmonically varying propeller rate provide a complete range of hydrodynamic advance angles ε^* for the first quadrant of operation (ε^* from 0 to 90 deg). As was mentioned during the analysis of the measurements, a distinction is made between tabular models based on a regression analysis of the increasing and decreasing phase. Hydrodynamic pitch angles ε^* between 0 and around 30 degrees belong to the most frequent conditions during harbour manoeuvres. Nevertheless, a clear relationship between ship velocity and apparent hydrodynamic advance angle ε^* is summarised in Table 5.3.

Table 5.3 Relationship between ship velocity and apparent advance angle for a propeller rate of 25 rpm full scale and a propeller diameter of 8.1 m.

Velocity (knots)	1	2	3	4	5	6	7	8	9	10	15	20
ε^* (deg)	3.9	7.8	11.7	15.4	19	22.5	25.8	28.9	31.8	34.6	46	54

As the total ship velocity increases, the difference between tabular models for the increasing and decreasing phase diminishes. At low speed manoeuvring (F_n=0.016 and F_n=0.032) and decreasing propeller revolutions wake factor 1-w_P is negative for almost all hydrodynamic advance angles and drift angles. Lower thrust coefficients K_T during the increasing phase lead to positive wake factors 1-w_P at F_n=0.032. Fluctuations in the K_T curve during a straight ahead motion at low speed and increasing propeller revolutions result into fanciful linear regression lines.

A better agreement between stationary and multi-modal test results is obtained at ordinary speed manoeuvring and decreasing propeller revolutions. A global tendency of increasing wake factor 1-w_P at increasing propeller loading (or decreasing hydrodynamic pitch angle ε^*) is observed. In addition, non-zero drift angles give a rise in the calculated wake factors 1-w_P and a drop in the modelled propeller thrust.

Instead of calculating *models per Froude number* a *global model* incorporating all Froude numbers has been calculated for the distinctive test types. The influence of ship velocity can now only be visualized based on the hydrodynamic advance angle ε^*. On Figure 5.30 results of tabular models for w_P are shown for different test types and straight ahead motion (quadrant 1 and 2). For stationary tests the expected values for w_P greater than 1 at low speed manoeuvring are not found anymore due to the global model calculation method. Instead the accuracy at low ε^* values is small (large error bars). Multi-modal tests of type A give once again the lowest values for w_P for the first quadrant.

w_P values for the second quadrant have only been obtained for stationary tests and multi-modal tests of type A. A value w_P which equals zero is not really expected as the inflow velocity at the propeller behind the ship model should then be the same as the inflow during open water propeller tests. During a motion ahead the ship is still going in front of the propeller contrary to a motion astern. Non-zero values have been found (Figure 5.30), although near ε^*=180 deg (low speed / high propeller loading) a zero value could be adopted.

If a global model is used for multi-modal tests of type B a limitation of examined propeller rates is necessary so that low rpm conditions are excluded. If all propeller rates (even values going to zero) are maintained very low values are calculated near zero drift angle (Figure 5.31, left) compared to the calculation for rpm values greater than 35% of the reference propeller rate n_0 (right figure).

For stationary tests (Figure 5.32) different values are calculated for w_P and w_Q. At increasing drift angle |β| the inflow into the propeller increases with lower values for $w_{P,Q}$.

For multi-modal tests type B more drift angles have been examined (Figure 5.33, increasing

propeller rate). Positive and negative drift angles do not give symmetrical values, so that a small difference can be explained based on the sense of rotation of the propeller. Values obtained during the decreasing phase (Figure 5.34) give higher values for w_P compared to the increasing phase. At low ε^* values, tending to zero, values for w_P higher than 1 are found for some drift angles.

For model E only a global model for all Froude numbers is represented in Figure 5.35 for the first quadrant based on stationary and multi-modal tests of both type A and B. In accordance with the restriction applied to the propeller rate ($n>35\%n_0$) for the determination of the wake factor for model D, the propeller rate has also been restricted in Figure 5.35. Some observations can be summarized comparing the models for 20% and 50% UKC:

❏ For both water depth to draught ratios the wake factor at zero drift angle is larger than the one for non-zero drift angle. Due to the oblique flow, the wake flow $w_P U_P$ at the ship's stern decreases. In addition, the wake at 50% UKC is lower taking into account the increased clearance between bottom and keel.
❏ At low propeller loading ($\varepsilon^*<10$ deg) values for w_P sometimes increase to a value greater than 1 with once again a shift from quadrant 1 to quadrant 4 or a negative inflow into the propeller. In the final model, used for validation, these values will nevertheless be restricted to 1.
❏ Globally, wake factor w_P decreases with increasing propeller loading or decreasing propeller rate.
❏ The values for the second quadrant are not included and expected to be negligible small and subject to large errors.

5.2.2.3 Negative ship velocity: third and fourth quadrant of operation

Tabular models for the ship going straight astern according to the different test types are shown in Figure 5.36. Error bars are large for both quadrants except for multi-modal tests of type A and quadrant 3 but these values are negative. The influence of drift angle has been examined based on multi-modal tests of type B (Figure 5.37) although the accuracy is so poor that zero values for wake factors w_P and w_Q will be adopted for the third and fourth quadrant of operation. During a motion astern the inflow at the propeller will consequently reach the free stream condition.

5.2.2.4 Model for validation: wake factor

In the preceding sections a detailed model per Froude number and a global model have been determined for model D. A distinction as was made in the model from Hydronautics Research Inc. (chapter 1) based on the ship propulsion ratio η, can also be found here taking into account the dependence of the propeller loading ε^*. For $\varepsilon^*=0$ a bollard pull condition is reached, while for $\varepsilon^*=90$ deg the propeller is stopped. The importance of detailing the model for wake factors $w_{P,Q}$ and considering tabular models depending on the speed levels (low speed, e.g. lower than 4 knots, and ordinary speed) could be examined during validation (chapter 7) where the sensitivity of each module of a manoeuvring ship simulation model will be examined. A proposed model for the first and second quadrant of operation for model D is shown in Figure 5.38 and is based on a global model for all Froude numbers. For drift angles 0, 5 and -5 degrees results of stationary tests are used while for larger (positive and negative) drift angles results of multi-modal test of type B for both increasing and decreasing propeller revolutions will be combined.

In Figure 5.39 the tabular models for model E are shown for both water depths. Values have been restricted to the physically excepted range of [0,1].

These tabular models are not necessarily smooth as modelled values are determined by a regression analysis based on arbitrary chosen input values ε^*. This lack of smooth lines in the available models can affect the resultant motions (like accelerations and turning circles) to a small extent compared to the use of polynomials while modelling. Nevertheless taking into account the ranges of error bars, tabular models are valuable and can be slightly modified if necessary.

5.3 Longitudinal force: thrust deduction

5.3.1 Description of model for thrust deduction

The longitudinal force X_P executed on the ship's hull due to propeller action differs from propeller thrust T by the proportion $t_P T$ with t_P denoting thrust deduction, a hull-propeller interaction coefficient. While deriving values for thrust deduction t_P two calculation methods could be used:

❏ hull force X_H is calculated together with the thrust deduction and propeller thrust T is based on measured values instead of modelled values.

❏ hull force X_H is given and based on previous calculations and the reduced longitudinal force:

$$X_{reduced} = X - X_H = (1 - t_P)T \tag{5.15}$$

will be used to predict t_P. Measured values of thrust T are used as well.

Although both methods have been examined, the last one (5.15) will be preferred because problems occur during the regression analysis (no parameter convergence).

Thrust deduction t_P will be modelled like wake factor $w_{P,Q}$ so that $t_P(\varepsilon^*, \beta_P)$ is a two-dimensional table. ε^* and β_P are defined as in 5.2.2.1. The dependence of thrust deduction on propeller loading for the four quadrants had already been examined in [89] with positive values for t_P for quadrant 1 and for the quadrants corresponding to going astern and negative values or an increase of longitudinal force X_P compared to propeller thrust T for quadrant 2 (stopping from headway).

5.3.2 Positive ship velocity: first and second quadrant of operation

For ship model D and the first quadrant of operation tabular models for $1-t_P$ are calculated according to the various test types with a distinction on Froude number (*model per Froude number*):

❏ For **stationary drift angle tests** (limited to *propeller action without rudder deflection*) a distinction is made between low speed manoeuvring ($F_n = 0.016$) and ordinary speed manoeuvring ($F_n \geq 0.049$, Figure 5.40). Low speed manoeuvring is once again limited to a small range of ε^*, more specifically [1.5deg; 3.5deg]. For this range and straight ahead motion (zero drift angle) thrust deduction $(1-t_P)$ does not change significantly (mean value is 1), while at ε^* around 3.5deg and non-zero drift angle $(1-t_P)$ decreases to a mean value for all tested drift angles of about 0.89. As for the wake factor, some doubt may arise about the accuracy of the results. An increasing propeller thrust at low speed with increasing drift angle $|\beta|$ (wake factor larger than 1) results apparently in a decrease of ratio $(1-t_P)$ for the calculation of the longitudinal force X_P.

For ordinary speed manoeuvring (straight ahead and small drift angles) within a range of ε^* [4.5deg; 25deg], lower values $(1-t_P)$ are found for a straight ahead motion compared to oblique towing, which is in contrast with the observations for low speed. A decreasing propeller loading (increasing ε^*) gives decreasing thrust deduction values from almost 0.95 to about 0.8. For non-zero drift angles higher values are obtained. Thrust deduction values for $(1-t_P)$ greater than 1 can hardly be accepted on a physical base but especially appear at lower propeller loading (ε^* near 25 degrees) which condition is characterised by low measured thrust values and some uncertainty.

Based on these results an important remark can be made. Lower values for $(1-t_P)$ are obtained for low speed and oblique towing compared to ordinary speed while values of thrust coefficient K_T are higher. For ordinary speed higher values for $(1-t_P)$ are measured for oblique towing compared to straight ahead motion while propeller thrust is decreasing with drift angle. This means that as modelled resistance force X_H has been used, modelled thrust deduction (an interaction coefficient) and modelled thrust coefficient compensate each other.

It is not clear if this could be concluded for all ship models. Probably it depends on ship type or even ship geometry.

❑ Calculations made for **multi-modal tests type A** (straight-line tests, *propeller with rudder deflection*) make use of a hull force model for $X'^{(\beta)}(u,0,0)$ which is based on results from stationary straight-line tests depending on Froude number F_n (Table 5.4)

Table 5.4 Model D, model for hull force $X'^{(\beta)}$ for a straight ahead motion depending on Froude number

F_n	0.016	0.032	0.049	0.065	0.077	0.081	0.116	0.122	0.154
$X'^{(\beta)}$	-0.0192	-0.0221	-0.0252	-0.0249	-0.0247	-0.0247	-0.0244	-0.0244	-0.0244

A reduced longitudinal force $X_{reduced}$, together with modelled values of thrust T and measured values of rudder force F_X have been used to calculate the thrust deduction values $(1-t_P)$ for each individual run (ε^* is constant, Figure 5.41). Measured values of F_X are based on rudder forces F_{RT} and F_{RN} (see chapter 6). Values for $(1-t_R)$ are calculated for a table of rudder angles with a step of 5 degrees:

$$X_{reduced} = X - X^{(\beta)}(u,0,0) = (1-t_P)T + (1-t_R)F_X \qquad (5.16)$$

At zero rudder deflection measured values of F_X are small (negative or positive values depending on propeller loading, see chapter 6) and are expected not to influence model values of thrust deduction.

❑ The influence of drift angle is also examined based on **multi-modal tests type B** (*propeller action with rudder deflection*) where drift angle β is kept constant during each individual run. The model for hull force $X'^{(\beta)}$ is based on a combination of stationary and multi-modal tests depending on the drift angle (Table 5.5). Contrary to the evaluation of multi-modal tests of type A no distinction is made according to the Froude number.

Table 5.5 Model D, symmetrical model for hull force $X'^{(\beta)}$ with indication of model test type

β (deg)	$X'^{(\beta)}$	test type
0	-0.02329	stationary test type
2.5	-0.02124	multi-modal type B
5	-0.02113	multi-modal type B
10	-0.01439	multi-modal type B
30	0.00738	multi-modal type B
60	-0.03707	multi-modal type B
90	-0.05363	multi-modal type B
120	-0.02023	multi-modal type B
150	0.00253	multi-modal type B
170	0.03416	stationary test type
175	0.03170	stationary test type
177.5	0.03416	stationary test type
180	0.03313	stationary test type

The same model (5.16) has been used as for multi-modal tests of type A although thrust deduction $(1-t_P)$ is calculated as function of propeller loading coefficient ε^* for each applied Froude number and drift angle (Figure 5.42, Figure 5.43 and Figure 5.44). Although propeller thrust is lower for the increasing phase compared to the decreasing phase thrust deduction factor $(1-t_P)$ is lower than 1 for all Froude numbers, drift angles and propeller loadings while propeller rate is increasing. This is not found for the decreasing phase although propeller thrust is larger than measured values during stationary tests. This conclusion is rather unexpected and it seems that the way of executing tests (e.g. during multi-modal tests of type B) do not only affect the propeller thrust but even the total longitudinal force.

❑ **PMM yaw tests** have not been examined individually but as for the wake factor yaw rate

angle γ is expected no to influence thrust deduction coefficient.

The results of these distinctive captive model tests for thrust deduction t_P can be compared to the values obtained based on a global model where no distinction is made according to the Froude number. The results of stationary tests are for the first and the second quadrant shown in Figure 5.45. Due to the oscillations which have been discussed in 5.1.2 and which even result into fluctuations of the longitudinal force at reversed propeller action and high propeller loading (Figure 5.62), the determination of thrust deduction based on mean values of measured forces could lead to a simplification of the observed phenomena, but will nevertheless be adopted. Values for thrust deduction t_P vary from positive to negative values in quadrant 2.

In Figure 5.46 values for t_P are shown based on a global model for multi-modal tests of type B subdividing into a model for the complete test run, the increasing propeller phase or the decreasing propeller phase. Negative values for t_P based on the decreasing phase correspond to factors (1- t_P) higher than 1 as obtained for the model per Froude number.

Modelled tables for model E are shown in Figure 5.47 for quadrant 1 and Figure 5.48 for quadrant 2 and are based on stationary and multi-modal tests. Except for a straight motion or some large inflow angles thrust deduction t_P is negative for quadrant 1 what can physically not be motivated. For the second quadrant an increasing under keel clearance gives less scatter as can be seen comparing the results at 20% and 50% UKC. Once again it can be concluded that the flow around a ship model is more complex in shallow than in medium deep water and gives rise to physically unexpected phenomena.

5.3.3 Negative ship velocity: third and fourth quadrant of operation

For ship model D going astern and ahead or reversed propeller, modelled values for t_P are represented in Figure 5.49 (quadrant 4) for multi-modal tests of type B and in Figure 5.50 for stationary tests (quadrant 3 and 4). Comparing the different phases of a harmonically changing propeller rate only the increasing phase gives small error bars and positive values for t_P. As for the first quadrant higher values are seen for a straight astern motion (β=180 deg) compared to an oblique motion in Figure 5.49 what could also be concluded for the third quadrant in Figure 5.50.

For model E positive values are found in Figure 5.51 for the third quadrant except for a pure cross flow while for quadrant 4 both positive and negative contributions are shown in Figure 5.52 probably due to the instable flow around the ship's stern.

5.3.4 Model for validation: thrust deduction

The model for thrust deduction for ship model D is based on the global models for the different test types where values are evaluated based on their error bars (significance of modelled values) and the assumption that thrust deduction must be positive except for the second quadrant. Tabular models for the four quadrants of operation are resumed in Figure 5.53 for model D. For ship model E t_P will be restricted for all quadrants within the range [0,1] except for the second quadrant. Selected tabular models are shown in Figure 5.54 for quadrant 1 and 2 and in Figure 5.55 for quadrant 3 and 4.

5.4 Lateral force and yawing moment

5.4.1 Observations

The propulsive power of the engine-propeller combination is not only necessary for the forward or backward motion of the ship but even for the total manoeuvring behaviour as the propeller slipstream also determines the rudder effectiveness. In addition, the propeller does not only influence the longitudinal force and rudder forces but even the lateral force and yawing moment at zero rudder deflection. In deep water and design conditions the effect is limited, but in harbour conditions with four-quadrant manoeuvring the dependence of Y and N on propeller revolutions

n or propeller thrust T can not be neglected. For a ship in oblique motion (influence of drift angle) measured lateral force and yawing moment increase due to a positive propeller action (quadrant 1 and 4, Figure 5.56). Preferably, a distinction will be made between the odd quadrants (quadrant 1 and 3) where the wake flow and the propeller working direction are the same and the even quadrants (quadrant 2 and 4) where wake flow and propeller action are opposite. At some point, e.g. while making figures, this choice will be omitted (see Figure 5.56).

5.4.1.1 Odd quadrants: quadrant 1 and 3

During an oblique motion in shallow water lateral force and yawing moment increase with increasing propeller rate, both for a motion ahead (Figure 5.56, model E) and a motion astern (Figure 5.57, model D). This growth seems to be proportional to the lateral force induced by swaying. The point of application of this additional force can be found while dividing the yawing moment and the lateral force:

$$x'_Y = \frac{N_P}{Y_P L_{PP}}$$

(5.17)

In Figure 5.58 the influence of a positive propeller rate on lateral force and yawing moment is presented for an individual PMM yaw test. According to this test, the propeller asymmetry effect induced by a right-handed single screw propeller near zero yaw rate angle gives a negative lateral force and a positive yawing moment. In general, such an effect is expected during a stopping manoeuvre and it seems that the test parameters during a PMM yaw test also determine the propeller asymmetry effect. While increasing the yaw amplitude (from 15 to 25 deg), the propeller induced yawing moment becomes negative although the errors on lateral force near zero yaw rate angle does not give a clear relationship (Figure 5.59). For a backward motion (quadrant 3, Figure 5.60) the yawing moment induces a positive turn (to starboard) near 180 deg yaw rate angle so that somewhat larger yawing moments are measured during a starboard turn. The point of application of the propeller induced lateral force is now positioned near the ship's bow as lateral force and yawing moment take the same sign. This relationship between yaw rate angle, lateral force and yawing moment corresponds to the global model determined for the velocity dependent hull force and moment in chapter 4.

5.4.1.2 Even quadrants: quadrant 2 and 4

During a stopping manoeuvre from headway in the towing tank (quadrant 2, Figure 5.61) an oscillating flow can be observed which is pronounced at large reversed propeller revolutions (e.g. full harbour astern or -80% of the reference propeller rate) and rather modest at moderate (-50% n_0) revolutions. This oscillating flow can be composed of large eddies which are shed from the stern of the model resulting into slowly fluctuating lateral forces and yawing moments (Figure 5.62). The amplitude of these oscillations for the lateral force may even exceed the steady term and these fluctuations are typical for shallow water conditions (see figure 16 in [84]). An increasing oblique flow reduces the amplitude of the oscillating term (Figure 5.63) as the directions of wake flow and propeller slipstream are no longer parallel which reduces the effect.

During harmonic yawing tests (Figure 5.64, Figure 5.65 and Figure 5.66) the period of oscillations differs from the period of the harmonic yawing motion. A reversed propeller induces a very unstable flow at the aft body with maximum values of lateral force and yawing moment which are 4 to 10 times higher than the values measured without propeller action as can be seen on Figure 5.64 for low speed (F_n=0.016). Seven oscillation cycles have been executed and no clear tendency can be seen depending on the maximum yaw amplitude ψ_A of 15, 25 or 35 degrees which corresponds to maximum yaw rate angles γ_A of respectively 24, 36 and 46 degrees. Due to a constant change of yaw rate angle and consequently a varying flow at the aft body similar effects as at an increasing drift angle during stationary oblique towing tests can not be observed during these test types. The harmonic yawing tests executed at Froude number 0.049 without propeller action are of type PMMPSI2 (see chapter 3) and consists of two test phases (Figure 5.65 and Figure 5.66): phase 1 consists of three oscillation cycles with varying yaw amplitude and phase 2 starts with a decreasing yaw amplitude from maximum to zero

during the first half period and corresponds to a straight motion during the remaining test time (1.5 oscillation cycles).

The yawing tests with reversed propeller action correspond to test type PMMPSI0 with 5 identical oscillation cycles. The relationship between maximum yaw amplitude ψ_A and maximum yaw rate angle γ_A is: for ψ_A values of 15, 25 or 35 degrees the angles γ_A are respectively 16, 26 and 34 degrees. At this ordinary speed and -100% of the reference propeller rate, measured lateral forces are also 4 to 10 times higher than the maximum values measured without propeller action (Figure 5.65). At a propeller rate of -75% which corresponds more or less to a full astern telegraph position (Figure 5.66), the influence is much smaller for both lateral force and yawing moment. Except some disturbances at rather smaller yawing motion (15 degrees), the oscillation period matches the imposed oscillation period of the test run.

According to Harvald (see chapter 2) the conditions are very unstable during a run with a positive propeller rate and a backward velocity or quadrant 4. This phenomenon has been introduced in chapter 2 based on photographs in a deep water condition. A very shallow water condition with ship model U at an UKC of 10% is here shown in Figure 5.67. While the unstable flow in deep water is more or less extended straight behind the ship's stern, in shallow water due to the reduced under keel clearance the unstable flow searches a way out once to the port side and subsequently to the starboard side resulting into positive and negative lateral forces and yawing moments.

Although oscillations in lateral force and yawing moment occur during the complete stationary test run, during a multi-modal test of type B with harmonically varying propeller rate (from zero to a maximum positive value or the increasing phase and back from maximum to zero or the decreasing phase) oscillations in the lateral force stay away as long as the propeller rate is still increasing (Figure 5.68). This unusual phenomenon is not only time dependent for a chosen speed-propeller combination but even depends on the actual and prevailing status of the propeller (increasing, regime or decreasing) which makes it still more complex.

In Figure 5.69 the influence of propeller action during a PMM yawing test and stopping from sternway is probably restricted to an increase depending on the yaw rate angle (or yaw velocity r). Comparing the oscillating lateral force and yawing moment with the time dependence of the course angle ψ a shift of half a period is found. No oscillations have been observed although the measured force and moment are not identical during each harmonic cycle, especially at a propeller rate full ahead.

5.4.2 Modelling of lateral force and yawing moment

Modelling lateral force and yawing moment due to propeller action, the influences must be incorporated of the kinematical parameters u, v and r through for example the drift angle and yaw rate angle and of the propeller loading (intensity of the propeller effect) through the advance angle ε^*. For a straight forward or backward motion the propeller effect on Y and N is limited for the odd quadrants while it is remarkable for the even quadrants due to the occurrence of oscillations together with a mean propeller effect. An oblique or yawing motion influences the propeller effect for both the odd and even quadrants. The amplitude of the oscillations is clearly diminished if the oblique flow is increasing so that the propeller flow and wake flow are more perpendicular to each other. For the influence of a yawing motion the analysis is not always easy as the research can only be based on non-stationary PMM yaw tests.

The mathematical models describing the contributions Y_P and N_P in this section will be based on the models of section 5.1.2 (restricted to the first quadrant) and a model developed for the project Mod582 Nautical Bottom [90] which is partly based on earlier work of the author [84]. According to [90] the following equation is proposed for the lateral force and for four quadrants:

$$Y_P = \frac{n}{n_0}\left(Y_{\dot{v}}^{n}\,\dot{v} + Y_{\dot{r}}^{n}\,\dot{r}\right) +$$

$$[[Y_{PT}(\beta,\varepsilon^*) + Y_{PT}(\gamma,\varepsilon^*)]F_n(K_1) + [Y_{PTA}(\beta,\varepsilon^*,K_2)][\cos(\omega(\beta,\varepsilon^*)t + \phi(\beta,\varepsilon^*))]]T_P(\varepsilon^*) \qquad (5.18)$$

In this equation the following parameters denote:

- ❏ n_0: the reference propeller rate of the propeller ($n_0 = n_{MAX}$, for both model D and model E this propeller rate is 100 rpm at full scale);

- ❏ $Y_{\dot{v}}^{n}$: contribution of the propeller to the added mass due to sway;

- ❏ $Y_{\dot{r}}^{n}$: contribution of the propeller to the acceleration derivative due to yaw;

- ❏ F_n: the Froude number;

- ❏ Y_{PT}: contribution of the propeller to the mean value for the lateral force (index P propeller, index T thrust);

- ❏ Y_{PTA}: contribution of the propeller to the amplitude of the oscillating lateral force (index A amplitude);

- ❏ ω: frequency of the oscillating lateral force;

- ❏ ϕ: phase of the oscillating lateral force;

- ❏ t: timestep (seconds), starting with the moment the propeller direction is changed (transition between quadrant 1 and 2 for a motion ahead and quadrant 3 and 4 for a motion astern)

- ❏ K_1: constant depending on the actual quadrant: the influence of the Froude number F_n is incorporated in the first quadrant ($F_n(K_1=1)=F_n$) while the influence is ignored in the other quadrants ($F_n(K_1\neq 1)=1$);

- ❏ K_2: constant depending on the actual quadrant: $K_2=1$ for quadrants 1 to 3, while K_2 varies between 0 and 1 for quadrant 4 and incorporates the influence of yawing on the oscillations occurring in quadrant 4.

- ❏ $T_P=T$: propeller thrust

The model for the yawing moment is found if letter Y is replaced by N and the complete model is multiplied with the length between perpendiculars L_{PP}. Taking into account the variation of the acceleration derivatives with test frequency, test amplitude and ship velocity discussed in chapter 4 the influence of the propeller on the acceleration derivatives is less important compared to the influences of test parameters. The influence of a yawing motion on the oscillatory component is not clear so that this effect will be neglected. In addition, the propeller thrust T_P is not only a function of the apparent advance angle but also of the inflow angle at the propeller β_P (see section 5.2.2) so that equation (5.18) will be changed to:

$$Y_P = [[Y_{PT}(\beta,\varepsilon^*) + Y_{PT}(\gamma,\varepsilon^*)]F_n(K_1) + [Y_{PTA}(\beta,\varepsilon^*)][\cos(\omega(\beta,\varepsilon^*)t + \phi_Y(\beta,\varepsilon^*))]]T_P(\varepsilon^*,\beta_P) \qquad (5.19)$$

and for the yawing moment:

$$N_P = [[N_{PT}(\beta,\varepsilon^*) + N_{PT}(\gamma,\varepsilon^*)] + [N_{PTA}(\beta,\varepsilon^*)][\cos(\omega(\beta,\varepsilon^*)t + \phi_N(\beta,\varepsilon^*))]]L_{PP}T_P(\varepsilon^*,\beta_P) \qquad (5.20)$$

5.4.2.1 Odd quadrants: quadrant 1 and 3

Stationary tests without rudder deflection and multi-modal tests of type B with and without rudder deflection have been executed with the fully appended ship in the first quadrant of operation. Although the hull-propeller combination is studied in this chapter, the propeller effect on lateral force and yawing moment will be compared for the two test types where the mathematical model is extended with the rudder module for the multi-modal tests with rudder deflection (see chapter 6). Modelling of lateral force and yawing moment during a combination of oblique towing and propeller action (zero rudder deflection) will first of all be based on the models described in section 5.1.2.

These models were extended so that they do not only incorporate the effect of a drift angle or

oblique motion but also of the yaw rate angle or a turning motion.

$$Y_P = \left[Y^{(\beta)}C_n(\beta) + Y^{(\gamma)}C_n(\gamma) \right] \left(\frac{n}{n_0} \right)^2$$

$$N_P = \left[x_Y(\beta)Y^{(\beta)}C_n(\beta) + x_Y(\gamma)Y^{(\gamma)}C_n(\gamma) \right] \left(\frac{n}{n_0} \right)^2 \qquad (5.21)$$

$$= \left[x_Y(\beta)Y^{(\beta)}C_n(\beta) + Y^{(\gamma)}C_n *(\gamma) \right] \left(\frac{n}{n_0} \right)^2$$

Except for the smallest drift angles near zero drift angle the coefficient $C_n(\beta)$ takes a value between 0.5 and 1.0 for low speed manoeuvring (Figure 5.70) and between 0 and 0.5 for ordinary speed manoeuvring (Figure 5.71). These results are obtained by executing calculations according to (5.21) for each Froude number where hull contribution $Y^{(\beta)}$ and propeller contribution $C_n(\beta)$ are determined at the same time. Differences in $C_n(\beta)$ between low and ordinary speed could be explained based on differences in $Y^{(\beta)}$, although lower values for $Y^{(\beta)}$ do not necessarily give higher values for $C_n(\beta)$ as can be concluded based on Figure 5.73. In addition, near zero drift angle the error bars, especially at low speed, are large as the lateral force due to drifting reaches low values. For the multi-modal tests with rudder action (Figure 5.72 and Figure 5.73) differences between these tests and the results of stationary tests without rudder deflection are growing even if the increasing and decreasing phase are separated. Combining the effects of all modules at once (hull, propeller and rudder) during the determination of the mathematical models leads to different model results as some influences will be rearranged between these modules. The same remark will be made for the rudder contribution to the hull forces as hull forces at all drift angles and yaw rate angles are determined with the fully appended ship where the rudder profile represents an additional lifting body compared to the isolated hull.

The same calculations have been made for the non-dimensional application point $x'_Y(\beta)$ of the propeller force Y_P. This application point is situated near midship with a tendency to the aft body of the ship (Figure 5.74 and Figure 5.75). The position varies over a larger range if tests with rudder deflection are considered (Figure 5.76 and Figure 5.77). A conclusion could be while comparing these figures that it is preferable to phase the determination of the different parts of a modular model so that first the hull contribution is modelled followed by the hull-propeller combination and ended with the complete ship model contribution.

Coefficient $C_n(\gamma)$ for the propeller contribution to the lateral force (Figure 5.78) during a pure yaw motion is much larger than coefficient $C_n(\beta)$ which could be understood taking into account the variation of hull force $Y^{(\gamma)}$ with the yaw rate angle for ship model D. According to the results in chapter 4 the velocity dependent lateral force due to yaw tends to zero for yaw rate angles $|\gamma|$ between 20 and 30 degrees. This zero point is first reached for Froude number 0.032 and latest for $F_n = 0.065$ (Figure 4.67). The application point $x'_Y(\gamma)$ is more situated aft compared to $x'_Y(\beta)$ and increases with an increasing absolute value of the yaw rate angle (Figure 5.79).

The discrepancy between Froude numbers for the hull dependent force explains the large difference in $C_n(\gamma)$ for yaw rate angles of 20 to 30 degrees. Therefore, it could be preferred to develop a model for the propeller induced lateral force and yawing moment which do not depend on the hull force and moment. Especially in shallow water, propeller action does not only influence the flow at the ship's stern but forces on the complete hull-propeller combination are modified. A model as was proposed in (5.19) for the lateral force and in (5.20) for the yawing moment will be used. This model has still some disadvantages for propeller induced forces and moments:

❑ As lateral force and yawing moment are not really coupled in these equations, the application point of the propeller induced force could take values which lie beyond the physically

accepted positions of [-0.5L_{PP}; 0.5L_{PP}].

❑ The lateral force Y_P for the first quadrant depends on the Froude number and thus the ship velocity while this dependency has not been considered for the yawing moment. For low speed manoeuvring (or Froude numbers tending to zero), e.g. during acceleration manoeuvres, the application point will instantaneously take extremely high values.

Tabular models for propeller induced lateral force and yawing moment due to sway and yaw are presented in Figure 5.80 for quadrant 1 and in Figure 5.81 for quadrant 3, for which the propeller thrust takes a negative value. For model E at 50% UKC an example is given of the influence of the chosen test type on modelled force and moment in Figure 5.82. Depending on the test type at a straight ahead motion a positive or negative value is modelled so that the propeller asymmetry effect induced by a right-handed propeller is not clearly determined. The results for model E and both water depths are compared in Figure 5.83.

5.4.2.2 Even quadrants: quadrant 2 and 4

Modelling propeller induced lateral force and yawing moment for the second and fourth quadrant depending on drift angle β, is based on a procedure containing two steps:

1. First of all, a regression analysis is performed on measured lateral force and yawing moment during stationary oblique towing tests according to the equations:

$$Y = Y_H + Y_P = Y^{(\beta)} + Y_P = Y^{(\beta)} + Y^{(0)} + Y^{(1)}\cos\left(2\pi\frac{t-t_0}{T_Y} + \phi_Y\right)$$

$$N = N_H + N_P = N^{(\beta)} + N_P = N^{(\beta)} + N^{(0)} + N^{(1)}\cos\left(2\pi\frac{t-t_0}{T_N} + \phi_N\right)$$

(5.22)

The start values for the regression analysis seem to be important and will therefore be based on the results of a pre-process executing a Fourier analysis through a Fourier Fast Transform. This step will be summarized in section 5.4.2.2.1.

2. Secondly, the resultant mean values, amplitudes, periods and phases found for equation (5.22) are examined to detect the influence of drift angle and propeller loading. Therefore, these parameters are represented in a non-dimensional form and evaluated proposing a tabular model of two dimensions, one for the propeller loading and one for the drift angle. This step can be found in section 5.4.2.2.2.

5.4.2.2.1   Regression analysis of measured force and yawing moment

Stationary oblique towing tests with forward speed and reversed propeller rate were performed with ship model D at 20% UKC. The lateral force and yawing moment measured during these tests were approximated according to equation (5.22). The following figures are based on a former calculation where the Fourier analysis and the regression analysis were not performed automatically. The developed models in 5.4.2.2.2 are instead based on the automatic determination of the different parameters giving the oscillatory behaviour of lateral force and yawing moment. This explains small differences that can be found comparing the derived parameters and the resultant tabular models.

Quadrant 2

Hull force and moment $Y^{(\beta)}$ and $N^{(\beta)}$ in equation (5.22) are based on the modelled values (see chapter 4). On Figure 5.84 to Figure 5.86 the periods T'_Y and T'_N are represented in a non-dimensional way, as suggested by Ch'ng in [88]:

$$T'_Y = T_Y \frac{V}{L_{PP}}$$

$$T'_N = T_N \frac{V}{L_{PP}}$$

(5.23)

The non-dimensional period T' equals the distance in ship lengths (L_{PP}) covered in one period. T' is displayed as a function of the apparent advance ratio J' based on the total ship velocity V.

An identical period is expected for the lateral force and the yawing moment as lateral force and yawing moment are linked with each other through the application point of the lateral force. Nevertheless, two distinct values T_Y and T_N are determined during the regression analysis based on (5.22). Comparing for example Figure 5.85 and Figure 5.86 for the tests with one propeller rate per run learns that both periods can be considered to be almost the same so that one model for the period T will be determined.

On Figure 5.84 to Figure 5.86 a distinction is made between:

- test series: series D1 is based on stationary captive model tests with three different propeller rates during one test run (Figure 5.84), while series DA is based on stationary captive model tests with either one propeller rate or three different propeller rates during one test run. The problem with combining three different conditions of reversed propeller during one test run is that the duration of one condition is sometimes too short to determine the period with enough accuracy.

- for test series D1 a ship velocity varying between 1.7 and 12 knots has been applied. A combination of high forward velocity (for example 12 knots) with reversed propeller is unrealistic as ship velocity has to be fallen down before the direction of rotation of a fixed pitch propeller can be changed. Based on this assumption a distinction is made between Froude numbers lower than or equal to 0.049 (5 knots full scale) and Froude numbers higher than or equal to 0.077 (8 knots full scale). This division is only based on the Froude numbers applied during the model tests.

- for test series DA a distinction is made between the test runs with one propeller rate or with three different propeller revolutions during one test run. A comparison of these results tells something about the way these tests have to be executed. The test parameters were nevertheless not the same for both conditions (one rpm value per run or three rpm values per run).

Some tendencies for the non-dimensional period T'_Y and T'_N can be summarized:

- A restriction of the number of combinations of velocity and propeller rate (V,n) during one test run leads to less scatter. This can be clearly seen on Figure 5.85 for T'_Y and Figure 5.86 for T'_N. At an apparent advance ratio J' of approximated -0.35 non-dimensional period T'_N is restricted to values lying between 0.9 and 1.3 ship lengths for all tested drift angles and one propeller rate per run while values for T'_N vary between 0.9 and 3.9 ship lengths for a higher number of sub-runs. A model for the non-dimensional period T' ($T'_Y = T'_N$) as function of the apparent advance ratio J' will be based on Figure 5.85 and Figure 5.86 for the test runs with only one combination (V,n).

- The scatter on modelled period is also higher if high forward velocities are combined with a reversed propeller compared to lower forward velocities (Figure 5.84).

- During a straight ahead motion (drift angle $\beta=0$ deg) non-dimensional period T' increases or circular frequency ω decreases with decreasing advance ratio J'. For a ship velocity of for example 4 knots full scale, period T' is larger at a propeller rate corresponding to full astern compared to dead slow astern. This can also be observed on Figure 5.62 where period T_Y is

lower at a propeller rate of -33% of the reference propeller rate n_0 compared to a propeller rate of almost -97%. At full scale, periods vary from about 35 seconds (relatively high speed, for example 6.7 knots, low rpm) to about 9 minutes (low speed, high rpm).

❑ The influence of the drift angle on non-dimensional period T' is not clear (Figure 5.63). Depending on the drift angle and the advance ratio J' lower or higher values can be found. Consequently, this influence could be ignored or could be of minor importance as period and amplitude of an oscillating term are linked to each other.

A suitable way of displaying $Y^{(0)}$, $Y^{(1)}$, $N^{(0)}$ and $N^{(1)}$ is obvious to find. Following representation appeared to yield acceptable results [84]:

❑ The lateral force components are referred to the (negative) propeller thrust ($Y^{(0)}/T=Y_{PT}$, $Y^{(1)}/T=Y_{PTA}$) and displayed as functions of the apparent advance angle ϵ^* (equation (5.11)).
❑ The yawing moment components are divided by the respective lateral force components in order to obtain the location of the application points:

$$x'_Y\left(i\right) = \frac{N^{(i)}}{Y^{(i)}L_{PP}} \quad \left(i = 0,1\right) \tag{5.24}$$

According to equation (5.22) two distinguished values are determined for the phase angles ϕ_Y and ϕ_N. Although the phase shift between these two values usually approximates 180 deg, two application points $x_Y'(1)$ are determined corresponding to the cosine component and the sine component of harmonic lateral force and yawing moment:

$$Y^{(1)}\cos\left(\omega\left(t-t_0\right)+\phi_Y\right) = Y^{(1)}\cos\phi_Y\,\cos\omega\left(t-t_0\right) - Y^{(1)}\sin\phi_Y\,\sin\omega\left(t-t_0\right)$$

$$N^{(1)}\cos\left(\omega\left(t-t_0\right)+\phi_N\right) = N^{(1)}\cos\phi_N\,\cos\omega\left(t-t_0\right) - N^{(1)}\sin\phi_N\,\sin\omega\left(t-t_0\right) \tag{5.25}$$

$$x'_{YCOS}\left(1\right) = \frac{N^{(1)}\cos\phi_N}{Y^{(1)}L_{PP}\cos\phi_Y}$$

$$x'_{YSIN}\left(1\right) = \frac{N^{(1)}\sin\phi_N}{Y^{(1)}L_{PP}\sin\phi_Y} \tag{5.26}$$

The steady component $Y^{(0)}$ is shown on Figure 5.87 and Figure 5.88. This propeller induced lateral force $Y^{(0)}$ is expected to be negative ($Y^{(0)}/T$ is positive for the second quadrant) and to create a positive turning moment (to starboard).

❑ For a straight ahead motion (drift angle $\beta=0$ deg) the apparent advance angle ϵ^* can be considered to influence the steady component so that at bollard pull condition ($\epsilon^*=180$ deg) $Y^{(0)}$ is negligible while values up to one time the propeller thrust can be found for ϵ^* within the range [171 deg; 177 deg] (Figure 5.88). At decreasing advance angle (increasing velocity, decreasing rpm) values are getting smaller to half the propeller thrust at $\epsilon^*=167$ deg and almost zero from a value of $\epsilon^*=157$ deg (Figure 5.87).
❑ The influence of the drift angle is not clear. This can be caused by a mean model for hull force $Y^{(\beta)}$ for all velocities and the influence of this predicted value on the steady component. Nevertheless, as a general rule lower ratios $Y^{(0)}/T$ could be expected with increasing (absolute) drift angle if the propeller is reversed at moderate ship velocities.
❑ The influence of the yaw rate angle (see section 5.4.1.2) on the mean value $Y^{(0)}$ is not clear at all. The execution of stationary rotating arm tests could be proposed but in the meantime the influence of yawing on $Y^{(0)}$ will be neglected.

The oscillatory component $Y^{(1)}/T=Y_{PTA}$ is shown on Figure 5.89 and Figure 5.90. Comparable tendencies can be seen as for the steady component. The left figure of Figure 5.90 will be used as basis.

- ❏ For the ship running straight ahead (drift angle β=0 deg) a maximum value for the oscillatory component of 2.75 times the propeller thrust (with change of sign, negative propeller thrust, positive component $Y^{(1)}$) is expected within the range ε* [171 deg; 174 deg]. At lower values (increasing velocity and decreasing rpm) or higher values up to bollard pull (ε*=180 deg) ratio $Y^{(1)}/T$ in absolute value decreases to negligible influences which means that no oscillations will be observed. Taking a look at Figure 5.89 (series D1, F_n values of 0.016 and 0.049) even higher values to 4 times the propeller thrust (ε*=175 deg, F_n=0.016) are modelled which could be explained due to a low forward speed compared to Figure 5.90 where the minimum speed corresponds to F_n=0.032. A distinction between low and ordinary speed manoeuvring could also be useful.
- ❏ Tests executed at a non-zero drift angle give a lower (absolute) ratio $Y^{(1)}/T$. This is also observed on Figure 5.89. At a drift angle of 40 to 50 degrees the oscillatory component is diminished to about -0.5 times the propeller thrust (which is negative).

Even during PMM yawing tests oscillations are observed with a period which differ from the test period of the harmonic yaw motion. This contribution to the oscillatory component is nevertheless restricted for common propeller rates for the reversed propeller. Therefore, Y_{PTA} will not depend on yaw rate angle.

The point of application of the lateral force components $Y^{(0)}$ and $Y^{(1)}$ is expected to be located at the aft body as it is caused by propeller action.

Non-dimensional position $x'_Y(0)$ of the steady component is shown on Figure 5.91 and Figure 5.92. Values must be restricted between –0.5 and 0.5 times the ship length as the application point has to be on the ship. Large scatter occurs on all figures except the left figure of Figure 5.92 where one value of the propeller rate of turn is applied during each test run:

- ❏ the application point $x'_Y(0)$ during a straight ahead motion is situated amidships within the range ε* [176 deg; 180 deg] (see also Figure 5.91) and increases to a value of -0.4L_{PP} at an advance angle of 173 deg. Within the range [155 deg; 173 deg] $x'_Y(0)$ varies between -0.5 and -0.2L_{PP}.
- ❏ during an oblique motion and low forward speeds ($F_n \leq 0.032$) $x'_Y(0)$ is located more fore or aft the position at β=0 depending on the drift angle. At higher velocities ($F_n \geq 0.049$) position $x'_Y(0)$ is shifting towards the fore body.

The sine or cosine components of the non-dimensional position $x'_Y(1)$ of the oscillatory component are shown on Figure 5.93 and Figure 5.94. The scatter on these modelled positions is large so that a clear relationship between the apparent advance angle and the positions $x'_{YCOS}(1)$ and $x'_{YSIN}(1)$ can not be found.

The analysis of test results in shallow water reveal that lateral forces and yawing moments due to reversed propeller rate cannot be simulated in an adequate way by means of a steady term which only depends on the propeller rpm or the propeller thrust:

- ❏ even if only average values are taken into account, the latter cannot be expressed as a constant fraction of propeller thrust;
- ❏ the fluctuating component and the steady term are of comparable importance.

The question arises whether these phenomena also occur at full scale. The data published by Ch'ng & Renilson indicate that, to some extent, scale effects are not of major importance, as the scale of the ship models used for the investigation described in [88] differs from the scale used in [91] (L=1.75 m). However, this preliminary conclusion should be confirmed by observations at larger or full scale.

In addition, the non-stationary flow phenomena occur especially at low speed and higher reversed propeller rates, conditions which are typical for harbour manoeuvres where tug assistance could also take an important role.

Quadrant 4

An identical analysis is used for the lateral force and the yawing moment measured during model tests executed in quadrant 4 (Figure 5.95) as for tests executed in quadrant 2. Figures are made for model D at 20% UKC according to the test results of series D1 and series DA:

❑ test series: series D1 is based on stationary captive model tests with three different propeller revolutions during one test run, while series DA is based on stationary captive model tests with either one propeller rate (most of the executed tests) or two propeller rates per run.

❑ for test series D1 ship velocity corresponds to -1.7 knots full scale (F_n=-0.016) while for test series DA two backward velocities have been used: -1.7 and -3.4 knots full scale (F_n=-0.016 and -0.032).

Periods T'_Y and T'_N in Figure 5.96 and Figure 5.97 are calculated based on:

$$T'_Y = T_Y \frac{|V|}{L_{PP}}$$

$$T'_N = T_N \frac{|V|}{L_{PP}}$$

(5.27)

with V the total ship velocity. In Figure 5.96 only two propeller loading conditions are presented, while in Figure 5.97, thanks to the combination of periods T'_Y and T'_N, a relationship between propeller loading, drift angle and these periods can be recognized and corresponds more or less to the observations for the period of oscillation in the second quadrant. There are some outstanding values but generally during a straight astern motion the period increases with decreasing advance ratio $|J'|$. As the inflow angle into the propeller increases (or decreasing $|\beta|$), the period of the oscillations increases with no clear relationship with propeller loading if the flow tends to a cross flow ($|\beta| \rightarrow$ 90deg).

Modelled values for the steady component $Y^{(0)}/T$ (Figure 5.98) could be compared to modelled values based on equation

$$Y_P = Y^{(\beta)} C_n (\beta) \left(\frac{n}{n_0} \right)^2$$

(5.28)

where this model has been used to calculate the influence of a positive propeller rate during oblique towing at forward and backward velocity. The absolute value of the steady component is increasing with the (absolute value of the) drift angle or with an increasing inflow angle compared to a straight astern motion. This means that for a straight astern motion (β=-180 deg) the steady component is almost zero while for increasing drift angle (for example series DA and 110 deg drift angle) the ratio increases to values of two times the propeller thrust for the steady component. Additionally, an influence of the propeller loading could be recognized.

On Figure 5.99 the oscillatory component $Y^{(1)}/T$ for series D1 decreases with decreasing (absolute value of the) drift angle compared to the straight astern motion (drift angles near 180 deg have a ratio Y_{PTA} of 0.8 while for drift angles $|\beta|$ near 130 deg Y_{PTA} is 0.25). This is not so clear for series DA. There could also be a dependence of the propeller loading through the apparent advance angle although inaccuracies could occur for the ratio at lower propeller loading due to the division by the propeller thrust. In addition, for series DA problems have been recognized with the measurements of propeller thrust T.

The maximum oscillatory component for quadrant 4 is much smaller than for quadrant 2 and for PMM yawing tests executed with a higher yaw amplitude no oscillations have been observed (see section 5.4.1.2). Instead, the steady component in quadrant 4 will be influenced by the yaw rate angle.

For the non-dimensional position $x'_Y(0)$ of the steady component (Figure 5.101) especially positive values are found for series D1. Rather high positive values are found for a motion nearby the straight astern motion. Nevertheless the steady component at these angles is small so that the yawing moment is also negligible. For drift angles in the range [130 deg; 160 deg] the position is nearby the middle of the ship. For series DA mainly negative values are found.

A distinction is made between positions $x'_{YCOS}(1)$ (Figure 5.102) and $x'_{YSIN}(1)$ (Figure 5.103) for the application point of the oscillatory component. For drift angles nearby the straight astern motion the application point is located nearby the aft perpendicular while the position is moving to the middle and the fore body for drift angles around a pure lateral motion.

For model E the availability of test results was smaller than for model D. Furthermore, at 50% UKC only test runs with three sub-runs were executed. Although these non-stationary phenomena disappear with increasing UKC, the scatter on results at 50% UKC is large. Results for model E in shallow water are presented in Figure 5.104 to Figure 5.107 for the second quadrant and Figure 5.108 to Figure 5.111 for the fourth quadrant.

5.4.2.2.2   Modelling of derived parameters

Two-dimensional tables have been determined for the following parameters determining propeller induced lateral force and yawing moment based on equations (5.19) and (5.20):

❑   the non-dimensional period T' for quadrant 2 and quadrant 4 (Figure 5.112);
❑   the steady components Y_{PT} and N_{PT} for quadrant 2 (Figure 5.113) and quadrant 4 (Figure 5.114);
❑   the oscillatory components Y_{PTA} and N_{PTA} for quadrant 2 (Figure 5.115) and quadrant 4 (Figure 5.116);

These figures for model D are mainly based on the test runs of series DA with one propeller rate/velocity combination per run. The two-dimensional tables are derived while calculating mean values per selected drift angle/advance angle combination.

The tabular models for model E will not be shown. For the shallow water condition these tables correspond to the values shown in Figure 5.104 to Figure 5.111 while for medium deep water the applicability of the derived parameters is questioned due to the combination of three sub-runs per test run.

6 Modelling of rudder forces and moments

A mathematical model for the prediction of rudder forces will be developed for the four quadrants of operation. First of all, measured longitudinal and lateral rudder forces F_X and F_Y will be observed during captive model tests and their dependence on ship speed, propeller loading and inflow angle to the rudder will be mapped out in section 6.1.1. The offset rudder angle δ_0, which is a result of the asymmetry induced by the propeller, is modelled in section 6.1.2 according to the MMG model. The axial momentum theory for an actuator disc will be used for the prediction of the propeller contribution. Three models making use of this philosophy are summarized and evaluated in 6.1.3. In the following sections a rudder model will be developed considering first of all a straight-line motion (section 6.1.4) followed by the incorporation of lateral velocity component v and turning rate r in 6.1.5. At least a model will be chosen that treats the contribution of the wake flow (wake factors $w_{R,X}$ and $w_{R,Y}$) and the propeller race (coefficients $K_{m,X}$ and $K_{m,Y}$) in a separate way. Resultant tabular models are presented in 6.1.6.

Rudder forces F_X and F_Y induce force and moment contributions on the fully appended ship's hull that are modelled through correlation parameters: the deduction parameter t_R for the longitudinal force X_R (section 6.2.1), the hull coefficient a_H for the lateral force Y_R (section 6.2.2) and the non-dimensional application point x'_H for the yawing moment N_R (section 6.2.3).

6.1 A four-quadrant model for rudder forces F_X and F_Y

Although the tangential rudder force F_{RT}, parallel to the rudder chord, is often neglected in favour of the normal rudder force F_{RN} for modelling rudder forces F_X and F_Y in a ship fixed axis system, the latter are here defined as:

$$F_X = F_{RT}\cos\delta_R - F_{RN}\sin\delta_R$$
$$F_Y = F_{RT}\sin\delta_R + F_{RN}\cos\delta_R$$

(6.1)

The influence of ship motion, propeller rate and rudder deflection on these forces will be examined in section 6.1.1.

Rudder forces F_X and F_Y will be modelled based on the open water characteristics $C_{FT}(\alpha_R)$ and $C_{FN}(\alpha_R)$, made symmetrical and anti-symmetrical, respectively, as shown in Figure 6.1 for the rudder profile of model D and Figure 6.2 for model E:

$$F_X = \frac{\rho}{2}A_R V_R^2 \{C_{FT}(\alpha_R)\cos\delta_R - C_{FN}(\alpha_R)\sin\delta_R\}$$
$$F_Y = \frac{\rho}{2}A_R V_R^2 \{C_{FT}(\alpha_R)\sin\delta_R + C_{FN}(\alpha_R)\cos\delta_R\}$$

(6.2)

A_R is the rudder area and V_R the inflow velocity at the position of the rudder. For a specific hull-propeller-rudder combination this velocity depends on:
❑ ship motion characterized by the velocity components u, v and r;
❑ propeller loading (propeller thrust coefficient K_T and propeller rate n);
❑ geometry of the hull-propeller-rudder combination such as the area affected by the propeller slipstream compared to the rudder area (often presented by the ratio η of the propeller diameter D_P to the rudder height H_R) or the distance between the propeller and the rudder.

The inflow velocity V_R at the rudder position is composed of the longitudinal component u_R, especially affected by the propeller slipstream and discussed in detail during a straight motion (section 6.1.4), and the lateral component v_R, function of the lateral velocity component v and the yaw velocity r (section 6.1.5).

The open water characteristic for the normal force coefficient C_{FN} for the rudders of models D and E are quite different. For model D stall occurs at an inflow angle near ±15 deg while for the rudder of model E stall is only reached near 30 deg. As the maximum rudder angle for all ship

types equipped with a normal rudder is generally 35 deg, stall could probably be observed during the execution of captive model tests taking into account the small stall angle for model D during a motion ahead.

6.1.1 Observations during captive model tests

Similar test types as used for the determination of propeller thrust can be executed to measure rudder forces in four quadrants of operation where the influence of Froude number (longitudinal and lateral velocity), yaw velocity, propeller rate (or loading) and rudder deflection will be examined:

❑ During a *stationary test* run, Froude number, propeller rate and rudder angle are kept constant so that discrete values are measured for tangential and normal rudder forces $F_{RT}(F_n,n,\delta_R)$ and $F_{RN}(F_n,n,\delta_R)$ in a rudder fixed axis system. Oblique motions can be applied by imposing a drift angle β. According to the ship model's velocity, the propeller rate is varied below and above the model self propulsion point to cover a wide range of operation conditions.

❑ During a *multi-modal test* two test types are considered: a run with constant propeller rate and harmonically varying rudder angle (test type A) or a run with harmonically varying propeller rate and rudder angle (test type B).

❑ During a *PMM yaw test* with propeller action Froude number, propeller rate and rudder angle are kept constant while the influence of yaw rate angle and possibly drift angle on rudder forces is measured.

Due to inaccuracies during stationary and some PMM yaw tests, measurements of tangential force F_{RT} on ship model D are doubtful. These less reliable measurements affect the longitudinal rudder force F_X especially at low rudder angles ($F_{RT}\cos\delta_R$). Although F_X is expected to represent an additional resistance force during a motion ahead, a decrease of resistance due to rudder action may be observed. The influence of inaccuracies are rather small for the lateral rudder force F_Y but the effect also depends on the propeller loading as lower values F_{RN} are measured at low propeller thrust loading.

6.1.1.1 First quadrant of operation: going ahead

❑ **Straight ahead motion**
Due to the inaccuracies for component F_{RT}, longitudinal rudder force F_X and lateral rudder force F_Y derived from stationary tests are defined as:

$$F_X = -F_{RN}\sin\delta_R$$
$$F_Y = F_{RN}\cos\delta_R$$

(6.3)

For model D, these forces are displayed in Figure 6.3 based on three propeller thrust loading conditions:

1. *No propeller action*: the propeller has been stopped (in contrast with a free wheeling propeller, with nevertheless comparable results) and rudder forces result from the forward motion of the ship. This can be compared to a free-stream situation where the propeller-rudder system is placed in the wake induced by the hull. Contrary to the straight ahead motion of the ship model, the inflow angle at the rudder position is non-zero for higher Froude numbers as the lateral force F_Y only becomes zero for small positive rudder angles. A rudder angle to port is necessary to counteract the small forces induced by the wake.

2. *Moderate propeller thrust loading*: propeller rate equals 50% of the reference propeller rate (100 rpm full scale). Stall is not obtained although rudder lift force F_Y stagnates for positive rudder angles of 30 and 40 degrees. An increase of the lift curve slope at small rudder angle with increasing propeller thrust loading is clearly seen for each Froude number. Propeller action straightens the flow at the stern compared to the free stream condition so that only a small offset rudder angle is needed.

3. *High propeller thrust loading*: propeller rate equals 100% of the reference propeller rate. Remarks made for the occurrence of stall and the lift curve slope are similar to those for

a moderate propeller thrust loading. Stall will probably only appear at higher Froude numbers. At higher ship velocity ($F_n \geq 0.077$) a small negative rudder angle (to starboard) eliminates the rudder action. The offset rudder angle δ_0 changes sign.

These measurements can be compared to rudder forces F_X and F_Y based on equation (6.1) and derived from multi-modal straight-line tests with constant propeller rate and harmonically varying rudder angle (type A). Equation (6.1) has been used as both rudder force components F_{RT} and F_{RN} are expected to be reliable for these tests in contrast with the stationary rudder angle tests. Rudder angle δ_R is oscillating during several consecutive cycles which number depends on the ship velocity and the useful tank length. Small differences between the various cycles can be observed.

Multi-modal straight ahead tests for ship model D have been executed in two test series at different points in time: first, series with Froude numbers: F_n=0.016, 0.032, 0.049, 0.065, 0.081 and secondly, series with Froude numbers: F_n=0.077, 0.122, 0.154. A small difference between these two series is clearly seen for the longitudinal rudder force F_X at small rudder angles and Froude numbers F_n=0.077 and 0.081 in the free-stream condition behind the ship's hull (Figure 6.4). An increase of ship velocity or Froude number F_n results in an increase of the absolute value of the tangential force F_{RT} and, consequently, the longitudinal rudder force F_X. Nevertheless, this growth does not match for the two test series and although differences are small, discrepancies in measurements must be avoided for low speed manoeuvring.

The longitudinal and lateral rudder forces F_X and F_Y are shown on Figure 6.4 and Figure 6.5, respectively, for the same propeller revolutions as for the stationary tests. Some remarkable features can be summarised:

1. Rudder force F_X measured during multi-modal tests type A is based on tangential and normal rudder force. The incorporation of tangential force F_{RT} gives cause for additional resistance forces measured at the rudder if the propeller is stopped. At high propeller loading nevertheless, the resistance force turns into a positive contribution at small rudder angles. This physically unrealistic phenomenon was investigated during bollard pull tests (zero speed) where flows at the aft ship are visualised making use of fibres attached to the rudder profile or of a coloured liquid. The flow at the rudder is clearly not turning 180 deg near zero rudder angle and, therefore, a reason can hardly be found. No pressure measurements have been executed over the rudder profile although these could probably give more insight into the variation of rudder forces over the rudder height.

2. All captive model tests are executed with the fully appended ship model (hull, propeller and rudder). The longitudinal rudder force measured during these tests, is in general already included in the total hull resistance (longitudinal force X_H). Consequently, modelling of longitudinal rudder force F_X based on equations (6.1) or (6.3) will be compensated using different values for the hull-rudder interaction coefficient t_R.

3. Independent of the calculation formula, (6.1) or (6.3), rudder forces F_X and F_Y are not symmetric for port and starboard rudder angles. A small asymmetry is probably caused by the propeller rotational direction of a single screw ship. Flow asymmetries induced by the ship's hull are physically not expected as the hull is symmetrical along the longitudinal axis.

4. As was notified by Molland in [42] stall occurs later if the free-stream velocity decreases. In addition, the absolute value of the stall angle for a specific propeller-rudder combination increases with increasing propulsion loading. Stationary tests are executed with a maximum Froude number of 0.116 while multi-modal tests of type A go up to F_n=0.154. At Froude numbers 0.122 and 0.154 (Figure 6.5) fluctuations in measured lift force F_Y occur probably caused by the occurrence of stall. In addition, due to the harmonic character of these rudder angle tests no regime is established in the flow around the rudder resulting in unstable force measurements which even depend on the propulsion loading and the direction and the magnitude of the rudder deflection.

□ *Ship motion affected by swaying and yawing*

Stationary oblique towing tests with ship model D are executed at two distinct drift angles, namely $\beta=-5$ deg and $\beta=+5$ deg. A negative drift angle produces a flow approaching the ship's stern from the starboard side. Rudder resistance F_X is in general augmented for starboard rudder angle ($\delta_R<0$) compared to the straight ahead run (Figure 6.6). Lateral rudder force F_Y requires a higher rudder angle to port to stabilise the additional flow at the stern (Figure 6.7). Based on measured lateral rudder forces shown on Figure 6.7 for zero propeller action a shift with almost 5 degrees appears compared to straight ahead motion (Figure 6.3). The opposite is occurring for positive drift angles as the flow is coming in from the port side of the ship. Flow straightening at both positive and negative drift angles is especially observed at small rudder angles but depends clearly on propeller loading and ship velocity.

A drift angle influences the occurrence of stall. The lift force F_Y stagnates at maximum Froude number 0.116 and higher rudder deflections. In addition, an increase of propulsion thrust loading from 50% to 100% delays the occurrence of stall. This phenomenon is even more noticeable for a positive drift angle ($\beta=5$deg) and rudder deflections to starboard.

Longitudinal and lateral rudder forces F_X and F_Y measured during PMM yaw tests with or without drift angle are mean values derived from a Fourier analysis of forces F_{RT} and F_{RN} (6.1). The test parameters are shown in Table 6.1: non-dimensional frequency and yaw amplitude are kept constant for all Froude numbers, ship velocity is varied between low ($F_n=0.032$) to ordinary ($F_n=0.065$) speed and propeller loading changes from stopped to overload condition.

Table 6.1 Test parameters during PMM yaw tests with ship model D

	F_n	n (% n_0)	β (deg)	ω'	ψ_A (deg)
Figure 6.8	0.032	100	0	2.25	25
Figure 6.9	0.049	50, 100	0	2.25	25
Figure 6.10	0.049	50	±2.5	2.25	25
Figure 6.11	0.065	0, 75, 100	0	2.25	25

Rudder forces F_X and F_Y are shown as a function of rudder angle for different yaw rate angles γ. This yaw rate angle corresponds to the inflow angle at the rudder position due to turning (or yaw velocity r) and can be compared to the drift angle during oblique towing tests. Zero yaw rate angle stands for instantly straight ahead motion (if β is zero) and in general measured rudder forces at this angle do not differ from forces measured during multi-modal straight ahead tests (type A).

Following remarks can be made for the longitudinal rudder force F_X:

1. Similar to stationary and multi-modal tests a positive contribution is seen at higher propeller loading and small rudder angles (e.g. Figure 6.8).
2. Influences of turning direction and rudder deflection are coupled. For a rudder deflection to port a positive turning motion increases the rudder resistance force while turning to the port side is accompanied with a decrease in the absolute value of F_X as the inflow to the rudder is hindered because of the turning motion. For a negative rudder angle the effects are opposite.
3. The overall influence of ship velocity is an increase of resistance force F_X with increasing Froude number.
4. The effect of propeller thrust loading is more important than the effect of ship velocity as the propeller slipstream is stronger than the stern wake (for these rather low velocities corresponding to 3.4, 5.1 and 6.7 knots full scale).
5. A stopped propeller gives very low measured forces although a clear tendency can be observed in this free-stream condition behind the ship's hull (Figure 6.11). There is almost no influence of turning rate for a turning motion to port and a rudder deflection to port as the flow into the rudder is blocked due to the turning motion. Similar observations

132

are made for a turning motion to starboard and a negative rudder angle. The opposite turning direction compared to rudder deflection shows a significant influence of yaw velocity.

6. Figure 6.10 reveals the influence of a combination of swaying and yawing. For a test run with F_n=0.049 and a propeller rate of 50% of the reference value, the drift angle β is nevertheless small (absolute value of 2.5 degrees) and a considerable change in measured F_X values is not observed.

The rudder lift force F_Y induces a yawing motion that, for its part, affects the measured lift force:

1. The yaw motion influences the rudder force F_Y especially at small rudder angles ($|\delta_R|$<20 degrees). A positive turning sense causes an increase of the rudder force F_Y as a flow coming from port side into the rudder, even at zero rudder deflection, creates a positive lateral force on the rudder profile.

2. For almost all tested Froude numbers and propeller rates the influence of the yaw rate angle at hard over port rudder is much smaller than for hard over starboard rudder. An explanation can probably be found in the turning direction effect of a single screw on the rudder.

3. As the yaw rate angle increases both for port and starboard turning, the effect of rudder deflection diminishes or stall is reached at lower rudder deflections if rudder angle and yaw rate angle have the same sign. For a range of a rudder angle between 10 and 40 degrees, Figure 6.9 hardly shows any influence on measured lateral force for yaw rate angles γ higher than 7 degrees.

4. Depending on the sign of yaw rate angle and drift angle compared to each other, the measured lateral rudder force will increase or decrease. If the sign is equal, the magnitude of the rudder force F_Y increases while for opposite signs $|F_Y|$ decreases (less positive or less negative, Figure 6.10).

5. Modifications of the flow pattern at the stern during oblique towing or turning can be compared. Evaluations are based on Figure 6.12 for a propeller rate of 100% and on Figure 6.13 for a moderate propeller rate (50% n_0). Lateral rudder forces agree qualitatively although quantitatively small differences can be interpreted as resulting from the typical (stationary or harmonic) character of the executed captive model tests. In addition, different expressions have been used to calculate rudder force F_Y based on stationary tests (only rudder normal force F_{RN}) and PMM yaw tests (rudder forces F_{RT} and F_{RN}).

Multi-modal tests of type B (harmonically varying rudder angle and propeller rate) are executed with a constant Froude number and drift angle from straight ahead to pure swaying (β=90deg). Measurements are not shown here due to a wide variation of rudder angle and propeller loading both with different test periods and will be discussed in the modelling phase.

6.1.1.2 Second quadrant of operation: stopping from headway

Rudder action during stopping from headway is influenced by the two opposite flows generated by the ship motion ahead and the reversed propeller. Depending on the strength of each flow the contribution of the wake or of the propeller slipstream will dominate. Besides this, measured longitudinal and lateral rudder forces are small.

❑ *Straight ahead motion*

Results of stationary tests based on equation (6.3) are shown in Figure 6.14 and results of multi-modal tests type A in Figure 6.15. Varying Froude numbers with varying propeller rates reveal a rather dominating wake at -35%n_0, while only the highest Froude number (F_n=0.116) still generates a resistance force F_X on the rudder at -50%n_0. At -100%n_0 (or -100 rpm full scale, a reversed propeller rate which is in practice not reached with existing containerships) the resistance force F_X during normal propeller operation, turns into a positive flow for all Froude numbers (Figure 6.14, left). The lateral rudder force in this condition is affected by unstable phenomena for a rudder angle to port (positive δ_R, fluctuating forces) while for

negative rudder angles the combination high speed-high propeller rate gives an increasing force F_Y with rudder angle. The combination $F_n=0.116$ and $n/n_0=-100\%$ will not appear during real manoeuvres, so that based on these measured forces the contribution of a rudder in the second quadrant during a straight ahead motion is negligible.

Non-conventional multi-modal tests with harmonically varying rudder angle during one test run show no clear tendency between measured rudder forces and imposed rudder angles. In Figure 6.15 rudder forces measured during individual test runs are replaced by tabular models with a step of 10 deg rudder angle using a regression analysis. Even at high astern propeller rate no tendency as for stationary tests can be observed for any of the rudder force components. Probably, the unstable fluctuating flow around the aft body, imposed by the reversed propeller, is interfering with the flow at the rudder, characterized by the harmonically varying rudder angle.

❑ **Ship motion affected by swaying and yawing**
During stationary oblique towing tests the drift angle is limited to only small values so that the effect of an oblique flow can not be fully evaluated (Figure 6.16). For a small ahead speed ($F_n=0.016$) only extreme reversed propeller ($-100\%n_0$) gives some what higher values for measured rudder forces.

High turning rates are obtained during PMM yawing tests and the effect of the strength of wake (depending on Froude number) compared to a propeller slipstream at $-100\%n_0$ is shown on Figure 6.17. At low forward speed (top) the slipstream dominates while at $F_n=0.049$ both flows result into measured forces around zero.

Comparing the influence of speed and turning rate combined with realistic values for the astern propeller rate, rudder forces induced during the second quadrant of operation could be considered to be small and will therefore not be modelled in a rudder model for four quadrants.

6.1.1.3 Third quadrant of operation: going astern

Compared to the second quadrant, the third quadrant of operation is smooth and less complicated. It is characterized by more or less stable flows from the motion astern of the ship and the reversed propeller. Both flows act in the same sense, although the rudder profile will not create large rudder forces due to the weak backward motion and the reversed propeller slipstream which is turned to the aft body of the ship, away from the rudder.

❑ **Straight astern motion**
The results of stationary tests (series DA with ship model D, based on equation (6.1)) can be compared with those of non-conventional multi-modal tests type A. The astern speed is still restricted to rather small values (-3.3 knots full scale). Some differences can be seen between Figure 6.18 and Figure 6.19. Positive and negative rudder angles do not always give symmetrical (force F_X) or anti-symmetrical (force F_Y) values. At a rudder angle around zero and $F_n=-0.032$ the longitudinal rudder force is even negative at low propeller rates astern although a positive force is expected. This is not in accordance with the unexpected phenomenon for quadrant 1 in Figure 6.4 where positive values near zero δ_R are only measured for F_X at high propeller rates. For the non-conventional rudder tests forces differ for positive and negative rudder angles at low astern speed ($F_n=-0.016$), although at higher speed ($F_n=-0.032$) values are rather (anti-)symmetrical. Stall is not observed.

❑ **Ship motion affected by swaying and yawing**
An influence of ship velocity is found in Figure 6.20, although at positive drift angle and 40 degrees rudder (to port) or negative drift angle and -40 degrees rudder (to starboard) the influence diminishes. The effect of a drift angle or a yaw rate angle can be compared (Figure 6.21 for oblique towing and Figure 6.22 and Figure 6.23 for PMM yawing tests). A positive drift angle ($\beta<180$ deg) or a positive yaw rate angle ($\gamma<180$ deg) give an increase of the lateral rudder force F_Y for all rudder angles compared to a straight astern motion. The flow is

coming into the rudder from the port side of the ship inducing an increase in measured force F_Y. For negative drift angle or yaw rate angle (>180 deg) the opposite is found.

6.1.1.4 Fourth quadrant of operation: stopping from sternway

The fourth quadrant of operation is, just as the second quadrant, more complex although the positive flow of the propeller slipstream over the rudder generates a more pronounced rudder effect. Examining the hull-propeller combination in chapter 5 the unsteady phenomena caused by the two opposite flows from the motion astern and the propeller will influence measured rudder forces.

❏ *Straight astern motion*

Only non-conventional multi-modal tests of type A are available for model D. The strength of the two opposite flows is determined by the ship speed for the astern wake and propeller revolutions for the slipstream. In Figure 6.24 it can be clearly seen how these two contributions relate one to another. For the longitudinal rudder force F_X positive and negative rudder angles give more or less symmetrical values for low astern speed, while at higher speed F_n=-0.032 the resistance force is more pronounced at rudder to port. This can probably be explained based on the unsteady flow at the aft body with eddies more concentrated at the starboard side of the ship. Just as for the first quadrant of operation, near zero rudder angle the force F_X changes from a negligible value to a force acting forward with increasing propeller rate. For the stronger astern wake at F_n=-0.032 a lateral force F_Y is only generated if the propeller ahead range is sufficiently large (n/n$_0$≥75% or 75 rpm full scale). In addition, stall can be notified especially for rudder angle to starboard at -30 degrees.

❏ *Ship motion affected by swaying and yawing*

The occurrence of stall is also pronounced during PMM yawing tests (Figure 6.25 and Figure 6.26). At F_n=-0.016 and maximum propulsion ahead (100%n$_0$) lateral force F_Y decreases from an angle of -20 degrees during a turning motion to port, while longitudinal force F_X is almost zero. For rudder angles to port this is not found. At larger backward speed stall even occurs at a rudder angle to port for a strong turning motion to starboard.

Stall especially occurred in the first quadrant while swaying and yawing (or with increasing speed). This effect must also be taken into account for a stopping manoeuvre from sternway.

6.1.2 Modelling of the offset rudder angle δ_0

δ_0 is the offset rudder angle for a straight ahead motion which is incorporated in the equation for the inflow angle α_R into the rudder:

$$\alpha_R = \delta_R + \delta_0 + \beta_R \tag{6.4}$$

where β_R=0 for a straight motion (v=r=0). The offset rudder angle δ_0 is mostly considered in literature as a function of the propeller slipstream s (see chapter 2, MMG model):

$$s = 1 - \frac{u_P}{nP} = 1 - \frac{(1-w_P)u}{nP} \tag{6.5}$$

Table 6.2 Model D and model E, tabular models for offset rudder angle δ_0

Model D		Model E at 50% UKC		Model E at 20% UKC	
Slipstream s	Rudder angle δ_0 (deg)	Slipstream s	Rudder angle δ_0 (deg)	Slipstream s	Rudder angle δ_0 (deg)
0	0.28	0	-0.77	0	-1.62
0.7	0.28	0.96	-0.77	0.83	-1.62
0.8	0.07	0.998	-0.08	1.0	0.45
0.9	-0.14	1.0	0.11	1.1	0.91
1.0	-0.36	1.1	-0.50	1.19	1.95
1.2	6.41	1.2	-0.58	1.2	1.93

The determination of this angle can be based on stationary or multi-modal tests of type A, but for

both ship models D and E, no clear relationship between slipstream s and offset rudder angle can be derived, resulting in a tabular model with rather arbitrary elements although they are based on a linear regression analysis (Table 6.2). No values are available for slipstream ratios lower than 0.7 for model D and lower than 0.83 for model E at 20% UKC (0.96 for model E at 50% UKC) so that the value for this slipstream is extended to s=0. To incorporate a stopping manoeuvre from sternway (fourth quadrant with u<0 and n>0) the slip ratio is extended to values greater than 1.

6.1.3 Selected models for the inflow velocity at the rudder

Modelling the rudder effect on a manoeuvring ship the contribution of the wake at the rudder position, given by the wake factor w_R, and the contribution of the propeller slipstream, given by the velocity u_{RP}, are of utmost importance together with the flow-straightening effect of hull-propeller-rudder combination while turning and swaying. The proposed model of the MMG-group is limited to the first quadrant of operation while the HSVA model is extended to four quadrants. Mod582 model is derived from the MMG model and extended to four quadrants, but differs from it in some features. These three models make use of the axial momentum theory for an actuator disc to express the speed in the propeller slipstream (Figure 6.27) and will be evaluated in this section.

6.1.3.1 MMG model

According to the MMG-group the effective rudder inflow velocity u_R can be expressed by a simple weighted average depending on the two flow areas:

$$u_R = \sqrt{\eta u_{RP}^2 + (1-\eta)u_{R0}^2}$$
(6.6)

with η the propeller diameter to rudder height ratio. Equation (6.6) equals:

$$u_R = \zeta u_P \sqrt{\eta \left\{1 + k\left(\sqrt{1 + \frac{8K_T}{\pi J^2}} - 1\right)\right\}^2 + (1-\eta)}$$
(6.7)

with k given by:

$$k = \frac{K_m}{\zeta} \quad \text{and} \quad \zeta = \frac{1 - w_{R0}}{1 - w_{P0}}$$
(6.8)

with ζ the ratio of resulting wake factor at the rudder $1-w_{R0}$ to wake factor at the propeller $1-w_{P0}$ during a straight motion. According to the MMG-group, ζ and K_m (or k) are experimental coefficients where for example in [47] the K_m value can be estimated as approximated 0.6 for the Esso Osaka model in deep water. If the coefficients ζ and k are determined experimentally such as on figure 3.9 in [47] which is based on equation (6.7), values reveal for ζ of 1.718, for k of 0.264 so that K_m will be 0.45. These estimations are based on measurements on a 2.5 m model of the Esso Osaka. Although K_m is expected to lie between 0.5 (position of the propeller) and 1.0 (far away from the propeller, see Table 6.6) according to other authors, experimentally determined values using the MMG modelling technique can differ from these physically expected values.

The flow at the rudder of single-screw ships is characterized by an asymmetry due to the propeller action even in a straight ahead motion. Consequently the rudder normal force F_{RN} is non-zero for a rudder in the neutral position. An offset rudder angle δ_0 is necessary to counteract the asymmetrical flow at the rudder which induces a lateral velocity component:

$$v_R = \delta_0 u_R = k_P s u_R$$
(6.9)

The coefficient k_P will be experimentally determined. Due to swaying and yawing, the lateral component of the effective inflow velocity at the rudder is increased by:

$$v_R = k_P s u_R + g(v', r')$$
(6.10)

6.1.3.2 HSVA model

For a rudder outside the propeller slipstream the interaction between hull and rudder is represented by the wake factor at the position of the rudder w_R and the flow rectification factor k_{HR}. The longitudinal and transverse flow velocity components into the rudder are:

$$u_R = (1 - w_R)u$$
$$v_R = k_{HR}(v + rx_R)$$
(6.11)

The flow rectification factor k_{HR} based on expression (6.11) is only function of the hull-rudder combination and is not influenced by the propeller slipstream.

The inflow velocity into a rudder, placed in the propeller slipstream, u_{RP} is increased compared to velocity u_R and a model can be based on the elementary momentum theory. The axial velocity increment in the slipstream at infinity is:

$$u_{A\infty} = (\text{sgn}\,u)\sqrt{u_P^2 + (\text{sgn}\,u)\frac{2T}{\rho A_0}} - u_P$$
(6.12)

with $\dfrac{2T}{\rho A_0} = \dfrac{8K_T}{\pi \dfrac{1}{n^2 D_P^2}} = u_P^2 \dfrac{8K_T}{\pi J^2}$
(6.13)

The axial velocity at the position of the rudder becomes:

$$
\begin{aligned}
u_{RP} &= u_P + \left[\left(k_{PR} - \frac{1}{2}\right)(\text{sgn}\,u) + \frac{1}{2}\right]u_{A\infty} \\[2mm]
&= u_P + \left[\left(k_{PR} - \frac{1}{2}\right)(\text{sgn}\,u) + \frac{1}{2}\right]\left[(\text{sgn}\,u)\sqrt{u_P^2\left(1 + (\text{sgn}\,u)\frac{8K_T}{\pi J^2}\right)} - u_P\right]
\end{aligned}
$$
(6.14)

The coefficient k_{PR} has the same meaning as coefficient K_m in (6.8) and depends on the relative distance between the propeller and the rudder. K_m takes a value within the range [0.5, 1] according to [13]. Using equation (6.14) the axial velocity u_{RP} can be calculated for each quadrant where a practical estimation of this inflow is made based on the open water curve K_T for model D (Figure 6.28).

The use of sgn(u) under the root sign gives no practical values in quadrants 2 and 4 and is rather unusual as ratio $8K_T/\pi J^2$ is function of the propeller loading while the introduction of sgn() is based on the ship velocity (Table 6.3).

Table 6.3 A four-quadrant model for velocity u_{RP} according to the HSVA model

Quadrant 1 $u \geq 0,\ n \geq 0$	$u_{RP} = u_P + [K_m]\left[\sqrt{u_P^2\left(1 + \frac{8K_T}{\pi J^2}\right)} - u_P\right]$ $= u_P + K_m u_P\left(\sqrt{1 + \frac{8K_T}{\pi J^2}} - 1\right)$ where $\sqrt{1 + \frac{8K_T}{\pi J^2}}$ is definite for model D based on Figure 6.28
Quadrant 2 $u > 0,\ n < 0$	$u_{RP} = u_P + K_m u_P\left(\sqrt{1 + \frac{8K_T}{\pi J^2}} - 1\right)$ where $\sqrt{1 + \frac{8K_T}{\pi J^2}}$ is indefinite for model D based on Figure 6.28

Quadrant 3 $u \leq 0, n \leq 0$	$u_{RP} = u_P + [1 - K_m]\left[-\sqrt{u_P{}^2\left(1 - \dfrac{8K_T}{\pi J^2}\right)} - u_P\right]$ $= u_P - (1 - K_m)\left[\sqrt{u_P{}^2\left(1 - \dfrac{8K_T}{\pi J^2}\right)} + u_P\right]$ where $\sqrt{1 - \dfrac{8K_T}{\pi J^2}}$ is definite for model D based on Figure 6.28
Quadrant 4 $u < 0, n > 0$	$u_{RP} = u_P - (1 - K_m)\left[\sqrt{u_P{}^2\left(1 - \dfrac{8K_T}{\pi J^2}\right)} + u_P\right]$ where $\sqrt{1 - \dfrac{8K_T}{\pi J^2}}$ is indefinite for model D based on Figure 6.28

The rudder area A_{RP} influenced by the velocity u_{RP} can be estimated based on the diameter of the propeller slipstream D_{RP} at the position of the rudder given by the condition of continuity [13]:

$$D_{RP}^2 u_{RP} = D_P^2\left(u_P + \frac{1}{2}u_{A\infty}\right) \tag{6.15}$$

Considering a rudder partially immersed in the slipstream the average axial velocity can be defined by:

$$\overline{u}_R^2 = \frac{1}{A_R}\left[A_{RP}u_{RP}^2 + (A_R - A_{RP})u_{R0}^2\right] \tag{6.16}$$

6.1.3.3 Mod582 model

During the study of the concept Nautical Bottom for the Port of Zeebrugge, [90] and [92], a model was adopted for the longitudinal inflow velocity u_R at the rudder position which was based on an extension of the MMG model to four quadrants.

first quadrant of operation

$$u_R = \frac{1 - w_{R0}}{1 - w_P}\sqrt{\left[\eta[(1-k)\sin\varepsilon + k\sqrt{(C_T + \sin^2\varepsilon)}]^2 + (1-\eta)\sin^2\varepsilon\right]\left[((1-w_p)u)^2 + (0.7\pi nD_P)^2\right]} \tag{6.17}$$

or

$$u_R = \frac{1 - w_{R0}}{1 - w_P}u_P\sqrt{\eta\left\{1 + K_m\left(\sqrt{1 + \frac{8K_T}{\pi J^2}} - 1\right)\right\}^2 + (1-\eta)} \tag{6.18}$$

with the thrust coefficient C_T in open water:

$$C_T(\varepsilon) = \frac{T}{\dfrac{\rho}{2}A_0\left(u_P^2 + c_p^2\right)} \tag{6.19}$$

and the advance angle

$$\varepsilon = \text{Arctan}\left(\frac{u_P}{c_P}\right) \tag{6.20}$$

- A_0 : the area of the propeller disk;
- u_P : the inflow velocity at the propeller;
- c_P : $0.7\pi nD_P$;
- k is considered to be equal to K_m although k should correspond to equation (6.8) and depend on the wake factors w_P and w_R. The Mod582 model differs therefore from the MMG model.

138

Equation (6.18) for the first quadrant of operation was earlier examined by the author and reported in [93] and [94].

second quadrant of operation

$$u_R = \xi n + (1 - w_R) u \tag{6.21}$$

third quadrant of operation

$$u_R = \xi n + u \tag{6.22}$$

fourth quadrant of operation

$$u_R = (1 - w_R) \sqrt{\left[\eta \left[(1-k)\sin\varepsilon \right| - k\sqrt{(C_T + \sin^2\varepsilon)} \right]^2 - (1-\eta)\sin^2\varepsilon \right] \left[u^2 + (0.7\pi n D_P)^2 \right]} \tag{6.23}$$

or

$$u_R = |u_{R0}| \sqrt{\eta \left[1 - K_m \left(\sqrt{1 + \frac{8K_T}{\pi J^2}} + 1 \right) \right]^2 - (1 - \eta)} \tag{6.24}$$

This model is based on the following expressions and assumptions:

❑ The velocity due to the propeller slipstream u_{RP} can be written as:

$$
\begin{aligned}
u_{RP} &= u_{R0} + K_m u_\infty \\
&= u_{R0} + K_m u_P \left(-\sqrt{1 + \frac{8K_T}{\pi J^2}} - 1 \right) \\
&= u_{R0} - K_m u_P \left(\sqrt{1 + \frac{8K_T}{\pi J^2}} + 1 \right) \\
&= u_{R0} - K_m \left(-\sqrt{u_P^2 \left(1 + \frac{8K_T}{\pi J^2} \right)} + u_P \right) \\
&= u_{R0} + K_m \left(\sqrt{u_P^2 \left(1 + \frac{8K_T}{\pi J^2} \right)} - u_P \right) \\
&= u_{R0} + K_m \left(\sqrt{u_P^2 + \frac{8K_T n^2 D_P^2}{\pi}} - u_P \right)
\end{aligned}
\tag{6.25}
$$

For a bollard pull condition (no ship motion or u=0) velocity u_{RP} in (6.25) reduces to:

$$u_{RP} = K_m \sqrt{\frac{8K_T n^2 D_P^2}{\pi}}$$

which is positive (for a positive K_m value) and which corresponds to a positive propeller rate.

At stopped propeller (n=0) and backward velocity (transition between quadrant 3 and 4) according to equation (6.25) the velocity induced by the propeller slipstream does not equal the velocity u_{R0}:

$$
\begin{aligned}
u_{RP} &= u_{R0} + K_m \left(\sqrt{u_P^2 + \frac{8K_T n^2 D_P^2}{\pi}} - u_P \right) \\
&= u_{R0} + K_m \left(\sqrt{u_P^2} - u_P \right) \\
&= u_{R0} + K_m \left(|u_P| + |u_P| \right) \\
&= u_{R0} + 2K_m |u_P|
\end{aligned}
$$

Based on equation (6.25) a discontinuity between quadrants 3 and 4 cannot be avoided, but a discontinuity was overcome saying that equation (6.25) can only be used for full scale propeller rates larger than 11.5 rpm (full scale). Another formula will be introduced to cover the transition between positive and negative propeller revolutions.

❑ In addition, a mean inflow velocity u_R written as:

$$u_R = \sqrt{\eta u_{RP}^2 + (1-\eta)u_{R0}|u_{R0}|} = \sqrt{\eta u_{RP}^2 - (1-\eta)u_{R0}^2} \qquad (6.26)$$

is based on the assumption that u_{R0} is negative (which explains the absolute value) but does not take into account the possibility of inducing a negative velocity u_{RP} (for low propeller revolutions n).

Equation (6.26) becomes:

$$u_R = \sqrt{\eta\left[u_{R0} - K_m u_P\left(\sqrt{1+\frac{8K_T}{\pi J^2}}+1\right)\right]^2 - (1-\eta)u_{R0}^2} \qquad (6.27)$$

The final equation (6.24) uses the assumption that the wake factor w_P is zero (could indeed be adopted for quadrant 4, see chapter 5) and that u_P equals u_{R0} (or consequently u_{R0} equals u so that the wake factor w_R must also be zero contrary to the non-zero values determined based on a regression analysis).

In conclusion equations (6.23) and (6.24) are based on some not straightforward assumptions and do not avoid the appearance of discontinuities during a real-time simulation unless some tricks are used.

The lateral velocity component of inflow velocity at the rudder v_R is defined as in (6.11). Wake factors $w_{R,X}$ (based on the rudder force F_X) and $w_{R,Y}$ (based on the rudder force F_Y) are considered to be function of the rudder angle δ_R and the angles β and γ while the flow-straightening coefficient k_{HR} equals 1 in all conditions.

6.1.4 Modelling of straight motion: influence of velocity u and propeller loading

6.1.4.1 The inflow velocity at the rudder u_R

Modelling of the inflow velocity at the rudder due to the propeller slipstream u_{RP}

The equation for the inflow velocity at the rudder due to the propeller slipstream u_{RP} defined in Table 6.3 can only be used in the first and the third quadrant. A definition based on sgn(u) is rather strange if the axial velocity increment in the slipstream at infinity is related to the propeller working direction (ahead or reversed). A new concept is proposed using sgn(n) for the coefficient k_{PR} and sgn(K_T) for the propeller thrust coefficient K_T (to avoid indefinite values at the root sign). Sgn(u) will be used in relation with the velocity component u_P.

$$u_{RP} = u_P + (sgn\,n)\left[\left(k_{PR} - \frac{1}{2}\right)(sgn\,n) + \frac{1}{2}\right]\left[\sqrt{u_P^2\left(1+(sgn\,K_T)\frac{8K_T}{\pi J^2}\right)} - (sgn\,u)u_P\right] \qquad (6.28)$$

Sgn(K_T) has to be used instead of sgn(n) for the fraction $8K_T/\pi J^2$ as problems arise for the third quadrant at very low propeller rates. Using sgn(K_T) or sgn(n) give only small differences in all quadrants at low propeller loading. The equation for the first quadrant (sgn n and sgn u are positive) only changes at very low propeller rates where K_T becomes negative.

Table 6.4 A modified four-quadrant model for velocity u_{RP}

Quadrant 1 $u \geq 0, n \geq 0$	$u_{RP} = u_P + K_m \left[\sqrt{u_P^2 \left(1 + (sgn K_T) \dfrac{8K_T}{\pi J^2} \right)} - u_P \right]$
Quadrant 2 $u \geq 0, n < 0$	$u_{RP} = u_P - (1 - K_m) u_P \left(\sqrt{1 + (sgn K_T) \dfrac{8K_T}{\pi J^2}} - 1 \right)$
Quadrant 3 $u \leq 0, n \leq 0$	$u_{RP} = u_P - (1 - K_m) \left[\sqrt{u_P^2 \left(1 + (sgn K_T) \dfrac{8K_T}{\pi J^2} \right)} + u_P \right]$
Quadrant 4 $u \leq 0, n > 0$	$u_{RP} = u_P + K_m \left[\sqrt{u_P^2 \left(1 + (sgn K_T) \dfrac{8K_T}{\pi J^2} \right)} + u_P \right]$

A theoretical calculation is executed for this inflow velocity at different propeller rates using the open water curve $K_T(J)$ for ship model D:

○ $|n|$ = 25 rpm, Dead Slow Ahead or astern;
○ $|n|$ = 35 rpm, Slow Ahead or astern;
○ $|n|$ = 50 rpm, Half Ahead or astern;
○ $|n|$ = 65 rpm, Harbour Full Ahead or astern.

If the propeller rate is known, the inflow velocity at the propeller u_P can be calculated based on J for a straight forward or backward motion: $u_P = J n D_P$. In Figure 6.29 K_m equals 0.85 (an arbitrary value), while the propeller diameter D_P is 8.145m. Some practical calculations can be made for ship model D:

first quadrant of operation

$$u_{RP} = u_P + K_m \left(\sqrt{u_P^2 + (sgn K_T) \frac{8K_T n^2 D_P^2}{\pi}} - u_P \right)$$

For J → ∞ (propeller stopped, n = 0), $u_{RP} = u_P$

Nevertheless, at stopped propeller the inflow velocity at the rudder u_{R0} is expected over the total rudder height and this can not be obtained with the proposed equation. The equation from the MMG model could be used $u_{RP} = u_{R0} + \Delta u_S$ instead of $u_{RP} = u_P + \Delta u_S$.

For J → 0 (bollard pull, u = 0 or very low speed) u_P → 0 or $u_{RP} = K_m \left(\sqrt{(sgn K_T) \frac{8K_T n^2 D_P^2}{\pi}} \right)$

In the range [0; 0.5] the inflow velocity does not change remarkably at a constant propeller rate. An explanation can be found in the expression $u_{RP} = u_P + \Delta u_S$ where the inflow velocity u_P increases with u while the increment Δu_S decreases proportionally so that u_{RP} only changes slightly. The increment Δu_S decreases as the thrust coefficient K_T decreases with increasing J.

third quadrant of operation

$$u_{RP} = u_P - (1 - K_m) \left[\sqrt{u_P^2 + (sgn K_T) \frac{8K_T n^2 D_P^2}{\pi}} + u_P \right]$$

For J → -∞ (propeller stopped, n = 0), $u_{RP} = u_P$ (or a negative velocity). The same remark could be made as for the first quadrant of operation.

For J → 0 (bollard pull, u = 0) u_P → 0 or $u_{RP} = -(1-K_m)\left(\sqrt{(sgn K_T)\dfrac{8K_T n^2 D_P^2}{\pi}}\right)$ (or a negative

inflow velocity thanks to the propeller action)

fourth quadrant of operation

$$u_{RP} = u_P + K_m\left(\sqrt{u_P^2 + (sgn K_T)\dfrac{8K_T n^2 D_P^2}{\pi}} + u_P\right)$$

For J → -∞ (propeller stopped, n = 0) (...), $u_{RP} = u_P$ (see third quadrant)

For J → 0 (bollard pull, u = 0) u_P → 0 or $u_{RP} = K_m\left(\sqrt{(sgn K_T)\dfrac{8K_T n^2 D_P^2}{\pi}}\right)$ (or a positive inflow

velocity thanks to the propeller action)

Some doubts may arise about the use of coefficient K_m for the propeller ahead and $(1-K_m)$ for the reversed propeller. According to the MMG report this coefficient is determined experimentally.

Calculation of the rudder area A_{RP} influenced by the propeller slipstream

The rudder area A_{RP} influenced by the velocity u_{RP} can be estimated based on the diameter of the propeller slipstream D_{RP} at the position of the rudder given by the condition of continuity [13]:

$$D_{RP}^2 u_{RP} = D_P^2\left(u_P + \dfrac{1}{2} u_{A\infty}\right) \tag{6.29}$$

Ratio D_{RP}/D_P can be estimated based on the propeller open water characteristics of model D:

$$\left(\dfrac{D_{RP}}{D_P}\right)^2 = \dfrac{\left(u_P + \dfrac{1}{2} u_{A\infty}\right)}{u_{RP}} \tag{6.30}$$

Numerator and denominator in (6.30) change proportionally with the propeller rate so that isolines will be calculated based on arbitrary values for K_m, depending on the distance between the propeller and the rudder (Figure 6.30).

For a bollard pull condition (transition between quadrant 1 and 4 for positive propeller rate or quadrant 2 and 3 for negative propeller rate) u_P is zero so that:

$$\left(\dfrac{D_{RP}}{D_P}\right) = \dfrac{1}{\sqrt{2K_m}} \text{ for n>0}$$

$$\left(\dfrac{D_{RP}}{D_P}\right) = \dfrac{1}{\sqrt{2(1-K_m)}} \text{ for n<0}$$

Table 6.5 Estimated values for ratio D_{RP}/D_P at bollard pull condition

	n>0	n<0
K_m	D_{RP}/D_P	D_{RP}/D_P
0.5	1	1
0.65	0.88	1.20
0.75	0.82	1.41
0.85	0.77	1.50
0.95	0.73	1.50

As K_m usually takes values between 0.5 and 1, the expected ratio D_{RP}/D_P can be calculated for bollard pull condition (Table 6.5) with positive or negative propeller revolutions. For the reversed propeller ratios D_{RP}/D_P must be restricted to the rudder height to propeller diameter ratio (for model D, $H_R/D_P = 1.5 = 1/\eta$).

Calculation of the mean inflow velocity at the rudder

According to the MMG model the effective rudder inflow velocity u_R can be expressed by a simple weighted average depending on the two flow areas [47]:

$$u_R = \sqrt{\eta u_{RP}^2 + (1-\eta)u_{R0}^2}$$
(6.31)

As u_{RP} and u_{R0} are expected to have positive values in the *first quadrant* of operation the mean velocity u_R will also be positive. Equation (6.31) can nevertheless not be used for the other quadrants.

Quadrant 2 will not be considered as rudder forces and the mean rudder inflow velocity can be neglected in the normal working condition during a stopping manoeuvre (the ship velocity must be low enough to reverse the propeller).

For *quadrant 3* inflow velocities u_{RP} and u_{R0} are expected to be negative (backward motion and reversed propeller) so that the mean inflow velocity could be calculated as:

$$u_R = -\sqrt{\eta u_{RP}^2 + (1-\eta)u_{R0}^2}$$
(6.32)

If the calculation of u_{RP} will be based on $u_{RP} = u_{R0} + \Delta u_S$ equation (6.32) gives the following values for u_R in some special occasions:

- For $J \to -\infty$ (propeller stopped, n = 0), $u_R = -|u_{R0}|$ (or a negative velocity)

- For $J \to 0$ (bollard pull, u = 0), $u_R = -\sqrt{\eta u_{RP}^2} = -\sqrt{\eta(1-K_m)^2\left(\sqrt{(sgnK_T)\dfrac{8K_T n^2 D_P^2}{\pi}}\right)^2}$

For *quadrant 4* (ship going astern and propeller ahead) the apparent advance coefficient J' for a large backward velocity and a small propeller rate (e.g. corresponding to dead slow ahead) gives a kind of outstanding value for interpolations to determine the rudder effect. For a backward velocity of -5 knots and a propeller rate of 25 rpm the apparent advance coefficient J' is -0.76 for a propeller diameter of 8.145 m. For model D the inflow velocity at the rudder due to the propeller slipstream u_{RP} is estimated to be -0.08 m/s for J = (1-w_P)J' = J' = -0.76 so that although the propeller is working ahead a negative velocity is found. As velocities u_{RP} can be positive and negative in quadrant 4, a distinction has to be made while calculating a mean value for the rudder induced velocity u_R. Nevertheless, in a wide range of practical values for the (apparent) advance coefficient velocity u_{RP} will be positive while u_{R0} is negative.

For a four-quadrant model of the mean inflow velocity proposed by the MMG-group a distinction must be made:

- If $\eta u_{RP}^2 \geq (1-\eta)u_{R0}^2$ then

$$u_R = sgn(u_{RP})\sqrt{\eta u_{RP}^2 - sgn(u_{RP})(1-\eta)u_{R0}^2}$$
(6.33)

The contribution of the propeller with the effect coefficient η is estimated to be larger then the contribution of the backward velocity u_{R0}. The sign of the inflow velocity u_{RP} must be taken into account, as no negative values can be combined with a root sign. If u_{RP} is positive, the contribution of the propeller will determine the sign of the inflow into the rudder. If u_{RP} is negative, a negative mean inflow velocity will be calculated.

❑ If $\eta u_{RP}^2 < (1-\eta)u_{R0}^2$ then

$$u_R = -\sqrt{\left| sgn(u_{RP})\eta u_{RP}^2 - (1-\eta)u_{R0}^2 \right|}$$ (6.34)

If the calculation of u_{RP} will be based on $u_{RP} = u_{R0} + \Delta u_S$ equations (6.33) and (6.34) give the following values for u_R in some special occasions:

❑ For $J \to -\infty$ (propeller stopped, n = 0), $u_{RP} = u_{R0}$ so that $\eta u_{RP}^2 \geq (1-\eta)u_{R0}^2$ for η=0.66 and $u_R = -|u_{R0}|$ (or a negative velocity)

❑ For $J \to 0$ (bollard pull, u = 0), $u_R = \sqrt{\eta u_{RP}^2} = \sqrt{\eta K_m^2 \left(\sqrt{(sgnK_T)\dfrac{8K_T n^2 D_P^2}{\pi}} \right)^2}$

6.1.4.2 Evaluation based on forces F_X and F_Y measured for model D

For model D the influence of ship velocity and propeller loading during a straight motion can best be examined based on multi-model tests of type A because velocity and propeller revolutions are varied over a wide range for four quadrants of operation. Wake factor w_R will be determined for each individual test run where the influence of rudder angle δ_R will be expressed using a tabular model. The variation of the wake factor with rudder angle could be motivated based on the effective aspect ratio of the rudder which changes due to a modification of the rudder angle. For model D the gap between the hull surface and the rudder top in neutral position is small but will increase with increasing rudder angle to port or starboard. With no gap the effective aspect ratio is twice the geometric aspect ratio.

In addition, a difference will be made on the wake factor determined based on the longitudinal force F_X (namely, $w_{R,X}$) and based on the lateral force F_Y ($w_{R,Y}$), so that these two independent parameter values for the wake factor can accurately describe the dependencies in the two directions.

❑ *First quadrant of operation*
Calculations are made based on:

$$u_R = \zeta_{X,Y} u_P \sqrt{\eta \left\{ 1+k\left(\sqrt{1+(sgnK_T)\dfrac{8K_T}{\pi J^2}} -1 \right) \right\}^2 + (1-\eta)}$$

with k=K_m according to Mod582 model and $k = \dfrac{K_m}{\zeta_{X,Y}}$ according to the MMG model.

Ratio $\zeta_{X,Y}$ (or ε in chapter 2) was introduced to express the difference in wake factor at the rudder during a straight forward motion, w_{R0}, and the wake factor at the propeller, w_{P0}, due to the interactions between hull, propeller and rudder. As wake factor w generally decreases with increasing distance to the aft body, ratio $\zeta_{X,Y}$ could be expected to be greater than 1 (w_{R0} is smaller than w_{P0}).

The difference between these two assumptions for the unknown parameter k is that for k=K_m the velocity induced by the propeller is based on the inflow velocity at the rudder u_{R0}:

$$u_{A\infty} = u_{R0}\left(\sqrt{1+(sgnK_T)\dfrac{8K_T}{\pi J^2}} -1 \right) = \zeta_{X,Y} u_P \left(\sqrt{1+(sgnK_T)\dfrac{8K_T}{\pi J^2}} -1 \right)$$ (6.35)

while for $k = \dfrac{K_m}{\zeta_{X,Y}}$ the velocity $u_{A\infty}$ is based on the inflow velocity into the propeller u_P:

$$u_{A\infty} = u_P\left(\sqrt{1+(sgnK_T)\dfrac{8K_T}{\pi J^2}} -1 \right)$$ (6.36)

Equation (6.36) is preferred on a physical base as the inflow velocity into the propeller is not expected to equal the inflow velocity at the rudder.

Calculations were first of all made for an estimated value for K_m of 0.94 for model D, which is much larger than the experimental determined values for the Esso Osaka according to the MMG-group. This value for K_m was based on Table 6.6 where a relationship is given between the distance between the rudder and the propeller (x_{RP}) and coefficient K_m.

Table 6.6 Relationship between distance x_{RP} and coefficient K_m [95]

x_{RP}/D_P	0.00	0.25	0.50	0.75	1.00
K_m	0.50	0.79	0.88	0.94	0.96

For model D the distance between the propeller and the rudder is estimated to be 75% of the propeller diameter. For model E the distance is 25% of the propeller diameter or K_m is 0.79.

Results for ratio ζ_X and ζ_Y according to (6.35) are given in Figure 6.31, while results according to (6.36) are shown in Figure 6.32 where the influence of K_m is examined and is clearly notified (K_m=0.94, figures on the left and K_m=0.80, figures on the right). Calculated values of ratio $\zeta_{X,Y}$ lower than 1 give an apparent coefficient K'_m ($= \zeta K_m$) in equation (6.35) which is lower than K_m so that if K_m would be determined experimentally in equation (6.36) K_m should be lower than 0.94 (for example 0.80).

Low and negative values for $\zeta_{X,Y}$ (or values w_R>1) are found for low speed manoeuvring (low values for advance angle ε^*) or low rudder angles $|\delta_R|$ (<20 degrees). These values can not be motivated physically but they indicate that the contribution of the propeller slipstream is overestimated compared to the contribution of the wake flow. Values for $\zeta_{X,Y}$ greater than 1 appear only at higher advance angles (ordinary speed manoeuvring) and higher rudder angles which give a pronounced rudder effect.

A discontinuity can be determined in calculated ratios $\zeta_{X,Y}$ at an apparent advance angle of 4 degrees (Figure 6.32). At low speed manoeuvring (and bollard pull condition) the contribution of the propeller is probably overestimated so that (1-w_R) becomes negative using equation (6.36):

$$u_R = \sqrt{ \eta \left[(1-w_R)u + K_m \left(\sqrt{u_P^2 + (\text{sgn} K_T)\frac{8K_T n^2 D_P^2}{\pi}} - u_P \right) \right]^2 + (1-\eta)(1-w_R)^2 u^2 }$$

Values for ε^* lower than 4 are obtained during bollard pull tests and multi-modal tests with combinations of velocity and propeller rate as shown in Table 6.7.

Table 6.7 Model D, combinations of speed and propeller revolutions with low advance angles ε^*

Name	Model scale		Full scale		
	n (rpm)	u (m/s)	n (rpm)	u (knots)	ε^* (deg)
D1MA02	433.0	0.1	50	1.68	3.3
D1MA03	649.5	0.1	75	1.68	2.2
D1MA04	866.0	0.1	100	1.68	1.7
D1MA05	1056.6	0.1	122	1.68	1.4
D1MB04	866.0	0.2	100	3.37	3.3
D1MB05	1056.6	0.2	122	3.37	2.7

A lower value for K_m (0.80 instead of 0.94) gives a smaller discontinuity between ratios $\zeta_{X,Y}$ calculated above and below an advance angle of 4 degrees. The estimated value for K_m has clearly an important influence on modelled wake factors w_R.

Comparing results of equations (6.35) and (6.36), parameter ζK_m for the contribution of the propeller in (6.35) offers the advantage that additional parameters (like rudder angle) are used during the regression analysis. Equation (6.36) which is more based on a physical background, could therefore be improved if coefficient K_m should be determined experimentally and depends on parameters like rudder angle and apparent advance angle ε^* (difference between low and ordinary speed manoeuvring).

❑ *Third quadrant of operation*
Model (6.22) for u_R proposed in [90] was used to evaluate measured rudder forces F_X and F_Y during straight-line multi-modal tests. Only constant ξ has to be determined. The inflow velocity is expected to be a linear function of the propeller rate n. Wake factor (1- w_R) equals 1 so that at the transition from quadrant 3 to 4 (zero propeller rate) the model for (1- w_R) is expected to be 1 for quadrant 4 at an advance angle ε^* of -90 deg.

For model D different values for ξ have been determined based on F_X and F_Y for multi-modal straight-line tests of type A. The results are shown in Table 6.8.

Table 6.8 Model D, results for ξ according to equation (6.22)

	for F_X		for F_Y	
	Value	Error	Value	Error
ξ	1.15E-02	1.02E-04	1.42E-02	1.49E-04
SD ERROR on total result		5.27E-02		1.00E-01

Based on the model for the third quadrant proposed in 6.1.4.1 a tabular model is determined for the wake factor (1-w_R) as function of the rudder angle. The coefficient (1-K_m) is experimentally determined during the regression analysis.

Table 6.9 Model D, results for wake factor $w_{R,X,Y}$ according to 6.1.4.1

δ_R (deg)	1-$w_{R,X}$	SD Coeff	1-$w_{R,Y}$	SD Coeff
-40	1.00E+00	1.13E-02	1.46E+00	1.76E-02
-30	8.78E-01	1.57E-02	1.42E+00	2.04E-02
-20	6.80E-01	3.31E-02	1.03E+00	2.92E-02
-10	2.82E-01	8.59E-02	5.10E-01	4.63E-02
0	-3.61E-02	1.73E-01	1.18E+00	1.02E-01
10	1.22E-01	1.14E-01	1.86E-01	5.96E-02
20	4.35E-01	4.37E-02	9.44E-01	3.50E-02
30	7.31E-01	1.88E-02	1.39E+00	2.28E-02
40	9.35E-01	1.23E-02	1.54E+00	1.83E-02
1-K_m	1.96E-01	1.49E-03	1.79E-01	2.10E-03
SD Error on total result		2.84E-02		5.07E-02

According to these results a value of K_m could be proposed of 0.8 or 0.82 for the third quadrant of operation. For a rudder angle $|\delta_R|>20$ deg negative values for wake factor $w_{R,Y}$ are found which means that the contribution of the backward wake flow must be increased compared to lower rudder angles. The standard deviation error (SD Error) on the total result has been halved comparing results in Table 6.8 and Table 6.9. This is probably thanks to the additional dependence of wake factor w_R on rudder angle δ_R. A comparison of measured and modelled values for the rudder forces F_X and F_Y is shown in Figure 6.33 for all backward velocities (F_n=-0.016 and F_n=-0.032) and all propeller rates.

❑ *Fourth quadrant of operation*
Using the equations developed in section 6.1.4.1, the unknown is the wake factor w_R. For straight-line tests the wake factor w_P is expected to be zero in the fourth quadrant so that

146

$$\zeta = \frac{1 - w_{R0}}{1 - w_{P0}} = 1 - w_{R0}$$

A comparison of Mod582 model and the model proposed in section 6.1.4.1 is not presented in this report but the following two equations for the inflow velocity due to the propeller slipstream have to be considered:

$$u_{RP} = u_{R0} + K_m \left(\sqrt{u_P^2 + \frac{8K_T n^2 D_P^2}{\pi}} - u_P \right)$$

for Mod582 model where u_P is considered to

$$= u_{R0} + K_m \left(\sqrt{u_{R0}^2 + \frac{8K_T n^2 D_P^2}{\pi}} - u_{R0} \right)$$

equal u_{R0} although wake factor w_P is expected to be zero and

$$u_{RP} = u_{R0} + K_m \left(\sqrt{u_P^2 + \frac{8K_T n^2 D_P^2}{\pi}} + u_P \right)$$

for the model according to this research where u_P is

expected to equal u as wake factor w_P is considered to be zero.

The unknown wake factor w_R in Mod582 model belongs both to the "free" stream flow from the motion astern of the ship and the propeller slipstream, so that coefficient K_m will multiplied by a fraction according to the fraction $(1 - w_R)$.

In this section calculations will be based on the proposed model where coefficient K_m is varied using three arbitrary values (0.94, 0.85 and 0.80, Figure 6.34). Rudder angle δ_R has an important influence on modelled values for ζ_X and ζ_Y. Ratio ζ_Y takes values between 0 and 1 for high propeller loading (low advance angles $|\varepsilon^*|$), high rudder angles and values for K_m in the range [0.80; 0.85]. For ratio ζ_X these conditions are somewhat different. If the propeller slipstream is weaker than the wake flow due to the motion astern (more negative advance angles) the influence of K_m is indeed small while values for $\zeta_{X,Y}$ higher than 1 are still found.

6.1.5 Oblique or turning motion: influence of components v and r

6.1.5.1 The inflow velocity at the rudder v_R

According to Ogawa and Kasai in [12] the order of fixing the coefficients for velocities u_R and v_R by captive model tests is based on the following concept: the longitudinal component u_R (and coefficient k) is first of all determined using straight ahead tests with varying rudder angle, followed by the determination of flow-straightening coefficient γ and coefficient C_R of the MMG model based on tests with non-zero v and r (see also chapter 2). The priority or sequence in fixing the values is important.

This method will be used as starting point for the prediction of rudder action while swaying and turning. In this concept rudder forces measured during a straight ahead motion are modelled based on the wake factor at the rudder w_{R0}, while the influence of turning and swaying must be expressed based on the definition of the local drift angle at the rudder position β_R and thus the flow-straightening coefficient k_{HPR}. The influence of velocity components v and r was especially examined for the first quadrant of operation. How this concept must be used in the other quadrants is not always clear as wake flow and propeller slipstream differ essentially from quadrant to quadrant. For example, the question arises if the flow is straightened during a stopping manoeuvre from sternway (quadrant 4) where unstable flow patterns and large eddies occur. Examining measured rudder forces F_X and F_Y during PMM yaw tests with model D, different modelling methods will be evaluated in section 6.1.5.2 for going ahead or quadrant 1. Once the modelling technique is determined all quadrants will be evaluated using the proposed

model.

6.1.5.2 Evaluation based on forces F_X and F_Y measured for model D

❏ An evaluation of rudder forces F_X and F_Y was first of all based on the concept proposed by Ogawa and Kasai (*method 1*). The wake factor at the rudder w_{R0} is determined and the influence of advance angle (or propeller loading) and rudder angle is incorporated using a model with constant K_m (see section 6.1.4). Using this model for the longitudinal velocity component u_R at the rudder position, the lateral velocity component is determined as

$$v_R = \delta_0 u_R + k_{HPR}(v + x_R r) \tag{6.37}$$

Although coefficient x_R is often considered to be twice the position of the rudder stock in the MMG model (for example, [47]) x_R is here $-0.5L_{PP}$ or the longitudinal position of the rudder in (6.37). An apparent inflow angle β_R^* is defined and the flow-straightening coefficient k_{HPR} is considered to be function of this angle:

$$\beta_R^* = \text{Arctan2}(-(v + x_R r), u) \tag{6.38}$$

❏ In *method 2.a* the influence of propeller loading on wake factor w_R was neglected and wake factor components $w_{R,X,Y}$ (function of rudder angle δ_R) together with flow-straightening coefficients $k_{HPRX,Y}$ have been determined as functions of apparent inflow angle β_R^*. As wake factor w_P is considered to be function of the advance ratio, the drift angle and the yaw rate angle, wake factor w_R could be considered to incorporate the same influences although mostly wake factor w_R is expressed as a constant value in literature or is considered not to be influenced by advance ratio, drift angle and yaw rate angle. Method 1 and method 2.a did not give enough accuracy so that *method 2.b* was examined. Results of method 1 for a straight motion are combined with a dependence of wake factor $w_{R,X,Y}$ of inflow angle β_R^*:

$$w_{RX} = w_{R,X0}(\varepsilon^*, \delta_R) \text{Coeff}_{HPRX}(\beta_R^*, \delta_R)$$
$$w_{RY} = w_{R,Y0}(\varepsilon^*, \delta_R) \text{Coeff}_{HPRY}(\beta_R^*, \delta_R) \tag{6.39}$$

Flow-straightening coefficients $k_{HPR,X,Y}$ are still function of β_R^*. Some improvement can also be made if $k_{HPR,X,Y}$ is function of the propeller loading (apparent advance angle ε^*).

A comparison of method 1 and 2 for a set of data of PMM yaw tests is shown in Table 6.10 and Figure 6.35.

Table 6.10 Comparison of the accuracy for a set of data of PMM yaw tests

Model F_Y	R^2	y=ax
Method 1	0.81	y = 0.61x
Method 2.a	0.95	y = 1.00x
Method 2.b	0.96	y = 0.98x

At least, to incorporate the parameters rudder angle δ_R, apparent advance angle ε^* and apparent inflow angle β_R^* 3-dimensional tables are determined for wake factors $w_{R,X,Y}$ where the third dimension is the propeller loading through ε^*. Using this *method 3* (an extension of method 2.a) the accuracy can be improved to an R^2 value of 0.99 (Figure 6.36). As most test types (except multi-modal tests of type B) are executed with constant speed V and propeller rate n, classes could be chosen for the 2D tables based on $\varepsilon^*(V,n)$.

If wake factor $w_{R,X,Y}$ is considered to incorporate the influence of drifting and turning like the wake factor at the propeller w_P, the flow-straightening coefficient loses its significance and although the results are not identical a model with additional parameters $k_{HPR,X,Y}$ could be ignored. This means that although realistic values are determined for the flow-straightening coefficient (especially in the first quadrant of operation, not for the motion astern of the ship) the difference between the accuracy with or without this coefficient is small so that flow-straightening could be expressed with the wake factor dependence of the apparent inflow angle β_R^*.

Adding these three parameters in a rudder prediction model which already incorporates these values in the model for the inflow angle α_R (δ_R and β_R^*) and for the velocity at the propeller slipstream ($\varepsilon^*(V,n)$) could be strange but the incorporation of the propeller loading could be explained based on the fact that not only self propulsion will be modelled but all realistic combinations of speed and propeller revolutions during a manoeuvre. The distinction made for the inflow velocity at the rudder and based on the rudder angle is especially useful to give could predictions for all rudder angles (even low ones).

6.1.6 Proposed model for the inflow velocity components at the propeller u_R and v_R

Summarizing the results of sections 6.1.4 and 6.1.5 wake factor $w_{R,x,y}$ is expected to be function of the rudder angle and the apparent inflow angle β_R^*. The flow-straightening coefficient k_{HPR} is ignored or replaced by the dependence of the wake factor from the inflow angle. The explicit model for the inflow velocity u_R could be based on Mod582 model or on the proposed model in section 6.1.4.1. How the impact of a variation of K_m must be expressed can be found in this section.

Which model will be preferred for the inflow velocity at the rudder, was examined while validating the rudder model in chapter 7 during the execution of turning circles at full scale with model D. The impact of each rudder model on derived characteristic parameters like advance, transfer and tactical diameter could be evaluated. Two models were examined.

1. **Model 1**: the rudder model for the inflow velocity u_R is based on the MMG model for the first quadrant of operation and the extended model described in section 6.1.4.1 for the other quadrants with a *constant value for coefficient K_m*. Coefficient K_m is determined experimentally based on the straight astern motions in the third quadrant of operation. For model D the K_m values are 0.83 for F_x and 0.8488 for F_Y which differ a little from the values in Table 6.9 as these values were not only based on multi-modal tests of type A but all available test types for the third quadrant of operation. Wake factors $w_{R,x}$ (Figure 6.37) and $w_{R,y}$ (Figure 6.38) are determined as two-dimensional tables of rudder angle δ_R and apparent inflow angle β_R^* and this is done for several classes assigned to distinctive advance angles ε^*. The results of this validation will not be reported here because there are two main disadvantages related to this model:

   □ the physical meaning of wake factor $w_{R,x}$ and $w_{R,y}$ is hard to find as values are obtained for some combinations of rudder angle and advance angle (especially low angles ε^*.) which do not lie between the expected values of 0 (free-stream inflow) and 1 (no inflow). In addition, as the wake at the rudder position will be closer to the free stream condition compared to the wake at the propeller, the values for wake factor w_R should be smaller than these for w_P.

   □ a distinction according to some classes of advance angles depends strongly on the executed combinations of velocity and propeller rate during the captive model tests. An advance angle of 22 deg could be obtained during a test at low speed and low propeller rate or high speed and high propeller rate if the ratio u/n is identical. During a full scale test at manoeuvring speed (harbour full) for model D the advance angle will be nearby 20 deg while the rudder model for this advance angle will probably be based on tests at lower speed and propeller rate.

2. **Model 2**: the rudder model for u_R is also based on the MMG model for the first quadrant of operation and the extended model described in section 6.1.4.1 for the other quadrants but *coefficient K_m is experimentally determined* as function of rudder angle δ_R and the apparent inflow angle β_R^*. Wake factors $w_{R,x}$ and $w_{R,y}$ are determined as two-dimensional tables of rudder angle δ_R and apparent inflow angle β_R^*. This model could be considered as a link between Mod582 model and model 1 which suffers from varying w_R values depending on the imposed K_m value. The results of this model for ship model D are presented in Figure 6.39 and a comparison of the accuracy of both mathematical models is shown in Figure 6.40.

Wake factors $w_{R,X}$ and $w_{R,Y}$ are indeed smaller than the wake factor at the propeller position w_P summarized in chapter 5. In addition, as wake factor w_P decreases with increasing inflow angle $|\beta|$ an identical tendency could be determined for the wake factor at the rudder for inflow angles β_R^* near zero deg. The errors for higher inflow angles are probably caused by the model test type which is multi-modal of type B. The experimentally determined coefficients $K_{m,X,Y}$ are much lower than the expected value of 0.94 for model D according to Table 6.6. During validation values lower than 0.5 were not accepted on a physical base. These values are found for lower rudder angles. Error bars are once again increasing for inflow angles $|\beta_R^*|$ larger than 30 deg.

The advantage of model 2 is a clear distinction in contribution of the free-stream flow and the propeller race as was also proposed by Molland and Turnock (see chapter 2). Another advantage is the possibility of imposing a wake factor $w_{R,X} = w_{R,Y} = w_P = 0$ for the motion astern. For both ship models the error bars on experimentally determined wake factors at the rudder were too large so that it could be decided to suppose that, as for the wake factor at the propeller, the wake due to the ship's hull could also be neglected during a motion astern. Wake factors at the rudder for model E and both water depths are represented in Figure 6.41, while coefficients $K_{m,X,Y}$ are shown in Figure 6.42 for a positive turning rate (quadrants 1 and 4) and in Figure 6.43 for a negative propeller rate (quadrant 3).

6.2 A correlation model for hull-propeller-rudder combination

The forces executed on the rudder itself during an arbitrary manoeuvre are not necessarily extended to the complete hull-propeller-rudder combination. Correlation coefficients will be introduced and are especially based on the assumptions described by Ogawa & Kasai in [12]. Coefficients t_R, a_H and x'_H are correlation coefficients which are related respectively to the longitudinal force, lateral force and yawing moment and will be discussed in the following sections.

Regardless of the correlation coefficient to determine or the test type which captive model results will be used for the analysis, measured rudder forces F_X and F_Y and measured propeller thrust value T_P or K_T will be used for the correlation model so that model inaccuracies for F_X and F_Y will not influence the consecutive modelling procedure step.

Oltmann and Sharma do not make use of these correlation coefficients but develop another concept for the horizontal forces and yawing moment X_R, Y_R and N_R which represent the total system response to rudder application. The lift and drag characteristics of a rudder in the behind ship condition are considered not only to be based on the open water characteristics C_{LR}^0 and C_{DR}^0 but they take into account the effect of propeller loading and hull-propeller-rudder interaction:

$$C_{LR} = \left(1 + k_{LR}\frac{u_P}{u_R}\right)C_{LR}^0$$

$$C_{DR} = \left(1 + k_{DR}\frac{u_P}{u_R}\right)C_{DR}^0$$

(6.40)

Separate rudder forces have not been calculated and the equations for the horizontal forces and yawing moment are transformed into:

$$X_R = \frac{\rho}{2}A_R\left(\overline{u_R}^2 + v_R^2\right)\left(C_{LR}\sin\beta_R - C_{DR}\cos\beta_R\right)$$

$$Y_R = \frac{\rho}{2}A_R\left(\overline{u_R}^2 + v_R^2\right)\left(C_{LR}\cos\beta_R + C_{DR}\sin\beta_R\right)$$

(6.41)

$$N_R = \left(1 - k_{NR}\frac{u_P}{u_R}\right)Y_R x_R$$

For the tanker Esso Osaka the values for k_{LR}, k_{DR} and k_{NR} for 50 and 20% UKC are summarized in Table 6.11 [96].

Table 6.11 Values for the rudder coefficients k_{LR}, k_{DR} and k_{NR}

	50% UKC	20% UKC
k_{LR}	11.84	9.48
k_{DR}	4.85	2.80
k_{NR}	0.0	0.0

The concept proposed by Ogawa and Kasai will be examined in the next sections although propeller loading will effect one of these correlation coefficients as was supposed by Oltmann and Sharma.

6.2.1 Longitudinal force X_R

The contribution of the rudder to the longitudinal force on the fully appended ship model, contribution X_R, is given as:

$$X_R = (1 - t_R)F_X \qquad (6.42)$$

Correlation coefficient t_R could be defined as a rudder deduction parameter, so that for a motion ahead the resistance force F_X is reduced to a fraction $(1-t_R)$. Modelled values for t_R have first of all been determined for the first quadrant of operation for model D, propeller working ahead during a motion ahead. The results of stationary tests with a distinction according to low and ordinary speed manoeuvring are shown in Figure 6.44. The influence of small drift angles is incorporated. As rudder force F_X is only based on rudder normal force F_{RN} modelled values for 1-t_R could be expected to be higher as F_X will be underestimated compared to the total longitudinal force X measured. To know if this assumption is true, the results of these stationary rudder angle tests could be compared to these of multi-modal tests of type A where F_X is composed of tangential and normal rudder force F_{RT} and F_{RN} (Figure 6.45).

First of all, for model D it can be observed that values for $(1-t_R)$ are not necessarily lower than 1. Especially negative rudder angles (angles to starboard) give higher values. This can physically not be accepted and must probably be ascribed to the hull and/or propeller contribution through resistance force X_H and thrust deduction t_P. For a straight ahead motion an increasing Froude number gives decreasing values for fraction $(1-t_R)$ as rudder (resistance) force F_X increases with ship velocity. High propeller loading (100% instead of 50% of the reference propeller rate) gives less scatter and for rudder angles to port fraction $(1-t_R)$ is in between 80 and 100%, except for low rudder angles.

Table 6.12 Model E at 20% UKC, quadrant 3 and 4, constant values for the correlation coefficients

Quadrant	t_R	Error t_R	a_H	Error a_H	x_H	Error x_H
3	7.56E-01	6.08E-02	-6.13E-01	9.18E-02	-1.61E-01	1.35E-02
4	5.97E-01	1.28E-02	-1.55E-01	2.43E-02	-2.57E-01	3.98E-03

For model E rudder deduction t_R has been determined as a two-dimensional table of rudder angle δ_R and inflow angle β_R^* for the first quadrant of operation. For the other quadrants, except for the second quadrant where the rudder forces are negligible, only a constant value is calculated per quadrant (Table 6.12 for both positive and negative rudder angles). Only for the highest tested rudder angles the error bars are restricted in Figure 6.46, which may arise some doubt about the worth of this correlation parameter. The rudder deduction parameter t_R will determine the speed loss due to rudder action as the lower this parameter the higher the resistance force X_R induced by the rudder for the first quadrant. During validation the question will arise if the obtained speed loss for the Esso Osaka will correspond to the speed reduction during the full scale trials and the correlation parameter t_R will be judged at that moment.

6.2.2 Lateral force Y_R

The rudder induced lateral force Y_R:

$$Y_R = (1 + a_H)F_Y \tag{6.43}$$

is composed of the lateral force measured at the rudder position F_Y and the force component $a_H F_Y$ which is working on the ship's hull at a position x_H from the midship point (Figure 6.47). In the MMG model the coefficient a_H is mostly a constant value [12] although influence of the propeller loading is recognized.

For an inflow angle β_R^* approximating zero the contribution of the hull Y_H and the propeller Y_P could be considered to be small so that the hull correlation coefficient a_H can be estimated based on:

$$a_H = \frac{Y - F_Y}{F_Y} \tag{6.44}$$

For oblique towing tests a reduced lateral force is represented based on

$$Y_R = Y - Y_H - Y_P = Y - Y^{(\beta)}(u, v, 0) \left[1 + C_n(\beta) \left(\frac{n}{n_0} \right)^2 \right] = (1 + a_H)F_Y \tag{6.45}$$

and in equation (6.44) Y will be replaced by Y_R. The observations for model D are summarized in section 6.2.2.1, while a model will be developed in 6.2.2.2.

6.2.2.1 Observations of hull contribution a_H

Measured values and linear regression lines for coefficient $1 + a_H$ are represented in Figure 6.48 for low speed manoeuvring and Figure 6.49 for ordinary speed manoeuvring for *stationary straight-line tests*. In Figure 6.50 all Froude numbers for this test type and propeller rates of 0, 50% and 100% of the reference propeller rate are combined for the largest tested rudder angles to port and starboard. An influence of the propeller loading represented by the apparent advance ratio J' or the advance angle ε^* must be incorporated in the mathematical model for hull coefficient a_H. In addition, for **bollard pull tests** measured values and linear regression lines give hull coefficients $1 + a_H$ which approximate 1 so that there is no additional hull force if there is no flow around the ship model induced by the forward ship velocity (or J'=0). Values for the total lateral force measured at rudder angle δ_R=10deg are doubtful so that a modelled value of zero for hull coefficient a_H can be adopted for Froude number F_n=0.

Measured values and linear regression lines for coefficient $1 + a_H$ for *oblique towing tests* are represented in Figure 6.51 to Figure 6.54 for drift angles of –5 deg and 5 deg. Comparing these figures an increase of a_H with Froude number F_n can be recognized with maximum values up to 2 or 3. Due to the inclined flow compared to the flow during a straight ahead motion of the model, the hull correlation parameter a_H is growing. Some differences of rudder angle dependence can also be observed.

In an attempt to incorporate as much influences as possible models for a_H could be expected to be function of the propeller loading, the apparent inflow angle at the rudder and the rudder angle it self.

6.2.2.2 Model for correlation parameter a_H

A mathematical model for hull coefficient a_H was developed in [89] depending on the apparent advance ratio J':

$$a_H = \frac{A_1 J'}{J'^3 + A_2} \tag{6.46}$$

where coefficients A_1 and A_2 are defined as:

$$A_1 = 3a_{Hmax} J'^2_{max}$$
$$A_2 = J'^3_{max} \tag{6.47}$$

using the couple (J'_{max}, a_{Hmax}) which means that coefficient a_H reaches a maximum value of a_{Hmax} at a propeller advance ratio J'_{max}. The propeller advance ratio is based on the total ship velocity V during straight-line and oblique towing tests which means that:

$$J' = \frac{V}{nD_P} = \frac{\sqrt{u^2 + v^2}}{nD_P}$$

For bollard pull tests ($J'=0$) and tests with vary low propeller loading ($J' \rightarrow \infty$) hull coefficient a_H is expected to be zero.

Tabular models for (J'_{max}, a_{Hmax}) have been determined as function of rudder angle δ_R for low speed manoeuvring ($F_n=0.016$) and ordinary speed manoeuvring ($F_n \geq 0.049$) based on the stationary straight-line tests discussed in 6.2.2.1 (Figure 6.55). Errors are important for low rudder angles ($|\delta_R| \leq 10deg$). Values J'_{max} are, as expected, lower for low speed manoeuvring compared to ordinary speed manoeuvring while the opposite applies to hull coefficients a_H. Resulting mathematical models are shown in Figure 6.56. During straight-line tests and ordinary speed higher values a_{Hmax} can be found in general for rudder deflections to portside compared to the same absolute values for the rudder deflections to starboard side.

During oblique towing tests (drift angle $|\beta|=5deg$) hull coefficient a_{Hmax} increases considerably for ordinary speed (Figure 6.57). For low speed the increase is less striking. For a drift angle β of -5 deg positive rudder angles or rudder deflections to portside give higher values for a_{Hmax} compared to negative rudder angles. For oblique towing tests with $\beta = 5$ deg and ordinary speed the opposite is true while the difference between positive and negative rudder angles is furthermore more important for this drift angle. This tendency could be explained based on the opposite directions of oblique flow and rudder angle. During a turning circle manoeuvre to for example starboard the drift angle will be positive for a (negative) rudder angle to starboard. The rudder induced hull effect will be more important than if the rudder angle would be instantaneously turned to port.

These models which are based on stationary tests with individual (V,n,δ_R) combinations per test run could be compared for model D to the tabular models for coefficient $1+a_H$ which have been determined as function of rudder angle δ_R for each individual *multi-modal straight-line test of type A*. Each test run of this type represents one apparent advance ratio J' or advance angle ε^*. Modelled hull coefficient values $1+a_H$ for rudder angles $\delta_R=-40deg$ and $\delta_R=40deg$ are shown on Figure 6.58. For the first quadrant of operation and a straight ahead motion the relationship between the apparent advance ratio J' and the advance angle ε^* is:

$$\varepsilon^* = Arctan2(J', 0.7\pi) \tag{6.48}$$

In general the change of a_H with the apparent advance angle differ from the proposed model in (6.46). At low propeller loading or higher values for the apparent advance ratio or advance angle coefficient a_H is determined with less accuracy (due to the small rudder forces) but model values do not necessarily tend to a zero value. A constant value could also be adopted instead of a decreasing value to zero. The model proposed in (6.46) could also be less interesting as small values are found near advance angles which correspond to the manoeuvring speed ratio during full scale trials. For the containership this ratio ε^* is approximately 20 deg. For a range of ε^* [0, 10 deg] the maximum value a_{Hmax} from stationary tests is higher than the hull coefficient a_H obtained from multi-modal tests of type A with harmonically varying rudder angle and constant propeller rate. Due to the oscillating character of this test type the flow around the ship model differ probably from the flow developed during stationary tests which are characterized by a regime condition. In addition, it could be expected that during multi-modal tests of type B with varying propeller rate and rudder angle this could be still worse or more complicated.

An example of modelled hull coefficient a_H (tabular model of yaw rate angle γ) for *pure yawing tests with propeller and rudder action* is shown in Figure 6.59. The influence of rudder angle could be of minor importance if the rudder angle is large enough ($|\delta_R| \geq 20deg$). For an

instantaneous straight motion (or $\gamma=0$) the a_H coefficient is almost identical for positive and negative rudder angles. In addition, a_H values are qualitatively the same for a combination ($\delta_R<0$, $\gamma>0$) and ($\delta_R>0$, $\gamma<0$) which combinations are realized during turning circles. For the opposite combinations the hull coefficient a_H decreases compared to the straight ahead motion.

During validation two-dimensional tables have been used for a_H as function of the inflow angle $\beta_R{}^*$ and the advance angle ε^*. For model D this table is based on the maximum values found for positive and/or negative rudder angles for each combination (ε^*, $\beta_R{}^*$) (Figure 6.60, all test types have been used for the modelling). This choice could be considered as artificial but hull coefficient a_H seems to have an important influence on the characteristics of a turning circle (see chapter 7). The hull coefficient a_H at ε^* zero has been determined during the regression analysis and these values have been kept during the validation.

For model E tabular models used during validation are presented in Figure 6.61. For the third and the fourth quadrant hull coefficient a_H is negative according to the results in Table 6.12 so that the rudder induced lateral force Y_R will be smaller than lateral rudder force F_Y.

For both ship types the errors on coefficient a_H at an advance angle of 25 deg are high (between 50% and 100% of the value) so that the influence of this parameter should be investigated during validation.

6.2.3 Yawing moment N_R

The application point of the additional rudder induced force $a_H F_Y$ will be made non-dimensional based on the length between perpendiculars L_{PP}:

$$N_R = \left(x_R + x'_H L_{PP} a_H\right) F_Y \tag{6.49}$$

The position x_R is the longitudinal position of the rudder stock or $-0.5 L_{PP}$. The longitudinal position x'_H for model D is presented for different model types in Figure 6.62 for stationary rudder angle tests, in Figure 6.63 for multi-modal tests of type A and in Figure 6.64 and Figure 6.65 for PMM yawing tests. Based on stationary tests non-dimensional positions between 0 and -0.2 have been found for both straight-line and oblique towing tests. The multi-modal straight ahead tests do not give any clear influence of Froude number or apparent advance angle and gives positions which are more concentrated on the aft body compared to stationary rudder angle tests. Probably a smaller hull coefficient a_H due to the oscillating rudder angle gives rise to an additional rudder force which is moved to the aft body compared to stationary tests. For the PMM yaw tests which are stationary in the imposed rudder angle but harmonic in the inflow angle to the rudder more or less stable positions can be found for combinations of ($\delta_R<0$, $\gamma>0$) and ($\delta_R>0$, $\gamma<0$) concentrated at the aft body with values for x'_H which do not differ a lot from the values found during stationary tests. If rudder angle and inflow angle take the same sign, the flow induced on the ship's hull is unstable and the non-dimensional application point moves from the fore to the aft body or vice versa.

Tabular models for x'_H as function of rudder angle δ_R and inflow angle $\beta_R{}^*$ based on all available test types are shown for model D in Figure 6.66. The errors are smaller for the combinations ($\delta_R<0$, $\gamma>0$) and ($\delta_R>0$, $\gamma<0$) and rudder angles $|\delta_R|$ which are at least 20 degrees but still variations in x'_H must be taken into account. For model E a comparison is made between non-dimensional positions x'_H for medium deep and shallow water (Figure 6.67). The results for positive rudder angles are doubtful and probably suffer from the bad chosen combinations of propeller rate and rudder angle during multi-modal tests of type B. Another explanation is hard to be found. If the water depth increases, the application point moves to the ship's stern. Values for x'_H are nevertheless restricted to values between -0.5 and 0.5.

7 Validation of the mathematical model

A mathematical manoeuvring model only gives a taste of its quality at the validation process. Validating means comparing the predicted results of the developed mathematical model with the expected results in real-time. This validation is a difficult task as measurements of real ship behaviour during manoeuvres are still unusual although techniques like GPS could offer a valuable tool. In section 7.1 the difference between objective and subjective validation (section 7.1.1) is discussed and some standard full scale trials which could be used during the validation are selected (section 7.1.2). The full scale trials with the Esso Osaka are executed at low speed and some background about low speed manoeuvres is given in section 7.1.3. The usefulness of the full scale trials executed with the Esso Osaka in deep, medium and shallow water will be considered in section 7.1.4.

Scale effects are inextricably related to the derivation of mathematical models using scale models even if the scale ratio λ is taken as small as possible. Only a short description of possible scale effects is given in section 7.2 where the proposed correction of ship resistance is described.

Due to a lack of knowledge about the scale effects and a lack of validation data like characteristics of full scale trials, the validation process will be accompanied or replaced by a sensitivity analysis (section 7.3) with the objective to determine the sensitivity of individual model components on the final results, e.g. characteristics of turning circles or other standard manoeuvres. Some background about sensitivity analyses is given in section 7.3.1. The validation starts for the Esso Osaka in 7.3.2 as the manoeuvrability of this ship is best documented in both deep and shallow water. Although a four-quadrant model for harbour manoeuvres was the objective, the validation for the Esso Osaka will only be executed for the first quadrant based on the available low speed manoeuvres. The reasons for this choice are:

❑ The documented full scale trials for the Esso Osaka are only part of quadrant 1 and 2 where quadrant 2 is only reached during a stopping manoeuvre.
❑ There is a lack of data from the captive model tests for the quadrants 3 and 4.

Based on the findings for the Esso Osaka the analysis will be undertaken for the fourth generation containership or model D (section 7.3.3), once again focussed on the first quadrant. As predicted and validated manoeuvring characteristics of containerships in (very) shallow water are rare and hardly found in literature, a comparison will be made of the manoeuvring characteristics of this ship for the following combinations:

❑ draught d = 13.5 m and 26% UKC
❑ draught d = 15.0 m and 20% UKC.

The results for the intermediate draught of 13.5 m and an under keel clearance nearby 20% are generated within the project reported in [90]. As the mathematical model is derived from a modified test program compared to the tests results used in this research, some differences in observed characteristics could be notified. In addition, containerships often travel at intermediate draughts from port A to B so that this comparison could be justified. As no full scale trials are available for the containership, the real validation of the four-quadrant simulation model must be based on the experience of pilots; this type of validation is out of the scope for this thesis, but is planned in the near future (see chapter 8).

7.1 Prediction of full scale trials

7.1.1 Objective or subjective validation

For the validation of ship manoeuvring mathematical models three main methods can be recognized:

❑ The validation of the derived mathematical models through comparison of predicted results with carefully planned and executed full scale trials can be considered to be objective as the influence of human factor is minimised as much as possible.

❑ Validation of ship manoeuvring models by captains or pilots on for example a ship manoeuvring simulator is subject to interpretations; therefore, the results of the validation may differ from pilot to pilot (subjective validation).

❑ If free model tests are used to validate the simulation models scale effects have still to be considered and could cause some discrepancies between model scale and full scale.

During the last decades the International Maritime Organization [97] has tried to increase the knowledge concerning ship manoeuvrability by the introduction of the Standards (see Appendix A). Full scale trials at fully loaded draught, nevertheless, are still poorly documented - often only turning circles and crash stops are presented - so that manoeuvring models running on a ship manoeuvring simulator are often validated based on the experience of its users only.

It is a permanent objective of the Manoeuvring Committee (MC) of the ITTC [58] to provide benchmark data for the validation of mathematical manoeuvring models. Ideally, there should be a list of benchmark ships of different ship types making a distinction between data based on either predictions in model scale or predictions in full scale. The opinion of the MC is that there is still a lack of validation even at model scale. The Esso Osaka benckmark, which provide data in full scale (see section 7.1.4) and in model scale, shows that very different results exist for hydrodynamic forces from published captive model tests executed at various institutes. Based on the results discussed in the chapters 4 to 6 in this report, the statement of the MC that captive model tests can be carried out in numerous ways, must be confirmed. The consequences of this opinion will be discussed in detail in section 7.3.2 while validating the obtained mathematical models for the fully appended ship model of the Esso Osaka.

7.1.2 Standard manoeuvres

The standard manoeuvres (turning circle, zigzag manoeuvre and crash stop) are executed in the following way:

❑ *Turning circle*: The ship is travelling at a certain propeller rate – speed combination with minimum rudder angle to maintain a straight course. The turning circle starts when the rudder angle is put to a prescribed value (for example 35 degrees to port or starboard). The ship follows a path which looks like a circle, a turning circle, with some characteristic distances (Figure 7.1):
   - *the advance*: the distance measured parallel to the original course of the ship, from the moment the rudder angle is put to the required value and the moment the course change is 90 degrees;
   - *the transfer*: the distance measured orthogonal to the original course, from the moment the rudder angle is put to the required value and the moment the course change is 90 degrees;
   - *the tactical diameter*: the distance measured orthogonal to the original course, from the moment the rudder angle is put to the required value and the moment the course change is 180 degrees;
   - *the radius* of the turning circle: the radius of the turning circle described by the ship when a regime has obtained.

❑ *Zigzag manoeuvre or overshoot tests*: The ship starts with a chosen propeller rate – speed combination. A rudder angle δ_R is imposed so that a course change is occurring. At the moment the course change ψ equals δ_R the rudder angle is changed to $-\delta_R$ until the course change is $-\delta_R$. The rudder angle is then replaced to the δ_R value. This process can be repeated several times. Mostly zigzag manoeuvres are executed with a 10/10 or a 20/20 change for the rudder/course change $\tilde{\delta_R}/\psi$. The manoeuvre can be evaluated using (Figure 7.2):

○ *the overshoot angle*: this is the extra course change (compared to a course change of for example 10 or 20 degrees) after changing the rudder angle to the opposite value;

○ *the overshoot width*: the extra lateral displacement of the ship after changing the rudder angle to the opposite value;

○ the *time* necessary to reach a course angle ψ after changing the rudder angle to δ_R.

❑ **Crash stop**: The ship travels with a certain propeller – speed combination followed by a reversal of the propeller to a full astern condition. The trajectory is characterized by:

○ *the head reach*: this is the distance between the position at the full astern command and the position of the standstill of the ship, measured parallel to the original course;

○ *the lateral deviation*: the distance between the position at the full astern command and the position of the standstill of the ship, measured orthogonal to the original course;

○ *the track reach*: the distance of trajectory between the position of the command and the position of a standstill.

7.1.3 Selection of low speed manoeuvres

As was stated by Dand in [22], a conflict exists between the necessity of a ship to be quite directionally stable during the long ocean passages and the necessity of having good turning ability and less directional stability during harbour approaches. Low speed manoeuvres which have to give some insight into this turning ability are proposed by Hwang et al. and are shown in Table 7.1. Some other additional low speed tests in [23] concern tests for twin-screw ships and tests for both bow and stern thrusters. The default test conditions for all tests include open deep and shallow water with 20% UKC, calm weather, moderate uniform current, loaded and ballast draft.

Table 7.1 Suggested basic low speed manoeuvres according to [23]

Name of manoeuvre	Test purposes
Minimum effective rudder (MER)	Least rudder angle that can be applied and still effect yaw-checking at speeds ranging from cruising to low speed at each engine order
Crash stop from Half AHD speed	Ship's stopping capabilities from a speed which is relevant in harbour operation Ship's dynamic response to throttle order when operating in transition from Quadrant 1 → 2 Paddlewheel effect / Stern walk
Acceleration / Deceleration Combinations (Start from and back to Dead in water)	Ship's dynamic response to throttle order when operating in transition from Quadrant 1 → 2 → 3 Paddlewheel effect / Stern walk
Backing / Stopping combinations (Start from and back to Dead in water)	Ship's dynamic response to throttle order when operating in transition from Quadrant 3 → 4 → 1 Paddlewheel effect / Stern walk
35 deg Accelerating turn starting from Dead in water with Slow AHD bell	Ship's ahead turning capability during acceleration at low speed
35 deg Coasting turn from Slow AHD	Ship's ahead turning capability at low speed during deceleration with propeller(s) wind milling or possibly stopped
20/20 Overshoot test with Slow AHD approaching speed	Ship's yaw checking capability at a speed which is relevant in harbour operation
20/20 Accelerating overshoot test starting from Dead in water with Slow AHD bell	Ship's yaw checking capability during acceleration ahead at low speed
20/20 Coasting overshoot test with Slow AHD or Half AHD approaching speed	Ship's yaw checking capability at low speed during coasting ahead with propeller(s) wind milling or possibly stopped
Back & fill with fill first (for both starboard filling and port filling)	Ship's manoeuvrability in tight space Interaction between hull, propeller and rudder when operating in transition from Quadrant 1 → 2 → 3

Name of manoeuvre	Test purposes
Back & fill with back first (for both starboard backing and port backing)	Ship's manoeuvrability in tight space Interaction between hull, propeller and rudder when operating in transition from Quadrant 3 → 4 → 1

The accelerating and coasting manoeuvres will be discussed in 7.1.4.

7.1.4 The Esso Osaka full scale trials [73]

The full scale trials executed with the tanker *Esso Osaka* in the late seventies have been considered to be invaluable for the prediction of ship manoeuvrability. The 21st, 22nd, 23rd and 24th International Towing Tank Conferences (ITTC) have carried out some studies on the Esso Osaka. During the 23rd ITTC the Specialist Committee on Esso Osaka [98] reported some conclusions concerning captive model test data and proposed benchmark data exclusively for the deep water condition. The Committee could after all not get sufficient data for the shallow water conditions due to a lack of information on experiments and analysing procedures. The 24th Manoeuvring Committee [58] succeeded in collecting some data of captive model tests for the Esso Osaka in shallow water from seven different sources. Some important conclusions will be summarized in section 7.3.2.2.

Table 7.2 Esso Osaka particulars

Hull		
Length overall	343.00	m
Length between perpendiculars	325.00	m
Breadth molded	53.00	m
Depth molded	28.30	m
Designed load draft, molded	22.05	m
Assigned summer freeboard draft, extreme	22.09	m
Full load displacement at assigned summer freeboard draft	328 880	mt
Block coefficient, summer freeboard draft	0.831	
Draft, molded, at trials	21.73	m
Draft, extreme, at trials	21.79	m
Trim in still water, at trials	0	
Displacement at trials	319400	mt
Longitudinal CG at trials, forward of amidship	10.30	m
Bow	Bulbous type	
Stern	Transom type	
Rudder		
Number of rudders	One	
Rudder area	119.817	m^2
Engine		
Hitachi Impulse 2-Cylinder Cross-Compound Main Steam Turbine		
Continuous full output, at 82 rpm	36 000	HP
Service output, at 81 rpm	35 000	HP
Propeller (single, right-handed, 5 blades)		
Diameter	9.1	m
Propeller pitch	6.507	m
Expanded area	44.33	m^2
Projected area	37.22	m^2
Disk area	65.0	m^2
Pitch ratio	0.71505	
Expanded area ratio	0.682	
Projected area ratio	0.572	
Rake angle	4 deg 24 min	

Manoeuvring trials of the 278 000-dwt tanker were made in two shallow water and one deep water site in the Gulf of Mexico during July/August 1977 providing 20, 50 and 320 percent

bottom clearance (Figure 7.3). The principal objective at that time was to develop data for improving the quality of computer simulations of ship-handling for training and for research and design. Although the trials were carried out with unusual care, inaccuracies (e.g. in bottom clearance) and lack of information still remain which makes a comparison between prediction and full scale a difficult task. The time dependence of the rudder and the propeller during for example accelerating and coasting manoeuvres influences the manoeuvring behaviour so that the exact behaviour of the steam turbine becomes important.

The particulars of the Esso Osaka are summarized in Table 7.2. Especially the propeller and the rudder characteristics do not correspond exactly with those of the scale model as was stated in chapter 3. The rudder of the ship model is 5% larger at full scale ratio than the rudder of the Esso Osaka, while the propeller diameter of the model is 4% smaller.

The low speed manoeuvres and their approach speeds are listed in Table 7.3; some of them clearly correspond to the low speed manoeuvres suggested in Table 7.1. The validation of the derived mathematical models for the Esso Osaka in shallow water will only be performed based on the described low speed manoeuvres.

Table 7.3 Trial agenda of full scale trials Esso Osaka

Type of manoeuvre or calibration run	Speed of approach to manoeuvres, knots		
	h/d= 1.2	h/d=1.5	h/d=4.2
1. Manoeuvres			
Turn, port, 35 deg L	5, 7	7	7
Turn, stbd, 35 deg R	5, 7	7	7, 10
Turn, accelerating, 35 deg R	0+	0+	
Turn, coasting, 35 deg R	5	5	5
zigzag manoeuvre, 20/20	7	7	7
zigzag manoeuvre 20/20 coasting	5	5	5
zigzag manoeuvre 10/10	7	7	7
Biased zigzag manoeuvre	7	7	7
Spiral	7	7	7
Stop, 35 deg L	3.5		3.5
Stop, 35 deg R	3.5	3.5	3.5
Stop, controlled heading	3.5		3.5
Stop, steering for constant heading			3.5
2. Calibration runs			
Speed/rpm, taken during steady runs Prior to chosen manoeuvres	3.5, 6, 8.5	5, 7.5	7, 10

A series of speed-versus-rpm calibration runs (or acceleration tests) were completed prior to conducting the manoeuvring trials at each site. A conventional turning circle, stopping and zigzag manoeuvre are described in 7.1.2 while the other low speed manoeuvres selected for the Esso Osaka need some comment:

❑ *Acceleration test or calibration run*: The ship starts at zero speed and the speed is gradually increased due to an imposed propeller rate (corresponding to the available telegraph positions for manoeuvring in shallow water: dead slow, slow, half and harbour full). The full scale trial ends when the longitudinal acceleration component is negligible and a constant (forward or backward) speed is reached. Important results are the regime speed and the time and distance necessary to obtain this speed. A lateral deviation is also possible due to the non-symmetric flow induced by the single right-handed propeller.

❑ *Accelerating turn*: This trial begins from dead in the water (zero speed). The rudder is set to 35 deg and the engine simultaneously ordered to 55 rpm ahead.

❑ *Coasting turn*: The coasting turn is similar to a conventional turning circle, except that the engine is ordered stopped at the instant the initial rudder execute command is given. Due to

the low approach speed and the ship slowdown only a partial turn can be performed.

❑ *Coasting zigzag manoeuvre*: This trial is similar to the conventional zigzag manoeuvre except that the engine is ordered stopped at the instant the first rudder execute command is given. The zigzag manoeuvre is continued until the ship's heading no longer responds to rudder. In the present trials for the Esso Osaka only two or three rudder commands were made before control was lost at very low speed. Therefore, modified performance indices where used, such as maximum lateral deviation and corresponding advance at maximum lateral deviation. These are in addition to first yaw angle overshoot.

❑ *Biased zigzag manoeuvre*: A zigzag manoeuvre according to steering procedures in a sequence of rudder angles and ordered time durations provided by the Massachusetts Institute of Technology. Based on these manoeuvres transient data could be obtained in the non-linear turning range as required for systems identification.

These manoeuvres and their manoeuvrability characteristics will be discussed in section 7.3.2.1, where the predictive power of the derived mathematical models will be evaluated.

7.2 Extrapolation from model to full scale

The transition from model scale to full scale requires several actions. First of all, the propeller rate during captive model tests is imposed while during simulations an engine model has to be available for a realistic variation of the propeller rate. The engine model of the ship simulator is discussed in section 7.2.1. From the moment model tests have been executed at scale factor λ, scale effects have to be considered. The prediction method to correct measured ship resistance is well known and discussed in section 7.2.2, but scale effects will play a part in all the modules of a manoeuvring ship, i.e. hull, propeller and rudder. Many questions about the impact of scale effects on the predicted ship manoeuvres stay unanswered; it is e.g. unclear whether additional influences exist for model tests executed in shallow water. In [12] Ogawa and Kasai denote a chapter to the model/full-scale correlation in manoeuvrability and conclude that there is only little information about the scale effect for the rudder contribution while for the wake and the propeller loading some useful concepts exist. These concepts will not be discussed here but some remarks about scale effects will be made during the sensitivity analysis in section 7.3.

7.2.1 A general formulation for the engine

The engine model has to describe the behaviour of the motor-propeller combination during the selected manoeuvres. The equation for the accelerating or decelerating of the propeller rate $\dot{n}$ is given by:

$$2\pi I_{pp}\dot{n} = Q_E - Q_P \tag{7.1}$$

The propeller torque Q_P is modelled based on the wake factor w_Q thanks to the torque identity method (chapter 5), while the engine torque Q_E is modelled using a simplified linear relationship between torque and rate n. Different conditions have been considered depending on the actual and the desired propeller rate:

❑ propeller action ahead is required:
  • Accelerating propeller (e.g. from *slow astern* to *half ahead*):
    IF $(n < -n_{min})$ THEN

$$Q_E = CoefC * B^- |n| \tag{7.2}$$

  IF $((n > -n_{min})$ AND $(n < n_{min}))$ THEN

$$Q_E = CoefD * \left(A^+ + B^+ |n|\right) \tag{7.3}$$

  IF $(n > n_{minimum})$ THEN

$$Q_E = CoefE * \left(A^+ + B^+ |n|\right) \tag{7.4}$$

  • Decelerating propeller (e.g. from *full ahead* to *slow ahead*):

$$Q_E = -CoefF * |B^+ n| \tag{7.5}$$

❑ propeller stopped is required:
- Stopping from reversed propeller:

$$Q_E = CoefF * |B^- n| \qquad (7.6)$$

- Stopping from propeller ahead:

$$Q_E = -CoefF * |B^+ n| \qquad (7.7)$$

❑ reversed propeller action is required:
- Decelerating propeller (e.g. from *full astern* to *slow astern*):

$$Q_E = CoefF * |B^- n| \qquad (7.8)$$

- Accelerating propeller (e.g. from *slow ahead* to *half astern*):

IF (n > n$_{min}$) THEN

$$Q_E = CoefC * B^+ |n| \qquad (7.9)$$

IF ((n > -n$_{min}$) AND (n < n$_{min}$)) THEN

$$Q_E = CoefD * \left(A^- + B^- |n|\right) \qquad (7.10)$$

IF (n < -n$_{min}$) THEN

$$Q_E = CoefE * \left(A^- + B^- |n|\right) \qquad (7.11)$$

The coefficients A^+, B^+, A^-, B^-, CoefC, CoefD, CoefE and CoefF can be tuned so that the evolution of the propeller rate corresponds to the real manoeuvre.

7.2.2 Scale effects on ship resistance

Although scale effects have not only to be considered for the difference in frictional resistance comparing model test data and full scale data, at this stage only a correction of the resistance is adopted according to the 1978 ITTC Performance Prediction Method.

7.2.2.1 Correction of resistance force: 1978 ITTC Performance Prediction Method

The non-dimensional hull force X' will be corrected for the increased frictional resistance measured during model tests so that the component $X'^{(\beta)}$ will be modified to a lower value.

❑ The resistance measured on the ship model (index M) during straight-line tests is made non-dimensional based on the wetted surface area S:

going ahead $$C_{TM} = \frac{X'^{(\beta)}(\beta = 0) L_{PP} d}{S} \qquad (7.12)$$

going astern $$C_{TM} = \frac{X'^{(\beta)}(\beta = 180 \deg) L_{PP} d}{S} \qquad (7.13)$$

❑ The specific total resistance coefficient C_{TM} depends on the Froude number F_n, the Reynolds number R_n and a non-dimensional pressure $p/\rho V^2$:

$$F_n = \frac{V}{\sqrt{gL}} \qquad (7.14)$$

$$R_n = \frac{VL}{\nu} \qquad (7.15)$$

The Froude number will be equalized for model and ship based on the scale factor λ so that if the length L is λ times smaller for the model, the model will be moved with a velocity that is $\sqrt{\lambda}$ times smaller than the velocity of the ship. In practice, the Reynolds number can not be identical for ship and model.

□ The specific total resistance coefficient C_{TM} consists of the frictional resistance C_F, function of the Reynolds number, and the residuary resistance C_R, function of the Froude number and thus equal for ship and model:

$$C_{TM} = (1+k)C_{FM} + C_R \tag{7.16}$$

The frictional resistance coefficient C_F will be calculated based on the ITTC-1957 ship-model correlation line:

$$C_F = \frac{0.075}{(\log R_n - 2)^2} \tag{7.17}$$

The correlation factor or form factor k depends on the ship's form and can be calculated based on the empirical formula of Prohaska:

$$k = 0.11 + 0.128 \frac{B}{d} - 0.0157 \left(\frac{B}{d}\right)^2 - 3.10\, C_B \frac{B}{L_{PP}} + 28.8 \left(C_B \frac{B}{L_{PP}}\right)^2 \tag{7.18}$$

or can be estimated based on model test results at low speed.

□ Taking into account the equality of $C_{RM} = C_{RS} = C_R$ the total specific resistance coefficient for the ship C_{TS} will be:

$$C_{TS} = (1+k)C_{FS} + C_R + \Delta C_F + C_{AA} \tag{7.19}$$

where the additional resistance coefficients C_{AA} (air resistance) and ΔC_F (roughness allowance) can first of all be chosen to equal zero.

7.2.2.2 Correction of resistance force for oblique towing

The 1978 ITTC Performance Prediction Method is based on the prediction of ship resistance during a straight course with minimum steering to maintain this course. During harbour manoeuvres the drift angle β will not necessarily be zero or 180 degrees so that a decision has to be made how the non-dimensional longitudinal force $X'^{(\beta)}$ will be corrected. $X'^{(\beta)}$ can be written as:

$$X'(\beta) = \frac{X(\beta)}{\frac{1}{2}\rho L_{PP} d(u^2 + v^2)} = \frac{X(\beta)}{\frac{1}{2}\rho L_{PP} d u^2 \left[1 + (\tan\beta)^2\right]} = \frac{f\, X(\beta)}{\frac{1}{2}\rho L_{PP} d u^2} \tag{7.20}$$

where the factor f, depending on the drift angle β, will be used to transform the $X'^{(\beta)}$ curve to a curve $X'^{(\beta)}{}_{corr}$ which incorporates the real specific resistance of the ship at full scale C_{TS}. Two correction methods have been compared:

□ method 1: $X'^{(\beta)}{}_{corr} = f\, C_{TS}(\text{ahead}) + (1-f)\, X'^{(\beta)}$ for $|\beta| \in$ [0; 90deg]   (7.21)

$X'^{(\beta)}{}_{corr} = f\, C_{TS}(\text{astern}) + (1-f)\, X'^{(\beta)}$ for $|\beta| \in$ [90; 180deg]   (7.22)

□ method 2: $X'^{(\beta)}{}_{corr} = f\, X'^{(\beta)} \dfrac{C_{TS}(\text{ahead})}{C_{TM}(\text{ahead})} + (1-f)\, X'^{(\beta)}$ for $|\beta| \in$ [0; 90deg]   (7.23)

$X'^{(\beta)}{}_{corr} = f\, X'^{(\beta)} \dfrac{C_{TS}(\text{astern})}{C_{TM}(\text{astern})} + (1-f)\, X'^{(\beta)}$ for $|\beta| \in$ [90; 180deg]   (7.24)

Finally, method 2 has been chosen as the influence of drift angle β on $X'^{(\beta)}$ at model scale corresponds better to the influence at full scale for non-zero drift angles.

162

7.3 Sensitivity analysis

7.3.1 Sensitivity analysis: introduction

The validation of the derived mathematical models for ship manoeuvrability in shallow water will be accompanied with or replaced by a sensitivity analysis of the isolated force components related to the hull, propeller and rudder modules. Taking into account the uncertainty concerning scale effects and the restrictions imposed by the chosen test types and parameters during the execution of model tests (see preceding chapters according to hull, propeller and rudder modelling), the standard manoeuvres predicted by the mathematical model will certainly not coincide with the full scale manoeuvres. A sensitivity analysis was performed by Martinussen and Ringen in [99] and will be summarized in the section 7.3.1.1. To clearly understand the impact of velocity dependent hull forces on ship manoeuvres the theory of the dynamic stability indices can be used according to 7.3.1.2. With this information a sensitivity analysis is applied to the Esso Osaka and the fourth-generation containership D.

7.3.1.1 A classification into important and less important coefficients

An example of a sensitivity analysis can be found in [99], where a description is given of the manoeuvring prediction program and the ship-handling simulation program which is in use at MARINTEK, Norway. Although it concerns design stage and therefore deep water conditions, the ship-handling model was extended to all four quadrants of ship operation and could predict manoeuvres in the complete speed range from zero speed to service speed with sufficient accuracy. The program is modular with individual program routines for the different physical phenomena.

Table 7.4 Classification of parameters of the mathematical model according to [99]

Important parameters	Less important parameters	Parameters of small importance
linear damping coefficients Y_v, Y_r, N_v and N_r	added mass due to surge $X_{\dot{u}}$	yaw acceleration derivative $Y_{\dot{r}}$
added mass due to sway $Y_{\dot{v}}$	added moment of inertia $N_{\dot{r}}$	sway acceleration derivative $N_{\dot{v}}$
moment of inertia I_{zz}	wake factor at the propeller position w_P at service speed	coefficient for ideal fluid X_{rr}
resistance force X_{res}	propeller side force	coefficient for ideal fluid X_{vr}
sectional cross flow drag coefficient	wake factor at the rudder w_R	distance between propeller and rudder stock
section for flow separation on hull	wake factor at the rudder for the rudder area above the propeller race w_{AR}	wake at instantaneous speed as fraction of wake at service speed
open water drift angle at propeller position	wake factor at the rudder for the rudder area below the propeller race w_{BR}	thrust deduction at instantaneous speed as fraction of thrust deduction at service speed
effect of propeller on the angle of flow to the rudder or flow straightening	wake factor at the propeller w_P at instantaneous speed as function of drift angle	initial gap between rudder and hull surface
correction of lift in case of rudder with horn		increased with rudder angle of gap between rudder and hull surface
		rudder sweep angle

A sensitivity analysis was made during the development of the prediction program and contains the following method: the results of a calculation with a 20% increase and a 20% decrease in the value of a selected coefficient were compared to the results with the original value of the coefficient. The qualitative analysis was based on the results of turning circles and 10/10 and

20/20 zigzag manoeuvres and a classification into *"important parameters, less important parameters and parameters of small importance"* can be found in Table 7.4.

The linear and non-linear velocity dependent hull coefficients have an important influence on the characteristics of ship manoeuvres; the way these coefficients determine manoeuvring characteristics will be discussed in the following section. Although the modification to shallow water prediction is often restricted to the hull part of a mathematical model, Table 7.4 shows clearly that even for the deep water condition some combined hull-propeller-rudder effects like inflow angle and flow straightening are of great importance and their changes due to a decreasing water depth must be accounted for. The sensitivity analysis will focus on the important and less important parameters which belong especially to the hull and the rudder contribution.

7.3.1.2 Sensitivity of hull forces based on the dynamic stability indices

The 23rd ITTC Manoeuvring Committee [100] considered a review of the course stability problem to be helpful for a good understanding of the various parameters which determine the influence of hull forces on ship manoeuvrability. The linear equations of sway and yaw motions for a fully equipped ship model running at the self-propulsion point are:

$$Y'_v \, v' + (Y'_{\dot{v}} - m') \dot{v}' + (Y'_r - m') r' + Y'_{\dot{r}} \, \dot{r}' = -Y'_\delta \, \delta$$
$$N'_v \, v' + N'_{\dot{v}} \, \dot{v}' + N'_r \, r' + (N'_{\dot{r}} - I'_{zz}) \dot{r}' = -N'_\delta \, \delta \tag{7.25}$$

These differential equations have the following solution:

$$v' = C'_{v1} \, e^{\sigma'_1 t'} + C'_{v2} \, e^{\sigma'_2 t'}; r' = C'_{r1} \, e^{\sigma'_1 t'} + C'_{r2} \, e^{\sigma'_2 t'} \tag{7.26}$$

with

$$\sigma'_{1,2} = \frac{1}{2} \left(-\frac{B}{A} \pm \sqrt{\left(\frac{B}{A}\right)^2 - 4\frac{C}{A}} \right) \tag{7.27}$$

using following notations:

$$A = (Y'_{\dot{v}} - m')(N'_{\dot{r}} - I'_{zz}) - Y'_{\dot{r}} \, N'_{\dot{v}}$$
$$B = Y'_v \, (N'_{\dot{r}} - I'_{zz}) + (Y'_{\dot{v}} - m') N'_r - (Y'_r - m') N'_{\dot{v}} - Y'_{\dot{r}} \, N'_v \tag{7.28}$$
$$C = Y'_v \, N'_r - (Y'_r - m') N'_v$$

$\sigma_{1,2}$ are the straight-line stability indices of the ship with zero rudder angle. When the straight course of a ship is disturbed by an external force, the sway velocity v and yaw rate r will approach zero with increasing time and the ship will follow again a straight course if the real parts of $\sigma_{1,2}$ are negative. This criterion is reached if C>0 or the stability levers l'_v and l'_r relate to each other as:

$$l'_v \equiv \frac{N'_v}{Y'_v} < \frac{N'_r}{-m' + Y'_r} \equiv l'_r \tag{7.29}$$

which implies that straight-line stability is obtained if the point of application of the forces due to sway is located aft of the point of application of the forces due to yaw. While turning the damping moment due to yaw, which always resists the turning, is stabilising and the moment associated with the side force due to sway is destabilising. In addition, due to a stern trim, a common situation in ballast condition, the lever l'_v will move to the ship's stern and the ship will become more stable.

This short description of theoretical assumptions will be used in the next sections for the validation and sensitivity analysis of hull forces.

7.3.2 Tanker Esso Osaka

7.3.2.1 Comparison with full scale trials

The full scale trials of the Esso Osaka will of course be used as reference for the validation of the derived mathematical models in chapter 4 to 6. The sensitivity analysis will be executed in progress using the available manoeuvres from calibration tests to turning circles and zigzag manoeuvres. The trajectories of the midship point of the Esso Osaka for the different low speed manoeuvres are presented in Figure 7.4. While interpreting these records it must be taken into account that the tracks of the full scale trials are detected with a pre-GPS equipment and some inaccuracies can arise. Manoeuvring characteristics related to these low speed manoeuvres are summarised in Table 7.5 for the conventional turning circles, Table 7.6 for the coasting turn, Table 7.7 for the accelerating turn and Table 7.8 for the conventional zigzag manoeuvres. Small differences between Figure 7.4 and the tabular results can be found and must be dedicated to the fact that the figures are derived from the figures in [73] while no digital information was available.

Table 7.5 Conventional turning circle results versus water depth for the Esso Osaka [73]

Rudder angle	h/d	At 90 deg heading change			At 180 deg heading change	
		Advance (m)	Transfer (m)	Speed (kts)	Tactical diameter (m)	Speed (kts)
35-deg left	4.2	1005	310	4.55	895	3.08
35-deg left	1.5	915	385	4.76	1075	3.78
35-deg left	1.2	1190	555	5.18	1565	4.2
35-deg right	4.2	1015	360	4.69	925	2.94
35-deg right	1.5	990	405	4.69	1075	3.5
35-deg right	1.2	1180	705	4.55	1590	4.2

Table 7.6 Water depth effect on advance in the coasting turn (*deep, advance at 45 deg heading change), with propelled turn shown for comparison [73]

Depth/Draft	Propelled turn (m)	Coasting turn (m)
4.2	706*	1906*
1.5	990	1140
1.2	1182	1616

The characteristics in Table 7.5 must be considered with care. A decrease of the speed loss at 90 and 180 deg heading change is expected with decreasing UKC and observed for the left turn. Nevertheless, for the right turn at 90 deg heading change, the speed loss is somewhat higher at 20% UKC compared to the other water depths. This could perhaps explain the significant difference in transfer comparing the left and right turn at 90 deg heading change and 20% UKC.

Table 7.7 Accelerating turning circle results versus water depth for the Esso Osaka [73]

Rudder angle	h/d	At 90 deg heading change		At 180 deg heading change
		Advance (m)	Transfer (m)	Tactical diameter (m)
35-deg right	1.5	470	190	800
35-deg right	1.2	490	375	1060

Table 7.8 20/20 Zigzag manoeuvre indices versus water depth [73]

	Deep	Medium	Shallow
1st yaw angle overshoot, deg	9.5	11.2	7.8
maximum lateral deviation, m	460	590	505
advance, at maximum lateral deviation, m	1540	1650	1400

Before executing these low speed manoeuvres making use of the simulation models, a modification has been made to the open-water characteristics of the propeller. As the propeller mounted on the ship model differs from the propeller of the Esso Osaka the open water characteristics for thrust and torque coefficient have been altered to the characteristics of a

Wageningen B-series propeller with the same geometrical characteristics as in Table 7.2. Although the rudder at model scale is somewhat larger, only the area of the modelled rudder is scaled without any further correction.

7.3.2.2 Comparison of velocity dependent hull forces

While the 23rd ITTC Manoeuvring Committee performed a comparison for the deep water condition, a detailed comparison of lateral force and yawing moment dependence on drift angle (restricted to 8 degrees) and non-dimensional yaw rate r' (restricted to 0.9) in deep and shallow water has been discussed in the 24th ITTC [58]. The results of seven institutes are summarized of which two will also be discussed here. The Manoeuvring Committee (MC) emphasizes that before comparing results, it is important to know the exact conditions of the tests. Besides the important parameters determining the simulation model according to Table 7.4, there are also important test parameters which are:

- ❏ the *scale of the model* or the ship length which varied between 1.6 and 8m.
- ❏ *bare hull* or *appended hull* testing
- ❏ *ship* or *model self-propulsion point*: according to the 24th ITTC MC, especially in shallow water, the suction of the propeller is expected to have a major influence on the overall measured lateral force and yawing moment.
- ❏ *approach speed*: for the full scale trials the approach speed is 7 knots which is considered to fall within the "low speed" category and which is in contrast with the distinction in "low" and "ordinary" speed in chapter 5. According to the experience of FORCE Technology (Denmark, see chapter 1) less consistent results sometimes occur at lower speeds.
- ❏ *free* or *fixed* to heave and pitch
- ❏ *origin of the axis system*: centre of gravity (COG) or amidships
- ❏ *turbulence stimulation* which has an influence on the boundary layer developed on the ship model and which causes more or less important scale effects
- ❏ the *model test program* itself such as the selection of speed.

The comparison is based on the measured forces and moments in such a way that uncertainties due to the fairing process and the choice of mathematical model are avoided. Conclusions which are also important for this research are:

- ❏ The spread in the model test results is large due to differences in scale, test parameters, test facility, equipment and analysis methods. Test parameters like speed and propeller rate are spread over wide ranges, which may have an influence on particular components of the simulation model.
- ❏ If tests are executed with positive or negative drift angles only, the results are not necessarily (anti-)symmetrical.
- ❏ For the lateral force the variation with water depth (or UKC) seems to depend on the model size so that in shallow water the lateral force increases with decreasing model length.

In the above discussion, test results have been used from two institutes:

- ❏ Versuchsanstalt für Binnenschiffbau Duisburg (VBD) in Germany where tests were performed at scale 65 or a 5 m model [101];
- ❏ Bulgarian Ship Hydrodynamics Centre (BSHC), Varna, Bulgaria where an 8 m model or scale 40 was used [102].

Table 7.9 Maximum drift and yaw rate angle during captive model tests

Institute	drift angle β	yaw rate angle γ
VBD	[-24deg; 24deg]	15 deg max.
BSHC	[-20deg; 8deg], for F_n = 0.0655	15 deg max.
FHR	[-180deg; 180 deg]	50 deg max.

Model tests were performed at the ship self-propulsion point with an approach speed of approximately 7 knots full scale for the three water depths. Only the medium deep and shallow water results will be compared and it has to be taken into account that the lateral force and yawing moment from Flanders Hydraulics Research (FHR) only belong to the hull contribution according to the results obtained in chapter 4. The maximum drift and yaw rate angle realized during the tests are shown in Table 7.9.

The results published by VBD are based on the following mathematical models with non-dimensional coefficients summarised in Table 7.10:

❏ Mathematical model for pure drift:

$$Y = Y_0 + Y_v v + Y_{vvv} vvv + Y_u u$$
$$N = N_0 + N_v v + N_{vvv} vvv + N_u u$$

(7.30)

❏ Mathematical model for pure yaw:

$$Y = Y_0 + Y_r r + Y_{rrr} rrr + Y_u u$$
$$N = N_0 + N_r r + N_{rrr} rrr + N_u u$$

(7.31)

Table 7.10 Non-dimensional hydrodynamic coefficients according to VBD [101] based on $L_{pp}d$

h/d	1.2	1.5	h/d	1.2	1.5
Y'_0	-2.92E+07	5.89E+07	N'_0	-1.79E+06	4.24E+07
Y'_u	-2.15E+07	-7.77E+07	N'_u	7.76E+06	4.77E+06
Y'_v	-1.59E+10	-1.19E+10	N'_v	-8.30E+09	-2.79E+09
Y'_{vvv}	-1.40E+11	-5.45E+10	N'_{vvv}	-1.13E+10	-5.06E+09
Y'_r	2.62E+09	2.67E+09	N'_r	-1.10E+09	-6.96E+08
Y'_{rrr}	1.54E+09	6.15E+08	N'_{rrr}	-1.94E+09	-8.40E+08

The results published by BSHC are based on the following mathematical models with non-dimensional coefficients summarised in Table 7.11:

❏ Mathematical model for pure drift:

$$Y = Y_0 + Y_v v + Y_{v|v|} v|v|$$
$$N = N_0 + N_v v + N_{v|v|} v|v|$$

(7.32)

❏ Mathematical model for pure yaw:

$$Y = Y_0 + Y_r r + Y_{r|r|} r|r|$$
$$N = N_0 + N_r r + N_{r|r|} r|r|$$

(7.33)

Table 7.11 Non-dimensional hydrodynamic coefficients according to BSHC [102] based on $L_{pp}d$

h/d	1.2	1.5	h/d	1.2	1.5
Y'_0	8.95E+06	5.97E+06	N'_0	-4.47E+06	-2.98E+06
Y'_v	-1.34E+10	-4.88E+09	N'_v	-4.62E+09	-2.51E+09
$Y'_{v|v|}$	-7.15E+10	-2.83E+10	$N'_{v|v|}$	0.00E+00	5.43E+08
Y'_r	2.00E+09	1.47E+09	N'_r	-5.61E+08	-5.19E+08
$Y'_{r|r|}$	1.94E+09	3.35E+08	$N'_{r|r|}$	-9.74E+08	-4.71E+08

The coefficients Y_0 and N_0 represent the propeller induced lateral force and yawing moment during a straight motion. Although the contribution of these coefficients should be subtracted from the presented force and moment in the comparative figures, this has not been done as the influence of propeller is also incorporated in the other coefficients. Presented non-dimensional lateral force and yawing moment must nevertheless be interpreted in this way. Although the comparison in [58] was restricted to positive drift angles with a maximum of 8 degrees, in Figure 7.6 the comparison is extended to the maximum available drift angle according to the three test

programs. Differences for the drift dependency are especially found for the yawing moment with lower values for the results of BSHC (largest ship model) and both water depths. This can also be concluded for the lateral force at 50% UKC. The results of FHR lie mostly in between the results of the other institutes although differences exceed sometimes more than 20% (with the FHR-values as reference), a value which will be used during the sensitivity analysis.

For the yaw rate dependency for both lateral force and yawing moment the lowest values are determined according to the FHR models (Figure 7.7). Taking into account the propeller effect on Y and N discussed in chapter 5 and the model test results for VBD and BSHC which are based on the ship self-propulsion point, especially for the yawing moment the FHR models for Y_H and N_H could still overestimate the full scale dependency on yaw rate. The ranges in which these results vary, could explain the choices that will be made during the sensitivity analysis.

7.3.2.3 Validation based on acceleration manoeuvres

During calibration tests the speed-rpm table is determined and the main force acting on the ship is the longitudinal force with a contribution of the hull and the propeller. The rudder is kept in the midship position. Due to the asymmetry induced by a right-handed propeller a positive propeller force Y_P is expected with a point of application at the stern so that the moment N_P will be negative and the ship will turn to the left (port side). Nevertheless the results of spiral tests show a positive turning rate near zero rudder deflection for the Esso Osaka at both water depths (Figure 7.5). Some doubt about the propeller effect may arise and the results of the model tests discussed in chapter 5 will be used with different contributions of swaying and yawing.

Acceleration tests have been executed starting from dead in water and have been stopped at the moment a regime is installed with constant speed. The results for going ahead are shown in Figure 7.8. To obtain a good correspondence between trial and prediction the non-dimensional longitudinal force $X'^{(\beta)}$ has been increased with 20% for all drift angles and for both water depths. An increase of the resistance coefficient with 20% for 50% UKC gives a decrease of the velocity with 6%. The correction for the scale effect between model and ship as was proposed in 7.2.2, could lead to an underestimation of the resistance at full scale. The increase of the resistance $X'^{(\beta)}$ with 20% corresponds to a scale effect correction for the resistance with form factor k = 0 instead of 0.44 which value was obtained according to the Prohaska prediction formula. For k zero the total resistance at model scale becomes:

$$C_{TM} = C_{FM} + C_R$$

and the residuary resistance coefficient C_R which is expected to be equal for model and ship, will increase.

The wake factor w_P could also be modified as due to scale effects the wake factor at the ship's stern is expected to be smaller for the full scale ship than for the scale model. Nevertheless, a decrease of the wake factor gives a decrease of the propeller thrust (closer to the open water results) so that for manoeuvres where rudder forces will take a major part, even these rudder induced forces will be smaller. An increase of thrust deduction is not really expected based on the test results in chapter 5 where even negative values were obtained for increasing propeller loading. During validation these t_P values have been restricted to a minimum value of 0.

Finally, an increase of the resistance force or a recalculation of this force with form factor k=0 was preferred based on the following reasons:

❑ During turning circle manoeuvres, discussed in the following section, the expected speed loss has not been reached, so that an underestimation of hull resistance could be supposed.
❑ The rudder induced longitudinal force is also responsible for this speed loss and will increase with increasing contribution of the propeller slipstream (or thus propeller thrust) so that wake factor should not be diminished.

An approach speed of 7 knots is at least reached with 40 rpm at 20% UKC and 38 rpm at 50% UKC.

7.3.2.4 Validation based on turning circle manoeuvres

Conventional turning circles have been executed with both manoeuvring mathematical models which hull, propeller and rudder contributions are discussed in chapter 4 to 6. During the validation process, nevertheless, some assumptions or modifications have been made:

❑ During the determination of tabular models and derivatives the influences of test parameters of PMM tests - Froude numbers, propeller loading and rudder angles - have been incorporated as much as possible. In addition, velocity dependent hull tables have not been made (anti-)symmetrical except for the longitudinal force $X'^{(\beta)}$. This large variation of dependencies based on the available captive model tests could nevertheless cause an important asymmetry between for example a right and a left turn, as was at first obtained for the Esso Osaka at 20% UKC. Instead, based on the full scale trials the turning circles to port and starboard do not differ significantly (see Table 7.5). The question arises how this discrepancy between model and full scale must be handled. According to the MMG model an interaction coefficient C is used which incorporates the difference in interaction between the propeller and the rudder for a starboard or port turn.

Most mathematical models describing the manoeuvring behaviour of the Esso Osaka or any ship in general (e.g. the HSVA model discussed in chapter 2) only have an asymmetry effect induced by the propeller while for the hull and rudder induced forces the models have comparable values for positive and negative inflow angles and rudder angles to port or starboard. As a consequence, to reduce the asymmetry between a left and a right turn for the shallow water condition rudder dependent coefficients like wake factor $w_{R,x}$ and $w_{R,Y}$ and coefficients $K_{m,X}$ and $K_{m,Y}$ have been based on the values obtained for the negative rudder angle (combined with a positive inflow angle $\beta_R{}^*$) which gave a better result for the turn to port. The values for a_H at a positive inflow angle $\beta_R{}^*$ have been copied to the corresponding negative inflow angle. In addition, for both water depths the velocity dependent tabular models in function of drift angle and yaw rate angle have been made (anti-)symmetrical.

❑ Rudder dependent coefficients have not been made (anti-)symmetrical in the way it has been applied to the hull forces because the captive model test program will influence the derived mathematical models for this module. This is in accordance with the remarks made in 7.3.2.2 while comparing the velocity dependent hull forces of different institutes. For both water depths the coefficients describing rudder forces and correlation forces for hull-propeller-rudder combination are especially determined based on multi-modal tests of type B. These tests have a disadvantage of combining propeller rate and rudder angle in a wide range resulting into situations with test parameters for positive and negative rudder angles which are surely not identical. This was observed for the application point x'_H of the rudder induced force on the hull at 50% UKC with unrealistic values for negative rudder angles and realistic values (near $-0.4L_{PP}$) for positive rudder angles (see chapter 6; in [96] realistic data for the rudder application point can also be found). The latter has consequently been used for both rudder directions. For the other rudder coefficients a choice will be made while validating to use the coefficients related to a positive (port) or a negative (starboard) rudder angle if differences are too large.

❑ Although the propeller rate is expected to be constant during a conventional turning circle some doubts arise about the variation of the rudder angle in time. Generally a rudder is moved with a velocity of 2 to 3 deg/s. Based on the registered rudder angle variation during the conventional turn to starboard (see figure 29 in [73]) where it takes almost 60 seconds to obtain a rudder angle of 35 deg this velocity could be overestimated and will be reduced during the calculations to a value of 0.5 deg/s. For a turning circle at 20% UKC this modification (from 3 to 0.5 deg/s) gives an increase of the advance with almost 10%, while the transfer change hardly and the tactical diameter increases with 2%.

Different calculations have been executed for rudder angle variations from hard port (35 deg) to hard starboard (-35 deg) with a step of 5 deg and are summarized in Table 7.12. The trajectories

of a 35 deg left turn based on calculation 1 for both water depths are compared with the registered paths during the full scale trials in Figure 7.9. For both water depths the predicted turning circles are overestimated and differences in absolute value and percentages are shown in Table 7.13 and Table 7.15. The speed reduction which has an important influence on the swept path is smaller based on the mathematical model. The speed values of the prediction are valid for the 270 deg turn, while the speed loss for the trial is given for a 180 deg turn. It is expected that the speed will still reduce somewhat between the 180 and 270 deg turn. For all simulation test results that will be discussed further, the deduction parameter t_R for the correlation of rudder dependent longitudinal force X_R is expected to be zero. In spite of the values determined in chapter 6, the assumption of no deduction for the longitudinal rudder force F_X is necessary to obtain a speed reduction which does not differ extremely from the reduction during the trials.

Table 7.12 Description of the conditions accepted for the sensitivity analysis of model E, Esso Osaka

Calculation number	Description of the conditions
1	reference situation
2	decrease of $Y'^{(\gamma)}$ with 20%
3	decrease of $N'^{(\gamma)}$ with 20%
4	decrease of $Y'^{(\beta)}$ with 20%
5	increase of $N'^{(\beta)}$ with 20%
6	the experimental determined values for $K_{m,X}$ and $K_{m,Y}$ are replaced by the constant value 0.79 according to Table 6.6 (chapter 6)
7	decrease of wake factor $w_{R,X}$ and $w_{R,Y}$ with 20%
8	increase of a_H with 20%
9	increase of x'_H with 20%
10	a combination of calculations 2 to 5
11	a combination of calculations 6 to 9

Due to this overestimation the sensitivity analysis for hull and rudder will be based on the attempt to reduce the manoeuvring characteristics by modifying individual components of hull and rudder contributions as in Table 7.12. A variation of the propeller induced asymmetry force Y_P and moment N_P is not listed in this table as the obtained reduction is smaller than the one received for any other calculation for 20% UKC while for 50% UKC the reductions lie within the range of lowest reductions found for the other calculations. In addition, for 50% UKC the speed reduction is lower than for calculation 1.

A sensitivity analysis of acceleration derivatives is not performed as the acceleration dependent forces only take a smaller part of the total force contribution just at the start of the turning circle.

Table 7.13 Esso Osaka, at 20% UKC, comparison of expected (Exp) and calculated (Calc 1) characteristics of turning circles at an approach speed of 7 knots and 40 rpm

(a) non-dimensional characteristics, speed and turning rate

	Advance/Lpp		Transfer/Lpp		Tact.diameter/Lpp		Speed (m/s) at 270 deg		Turning rate r (deg/s)	
δ_R	Exp	Calc 1	Exp	Calc 1	Exp	Calc 1	Exp	Calc 1	Exp	Calc 1
-35	3.6	4.07	2.2	3.02	4.89	5.91	2.16	2.64	0.19	0.184
35	3.7	4.24	1.7	3.16	4.82	6.14	2.16	2.63	-0.17	-0.176

(b) required decrease (negative value) or increase (positive value) in % with calculation 1 as reference

	Advance/Lpp	Transfer/Lpp	Tact.diameter/Lpp	Speed (m/s) at 270 deg	Turning rate r (deg/s)
δ_R	Calc 1	Calc 1	Calc 1	Calc 1	Calc 1
-35	-11.6	-27.2	-17.3	-18.2	+3.3
35	-12.7	-46.2	-21.5	-17.9	-3.4

A comparison of the expected and calculated characteristics of a turning circle at an approach speed of 7 knots is shown in Table 7.13 for 20% UKC and in Table 7.15 for 50% UKC. The

turning rate for the full scale trials in these tables is taken from the spiral tests and the speed loss is given at 180 deg turn. All characteristic distances are overestimated although the turning rate for both starboard and port turn at 20% UKC differs only slightly from the one measured during the full scale spiral results. The objectives of a spiral test and a turning circle are totally different as regime is supposed during a "stationary" turning circle while the influence of the preceding is expected for the spiral test. Nevertheless, turning rates where only reported in [73] based on spiral tests.

As hull and rudder dependent forces and yawing moments are made "symmetrical" the asymmetry between a port and starboard turn at 20% UKC is caused by the propeller. The contributions of Y_P and N_P due to yaw rate angle and drift angle give opposite asymmetry effects near zero rudder angle (see chapter 5). If the tabular models $Y_{PT}(\gamma)$ and $N_{PT}(\gamma)$ are used for the drift angle dependence a propeller asymmetry effect to port is obtained and Table 7.13 modifies in Table 7.14.

Table 7.14 Esso Osaka, at 20% UKC, comparison of expected (Exp) and calculated (Calc 1) characteristics of turning circles at an approach speed of 7 knots and 40 rpm with a propeller asymmetry effect to port

(a) non-dimensional characteristic distances, speed and turning rate

δ_R	Advance/Lpp		Transfer/Lpp		Tact.diameter/Lpp		Speed (m/s) at 270 deg		Turning rate r (deg/s)	
	Exp	Calc 1	Exp	Calc 1	Exp	Calc 1	Exp	Calc 1	Exp	Calc 1
-35	3.6	4.34	2.2	3.19	4.89	6.21	2.16	2.68	0.19	0.177
35	3.7	3.97	1.7	2.97	4.82	5.79	2.16	2.56	-0.17	-0.183

Table 7.15 Esso Osaka, at 50% UKC, comparison of expected (Exp) and calculated (Calc 1) characteristics of turning circles at an approach speed of 7 knots and 38 rpm

(a) non-dimensional characteristic distances, speed and turning rate

δ_R	Advance/Lpp		Transfer/Lpp		Tact.diameter/Lpp		Speed (m/s) at 270 deg		Turning rate r (deg/s)	
	Exp	Calc 1	Exp	Calc 1	Exp	Calc 1	Exp	Calc 1	Exp	Calc 1
-35	3.1	3.92	1.3	2.55	3.31	5.05	1.80	2.13	N.A.	0.191
35	2.8	3.79	1.2	2.39	3.31	4.93	1.94	2.08	N.A.	-0.168

(b) required decrease in % with calculation 1 as reference

δ_R	Advance/Lpp Calc 1	Transfer/Lpp Calc 1	Tact.diameter/Lpp Calc 1	Speed (m/s) at 270 deg Calc 1	Turning rate r (deg/s) Calc 1
-35	-21.0	-49.1	-34.5	-15.5	N.A.
35	-26.1	-49.7	-32.8	-6.5	N.A.

For the Esso Osaka in medium deep water only velocity dependent hull forces have been made "symmetrical" while rudder coefficients have been used as derived from the model tests with a distinction for positive and negative rudder angles. Although characteristic distances are smaller for a port turn compared to a starboard turn, the turning rate is larger for a negative rudder angle. A discrepancy therefore still exists between trial and prediction as much higher yaw velocities are measured during the spiral test phases with positive rudder angle (Figure 7.5).

7.3.2.4.1 Sensitivity analysis of hull forces

According to the theory of dynamic stability (equation (7.24))

$$l'_v \equiv \frac{N'_v}{Y'_v} < \frac{N'_r}{-m'u'_1 + Y'_r} \equiv l'_r$$

the turning ability of a ship can be increased by increasing N'_v (or the tabular model $N'^{(\beta)}$) or decreasing the linear coefficients Y'_v, Y'_r or N'_r (or the corresponding tabular models $Y'^{(\beta)}$, $Y'^{(\gamma)}$ and $N'^{(\gamma)}$). A sensitivity analysis of hull forces will therefore focus on these modifications (Table 7.12) which are also motivated based on the comparative study between test results of VBD, BSHC

and FHR.

The influence of a variation of the velocity dependent tabular models for lateral force and yawing moment is presented for the advance, the transfer, the tactical diameter and for the reduction of speed due to turning in Table 7.16 for 50% UKC and in Table 7.17 for 20% UKC. The influence on the yaw velocity or turning rate is shown in Figure 7.10 for both water depths.

Table 7.16 Esso Osaka, 50% UKC, change of characteristic distances and speed (%) compared with reference condition Calc 1 during a sensitivity analysis of hull forces

δ_R (deg)	-35	-30	-25	-20	-15	-10	-5	5	10	15	20	25	30	35
change of advance (%) compared with reference condition Calc 1														
CALC	%	%	%	%	%	%	%	%	%	%	%	%	%	%
2	-3.4	-3.8	-5.9	-7.6	-7.2	-6.2	-5.9	-11.7	-9.6	-5.8	-6.1	-4.1	-4.0	-3.0
3	-12.5	-13.3	-16.3	-18.7	-17.4	-15.3	-13.7	-18.6	-16.1	-12.9	-13.0	-10.8	-10.5	-9.3
4	-3.9	-4.5	-7.1	-9.2	-8.6	-7.4	-7.6	-15.4	-11.2	-7.1	-7.4	-5.1	-5.1	-3.8
5	-9.3	-10.1	-12.7	-14.6	-13.8	-12.0	-11.6	-16.4	-13.7	-10.8	-10.9	-8.8	-8.5	-7.5
10	-25.3	-28.3	-32.0	-36.2	-36.6	-37.0	-39.7	-61.3	-34.3	-28.5	-26.9	-23.7	-23.1	-21.0
change of transfer (%) compared with reference condition Calc 1														
2	-6.0	-6.2	-10.1	-12.4	-10.6	-8.7	-7.1	-12.9	-12.3	-8.0	-9.2	-6.3	-7.6	-5.9
3	-14.8	-15.7	-20.9	-24.3	-21.1	-17.3	-14.4	-19.7	-18.3	-14.4	-14.3	-12.1	-12.5	-11.2
4	-6.9	-7.9	-12.4	-15.3	-13.2	-10.4	-9.1	-17.2	-14.8	-10.6	-11.7	-9.2	-9.8	-7.5
5	-10.5	-11.5	-16.3	-18.9	-16.5	-13.8	-12.2	-17.4	-15.8	-12.1	-12.0	-10.0	-10.6	-9.1
10	-32.5	-36.9	-41.9	-45.9	-45.5	-44.9	-44.8	-68.0	-40.3	-35.4	-32.1	-30.4	-31.8	-28.0
change of tactical diameter (%) compared with reference condition Calc 1														
2	-5.2	-5.4	-9.0	-12.4	-10.5	-8.5	-6.9	-12.8	-12.1	-7.7	-7.6	-5.8	-6.2	-4.4
3	-14.4	-15.2	-20.2	-24.2	-21.1	-17.7	-14.3	-19.6	-18.6	-14.5	-13.8	-12.3	-12.5	-10.9
4	-6.3	-6.8	-11.3	-15.3	-12.9	-10.4	-8.9	-17.0	-14.6	-10.4	-9.6	-8.0	-8.4	-6.4
5	-10.4	-11.1	-15.2	-18.9	-16.8	-13.8	-12.2	-17.3	-16.1	-12.3	-11.5	-9.9	-10.1	-8.7
10	-29.2	-34.8	-39.3	-43.1	-44.5	-44.4	-44.8	-67.8	-39.9	-34.5	-29.0	-27.8	-29.8	-25.8
change of speed (%) at 270 deg turn compared with reference condition Calc 1														
2	-3.3	-3.2	-5.9	-6.3	-3.8	-2.4	-0.6	-0.3	-4.1	-5.2	-2.9	-3.9	-3.1	-3.4
3	0.9	1.2	-2.7	-3.0	-2.8	-1.2	0.3	0.3	-4.1	-4.5	-1.6	-3.5	-2.6	-2.4
4	-4.2	-4.0	-7.0	-7.4	-4.7	-3.0	-0.8	-0.3	-5.6	-7.3	-4.1	-6.1	-4.8	-5.3
5	0.5	0.8	-2.0	-2.6	-2.5	-0.9	0.3	0.0	-3.5	-3.8	-1.6	-3.0	-2.2	-1.9
10	-6.6	-6.4	-12.9	-10.7	-11.7	-9.8	-2.8	-3.5	-15.0	-15.6	-9.8	-13.9	-14.0	-13.9

A change of yawing moment tabular models due to sway or yaw gives a larger variation in characteristic distances compared to a variation of the lateral force table for 50% UKC. A speed reduction is generally obtained although in some cases a small increase is observed. The largest changes are found for the transfer and the tactical diameter with a decrease of 15% and 11% for hard rudder to starboard, respectively hard rudder to port. Calculation 10 which combines all previous calculations, gives turning rates which are inline with the results of the spiral tests for a port turn but which overestimate these values for a starboard turn.

For the turning circles at 20% UKC the largest changes for the transfer and tactical diameter are now found for calculation 2 and 3 which implies a modification of the lateral force and yawing moment depending on drift angle.

7.3.2.4.2 Sensitivity analysis of rudder forces

The effect of rudder dependent coefficients on the manoeuvring characteristics of a turning circle will be examined while reducing the wake factor at the rudder position $w_{R,X}$ and $w_{R,Y}$ so that the inflow velocity at the rudder will increase or while increasing the propulsion dependent coefficients $K_{m,X}$ and $K_{m,Y}$ so that the contribution of the propeller slipstream will grow.

Only the correlation coefficients a_H and x'_H for the hull-propeller-rudder combination will be varied as deduction parameter t_R is supposed to be zero.

Table 7.17 Esso Osaka, 20% UKC, change of characteristic distances and speed (%) compared with reference condition Calc 1 during a sensitivity analysis of hull forces

change of advance (%) compared with reference condition Calc 1														
δ_R (deg)	-35	-30	-25	-20	-15	-10	-5	5	10	15	20	25	30	35
CALC	%	%	%	%	%	%	%	%	%	%	%	%	%	%
2	-7.2	-7.7	-9.3	-10.3	-12.5	-15.7	-16.5	-18.4	-16.2	-14.0	-10.6	-8.6	-7.1	-6.7
3	-12.0	-12.7	-14.3	-15.3	-17.4	-20.2	-19.6	-20.7	-20.7	-19.9	-16.5	-14.5	-12.8	-12.3
4	-4.2	-4.7	-6.0	-7.0	-9.1	-11.5	-13.3	-12.8	-11.1	-10.0	-7.0	-5.4	-4.4	-4.0
5	-6.7	-7.1	-8.2	-9.3	-10.8	-12.4	-13.3	-12.0	-11.7	-12.0	-9.6	-8.1	-7.0	-6.5
change of transfer (%) compared with reference condition Calc 1														
2	-10.0	-10.3	-12.6	-13.5	-15.2	-18.1	-17.3	-19.0	-18.1	-16.9	-14.2	-11.8	-9.8	-10.0
3	-12.8	-13.9	-15.9	-17.3	-19.0	-21.6	-20.0	-21.0	-21.9	-21.6	-18.5	-15.8	-14.0	-13.2
4	-5.0	-5.7	-7.2	-8.8	-10.9	-12.9	-13.8	-13.2	-12.2	-11.7	-8.8	-7.0	-5.8	-5.0
5	-6.5	-6.9	-8.7	-10.1	-11.5	-12.9	-13.4	-12.1	-12.1	-12.4	-10.2	-8.2	-7.2	-6.0
change of tactical diameter (%) compared with reference condition Calc 1														
2	-8.8	-10.8	-12.5	-13.5	-15.3	-17.8	-17.3	-18.9	-18.0	-16.8	-14.0	-11.6	-9.6	-8.7
3	-12.2	-14.0	-15.9	-16.9	-19.0	-21.5	-20.0	-20.9	-21.8	-21.4	-18.3	-15.9	-13.6	-12.2
4	-4.6	-5.9	-7.4	-8.7	-10.7	-12.7	-13.7	-13.1	-12.1	-11.6	-8.9	-6.8	-5.3	-4.7
5	-5.8	-7.1	-8.6	-9.8	-11.4	-12.9	-13.4	-12.1	-12.1	-12.5	-10.2	-8.3	-6.8	-5.6
change of speed (%) at 270 deg turn compared with reference condition Calc 1														
2	-3.4	-3.3	-3.2	-3.9	-1.7	-0.3	0.0	0.3	-0.3	-2.0	-4.2	-3.8	-4.0	-4.9
3	3.4	1.7	1.3	0.0	0.6	0.8	0.3	0.3	0.5	0.3	0.3	1.3	2.0	2.7
4	-1.5	-1.7	-1.6	-2.1	-1.1	0.0	0.0	0.3	-0.3	-1.1	-2.4	-1.9	-2.0	-2.3
5	1.5	0.7	0.6	0.0	0.3	0.5	0.3	0.3	0.3	0.3	0.3	0.6	0.7	1.1

The results of this sensitivity analysis of rudder induced forces and moment are presented in Figure 7.11 for the turning rate and in Table 7.18 and Table 7.19 for the characteristic distances and speed values. An increase of coefficients $K_{m,X}$ and $K_{m,Y}$ induces a large increase in all characteristic parameters for all rudder angles $|\delta_R|$ larger than 10 deg. Taking into account the experimental determined values (see chapter 6, $K_{m,X}$ nearby 0.6 and $K_{m,Y}$ nearby 0.7 for the maximum rudder angles) especially for the longitudinal rudder force and therefore the speed reduction an important change is realized. A modification of the other parameters gives only small changes at 50% UKC while for 20% UKC calculation 7 and 8 (decrease of w_R or increase of a_H) give almost the same variation.

The error bars for the coefficients $K_{m,X}$ and $K_{m,Y}$ at large rudder angles were restricted while wake factor at the rudder and correlation parameters a_H and x'_H could be expected to change within the ranges proposed in this sensitivity analysis. Based on the small change of turning rate at 50% UKC for rudder angles between 20 and 35 deg (Figure 7.11), a calculation was made with wake factors $w_{R,X}$ and $w_{R,Y}$ for $|\delta_R|>20$ deg based on the values for $|\delta_R|=20$ deg. This decision could seem artificial but taking into account that most simulation models do not use a distinction for wake factors based on the rudder deflection, this choice could be motivated. The results of calculation 1 and this "corrected calculation 1" are presented in Figure 7.12 for the trajectories and in Figure 7.13 for the changes of speed, course angle, lateral velocity v and turning rate r. The stationary values for v and r are almost identical while the overshoot values at the start of the turning circle are much higher. Encouraged by this result, the same calculation has been executed for the Esso Osaka at 20% UKC (Figure 7.14 and Figure 7.15). An overall increase of lateral and yaw velocity is now obtained and the trajectories of the prediction and the trial are almost the same. Nevertheless, comparing the time dependence of r during the trial (figure 29 in [73]) and the prediction a small overshoot had to be realized although none of the calculations proposed in Table 7.12 shows this overshoot. A small overshoot both in height and time is realized if all the rudder dependent coefficients and correlation parameters take constant

values. This ship behaviour and variation of turning rate were also examined based on a linear simulation model in [103], where the effect of keel clearance on linear derivatives and dynamic stability parameters is examined in navigation areas with very small UKC and even negative values referred to the water-mud interface. The absence of an overshoot is found for containership D at a draught of 13.5 m and UKC values of 15%, 26% and 32% above a solid bottom (see also section 7.3.3), while an overshoot occurs at keel clearances of 10% and lower. For the tanker Esso Osaka at 20% UKC the same variations can be found based on the manoeuvring model.

Table 7.18 Esso Osaka, 50% UKC, change of characteristic distances and speed (%) compared with reference condition Calc 1 during a sensitivity analysis of rudder forces

change of advance (%) compared with reference condition Calc 1														
δ_R (deg)	-35	-30	-25	-20	-15	-10	-5	5	10	15	20	25	30	35
CALC	%	%	%	%	%	%	%	%	%	%	%	%	%	%
6	-10.0	-11.2	-13.7	-13.3	-9.8	-4.2	3.8	-17.5	-3.3	-8.9	-14.9	-13.1	-14.1	-12.3
7	-5.0	-6.2	-6.7	-7.4	-6.9	-4.8	-7.2	-21.5	-12.5	-9.7	-9.5	-8.3	-8.7	-7.7
8	-3.4	-3.1	-3.9	-4.1	-3.3	-2.6	-1.0	-6.9	-8.1	-7.2	-8.3	-6.8	-6.6	-5.8
9	-2.2	-2.0	-2.2	-2.1	-1.8	-1.4	-0.5	-3.8	-0.8	-1.4	-2.8	-1.8	-1.1	-1.3
11	-17.7	-19.8	-21.8	-22.2	-18.7	-11.6	-6.9	-38.2	-18.9	-20.4	-24.9	-23.0	-24.2	-22.4
change of transfer (%) compared with reference condition Calc 1														
6	-12.2	-14.1	-17.5	-16.7	-11.3	-4.0	4.6	-17.6	-1.5	-6.9	-14.1	-13.1	-17.6	-14.9
7	-4.5	-6.9	-6.7	-7.2	-7.8	-5.0	-7.6	-22.3	-11.2	-6.6	-5.2	-5.0	-7.5	-7.1
8	-3.6	-3.2	-5.3	-5.1	-3.6	-2.9	-0.8	-7.1	-8.9	-7.1	-9.3	-7.7	-7.6	-6.7
9	-2.0	-1.9	-3.1	-2.2	-1.8	-1.4	-0.4	-3.8	0.2	-0.1	-0.4	-0.1	-0.1	-0.4
11	-20.4	-23.1	-25.2	-25.5	-21.0	-11.7	-6.5	-39.2	-16.2	-16.7	-20.5	-21.6	-27.2	-24.5
change of tactical diameter (%) compared with reference condition Calc 1														
6	-14.4	-16.1	-18.8	-18.4	-12.4	-4.1	4.5	-17.4	-1.2	-7.5	-14.1	-15.6	-20.3	-17.6
7	-4.8	-6.6	-6.0	-6.8	-7.7	-5.1	-7.6	-22.1	-11.0	-6.0	-3.5	-4.2	-6.9	-5.8
8	-4.0	-3.5	-5.0	-5.7	-4.0	-2.7	-0.9	-7.1	-8.7	-7.5	-8.6	-7.4	-7.5	-6.2
9	-2.4	-2.1	-2.7	-2.8	-2.0	-1.5	-0.4	-3.8	-0.1	-0.1	-0.4	-0.1	0.0	0.0
11	-21.6	-24.6	-25.8	-25.6	-21.6	-12.2	-6.5	-38.9	-15.9	-16.8	-19.4	-22.0	-28.2	-25.4
change of speed (%) at 270 deg turn compared with reference condition Calc 1														
6	-19.2	-14.1	-15.6	-10.7	-5.4	-1.2	-1.1	-0.8	-0.9	-6.6	-11.0	-20.8	-29.8	-34.1
7	-2.8	-3.2	-2.3	-1.9	-2.2	-0.9	-0.3	-0.5	-3.2	-2.4	-0.4	-1.3	-3.5	-4.3
8	-1.4	-0.8	-2.0	-2.6	-0.9	-0.3	0.0	0.0	-2.3	-3.5	-2.4	-3.5	-2.6	-2.9
9	0.0	0.4	-0.4	-0.7	-0.3	0.0	0.0	0.0	0.0	0.0	0.0	0.0	0.0	0.0
11	-23.0	-18.1	-18.0	-12.2	-8.2	-3.0	-1.4	-1.6	-5.3	-10.7	-13.1	-23.8	-36.0	-40.4

For the Esso Osaka at medium deep water and "calculation 1 corrected" the resultant trajectory is still larger than the expected one based on the full scale trials. Therefore, making use of the results for the sensitivity analysis of hull forces the manoeuvring model was modified by increasing the $N'^{(\beta)}$ table with 20% while $N'^{(\gamma)}$ was decreased with 20%. In this way, a better agreement between prediction and trial was obtained and the Esso Osaka, who seemed to be marginally unstable in medium water depth, looses some of its straight-line stability. The results of a conventional turning circle according to this modification are compared to the full scale trial results in Table 7.20. Differences still remain in the transfer and the speed loss.

This manoeuvring model at 50% UKC and the model based on "calculation 1 corrected" for 20% UKC without further modifications have been used to perform the non-conventional turning circles and the conventional zigzag manoeuvres in the following sections.

7.3.2.4.3   Accelerating turn and coasting turn

The results of an accelerating turn and a coasting turn do not only depend on the mathematical model for the ship motions but also on the applied engine model. The engine model as was

proposed in 7.2.1, was used and modified to simulate the behaviour of a steam turbine but finally it was not possible to verify if this behaviour corresponded to the time dependence of the propeller rate during the full scale trials.

Table 7.19 Esso Osaka, 20% UKC, change of characteristic distances and speed (%) compared with reference condition Calc 1 during a sensitivity analysis of rudder forces

δR (deg) CALC	-35	-30	-25	-20	-15	-10	-5	5	10	15	20	25	30	35
change of advance (%) compared with reference condition Calc 1														
	%	%	%	%	%	%	%	%	%	%	%	%	%	%
6	-21.0	-26.5	-28.8	-26.0	-28.5	-30.5	-21.7	-33.0	-35.5	-33.2	-29.2	-31.0	-28.4	-22.8
7	-8.7	-10.7	-10.6	-11.0	-12.8	-15.3	-19.9	-29.9	-18.0	-16.1	-12.4	-11.4	-11.3	-9.2
8	-7.0	-6.6	-7.4	-7.8	-8.4	-7.4	-5.3	-8.1	-8.1	-10.2	-8.6	-7.6	-6.9	-7.5
9	-3.7	-3.1	-3.2	-3.4	-3.6	-2.7	-1.1	-1.0	-2.8	-5.2	-3.9	-3.6	-3.6	-3.9
change of transfer (%) compared with reference condition Calc 1														
6	-24.1	-31.3	-34.0	-29.2	-31.2	-32.8	-22.2	-33.5	-37.7	-36.1	-32.9	-36.3	-33.8	-26.6
7	-9.1	-12.0	-11.3	-11.5	-13.3	-16.3	-20.4	-30.5	-18.9	-16.7	-13.0	-12.1	-12.2	-9.8
8	-8.2	-7.8	-8.8	-9.2	-9.5	-7.9	-5.4	-8.1	-8.7	-11.3	-10.2	-8.8	-8.5	-9.0
9	-3.7	-3.3	-3.5	-3.6	-4.0	-2.7	-1.1	-1.0	-2.9	-5.4	-4.5	-3.7	-3.6	-4.3
change of tactical diameter (%) compared with reference condition Calc 1														
6	-25.4	-33.2	-35.1	-30.3	-32.1	-32.9	-22.1	-33.4	-37.8	-36.8	-33.9	-37.7	-35.2	-27.3
7	-8.6	-12.3	-11.6	-11.3	-13.4	-16.2	-20.3	-30.3	-18.8	-16.9	-12.9	-12.2	-12.6	-9.1
8	-7.8	-8.1	-8.9	-9.3	-9.5	-7.9	-5.3	-8.1	-8.5	-11.3	-10.4	-9.1	-8.2	-8.4
9	-3.7	-3.4	-3.5	-3.7	-3.9	-2.8	-1.0	-1.0	-2.9	-5.5	-4.2	-3.9	-3.6	-4.0
change of speed (%) at 270 deg turn compared with reference condition Calc 1														
6	-15.2	-18.7	-15.5	-11.9	-7.3	-2.5	-0.8	-0.5	-2.5	-7.8	-13.6	-17.7	-21.1	-17.1
7	-3.8	-4.3	-3.2	-3.0	-1.7	-0.5	-0.5	-0.3	-0.8	-2.0	-3.0	-3.5	-4.4	-4.2
8	-0.8	-1.3	-1.3	-1.8	-0.6	0.0	0.0	0.3	0.0	-0.6	-1.8	-1.6	-1.3	-1.5
9	1.1	0.3	0.3	-0.3	0.0	0.3	0.0	0.0	0.0	0.0	0.0	0.3	0.3	0.8

Table 7.20 Esso Osaka, 50% UKC, comparison of conventional turning circle results for calculation and trial.

h/d = 1.5		At 90 deg heading change			At 180 deg heading change	
Rudder angle		Advance (m)	Transfer (m)	Speed (kts)	Tactical diameter (m)	Speed (kts)
35-deg left	trial	915	385	4.76	1075	3.78
35-deg left	calc	912	501	5.0	1064	3.87
35-deg right	trial	990	405	4.69	1075	3.5
35-deg right	calc	921	520	5.35	1056	4.28

The results for an accelerating turn are presented in Figure 7.16 and for both water depths the trajectories during the prediction are smaller. This will probably be caused by a difference in the variation of the propeller rate at the start of the accelerating turn. Qualitatively, the correspondence between trial and prediction is promising.

The time dependence of the propeller rate during a coasting turn determines the progress of this manoeuvre probably to a larger extent. Comparisons between trial and prediction for this manoeuvre have not been found in literature and will therefore not be discussed further.

7.3.2.5 Validation based on zigzag manoeuvres

A zigzag manoeuvre provides information about the yaw checking and course keeping qualities of a ship. The resultant trajectories for medium deep and shallow water are shown in Figure 7.17, while time dependencies of course angle, turning rate and rudder angle are presented in Figure 7.18. A good agreement is obtained for prediction and trial in medium deep water while some doubts arise about the correctness of the trajectory during the full scale trial in shallow water. Probably, the influence of the current is not made undone. The Esso Osaka is expected to become more directionally stable with decreasing water depth so that the variation from

medium deep to shallow water predicted by the model could be accepted.

Table 7.21 Esso Osaka, comparison of first overshoot angle of a 20/20 zigzag manoeuvre

		Medium	Shallow
1st yaw angle overshoot, deg	trial	11.2	7.8
1st yaw angle overshoot, deg	calc	13.2	5.4

A comparison of the first overshoot angles is summarized in Table 7.21. The angle is somewhat overestimated at 50% UKC and underestimated at 20% UKC.

7.3.3 Fourth generation containership

For the validation of model D at a draught of 15.0 m full scale (condition D150) and an under keel clearance of 20% no full scale tests are available. For existing containerships a few data can be found about the manoeuvring characteristics of turning circles or acceleration and stopping tests at design draught or at ballast condition. Nevertheless, these results in deep water can not be extrapolated to shallow water. During validation a comparison will be made of the mathematical model which has been developed for model D at a draught of 13.5 m above a solid bottom with a water depth of 1.26 times the draught (condition D135). This model belongs to a research project for the port of Zeebrugge where the nautical implications are studied of a muddy bottom [90].

First of all, a comparison will be made of the velocity dependent hull forces in 7.3.3.1. The acceleration derivatives are not compared as their influence on turning circles and zigzag manoeuvres is less important; for approaching manoeuvres of e.g. quay walls their influence will be important, especially in shallow water. The rudder dependent coefficients are not examined as the rudder models developed for both conditions differ to some extent so that a straightforward comparison is not possible.

As was performed for the Esso Osaka, a sensitivity analysis of hull and rudder forces will be executed to determine the dependence of an isolated component on manoeuvring characteristics of a turning circle. The variation of some components will also be determined based on the comparative study of the hull forces for the containership at both draughts.

7.3.3.1 Comparison of hull forces for model D at draughts of 13.5 and 15.0 m

Velocity dependent hull forces for model D, modified to full scale for $X'^{(\beta)}$, are compared in Figure 7.19 for the sway and yaw motion and in Figure 7.20 for the cross-coupling of lateral velocity v and yaw velocity r. The tabular models for condition D150 are made (anti-)symmetrical for the drift angle and the yaw rate angle dependence while the tabular models for χ- dependence have been modified taking into account the errors on the tabular coefficients. For condition D135 no model tests were available at 90 deg yaw rate angle.

The longitudinal force $X'^{(\beta)}$ gives for a motion ahead a smaller resistance for D150 compared to D135. This is in contrast with the larger draught and smaller UKC and must probably be dedicated to a difference in test program (applied speed ratio and model test type) and perhaps model-full scale correction. For the longitudinal force $X'^{(\gamma)}$ condition D135 represents for a motion ahead and non-zero yaw rate angles a resistance force in a much larger range of γ compared to D150. These differences will of course have their impact on the acceleration manoeuvres.

Lateral force and yawing moment due to sway or yaw can be determined with less uncertainty so that the discrepancies between D135 and D150 will also be smaller except for the lateral force due to pure yaw. Based on the results reported in chapter 4 where the influence of the test parameters of a PMM yaw test is demonstrated, the tabular form can vary remarkably around zero yaw rate angle depending on the test frequency, the yaw amplitude and the speed. The lateral force $Y'^{(\gamma)}$ for D150 had been determined based on a selection of model tests which gave accurate results for successive ranges. In addition, anti-symmetrical values are expected for either a positive turn (γ>0) or a negative turn (γ<0) what is not observed for D135 with negative

values near zero yaw rate angle for both turning directions. Lateral force $Y'^{(\beta)}$, and yawing moments $N'^{(\beta)}$ and $N'^{(\gamma)}$ are somewhat larger for D150 and the maxima for $N'^{(\beta)}$ are reached at drift angles closer to 0 for a motion ahead and closer to 180 deg for a motion astern.

The error bars are large for all tabular models depending on angle χ except for values near ±90 deg. In this range the correspondence between both conditions is good.

7.3.3.2 Validation based on acceleration manoeuvres

For the Esso Osaka the correction of resistance force $X'^{(\beta)}$ from model to full scale had to be reconsidered giving a larger value compared to the correction based on a non-zero form factor k. The same revision has been performed for containership D (tabular model in Figure 7.19 is based on this revision). The results of speed-rpm calibration tests are shown in Figure 7.21 and compared to the speed-rpm table for an S-class containership in deep water. This comparison is only indicative as propeller and hull form characteristics will probably differ. Additionally, this reference ship is chosen because of the large draught of model D compared to other fourth generation containerships. Nevertheless, compared to other 8000 TEU containerships the service speed of an S-class ship is modest.

For the Esso Osaka the decrease of ship speed with decreasing water depth was rather limited and probably an identical small change can be expected for a containership. At harbour full (or 65 rpm) the speed for D150 is almost 6% larger than for D135. This is in accordance with the differences for the longitudinal force. Turning circles for both conditions of model D will be executed at harbour full and the corresponding speed according to Figure 7.21.

Table 7.22 Description of the conditions accepted for the sensitivity analysis of containership D

Calculation number	Description of the condition
Determination of a reference condition	
1a	based on the derived mathematical model (see chapter 4, 5 and 6)
1b	"symmetry" in rudder induced coefficients: rudder angle to port as reference
1c	"symmetry" in rudder induced coefficients: rudder angle to starboard as reference
1d	constant values: $w_{R,X}=w_{R,Y}= 0.3$, $K_{m,X}= 0.75$, $K_{m,Y}= 0.85$, $a_H= 2.0$, $x'_H= -0.2$
1e	calculation 1b + change of open water curve C_{FN} for $\alpha_R = \pm20$ deg: reference situation
Sensitivity of velocity dependent hull forces	
2	decrease of $Y'^{(\gamma)}$ with 50%
3	decrease of $N'^{(\gamma)}$ with 20%
4	decrease of $Y'^{(\beta)}$ with 20%
5	increase of $N'^{(\beta)}$ with 20%
Sensitivity of rudder induced coefficients	
6	the experimental determined values for $K_{m,X}$ and $K_{m,Y}$ are replaced by the constant value 0.94 according to Table 6.6 (chapter 6)
7	decrease of wake factor $w_{R,X}$ and $w_{R,Y}$ with 20%
8	decrease of a_H with 20%
9	increase of x'_H with 20%

7.3.3.3 Validation based on turning circle manoeuvres

The same analysis has been executed as for the Esso Osaka, although a reference condition is determined before starting the sensitivity analysis. These calculations are summarized in Table 7.22 with number 1a to 1e. Calculation 1a was based on the simulation model for the hull-propeller-rudder combination as described in chapters 4 to 6. An asymmetry is observed between a port and a starboard turn with larger turning rates for a starboard than for a port turn (Figure 7.22). This is in contrast with the results for condition D135, characterized by a turning rate of -0.05 deg/s for zero rudder angle and consequently higher turning rates for a port than for a starboard turn. Besides, rudder induced coefficients for condition D135 are determined based on multi-modal tests of type A (constant propeller rate, harmonically varying rudder angle) which give more stable results than test type B used for D150. In addition, stall occurs clearly for a

starboard rudder angle and condition D150. During the captive model tests stall was indeed observed for high Froude numbers and negative rudder angles, while for rudder angles to port lateral rudder force F_Y took rather a constant value between 20 and 40 deg.

In calculation 1b wake factor at the rudder and coefficient $K_{m,X}$ and $K_{m,Y}$ for a port rudder angle have been copied to the values for a negative rudder angle. This decision has once again been made because of the difference in test program for positive and negative rudder angles. The deduction parameter t_R is again zero, while the other correlation parameters are also copied to the opposite rudder angle. For calculation 1c the rudder induced coefficients for a starboard rudder angle are preferred. For calculation 1b only the results for starboard rudder are shown in Figure 7.22 as the results for 1a and 1b are identical for a positive rudder angle. For calculation 1c only the results for port rudder are shown.

Table 7.23 Characteristic distances, speed and turning rate for reference condition 1e

δ_R	-35	-30	-25	-20	-15	-10	-5	5	10	15	20	25	30	35
Advance/Lpp	7.7	7.9	8.1	8.4	9.2	13.8	58.3	35.7	12.6	8.8	8	7.5	7.3	7.3
Transfer/Lpp	6.5	6.7	7.1	7.6	8.4	13.1	57.4	34.6	11.8	7.9	7.1	6.4	6	6.1
Tact.diam./Lpp	12.6	13.1	14.1	15.3	16.9	26.3	115.2	69.7	23.9	16	14.3	12.8	11.8	11.8
Speed (knots) at 270 deg	10.3	10.7	11.5	12.6	13.1	14	14.5	14.4	14	13.1	12.6	11.4	10.5	10.2
r (deg/s)	0.177	0.179	0.173	0.17	0.16	0.109	0.026	-0.042	-0.119	-0.168	-0.184	-0.191	-0.199	-0.191

Table 7.24 Containership D, 20% UKC, change of characteristic distances and speed (%) compared with reference condition Calc 1e during a sensitivity analysis of hull forces

change of advance (%) compared with reference condition Calc 1e														
δ_R (deg)	-35	-30	-25	-20	-15	-10	-5	5	10	15	20	25	30	35
CALC	%	%	%	%	%	%	%	%	%	%	%	%	%	%
2	-9.5	-13.2	-14.4	-11.2	-10.4	-11.6	-21.3	-20.1	-11.1	-14.8	-12.5	-16.1	-15.5	-10.6
3	-21.2	-26.6	-27.2	-22.2	-22.0	-21.8	-29.7	-28.2	-20.8	-26.0	-23.6	-30.8	-31.4	-22.9
4	-6.8	-9.5	-10.5	-8.2	-7.1	-8.0	-16.8	-19.2	-8.8	-12.6	-10.8	-13.7	-13.2	-8.7
5	-9.8	-12.1	-12.7	-10.6	-9.5	-9.9	-15.2	-17.5	-10.6	-13.2	-12.5	-14.9	-14.8	-11.4
change of transfer (%) compared with reference condition Calc 1e														
2	-12.1	-16.7	-18.4	-14.2	-13.9	-13.1	-21.9	-21.2	-12.8	-19.6	-15.8	-20.4	-19.9	-13.3
3	-23.8	-32.1	-32.1	-24.9	-25.4	-23.2	-30.3	-29.2	-22.1	-30.5	-26.4	-37.6	-39.5	-26.6
4	-8.9	-12.0	-13.3	-10.8	-9.6	-9.1	-17.3	-20.1	-10.1	-16.5	-13.4	-17.7	-17.8	-11.1
5	-11.1	-14.5	-14.8	-12.3	-10.6	-10.6	-15.4	-18.0	-11.4	-15.6	-13.9	-17.4	-18.3	-13.1
change of tactical diameter (%) compared with reference condition Calc 1e														
2	-11.2	-16.5	-17.7	-14.0	-14.0	-12.9	-21.9	-21.0	-12.5	-19.5	-14.8	-20.2	-20.3	-12.7
3	-24.8	-34.0	-33.1	-25.4	-26.3	-23.1	-30.3	-29.2	-22.2	-32.1	-27.2	-39.4	-40.3	-28.0
4	-8.3	-12.5	-13.1	-10.4	-9.5	-8.8	-17.2	-20.1	-9.8	-16.8	-12.6	-18.3	-19.3	-11.3
5	-11.5	-15.3	-15.3	-12.5	-10.4	-10.4	-15.5	-18.0	-11.2	-16.3	-13.7	-18.9	-20.7	-14.0
change of speed (%) at 270 deg turn compared with reference condition Calc 1e														
2	-1.7	-2.9	-2.4	-1.4	-2.5	-1.4	-0.4	-0.7	-1.4	-3.0	-2.0	-3.1	-4.8	-2.1
3	-3.0	-6.9	-3.6	-1.7	-2.8	-1.5	-0.4	-0.8	-1.5	-4.2	-2.8	-6.3	-7.6	-4.4
4	-1.3	-2.2	-1.7	-0.8	-1.8	-0.8	-0.3	-0.7	-1.1	-2.5	-1.5	-2.9	-5.0	-2.1
5	-1.3	-2.2	-1.5	-0.5	-1.0	-0.6	-0.3	-0.4	-0.7	-1.6	-0.9	-2.2	-5.0	-1.9

Maximum turning rates for some calculations occur at 15 and 20 deg rudder angle; therefore calculation 1d was made with constant values for all rudder induced coefficients. The variation of turning rate is now following more or less the open-water characteristics of the rudder attached to model D with maximum values for the normal rudder force coefficient C_{FN} at an inflow angle of ±15 deg. Stall occurs during the open-water tests while it is only observed in some isolated test conditions with the fully appended ship. To minimize this reduction calculation 1b has been repeated with a slightly increased value for the open-water characteristic C_{FN} for inflow angles α = ±20 deg. This calculation 1e has been chosen as reference condition for the sensitivity

analysis (Figure 7.23) and is a proof of the flexibility of this mathematical model as open-water characteristics of the individual modules can be easily modified.

The resultant characteristics for reference condition 1e are presented in Table 7.23. Time dependence of turning rate corresponds to the time dependence for the Esso Osaka at 20% UKC. No overshoot at the start of the turning circle is observed and containership D has probably an over-critical damped behaviour for either 13.5 m or 15.0 m draught at intermediate shallow water depths nearby 20% keel clearance.

7.3.3.3.1 Sensitivity analysis of hull forces

A decrease of 50% of lateral force $Y'^{(\gamma)}$ had been chosen instead of 20% because of the difference for tabular models of D135 and D150. Calculation 2, 4 and 5 in Figure 7.24 give almost the same increase of turning rate. An increase with more than 50% in turning rate is obtained for some rudder angles if non-dimensional yawing moment due to sway $N'^{(\beta)}$ is increased with 20%. This is remarkable and differs to some extent from the sensitivity analysis of the tanker Esso Osaka. In addition, calculation 3 gives turning rates nearby the turning rates obtained for model D at 13.5 m draught and 26% UKC. Changes of characteristic distances and speed are presented in Table 7.24.

Table 7.25 Containership D, 20% UKC, change of characteristic distances and speed (%) compared with reference condition Calc 1e during a sensitivity analysis of rudder induced coefficients

δ_R (deg)	-35	-30	-25	-20	-15	-10	-5	5	10	15	20	25	30	35
change of advance (%) compared with reference condition Calc 1e														
CALC	%	%	%	%	%	%	%	%	%	%	%	%	%	%
6	-28.6	-39.0	-44.9	-40.2	-45.0	-40.4	-71.1	-54.4	-38.7	-45.9	-41.3	-47.1	-41.7	-29.7
7	-7.0	-6.9	-9.0	-9.1	-8.6	-17.8	-35.1	-23.0	-14.8	-11.0	-10.1	-9.5	-7.0	-7.1
8	8.0	8.9	8.4	6.7	8.8	15.4	5.1	5.1	11.6	7.9	8.5	11.9	11.6	9.1
9	-2.9	-2.9	-2.6	-1.8	-2.1	-5.0	5.8	3.6	-4.0	-1.5	-2.2	-3.1	-3.4	-3.1
change of transfer (%) compared with reference condition Calc 1e														
6	-35.3	-47.8	-53.5	-46.8	-51.9	-44.5	-73.0	-56.2	-43.5	-53.0	-48.7	-56.9	-49.9	-37.2
7	-8.4	-7.6	-10.7	-10.9	-9.3	-18.8	-35.7	-23.7	-15.7	-13.1	-11.4	-10.9	-7.5	-8.2
8	11.1	13.5	11.1	7.6	9.8	16.1	5.4	5.5	12.5	8.7	10.8	15.6	16.4	11.4
9	-3.6	-3.7	-3.3	-2.4	-2.2	-5.3	5.9	3.7	-4.1	-1.5	-2.5	-3.4	-3.9	-3.7
change of tactical diameter (%) compared with reference condition Calc 1e														
6	-36.0	-48.7	-56.1	-48.3	-53.2	-45.4	-73.0	-56.1	-44.6	-54.4	-52.8	-58.4	-50.1	-38.5
7	-8.2	-8.0	-10.8	-10.9	-9.2	-18.4	-35.7	-23.6	-15.3	-13.5	-11.1	-11.1	-8.3	-8.4
8	11.8	14.9	12.3	7.6	9.7	16.0	5.3	5.4	12.5	8.8	11.0	16.4	16.9	12.3
9	-3.7	-4.3	-3.6	-2.3	-2.0	-5.2	5.9	3.7	-4.2	-1.6	-2.5	-3.9	-5.8	-4.3
change of speed (%) at 270 deg turn compared with reference condition Calc 1e														
6	-16.1	-19.3	-21.7	-18.0	-18.4	-11.5	-8.1	-7.0	-12.0	-19.5	-24.3	-23.0	-19.6	-18.4
7	-2.5	-2.0	-2.4	-1.8	-2.1	-2.5	-1.6	-1.5	-2.2	-2.5	-2.0	-2.7	-2.4	-2.5
8	1.1	1.8	1.4	0.5	1.2	0.7	0.0	0.1	0.8	1.2	0.6	1.7	2.6	1.7
9	-0.4	-0.5	-0.3	-0.2	-0.1	-0.3	0.0	0.0	-0.3	-0.3	0.0	-0.5	-1.3	-0.6

7.3.3.3.2 Sensitivity analysis of rudder forces

Correlation parameter a_H has been decreased with 20% because the errors on the derived values were large and based on the ratios a_H determined for individual test runs in chapter 6 smaller values could be adopted. The increase or decrease of turning rates for consecutive rudder angles is small for calculations 7 to 9. Only based on calculation 6 with a constant value for $K_{m,X}$ and $K_{m,Y}$ for all rudder angles a remarkable modification can be realized. For hard port or starboard rudder the increase is still limited and turning rates are obtained nearby the values for condition D135. For the other rudder angles the increase of coefficients K_m from the experimental determined value (see chapter 6) to 0.94 can give an increase of almost 100% for the turning rate. This change can physically not be motivated even if scale effects should play a

part but this calculation demonstrates how the turning characteristics could be easily modified for each individual rudder angle using these tabular models. Changes of characteristic distances and speed are presented in Table 7.25.

7.3.3.4 Validation based on zigzag manoeuvres

Zigzag manoeuvres have been executed for the reference condition and some calculations proposed in Table 7.22. The results for the 20/20 zigzag manoeuvre are compared to the results for condition D135 at 26% UKC. For this condition first a turning to port is executed, followed by a turning to starboard. Due to the asymmetry between a positive and negative turn the first and second overshoot angle differ considerably Table 7.26. For condition D150 the asymmetry for the reference calculation 1e and all other calculations is restricted and first a starboard turn is executed. The first and second overshoot angle only differ slightly. The overshoot angles are very small and correspond to the increased directional stability with decreasing water depth. Calculation 3 with increased tabular values for $N'^{(\beta)}$ and calculation 6 with reduced values for $K_{m,X}$ and $K_{m,Y}$ compared to the original calculation 6 give only a small increase of the overshoot angles.

Table 7.26 Containership D, comparison of overshoot angles for condition D135 and D150

Condition or calculation	1st overshoot	2nd overshoot
d = 13.5 m, 26% UKC	5.2	2.5
calculation 1e	1.70	1.80
calculation 3	1.90	2.10
calculation 6 but $K_{m,X} = 0.75$ and $K_{m,Y} = 0.85$	2.10	2.40

7.4 Concluding remarks

The validation process described in the preceding sections was restricted to the first quadrant of operation although a four-quadrant mathematical model has been determined for tanker Esso Osaka and containership D both at 20% UKC. This decision is caused by a lack of validation data based on free-running model tests or full scale trials in the four quadrants. A subjective validation performed by the pilots on the ship manoeuvring simulator is time-consuming and planned in the near future as part of a research project concerning the accessibility of 8000 TEU containerships to the port of Antwerp [104].

As little information can still be found about scale effects on hull forces (except ship resistance), propeller forces and rudder forces, especially in shallow water, a sensitivity analysis is chosen to give some insight into the dependence of ship manoeuvring characteristics on isolated components of the mathematical model. Not all the model coefficients and tabular models have been modified. The influence of wake factor at the propeller position w_P for example has not been examined as each variation of this coefficient has implications for the propeller thrust and therefore the approach speed of the considered manoeuvres. Once the calibration tests for the speed-rpm relation are executed, longitudinal hull force components, thrust deduction and wake factor are preferred to be kept unchanged.

The sensitivity analysis clearly demonstrates that a 20% change of an isolated component can give smaller or larger variations of the characteristics of a turning circle. These variations also depend on the ship's form itself. For the containership an increase of tabular model $N'^{(\beta)}$ gives an outstanding increase of the turning rate compared to a variation of the other velocity dependent hull forces, while for the tanker changes of these components are qualitatively similar.

The detailed analysis of hull, propeller and rudder dependent models executed for containership D in the chapters 4 to 6 have not been performed to the same extent during this sensitivity analysis. Nevertheless, as was concluded by Pawlowski in chapter 1, manoeuvring simulation is a *"task oriented activity"* so that depending on the field of application more functionalities (e.g. dependence into low and ordinary speed) could be added to the simulation model giving a well-founded prediction model although uncertainties still exist.

8 Conclusion and future work

The conclusions will be summarized according to the title of this research:

- Section 8.1 Selection of a mathematical model: The final form of the mathematical manoeuvring model will be presented and is considered to be applicable in both shallow and deep water conditions. A distinction is made between the different modules of a manoeuvring ship: hull forces, propeller induced forces and rudder induced forces. As the selection of the mathematical model and the determination method, i.e. experiments at model scale, are strongly linked one to another, the influence of test parameters on the different modules or coefficients will also be discussed.
- Section 8.2 Experimental determination of a mathematical model: For the determination of the mathematical model captive model tests have been used. In this section, the development of a global methodology for the execution of captive tests is discussed considering the possibilities and opportunities of the different test types, the implementation of the modular structure of the mathematical model into the experimental setup and the composition of a balanced and optimized test program.
- Section 8.3 Evaluation of a mathematical model: The quality of a mathematical model can be evaluated through the validation process. Validation is a difficult task as not much information is available for the comparison of prediction and reality. Nevertheless, introducing a sensitivity analysis, the lack of knowledge concerning e.g. scale effects can be overcome by varying individual components of the mathematical model towards the expected results for full scale.

8.1 Selection of a mathematical model

8.1.1 General conclusion

The preference is given to a modular manoeuvring model. In contrast with the formal or regression models, ship/fluid interaction is no longer treated as a black box and the hydrodynamic forces are linked to the three modules of a manoeuvring ship: hull (H), propeller (P) and rudder (R):

$$m\left(\dot{u} - vr - x_G r^2\right) = X_H + X_P + X_R$$
$$m\left(\dot{v} + ur + x_G \dot{r}\right) = Y_H + Y_P + Y_R \tag{8.1}$$
$$I_{zz}\dot{r} + mx_G\left(\dot{v} + ur\right) = N_H + N_P + N_R$$

These forces do not only incorporate the influence of the individual modules but also express the interaction effects occurring at the fully appended ship model. The modular model, based on a physical background, is highly suitable to meet the requirements of hydrodynamic models for ship simulation: functionality, validity, expandability and adjustability (chapter 1). In addition, future research concerning mathematical modelling has to develop towards a cross-reference use of mathematical models of different types like CFD (Computational Fluid Dynamic) models on the one hand and modular force models, based on (8.1), on the other. Taking into account the experimental facility at Flanders Hydraulics Research and the experience of the last decade, a co-operation with other institutes involved with CFD calculations, should be recommended for the evolution towards combined force-flow models.

As the selection of a mathematical model is based on experiments executed in medium deep and shallow water, the model is first of all suitable for the prediction of manoeuvres in conditions with restricted water depth. Nevertheless, the model can be extended to all open water conditions with or without vertical restrictions, taking into account that some phenomena do not occur in deep water so that the model dependencies can be reduced.

For the prediction of all kind of manoeuvres, i.e. low speed harbour manoeuvres and standard

manoeuvres at service speed, speed-propeller loading combinations must be available in four quadrants (Table 8.1). In addition, low speed manoeuvres will be influenced by so-called memory or time-history effects: hydrodynamic effects on the local flow at some part of the ship due to the earlier flow at another part of the ship. Nevertheless, a quasi-steady approach will be considered which means that no time dependent relations will be included in the mathematical model except the occurrence of unstable flows at the aft body in quadrants 2 and 4 due to propeller action.

Table 8.1 Four quadrants of operation for speed – propeller rate combinations

velocity u	propeller rate n	ε*	mathematical definition
positive	positive	[0; 90 deg]	quadrant 1
positive	negative	]90; 180 deg[	quadrant 2
negative	negative	[-180 deg; -90 deg]	quadrant 3
negative	positive	]-90 deg; 0 deg[	quadrant 4

8.1.2 Hull forces (chapter 4)

Hull forces are composed of <u>acceleration</u> dependent terms (8.1.2.1) and <u>velocity</u> dependent terms (8.1.2.2):

$$X_H = X_{Ha} + X_{Hv}$$
$$Y_H = Y_{Ha} + Y_{Hv}$$
$$N_H = N_{Ha} + N_{Hv}$$

(8.2)

In general, the horizontal forces and yawing moment measured during captive model tests in shallow and very shallow water conditions (h/d ≤ 1.5) are clearly influenced by the selected test parameters. In deep water conditions, this influence is negligible.

8.1.2.1 Acceleration dependent terms

The acceleration dependent terms for surge, sway and yaw are restricted to:

$$X_{Ha} = X_{\dot{u}}\dot{u}$$
$$Y_{Ha} = Y_{\dot{v}}\dot{v} + Y_{\dot{r}}\dot{r}$$
$$N_{Ha} = N_{\dot{v}}\dot{v} + N_{\dot{r}}\dot{r}$$

(8.3)

The choice of the parameters determining the harmonic captive tests (PMM tests) highly affects the most important acceleration derivatives, the added mass due to sway and the added moment of inertia due to yaw. The added mass due to sway is subject to non-stationary effects both for slender and full ships. The large scatter at low test frequencies can partly be explained based on the observation that the lateral force component due to sway acceleration becomes less important compared to the force component induced by sway velocity. In order to quantify the relative magnitude of the sway acceleration dependent terms, an angle φ was defined:

$$\phi = Arc\tan\left(\frac{Y_s^{[1]}}{Y_c^{[1]}}\right)$$

(8.4)

with $Y_s^{[1]}$ (related to sway velocity) and $Y_c^{[1]}$ (related to sway acceleration) the first harmonic sine and cosine component obtained by a Fourier analysis of the lateral force. If φ takes values near ±90 degrees, only a minor part of the total lateral force is caused by sway acceleration, so that some doubt may arise about the accuracy or the reliability of $Y_{\dot{v}}$. The accuracy can be increased by executing small amplitude and/or high frequency PMM sway tests.

Non-conventional sway tests were introduced to overcome some disadvantages of conventional tests: discontinuities in the sway acceleration at start and end and inaccuracies due to a maximum acceleration at zero velocity combination. The occurrence of non-stationary flow phenomena in the towing tank could nevertheless not be avoided so that these non-conventional sway tests should only be recommended in case the test parameters are selected with care (moderate frequency, link phase large enough).

For the added moment of inertia, especially the results for slender ships are influenced by the test parameters. On the other hand, the selected value of the yaw amplitude has an important influence on the acceleration derivative of lateral force. In addition, during a motion astern, this derivative changes sign which means that the flow at the aft body dominates the total lateral force. There are indications that conventional PMM yaw tests give more reliable results at high yaw amplitude. Finally, acceleration derivatives due to yaw are affected by combining yaw and drift, depending on the hull form and the test parameters.

8.1.2.2 Velocity dependent terms

Velocity dependent hull forces and yawing moment are presented as tabular models:

$$
\begin{aligned}
X_{Hv} &= X^{(\beta)}(u,v,0) + X^{(\gamma)}(u,0,r) + X^{(\chi)}(0,v,r) \\
Y_{Hv} &= Y^{(\beta)}(u,v,0) + Y^{(\gamma)}(u,0,r) + Y^{(\chi)}(0,v,r) \\
N_{Hv} &= N^{(\beta)}(u,v,0) + N^{(\gamma)}(u,0,r) + N^{(\chi)}(0,v,r)
\end{aligned}
\tag{8.5}
$$

The drift angle β, the yaw rate angle γ and the angle χ vary over four quadrants from -180 deg to 180 deg:

$$
\begin{aligned}
\beta &= \text{Arctan2}\,(-v,u) \\
\gamma &= \text{Arctan2}\left(\frac{rL_{PP}}{2}, u\right) \\
\chi &= \text{Arctan2}\left(\frac{rL_{PP}}{2}, v\right)
\end{aligned}
\tag{8.6}
$$

Non-dimensional expressions for the velocity dependent forces and yawing moment are formulated as follows:

❏ pure sway:

$$
X'^{(\beta)} = \frac{X^{(\beta)}}{0.5\rho L_{PP}d\left(u^2+v^2\right)},\ Y'^{(\beta)} = \frac{Y^{(\beta)}}{0.5\rho L_{PP}d\left(u^2+v^2\right)},\ N'^{(\beta)} = \frac{N^{(\beta)}}{0.5\rho L_{PP}^2 d\left(u^2+v^2\right)}
\tag{8.7}
$$

❏ pure yaw:

$$
X'^{(\gamma)} = \frac{X^{(\gamma)}}{0.5\rho L_{PP}d\left(u^2+\left(\frac{rL_{PP}}{2}\right)^2\right)},\ Y'^{(\gamma)} = \frac{Y^{(\gamma)}}{0.5\rho L_{PP}d\left(u^2+\left(\frac{rL_{PP}}{2}\right)^2\right)},
$$

$$
N'^{(\gamma)} = \frac{N^{(\gamma)}}{0.5\rho L_{PP}^2 d\left(u^2+\left(\frac{rL_{PP}}{2}\right)^2\right)}
\tag{8.8}
$$

❏ combination sway-yaw:

$$X'^{(\chi)} = \frac{X^{(\chi)}}{0.5\rho L_{PP} d\left(v^2 + \left(\frac{r L_{PP}}{2}\right)^2\right)}, \quad Y'^{(\chi)} = \frac{Y^{(\chi)}}{0.5\rho L_{PP} d\left(v^2 + \left(\frac{r L_{PP}}{2}\right)^2\right)},$$

$$N'^{(\chi)} = \frac{N^{(\chi)}}{0.5\rho L_{PP}^2 d\left(v^2 + \left(\frac{r L_{PP}}{2}\right)^2\right)} \tag{8.9}$$

Although the hull form is expected to be symmetrical compared to the Oxz plane, especially longitudinal force X_{Hv} is subject to unusual phenomena inducing non-symmetric tabular models for positive and negative inflow angles β and γ. Model tests, combining hull-propeller combination, are preferred as these tests reduce somewhat the difference between both directions. The longitudinal force $X'^{(\beta)}$ measured during oblique towing is affected by the hull form and the water depth to draught ratio. For full ships this force turns from a resistance force acting aft into a component acting forward as the drift angle increases. The involved drift angle, at which this effect occurs, is getting smaller as the water depth decreases.

The influence of test parameters on lateral force and yawing moment is restricted, except for the velocity dependent lateral force $Y'^{(\gamma)}$ both for full and slender ships. Testing parameters frequency and yaw amplitude have a significant influence, which is partly caused by an increasing sinkage occurring at maximum yaw velocity during PMM yaw tests.

To reduce the asymmetry between positive and negative inflow angles during the validation process, velocity dependent models depending on β and γ have been made (anti-)symmetrical. For the cross-coupling models depending on χ the results are only reliable for small ranges near ± 90 deg so that table values out of this range will be reduced.

8.1.3 Propeller induced forces (chapter 5)

The longitudinal force X_P acting on the ship's hull due to propeller action is the most important propeller induced force component during a forward motion and forward propeller rate. This force is proportional to the propeller thrust T and is reduced to a fraction $(1-t_P)$ with t_P the thrust deduction factor:

$$X_P = (1 - t_P)T \tag{8.10}$$

General formulations are:

❑ For the propeller thrust T and torque Q based on the open water curve $K_T(\varepsilon)$ and $K_Q(\varepsilon)$:

$$T = \rho n^2 D_P^4 K_T(\varepsilon)$$
$$Q = \rho n^2 D_P^5 K_Q(\varepsilon) \tag{8.11}$$

❑ For the hydrodynamic pitch angle ε depending on the wake factors w_P or w_Q:

$$\varepsilon = \text{Arctan2}\left((1 - w_{P,Q}(\varepsilon^*, \beta_P))U_P, 0.7\pi n D_P\right) \tag{8.12}$$

Wake factor and thrust deduction factor express the interactive phenomena between the propeller and the ship's hull and are affected by each elementary manoeuvre (drifting, yawing) and by the propeller loading. For the tanker and the containership, due to a lack of data from rotating arm tests, only the influence of lateral velocity component v (or angle $\beta=\beta_P$) will be incorporated, together with the apparent advance angle ε^*:

$$\varepsilon^* = \text{Arctan2}(U_P, 0.7\pi n D_P)$$
$$\beta_P = \text{Arctan2}(-v, u) \tag{8.13}$$

The ship velocity at the propeller position U_P depends on the total ship motion:

$$U_P = sgn(u)\sqrt{u^2 + v^2} \tag{8.14}$$

The influence of rudder angle on wake factor is not clear and will be ignored although all tests runs, even with rudder deflection, will be used for the determination; the influence will therefore be averaged. The open water characteristics of the propellers for both the containership and the tanker are estimated based on the Wageningen B-series and the wake factors w_P and w_Q will depend on these estimations using the thrust or torque identity method. A comparison of the wake factors of the containership and the tanker must be made carefully as different propellers are mounted to the ship models inducing different propeller thrust and torque values. Nevertheless, lower wake factors are observed for the containership thanks to the hull form of the aft body. Wake factors are non-zero for the first quadrant, zero (tanker E) or non-zero (container carrier D) for the second quadrant and expected to be zero for a backward motion (quadrant 3 and 4). Due to the large errors on wake factors for the ship model going astern, zero wake factors could indeed be adopted. The latter means that the inflow into the propeller, attached to the ship's hull, is identical to the inflow at a propeller in a free stream.

The influence of drift angle β on wake factors is clear: w_P and w_Q decrease with increasing drift angle $|\beta|$ so that the inflow into the propeller will better correspond to the open water inflow. The influence of propeller loading ε^* depends on the ship form with decreasing w_P values for increasing ε^* angle or decreasing propeller rate for tanker E. For the container carrier D this relationship is not clear. In addition, opposite phenomena are detected for both wake factor and thrust deduction factor considering on the one hand low speed manoeuvring and on the other ordinary speed manoeuvring. The division into low speed ($F_n < 0.016$ to 0.032) and ordinary speed is rather arbitrary for container carrier D and based on the available Froude numbers during the model tests. This distinction could consequently be optimized while selecting speed ranges for a test program and should furthermore be recommended to increase the accuracy of not only the propeller induced factors but also of the hull forces and rudder induced forces.

The influence of drift angle and propeller loading on thrust deduction t_P is not clear for both slender and full ships. Negative values for t_P are only accepted in quadrant 2 due to earlier research, so that negative values which are found for the tanker E in quadrant 1 will be equalized with zero. For all quadrants, thrust deduction is restricted to maximum values nearby 40%.

Lateral force and yawing moment due to propeller action are modelled based on:

$$Y_P = [[Y_{PT}(\beta, \varepsilon^*) + Y_{PT}(\gamma, \varepsilon^*)]F_n(K_1) + [Y_{PTA}(\beta, \varepsilon^*)][\cos(\omega(\beta, \varepsilon^*)t + \phi_Y(\beta, \varepsilon^*))]]T_P(\varepsilon^*, \beta_P)$$
$$N_P = [[N_{PT}(\beta, \varepsilon^*) + N_{PT}(\gamma, \varepsilon^*)] + [N_{PTA}(\beta, \varepsilon^*)][\cos(\omega(\beta, \varepsilon^*)t + \phi_N(\beta, \varepsilon^*))]]L_{PP}T_P(\varepsilon^*, \beta_P) \tag{8.15}$$

In this equation the following parameters denote:

- n_0: the reference propeller rate of the propeller ($n_0 = n_{MAX}$, for both model D and model E this propeller rate is 100 rpm at full scale);
- F_n: the Froude number;
- Y_{PT}: contribution of the propeller to the mean value for the lateral force (index P propeller, index T thrust);
- Y_{PTA}: contribution of the propeller to the amplitude of the oscillating lateral force (index A amplitude);
- ω: frequency of the oscillating lateral force;
- ϕ: phase of the oscillating lateral force;
- t: timestep (seconds), starting with the moment the propeller direction is changed (transition between quadrant 1 and 2 for a motion ahead and quadrant 3 and 4 for a motion astern)
- K_1: constant depending on the actual quadrant: the influence of the Froude number F_n is incorporated in the first quadrant ($F_n(K_1=1)=F_n$) while the influence is ignored in the other quadrants ($F_n(K_1 \neq 1)=1$);

❏ $T_P = T$: propeller thrust

Lateral force and yawing moment induced by the propeller represent generally a minor part in the total force equation although in shallow water conditions the following phenomena occur:

❏ For quadrant 1 and 3, characterized by the identical flow directions of wake and propeller slipstream, lateral force and yawing moment increase with increasing propeller rate. This could be compared to an extension of the total ship length due to propeller action. The importance of this effect can be illustrated as follows: at 90 deg drift angle an increase with 40% for the total lateral force at a propeller rate of 100% of the reference propeller rate is observed for tanker E at 20% UKC.
❏ For quadrant 2 and 4, characterized by two opposite flows for the ship motion and the propeller race, oscillating lateral forces and yawing moment are measured. The resultant steady component Y_{PT} and the amplitude Y_{PTA} of the oscillatory component depend on the propeller thrust, the propeller loading and the drift angle. The amplitude can take several times the propeller thrust. The period of the oscillatory component increases with increasing propeller rate and/or decreasing velocity $|U_P|$. If the inflow angle at the propeller position increases, these non-stationary phenomena are diminishing. Scale effects could play a part in this contribution although this effect has been observed at different scale ratios.

8.1.4 Rudder induced forces (chapter 6)

Forces and moment induced by the rudder are subdivided into:

❏ the longitudinal and lateral rudder force, F_X and F_Y, acting on the rudder itself;
❏ the rudder induced hull forces which are generally a fraction of forces F_X and F_Y.

Rudder forces F_X and F_Y are calculated based on the open water coefficients C_{FT} and C_{FN}, respectively tangential and normal rudder force coefficient, based on an equation where the inflow velocity into the rudder V_R and the inflow angle into the rudder α_R are the unknown parameters:

$$F_X = \frac{\rho}{2} A_R V_R^2 \{C_{FT}(\alpha_R)\cos\delta_R - C_{FN}(\alpha_R)\sin\delta_R\}$$

$$F_Y = \frac{\rho}{2} A_R V_R^2 \{C_{FT}(\alpha_R)\sin\delta_R + C_{FN}(\alpha_R)\cos\delta_R\}$$

(8.16)

with

$$V_R^2 = u_R^2 + v_R^2 \tag{8.17}$$

$$\alpha_R = \delta_R + \delta_0 + \beta_R \tag{8.18}$$

An evaluation is made of the expressions for the longitudinal and lateral components, u_R and v_R, found in literature and available for the four quadrants of operation. The longitudinal component, generally, depends on the wake factor at the rudder w_R, while the lateral component depends on the flow straightening coefficient k_{HPR}.

The effective rudder inflow velocity u_R will be expressed by a simple weighted average depending on the two flow areas (η = propeller diameter to rudder height ratio):

❏ quadrant 1: $u_R = \sqrt{\eta u_{RP}^2 + (1-\eta)u_{R0}^2}$ (8.19)
❏ quadrant 2: rudder forces neglected

❏ quadrant 3: $u_R = -\sqrt{\eta u_{RP}^2 + (1-\eta)u_{R0}^2}$ (8.20)
❏ quadrant 4:
  If $\eta u_{RP}^2 \geq (1-\eta)u_{R0}^2$ then

  $$u_R = sgn(u_{RP})\sqrt{\eta u_{RP}^2 - sgn(u_{RP})(1-\eta)u_{R0}^2}$$ (8.21)

186

If $\eta u_{RP}^2 < (1-\eta)u_{R0}^2$ then

$$u_R = -\sqrt{\left| sgn(u_{RP})\eta u_{RP}^2 - (1-\eta)u_{R0}^2 \right|} \qquad (8.22)$$

The rudder inflow velocity u_{R0} due to the wake of the ship motion and the inflow velocity u_{RP} due to the propeller race are defined as:

$$u_{R0} = (1-w_R)u \qquad (8.23)$$

$$u_{RP} = u_{R0} + (sgn\,n)\left[\left(K_m - \frac{1}{2}\right)(sgn\,n) + \frac{1}{2}\right]\left[\sqrt{u_P^2\left(1 + (sgn\,K_T)\frac{8K_T}{\pi J^2}\right)} - (sgn\,u)u_P\right] \qquad (8.24)$$

Finally, a tabular model was proposed for the wake factors $w_{R,X}$ and $w_{R,Y}$ and the propeller race dependent coefficients $K_{m,X}$ and $K_{m,Y}$, both related respectively to F_X and F_Y, function of the rudder angle δ_R and the inflow angle into the rudder β_R^*:

$$\beta_R^* = Arctan2(-(v + x_R r), u) \qquad (8.25)$$

In this concept the flow straightening coefficient k_{HPR} equals one as the influence of a locally oblique flow is incorporated in the wake factor w_R. Following this philosophy, wake factor at the propeller w_P and wake factor at the rudder w_R, which value is expected to be smaller than the value for w_P, vary similarly as function of β_P respectively β_R^*. For the ship going astern, w_R becomes zero, a value that was also accepted for wake factor w_P. In addition, the proposed model guarantees continuity at the transitions between the four quadrants.

The correlation coefficients t_R, a_H and x'_H, introduced in the MMG model, were examined and clearly depend on the water depth to draught ratio. Rudder deduction parameter t_R and the application point x'_H are function of rudder angle δ_R and inflow angle β_R^* for the first quadrant of operation, while hull coefficient a_H is determined as function of propeller loading and inflow angle β_R^*. The latter increases generally with decreasing under keel clearance while the application point shifts towards midships. The accuracy and physical meaning of t_R is questioned as negative values can be determined for the first quadrant. For the other quadrants constant values are determined.

8.2 Experimental determination of a mathematical model

All captive model tests have been executed with the fully appended hull forms without any turbulence stimulation. As a consequence, the three modules hull, propeller and rudder are interacting during each test run, although e.g. only hull-propeller interaction is expected to be determined and modelled. Models for the hull forces will therefore incorporate a small part of rudder induced forces which makes it difficult to exchange the individual modules and compose the same hull e.g. with another propeller and/or rudder. The modular form of the mathematical model should therefore be extended to the experimental setup. If a so-called modular or flexible mounting of the rudder can be realized with low costs in both time and actions, the determination of the hydrodynamic forces and moment can consequently be phased in hull-propeller interaction on the one hand and hull-propeller-rudder interaction on the other. This recommendation is hoped to improve the accuracy and the applicability of the EFD technique for the prediction of ship manoeuvres in a wide range of operational conditions.

The test program at FHR consists of conventional and non-conventional test types:
- ❑   Conventional test types are stationary tests, oscillatory tests and PMM sway and yaw tests.
- ❑   Non-conventional tests are non-conventional sway tests and multi-modal tests.

In accordance with the conclusions of comparative studies executed by the consecutive Manoeuvring Committees of the ITTC, a test program itself has an important influence on the derived mathematical model. For the container carrier D and the tanker E, summarized in chapter 3, the test programs were composed of rather arbitrarily chosen test types and test

parameters. Some conclusions, summarized below, have nevertheless led to the development of a balanced and optimized test program:

❑ PMM sway and yaw tests, characterized by a test frequency and a sway or yaw amplitude, induce non-stationary effects in the towing tank which can be determined introducing a run-out phase with a straight ahead or oblique motion. The guidelines summarized in chapter 3 and 4 must be kept in mind while selecting the test parameters. Non-stationary effects can indeed be diminished if non-dimensional test frequency is restricted to values below 4 and if sway amplitude is limited to e.g. 0.25 m. In addition, while executing tests at, at least, two frequencies the influence of this parameter can be examined.

❑ As no rotating arm facility is available, PMM yaw tests will be necessary to obtain the dependence of the tabular models on yaw rate angle. A comparison of these two test types could nevertheless give some insight into the variation of forces and moment using stationary and non-stationary test runs, a comparison that has been made for drift angle dependence.

❑ Non-stationary phenomena are also generated during multi-modal tests of type A (constant propeller rate, harmonically varying rudder angle) and type B (harmonically varying rudder angle and propeller rate). Test type B has been widely used in the test programs for the container carrier and the tanker. Test programs that have been executed after 2000, have been modified so that tests of type B are no more used for the determination of hull-propeller-rudder interaction. The harmonic variation of more than one parameter at once (exclusively for multi-modal tests of type B) must indeed be avoided and can be replaced by multi-modal tests of type A.

❑ Improvements could probably also be obtained for the multi-modal tests if the harmonically varying function should be replaced by a function with a linear variation in time of e.g. rudder angle between a minimum and a maximum value. In this way, the uneven division, typical for a harmonic function, can be avoided.

❑ The examination of non-stationary phenomena occurring in shallow water due to the opposite flows in quadrant 2 and 4, can only be executed with enough accuracy if the number of test runs is adapted to the expected frequency of oscillation taking into account the velocity and the useful tank length. The execution of test runs with three sub-runs must be avoided.

In 2004-2005 a shallow water and a deep water test program have been executed with model U, an 8000 TEU containership, at 9 combinations of draught (14.5, 13.5, 12 m) and under keel clearance (100%, 35% and 10% UKC) [105]. These test programs, summarized in detail in Appendix B, could be used as reference programs for the development of any test program that will be set up in the future, applicable for a four-quadrant determination of a mathematical manoeuvring model:

❑ The deep water and shallow water test program differ only slightly in the applied maximum model speed, maximum propeller rate and the occurrence of oscillating flow phenomena in the even quadrants; the differences are indicated with underlined values.
❑ The maximum speed is restricted to 10 (or 12) knots for the shallow water condition (10% UKC) and 16 knots for the deep water condition (35% and 100% UKC). The maximum speed astern is -4 knots.
❑ Sway acceleration derivatives are determined based on PMM sway tests, although these tests could be replaced by non-conventional sway tests. The influence of test frequency is examined with more test runs in shallow than in deep water and the sway amplitude is restricted to a small value of 0.2 m.
❑ The influence of yaw rate angle and yaw acceleration on all modules is examined based on PMM yaw tests. The maximum yaw rate angle is limited and depends on the applied yaw amplitude, test frequency and model speed (ahead or astern). For pure yawing with zero

speed, one oscillatory test has been added.

❑ Multi-modal tests of type B have been executed for the determination of hull-propeller interaction at different drift angles within a range of [-180 deg; 180 deg].

❑ For the examination of the hull-propeller-rudder combination multi-modal tests of type A with constant drift angle have been chosen. The rudder angle is harmonically varied between -40 deg starboard and 40 deg port. Based on the stationary tests that have been executed at zero and maximum rudder angle, the influence of the non-stationary character of multi-modal tests can be examined.

❑ The validation runs are added to be able to validate the derived mathematical model at model scale.

The deep water program is composed of 294 basic test runs and 58 optional runs; the shallow water program has 312 basic and 56 optional runs. These optional runs can be distinguished based on the italic form.

Generally, each test program must be adapted to the scope of the simulation model where speed ranges, ranges of drift angle and yaw rate angle, rudder angle and propeller loading must be determined not only to give test results in a broad spectrum of operation but at least to give results which correspond to the expected manoeuvres during the simulations.

The standard deviations which are determined for the tabular models during the regression analysis, give important information about the accuracy of the individual mathematical modules. Low speed manoeuvres induce smaller forces compared to high speed manoeuvres so that these forces will more suffer from measurement inaccuracies. An uncertainty analysis (UA) on model tests, as was proposed and performed by the 24th ITTC Manoeuvring Committee for the results of one institute, is not explicitly realized here although the initial impetus is given with the observed inaccuracies reported in chapter 3 considering quality control.

8.3 Evaluation of a mathematical model

The evaluation or validation of the mathematical manoeuvring models was completed using the full scale trials at low speed for the tanker Esso Osaka in shallow and medium deep water and the results of earlier research for the container carrier D, examined at a reduced draught of 13.5 m instead of 15.0 m. An exact correspondence between prediction and full scale for the Esso Osaka could not be realized on all fields (trajectories, speed reductions, etc.). This conclusion has different reasons:

❑ The registrations of full scale trials are accurate taking into account the pre-GPS equipment, but not complete. Information about the behaviour of the steam turbine and consequently the variation of propeller rate at full scale can hardly be found. This information is essential for the prediction of non-conventional manoeuvres like coasting and accelerating turning circles. The development of a realistic engine model, accompanied by the registration of engine orders and propeller rates during the full scale manoeuvres, must prevent simulations of being unrealistic especially for harbour manoeuvres, characterized by an operation in four quadrants.

❑ The lack of information about scale effects of model tests which are used to predict ship manoeuvring, still exists. Only resistance force $X'^{(\beta)}$ is scaled from model to full scale taking into account the difference in Reynolds numbers and therefore frictional resistance. Instead of estimating the influence of scale differences, a sensitivity analysis (SA) is executed to some isolated force components of the mathematical manoeuvring model.

The stability indices play an important part in the SA of hull forces. A variation of velocity dependent tabular models for lateral force and yawing moment (increase or decrease with 20%) give remarkable changes for the characteristics of a turning circle if the tables for the yawing moment are varied. For the rudder induced forces, the sensitivity of the correlation parameters a_H and x'_H is small, while the wake factor at the rudder and the coefficient K_m, which influences

the effect of the propeller slip stream, are important parameters.

As long as full scale trials are not available for the validation of a mathematical manoeuvring model, each determination of a mathematical model should be accompanied by a sensitivity analysis so that as much information as possible is available when the validation process starts making use of e.g. the experience of pilots. Although Flanders Hydraulics Research has the intention to install a device for the execution of free-sailing model tests, which could be of great help for the validation of the mathematical model on model scale, the registration of real manoeuvres of different ship type while entering a Flemish harbour or sailing on the river Scheldt could offer additional information for the validation of the real-time simulations.

The flexibility of the modular manoeuvring model, which offers the opportunity to change a module while the other modules are kept unchanged, has become clear during the validation process. A model must indeed meet the properties "functionality, validity, expandability and adjustability" before it can be a valuable tool in the prediction of ship manoeuvring for any research. As the validation for both ship types was only restricted to the first quadrant, the completion of this validation is planned to be realized with the assistance of the Flemish pilots within the framework of MOD 689/4, a research project which is a co-operation between Ghent University and Flanders Hydraulics Research [104]. The aim is to implement many functions (ship-ship interaction, bank effects) at a higher level than is now available, into the ship manoeuvring simulator to provide an up and running tool for the evaluation of existing entrance guidelines and for the training of the pilots.

Bibliography

[1]   Laforce E.

        Scheepsmanoeuvreersimulator: werking en toepassingen.
        Het ingenieursblad, oktober 1992.

[2]   Vantorre M.

        Waterbouwkundig Laboratorium installeert manoeuvreer-sleeptank.
        Het ingenieursblad, oktober 1992.

[3]   http://www.imo.org

[4]   http://ittc.sname.org

[5]   Abkowitz M.A.

        Lectures on ship hydrodynamics – Steering and manoeuvrability.
        Hydro- of Aerodynamisk Laboratorium, Report No. Hy-5. Lyngby, May 1964.

[6]   Ankudinov V., Kaplan P., Jacobsen B.K.

        Assessment and principal structure of the modular mathematical model for ship
        maneuverability prediction and real-time maneuvering simulations.
        Prepared for delivery at MARSIM '93, St. John's, Newfoundland, Canada, September
        1993.

[7]   Dand I.W.

        On modular manoeuvring models.
        International Conference on Ship Manoeuvrability. Prediction and achievement, Vol. 1,
        Paper 8, Londen, 1987.

[8]   Norrbin N.H.

        Theory and observations on the use of a mathematical model for ship manoeuvering in
        deep and confined waters.
        Swedish State Shipbuilding Experimental Tank, Publication No. 68. Göteborg, 1971.

[9]   Asinovsky V, Landsburg A.C., Hagen Grant R.

        Ship maneuverability analysis using the differential approach.
        International Conference on Ship Manoeuvrability. Prediction and achievement, Vol. 1,
        Paper 9, Londen, 1987.

[10]   Basin A.M.

        Propulsion and Maneuverability of Ships.
        Publishing House "Transport", 1968.

[11]   Fediaevsky K.K., Sobolev G.V.

        Maneuverability of Ships.
        Publishing House "Sudpromgiz", 1963.

[12]   Ogawa A. and Kasai H.

        On the mathematical model of manoeuvring motion of ships.
        International Shipbuilding Progress, Volume 25, No. 292, 306-319, December 1978.

[13]   Oltmann P. and Sharma S.D.

        Simulation of combined engine and rudder maneuvers using an improved model of hull-
        propeller-rudder interactions.
        Fifteenth Symposium on Naval Hydrodynamics, 1984 (proceedings published in 1985).

[14] Kose K., Misiag W.A., Inoue K.

Can one have a general, standardized maneuvering model?
IMSF Workshop, Florida, USA, 1995.

[15] Vantorre M.

Nauwkeurigheidsoverwegingen en optimalisatie van de parameterkeuze bij gedwongen maneuvreerproeven met scheepsmodellen.
Universiteit Gent, 1989.

[16] Pawlowski J.S.

Hydrodynamic modelling for ship manoeuvring simulation
International Conference on Marine Simulation and Ship Manoeuvrability, MARSIM'96, Denmark, September 1996.

[17] Bailey P.A., Price W.G., Temarel P.

A unified mathematical model describing the manoeuvring of a ship travelling in a seaway.
Transactions of the Royal Institution of Naval Architects, Vol. 140, Part B, pp. 131-149, 1998.

[18] PIANC, 1992

Capability of ship manoeuvring simulation models for approach channels and fairways in harbours.
Report of Working Group no. 20 of Permanent Technical Committee II, Supplement to PIANC Bulletin No. 77, 49 pp.

[19] Yasukawa H.and Kobayashi E.

Shallow water model experiments on ship turning performance.
Mini Symposium on Ship Manoeuvrability, pp. 71-83, Fukuoka, Japan, 26 May 1995.

[20] Gronarz A.

Rechnerische Simulation der Schiffsbewegung beim Manövrieren unter besonderer Berücksichtigung der Abhängigkeit von der Wassertiefe.
Dissertation zur Erlangung des akademischen Grades Doktor-Ingenieur, 1997.

[21] International Conference on Marine Simulation and Ship Maneuverability, MARSIM'03

Conference Proceedings, Volume I-III, Kanazawa, Japan, August 2003.

[22] Dand I.

Low speed manoeuvring criteria: some considerations.
International Conference on Marine Simulation and Ship Manoeuvrability, MARSIM'03, Volume I, Kanazawa, Japan, 2003.

[23] Hwang W-Y, Jakobsen B.K., Barr R.A., Ankudinov V.K., Fuller N.R., Vest L.C., Morris M.A., McGovern A.W., Landsburg A.C.

An exploratory study to characterize ship maneuvering performance at slow speed.
International Conference on Marine Simulation and Ship Manoeuvrability, MARSIM'03, Volume III, pp. RC-16-1 to RC-16-14, Kanazawa, Japan, 2003.

[24] Harvald SV.Aa.

Wake and thrust deduction at extreme propeller loadings.
Publications of the Swedish State Shipbuilding Experimental Tank, Nr. 61, Göteborg, 1967.

[25] Tanaka S.

On hydrodynamic forces acting on a ship at larger drift angles.
Transactions of the West-Japan Society of Naval Architects No. 91, pp. 81-94, 1996.

[26] Karasuno K., Igarashi K.

A physical-mathematical model of hydrodynamic forces and moment acting on a hull during large drifting and turning motion under the conditions of slow speed.
International Conference on Marine Simulation and Ship Manoeuvrability, MARSIM'93, St. John's, Newfoundland, Canada, September 1993.

[27] Kose K., Hinata H., Hashizume Y., Futagawa E.

On a new mathematical model for manoeuvring motions of ships in low speed.
Japanese Society of Naval Architects, Vol. 155, June 1984.

[28] Khattab O.

Ship handling in harbours using real time simulation.
International Conference on Ship Manoeuvrability. Prediction and achievement, Vol. 1, Paper 11, London, 1987.

[29] Kobayashi E., Asai S.

A simulation study on ship manoeuvrability at low speeds.
International Conference on Ship Manoeuvrability. Prediction and achievement, Vol. 1, Paper 10, London, 1987.

[30] Kose K., Misiag W.A., Hashizume Y., Nogami S., Ishioka Y.

A practical approach to the mathematical model of ship maneuvering in harbours.
Ship manoeuvring symposium, Ilawa, Poland, 1995.

[31] Goodman A., Gertler M., Kohl R.

Experimental techniques and methods of analysis used at Hydronautics for surface-ship maneuvering predictions.
11th ONR Symposium on Naval Hydrodynamics. Proceedings, pp. I.55-113, London, 1976.

[32] Roseman D.P. (Editor)

The MARAD systematic series of full-form ship models.
The Society of Naval Architects and Marine Engineers, Jersey City, 1987.

[33] Barr R.A.

Fax transmittal from Hydronautics Research, Inc., September, 2003

[34] Bishop R.E.D., Burcher R.K., Parkinson A.G., Price W.G.

Oscillatory testing for the assessment of ship maneuverability.
Proceedings of the 10th Symposium on Naval Hydrodynamics, pp. 109-130, Boston, 1974.

[35] Bishop R.E.D., Burcher R.K., Price W.G.

The determination of ship manoeuvring characteristics from model tests.
Transactions of the Royal Institution of Naval Architects, Supplement Papers, Vol. 117, pp. 215-231, July 1975.

[36] Imlay

The complete expressions for added mass of a rigid body moving in an ideal fluid. 1961.

[37] Karasuno K., Maekawa K.

An advanced physical-mathematical model of ship-hull hydrodynamic forces deduced from simplified vortex model during manoeuvring motion in slow speed.
International Conference on Marine Simulation and Ship Manoeuvrability, MARSIM'96, Copenhagen, Denmark, September 1996.

[38] Karasuno K., Maekawa K., Saito Y., Ikeda H.

An element-type mathematical model derived from a simplified 3D vortex system on ship-hull hydrodynamic forces during slow-speed maneuvering motion.
International Conference on Marine Simulation and Ship Manoeuvrability, MARSIM2000, Orlando, USA, May 2000.

[39]   Harvald S. A.

Wake and thrust deduction at extreme propeller loadings for a ship running in shallow water.
Trans RINA Vol 119,1977.

[40]   Vantorre M.

Stationary and non-stationary open water rudder tests.
Mini Symposium on Prediction of Ship Manoeuvring Performance (Editor: Kijima, K.), pp. 103-111, Tokyo, 2001.

[41]   Molland A.F., Turnock S.R.

The prediction of ship rudder performance characteristics in the presence of a propeller.
International Conference on Manoeuvring and Control of Marine Craft, MCMC'92, Southampton, UK, July 1992.

[42]   Molland A.F., Turnock S.R.

Prediction of ship rudder-propeller interaction at low speeds and in four quadrants of operation.
International Conference on Manoeuvring and Control of Marine Craft, MCMC'94, Southampton, UK, September 1994.

[43]   Molland A.F., Turnock S.R., Wilson P.A.

Performance of an enhanced rudder force prediction model in a ship manoeuvring simulator.
International Conference on Marine Simulation and Ship Manoeuvrability, MARSIM'96, Copenhagen, September 1996.

[44]   Kuiper G.

The Wageningen Propeller Series.
MARIN publication 92-001, May 1992.

[45]   Molland A.F., Turnock S.R.

The effect of hull on the manoeuvring performance of rudders.
International Conference on Ship Motions and Manoeuvrability, London, February 1998.

[46]   Kose K.

On a new mathematical model of maneuvering motions of a ship and its applications.
International Shipbuilding Progress, Vol. 29, pp. 205 – 220, August 1982.

[47]   The Research Committee of Dynamic Performance, Manoeuvring and Control Section.

Prediction of manoeuvrability of a ship.
Bulletin of the Society of Naval Architects of Japan, No. 668, 1985.

[48]   Kijima K., Nakiri Y.

On the practical prediction method for ship manoeuvrability in restricted water.
Transactions of the Society of Naval Architects of West Japan, No. 107, March 2004.

[49]   Kijima K.

Manoeuvrability of ship in confined water.
International Conference on Ship Manoeuvrability. Prediction and Achievement, Vol. 1, London, 1987.

[50]   Fujii J., Tsuda T.

Experimental researches on rudder performance (2) & (3) (in Japanese).
Journal of the Society of Naval Architects of Japan, Vol. 110 and 111. December 1961,
June 1962.

[51]   Yoshimura Y., Nomoto K.

Modeling of manoeuvring behaviour of ships with propeller idling, boosting and reversing.
Journal of the Society of Naval Architects of Japan, Vol. 144, December 1978.

[52]   Kijima K., Tanaka S., Furukawa Y., Hori T.

On a prediction method of ship manoeuvring characteristics.
International Conference on Marine Simulation and Ship Manoeuvrability, MARSIM'93,
St. John's, Newfoundland, Canada, pp. 285 – 294, September 1993.

[53]   Hirano M., Takashina J., Moriya S.

A practical prediction method of ship maneuvring motion and its application.
International Conference on Ship Manoeuvrability. Prediction and Achievement, Vol. 1,
London, 1987.

[54]   Jensen P.S., Chislett M.S., Römeling J.U.

DEN-Mark 1 – An innovative and flexible mathematical model for simulation of ship
manoeuvrability.
International Conference on Marine Simulation and Ship Manoeuvrability, MARSIM'93,
St. John's, Newfoundland, Canada, pp. 285 – 294, September 1993.

[55]   Chislett M.S.

A generalized math model for manoeuvring.
International Conference on Marine Simulation and Ship Manoeuvrability, MARSIM'96,
Copenhagen, Denmark, 1996.

[56]   Smitt L.W. and Chislett M.S.

Large amplitude PMM tests and manoeuvring predictions for a Mariner Class Vessel.
Proceedings of the 10th Symposium on Naval Hydrodynamics, Boston, 1974.

[57]   Bevernage E.

Implementatie van het rudder loading concept in de wiskundige modellering van
roerkrachten voor een manoeuvrerend schip.
Master thesis, Universiteit Gent, September 2005.

[58]   The Manoeuvring Committee of the 24th ITTC

Final report and recommendations. United Kingdom, September 2005.

[59]   Grim O., Oltmann P., Sharma S.D., Wolff K.

CPMC - A novel facility for planar motion testing of ship models.
Proceedings of the 11th ONR Symposium on Naval Hydrodynamics, pp. 115-131,
London, United Kingdom, 1976.

[60]   Vantorre M., Eloot K.

Requirements for standard harmonic captive manoeuvring tests.
Fourth IFAC Conference on Manoeuvring and Control of Marine Craft, pp. 93-98, Brijuni,
Croatia, September 1997.

[61]   22nd International Towing Tank Conference Proceedings

Final report and recommendations, Seoul and Shangai, 1999.

[62]   23rd International Towing Tank Conference Proceedings

Final report and recommendation, Venice, 2002.

[63]   International Towing Tank Conference, Quality Systems Manual

http://ittc.sname.org/manual.htm

[64]   Vantorre M.

Captive Maneuvering Tests with Ship Models: A Review of Actual Practice, Based on the 22nd ITTC Maneuvering Committee Questionnaire
Conference on Ship Manoeuvrability and Marine Simulation, MARSIM2000, Orlando, USA.

[65]   Van Leeuwen G.

Enkele problemen bij het ontwerpen van een horizontale oscillator.
Rapport No. 225, Lab. Scheepsbouwkunde, Technische Hogeschool Delft, 1969.

[66]   Vantorre M.

Accuracy and optimization of captive ship model tests.
5th International Symposium on Practical Design of Ships and Mobile Units.
Vol. 1, pp. 1.190-230. Elsevier Applied Science, London/New York, 1992.

[67]   Wehausen J.V. and Laitone E.

Surface waves.
Handbuch der Physik. Band IX: Strömungsmechanik III, pp. 446-778. Springer Verlag, Berlin, 1960.

[68]   Van Leeuwen G.

The lateral damping and added mass of an oscillating ship-model.
Shipbuilding Laboratory, Technological University Delft, Publication No. 23, 1964.

[69]   Nomoto K.

Ship response in directional control taking account of frequency dependent hydrodynamic derivatives.
Proceedings of the 14th International Towing Tank Conference, Vol.2 pp. 408-413.
National Research Council, Canada, Ottawa, 1975.

[70]   Milanov E.

On the use of quasisteady PMM-test results.
International Symposium on Ship Techniques, Rostock, 1984.

[71]   Vantorre M.

Towing tank for manoeuvres in shallow water, co-operation Flanders Hydraulics – Ghent University. Internal document, Flanders Hydraulics Research.

[72]   Eloot K.

Mod 673: Panama Canal: Conceptual Study Post-panamax locks: Fast-time simulator study for the optimization of the alignment to the post-panamax locks, 2002.

[73]   Crane C.L.

Maneuvering Trials of a 278 000-DWT Tanker in Shallow and Deep Waters.
SNAME Transactions, Vol. 87, pp. 251-283, 1979.

[74]   Vantorre M.

Genereren, valideren en uitwerken van gedwongen manoeuvreer- en zeegangsproeven.
Universiteit Gent, 1997.

[75]   The Specialist Committee on Procedures for Resistance, Propulsion and Propeller Open Water Tests

Proceedings of the 23rd International Towing Tank Conference (ITTC), pp. 369-377, Venice, 2002.

[76]   Gill A.D. and Price W.G.

196

Determination of the manoeuvring derivatives of a ship model using a Horizontal Planar Motion Mechanism in a Circulating Water Channel.
Transactions of the Royal Institution of Naval Architects, Vol. 119, pp. 161-176, 1977.

[77]   Gill A.D. and Price W.G.

Experimental evaluation of the effects of water depth and speed on the manoeuvring derivatives of ship models.
Transactions of the Royal Institution of Naval Architects, Vol. 120, pp. 149-160, 1978.

[78]   Mikelis N.E. and Price W.G.

Calculations of acceleration coefficients and correction factors associated with ships manoeuvring in restricted waters: comparisons between theory and experiments.
Transactions of the Royal Institution of Naval Architects, Vol.?, 1980.

[79]   Bailey P.A., Hudson D.A., Price W.G., Temarel P.

Theoretical and experimental techniques for predicting seakeeping and manoeuvring ship characteristics.
International Conference on Ship Motions and Manoeuvrability, London, February 1998.

[80]   Bailey P.A., Hudson D.A., Price W.G., Temarel P.

The measurement and prediction of fluid actions experienced by a manoeuvring vessel.
International Symposium and Workshop on Forces acting on a Manoeuvring Vessel, Val de Reuil, France, September 1998.

[81]   Karasuno K., Okano S., Miyoshi J., Maekawa K.

Prediction of ship's hull hydrodynamic forces and maneuvering motions at slow speed based on a component-type mathematical model.
International Conference on Marine Simulation and Ship Manoeuvrability, MARSIM'03, Kanazawa, Japan, August 2003.

[82]   Boggs P.T., Byrd R.H., Rogers J.E., Schnabel R.B.

User's Reference Guide for ODRPACK Version 2.01 Software for Orthogonal Distance Regression.
Center for Computing and Applied Mathematics, U.S. Department of Commerce, June 1992.

[83]   Eloot K., Vantorre M.

Non-conventional captive manoeuvring tests.
International Workshop on Ship Manoeuvrability at the Hamburg Ship Model Basin, Paper No. 3, Hamburg, Germany, October 2000.

[84]   Vantorre M., Eloot K.

Hydrodynamic phenomena affecting manoeuvres at low speed in shallow navigation areas.
Proceedings of the 11th International Harbour Congress, pp.535-546, Antwerp, Belgium,1996.

[85]   Eloot K., Vantorre M.

Development of a tabular manoeuvring model for hull forces applied to full and slender ships in shallow water.
International Conference on Marine Simulation and Ship Manoeuvrability, MARSIM'03, Kanazawa, Japan, August 2003.

[86]   Nakatake K., Yoshitake A., Shimomichi Y., Yamamoto T.

Measurement of wake distributions behind ships with yaw angle.
Transactions of the West-Japan Society of Naval Architects, No. 91, 1996.

[87]   Kijima K., Murakami M., Katsuno T., Nakari Y.

On the hydrodynamic force acting on ship in accelerating and decelerating motions.
Transactions of the West-Japan Society of Naval Architects, No. 66, August 1983.

[88]   Ch'ng P., Renilson M.R.

The effect of astern revolutions on manoeuvring behaviour.
The Naval Architect, pp. E35-E36, 1993.

[89]   Eloot K. and Heylbroeck B.

Efficiënt simuleren van schroef-roer-romp-interactie.
Afstudeerwerk ingediend tot het behalen van de academische graad van burgerlijk
scheepsbouwkundig ingenieur. Academiejaar 1994-1995. Universiteit Gent.

[90]   Delefortrie G., Laforce E., Vantorre M.

Bepaling van de nautische bodem in de haven van Zeebrugge: Onderzoek nautische
implicaties. Fase B: Eigenlijke onderzoeksfase: Eindrapport. Antwerpen, oktober 2004.

[91]   Ch'ng P.W., Doctors L.J., Renilson M.R.

A method of calculating the ship-bank interaction forces and moments in restricted
waters.
International Shipbuilding Progress, Vol. 40, No. 421, pp. 7-23, 1993.

[92]   Delefortrie G., Vantorre M., Eloot K.

Modelling navigation in muddy areas through captive model tests.
Journal of Marine Science and Technology, Vol. 10, No.4, pp. 188-202, 2005

[93]   Eloot K.

Ontwikkeling van een mathematisch manoeuvreermodel voor scheepsmanoeuvres in
ondiep water.
Interimrapport voor de doctoraatsopleiding, Universiteit Gent, juni 1999.

[94]   Eloot K., Vantorre M.

Prediction of low speed manoeuvring based on captive model tests: opportunities and
limitations.
31st Annual General Meeting of IMSF, september 2004, Antwerp, Belgium.

[95]   Society of Naval Architects and Marine Engineers (SNAME)

Principles of Naval Architecture, Volume III, Motions in waves and Controllability.

[96]   Oltmann P., Wolff K., Müller E; and Baumgarten B.

Zur Korrelation Modell-Großausführung bei Manövrierversuchen auf tiefem und flachem
Wasser.
Jahrbuch STG, Band 80, pp. 217-245, 1986.

[97]   International Maritime Organization, Maritime Safety Committee (MSC)

Explanatory notes to the Standards for ship manoeuvrability.
Resolution MSC.137(76), December 2002

[98]   23rd International Towing Tank Conference, The Specialist Committee on Esso Osaka

Final report and recommendations to the 23rd ITTC, Venice, 2002.

[99]   Martinussen K., Ringen E.

Manoeuvring Predicition During Design Stage
International Workshop on Ship Manoeuvrability at the Hamburg Ship Model Basin,
paper No. 8, October 2000.

[100]   23rd International Towing Tank Conference, The Manoeuvring Committee

Final report and recommendations to the 23rd ITTC, Venice 2002.

[101]   Gronarz A., Müller E.

Manövrierverhalten völliger schiffe auf begrenzter wassertiefe
Versuchanstalt für Binnenschiffbau, Duisburg, August 1988.

[102]   Bogdanov P. et al.

"Esso Osaka" tanker manoeuvrability investigations in deep and shallow water, using
PMM.
International Shipbuilding Progress, February 1987.

[103]   Delefortrie G., Vantorre M., Eloot K.

Linear manoeuvring derivatives in muddy navigation areas.
RINA, Transactions 2004 Part A4 – International Journal of Maritime Engineering.

[104]   Eloot, K., Vantorre, M.

Overeenkomst 16EB/05/06: technische bepalingen voor de uitvoering van de
aannemingsopdracht van diensten betreffende de op- en afvaartregeling voor 8000 (en
meer) TEU containerschepen tot de haven van Antwerpen bij een maximale diepgang
van 145dm.
Onderzoeksproject UGent 174C8905, WL Mod. 689/4. Gent / Antwerpen, mei 2005.

[105]   Eloot K., Vantorre M. et al.

WL Mod. 749, Het uitvoeren van proeven en opstellen van wiskundige
manoeuvreermodellen voor 8000 TEU containerschepen voor de toegang tot de
Vlaamse havens. Deelopdracht 1, oktober 2004.
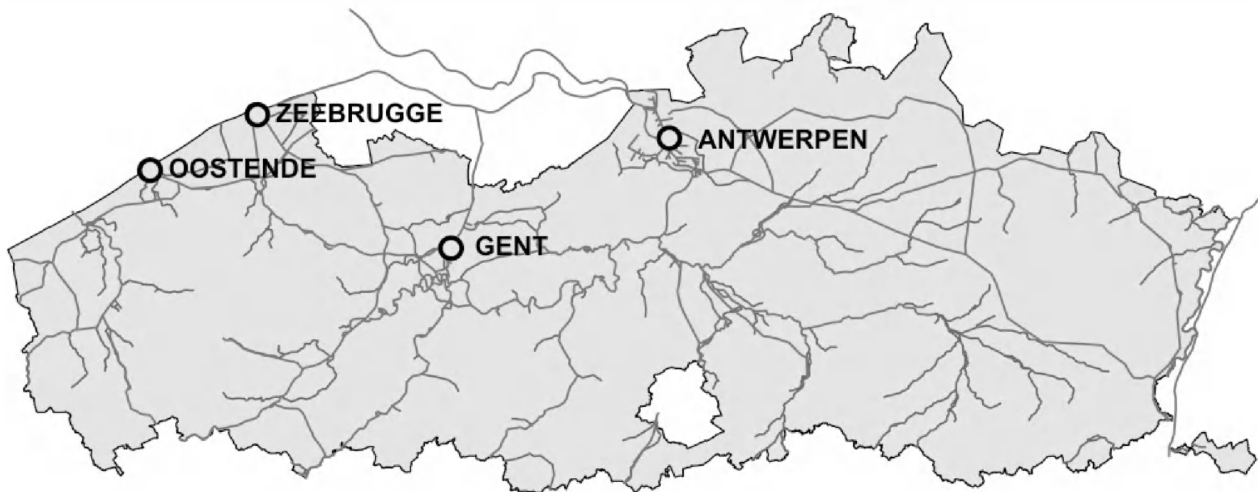
Overview of the areas where the four major ports of Flanders are situated

Figure 1.1 Ports at the coastline (left side): Port of Zeebrugge (top), Port of Oostende (bottom) and inland ports (right side): Port of Antwerp/Antwerpen (top), Port of Ghent/Gent (bottom)
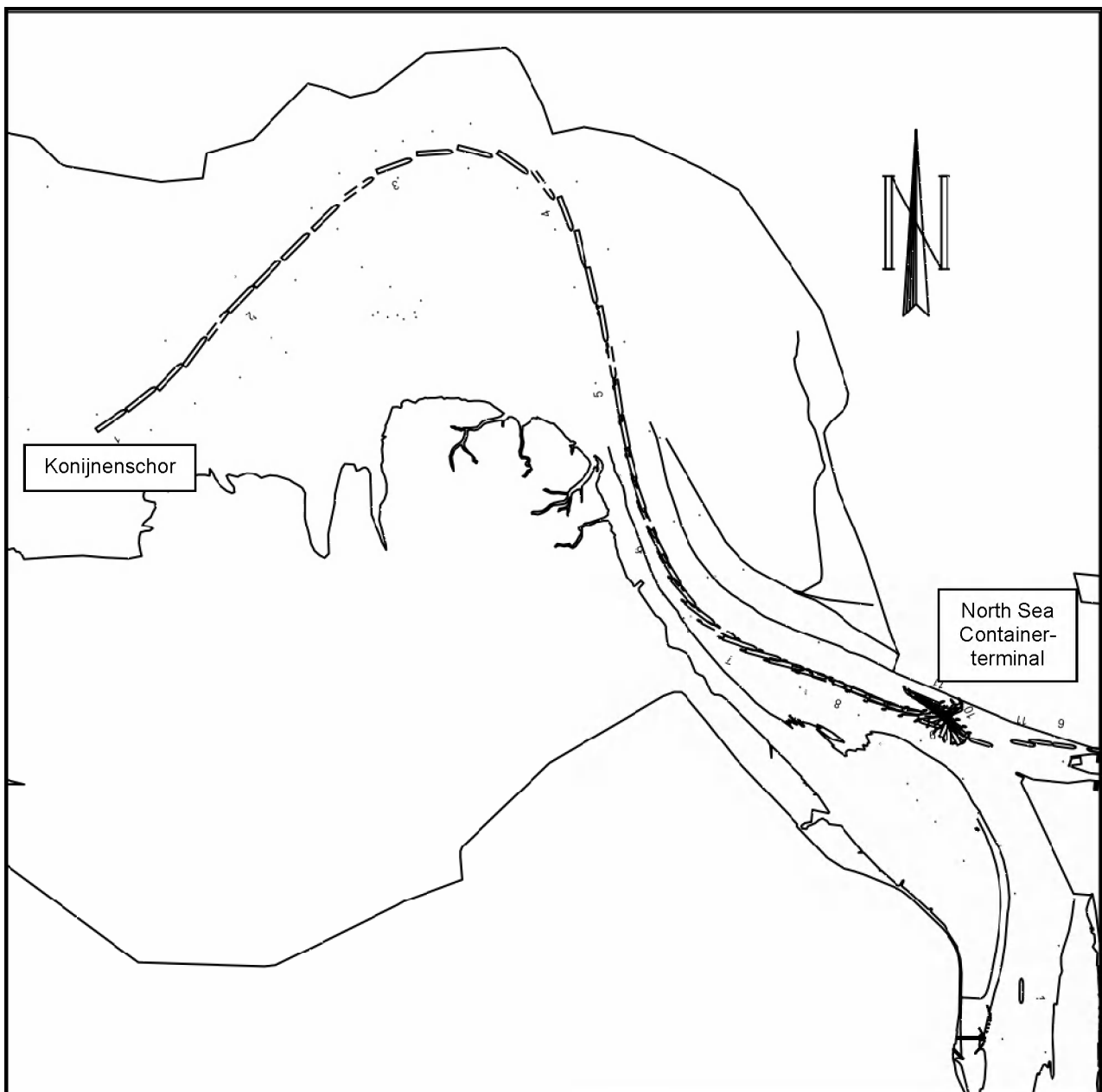
Skagen Maersk at the North Sea Container terminal   Skagen Maersk leaves the port of Antwerp

Figure 1.2 Model 689. Accessibility of S-class containerships to the port of Antwerp: run from Konijnenschor to the North Sea Containerterminal.

going ahead

stopping from
headway

going astern

swinging
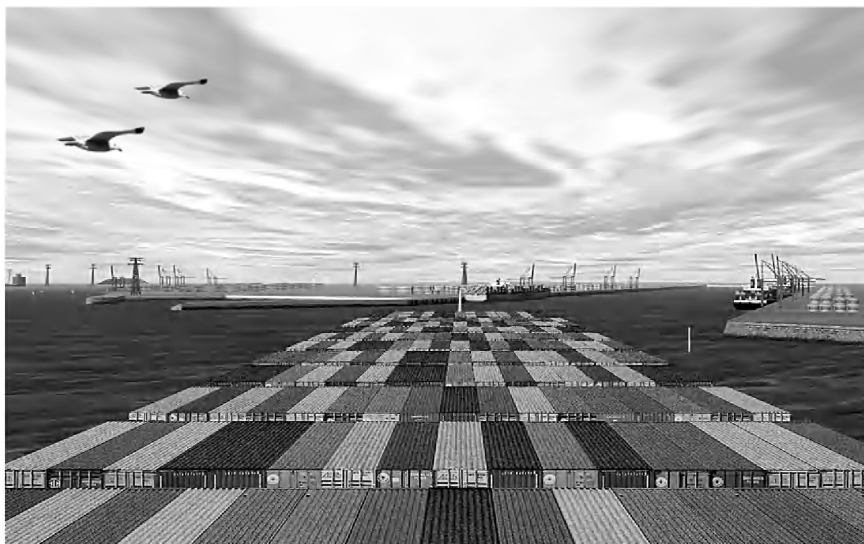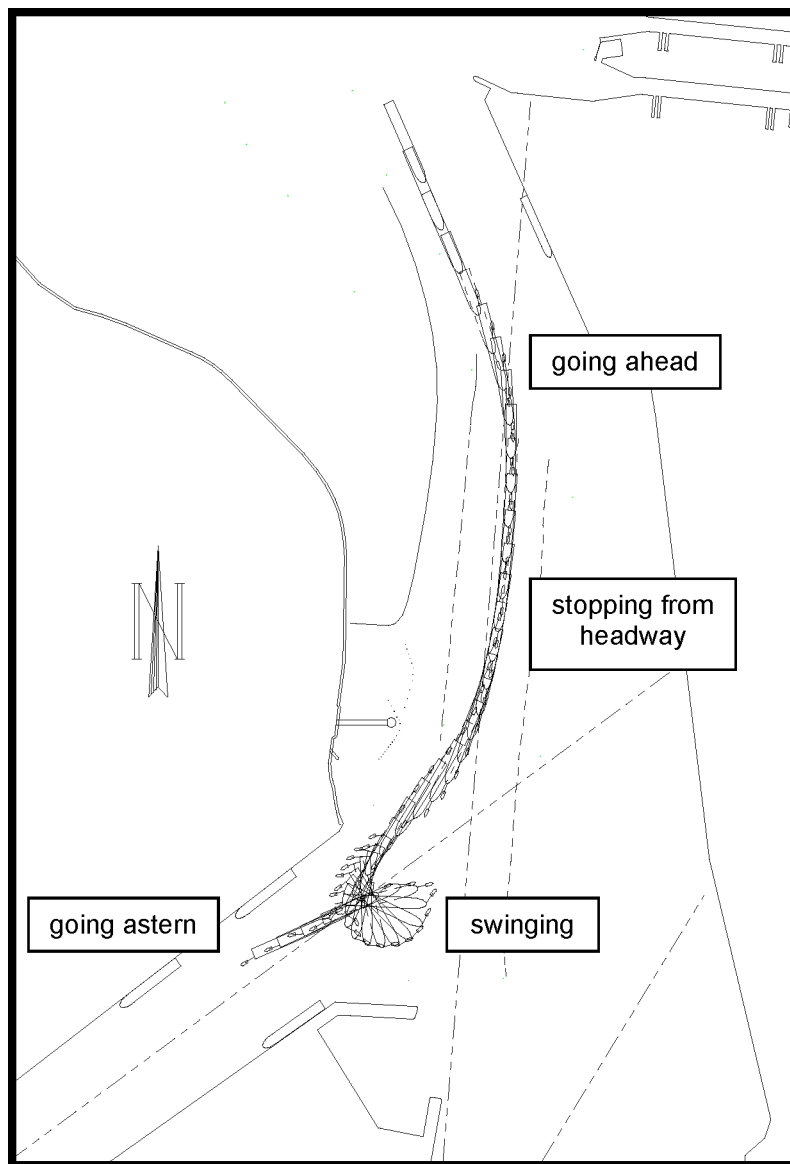
View at the ship manoeuvring simulator during an arrival at the tidal dock Saeftinge

Figure 1.3 Model 670. Port of Antwerp: tidal dock Saeftinge: an entering manoeuvre characterized by diverse operational conditions of ship speed and propeller rate
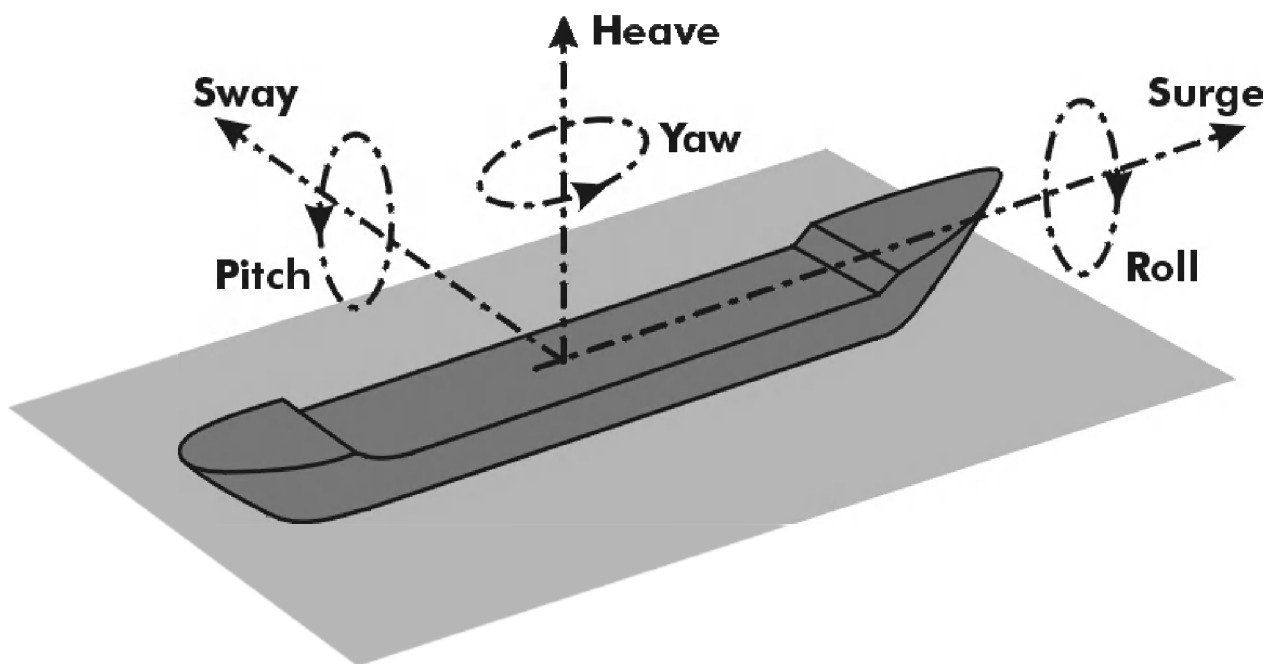
Figure 1.4 Ship motions: six degrees of freedom
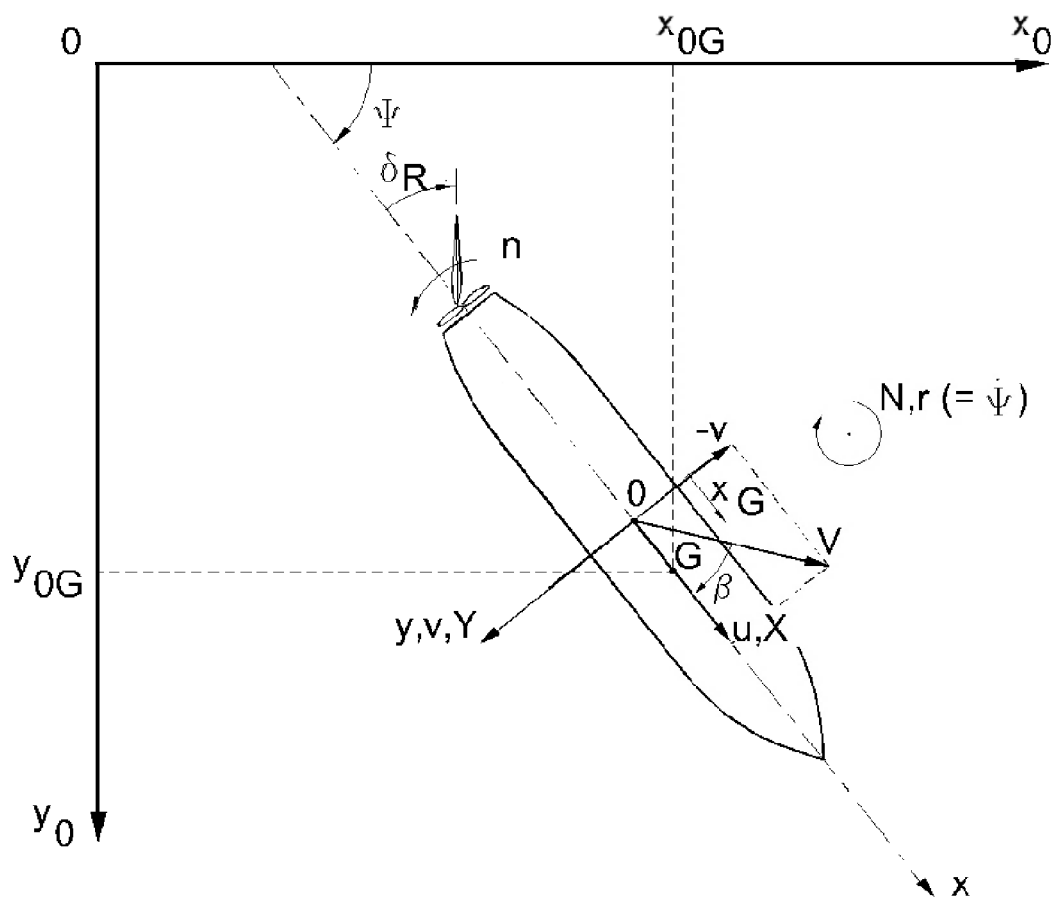
Figure 1.5 Space fixed and ship fixed axis system: conventions and symbols

Figure 1.6 Three interacting modules of a ship: hull, propeller and rudder
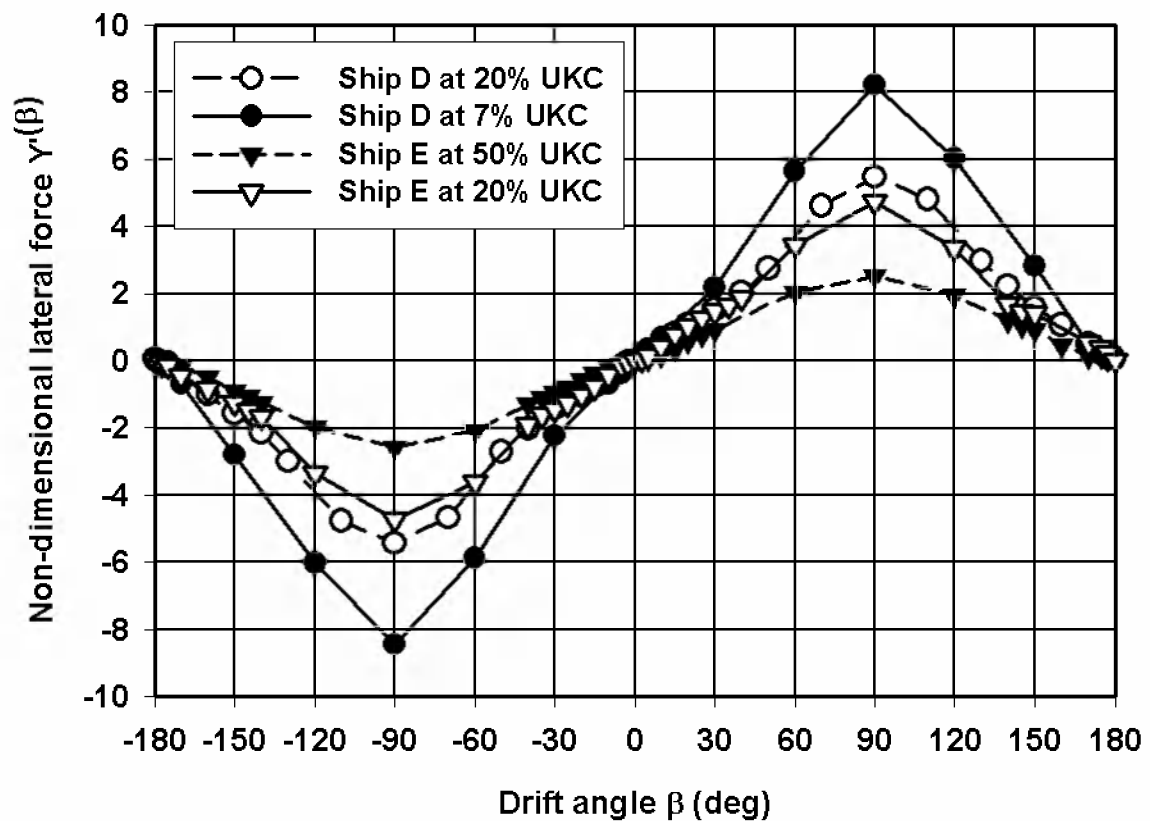
Figure 1.7 Influence of water depth on non-dimensional lateral force Y due to oblique towing for a containership (ship D) and a tanker (ship E)
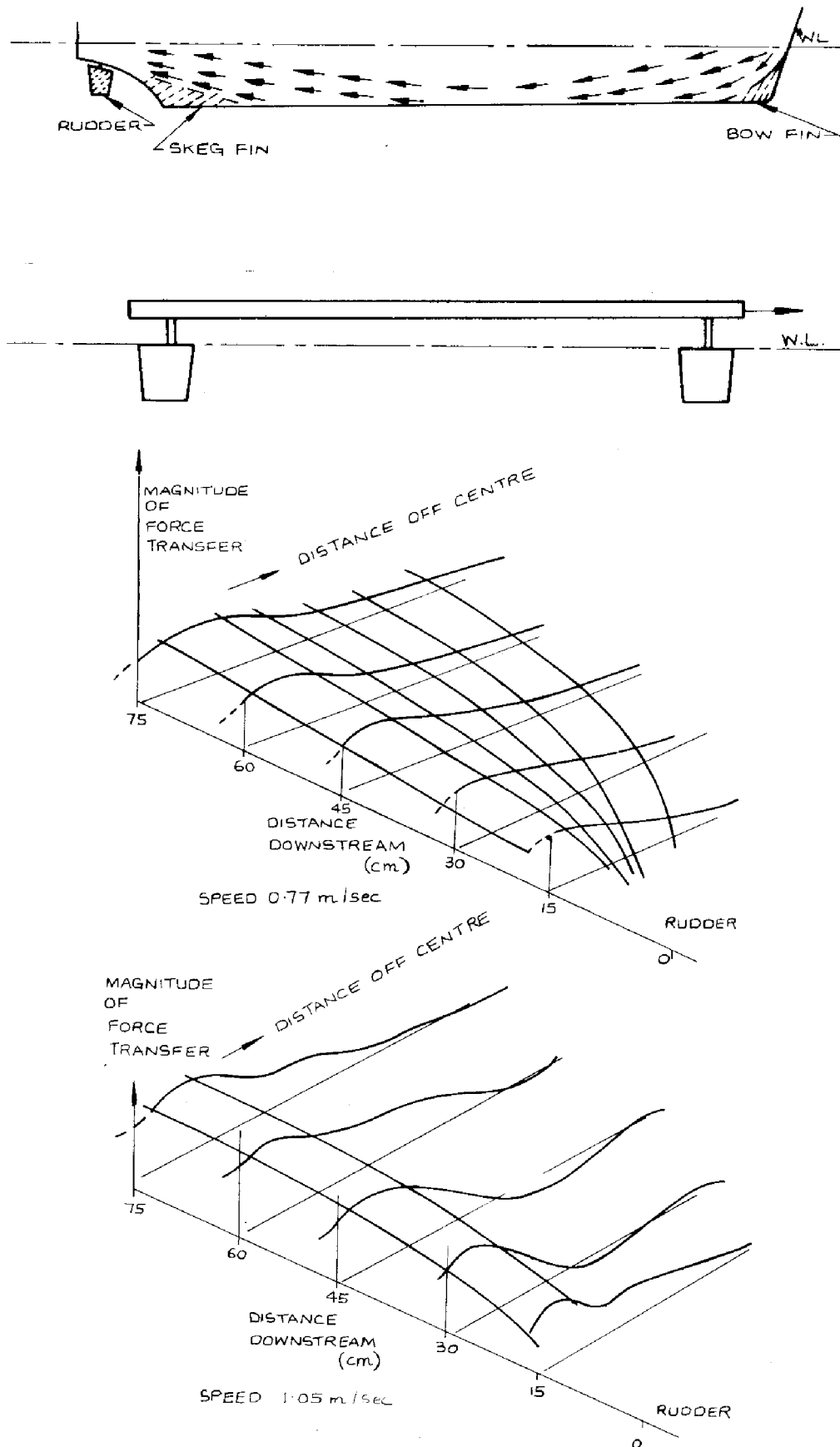
Figure 1.8 Demonstration of a "memory effect" on a simple craft with two vertical fins according to [35]

206
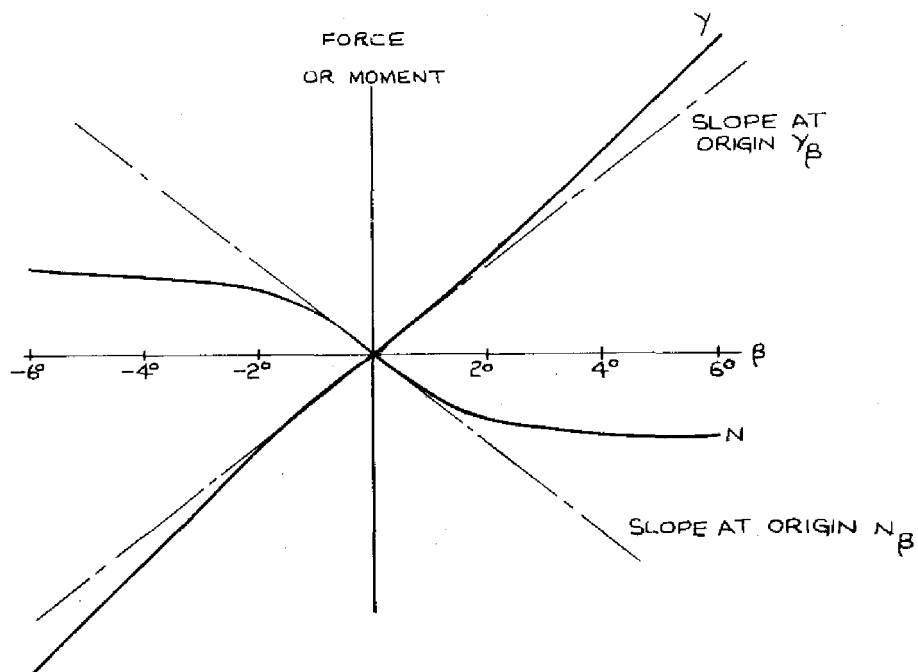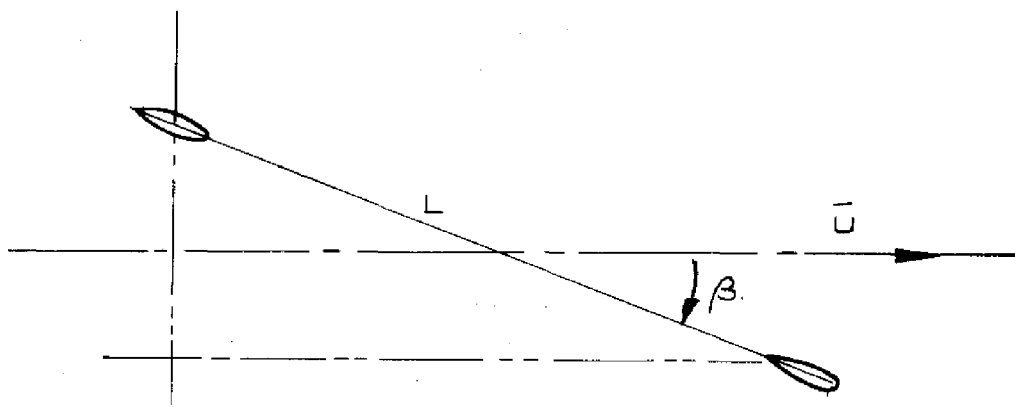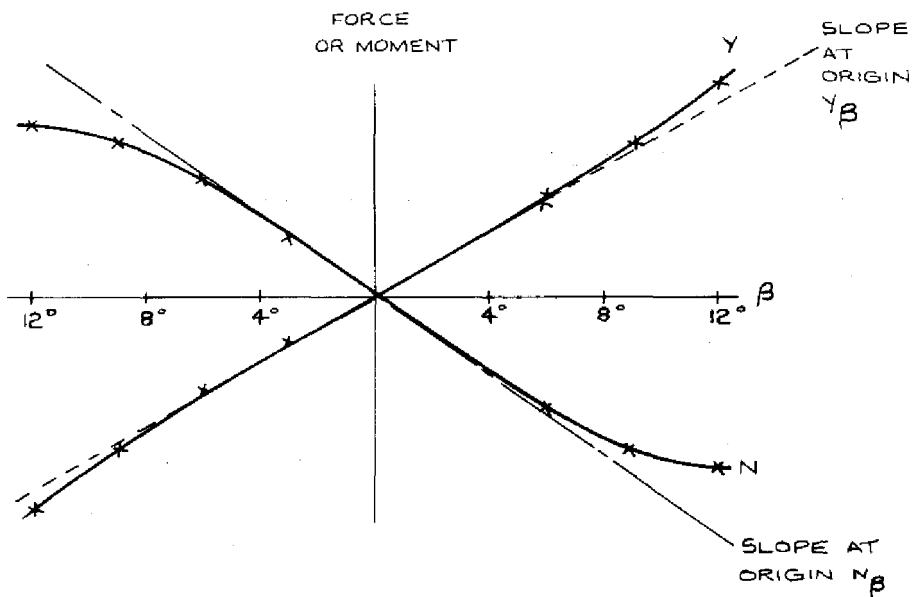
Figure 1.9 Demonstration of a "memory effect" during a steady sway motion of the two fin craft [35]
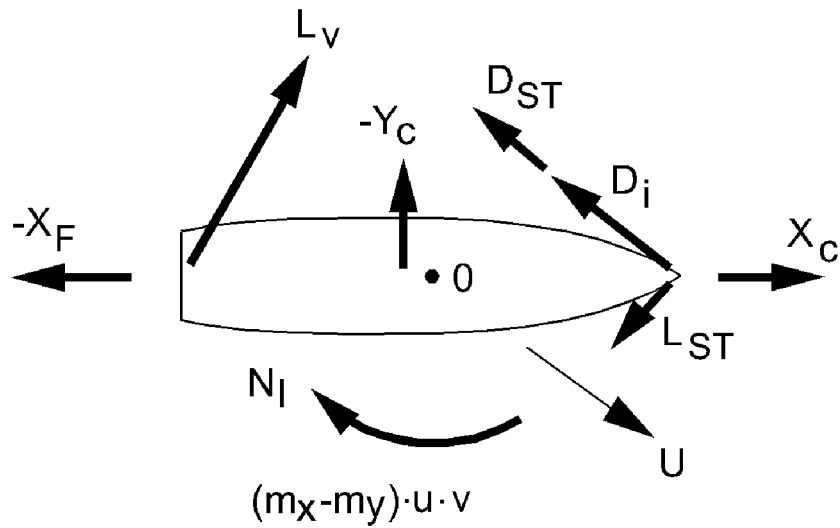
Figure 2.1 Schematic model of hydrodynamic forces according to [26]
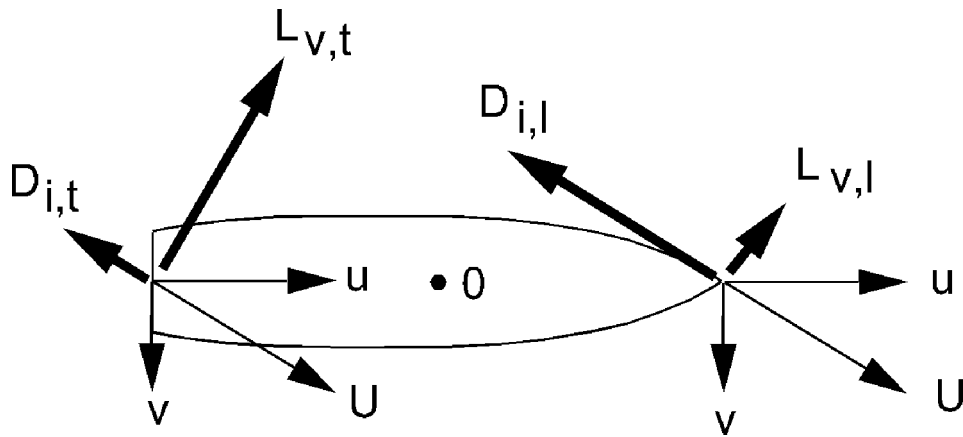
(a) schematic model of hydrodynamic forces during an oblique motion
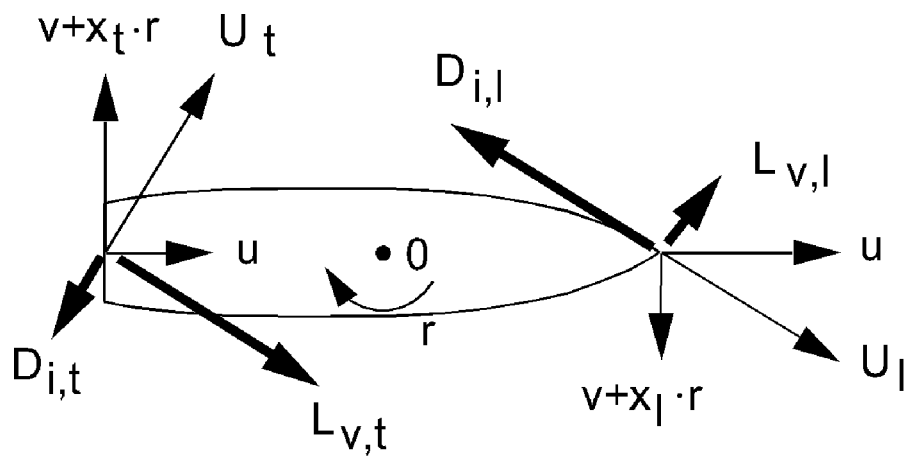
(b) schematic model of hydrodynamic forces during a turning motion

Figure 2.2 Schematic model of hydrodynamic forces during an oblique motion and a turning motion on the leading edge (l) and the trailing edge (t) according to [26]
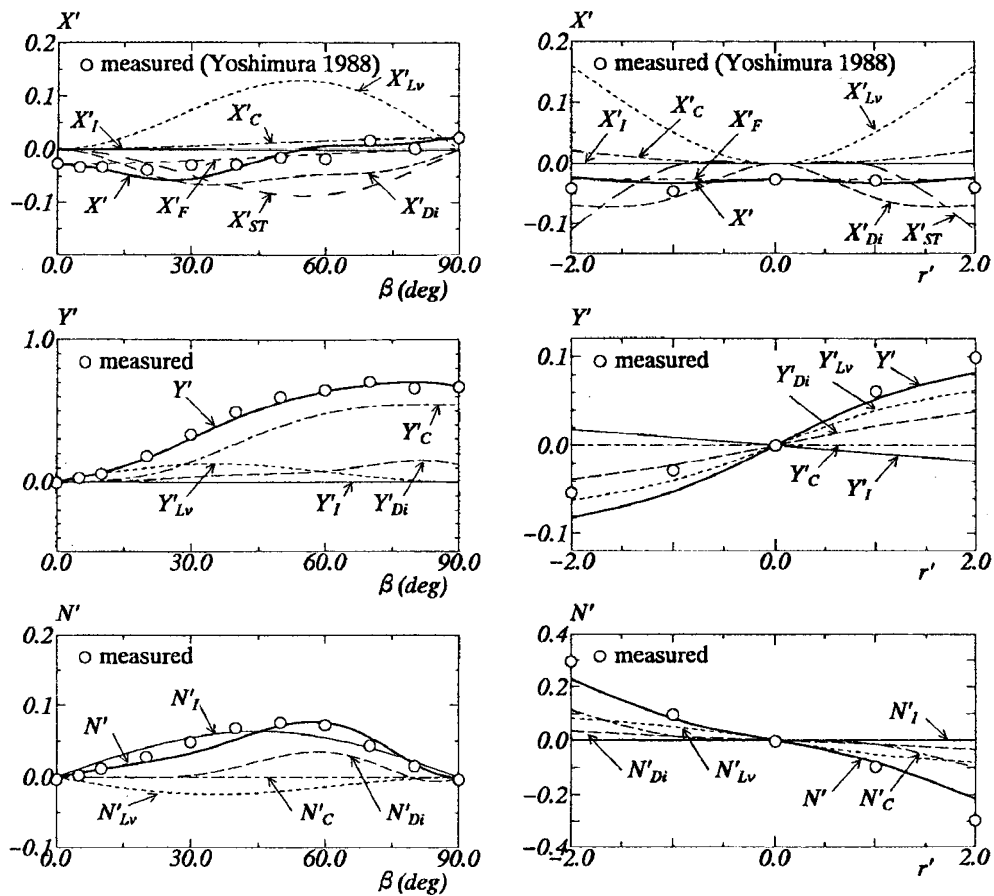
Figure 2.3 Analysed results of hydrodynamic forces in oblique motion (left) and turning motion (right) of pure car carrier model
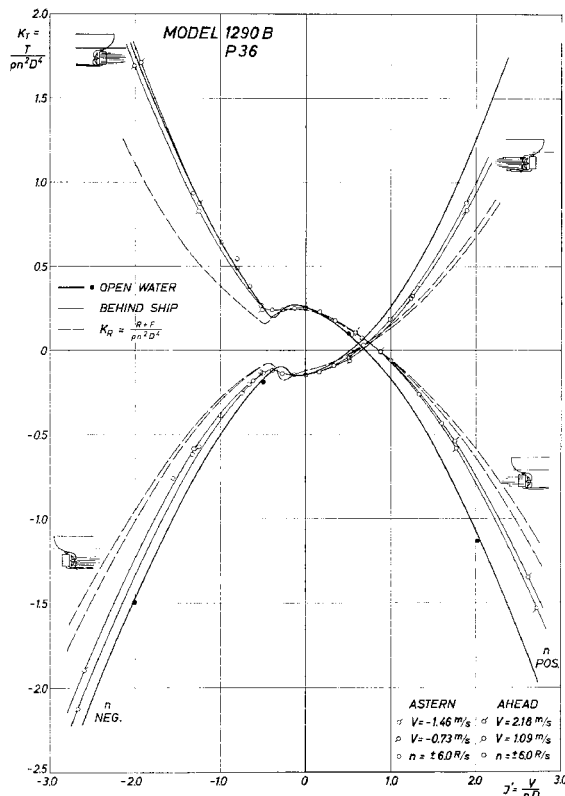
Fig. 12. K_T—J'-diagram, ship model 1290 B, propeller P 36.
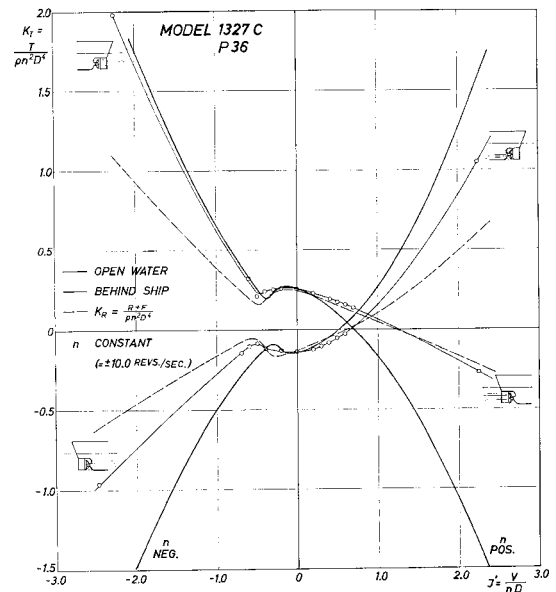
Fig. 16. K_T—J'-diagram, ship model 1327 C, propeller P 36, constant rate of revolution.

Figure 2.4 Thrust coefficient for the fishing trawler (left) and the bulk carrier (right) according to [24]

210

Top-left chart:

$w = \dfrac{J'-J}{J'}$ MODEL 1290 B P 36 4.QUADRANT

0.4
0.2
0.1
0
-0.1
-0.2

○ T – IDENTITY
● Q – IDENTITY

n NEG.

♂ V = 2.18 m/s
♀ V = 1.09 m/s

♂ V = -1.46 m/s
♀ V = -0.73 m/s

-3.0   -2.0   -1.0   0   1.0   2.0   3.0 $J' = \dfrac{V}{nD}$

Top-right chart:

$w = \dfrac{J'-J}{J'}$ 2.QUADRANT 1.QUADRANT

n POS.

♂ V = -1.46 m/s
♀ V = -0.73 m/s

♂ V = 2.18 m/s
♀ V = 1.09 m/s

-3.0   -2.0   -1.0   0   1.0   2.0   3.0 $J' = \dfrac{V}{nD}$

Bottom-left chart:

$w = \dfrac{J'-J}{J'}$ MODEL 1290 B P 39 4.QUADRANT

○ T – IDENTITY
● Q – IDENTITY

n NEG.

♂ V = 2.18 m/s
♀ V = 1.64 m/s
♀ V = 1.09 m/s

♂ V = -1.46 m/s
♀ V = -1.09 m/s
♀ V = -0.73 m/s

-3.0   -2.0   -1.0   0   1.0   2.0   3.0 $J' = \dfrac{V}{nD}$

Bottom-right chart:

$w = \dfrac{J'-J}{J'}$ 2.QUADRANT 1.QUADRANT

n POS.

♂ V = -1.46 m/s
♀ V = -1.09 m/s
♀ V = -0.73 m/s

♂ V = 2.18 m/s
♀ V = 1.09 m/s

-3.0   -2.0   -1.0   0   1.0   2.0   3.0 $J' = \dfrac{V}{nD}$

Figure 2.5 Wake factors for the fishing trawler equipped with propeller P36 (top) and P39 (bottom) according to [24]
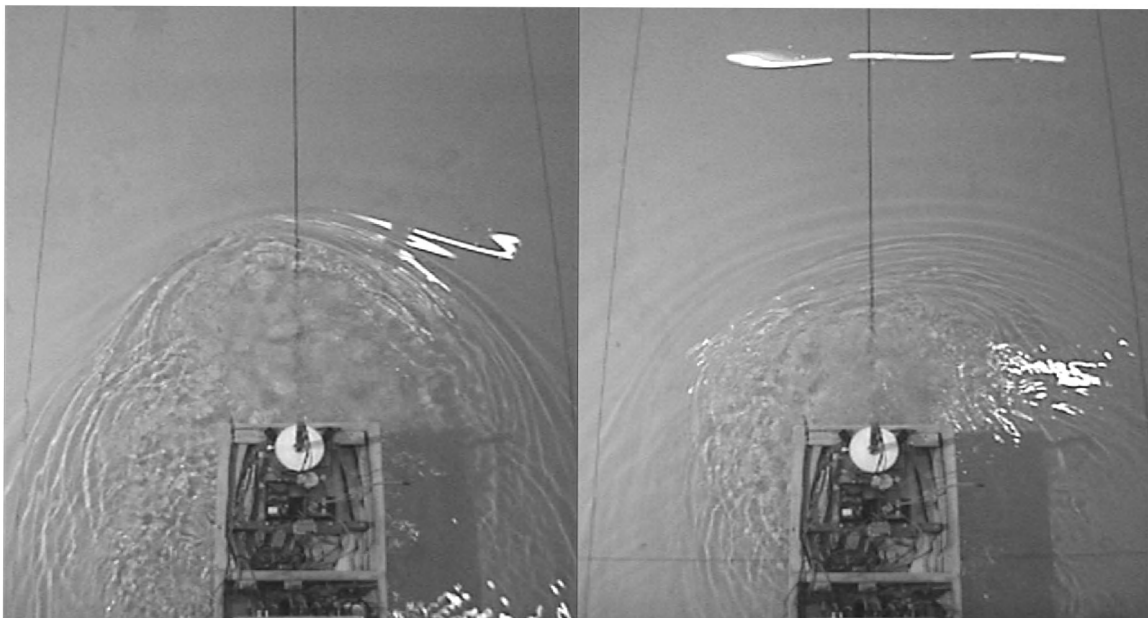
Figure 2.6 Quadrant 4: Development of an unstable flow at the aft body during a test run with a backward velocity (-4 knots full scale) and a positive propeller rate (60% of the reference rate). Model U is tested at a full scale draught of 12.0 m and 100% UKC. Photographs are taken with an interval of 30 seconds.
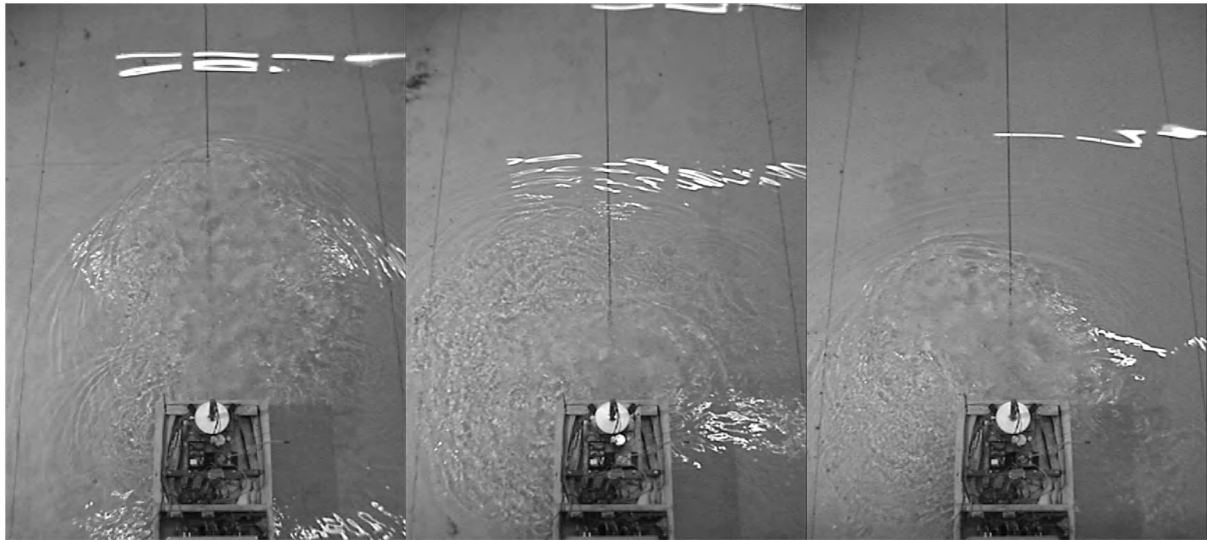
Figure 2.7 Quadrant 4: Development of an unstable flow at the aft body during a test run with a backward velocity (-4 knots full scale) and a positive propeller rate (80% of the reference rate). Model U is tested at a full scale draught of 12.0 m and 100% UKC. Photographs are taken with an interval of approximated 15 seconds.
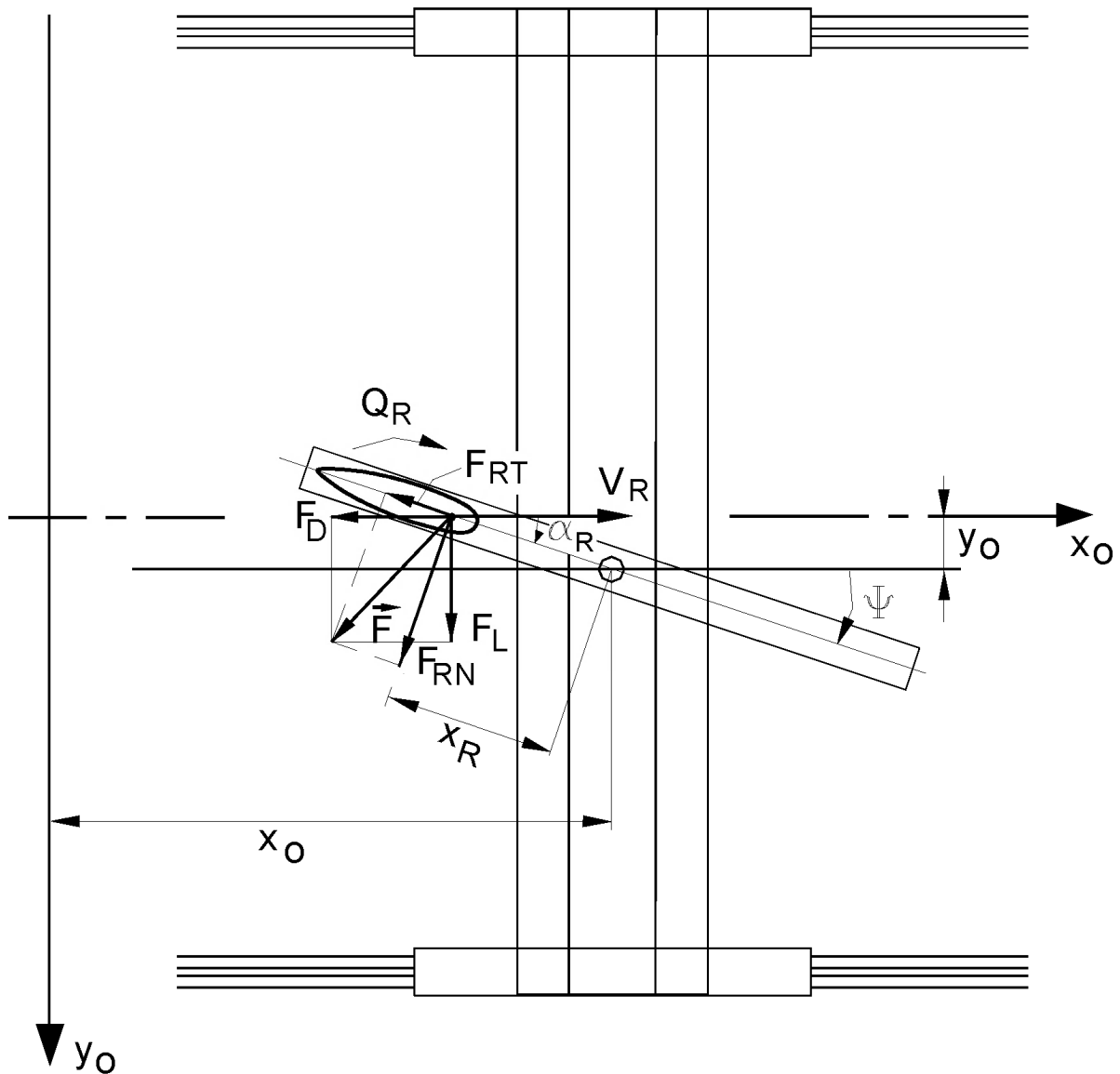
Figure 2.8 Definition of rudder forces (F_D, F_L) and (F_{RT}, F_{RN}) during open water rudder tests [40]
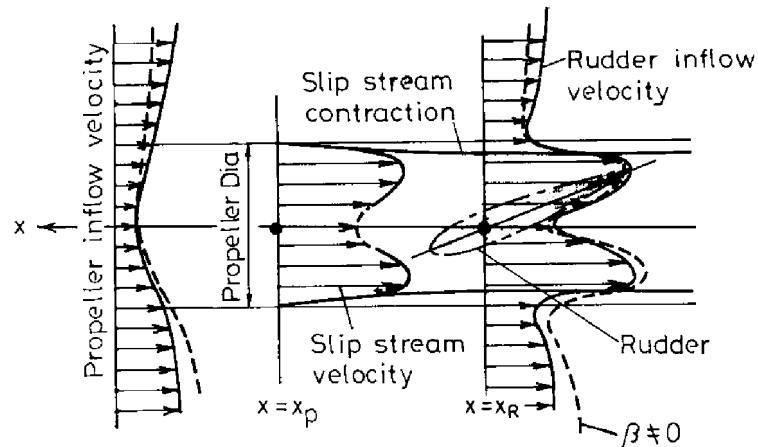
(1) Horizontal section through propeller center.
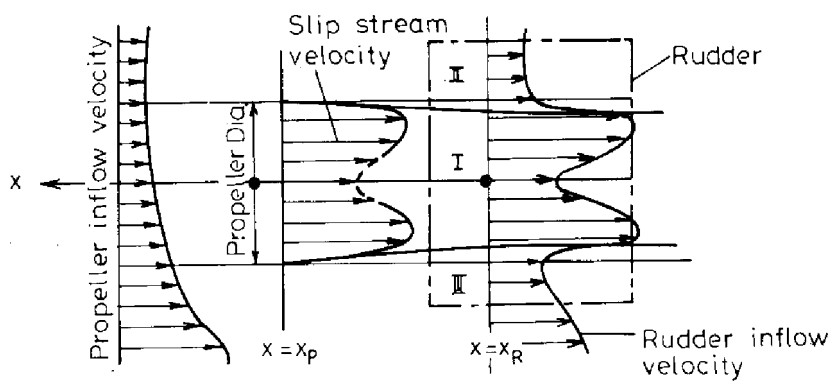
(2) Vertical section through propeller center.

Figure 2.9 The complex character of the rudder inflow for a manoeuvring ship [12]

H	: Ship hull	S	: Effect of streamline motion	W	: Wake generation
P	: Propeller	V	: Effect of viscosity	J	: Propeller flow field
R	: Rudder	G	: Effect of gravity	C	: Rudder flow field
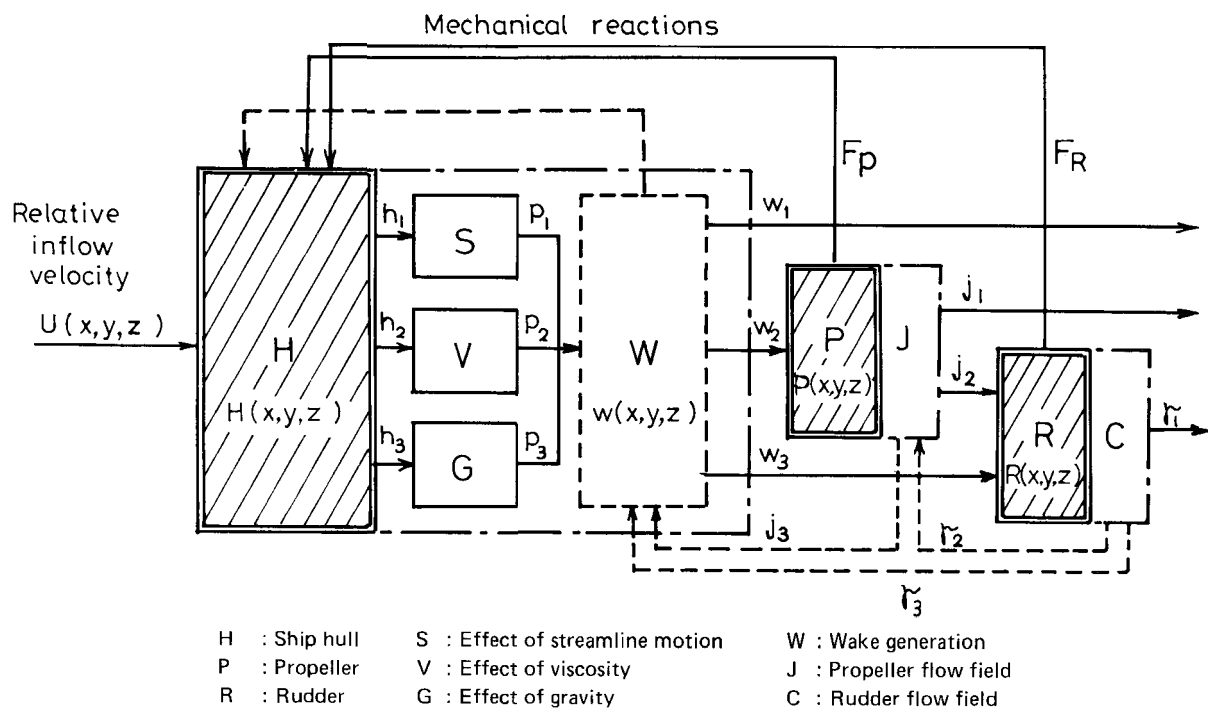
Figure 2.10 A block diagram taken from [12] for the flow effects around a manoeuvring ship
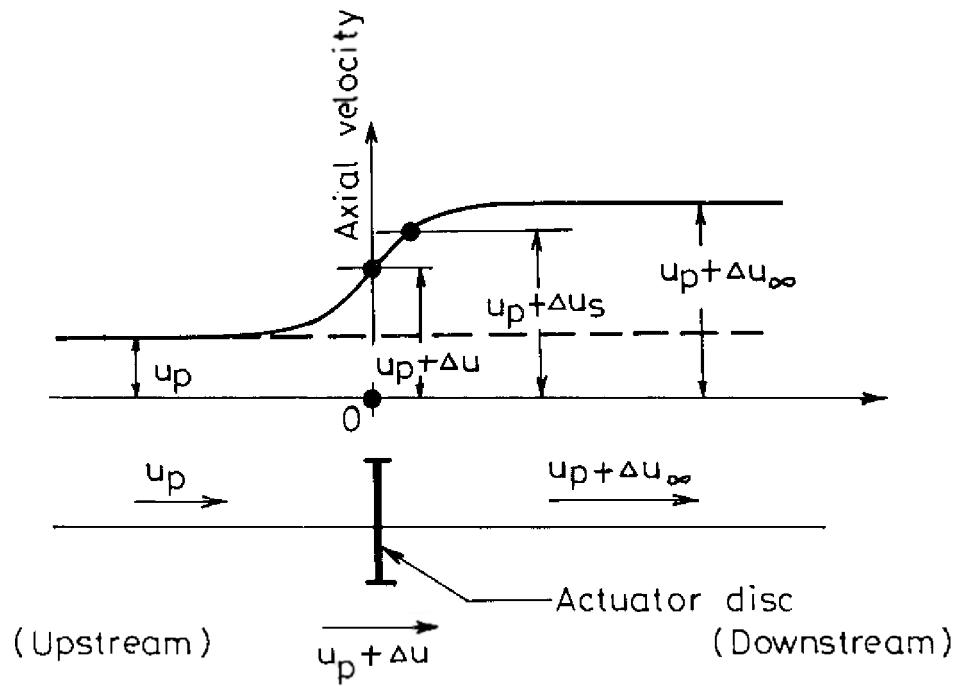
Figure 2.11 The average increase in rudder inflow due to propeller action estimated by use of the axial momentum theory for an actuator disc [12]
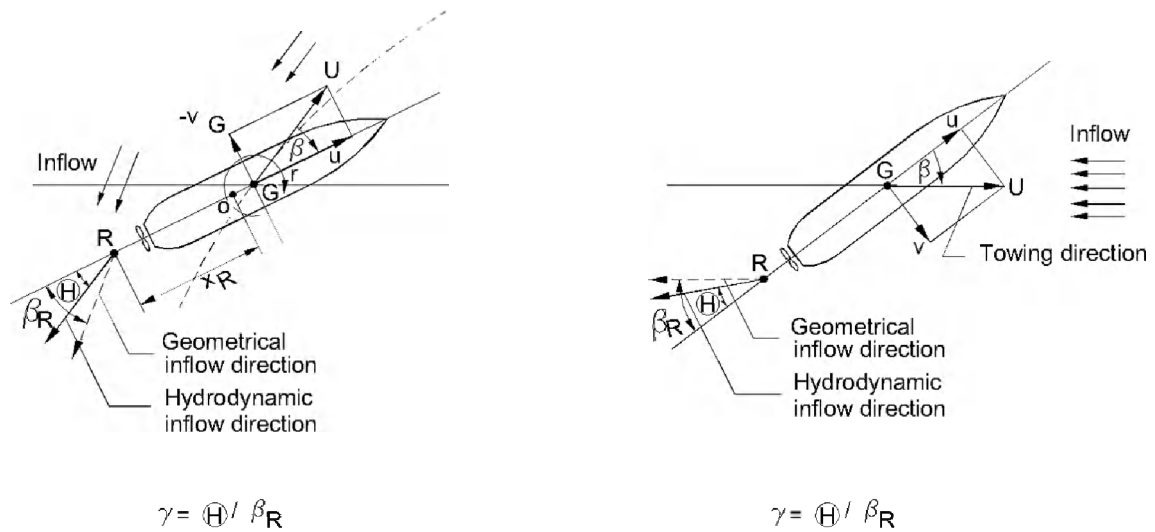
Figure 2.12 Definition of the flow straightening coefficient k_{HR} or γ in [12] for a turning motion (left) and an oblique motion (right)
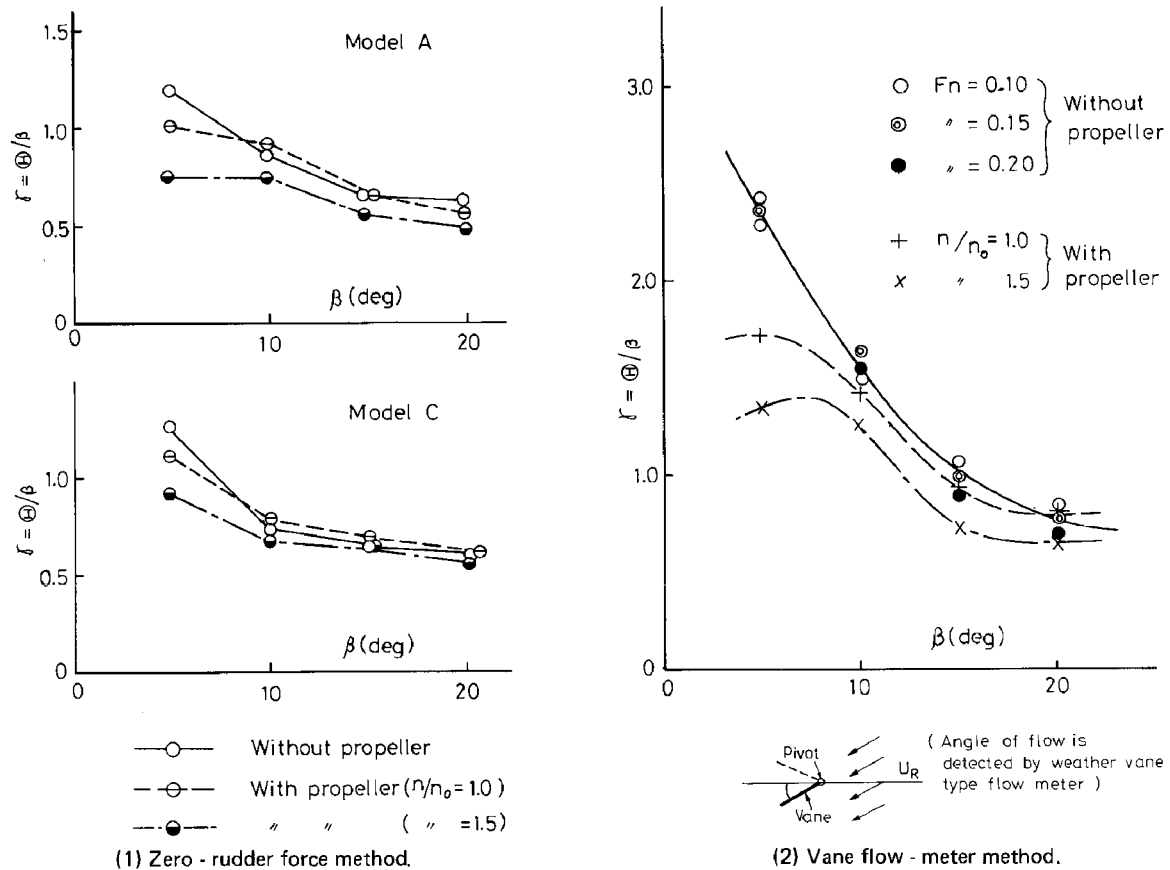
Figure 2.13 Measured flow straightening coefficients for model A and C as function of the drift angle β according to [12]
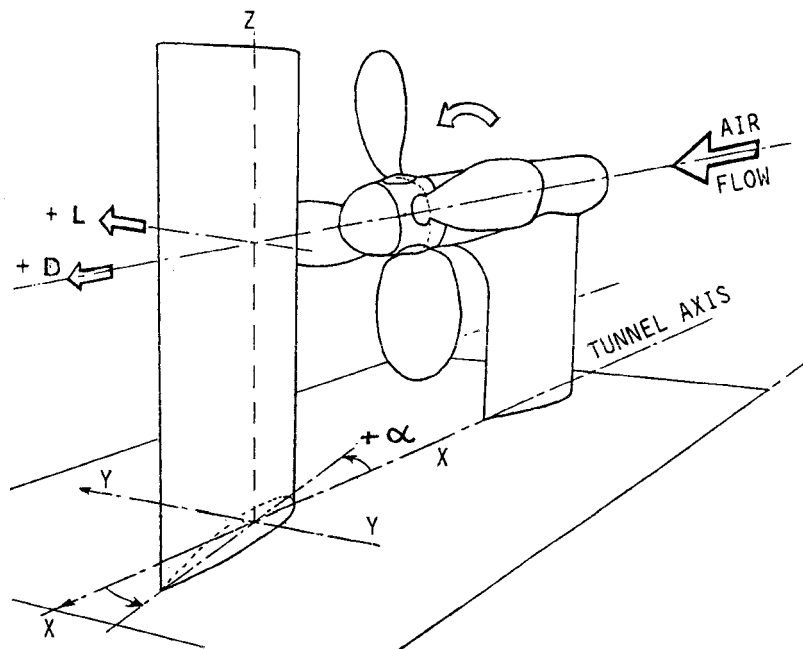
Figure 2.14 Schematic of rudder and propeller combination in a wind tunnel according to [41]
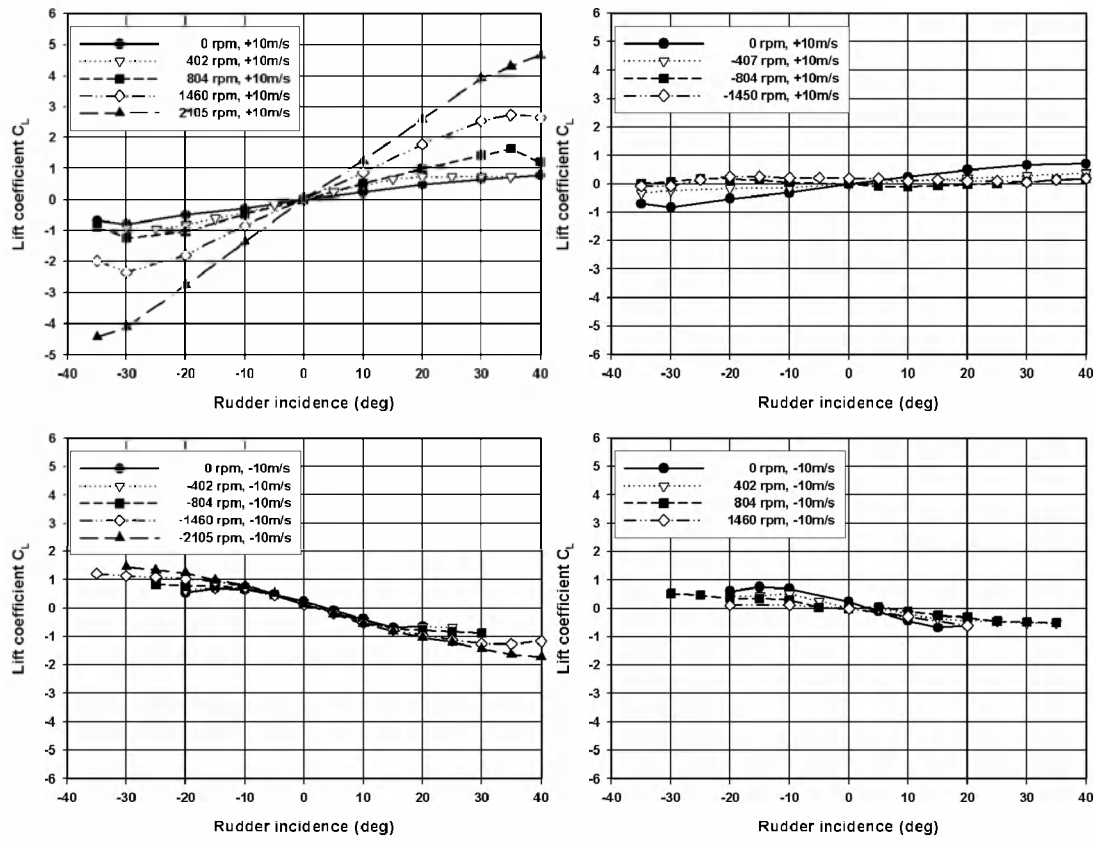
Figure 2.15 Measured lift coefficient for quadrant 1 (left, top), quadrant 2 (right, top), quadrant 3 (left, bottom) and quadrant 4 (right, bottom) according to [42]
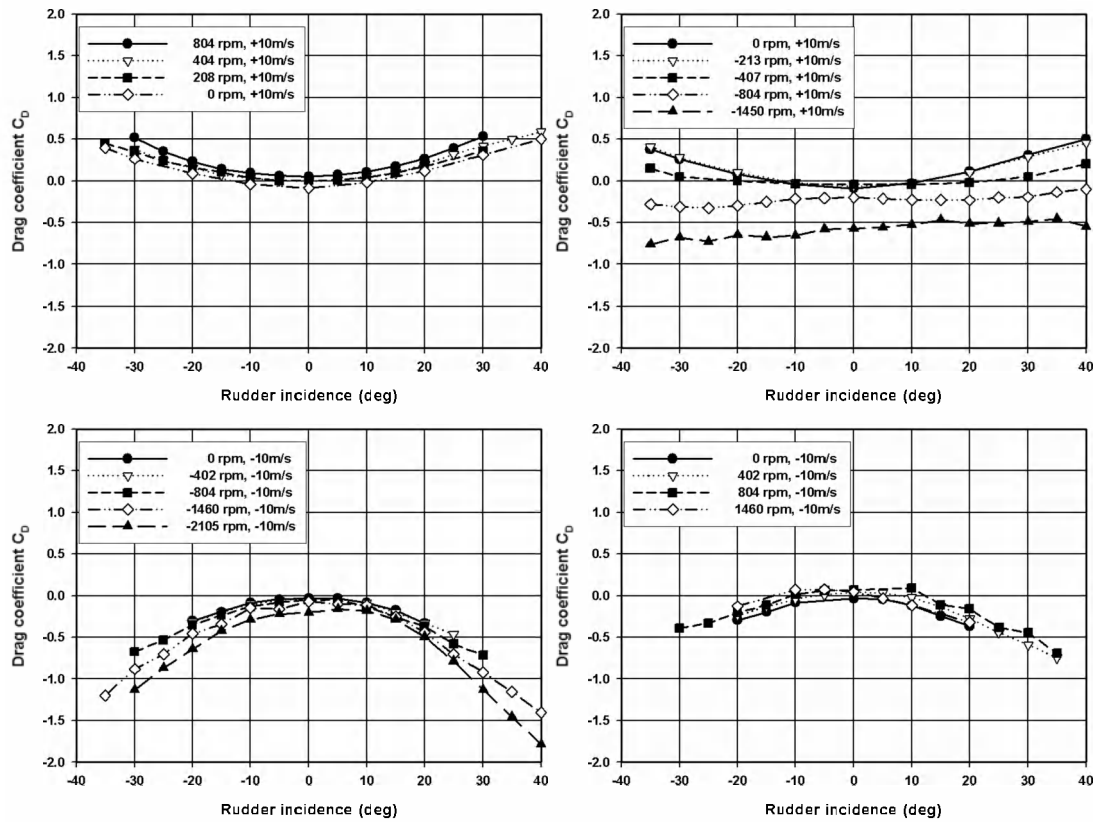
Figure 2.16 Measured drag coefficient for quadrant 1 (left, top), quadrant 2 (right, top), quadrant 3 (left, bottom) and quadrant 4 (right, bottom) according to [42]

216
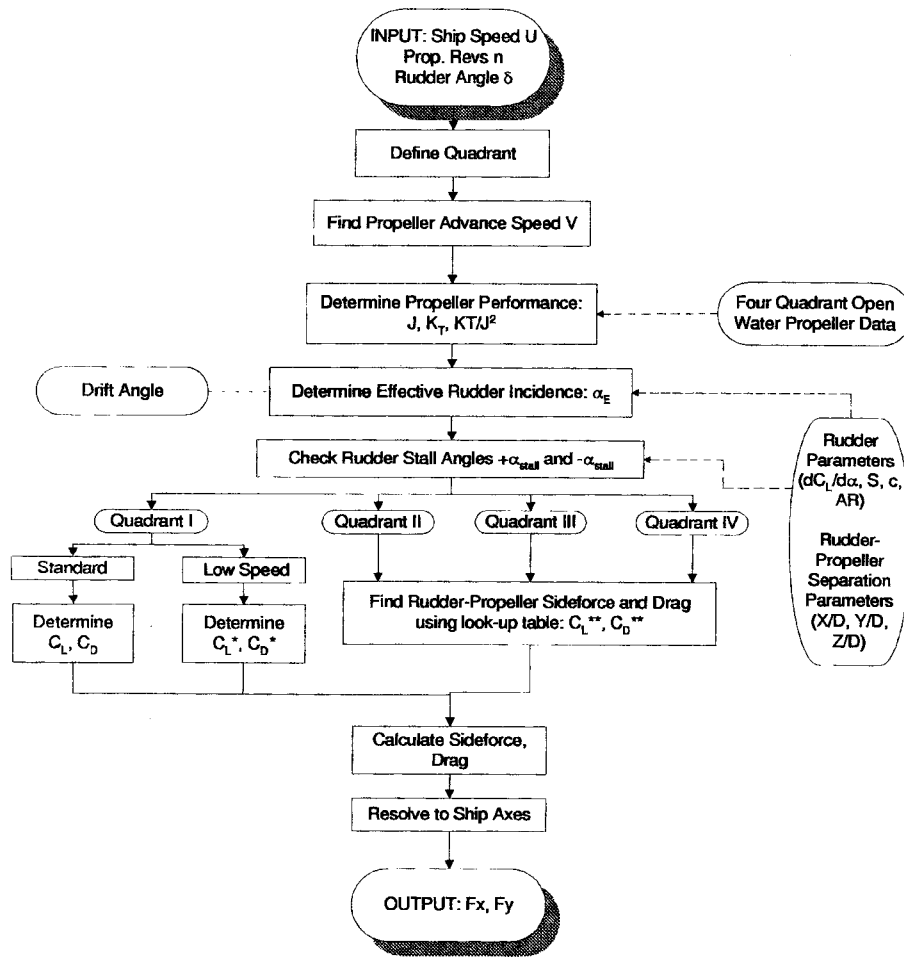
Figure 2.17 Flow chart for enhanced rudder force prediction algorithm [43]
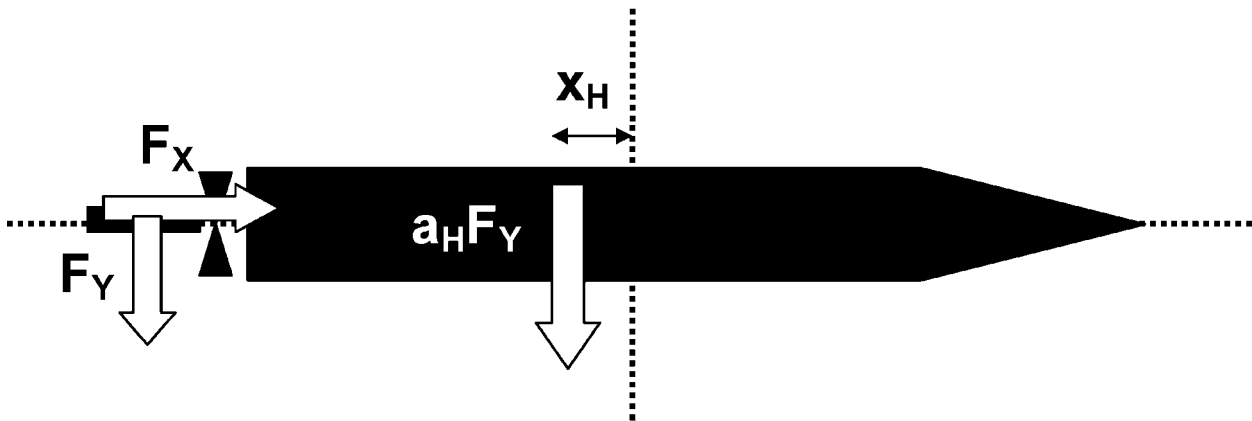
Figure 2.18 Schematic view of correlation parameters a_H and x'_H for the rudder induced lateral force on ship hull $a_H F_Y$ with an application point at a distance x_H from amidships
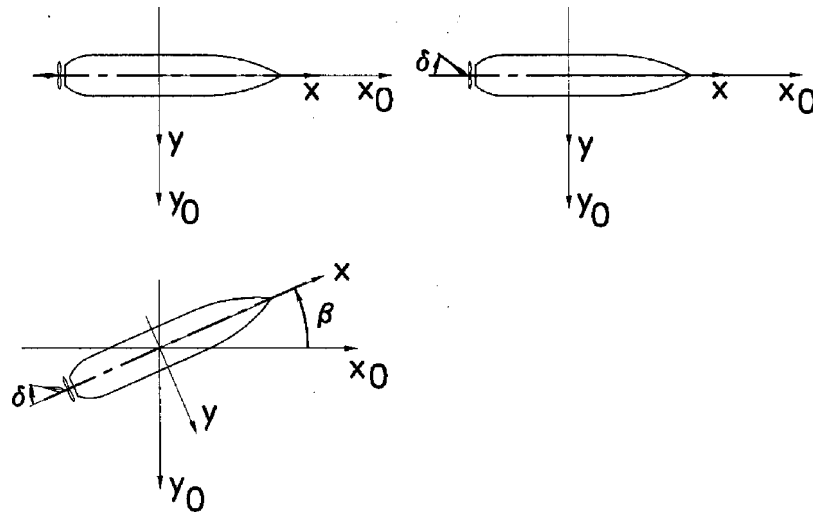
Figure 3.1 Schematic view of stationary oblique towing tests with variation of velocity components u and v and/or control parameters n and δ
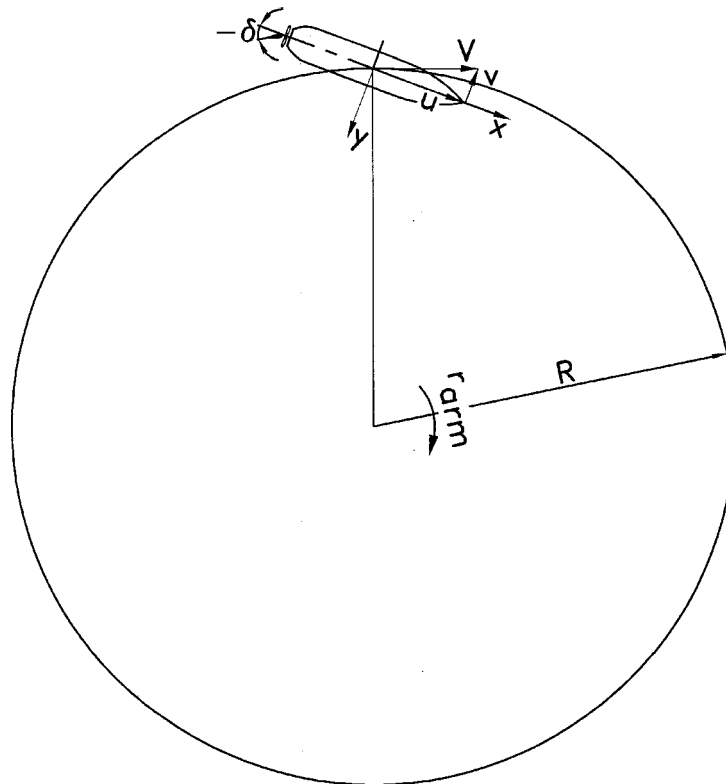
Figure 3.2 Schematic view of stationary circular motion tests with variation of velocity components u, v and r and/or control parameters n and δ
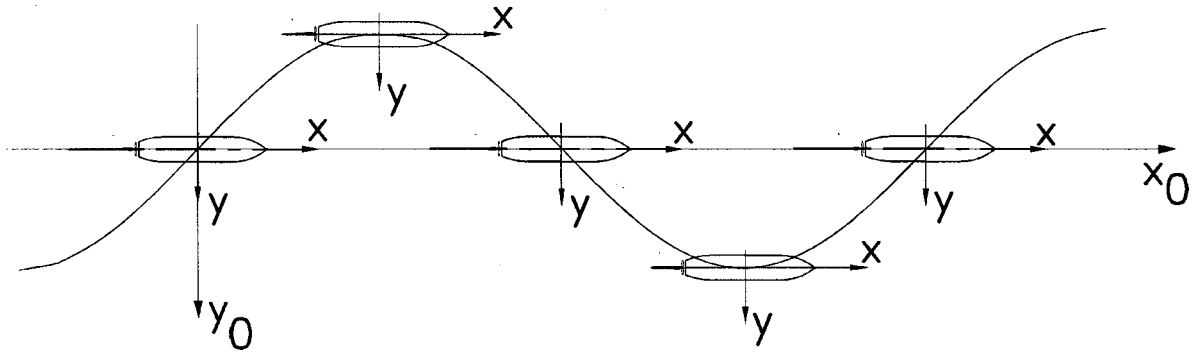
Figure 3.3 Schematic view of a harmonic sway test or PMM sway test with amplitude y_{0A} and period T
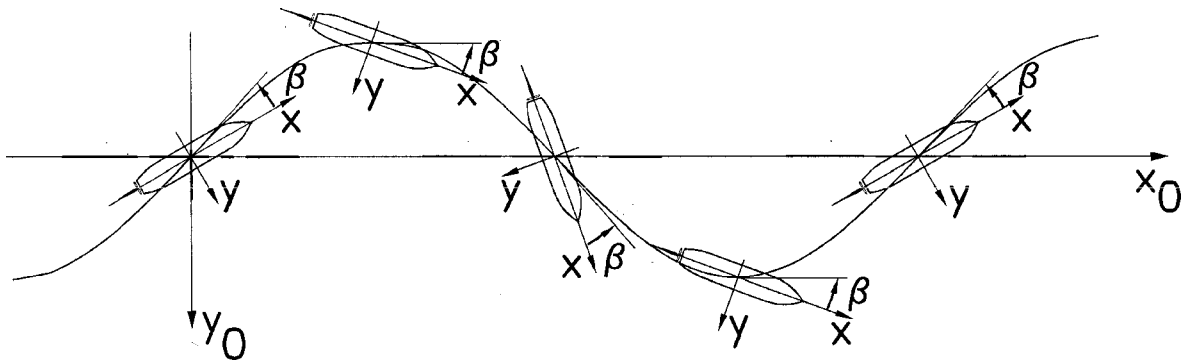
Figure 3.4 Schematic view of a harmonic yaw test or PMM yaw test with drift angle β, amplitude ψ_A and period T
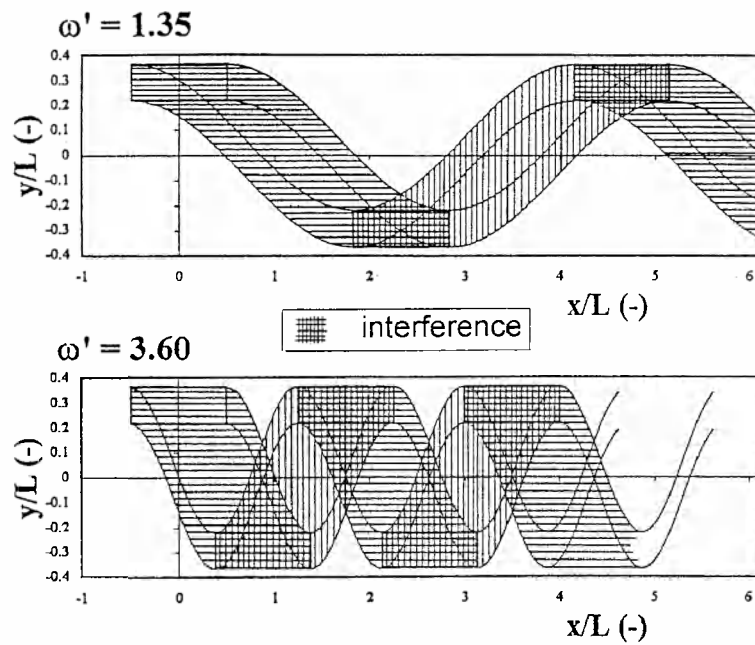
Figure 3.5 Swept path during harmonic sway tests: influence of non-dimensional frequency
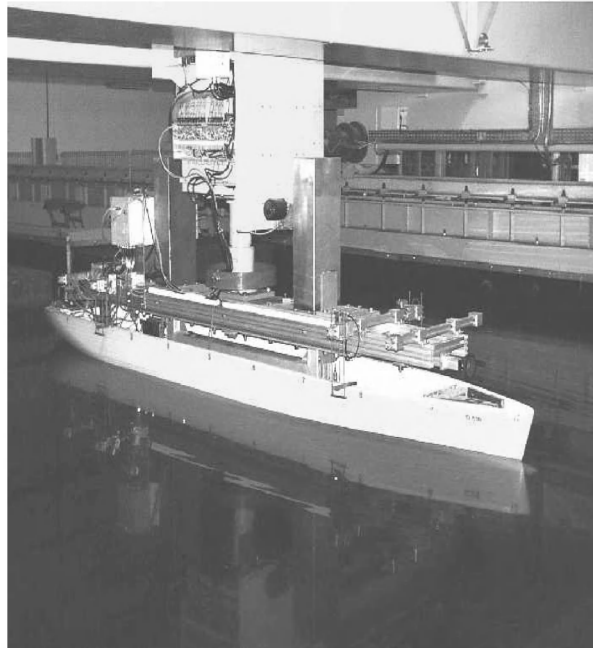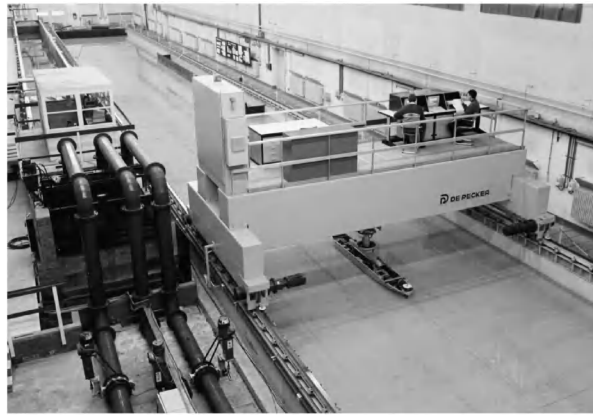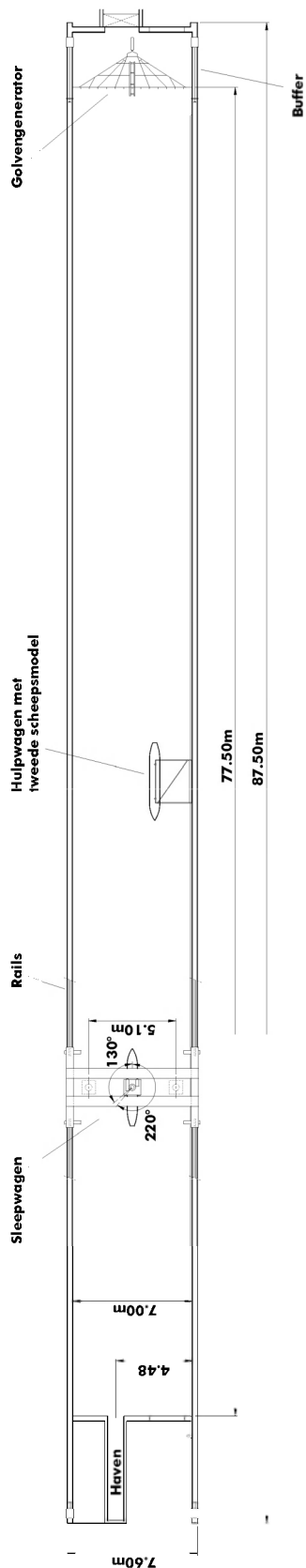
Figure 3.6 Towing tank for manoeuvres in shallow water (co-operation Flanders Hydraulics Research – Ghent University)

1	rudder mechanism	7	propeller rate of turn meter	13	propeller control
2	rudder control system	8	amplifier	14	leakage alarm
3	leakage pump	9	sinkage measurement (4x)	15	limit vertical motion (4x)
4	battery	10	long. dynamometer (2x)	16	vertical guidance
5	thrust & torque meter	11	lateral dynamometer (2x)	17	pitch and roll mechanism
6	propeller motor	12	roll moment measurement		
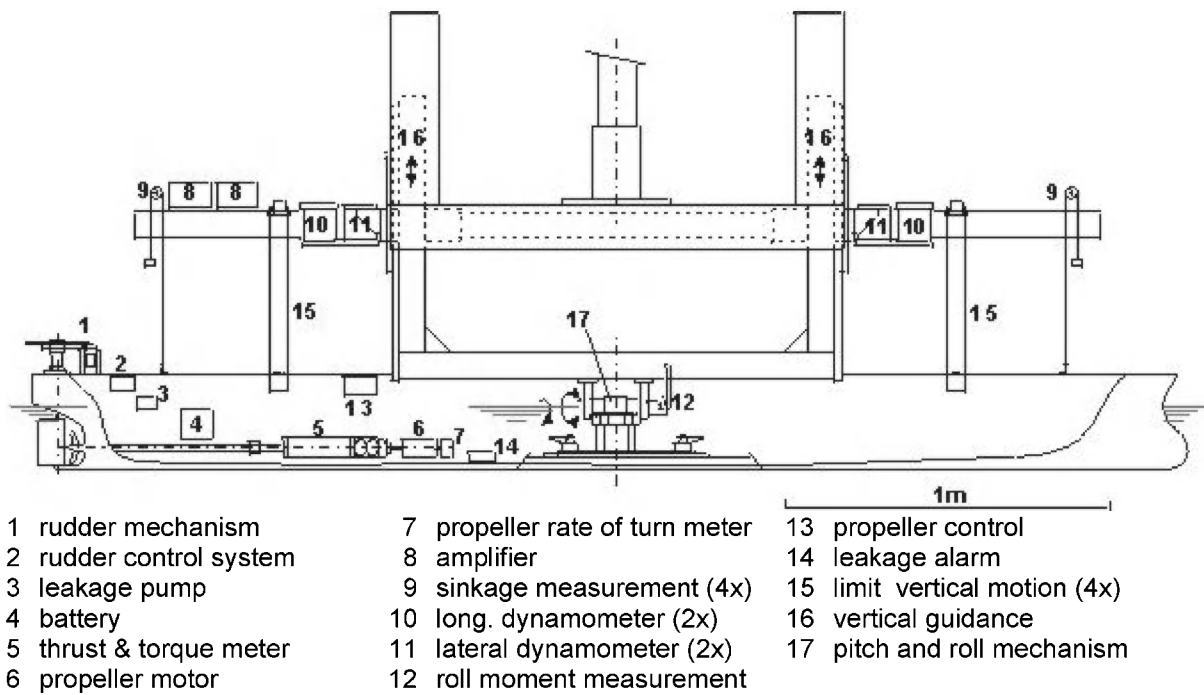
Figure 3.7 Ship model instrumentation for the present beam mechanism
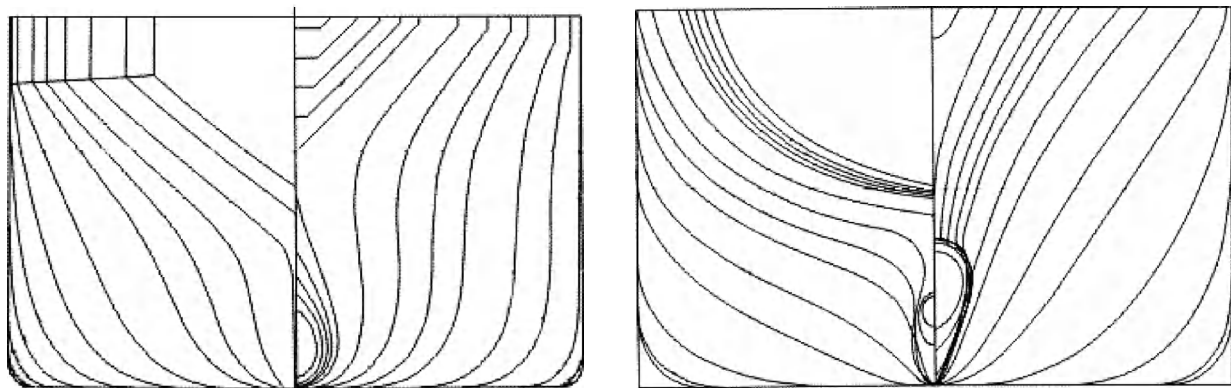
Figure 3.8 Section profile of model E (left) and model D (right)
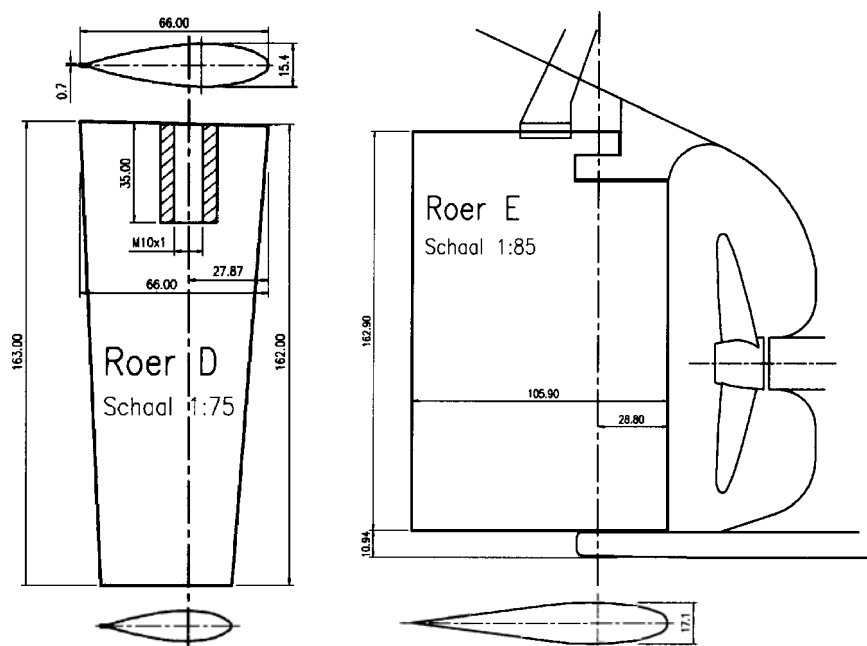
Figure 3.9 Rudder profile for model D (left) and model E (right)

222
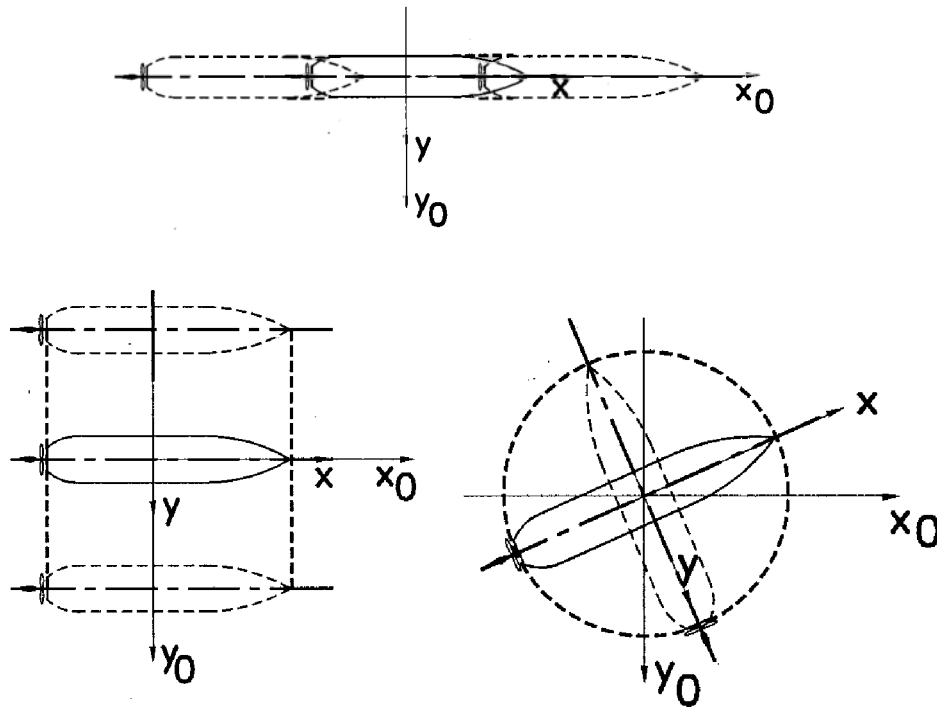
Figure 3.10 Schematic view of oscillatory tests in x-direction, y-direction or ψ-direction
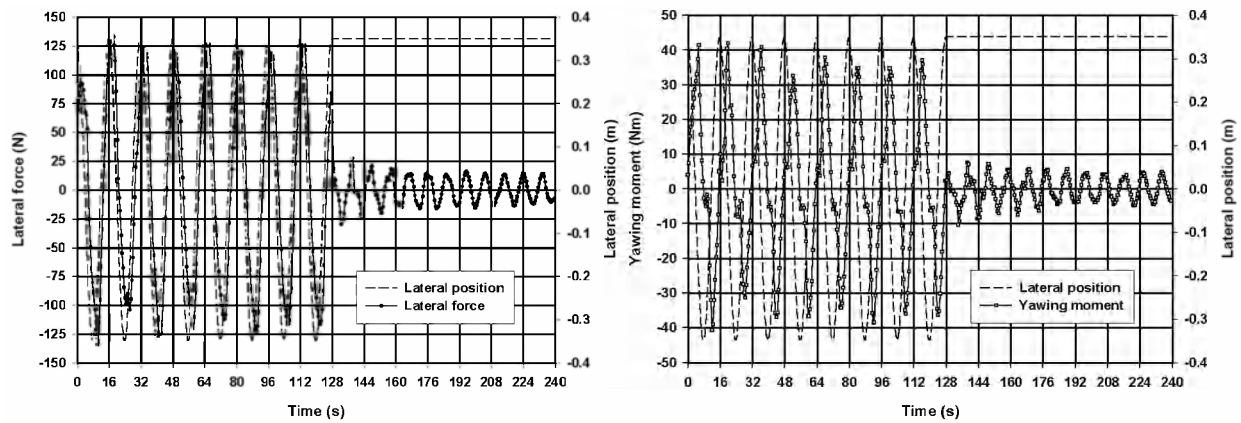
Figure 3.11 Lateral force and yawing moment measured during test type PMMY2 for model E at intermediate draught and 20% UKC (F_n=0.041)
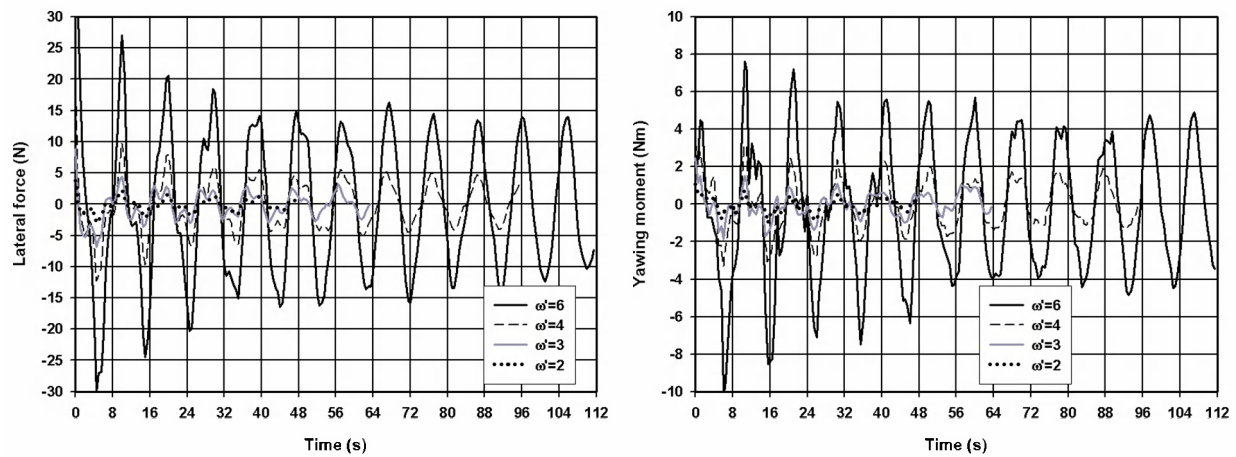
Figure 3.12 Lateral force and yawing moment measured during run-out phase for model E at intermediate draught and 20% UKC (F_n=0.041): influence of test frequency
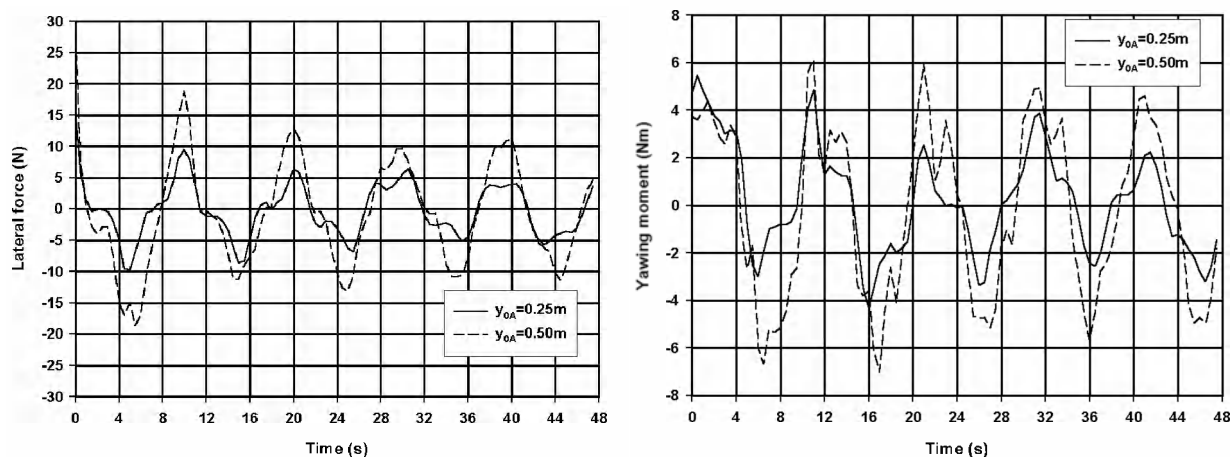
Figure 3.13 Lateral force and yawing moment measured during run-out phase for model E at intermediate draught and 20% UKC (F_n=0.057): influence of sway amplitude
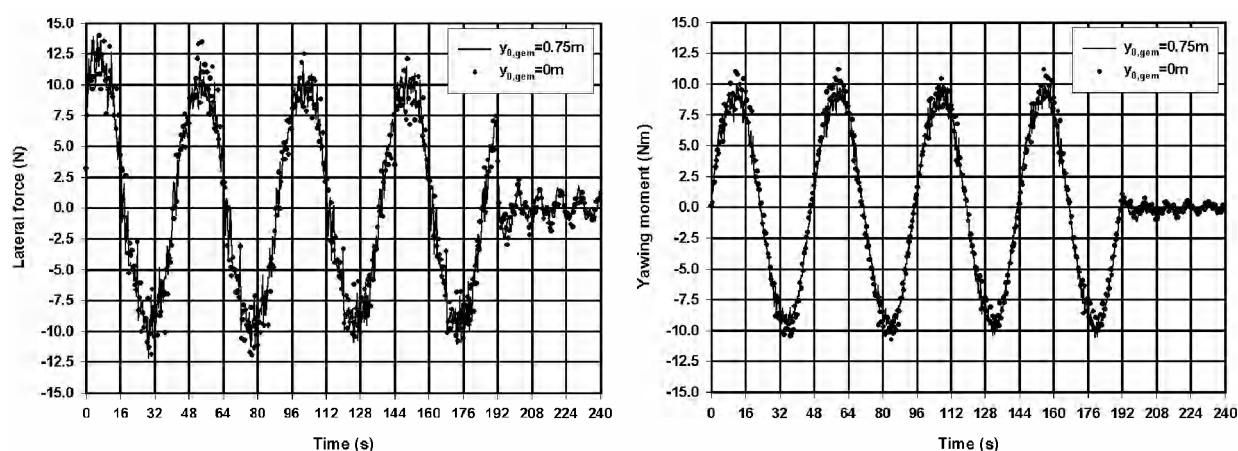
Figure 3.14 Lateral force and yawing moment measured during test type PMMY2 (period 48s, y_{0A}=0.35m) for model E at intermediate draught and 20% UKC (F_n=0.041): influence of mean lateral position
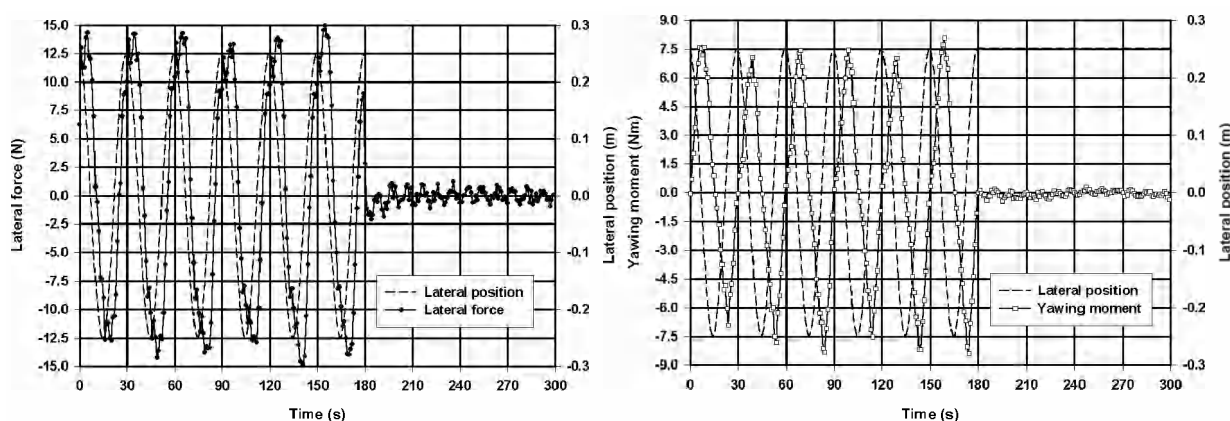
Figure 3.15 Lateral force and yawing moment measured during test type PMMY2 for model D at 20% UKC (F_n=0.032)

224
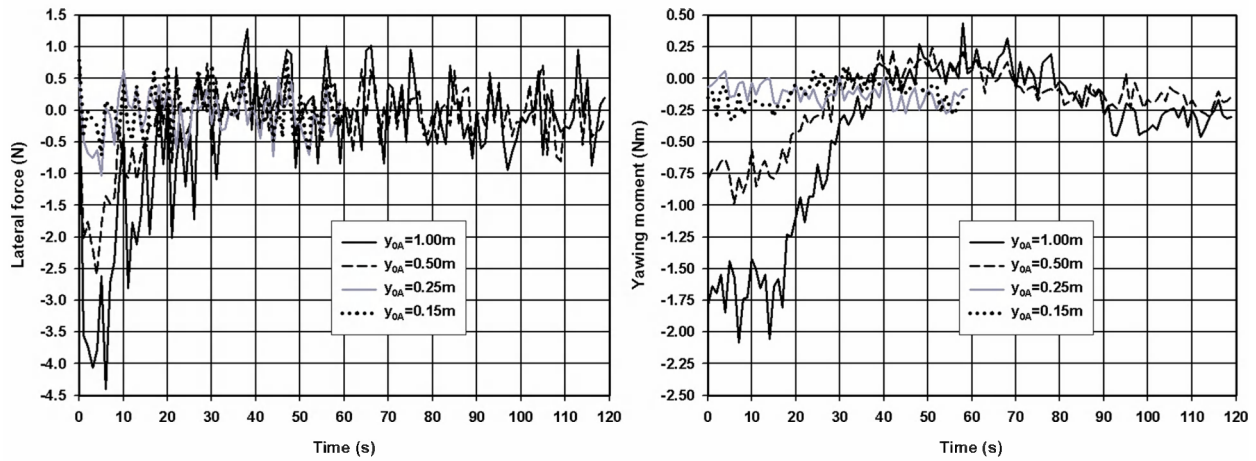
Figure 3.16 Lateral force and yawing moment measured during run-out phase for model D at 20% UKC (F_n=0.032 and period 60s): influence of sway amplitude
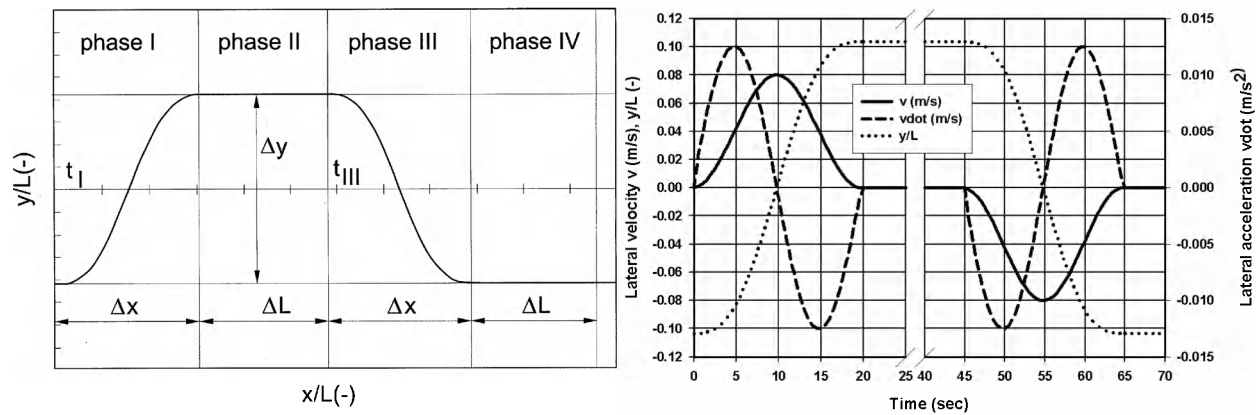
Figure 3.17 Trajectory of an alternative non-stationary sway test (type PMMY_L or PMMYL2) and variation of sway velocity and sway acceleration
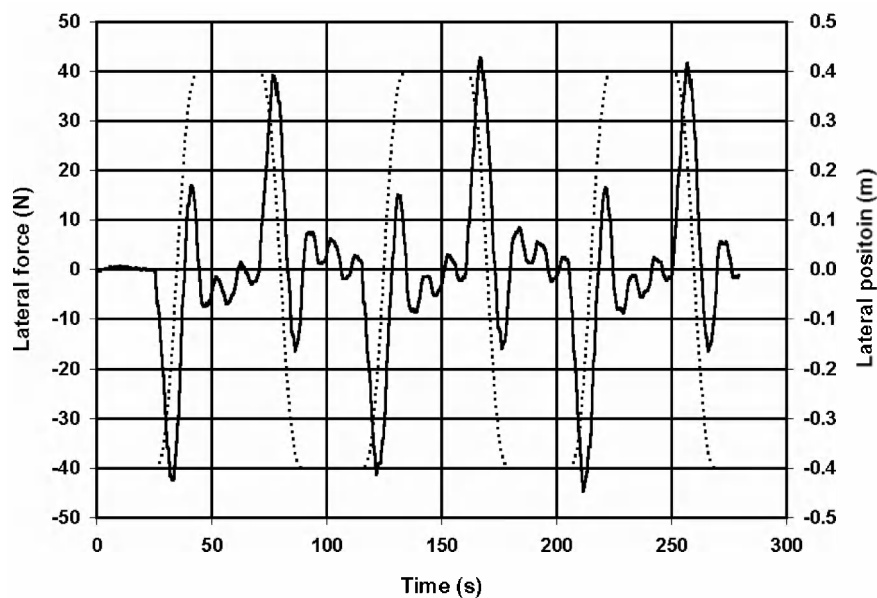
Figure 3.18 Model D: time history of lateral force during a non-conventional sway test executed at a non-dimensional frequency $\omega^{*'}$=6 (7% UKC, F_n=0.032)
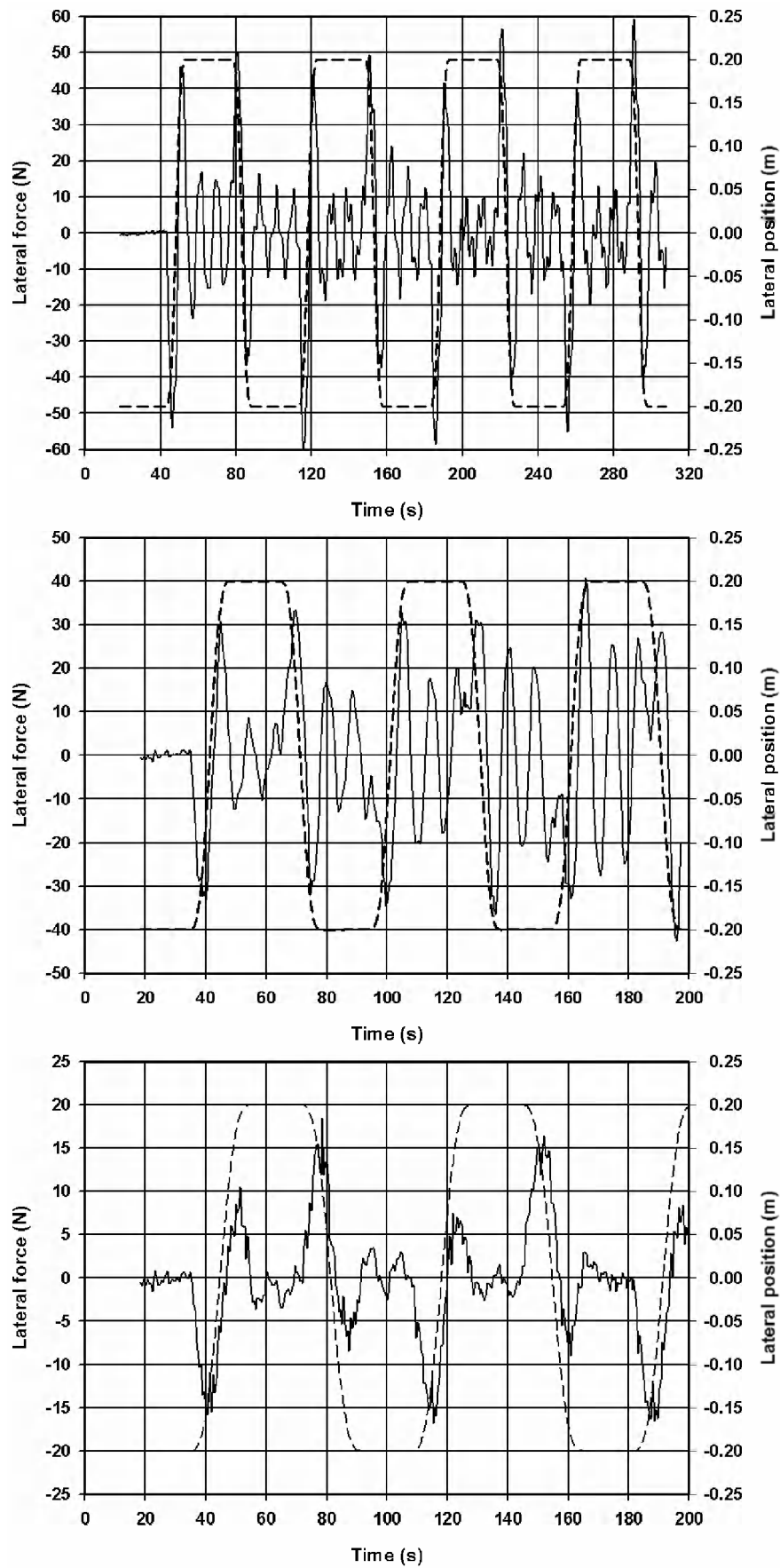
Figure 3.19 Model E at design draught and 20% UKC: time history of lateral force during a non-conventional sway test executed at a non-dimensional frequency ω*'=12 (Fₙ=0.033, top), a non-dimensional frequency ω*'=6 (Fₙ=0.049, centre) and a non-dimensional frequency ω*'=4 (Fₙ=0.049, bottom)
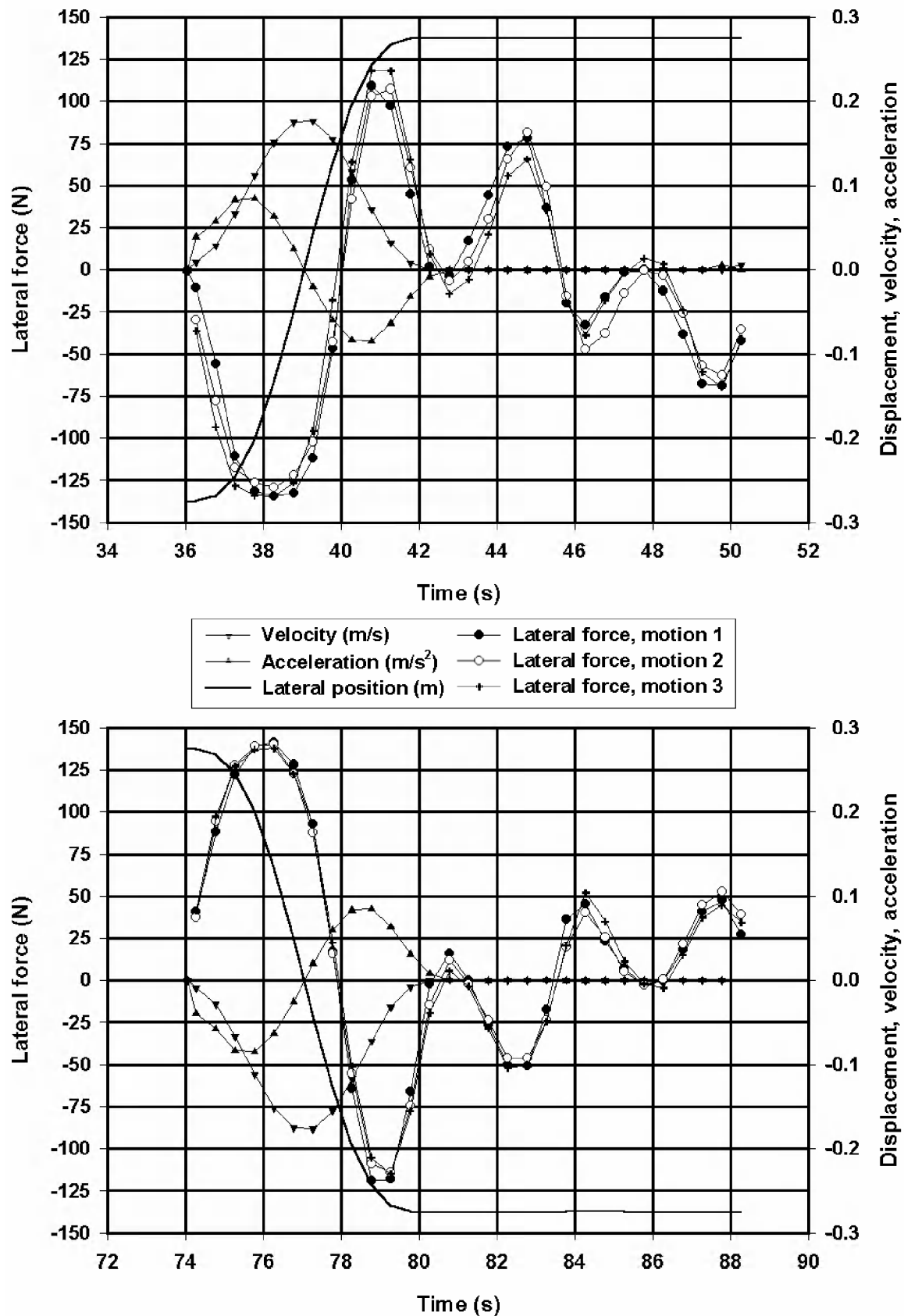
Figure 3.20 Model E at intermediate draught and 20% UKC: time history of lateral force during a non-conventional sway test executed at a non-dimensional frequency $\omega^{*\prime}=16$ ($F_n=0.041$), motions to starboard and link phases at the top, motions to port and link phases at the bottom
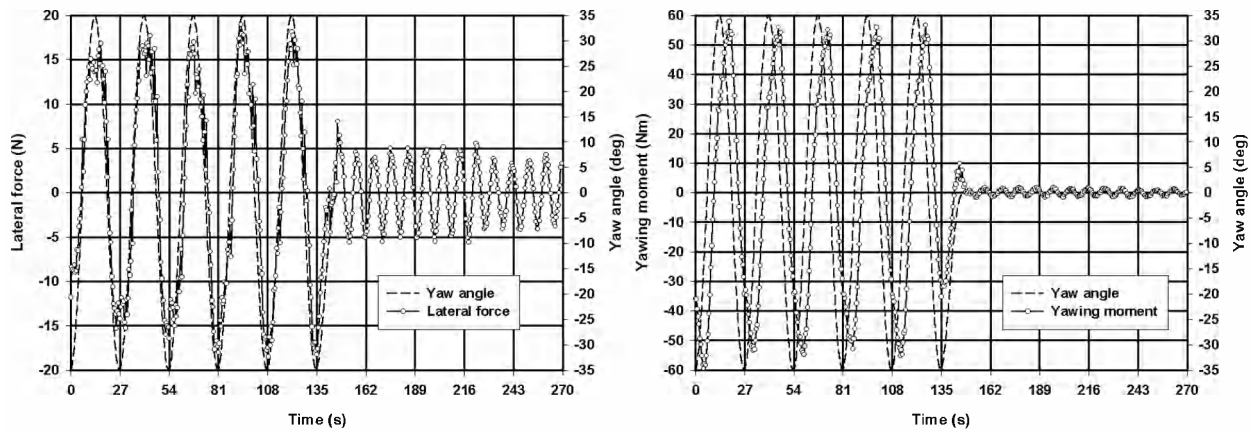
Figure 3.21 Lateral force and yawing moment measured during test type PMMPS2 for model E at intermediate draught and 20% UKC (F_n=0.033)
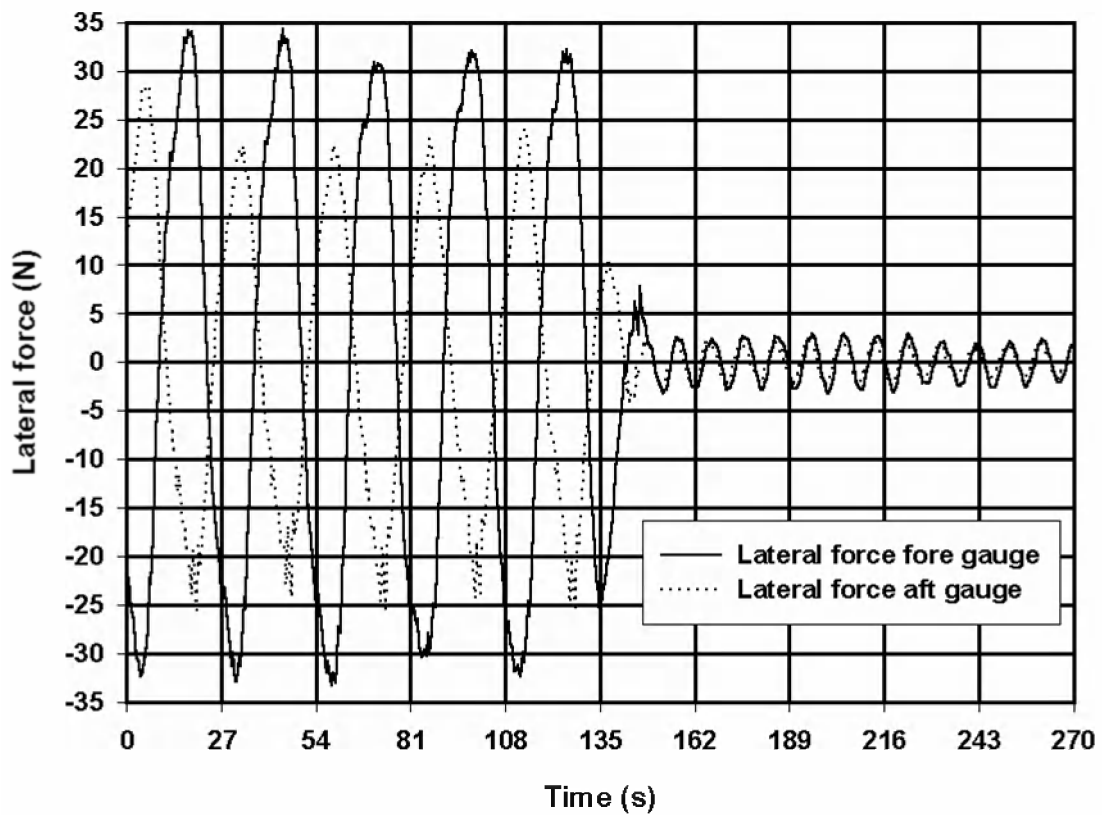
Figure 3.22 Lateral force measured on fore and aft gauges during test type PMMPS2 for model E at intermediate draught and 20% UKC (F_n=0.033)

228
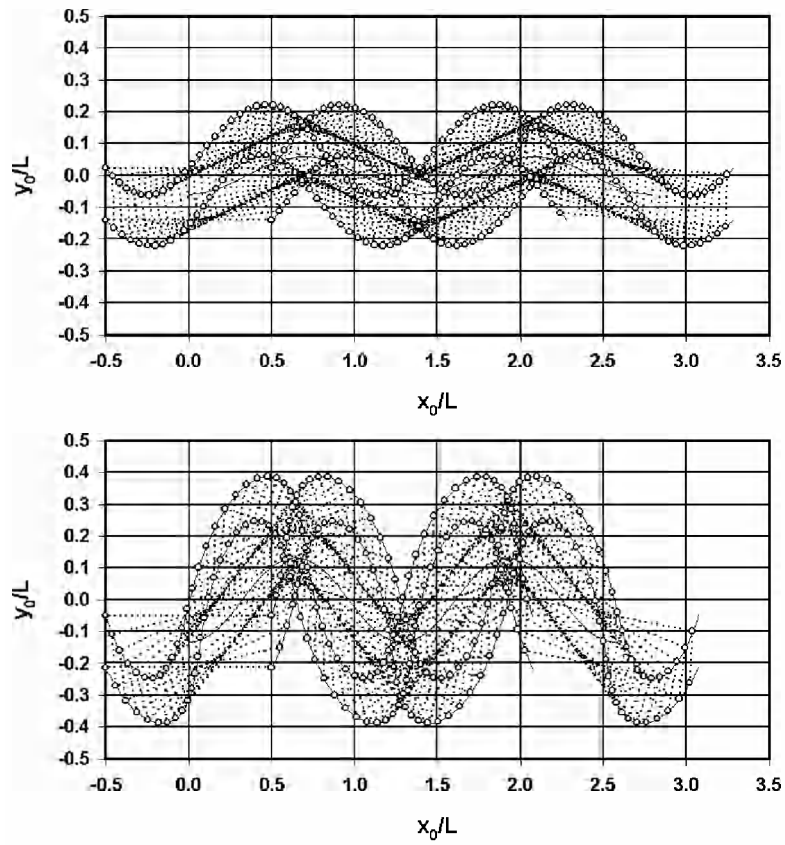
Figure 3.23 Swept path of a ship with B/L=0.16 during a harmonic yaw test with ω'=4.4, Ψ_A=15deg (top) or Ψ_A=35deg (bottom)
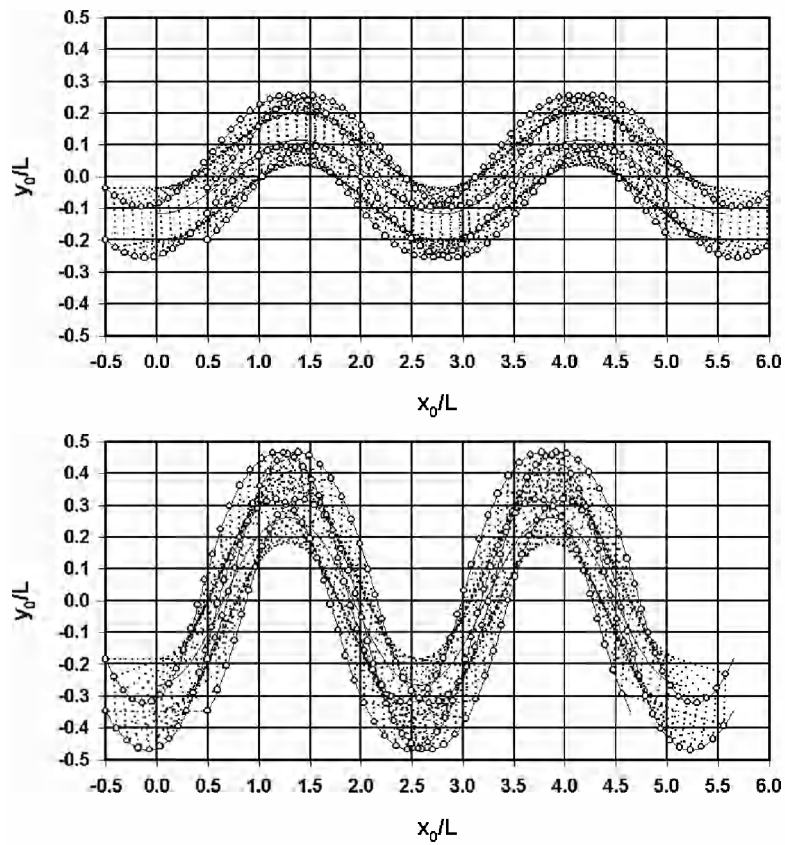
Figure 3.24 Swept path of a ship with B/L=0.16 during a harmonic yaw test with ω'=2.2, Ψ_A=15deg (top) or Ψ_A=35deg (bottom)

229
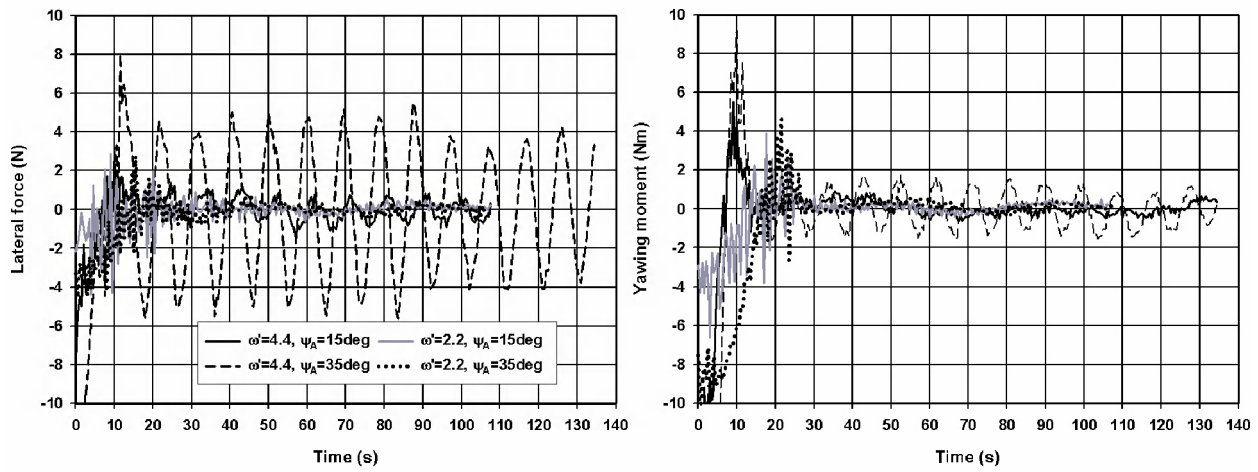
Figure 3.25 Lateral force and yawing moment measured during run-out phase for model E at intermediate draught and 20% UKC (F_n=0.033): influence of test frequency and yaw amplitude
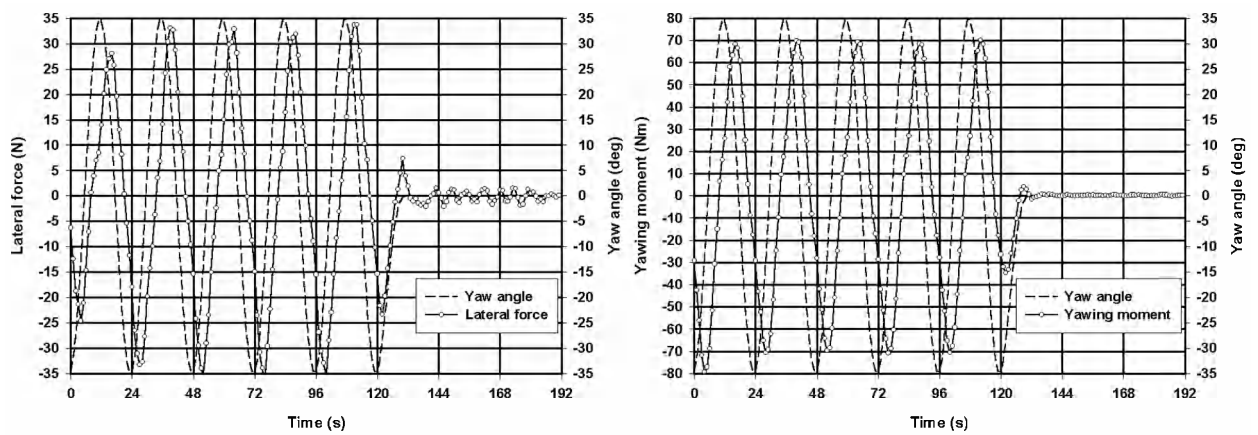
Figure 3.26 Lateral force and yawing moment measured during test type PMMPS2 for model D at 20% UKC (F_n=0.049)
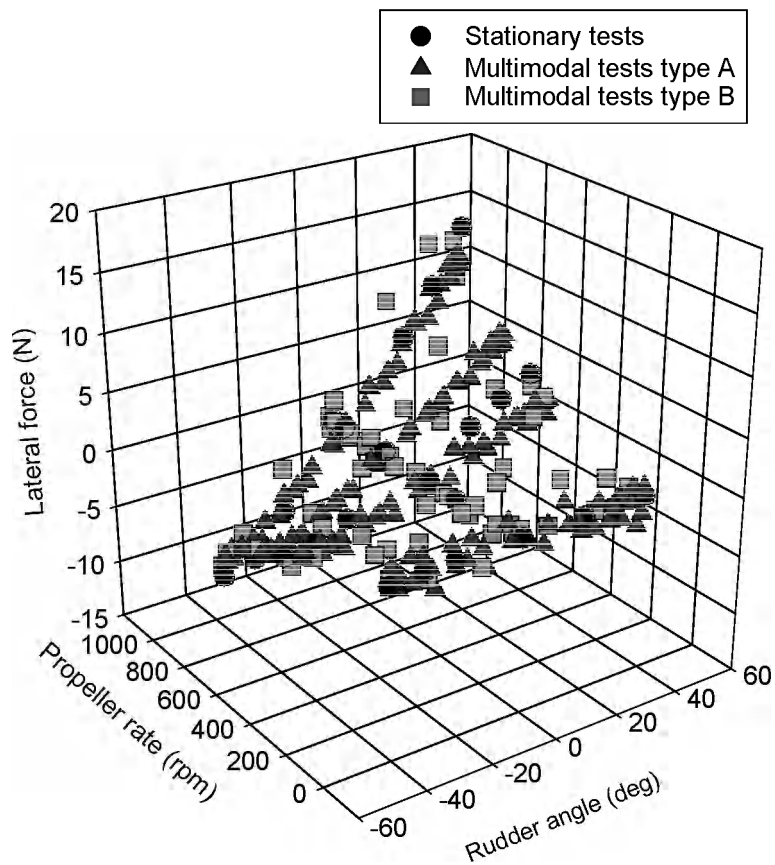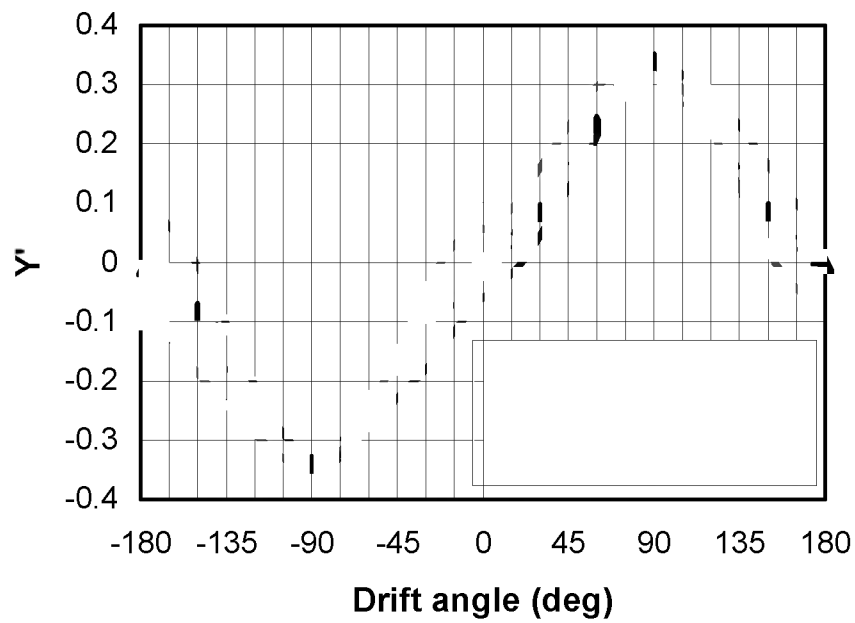
Figure 3.27 Comparison of measured lateral force during multi-modal and stationary tests: influence of drift angle on hull force at the top and influence of propeller rate and rudder angle at the bottom
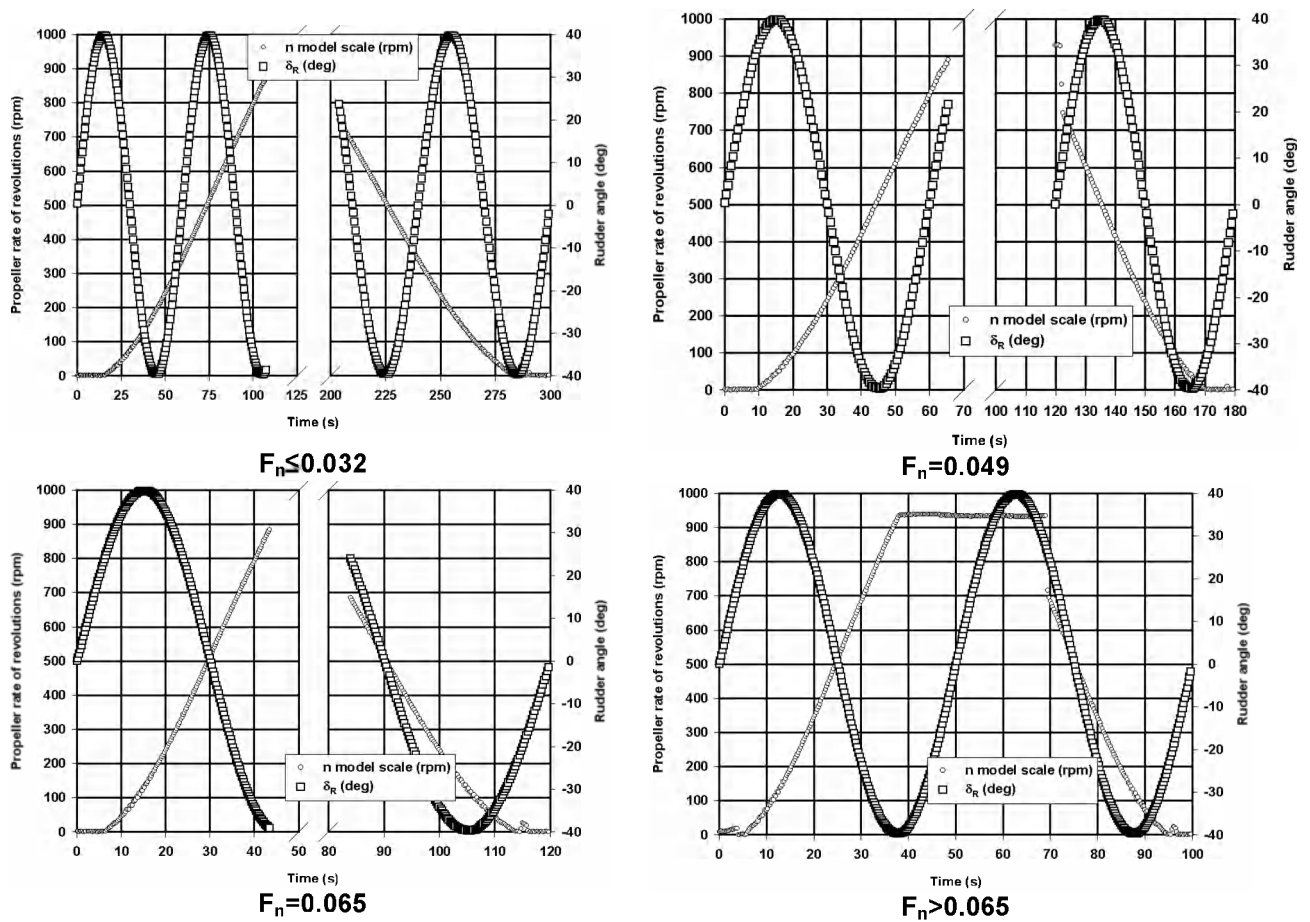
Figure 3.28 Multi-modal test of type B, variation of propeller rate and rudder angle during test runs with different Froude numbers
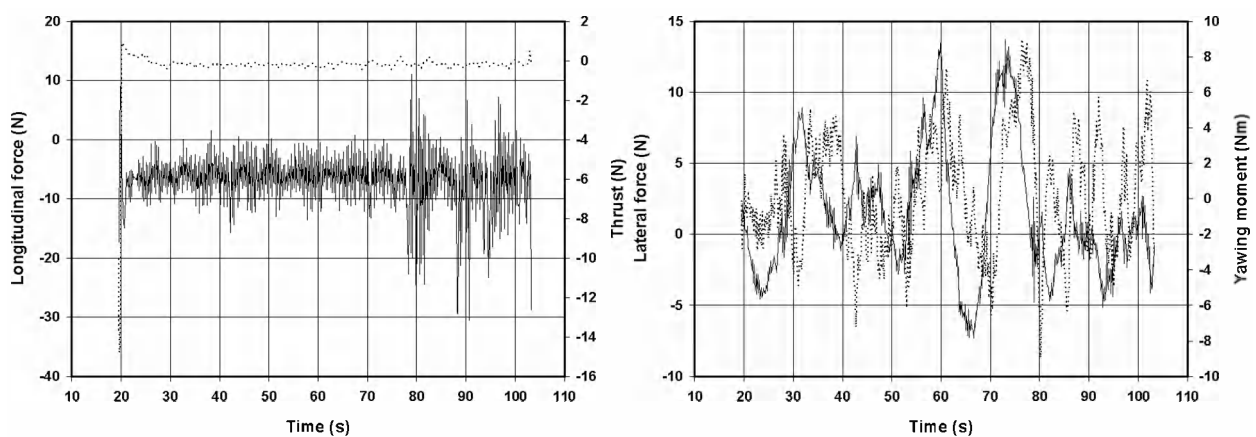
Figure 3.29 Model D at 7% UKC with a full scale speed of 12 knots: run D3_12100 (no propeller loading): left: longitudinal force (solid line) and thrust; right: lateral force (solid line) and yawing moment
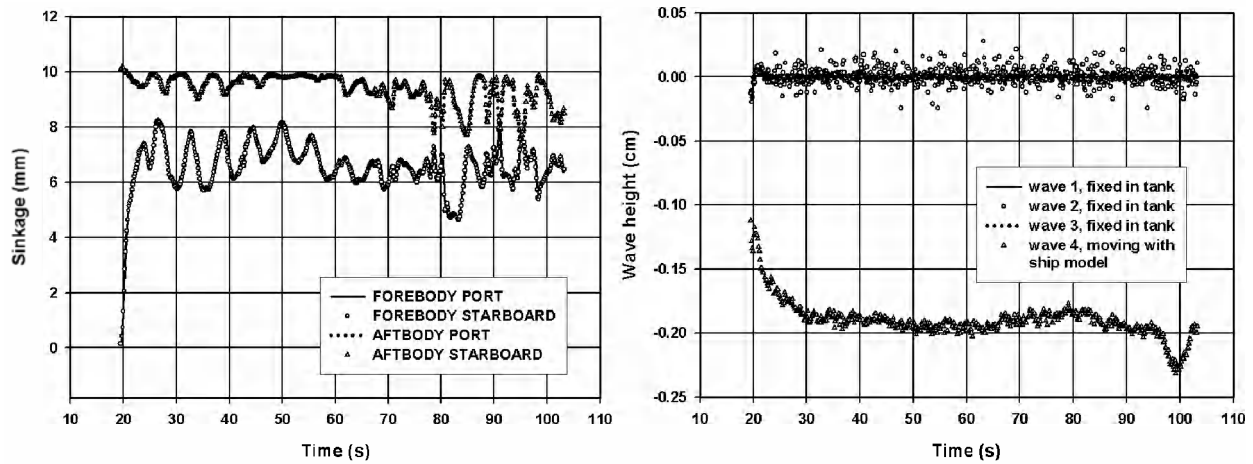
Figure 3.30 Model D at 7% UKC with a full scale speed of 12 knots: run D3_12100 (no propeller loading) sinkage at four positions of the ship model (left) and measurements of wave height on three positions fixed in the tank and one position in front of the ship model (right)
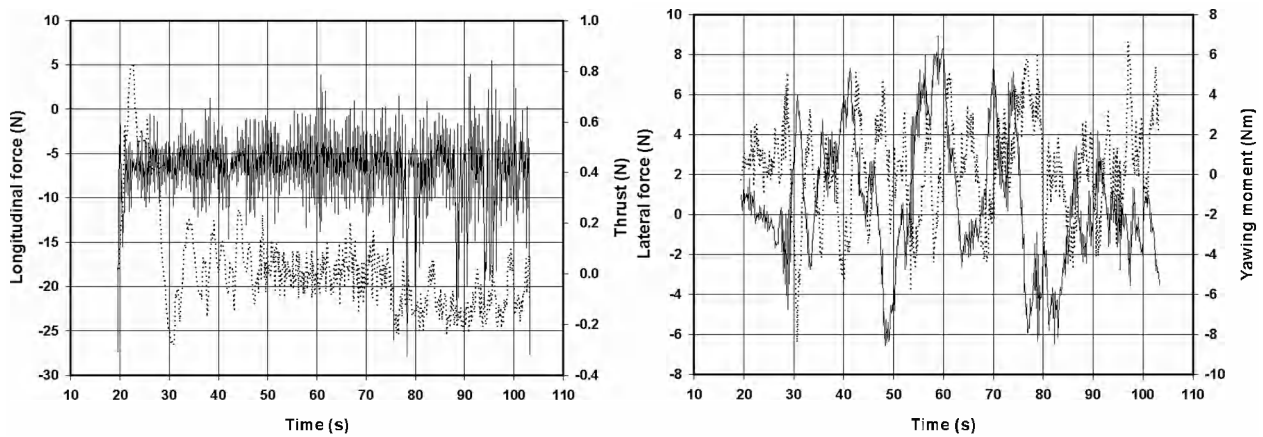
Figure 3.31 Model D at 7% UKC with a full scale speed of 12 knots: run D3_12200: left: longitudinal force (solid line) and thrust; right: lateral force (solid line) and yawing moment
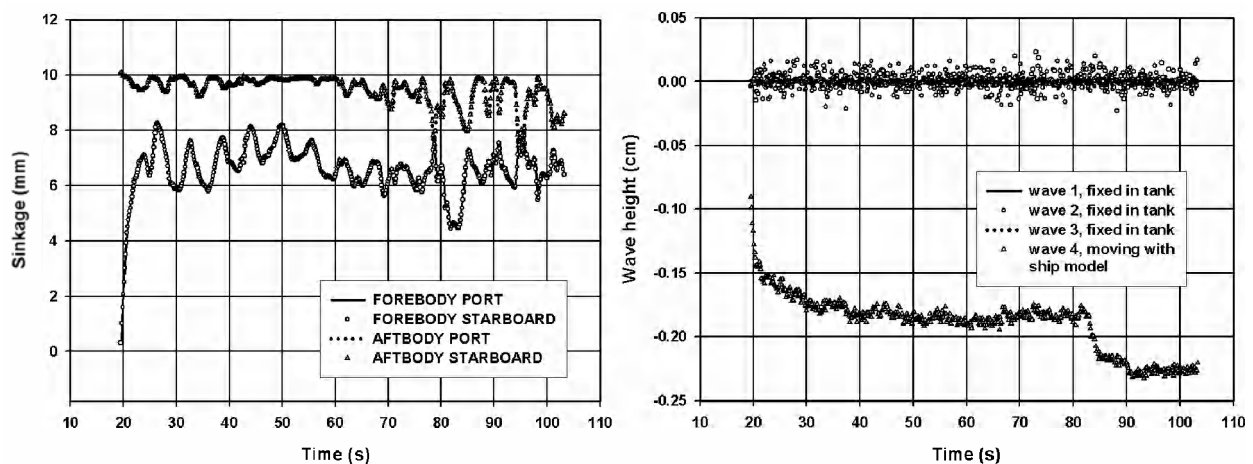
Figure 3.32 Model D at 7% UKC with a full scale speed of 12 knots: run D3_12200 sinkage at four positions of the ship model (left) and measurements of wave height on three positions fixed in the tank and one position in front of the ship model (right)

233
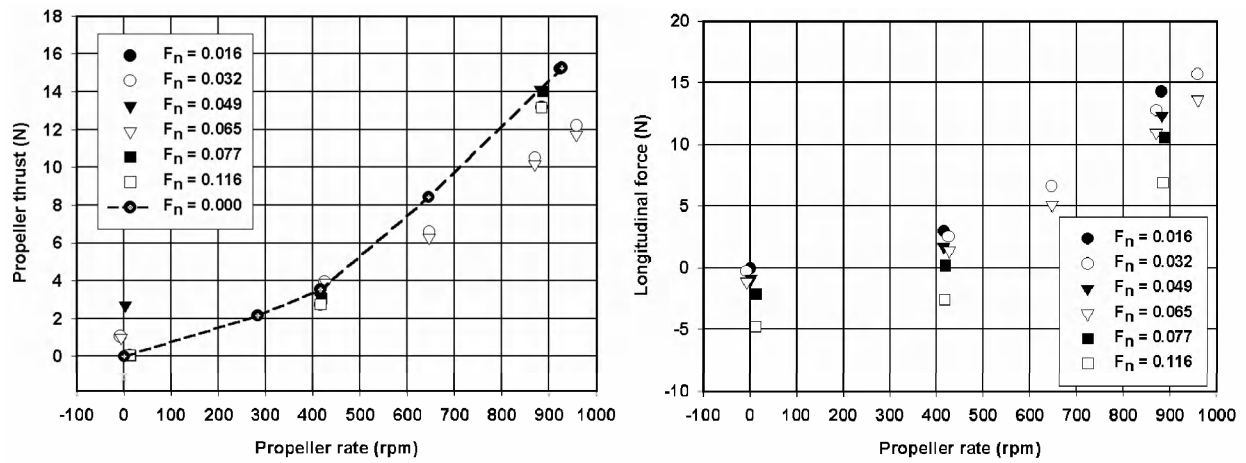
Figure 3.33 Model D at 20% UKC, inaccuracies of propeller thrust measurement (model scale) and corresponding measurement of longitudinal force
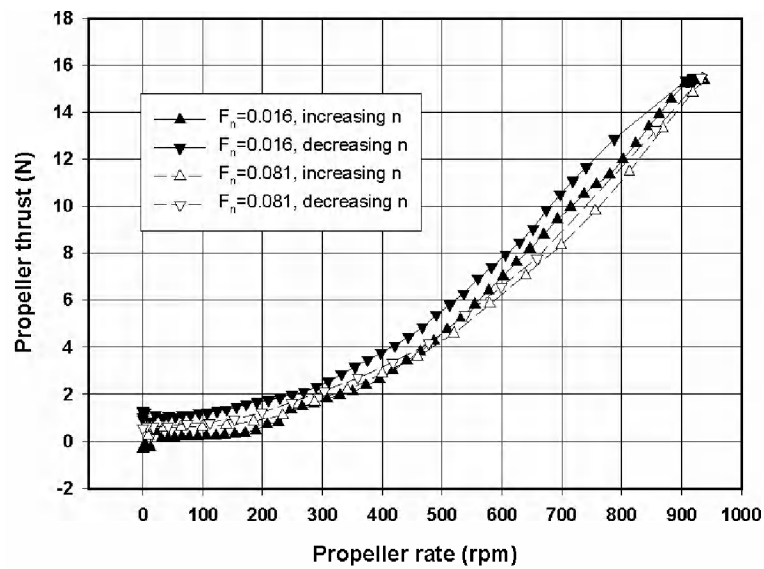
Figure 3.34 Model D at 20% UKC, propeller thrust as function of propeller rate measured during multimodal tests of type B (harmonically varying propeller rate and rudder angle)
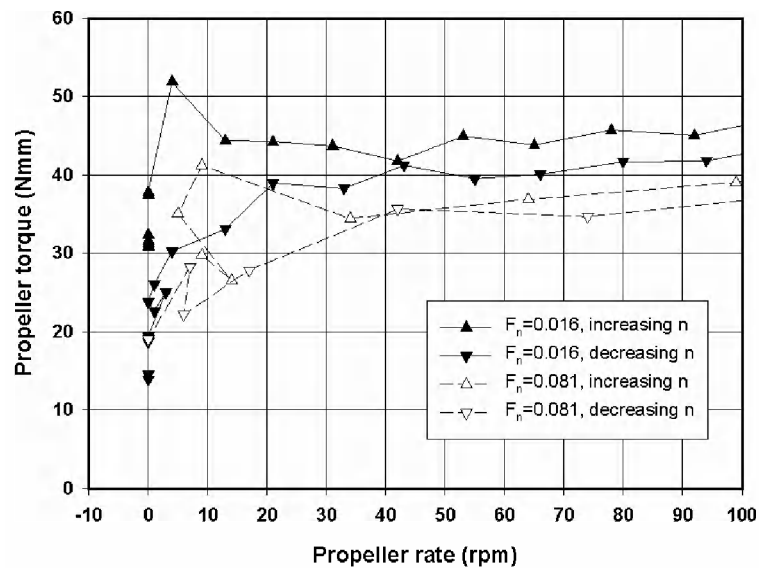
Figure 3.35 Model D at 20% UKC, propeller torque as function of propeller rate measured during multimodal tests of type B (only low propeller rate of turn)

234
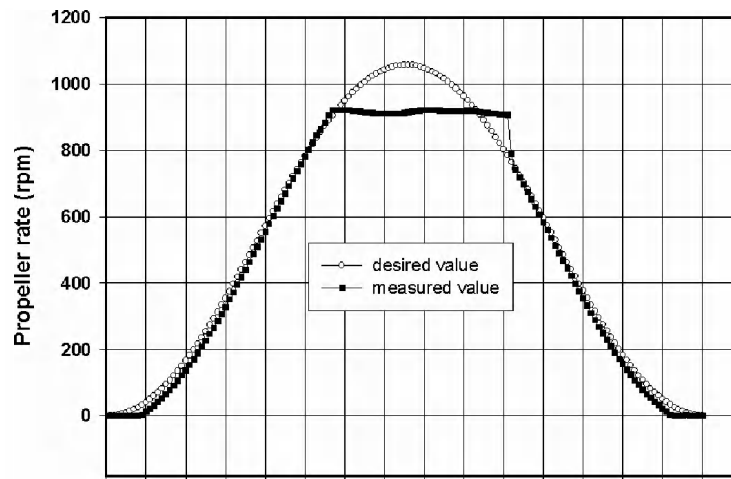
Figure 3.36 Model D at 20% UKC, comparison of desired and measured value of propeller revolutions
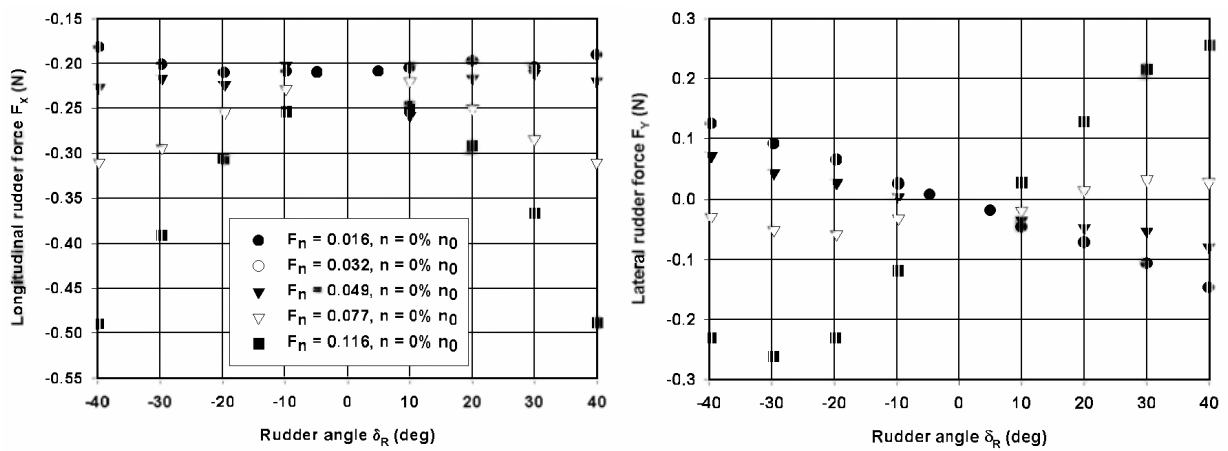
Figure 3.37 Model D at 20% UKC, longitudinal rudder force F_X and lateral rudder force F_Y based on rudder forces F_T and F_N for low to zero propeller rate
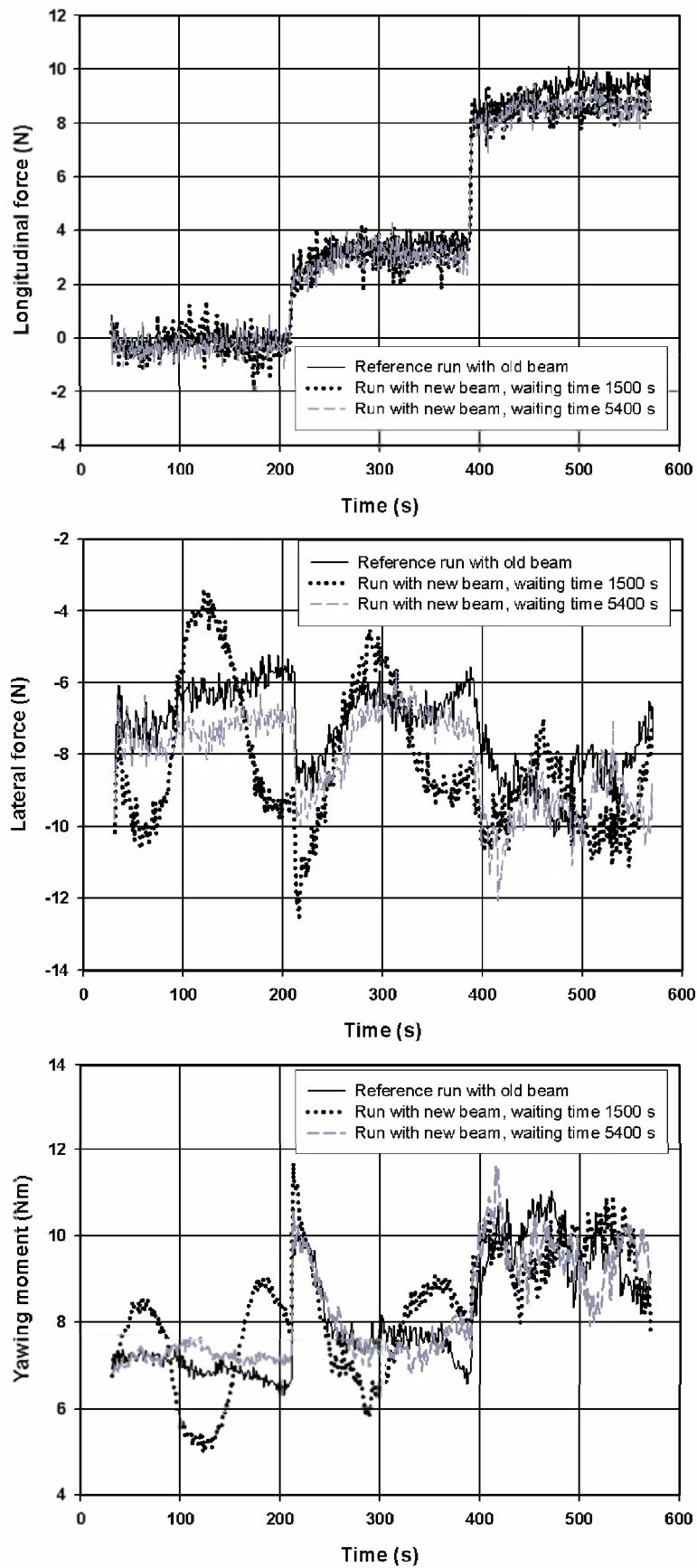
Figure 3.38 Model E at 20% UKC, comparison of measured longitudinal force, lateral force and yawing moment according to the influence of waiting time
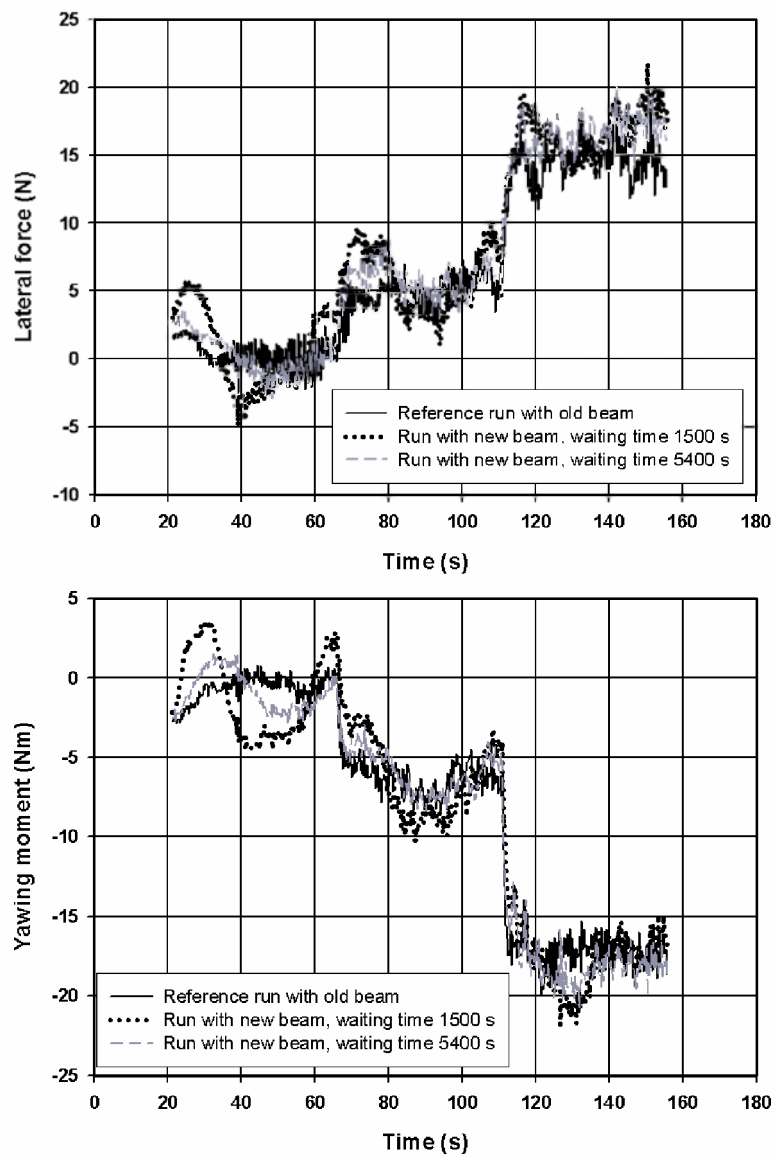
Figure 3.39 Model E at 20% UKC, comparison of lateral force and yawing moment according to the influence of waiting time
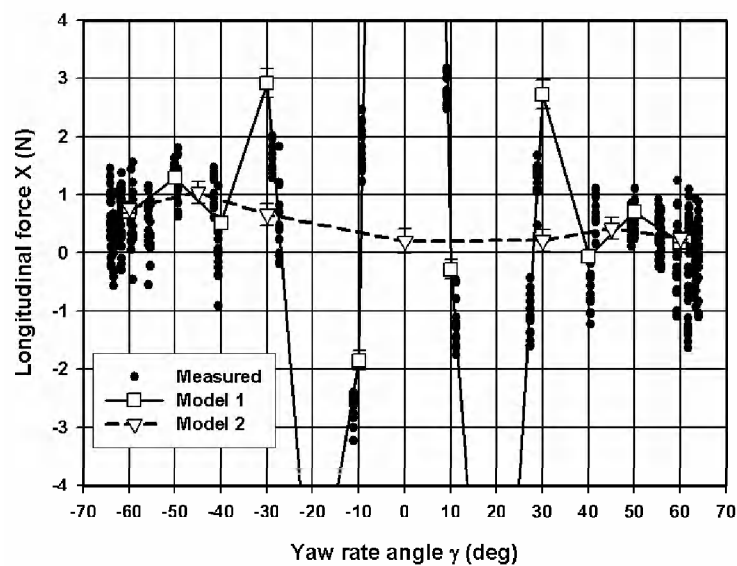
Figure 3.40 Model D at 20% UKC, influence of input parameters γ on tabular output parameters for a regression analysis using ODRPACK
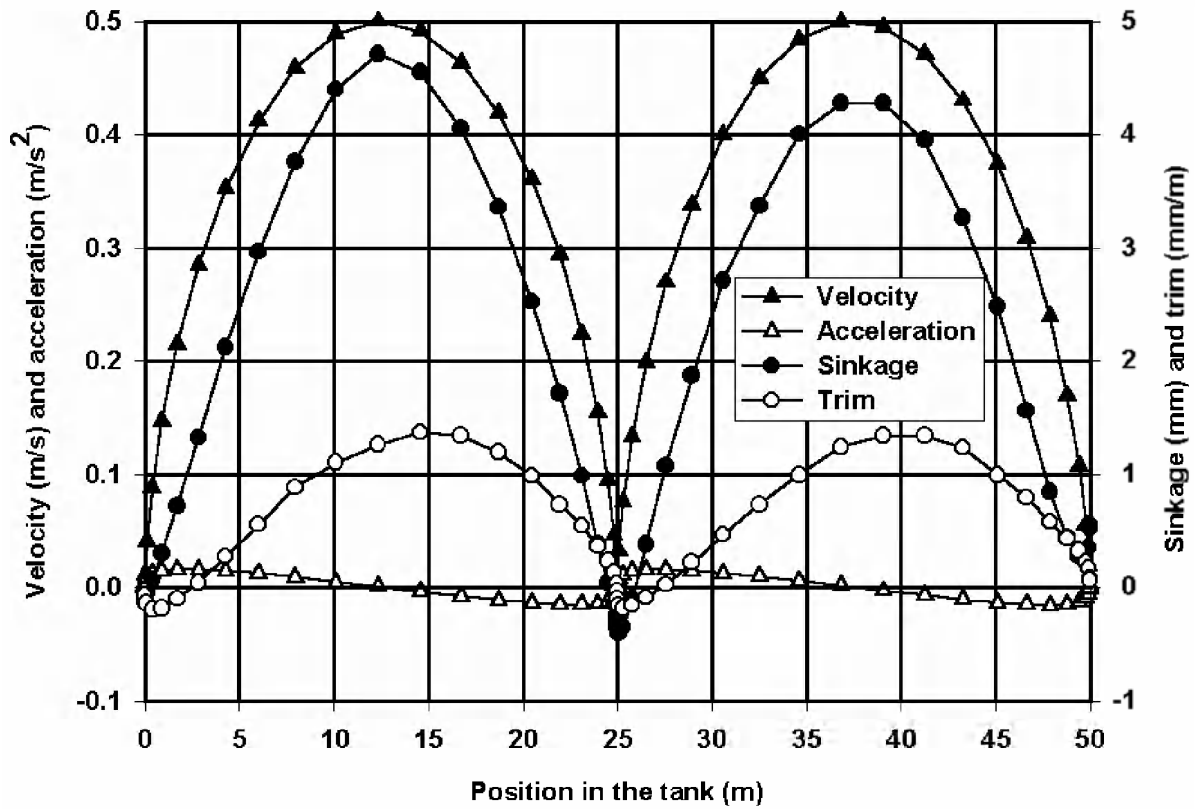
Figure 4.1 Model E, fully laden and 20% UKC, a multi-modal test for surge motion
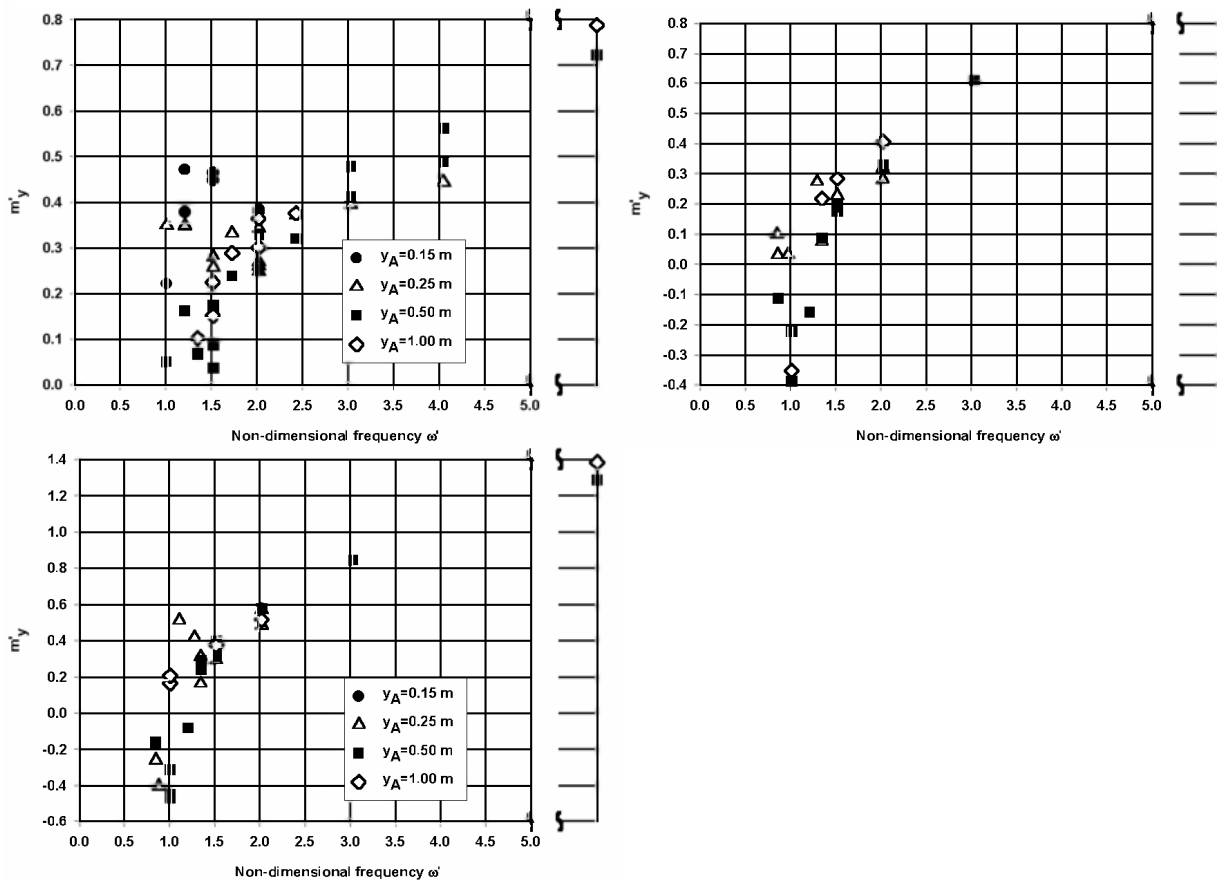
Figure 4.2 Model D, non-dimensional added mass due to sway as function of non-dimensional frequency ω' for 20% UKC (left, top), 13% UKC (right, top) and 7% UKC (bottom) (for reference non-dimensional ship's mass m'=0.17)
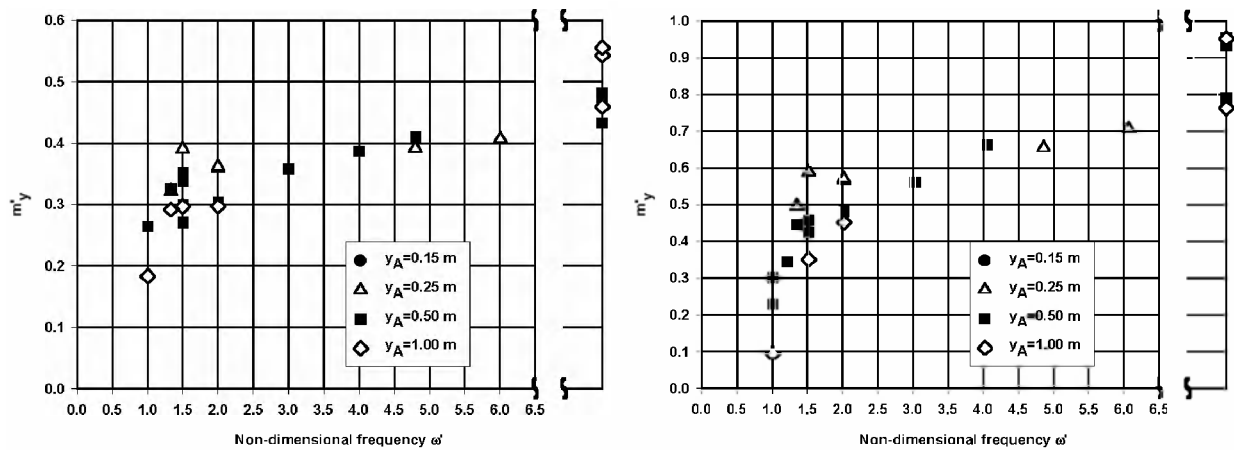
Figure 4.3 Model E, non-dimensional added mass due to sway as function of frequency ω' for 50% UKC (left) and 20% UKC (right) (for reference non-dimensional ship's mass m'=0.27)
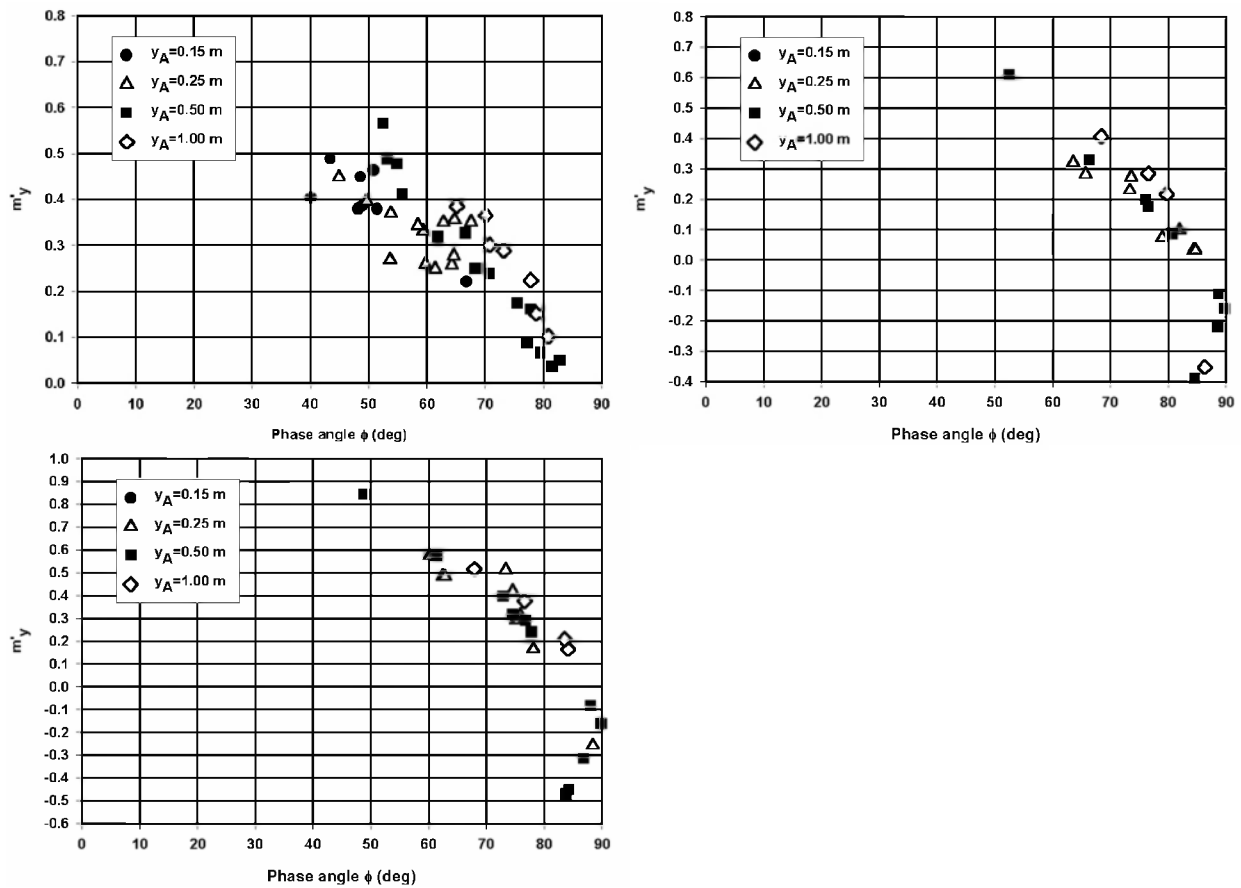
Figure 4.4 Model D, non-dimensional added mass due to sway as function of phase angle for 20% UKC (left, top), 13% UKC (right, top) and 7% UKC (bottom) (for reference non-dimensional ship's mass m'=0.17)

240
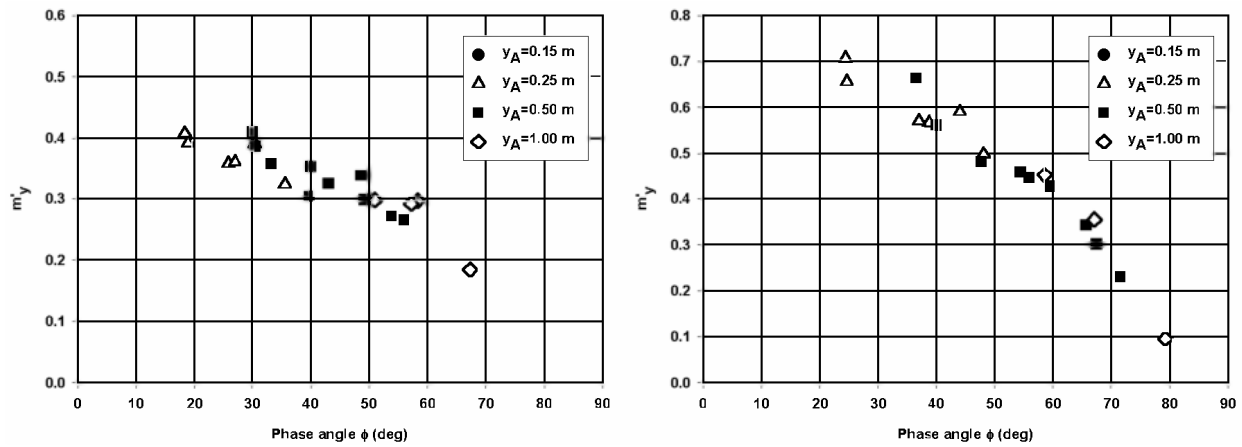
Figure 4.5 Model E, non-dimensional added mass due to sway as function of phase angle for 50% UKC (left) and 20% UKC (right) (for reference non-dimensional ship's mass m'=0.27)
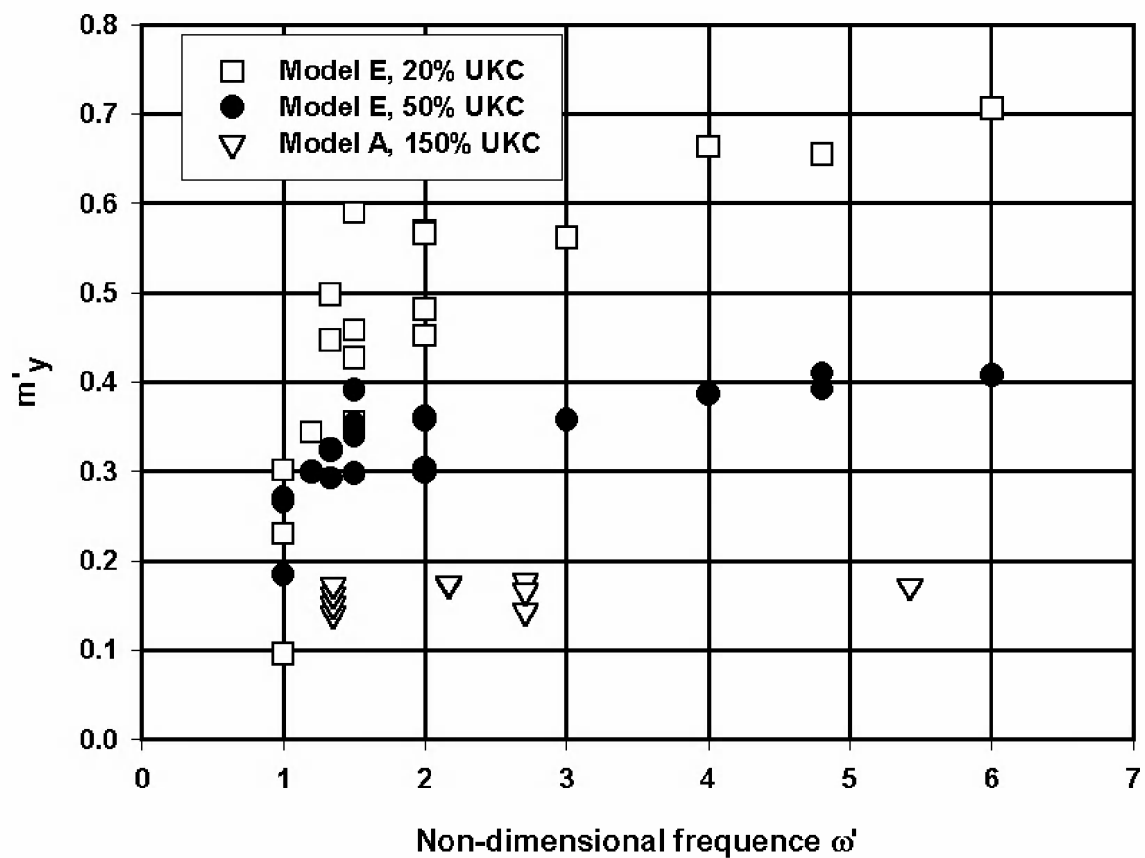
Figure 4.6 Frequency dependence of added mass with decreasing under keel clearance (full form)
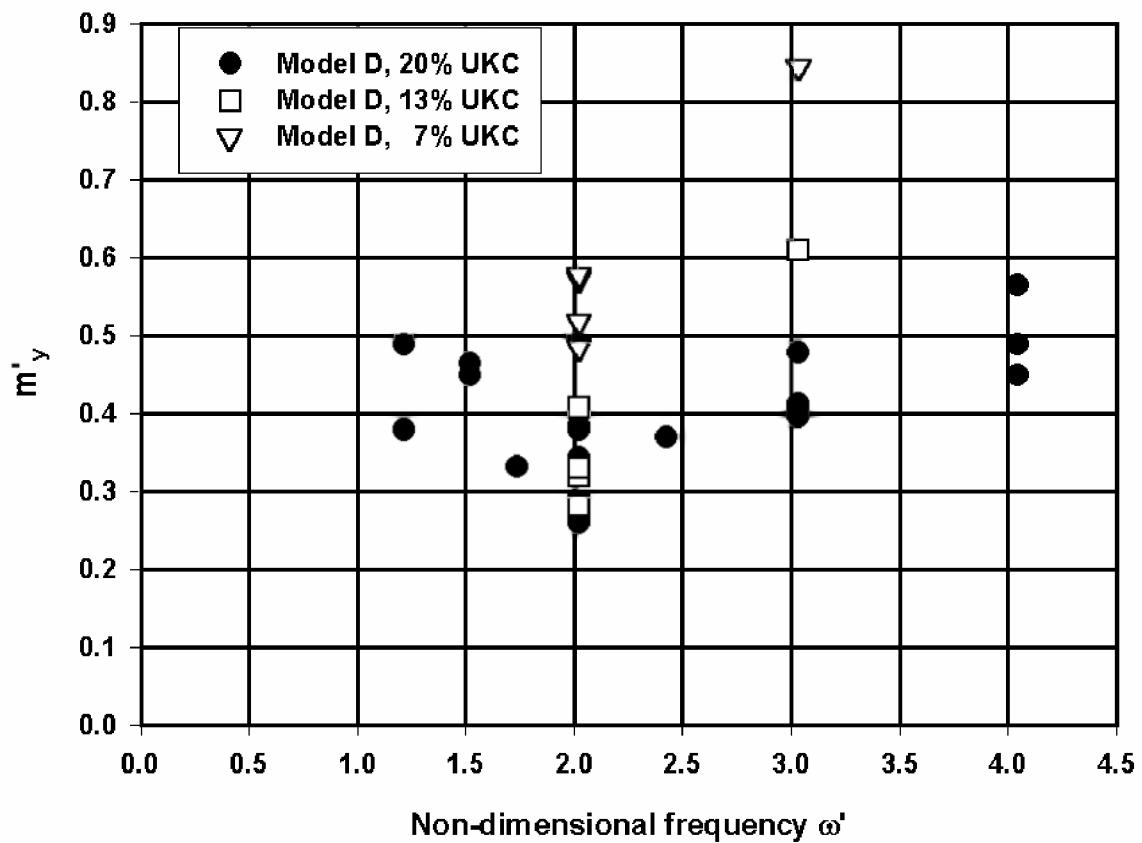
Figure 4.7 Model D, selection of added mass m_y based on phase angle ϕ (for reference non-dimensional ship's mass m'=0.17)
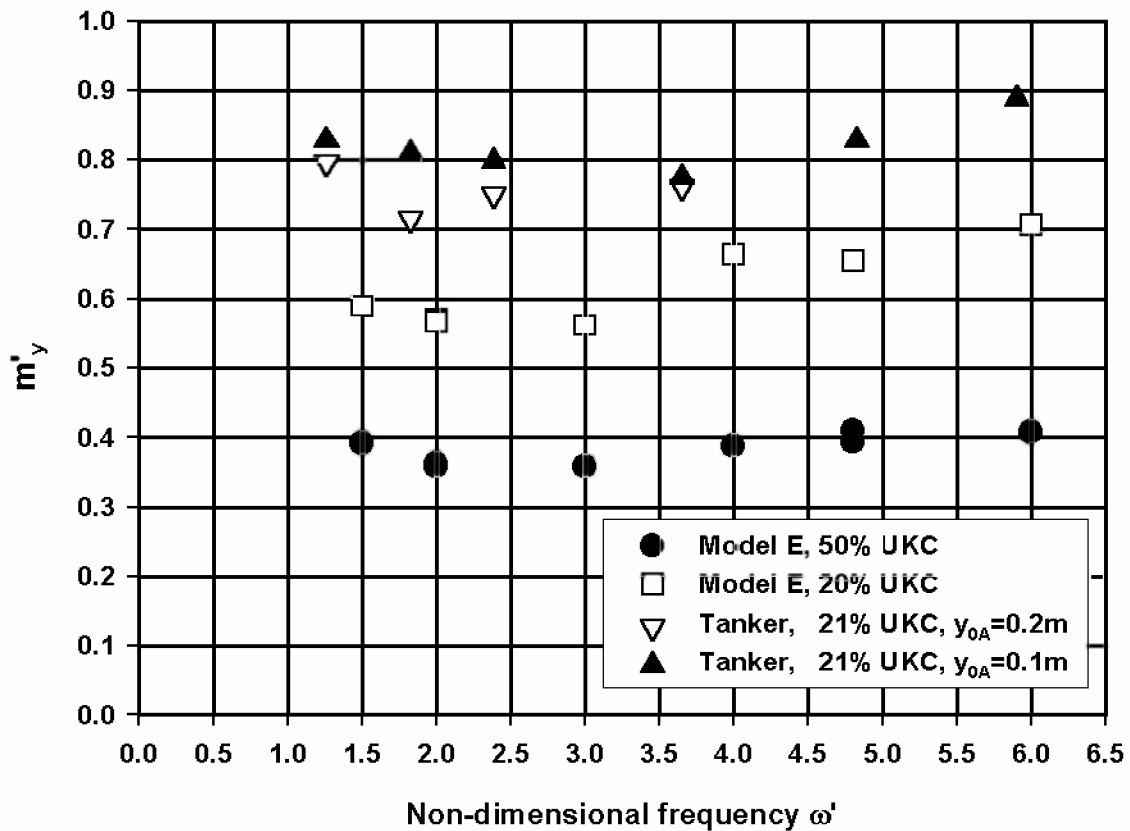
Figure 4.8 Model E, selection of added mass m_y based on phase angle ϕ (for reference non-dimensional ship's mass m'=0.27) and comparison with results reported in [77]

242
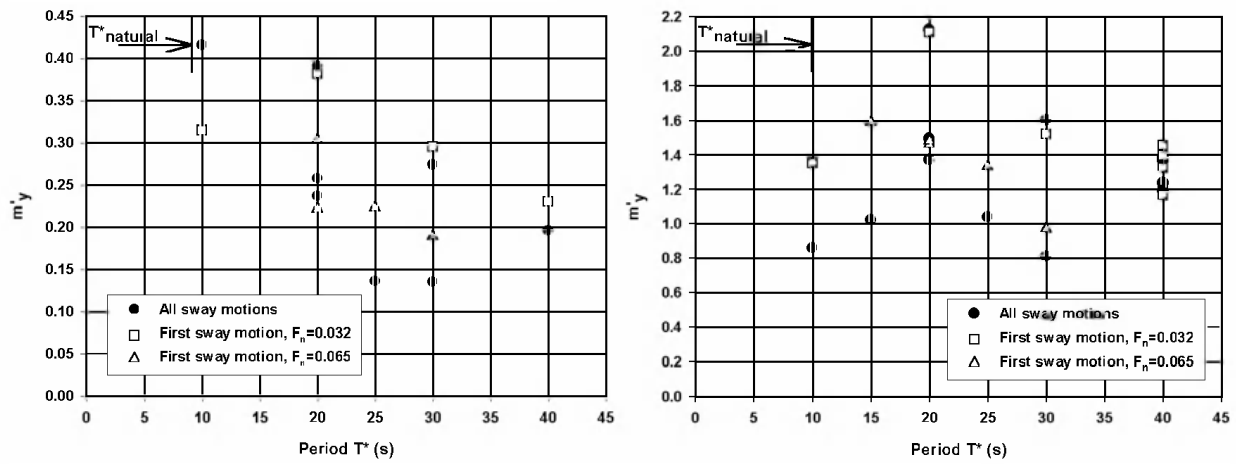
Figure 4.9 Model D, non-dimensional added mass as function of oscillation period during non-conventional sway tests for 20% UKC (left) and 7% UKC (right) (for reference non-dimensional ship's mass m'=0.17)
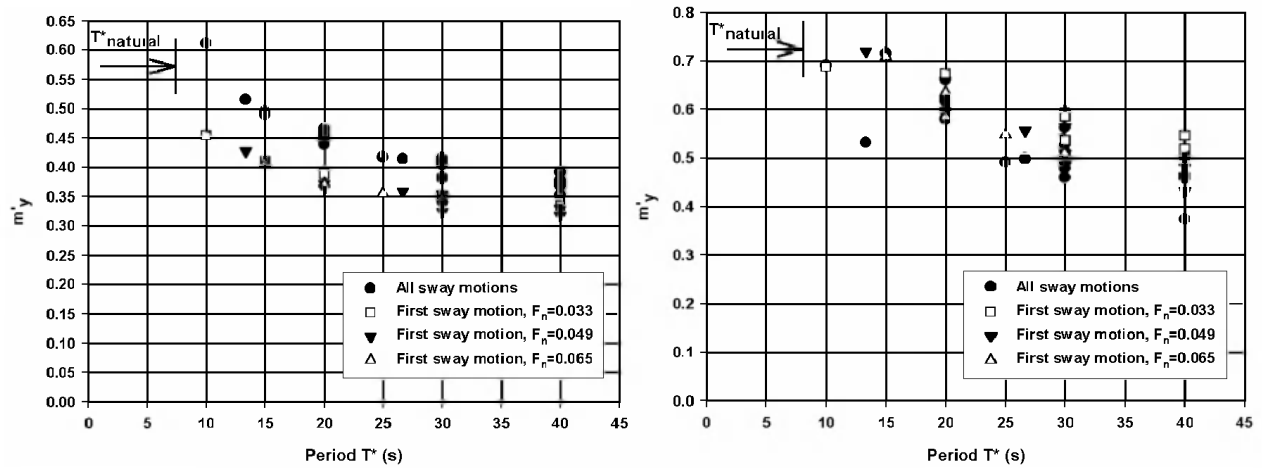
Figure 4.10 Model E, non-dimensional added mass as function of oscillation period during non-conventional sway tests for 50% UKC (left) and 20% UKC (right) (for reference non-dimensional ship's mass m'=0.27)
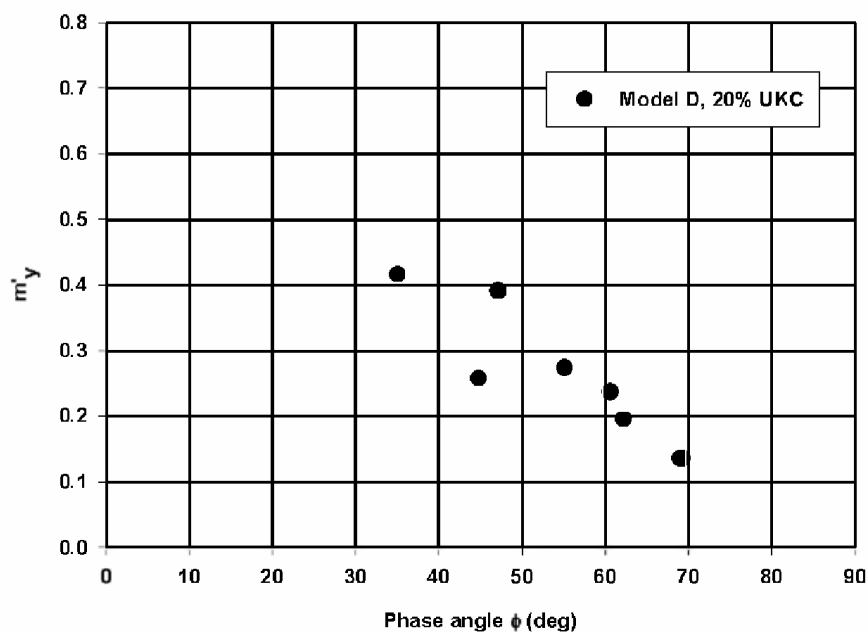
Figure 4.11 Model D, non-dimensional added mass as function of angle ϕ for alternative sway tests (for reference non-dimensional ship's mass m'=0.17)

243
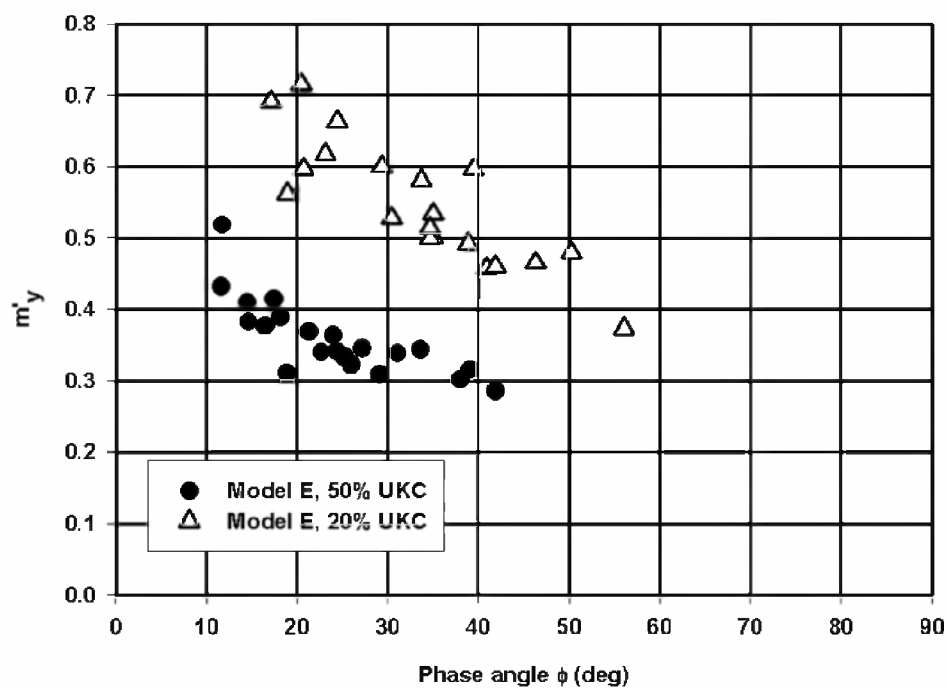
Figure 4.12 Model E, non-dimensional added mass as function of angle φ for alternative sway tests (for reference non-dimensional ship's mass m'=0.27)
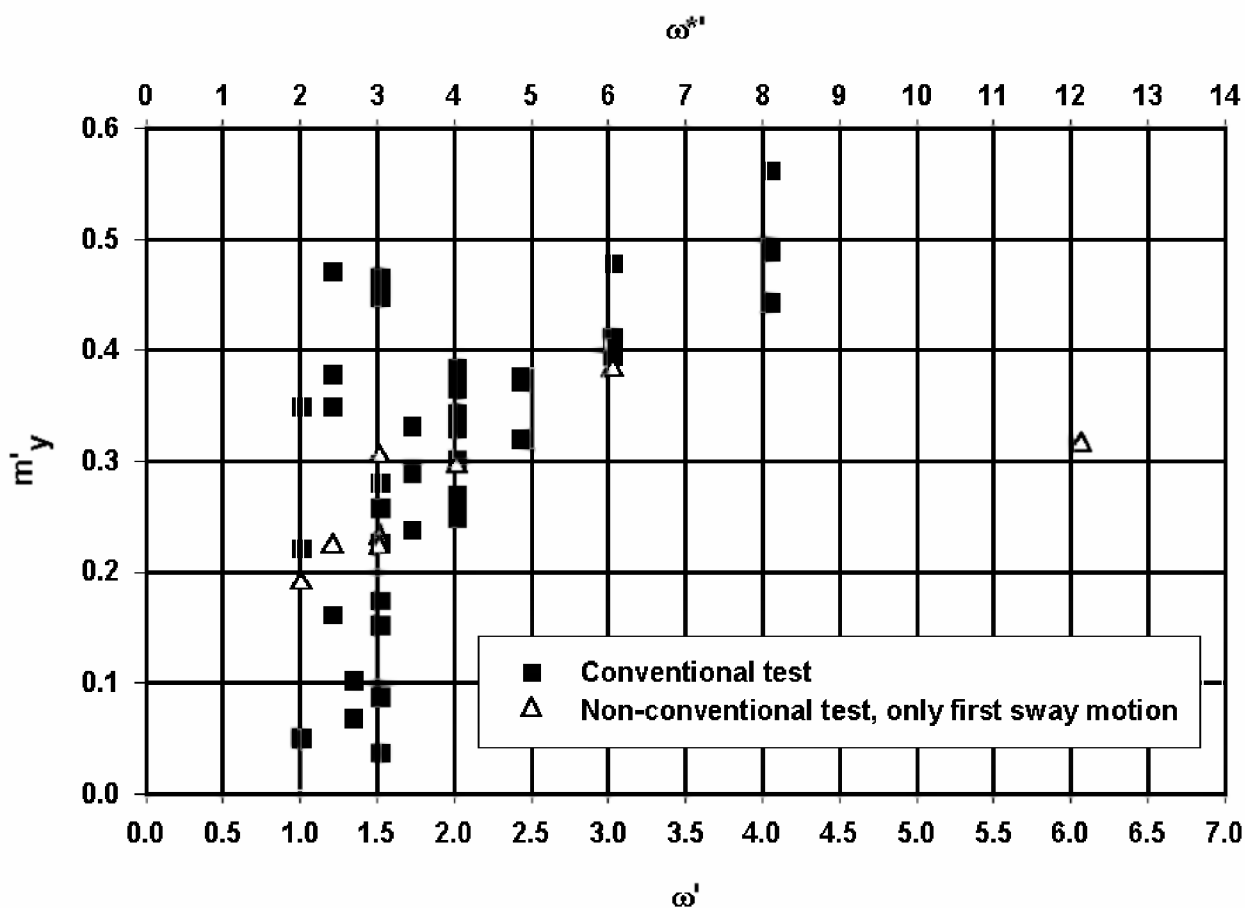
Figure 4.13 Model D, added mass due to sway, derived from harmonic and non-conventional sway tests as a function of test frequency (20% UKC) (for reference non-dimensional ship's mass m'=0.17)
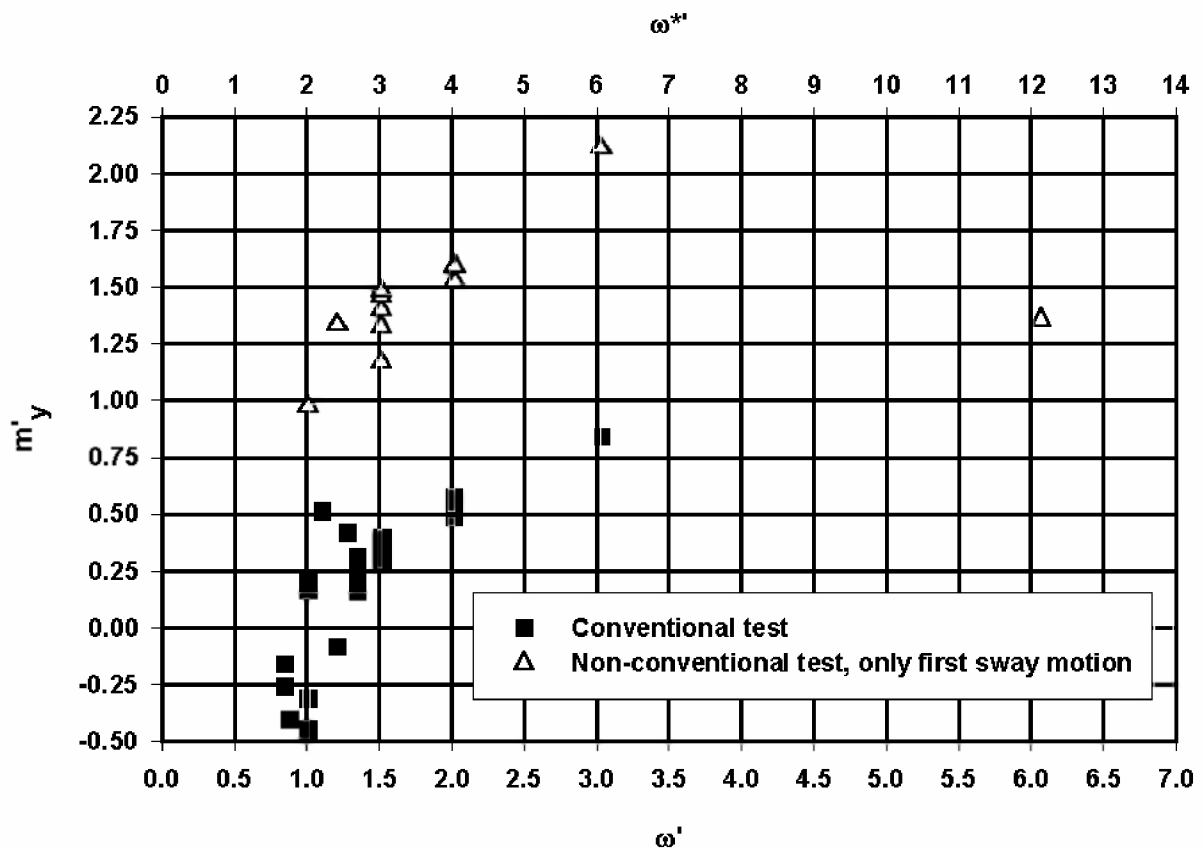
Figure 4.14 Model D, added mass due to sway, derived from harmonic and non-conventional sway tests as a function of test frequency (7% UKC) (for reference non-dimensional ship's mass m'=0.17)
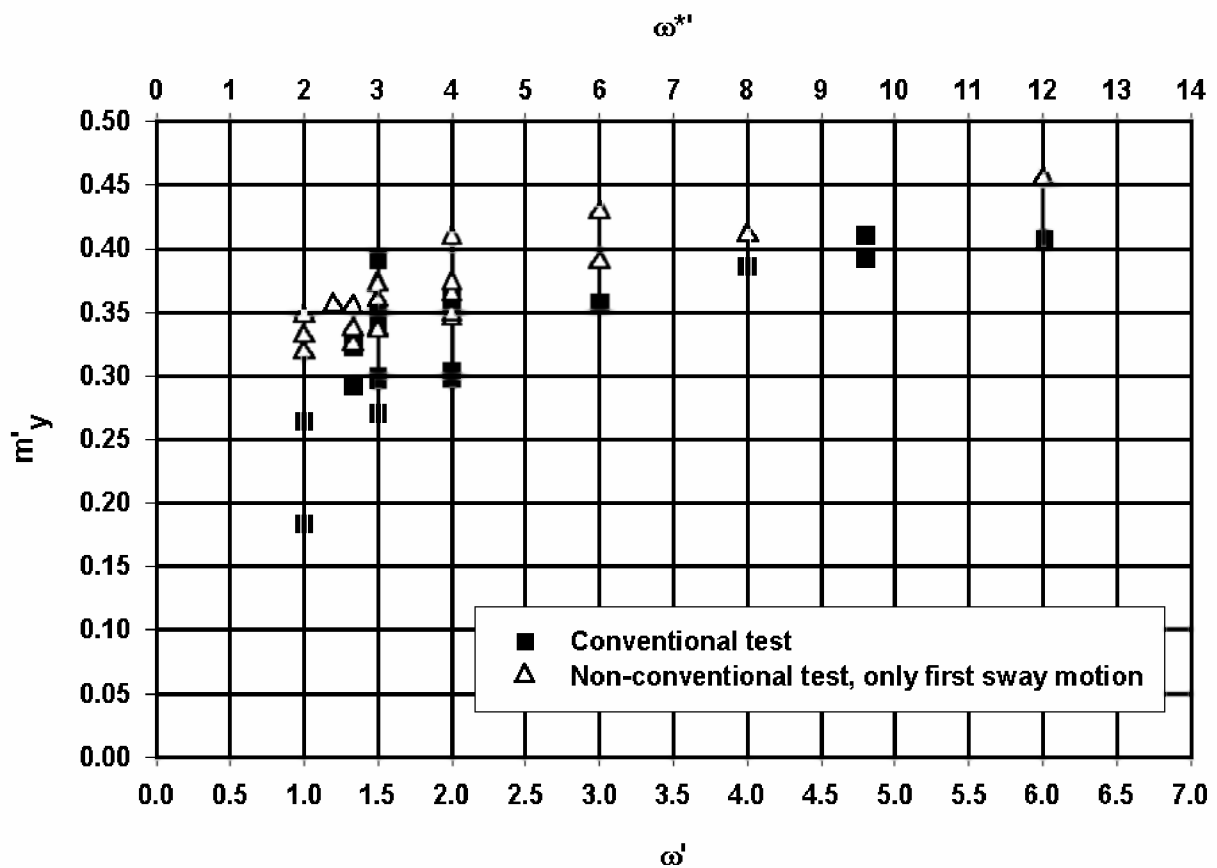
Figure 4.15 Model E, added mass due to sway, derived from harmonic and non-conventional sway tests as a function of test frequency (50% UKC) (for reference non-dimensional ship's mass m'=0.27)
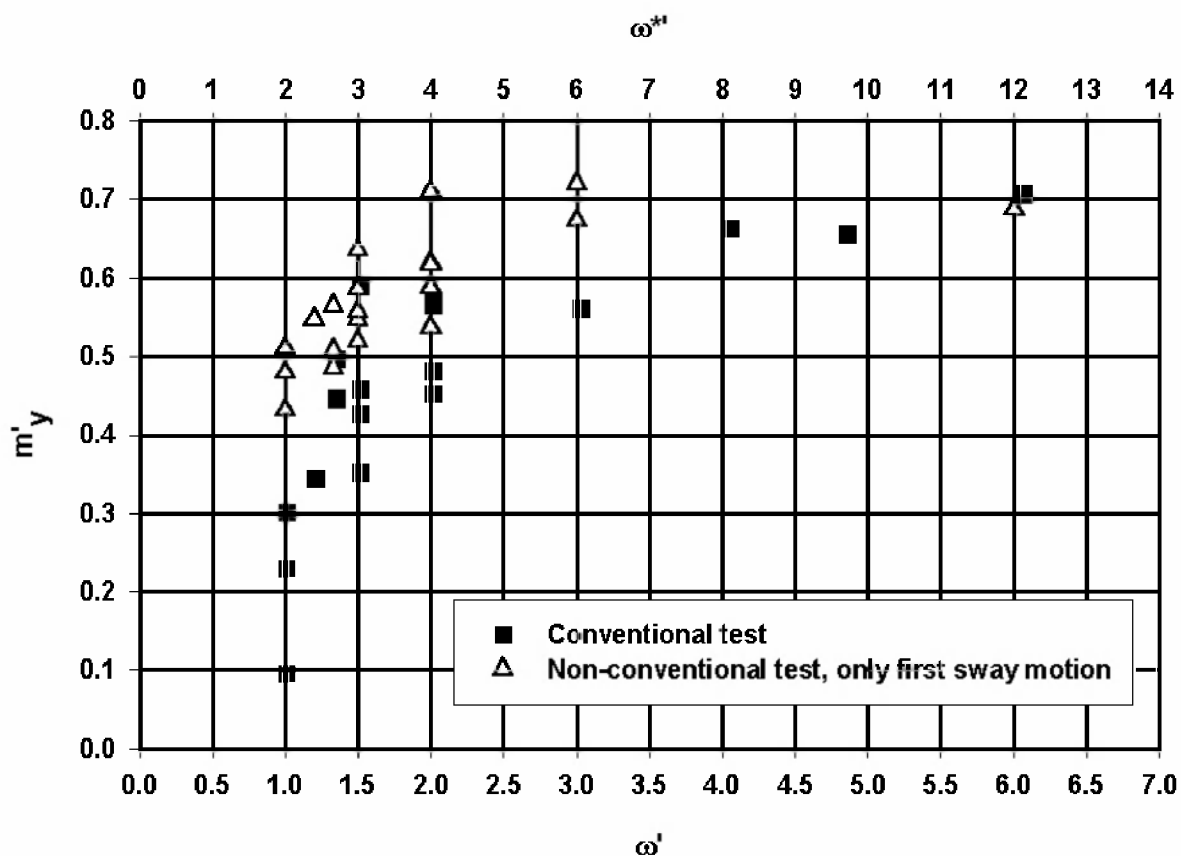
Figure 4.16 Model E, added mass due to sway, derived from harmonic and non-conventional sway tests as a function of test frequency (20% UKC) (for reference non-dimensional ship's mass m'=0.27)
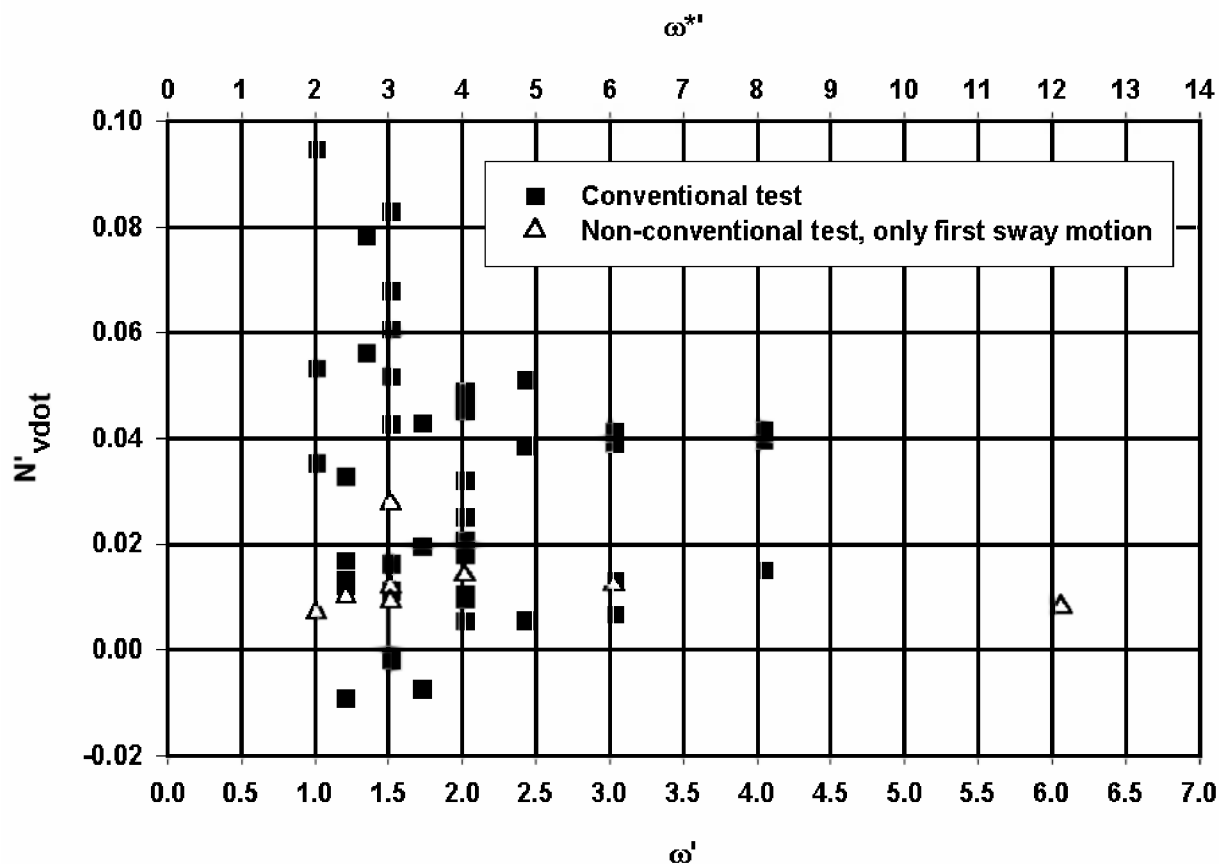
Figure 4.17 Model D, yawing moment acceleration coefficient, derived from harmonic and non-conventional sway tests as a function of test frequency (20% UKC)
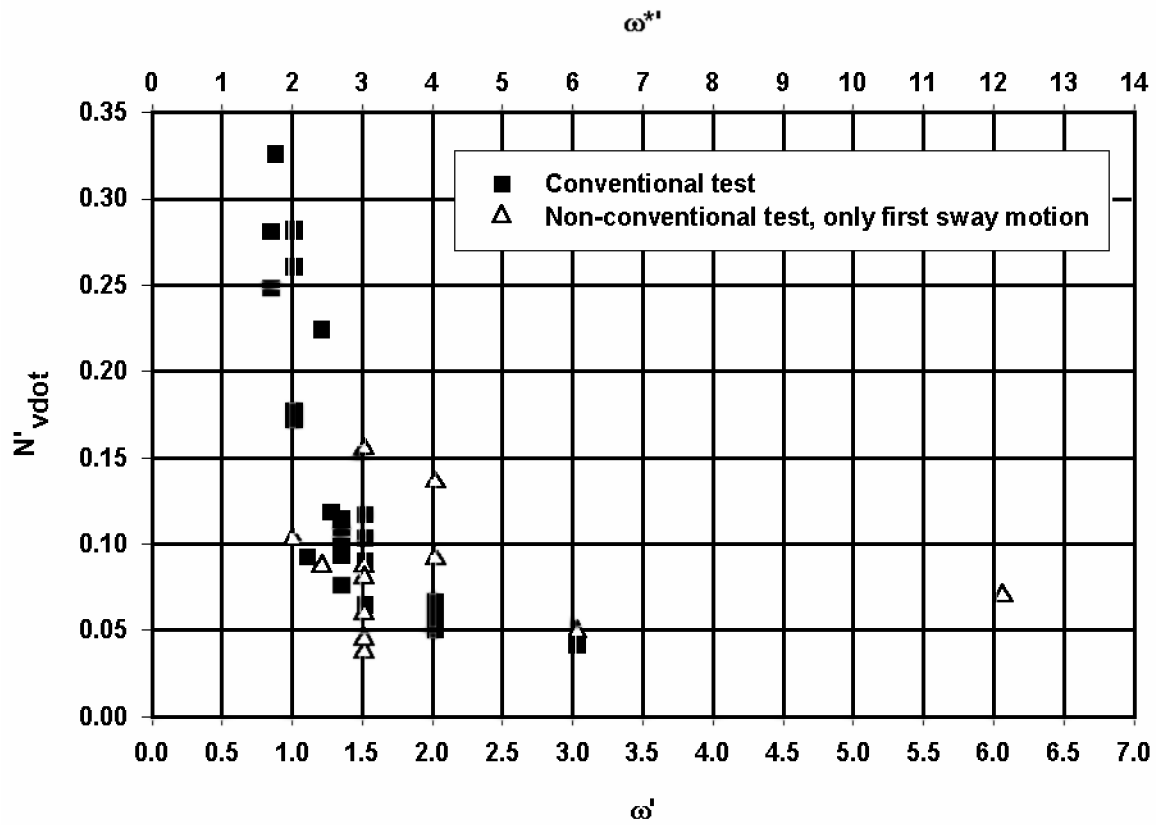
Figure 4.18 Model D, yawing moment acceleration coefficient, derived from harmonic and non-conventional sway tests as a function of test frequency (7% UKC)
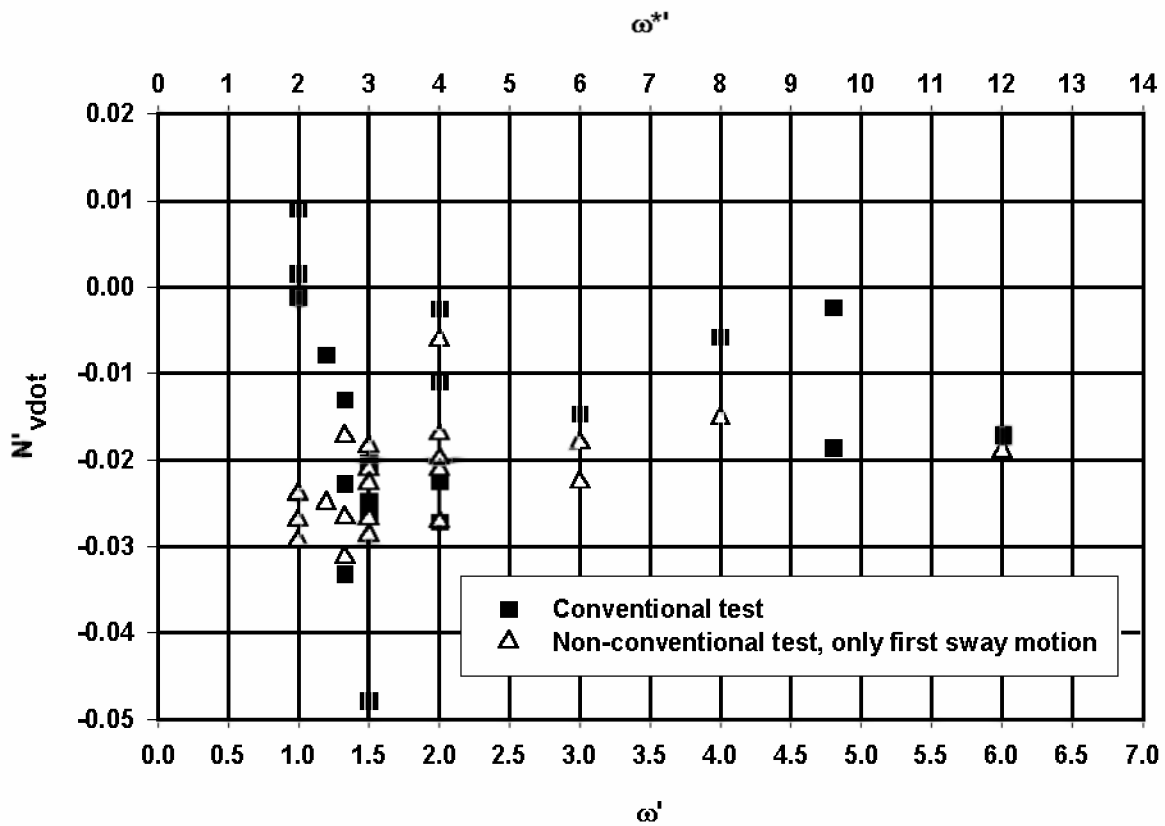
Figure 4.19 Model E, yawing moment acceleration coefficient, derived from harmonic and non-conventional sway tests as a function of test frequency (50% UKC)
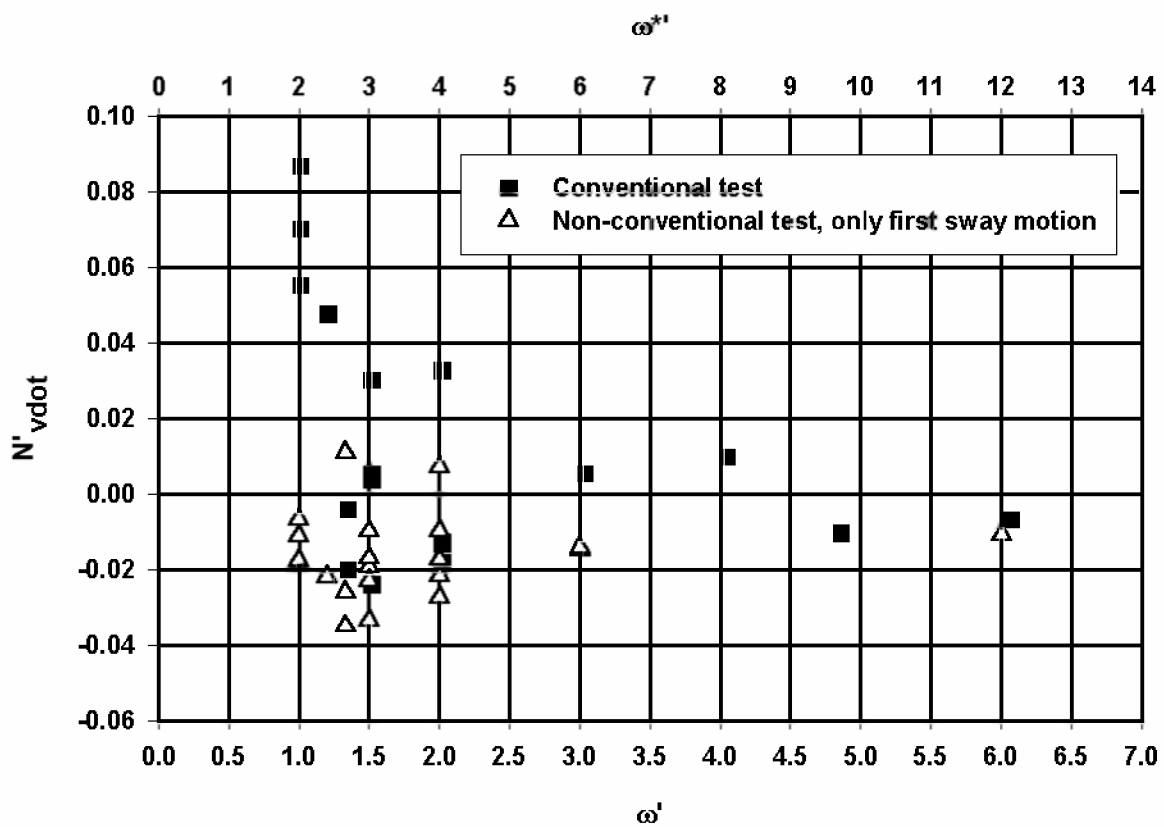
Figure 4.20 Model E, yawing moment acceleration coefficient, derived from harmonic and non-conventional sway tests as a function of test frequency (20% UKC)
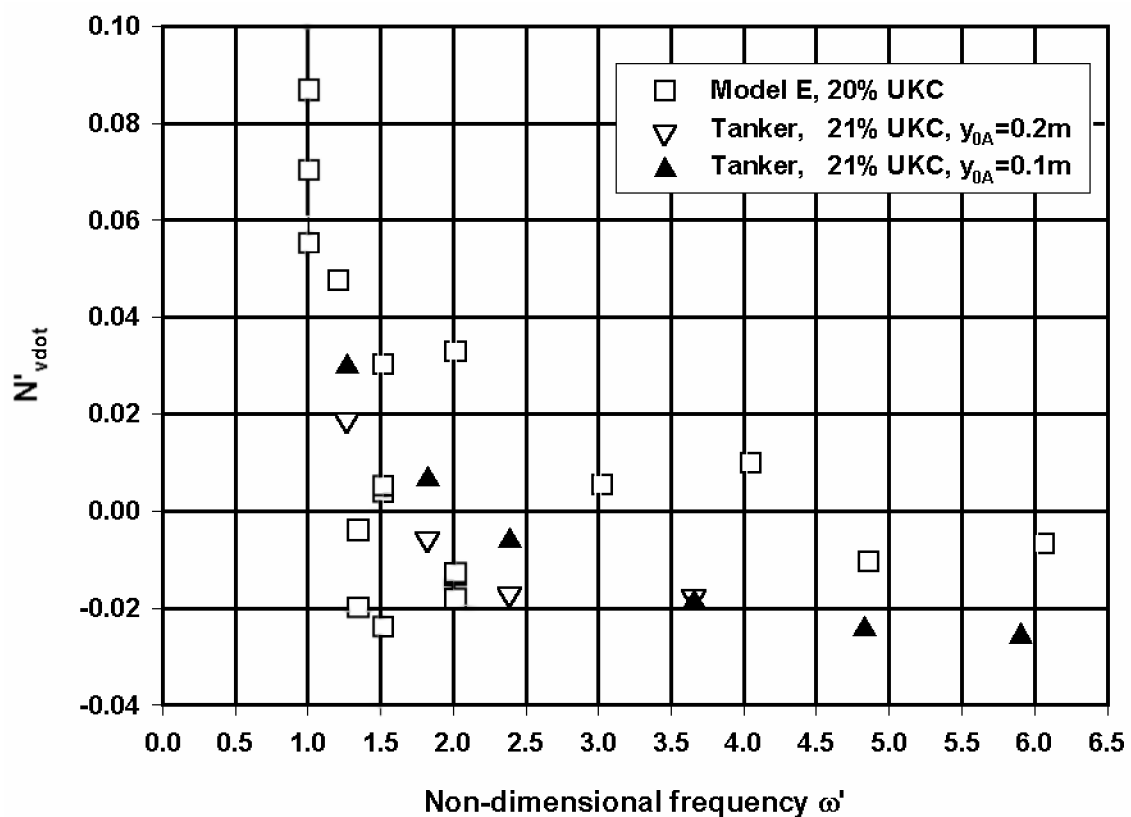
Figure 4.21 Comparison of yawing moment acceleration derivative for model E and a tanker reported in [77] only based on conventional sway tests

248
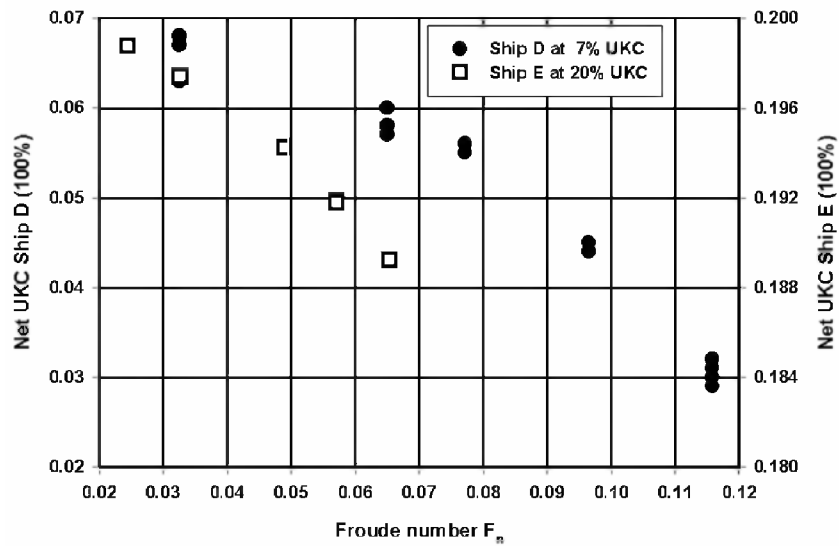
Figure 4.22 Net UKC as function of Froude number during resistance tests without propeller action
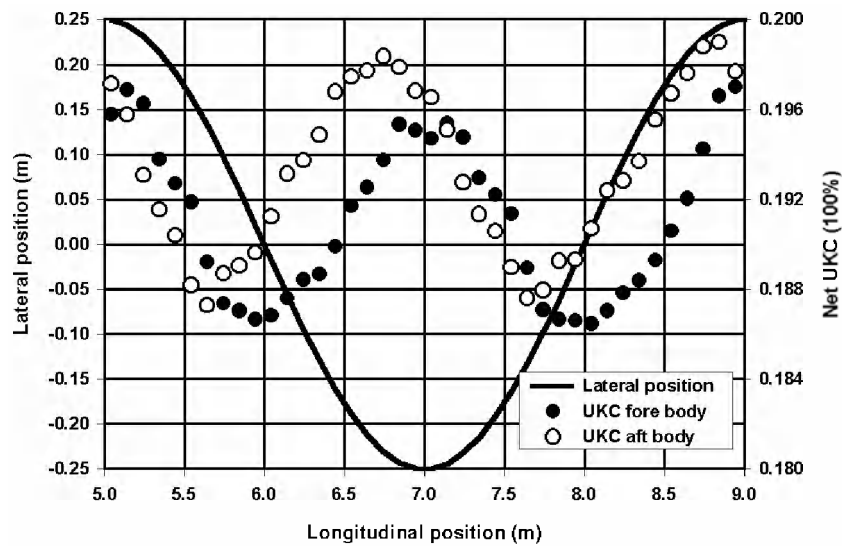
Figure 4.23 Model E, net UKC measured during a harmonic sway test (F_n=0.033, ω'=6, y_{0A}=0.25m) at a nominal UKC of 20%
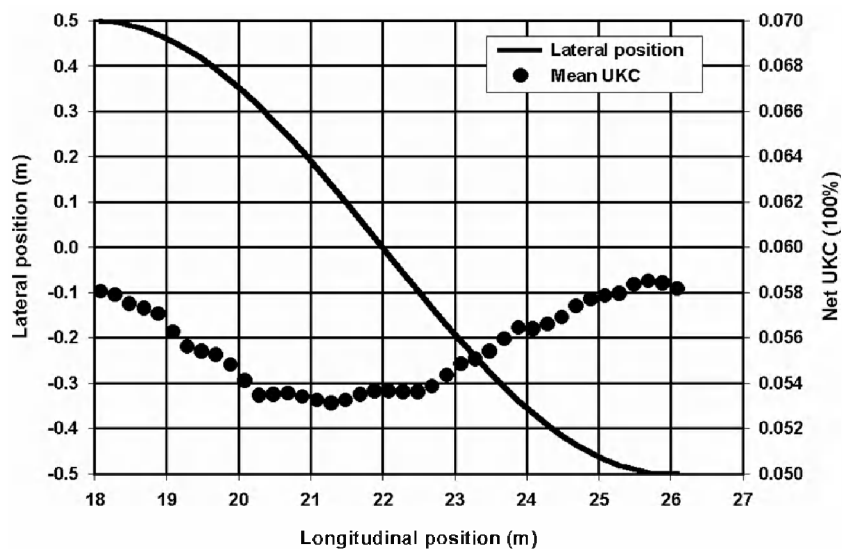
Figure 4.24 Model D, net UKC measured during a harmonic sway test (F_n=0.065, ω'=1.5, y_{0A}=0.5m) at a nominal UKC of 7%
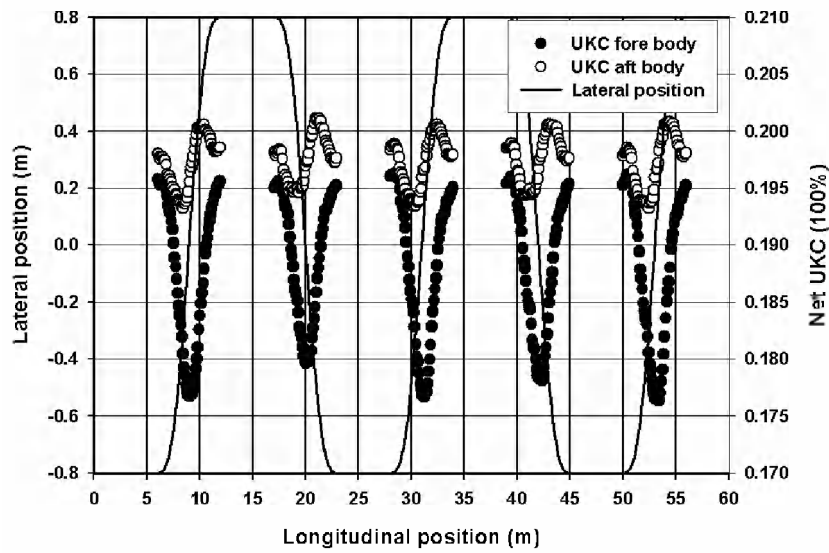
Figure 4.25 Model E, net UKC measured during a non-conventional sway test (F_n=0.033, ω*'=4, $\Delta y/2$ = 0.8m) at a nominal UKC of 20%
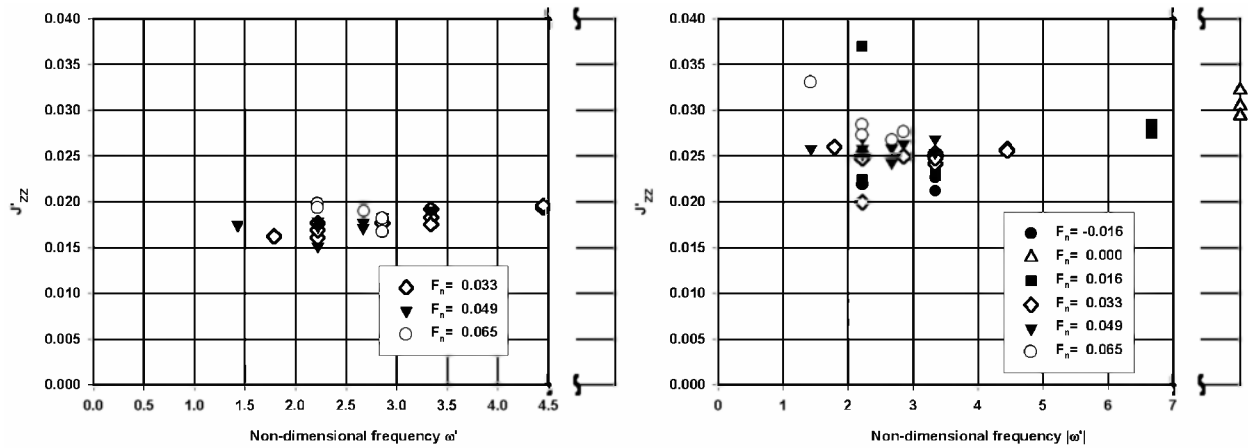
Figure 4.26 Model E, non-dimensional added moment of inertia as function of frequency for 50% UKC (left) and 20% UKC (right)
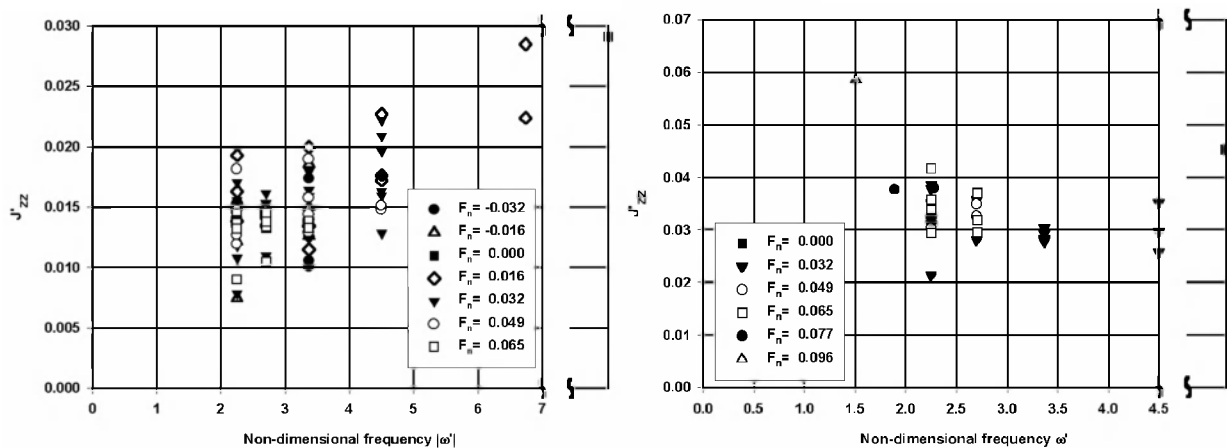
Figure 4.27 Model D, non-dimensional added moment of inertia as function of frequency for 20% UKC (left) and 7% UKC (right)
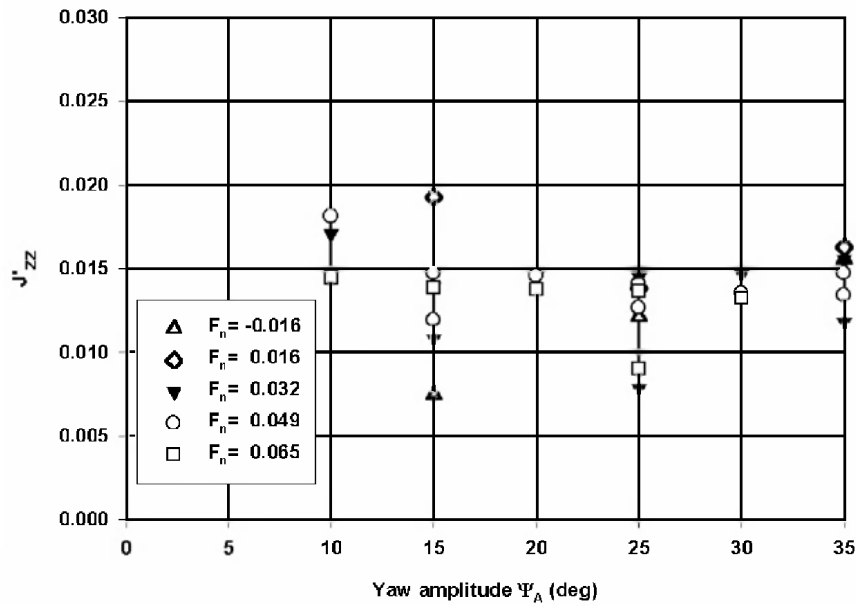
Figure 4.28 Model D, non-dimensional added moment of inertia as function of yaw amplitude for non-dimensional frequency $\omega'=2.25$ and 20% UKC
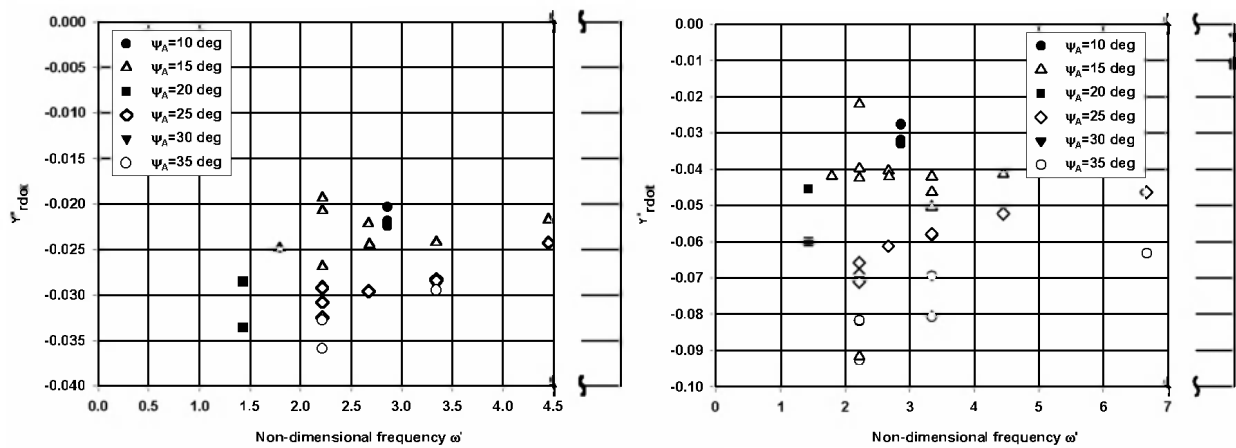
Figure 4.29 Model E, non-dimensional acceleration derivative Y'_{rdot} as function of frequency for 50% UKC (left) and 20% UKC (right)
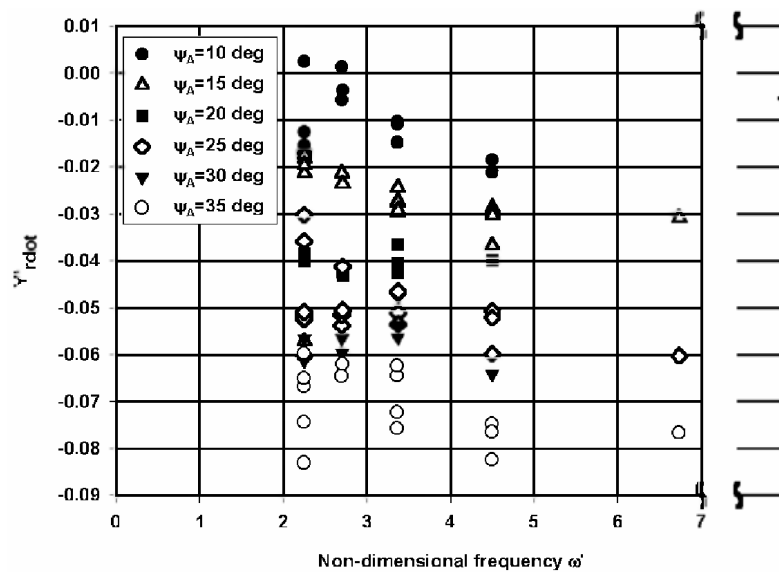
Figure 4.30 Model D, non-dimensional acceleration derivative Y'_{rdot} as function of frequency for 20% UKC

251
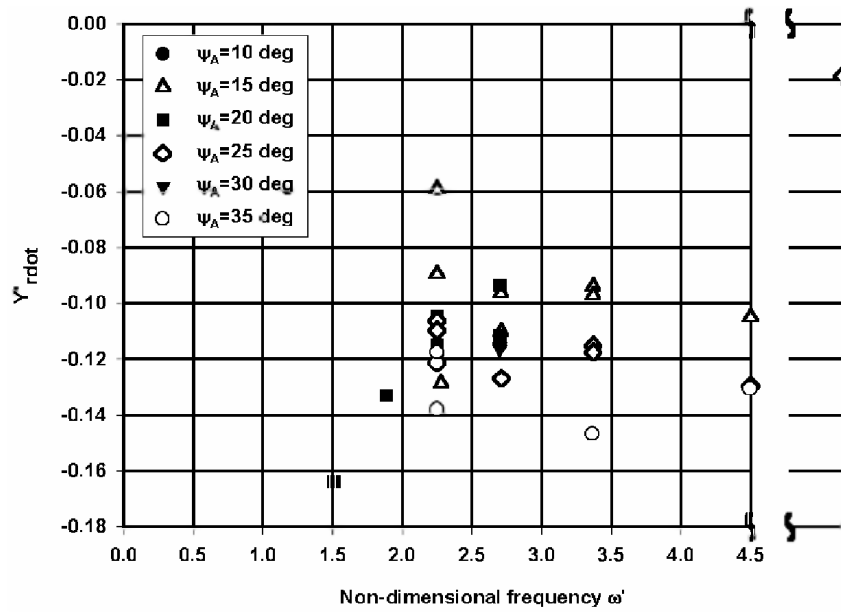
Figure 4.31 Model D, non-dimensional acceleration derivative Y'$_{rdot}$ as function of frequency for 7% UKC
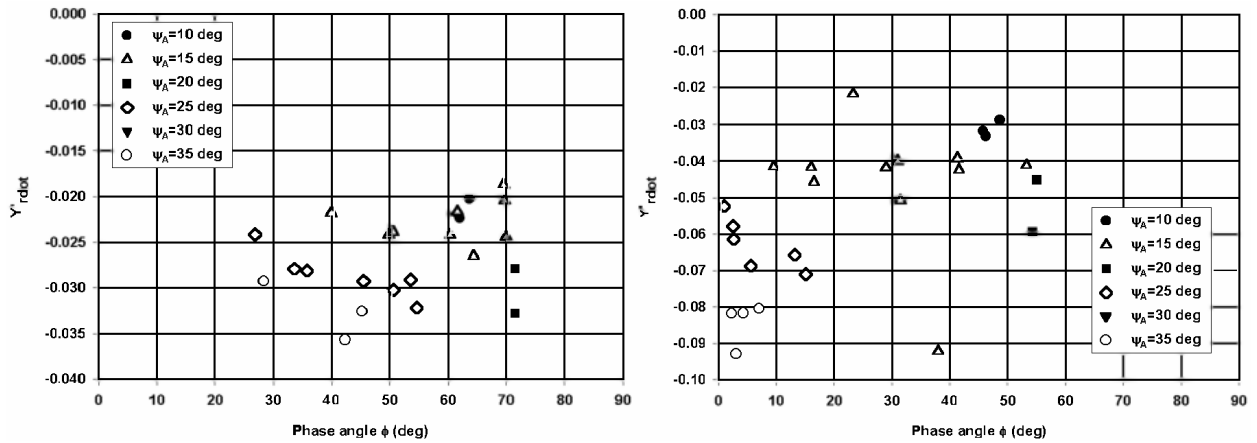
Figure 4.32 Model E, non-dimensional acceleration derivative Y'$_{rdot}$ as function of phase angle for 50% UKC (left) and 20% UKC (right)
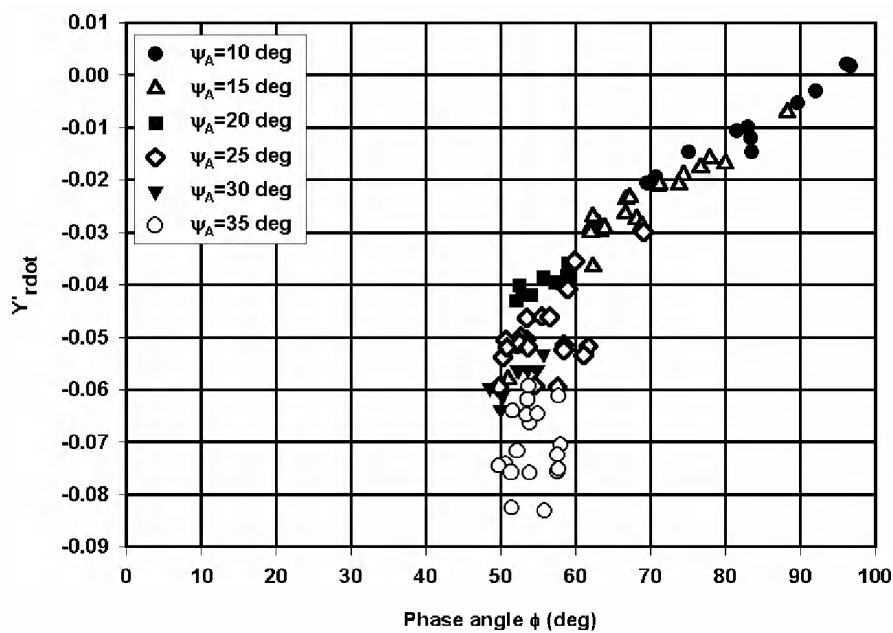
Figure 4.33 Model D, non-dimensional acceleration derivative Y'$_{rdot}$ as function of phase angle, 20% UKC

252
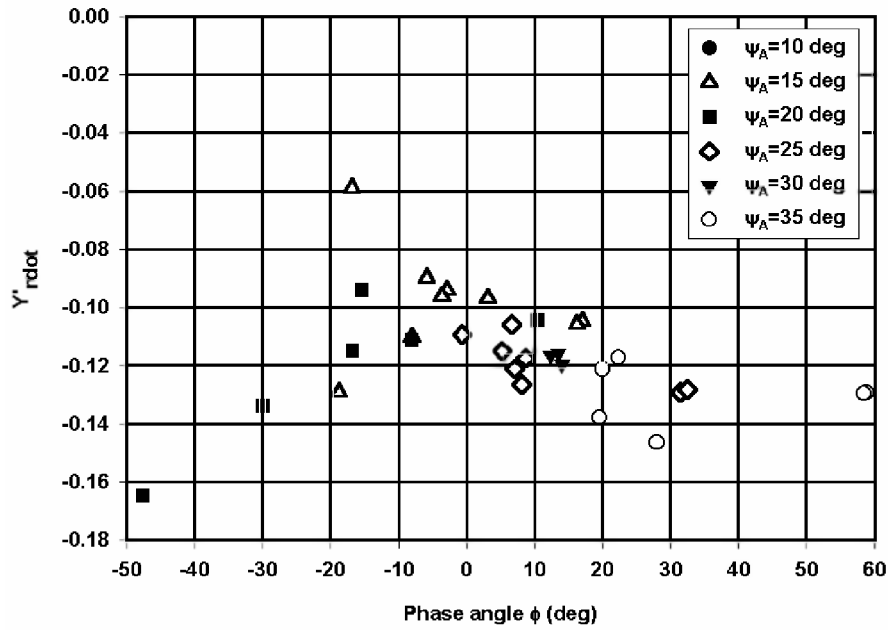
Figure 4.34 Model D, non-dimensional acceleration derivative Y'$_{rdot}$ as function of phase angle, 7% UKC
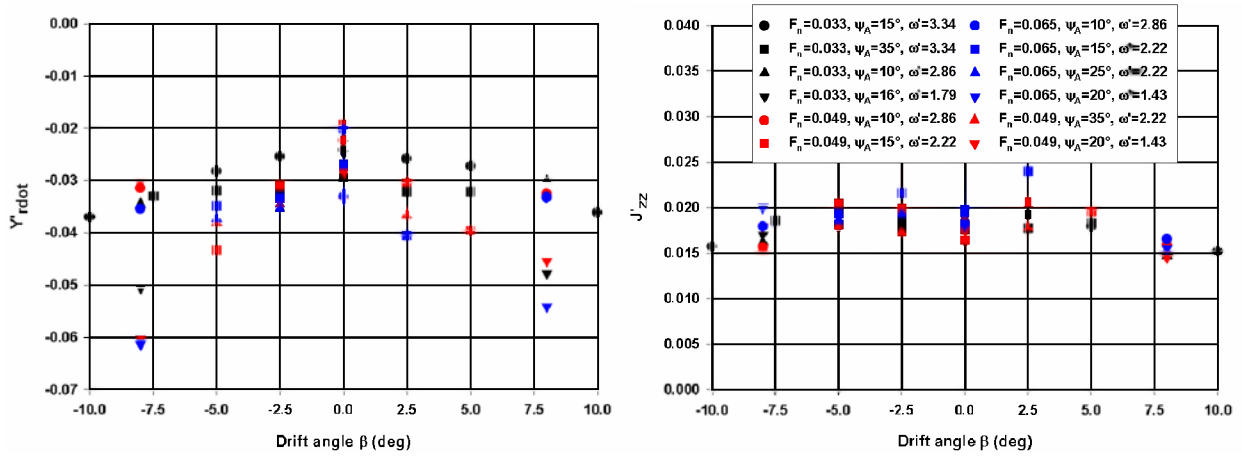
Figure 4.35 Model E, influence of drift angle on lateral force acceleration derivative Y'$_{rdot}$ and added moment of inertia J'$_{zz}$ for 50% UKC
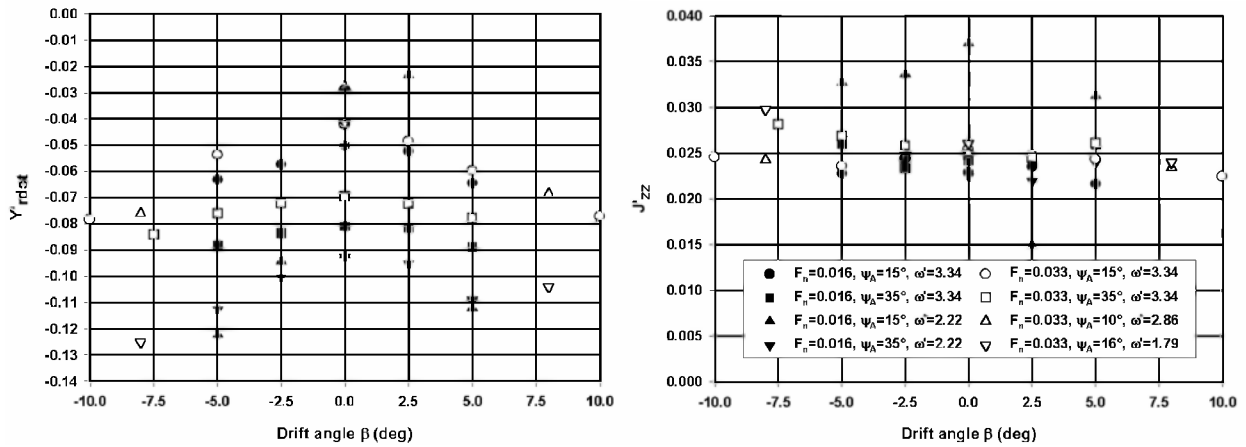
Figure 4.36 Model E, influence of drift angle on lateral force acceleration derivative Y'$_{rdot}$ and added moment of inertia J'$_{zz}$ for low speed manoeuvring and 20% UKC
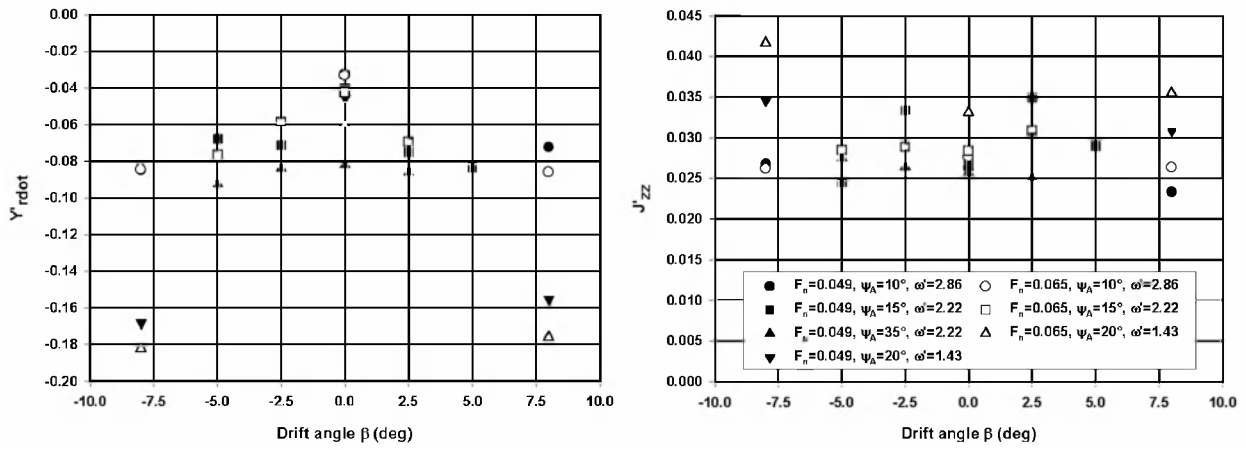
Figure 4.37 Model E, influence of drift angle on lateral force acceleration derivative Y'$_{rdot}$ and added moment of inertia J'$_{zz}$ for ordinary speed manoeuvring and 20% UKC
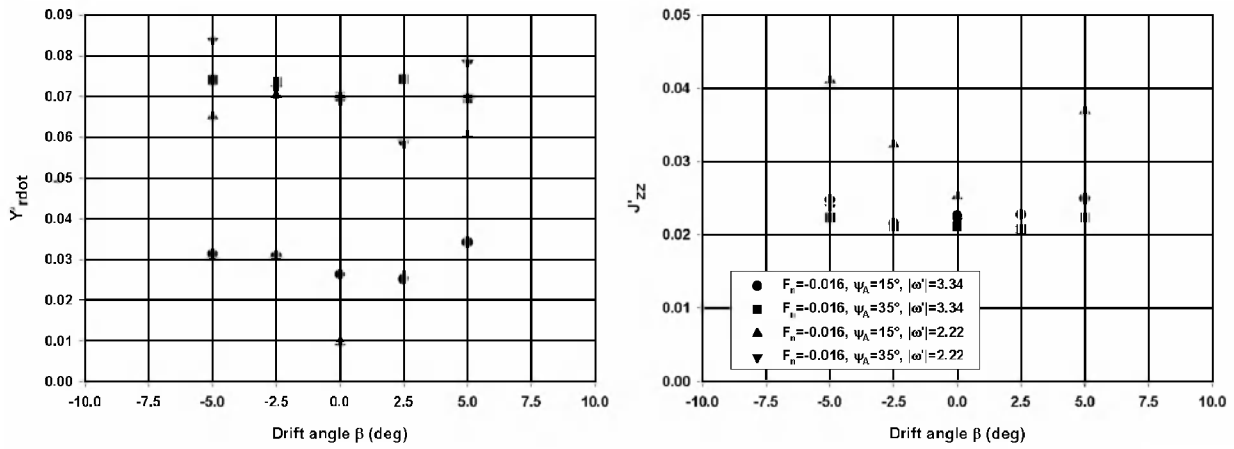
Figure 4.38 Model E, influence of drift angle on lateral force acceleration derivative Y'$_{rdot}$ and added moment of inertia J'$_{zz}$, going astern and 20% UKC
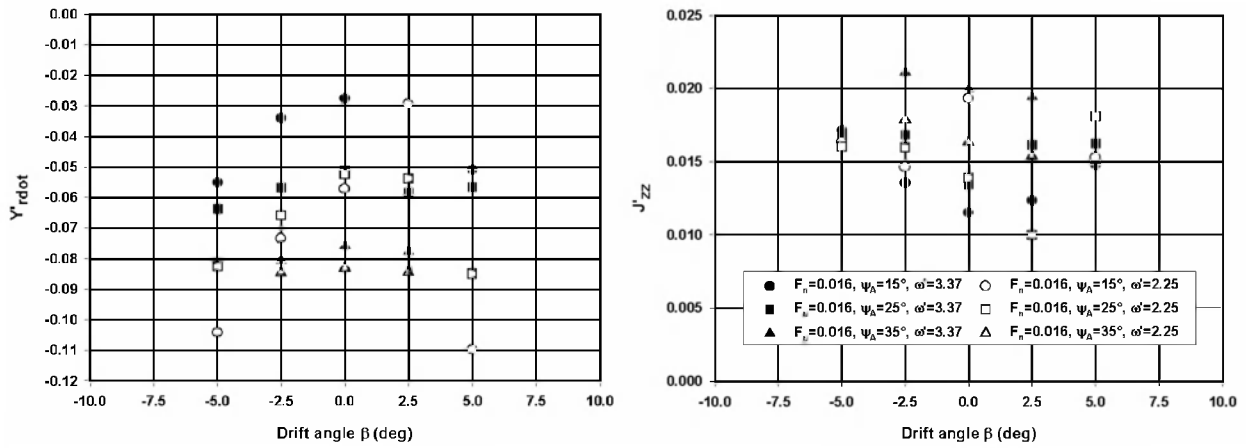
Figure 4.39 Model D, influence of drift angle on lateral force acceleration derivative Y'$_{rdot}$ and added moment of inertia J'$_{zz}$, F$_n$=0.016 and 20% UKC

254
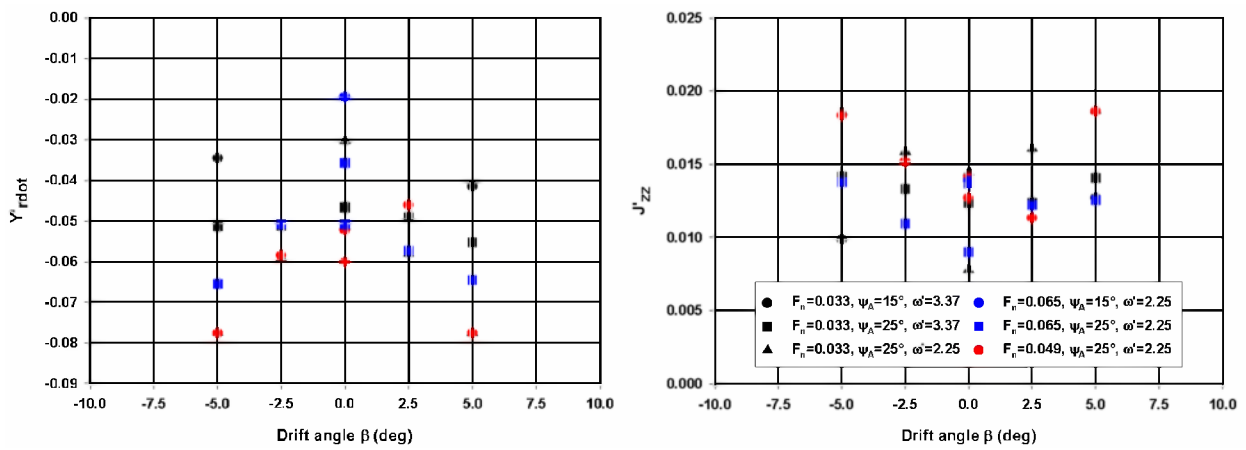
Figure 4.40 Model D, influence of drift angle on lateral force acceleration derivative Y'$_{rdot}$ and added moment of inertia J'$_{zz}$ for 20% UKC
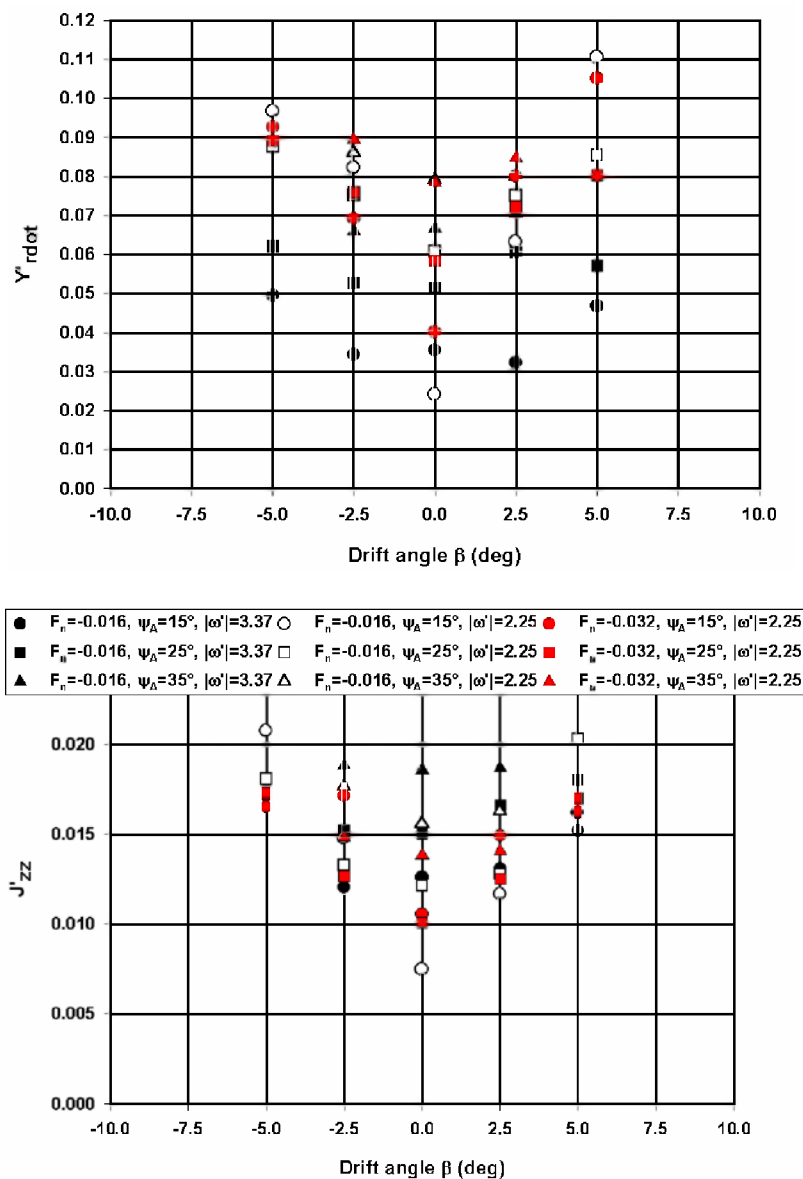
Figure 4.41 Model D, influence of drift angle on lateral force acceleration derivative Y'$_{rdot}$ and added moment of inertia J'$_{zz}$, going astern and 20% UKC

255
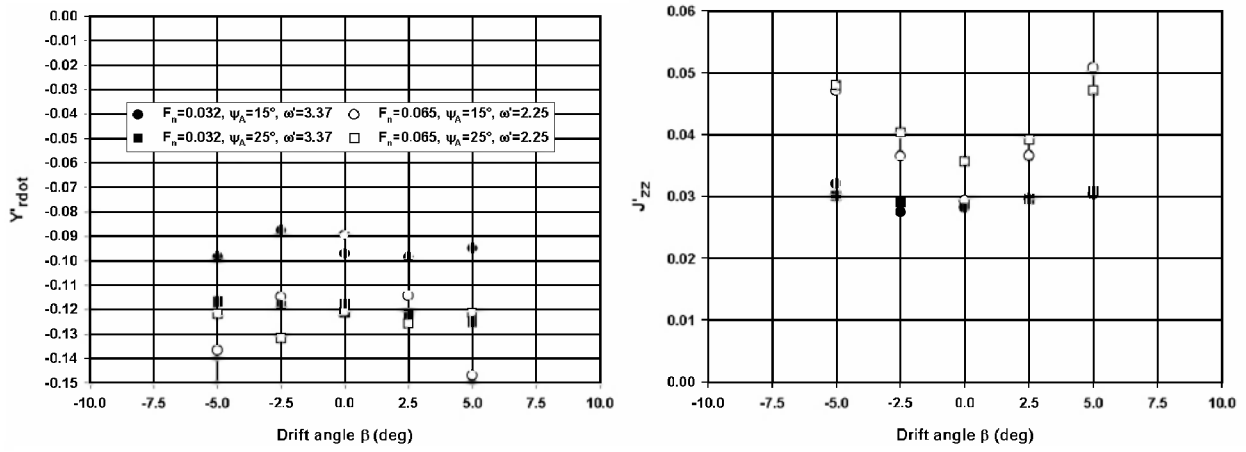
Figure 4.42 Model D, influence of drift angle on lateral force acceleration derivative Y'$_{rdot}$ and added moment of inertia J'$_{zz}$ at 7% UKC
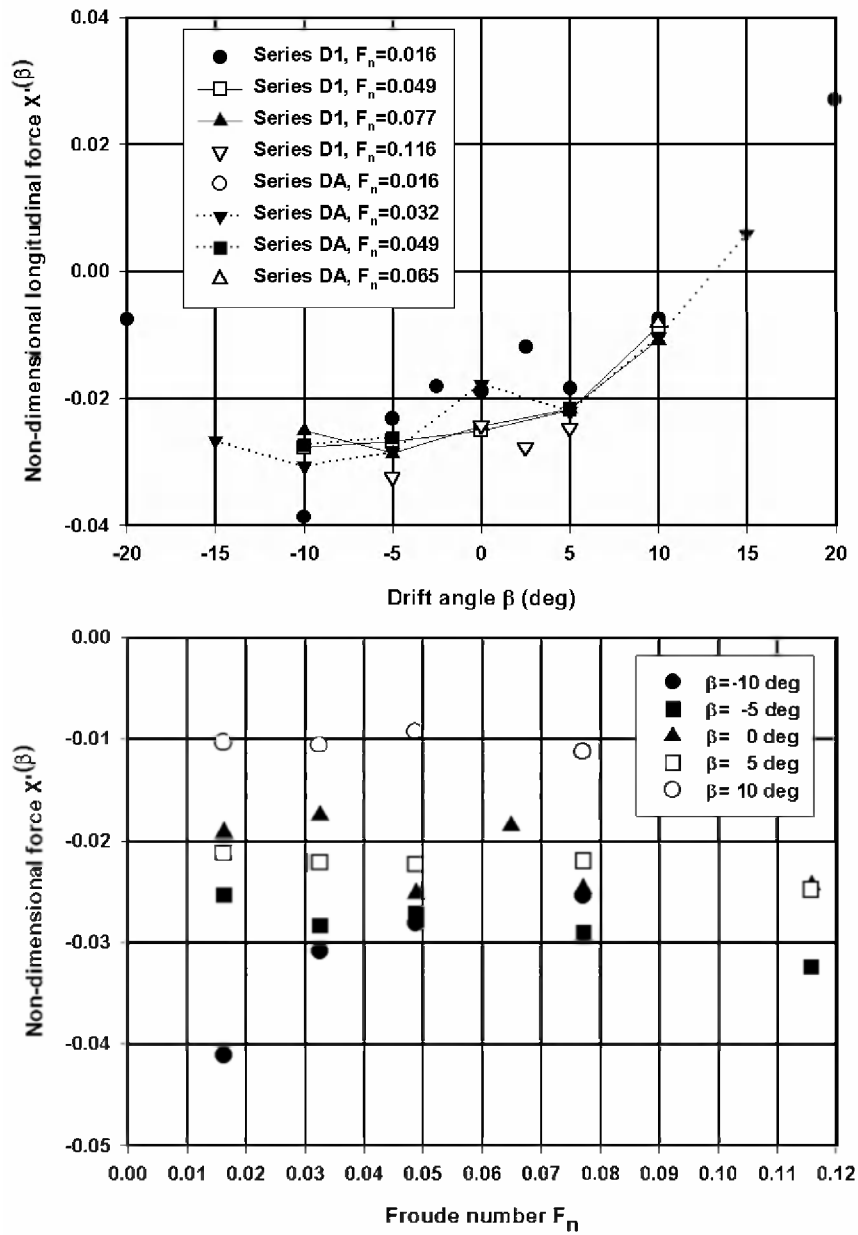
Figure 4.43 Model D, 20% UKC, non-dimensional longitudinal force X'$^{(\beta)}$ for oblique towing tests with small drift angles
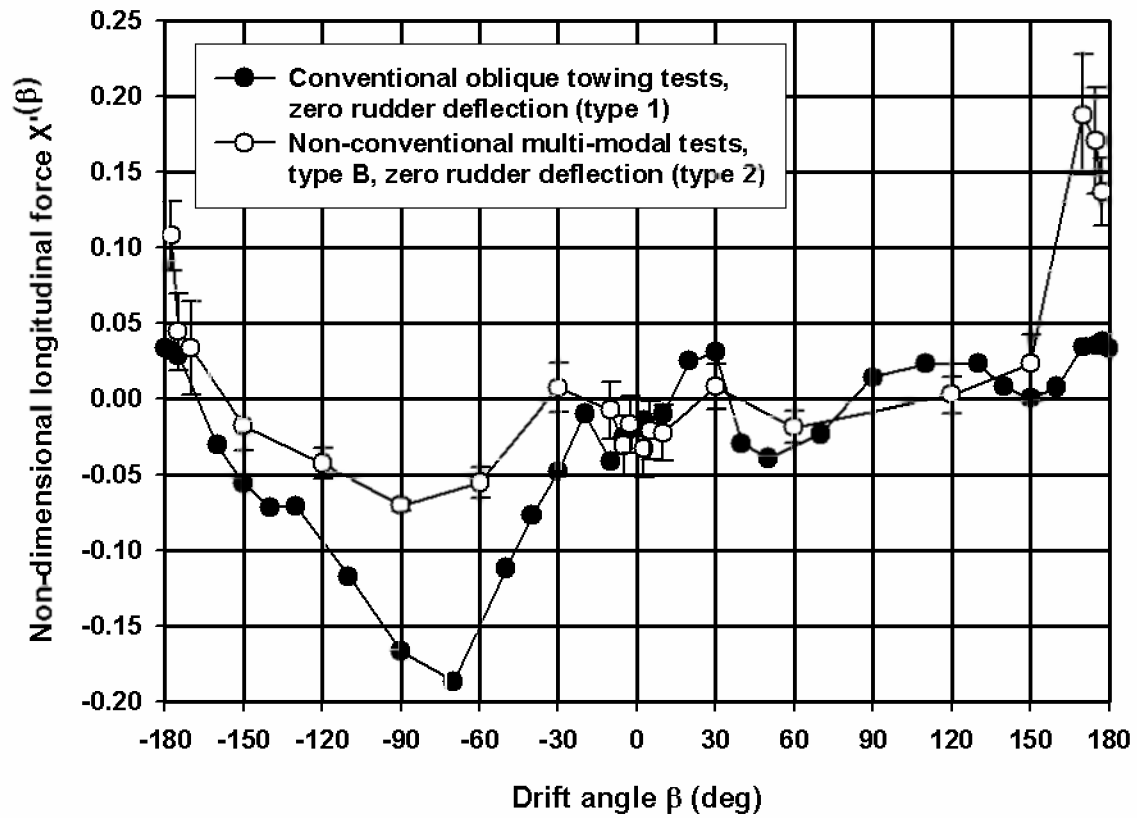
Figure 4.44 Model D, 20% UKC, comparison of non-dimensional longitudinal force for F_n=0.016 based on two test types
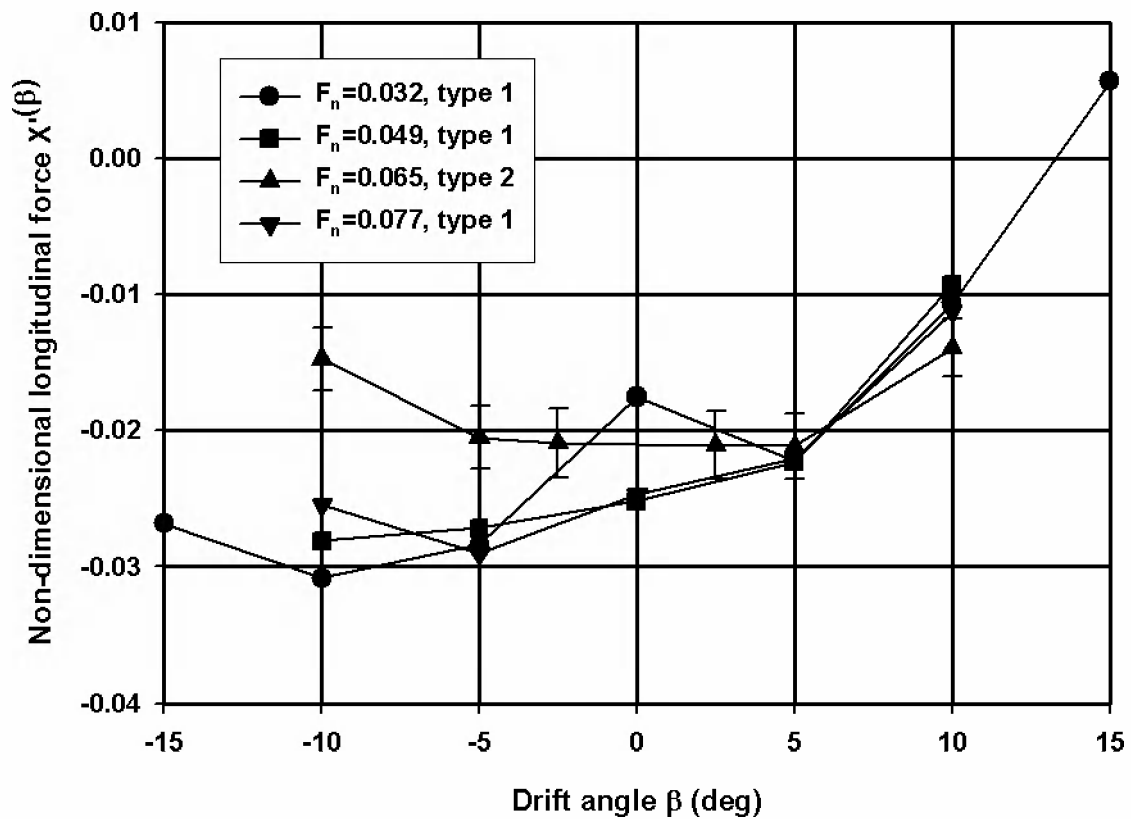
Figure 4.45 Model D, 20% UKC, comparison of non-dimensional longitudinal force for higher F_n based on two test types
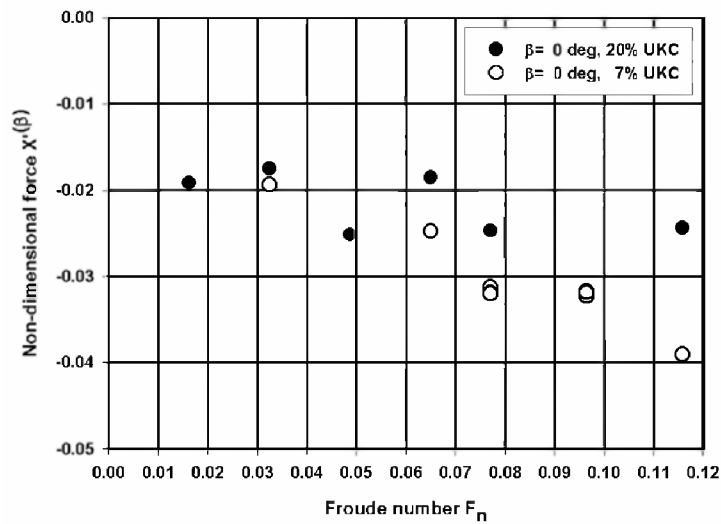
Figure 4.46 Model D, 20% and 7% UKC, comparison of non-dimensional longitudinal force measured during stationary straight-line tests
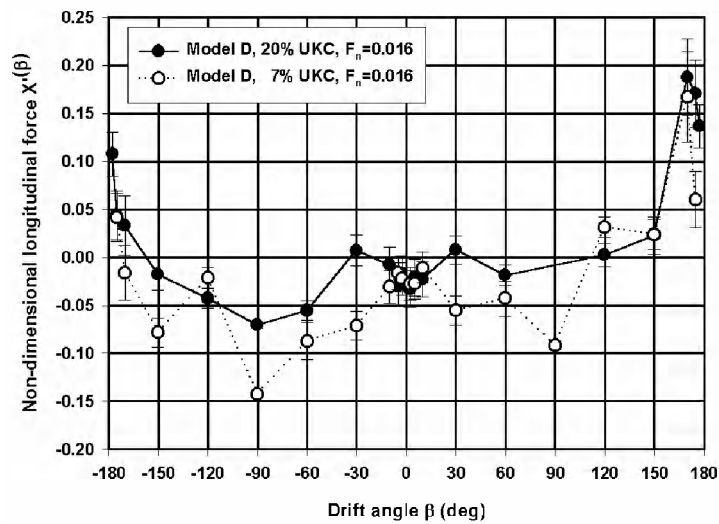
Figure 4.47 Model D, 20% and 7% UKC, comparison of non-dimensional longitudinal force measured during multi-modal tests (type 2) for $F_n=0.016$
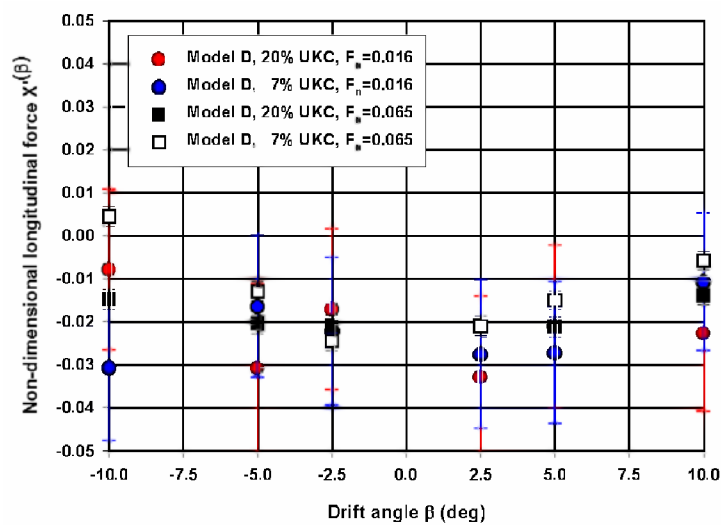
Figure 4.48 Model D, 20% and 7% UKC, comparison of non-dimensional longitudinal force measured during multi-modal tests (type 2) for small drift angles

258
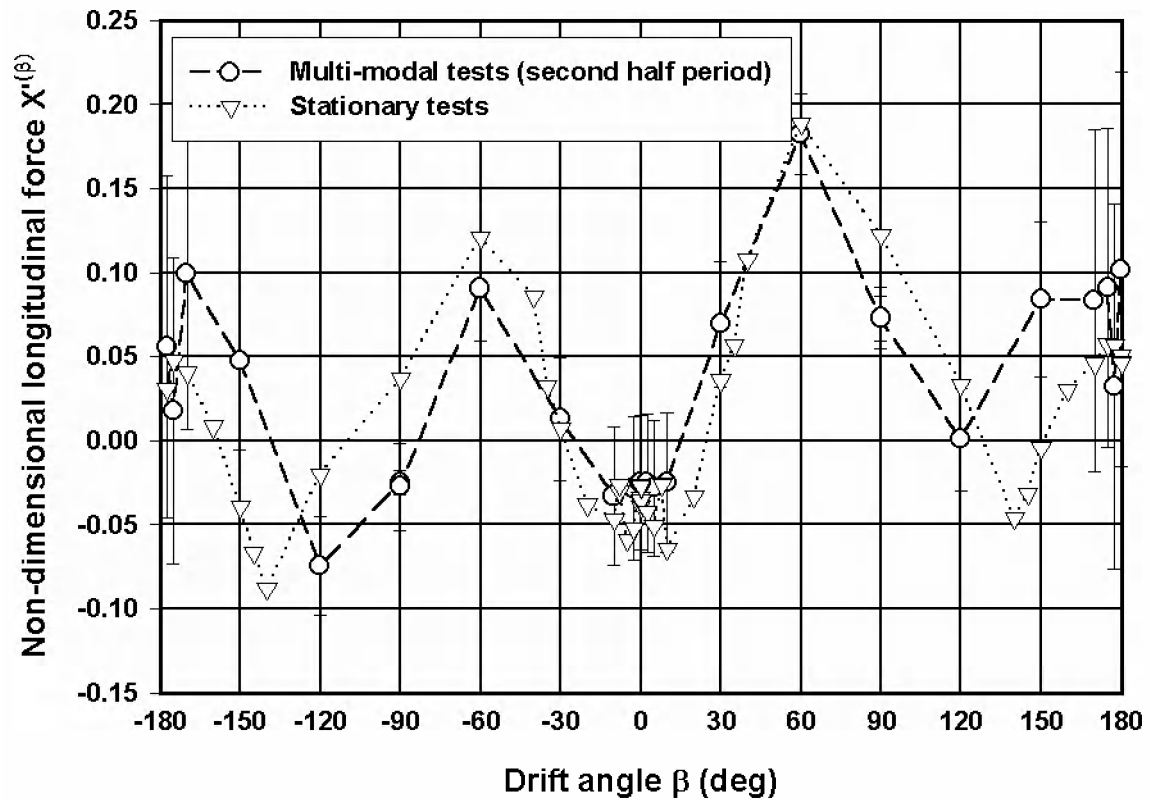
Figure 4.49 Model E, 50% UKC, comparison of non-dimensional longitudinal force for F_n=0.016 based on tests type 1 and 2
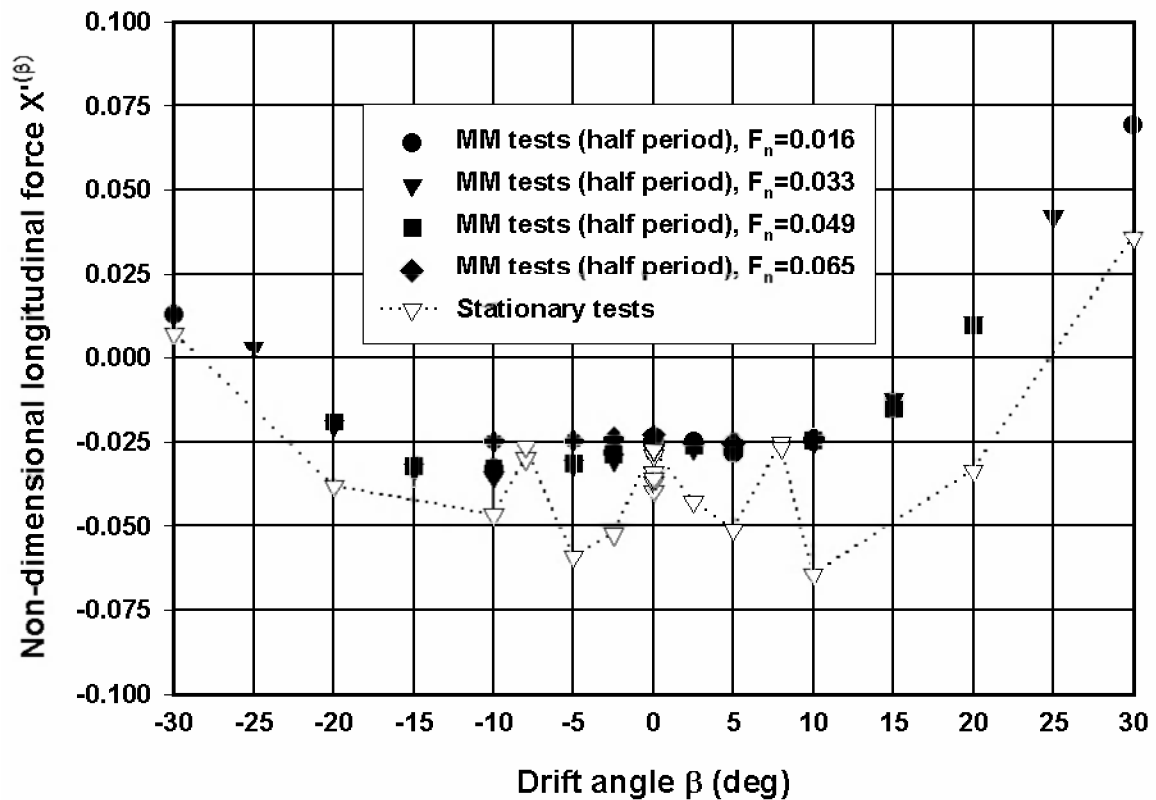
Figure 4.50 Model E, 50% UKC, comparison of non-dimensional longitudinal force for different F_n based on tests type 1 and 2
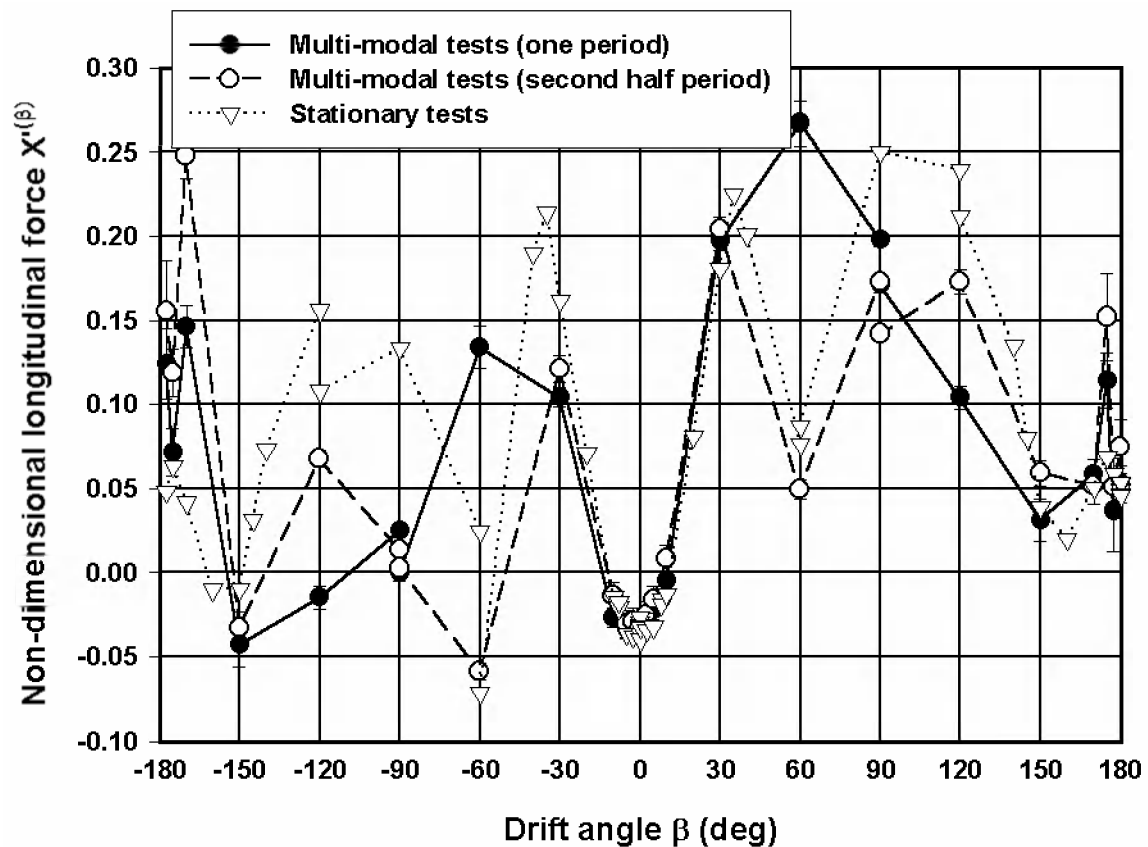
Figure 4.51 Model E, 20% UKC, comparison of non-dimensional longitudinal force for F_n=0.016 based on tests type 1 and 2
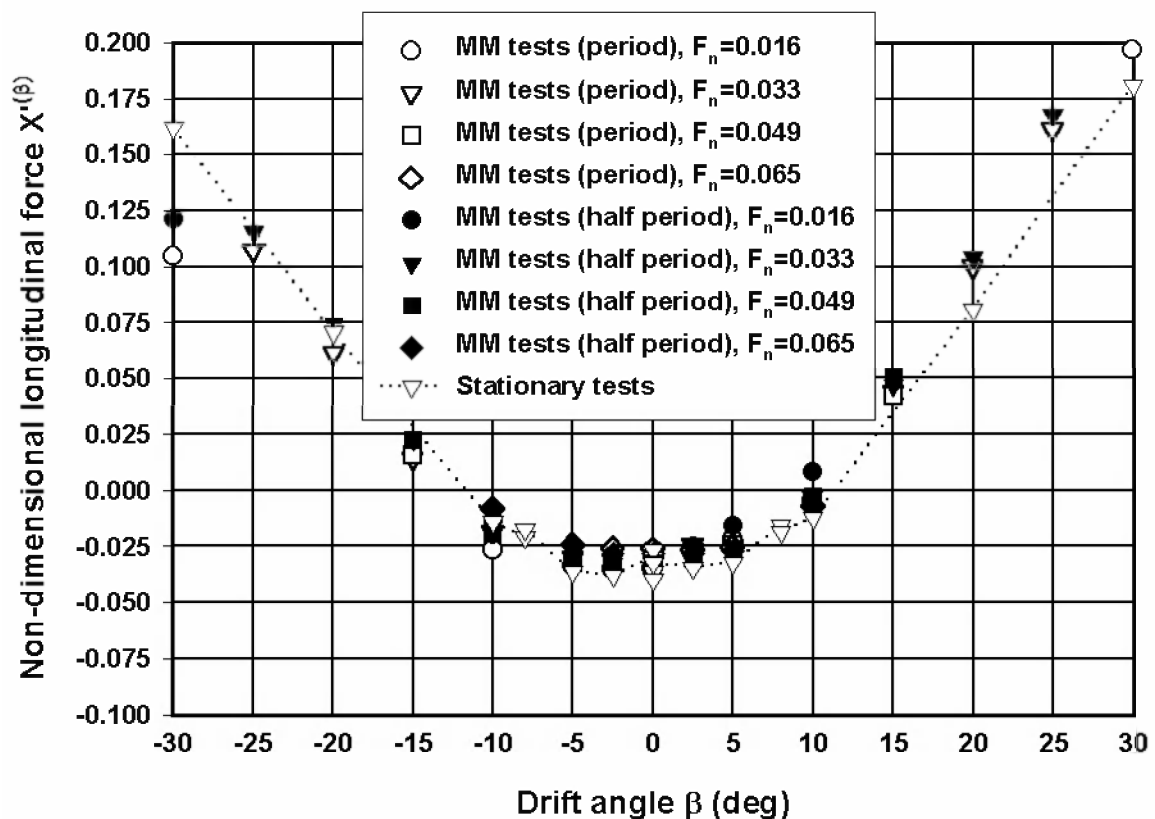
Figure 4.52 Model E, 20% UKC, comparison of non-dimensional longitudinal force for different F_n based on tests type 1 and 2

260
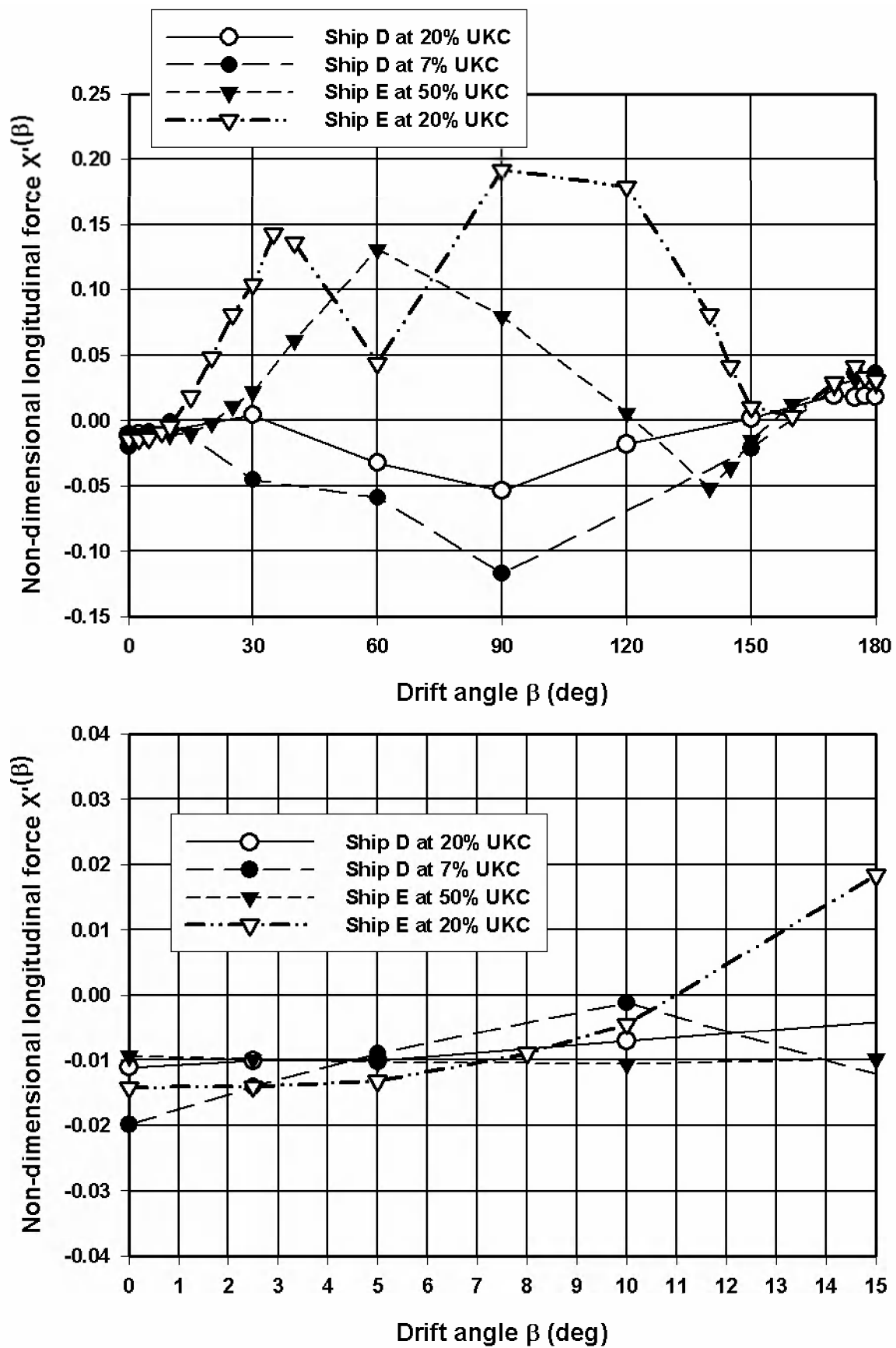
Figure 4.53 Comparison of selected tabular model for $X^{'(\beta)}$ for ship model D and E
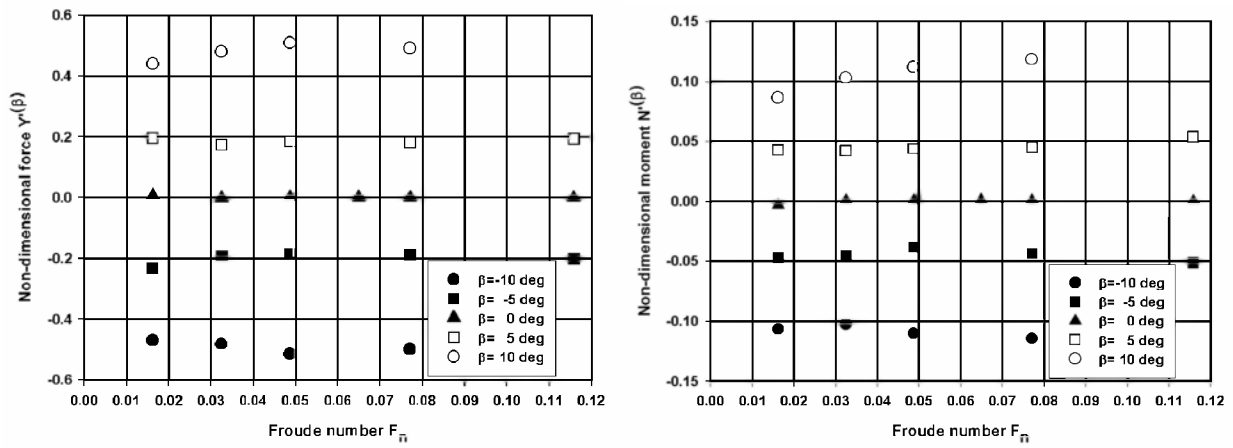
Figure 4.54 Model D, 20% UKC, non-dimensional lateral force and yawing moment as function of F_n
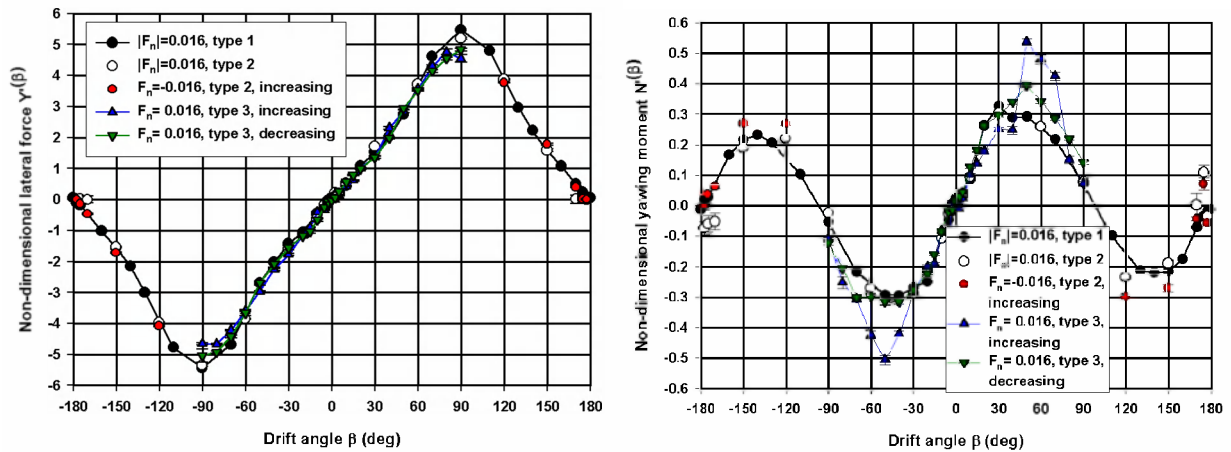
Figure 4.55 Model D, 20% UKC, comparison of non-dimensional lateral force and yawing moment for F_n=0.016 based on three different test types
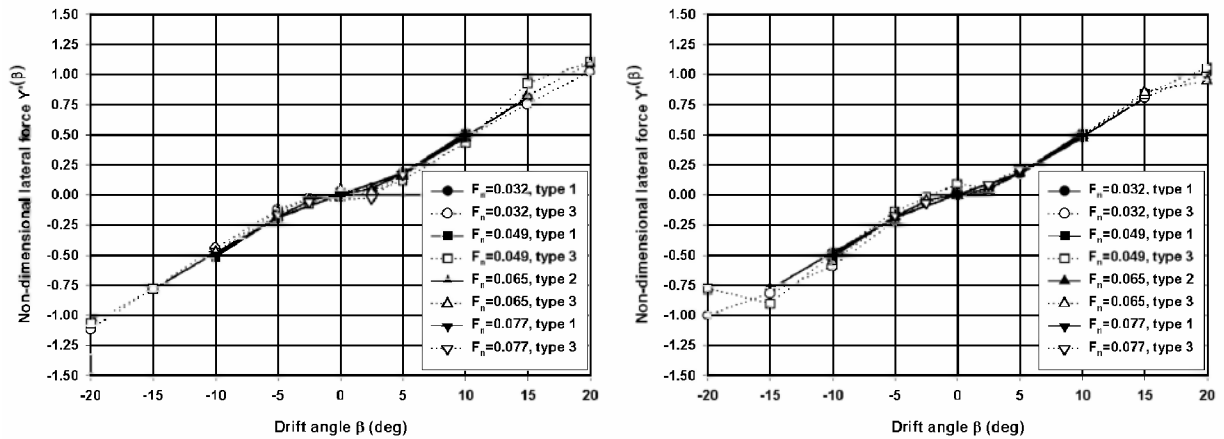
Figure 4.56 Model D, 20% UKC, comparison of non-dimensional lateral force for higher F_n (type 3 with increasing propeller rate of turn, left figure, or with decreasing propeller rate of turn, right figure)
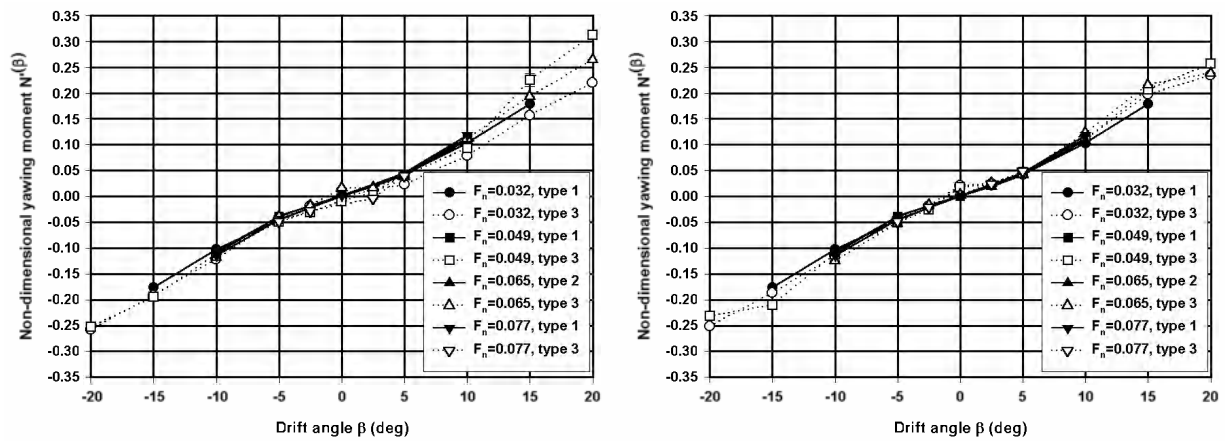
Figure 4.57 Model D, 20% UKC, comparison of non-dimensional yawing moment for higher F_n (type 3 with increasing propeller rate of turn, left figure, or with decreasing propeller rate of turn, right figure)
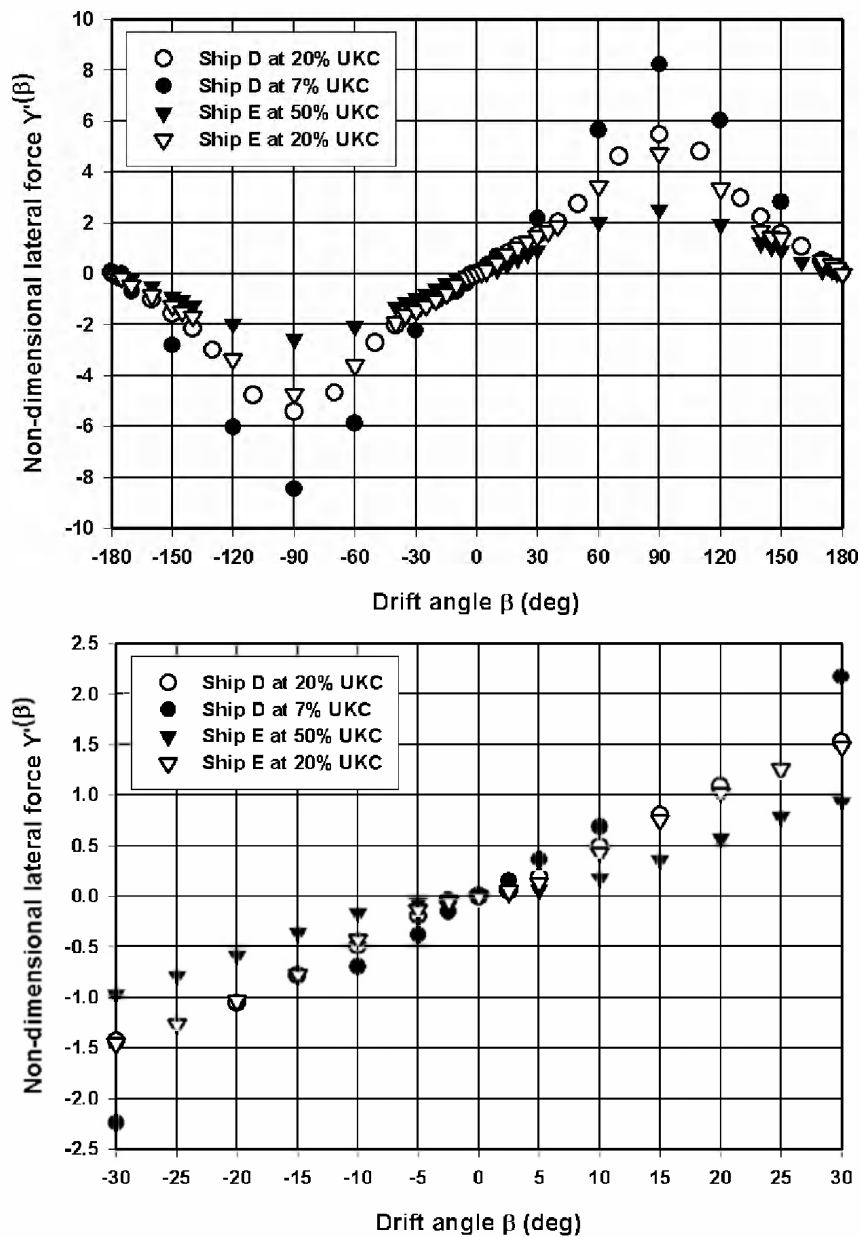
Figure 4.58 Comparison of selected tabular model for $Y'^{(\beta)}$ for ship model D and E
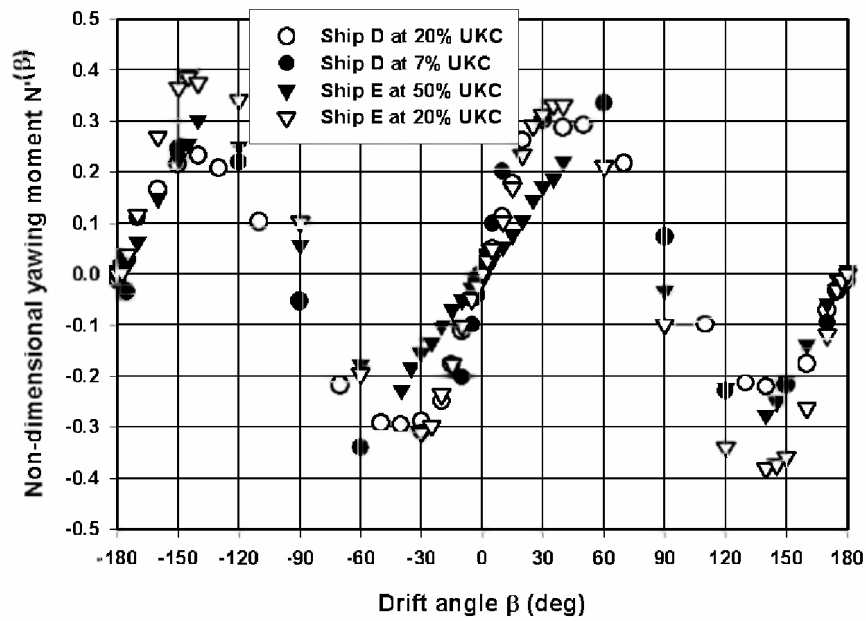
Figure 4.59 Comparison of selected tabular model for N'$^{(\beta)}$ for ship model D and E
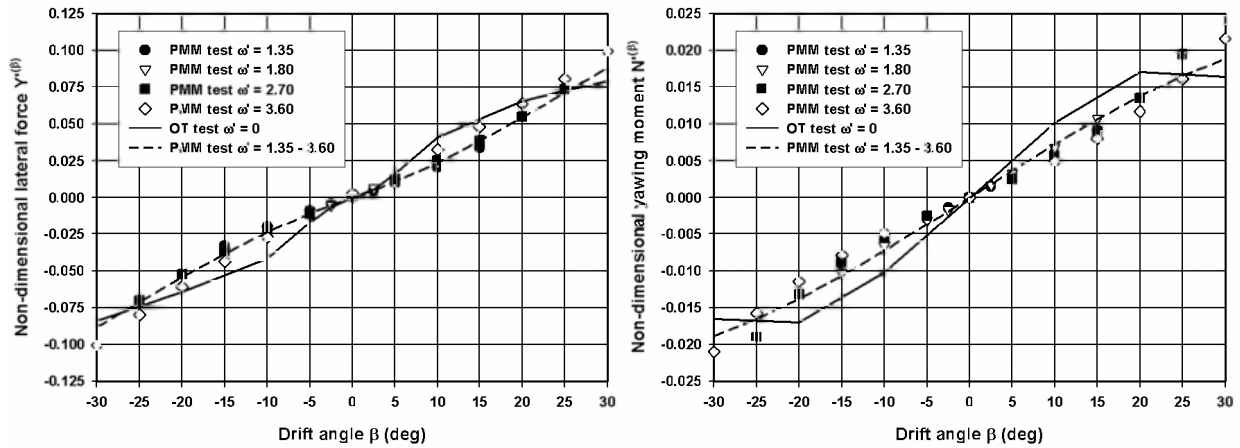
Figure 4.60 Model C, 10% UKC, comparison of non-dimensional lateral force Y'$^{(\beta)}$ and yawing moment N'$^{(\beta)}$ for stationary oblique towing (OT) tests and harmonic PMM tests
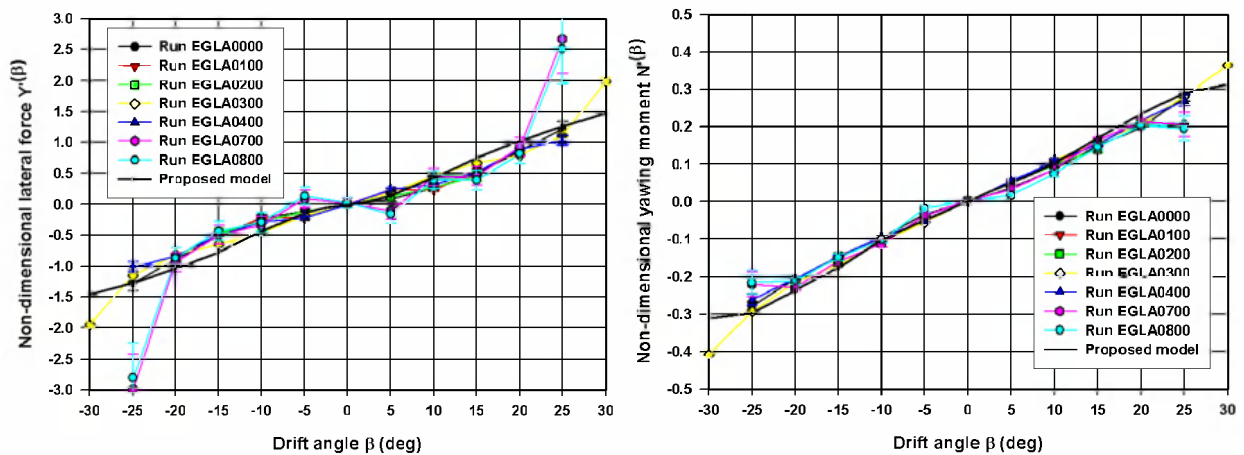
Figure 4.61 Model E, 20% UKC, comparison of non-dimensional lateral force Y'$^{(\beta)}$ and yawing moment N'$^{(\beta)}$ for the proposed model based on stationary tests and for non-conventional harmonic sway tests (F_n=0.033)

264
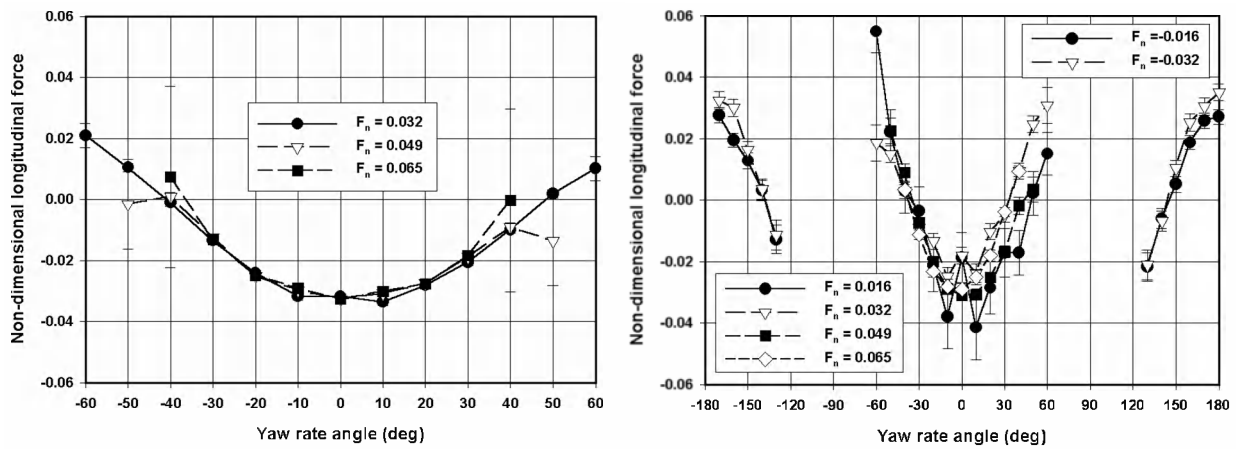
Figure 4.62 Model D, 20% UKC, non-dimensional longitudinal force (resistance included) during pure yawing tests per Froude number for going ahead and going astern, series D1 (left) and series DA (right)
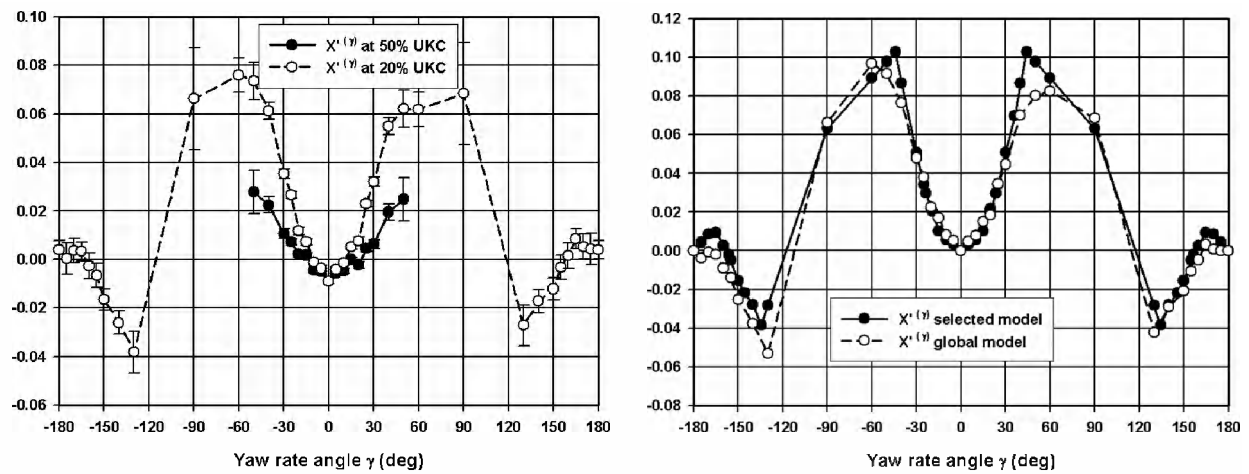
Figure 4.63 Model E, non-dimensional longitudinal force $X'^{(\gamma)}$ during pure yawing tests: comparison of a global model for 50% and 20% UKC (left) and comparison of a global corrected model and a model based on selected test runs for 20% UKC (right)
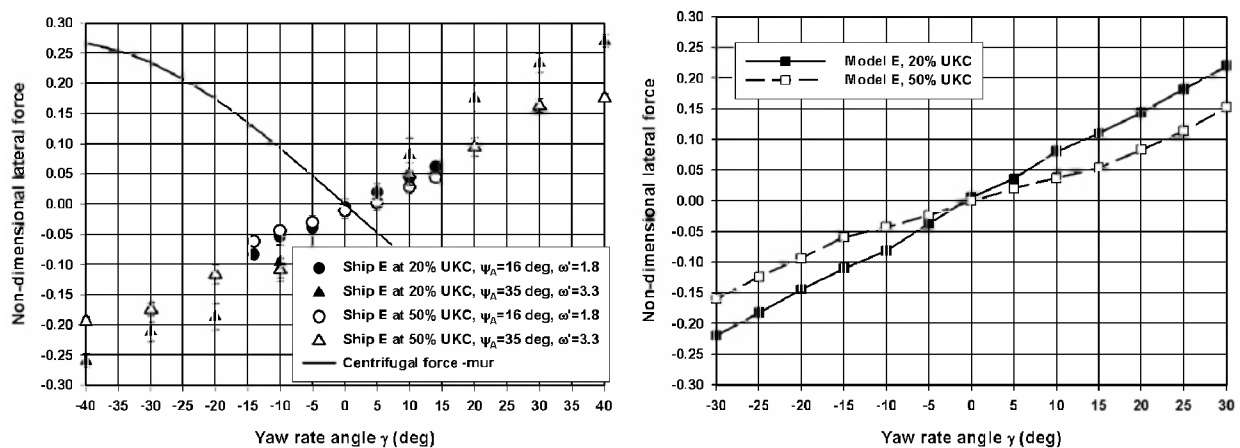
Figure 4.64 Model E, comparison of tabular models for non-dimensional lateral force during pure yawing tests: individual test runs for $F_n = 0.033$ at 20% UKC (left) and global models (right)
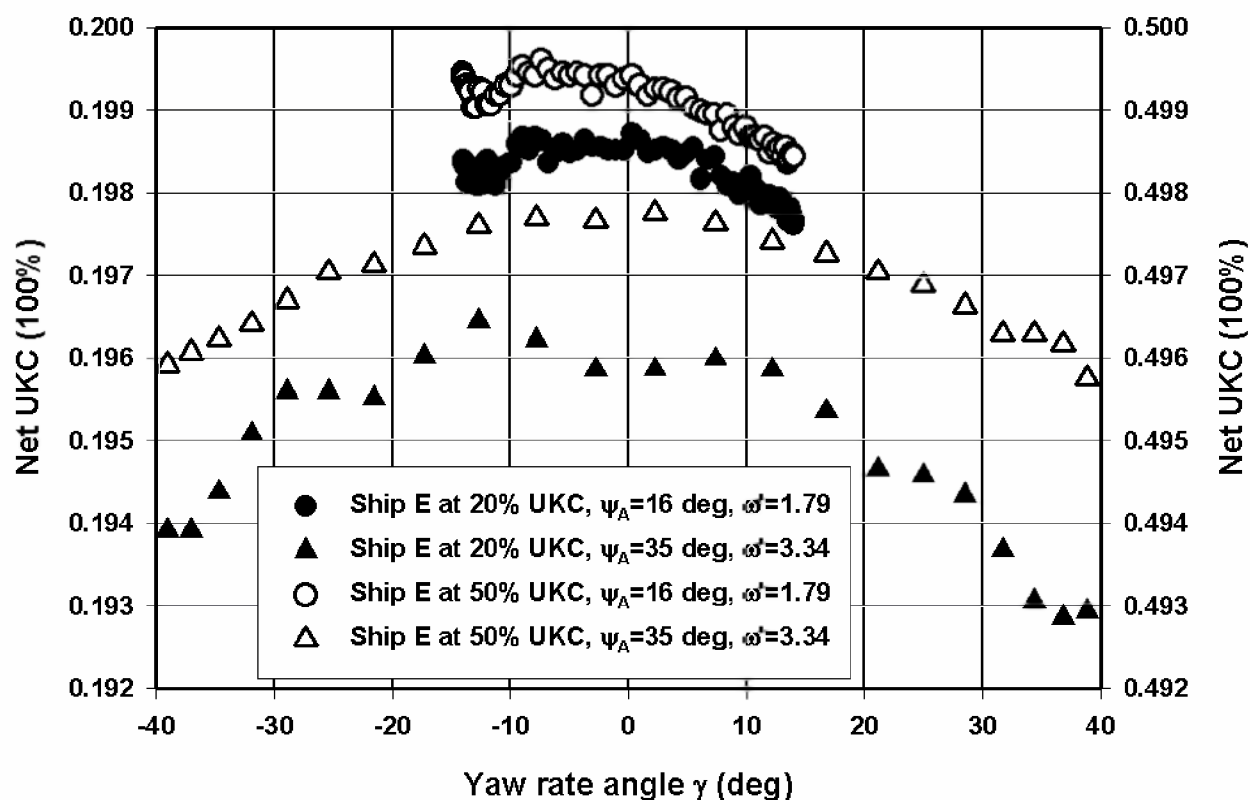
Figure 4.65 Model E, net UKC during harmonic yaw tests at under keel clearances of 20 and 50%.

RUN	UKC	F_n	ψ_A	ω'	RUN	UKC	F_n	ψ_A	ω'
DAGA02	20%	0.033	35°	4.5	DCGA06	7%	0.033	15°	2.3
DAGA06	20%	0.033	15°	2.3	DCGB03	7%	0.049	30°	2.3
DAGB05	20%	0.049	35°	3.4	DCGC01	7%	0.065	25°	2.7
DAGB11	20%	0.049	35°	2.3					
DAGC02	20%	0.065	35°	2.7					

■ DAGA0200	▲ DAGB0500	—— Centrifugal force -mur	
● DAGA0600	▼ DAGB1100	◆ DAGC0200	
○ DCGA0600	▽ DCGB0300	◇ DCGC0100	
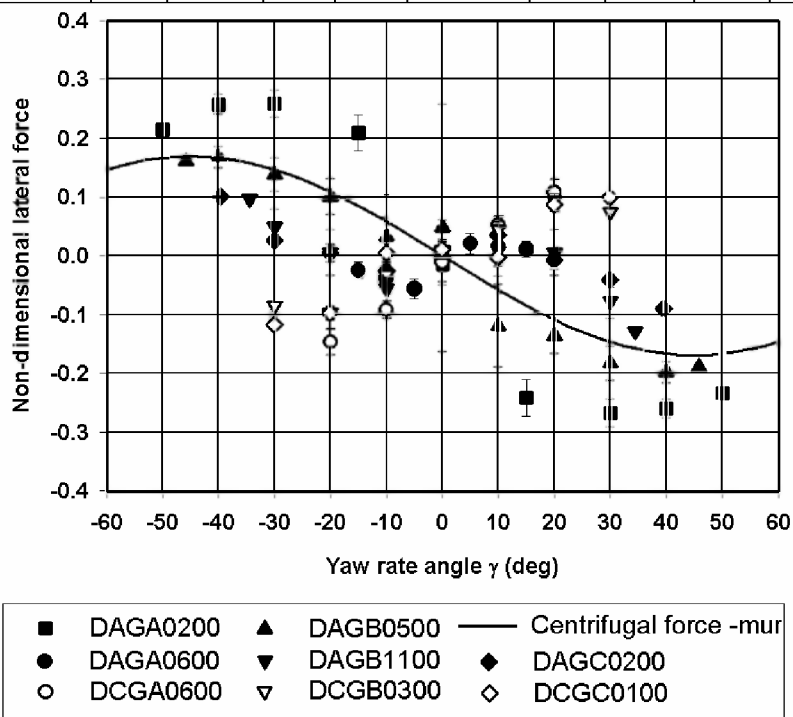
Figure 4.66 Model D, influence of test parameters frequency and amplitude on non-dimensional lateral force during pure yawing tests at 20% and 7% UKC
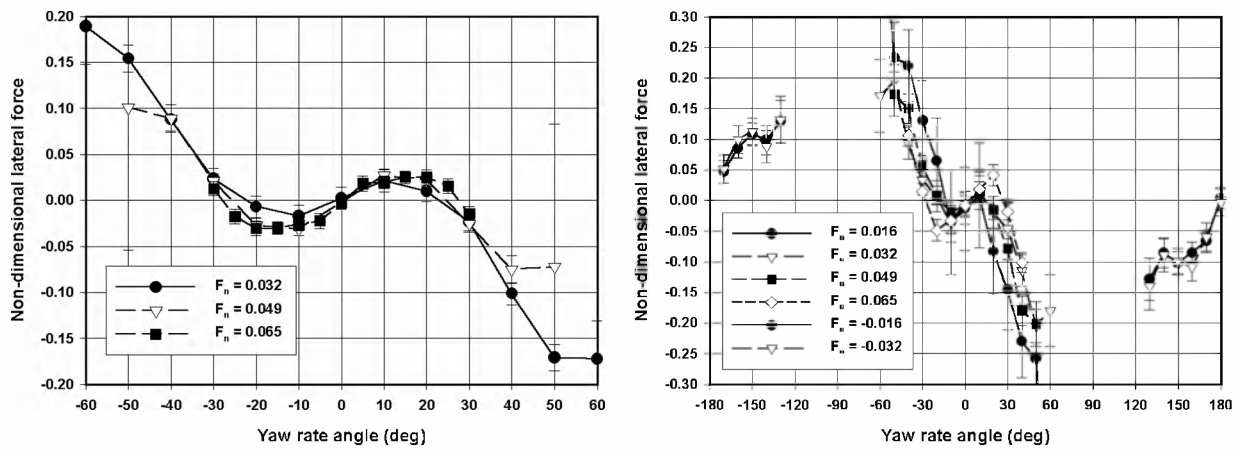
Figure 4.67 Model D, 20% UKC, non-dimensional lateral force during pure yawing tests per Froude number for going ahead and going astern, series D1 (left) and series DA (right)
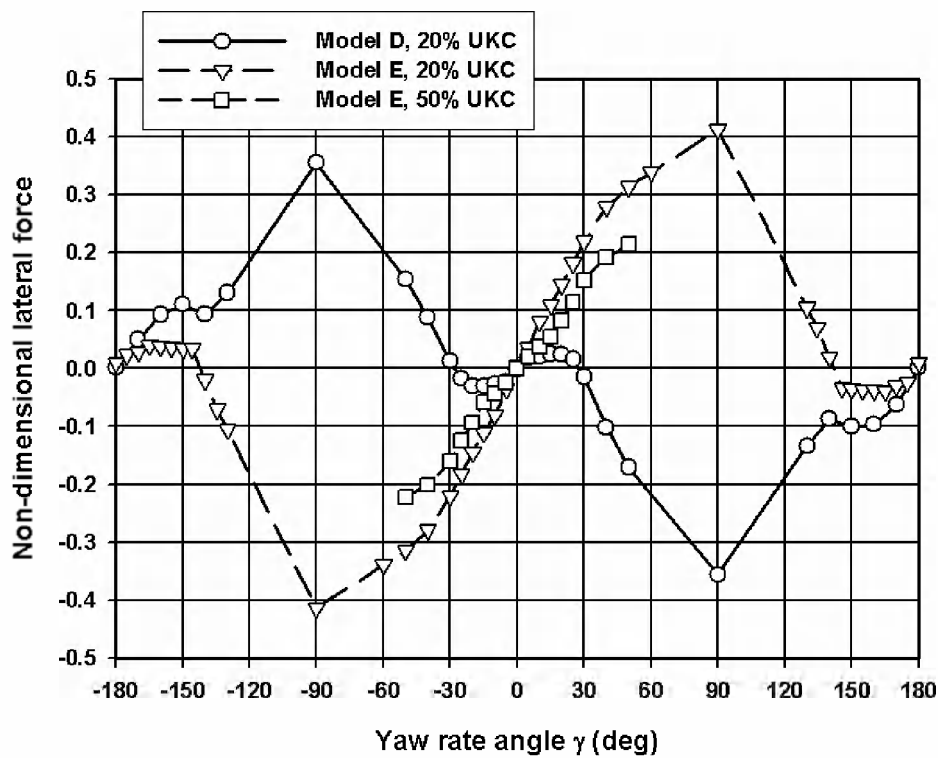
Figure 4.68 Comparison of tabular models for the non-dimensional lateral force during pure yawing tests for model D and model E
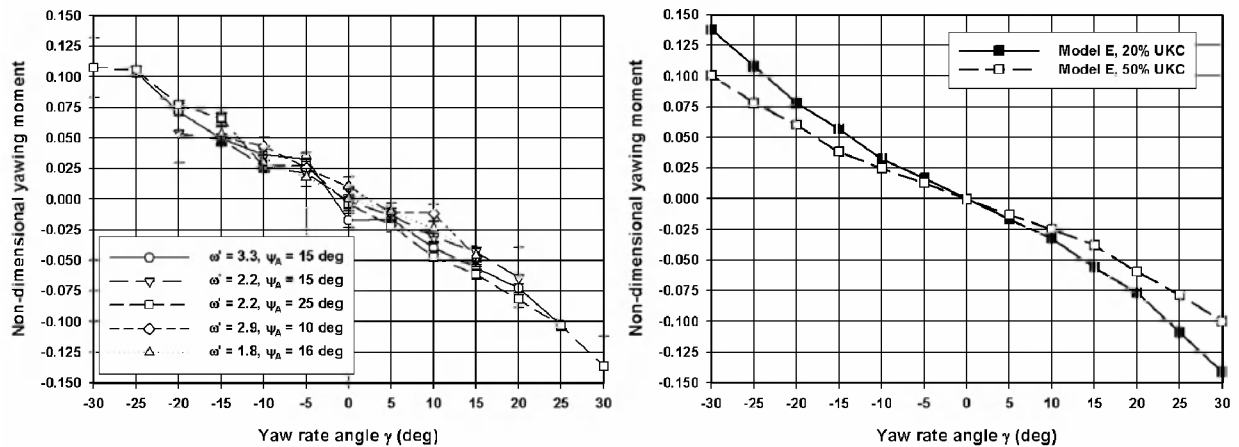
Figure 4.69 Model E, comparison of tabular models for non-dimensional yawing moment during pure yawing tests: individual test runs for $F_n = 0.033$ at 20% UKC (left) and global models (right)

267
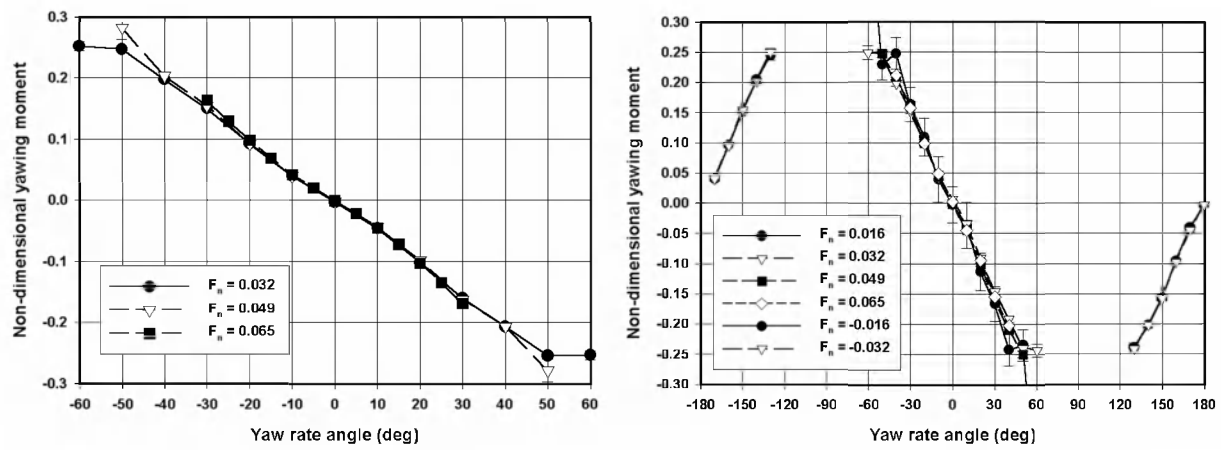
Figure 4.70 Model D, 20% UKC, non-dimensional yawing moment during pure yawing tests per Froude number for going ahead and going astern, series D1 (left) and series DA (right)
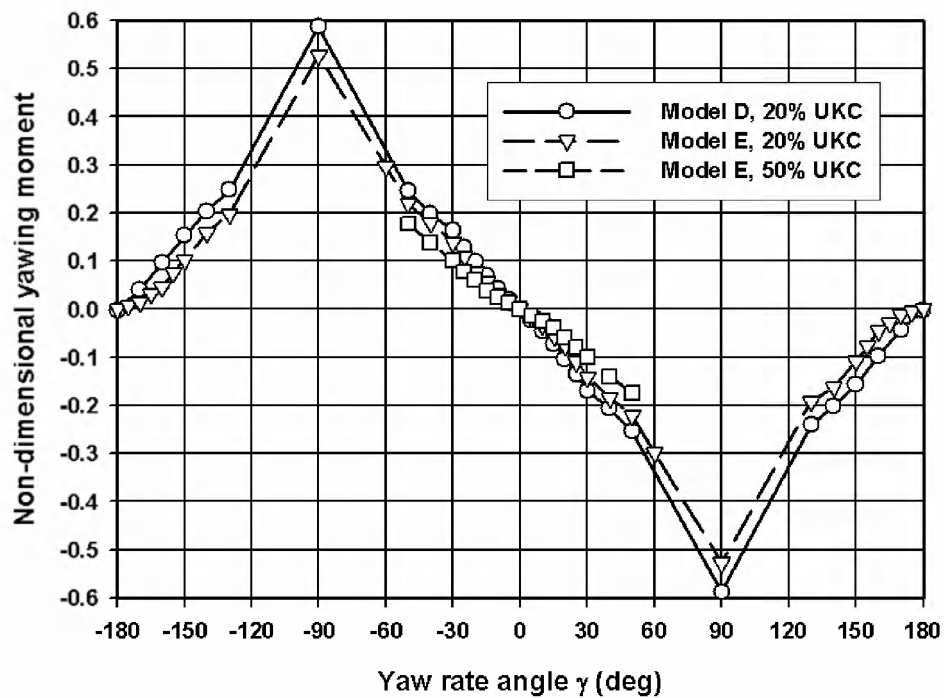
Figure 4.71 Comparison of tabular models for the non-dimensional yawing moment during pure yawing tests for model D and model E
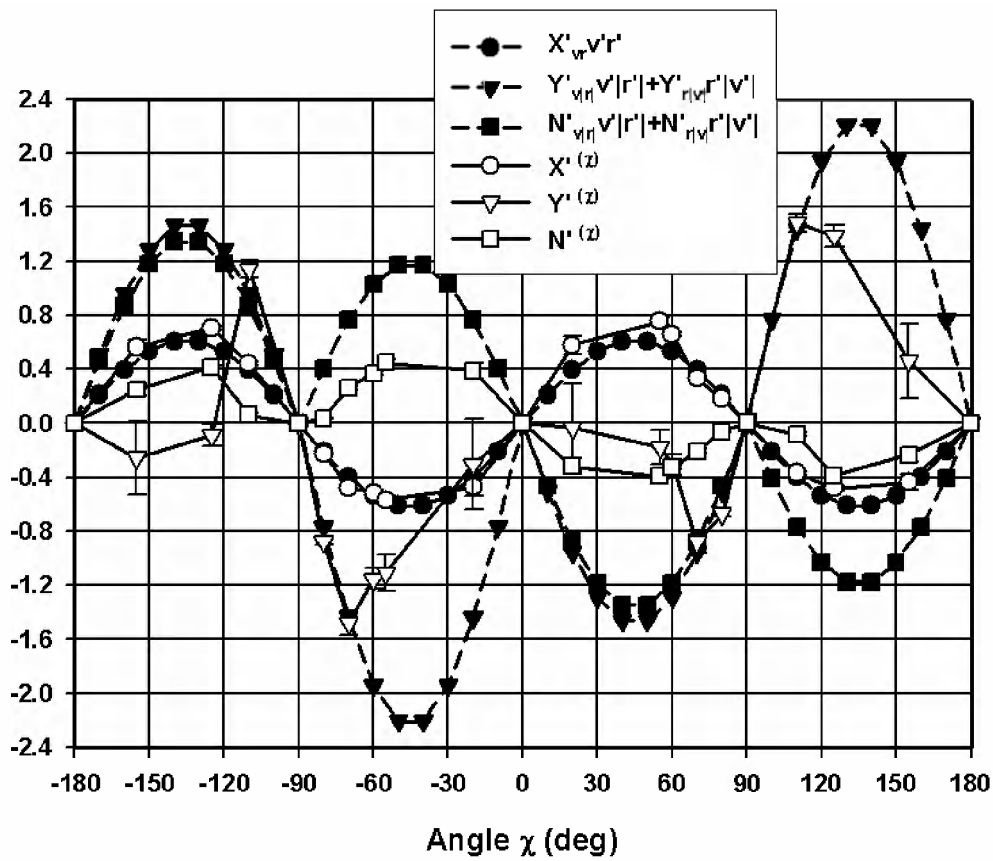
Figure 4.72 Model E, 20% UKC, comparison of a formal and a tabular model for non-dimensional forces and yawing moment due to a combination of sway and yaw
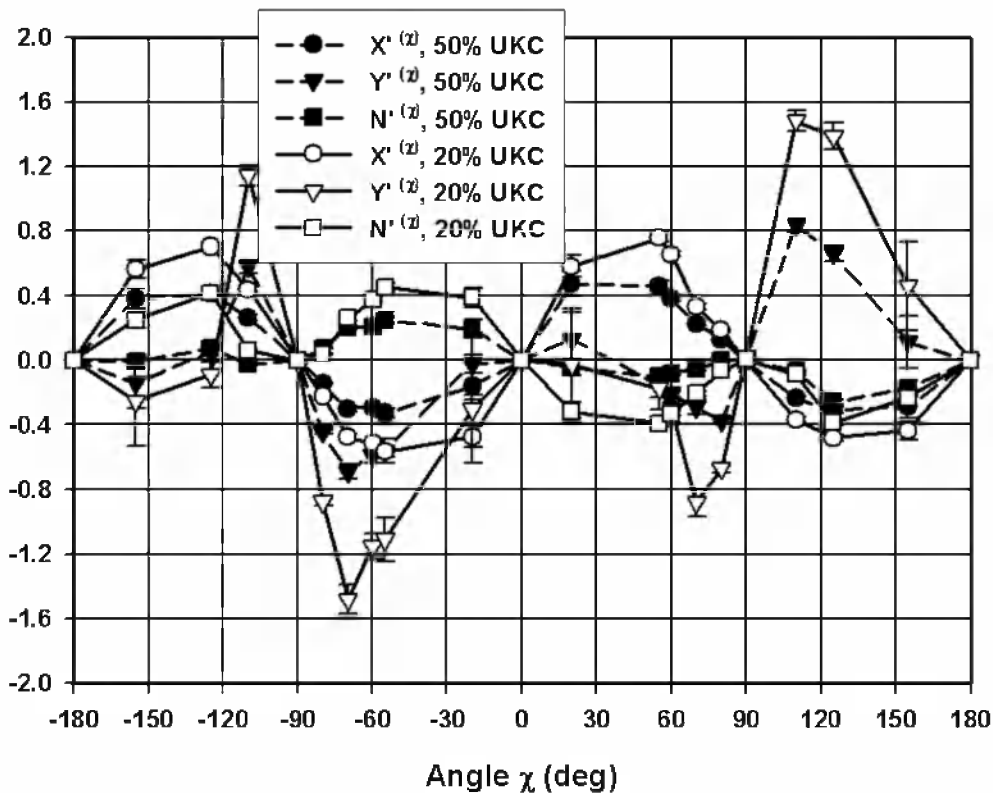
Figure 4.73 Model E, comparison of tabular models for non-dimensional forces and yawing moment due to a combination of sway and yaw

269
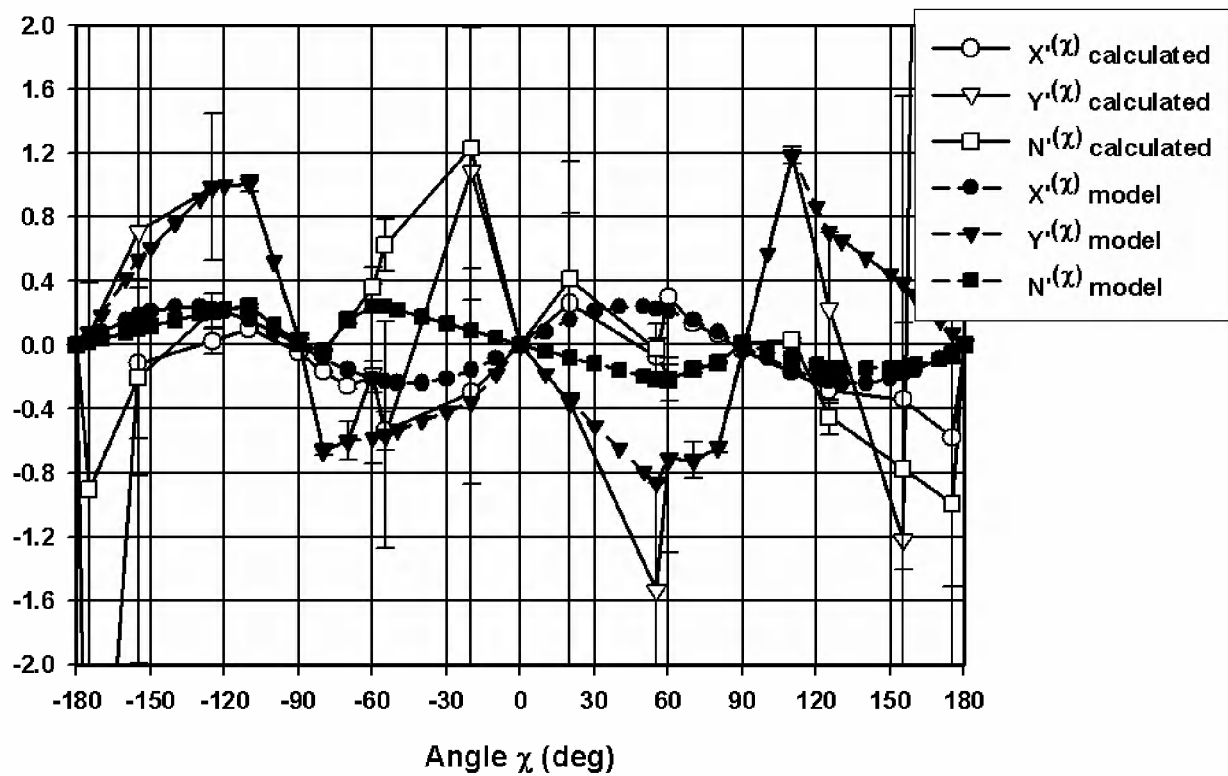
Figure 4.74 Model D, 20% UKC, comparison of calculated and corrected (model) tabular models for non-dimensional forces and yawing moment due to a combination of sway and yaw

270
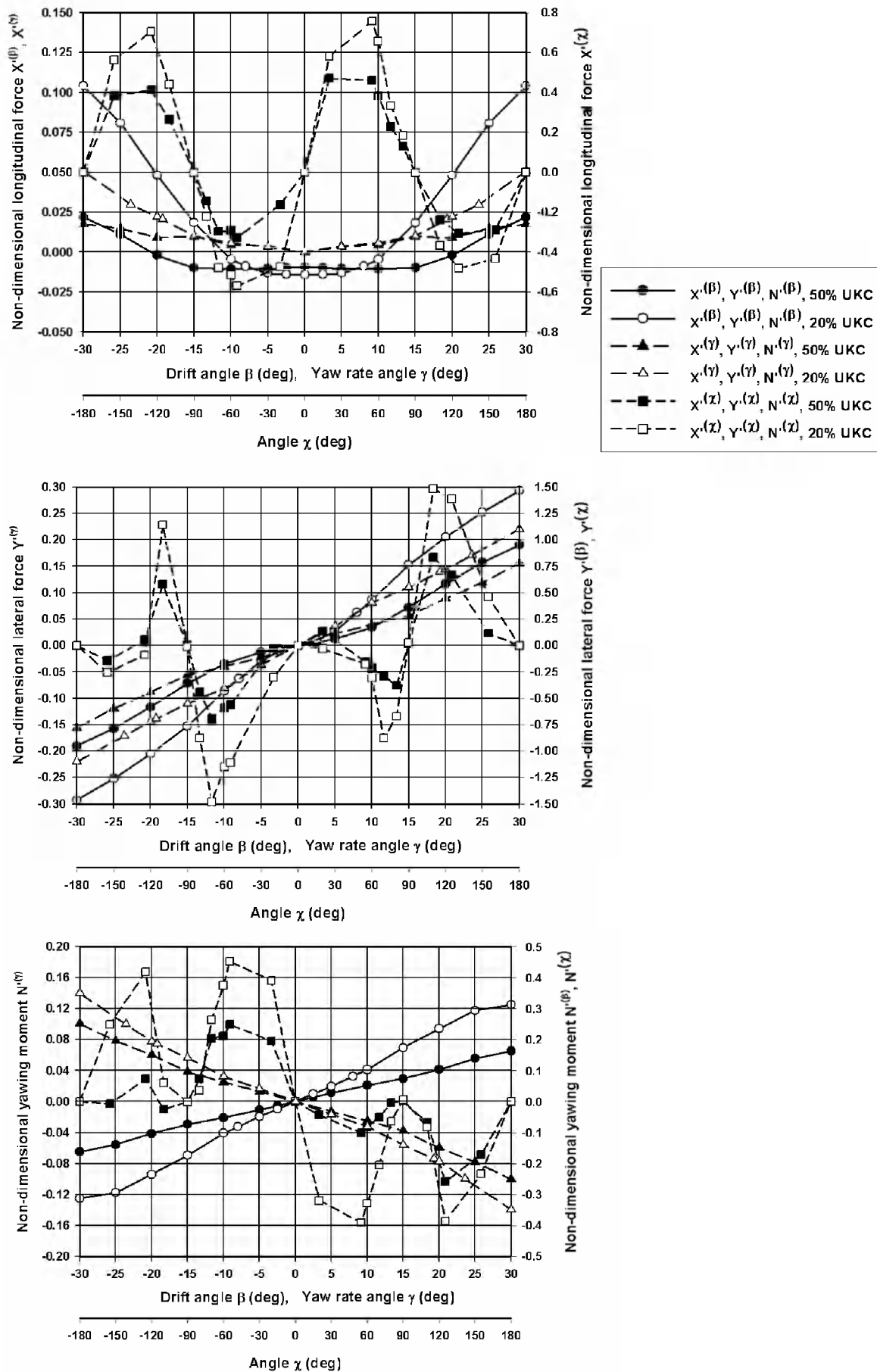
Figure 4.75 Model E, comparison of velocity dependent hull forces at 50% and 20% UKC
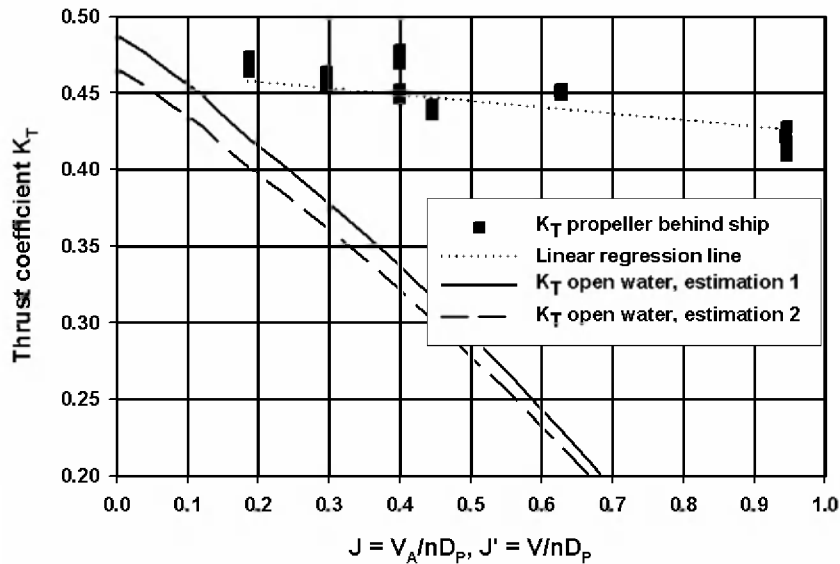
Figure 5.1 Influence of estimation of open water characteristics on wake factor
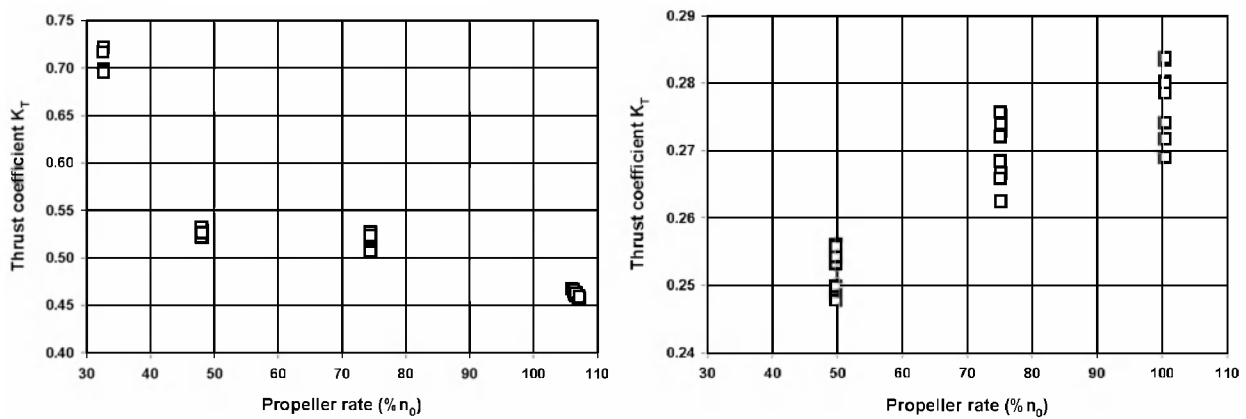
Figure 5.2 Propeller thrust coefficient K_T at bollard pull condition with rudder deflection, model D (left) and model E (right) at 20% UKC: transition between quadrant 1 and 4
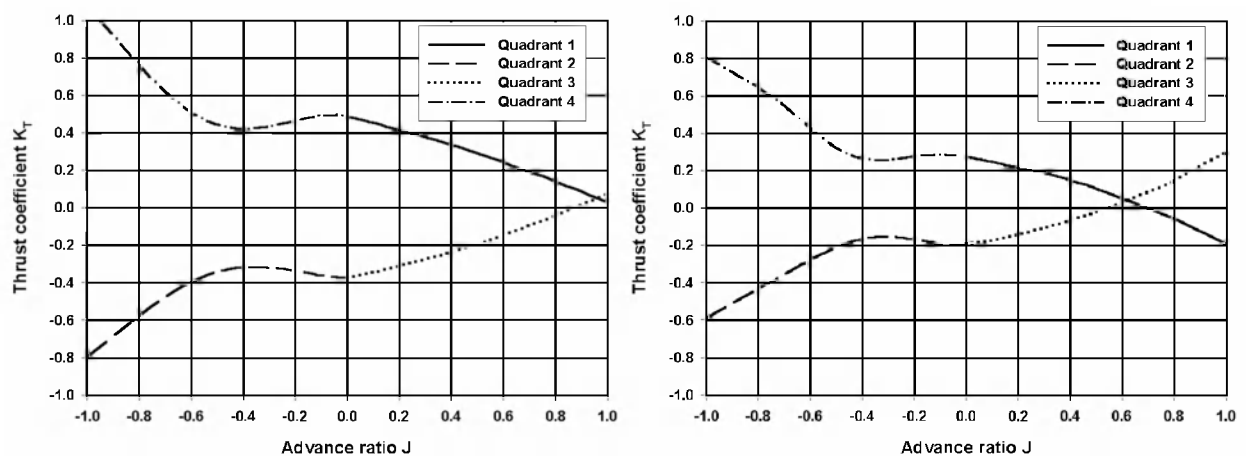
Figure 5.3 Estimated open water K_T curve for four quadrants of operation, containership D (left) and tanker E (right)
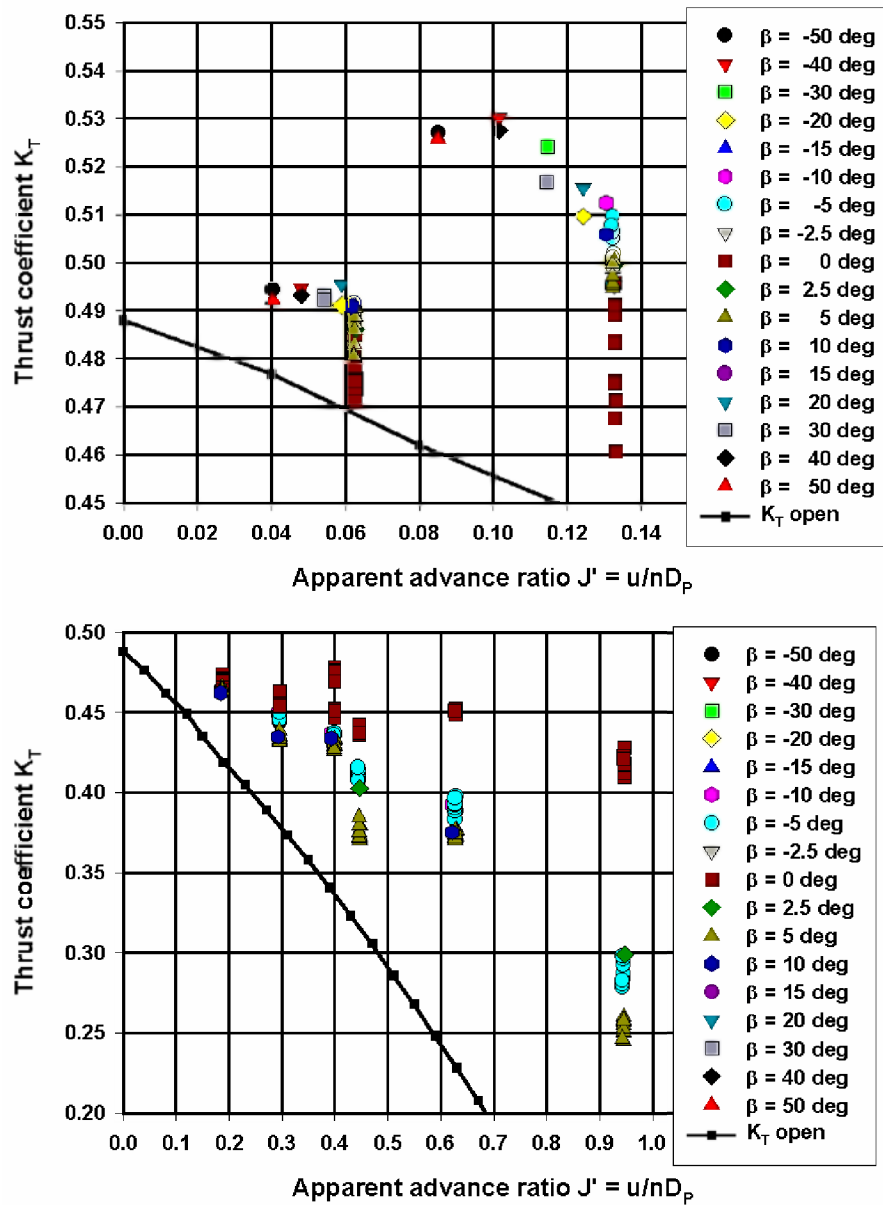
Figure 5.4 Model D, influence of drift angle on propeller thrust coefficient K_T (stationary tests F_n=0.016, top and F_n≥0.049, bottom)
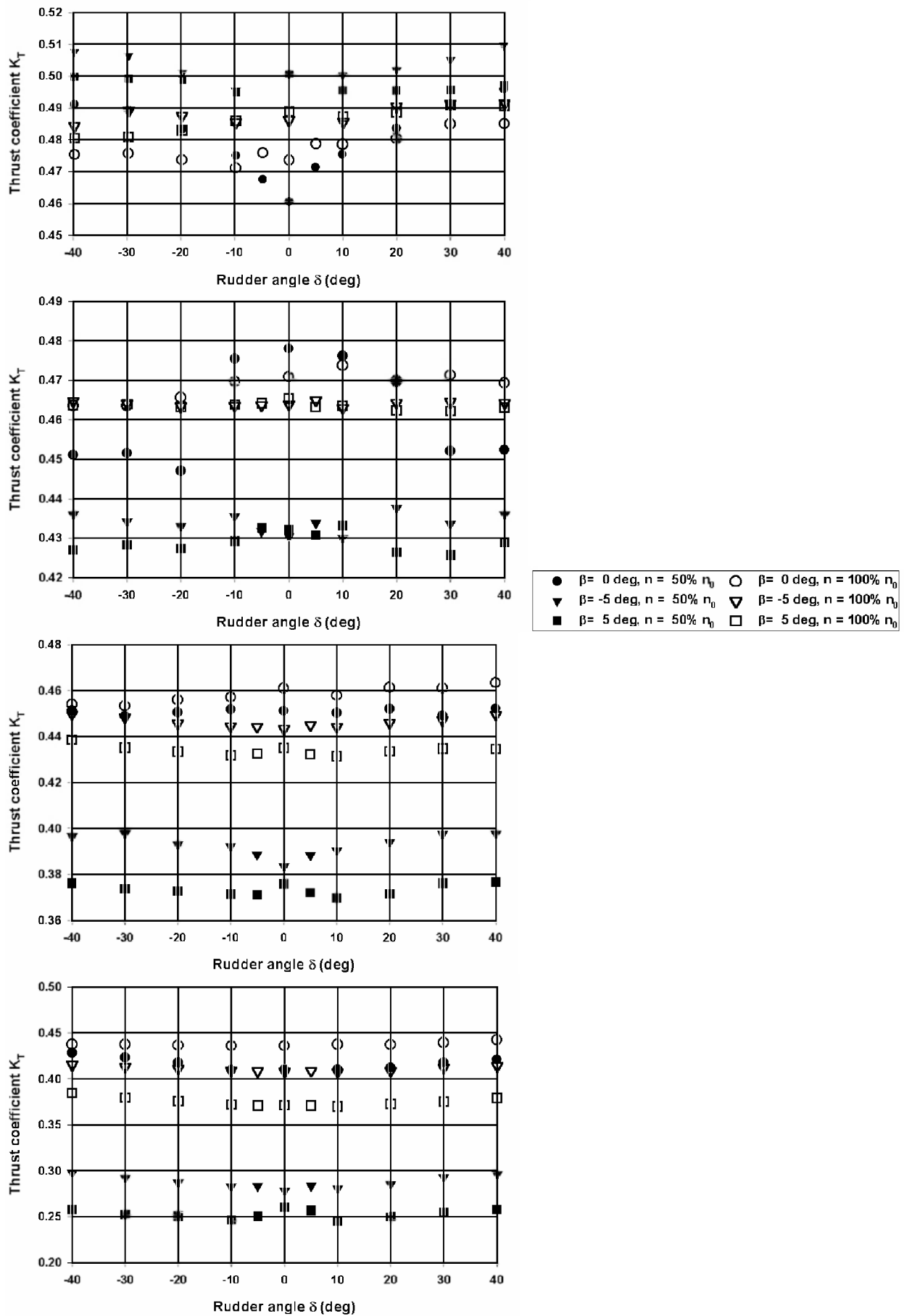
Figure 5.5 Model D, influence of steering on propeller thrust coefficient K_T (stationary tests, from top to bottom, F_n=0.016, F_n=0.049, F_n=0.077 and F_n=0.116)
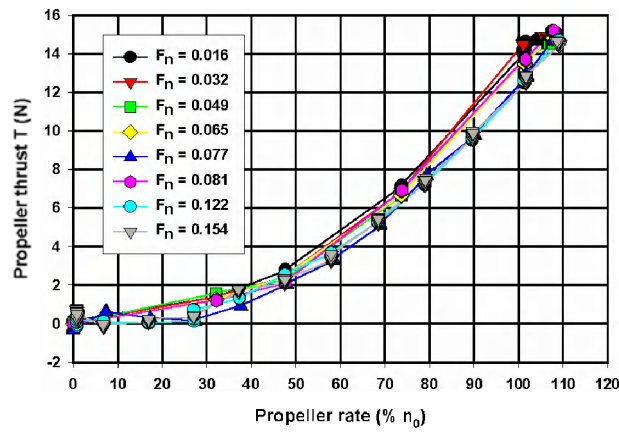
Figure 5.6 Model D, propeller thrust measured during multi-modal tests type A (straight ahead or $\beta=0$)
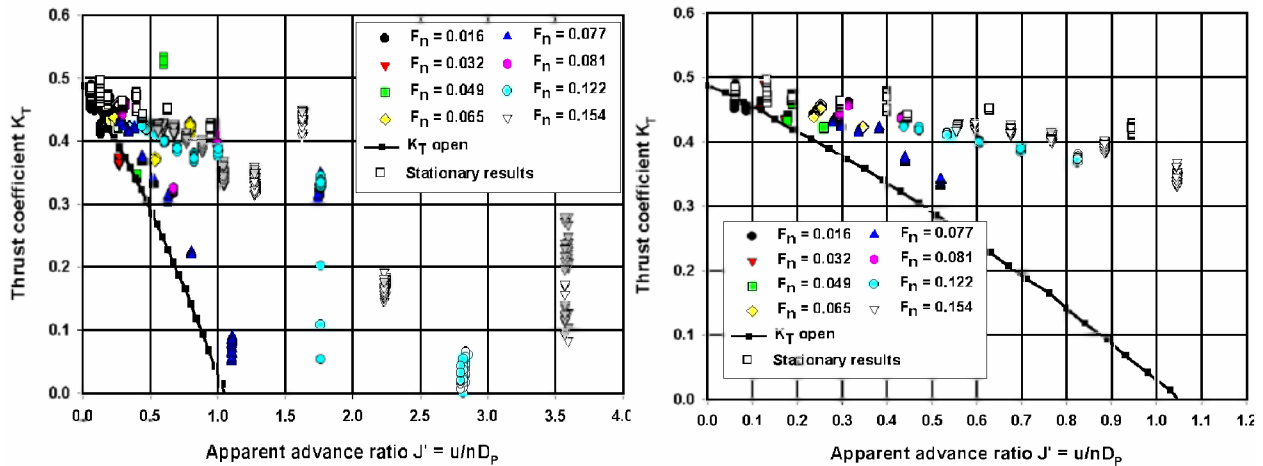
Figure 5.7 Model D, comparison between stationary and multi-modal K_T values (type A) during a straight ahead motion: all propeller rates (left) and a selection for propeller rate of turn > 50% n_0 (right)
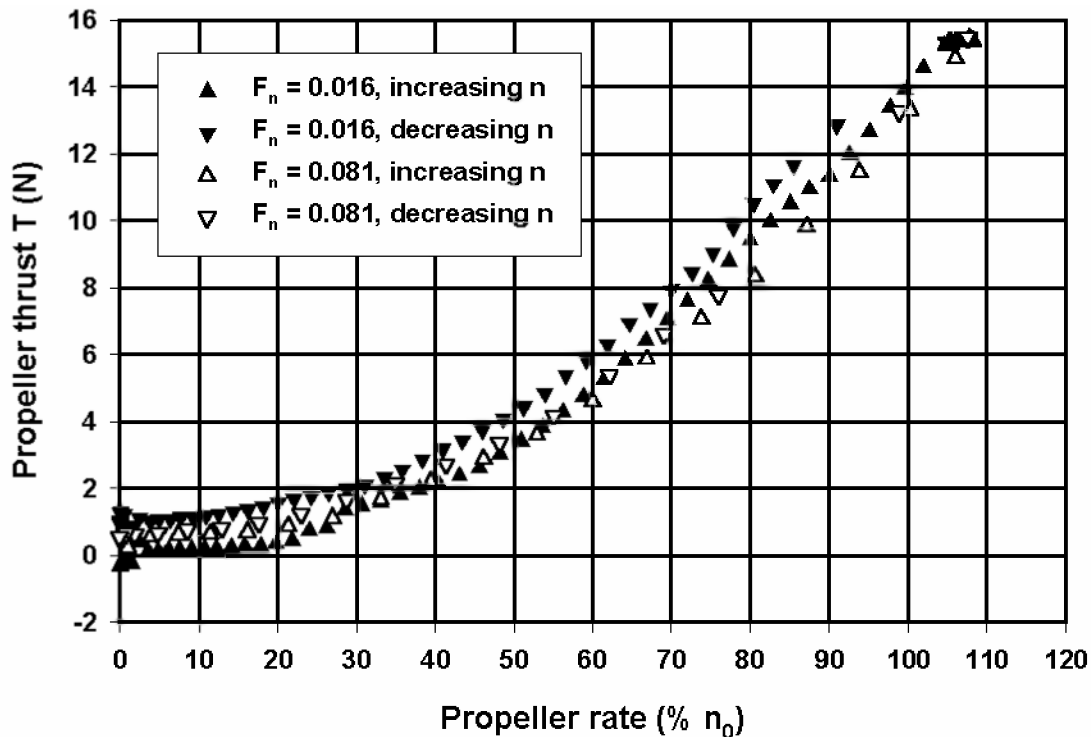
Figure 5.8 Model D, propeller thrust measured during multi-modal tests type B (straight ahead or $\beta=0$))

276
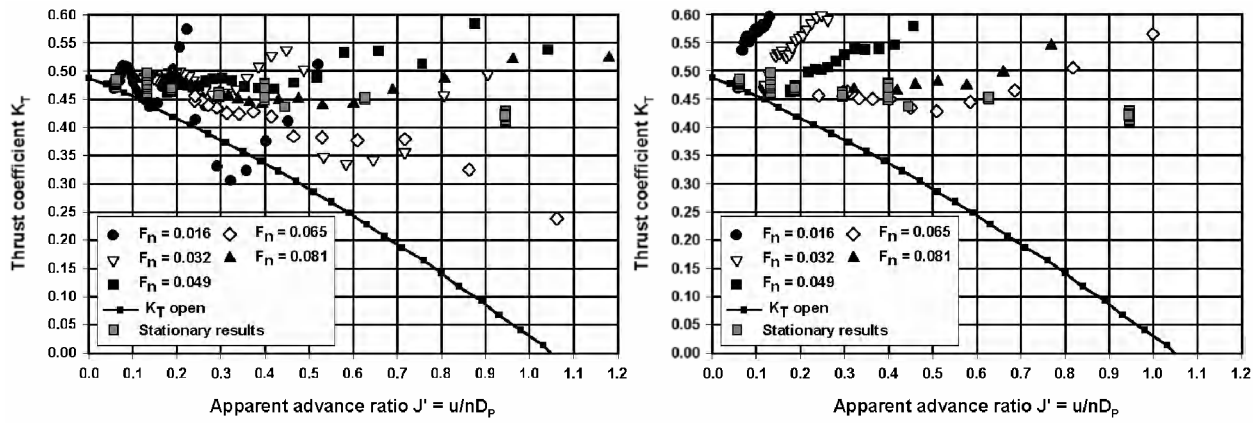
Figure 5.9 Model D, comparison between stationary and multi-modal K_T values (type B) during a straight ahead motion, increasing propeller rate (left) and decreasing propeller rate (right)
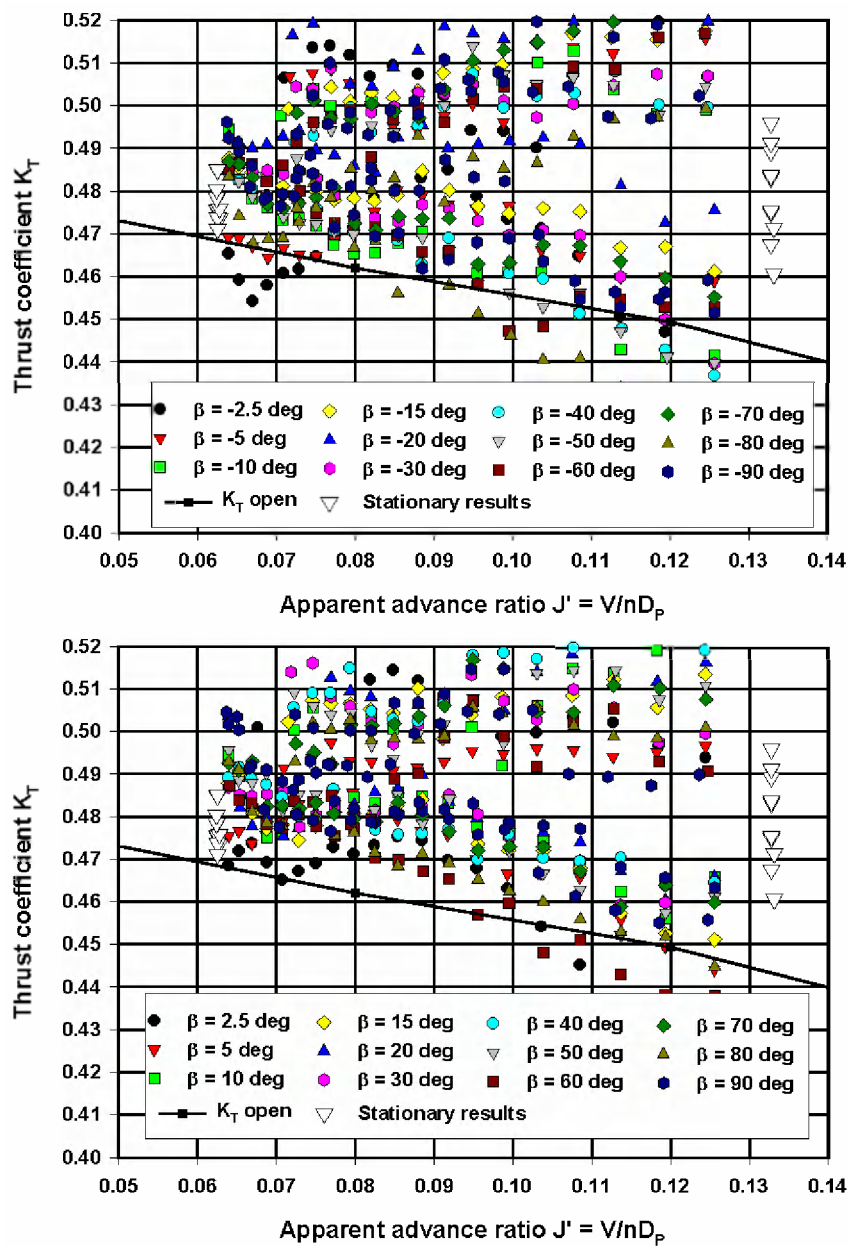
Figure 5.10 Model D, influence of negative (top) and positive (bottom) drift angles on K_T values (multi-modal tests type B, F_n=0.016). The stationary results are restricted to zero drift angle with rudder deflection.
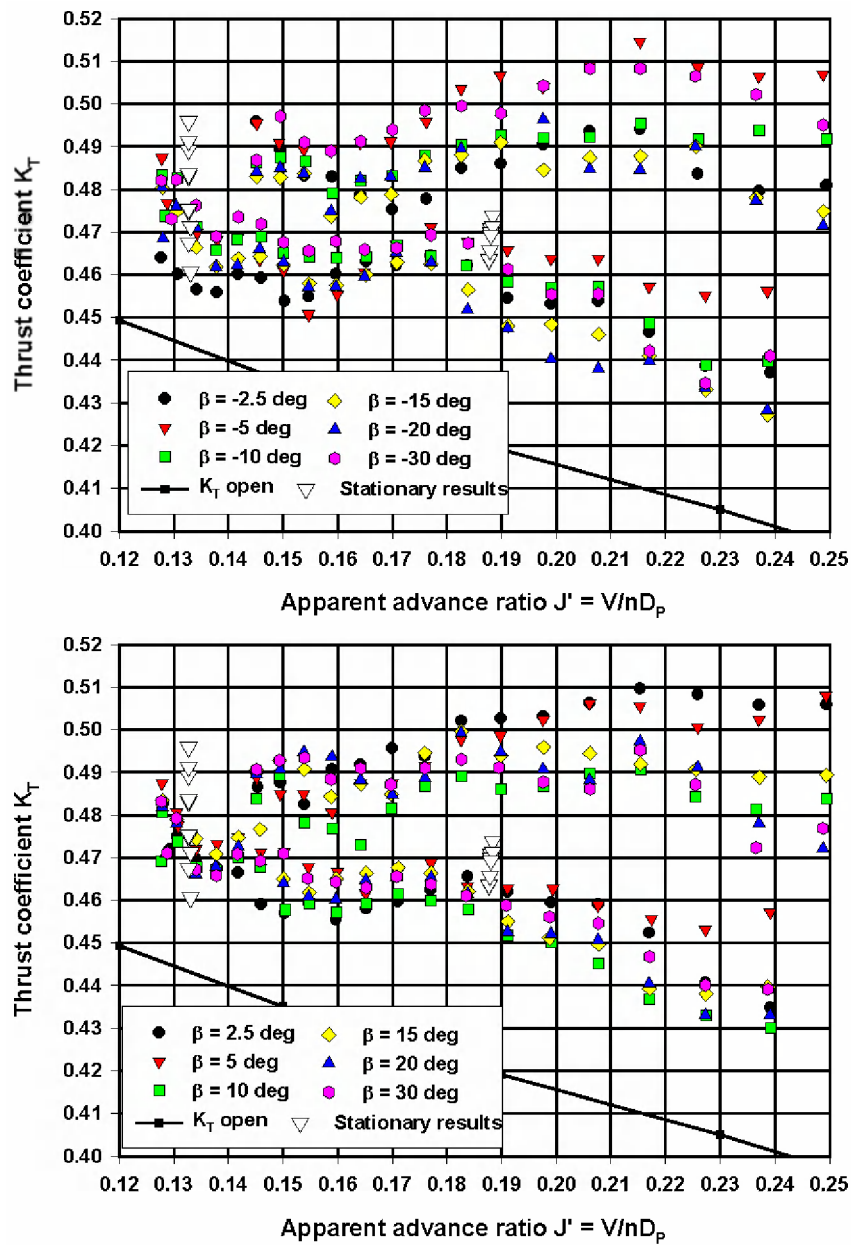
Figure 5.11 Model D, influence of negative (top) and positive (bottom) drift angles on K_T values (multimodal tests type B, F_n=0.032). The stationary results are restricted to zero drift angle with rudder deflection.
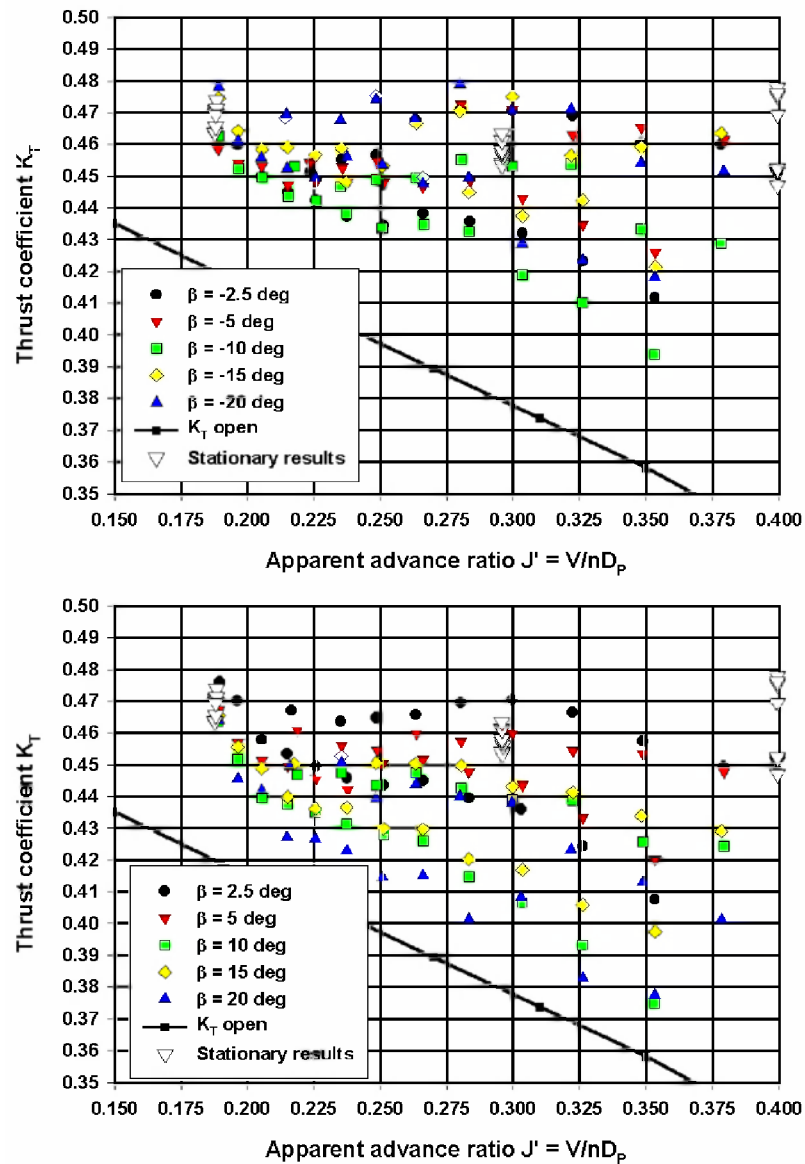
Figure 5.12 Model D, influence of negative (top) and positive (bottom) drift angles on K_T values (multi-modal tests type B, $F_n=0.049$). The stationary results are restricted to zero drift angle with rudder deflection.
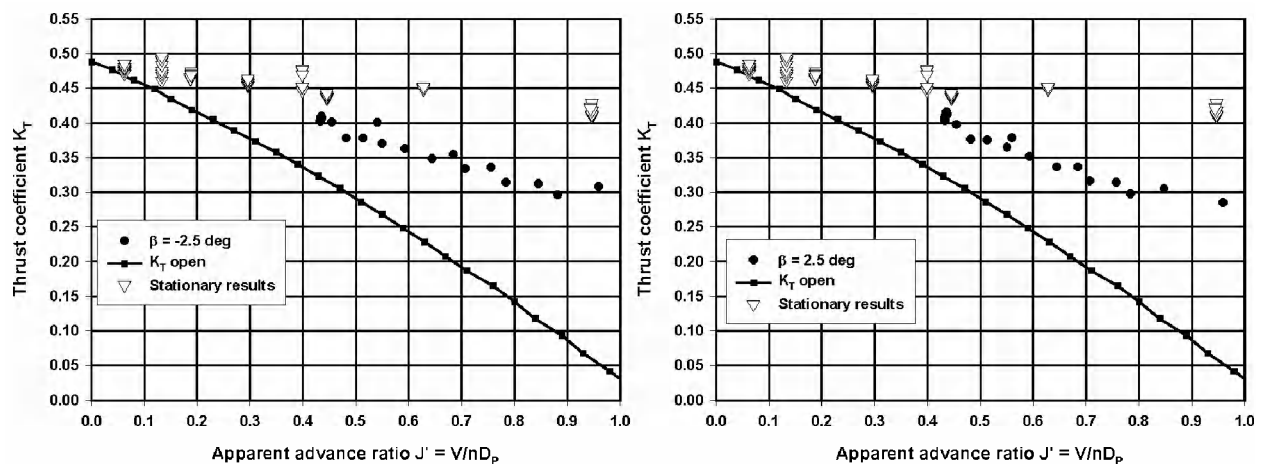
Figure 5.13 Model D, influence of drift angles on K_T values (multi-modal tests type B, $F_n=0.122$). The stationary results are restricted to zero drift angle with rudder deflection.
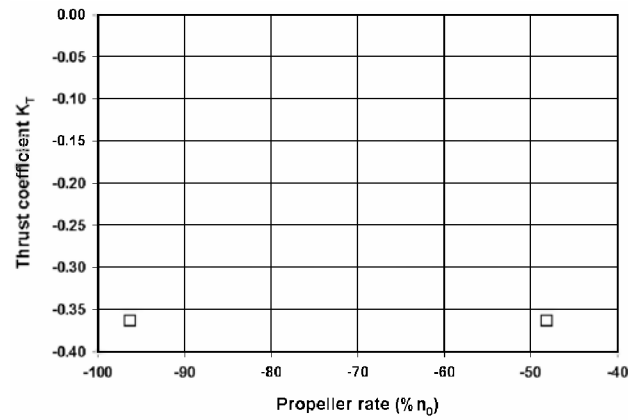
Figure 5.14 Propeller thrust coefficient K_T at bollard pull condition without rudder deflection, model D (left) and model E (right) at 20% UKC: transition between quadrant 2 and 3
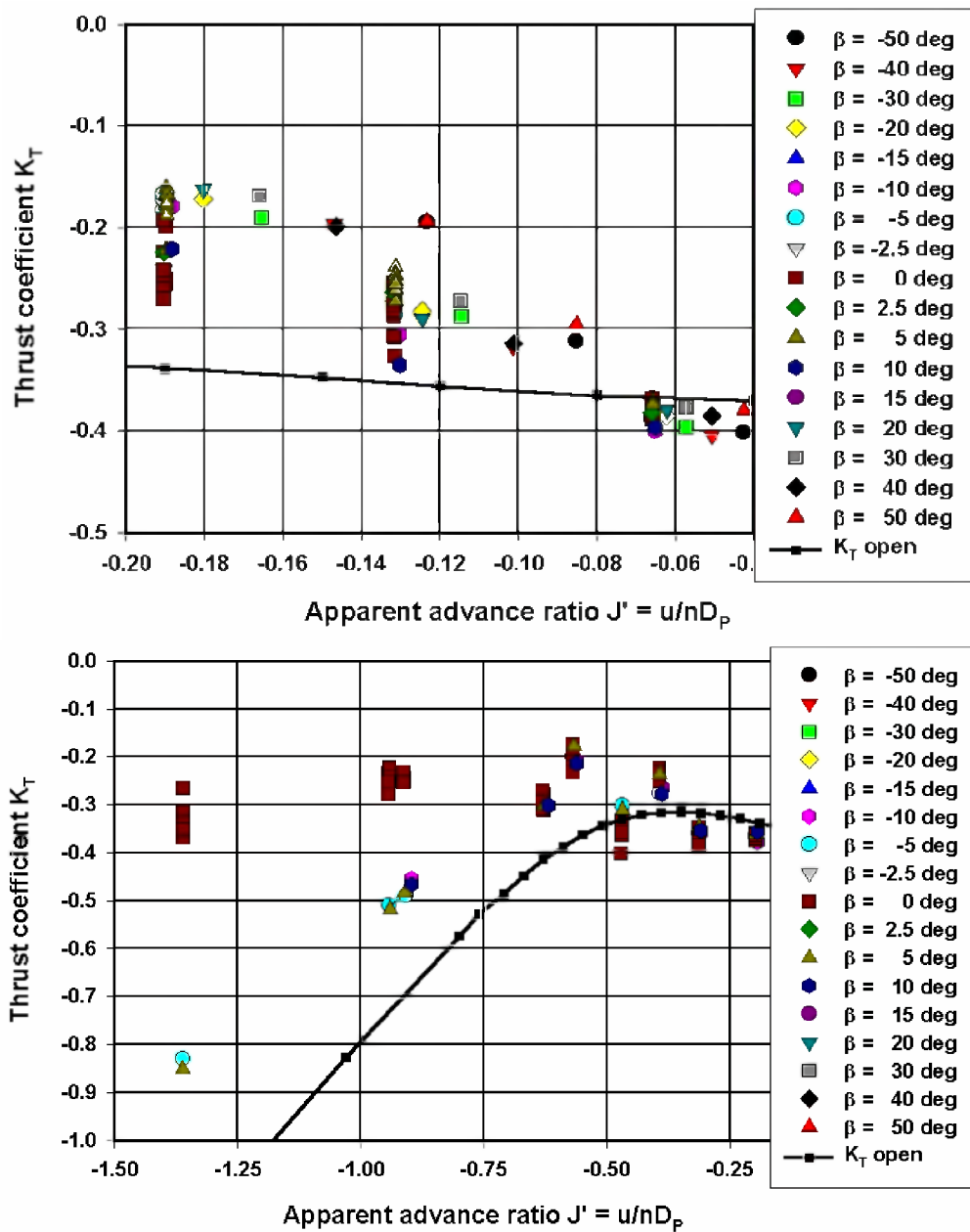
Figure 5.15 Model D, influence of drift angle on propeller thrust coefficient K_T (stationary tests, F_n=0.016, top and F_n≥0.049, bottom)
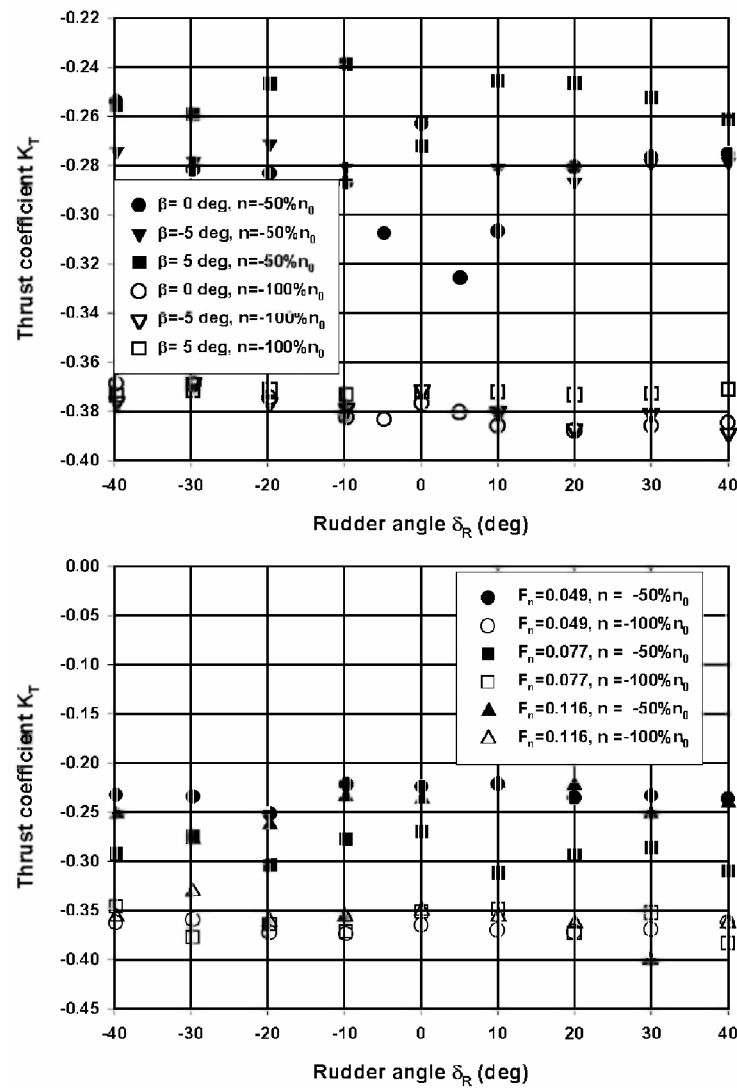
Figure 5.16 Model D, influence of steering on propeller thrust coefficient K_T (stationary tests, low speed or F_n=0.016 at top, ordinary speed at bottom)
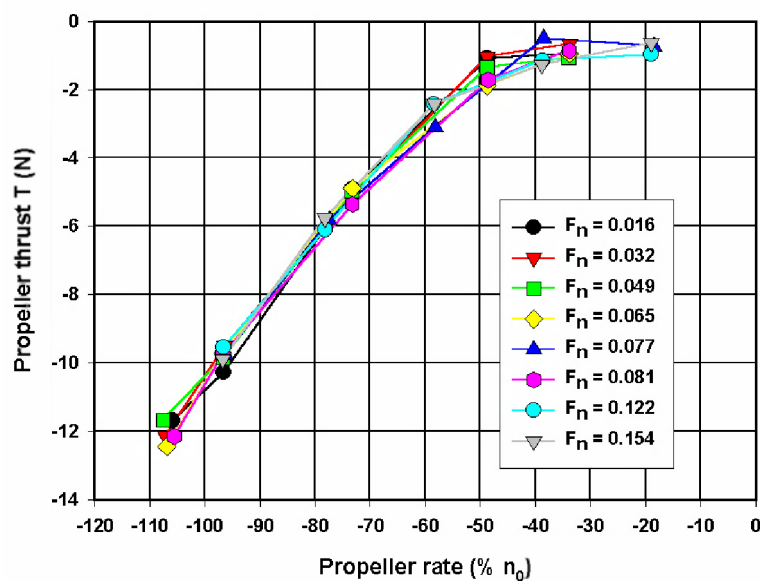
Figure 5.17 Model D, mean values of propeller thrust measured during multi-modal tests type A (stopping at β=0)
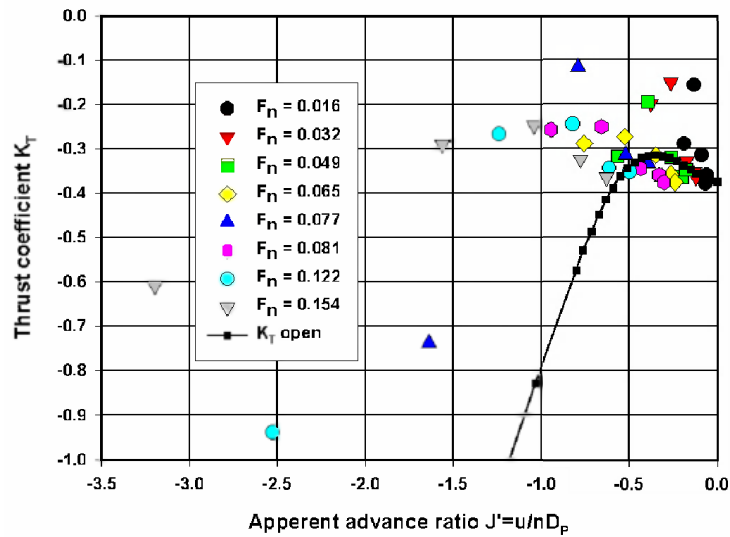
Figure 5.18 Model D, mean values of thrust coefficient K_T measured during multi-modal tests type A (stopping at $\beta=0$)
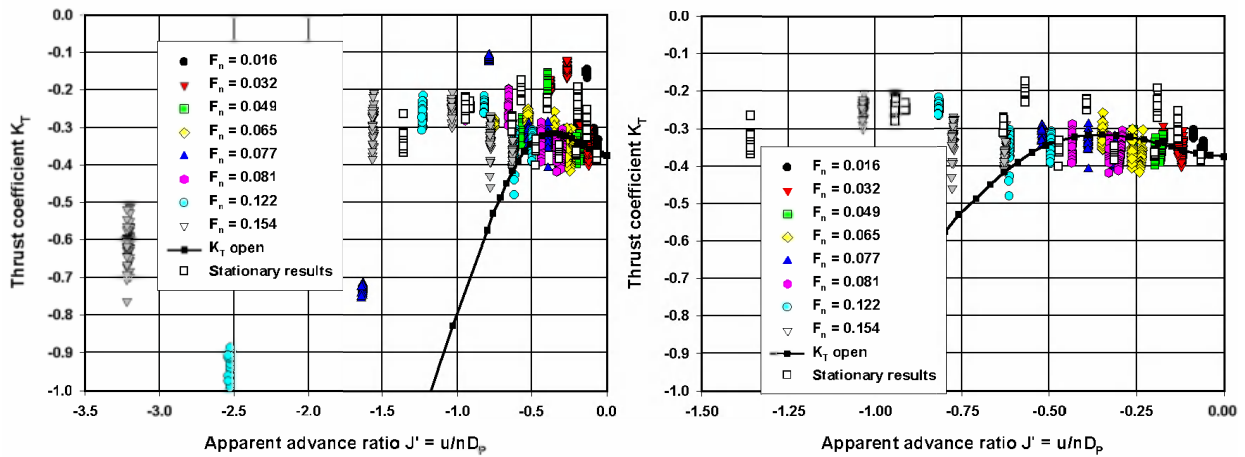
Figure 5.19 Model D, comparison between stationary and multi-modal K_T values (type A) during a straight ahead motion and stopping: all propeller rates (left) and a selection for propeller rate of turn < -50% n_0 (right)
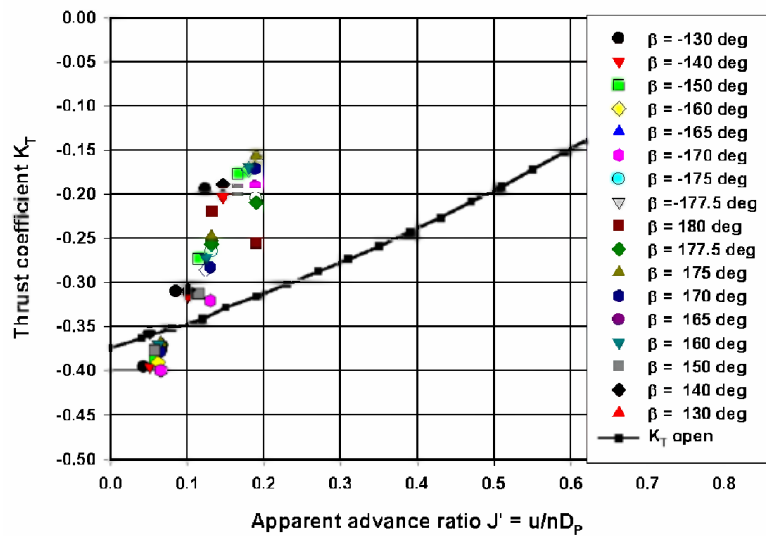
Figure 5.20 Model D, influence of drift angle on propeller thrust coefficient K_T for going astern (F_n=-0.016), stationary test results without rudder deflection

282
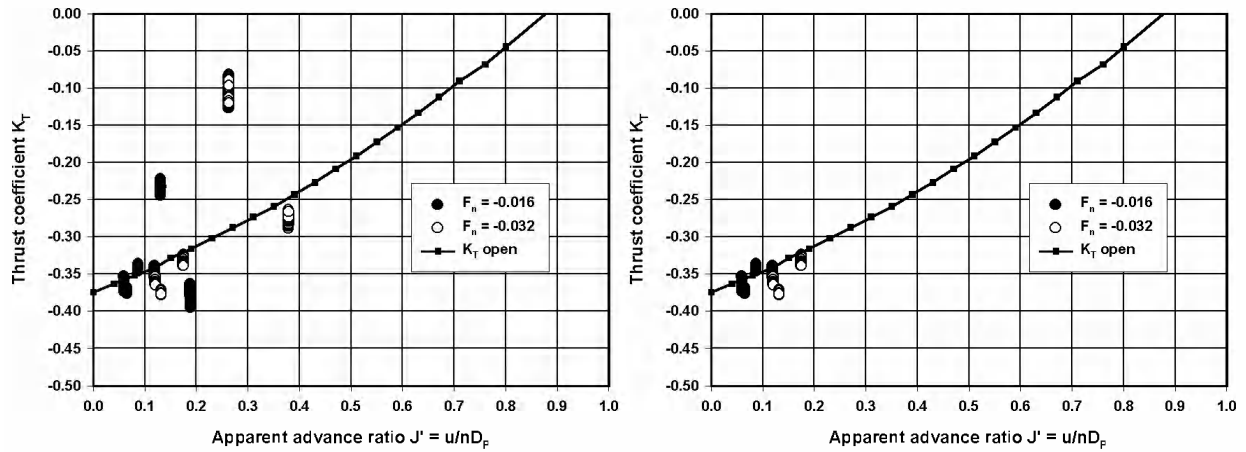
Figure 5.21 Model D, propeller thrust measured during multi-modal tests type A (going astern at β=0): all propeller rates (left) and a selection for propeller rate of turn < -50% n_0 (right)
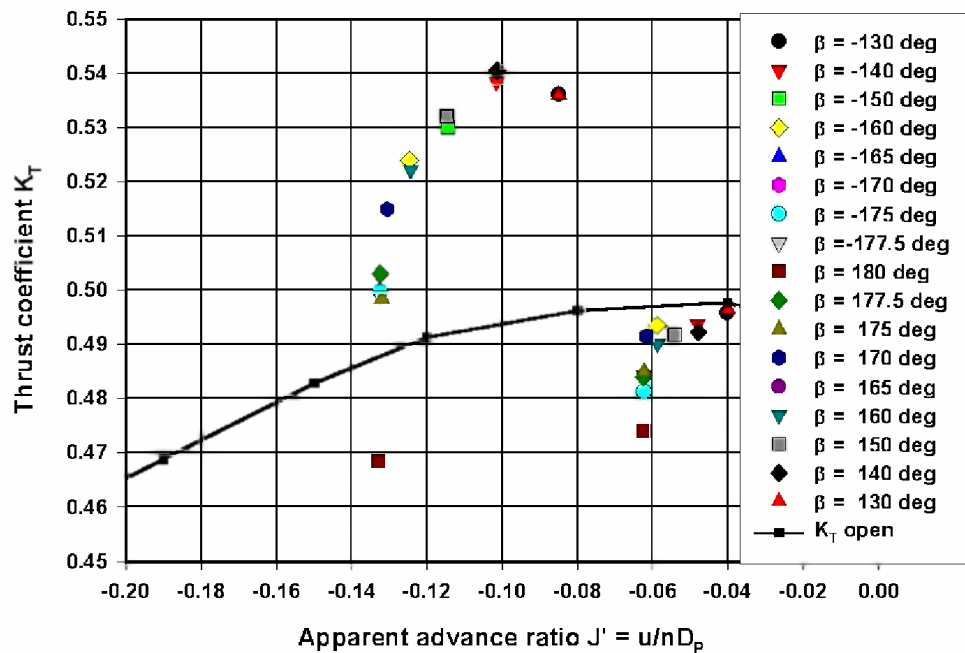
Figure 5.22 Model D, influence of drift angle on propeller thrust coefficient K_T stopping from sternway (F_n=-0.016), stationary test results without rudder deflection
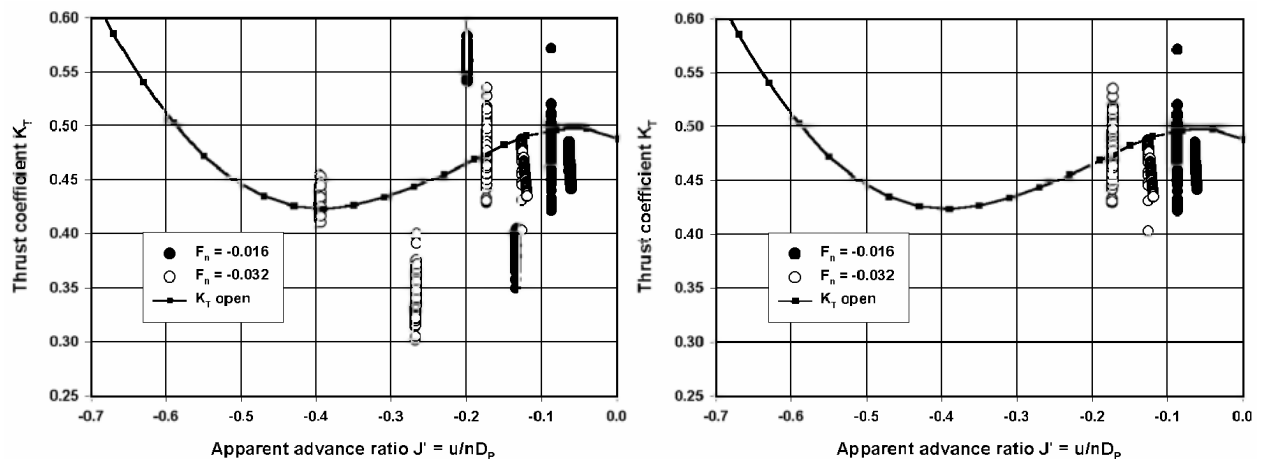
Figure 5.23 Model D, propeller thrust measured during multi-modal tests type A (going astern at β=0): all propeller rates (left) and a selection for propeller rate of turn > 50% n_0 (right)

283
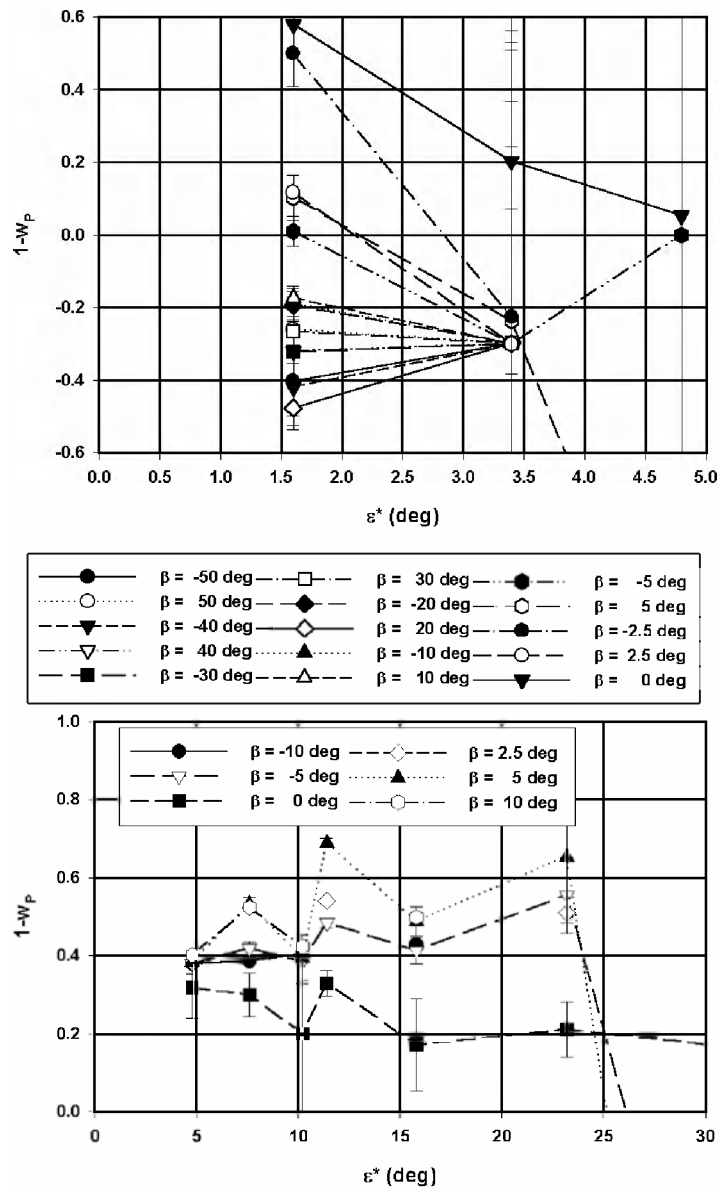
Figure 5.24 Model D, *model per Froude number*, tabular model for wake factor 1-w_P (stationary tests, low speed F_n=0.016 at top and ordinary speed F_n≥0.049 at bottom)
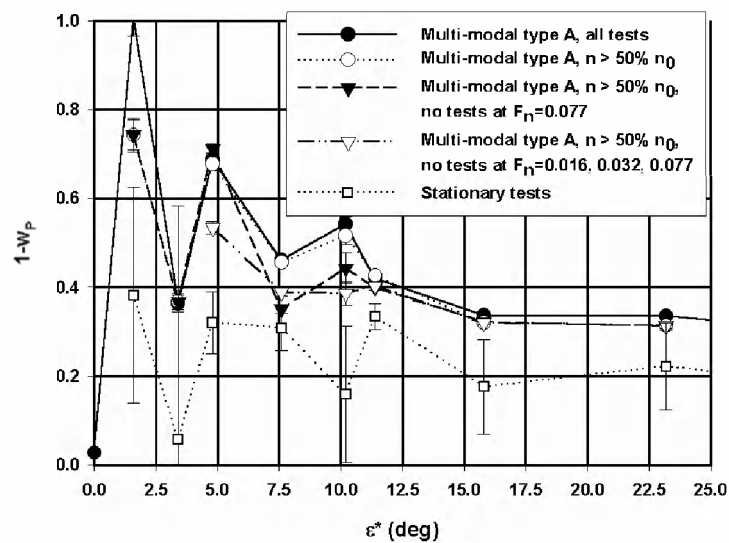
Figure 5.25 Model D, comparison of tabular models for 1-w_P (stationary and multi-modal tests type A, different selections)
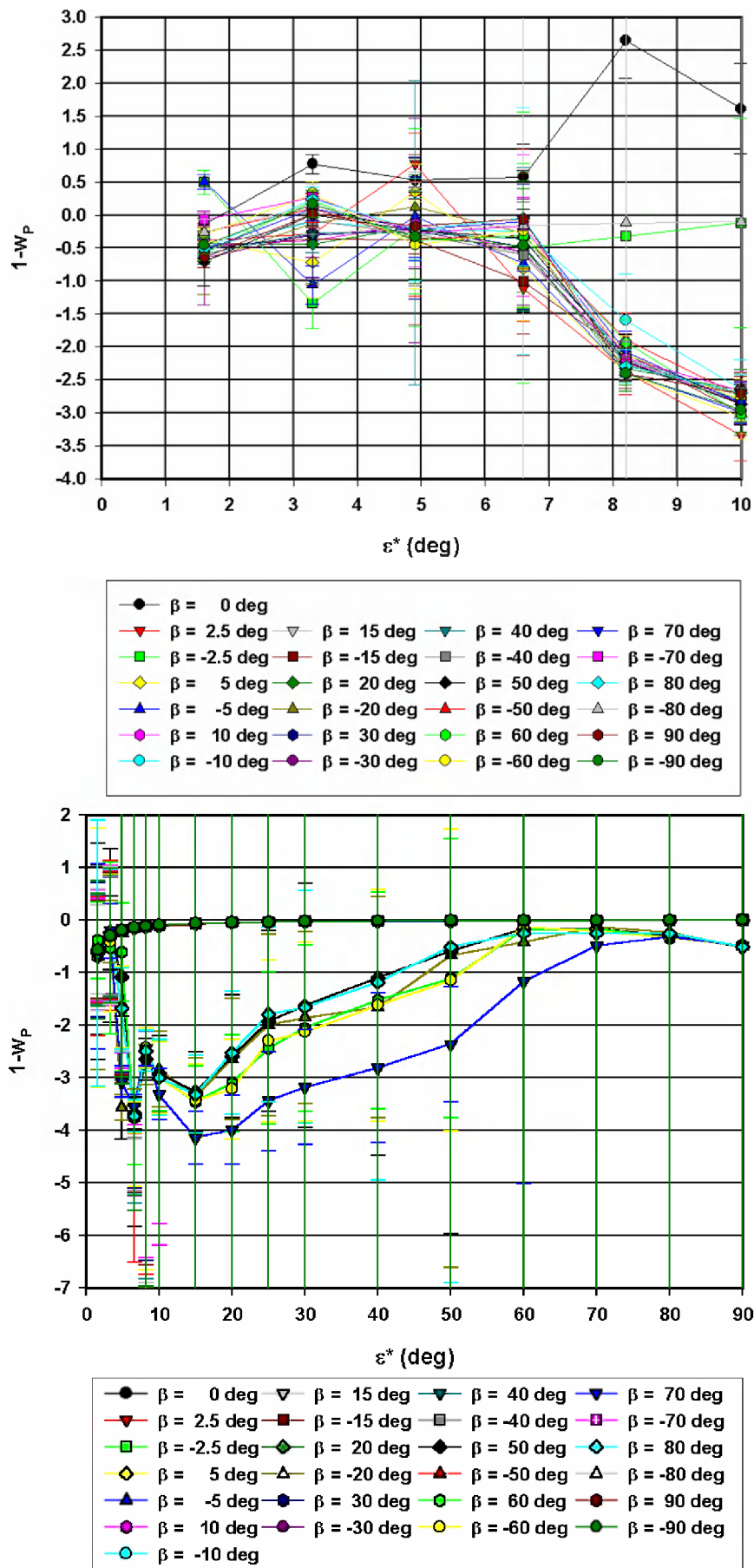
Figure 5.26 Model D, *model per Froude number*, tabular model for wake factor 1-w_P (multi-modal tests type B, F_n=0.016, increasing propeller rate at top and decreasing propeller rate at bottom)
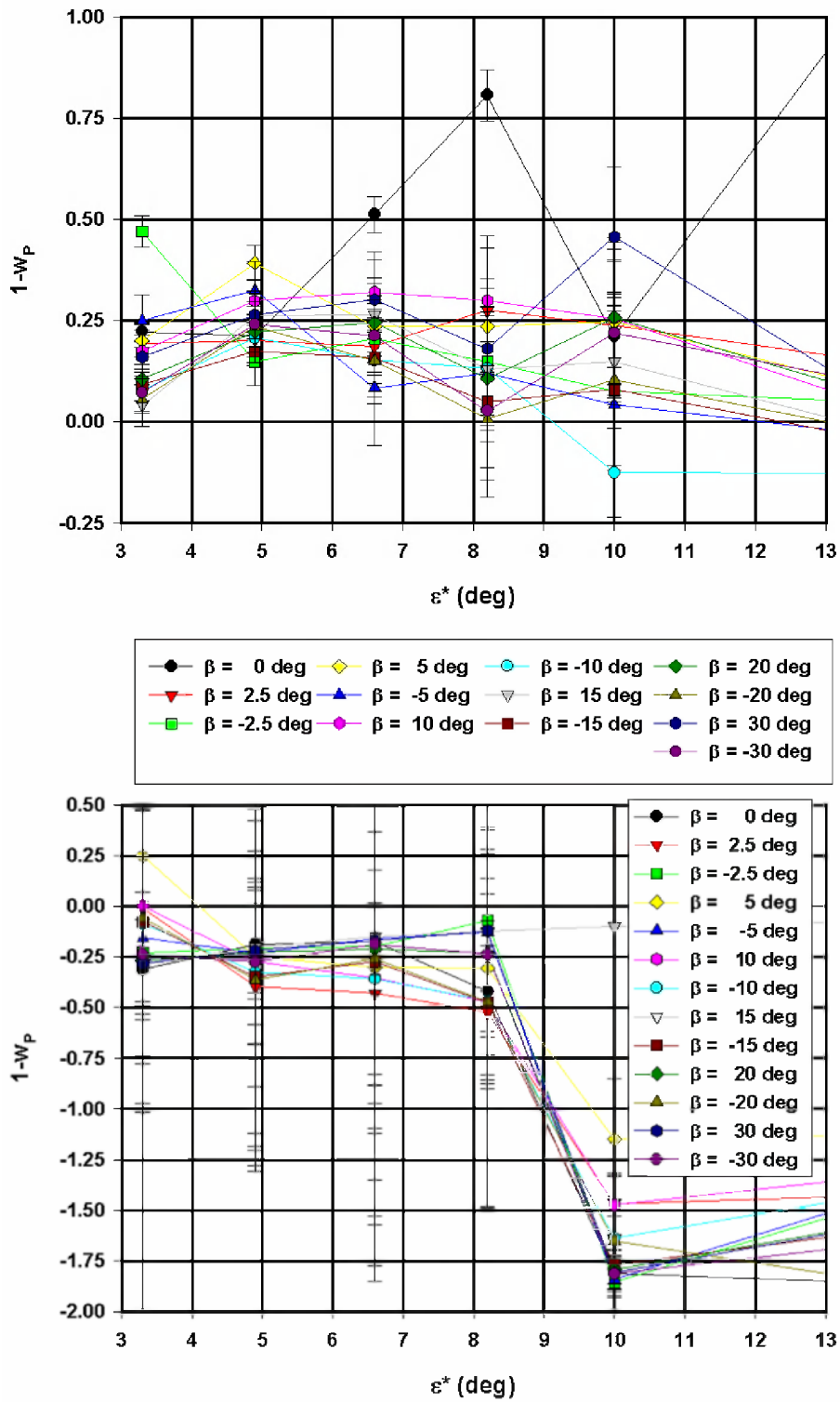
Figure 5.27 Model D, *model per Froude number*, tabular model for wake factor 1-w_P (multi-modal tests type B, F_n=0.032, increasing propeller rate at top and decreasing propeller rate at bottom)
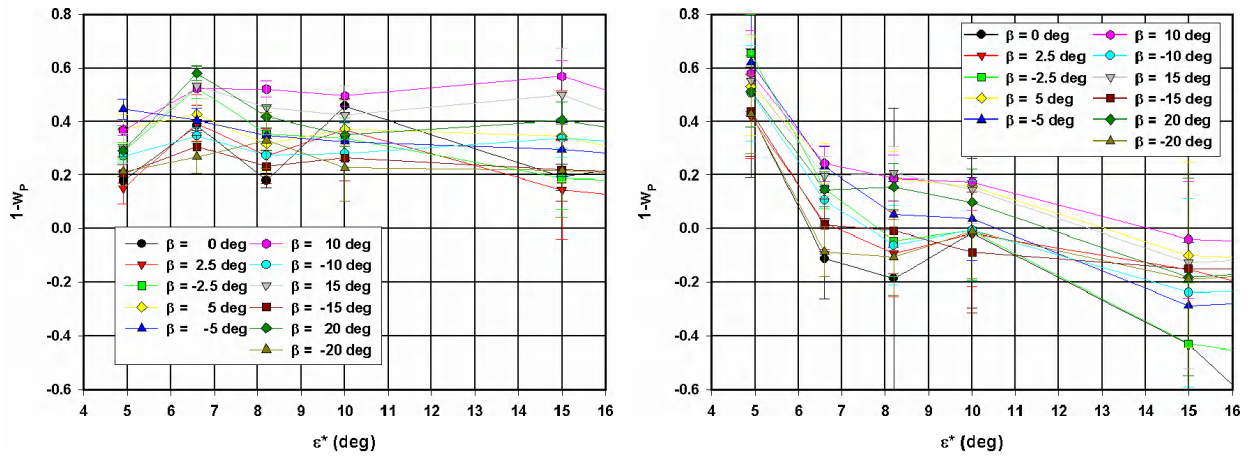
Figure 5.28 Model D, *model per Froude number*, tabular model for wake factor $1-w_P$ (multi-modal tests type B, $F_n=0.049$, increasing propeller rate left and decreasing propeller rate right)
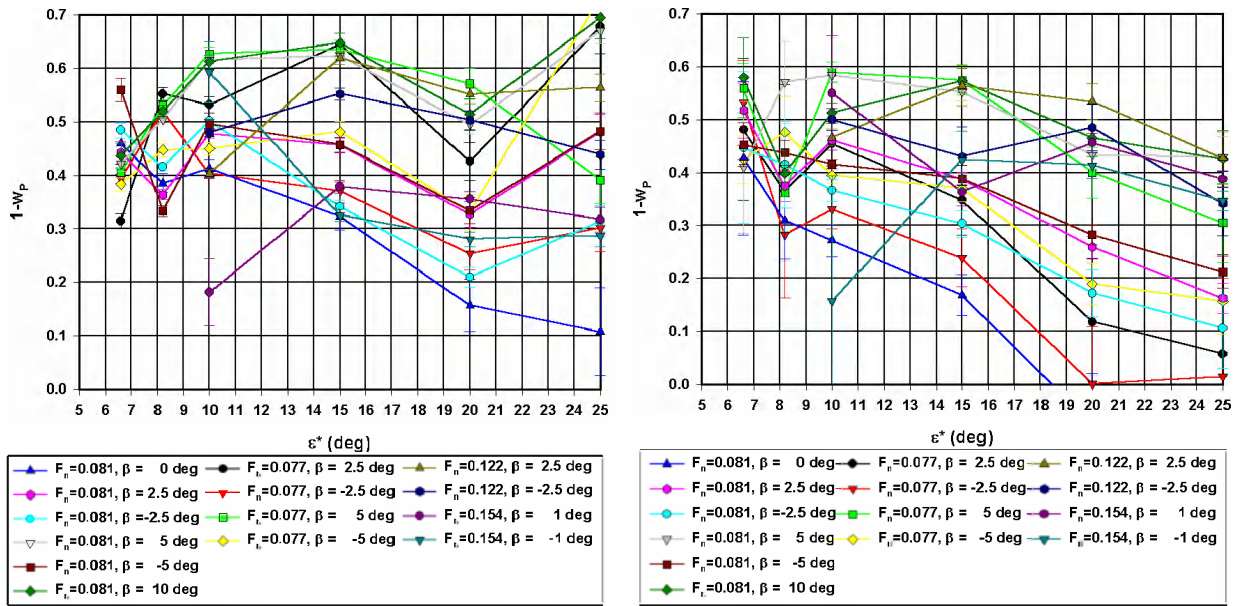
Figure 5.29 Model D, *model per Froude number*, tabular model for wake factor $1-w_P$ (multi-modal tests type B, Froude numbers $F_n \geq 0.077$, increasing propeller rate left and decreasing propeller rate right)
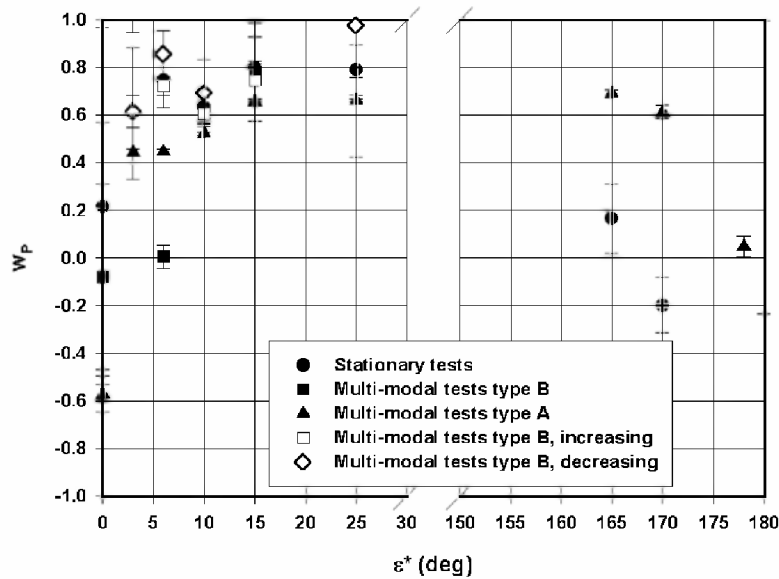
Figure 5.30 Model D, *global model*, comparison of wake factor w_P for a straight ahead motion and different test types (quadrant 1 and 2)
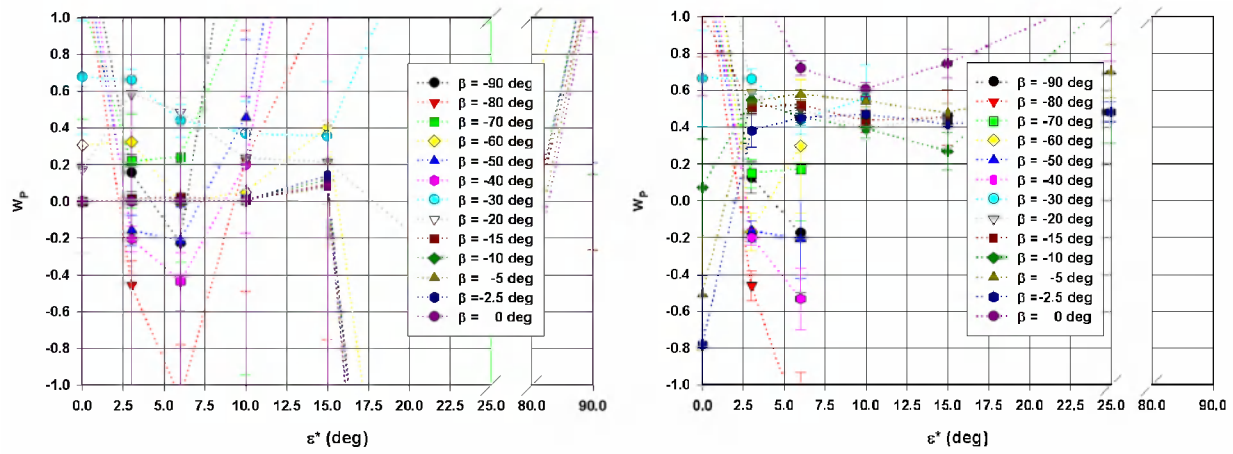
Figure 5.31 Model D, *global model*, influence of a restriction of propeller rate on modelled wake factors (multi-modal tests type B, increasing phase, all propeller rates, left, propeller rates > 35% n_0, right)
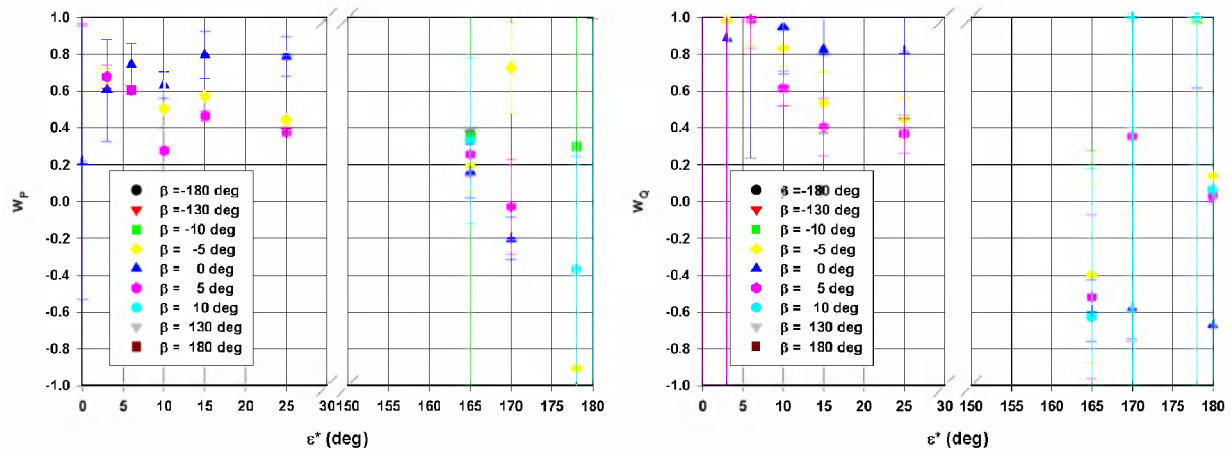
Figure 5.32 Model D, *global model*, tabular model for wake factor w_P and w_Q (stationary tests, quadrant 1 and 2)
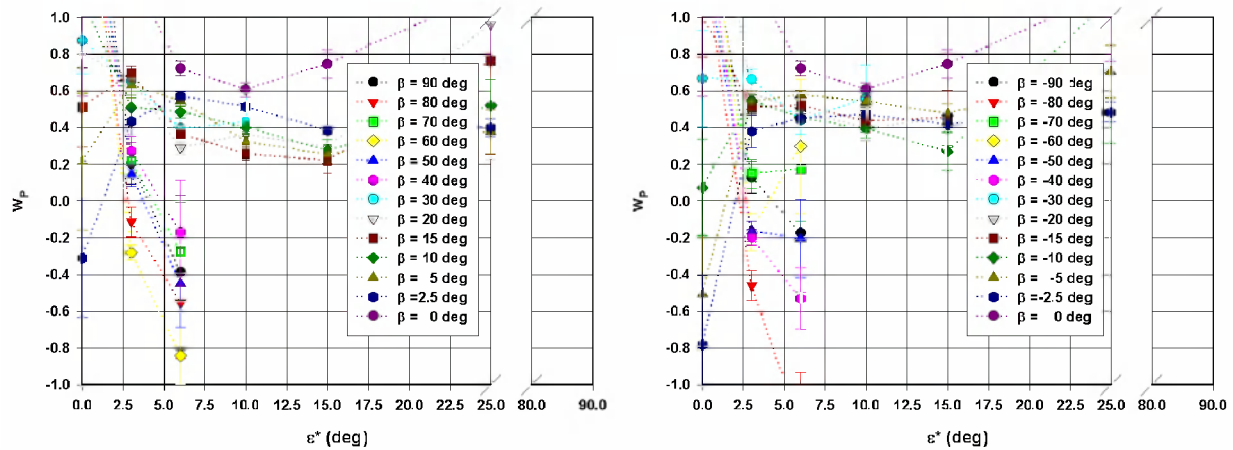
Figure 5.33 Model D, *global model*, tabular model for wake factor w_P (multi-modal tests type B, quadrant 1, increasing propeller rate)
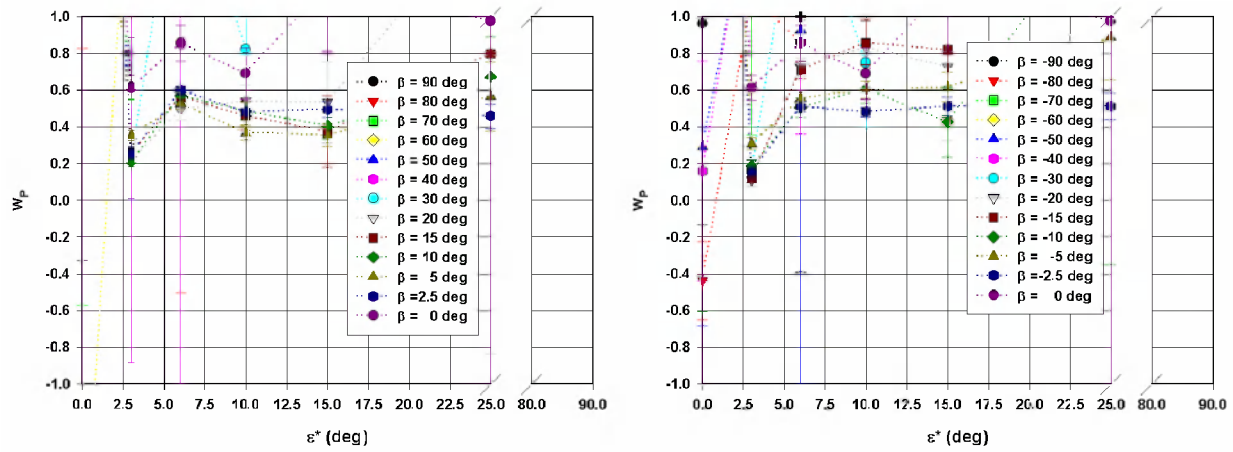
Figure 5.34 Model D, *global model*, tabular model for wake factor w_P (multi-modal tests type B, quadrant 1, decreasing propeller rate)
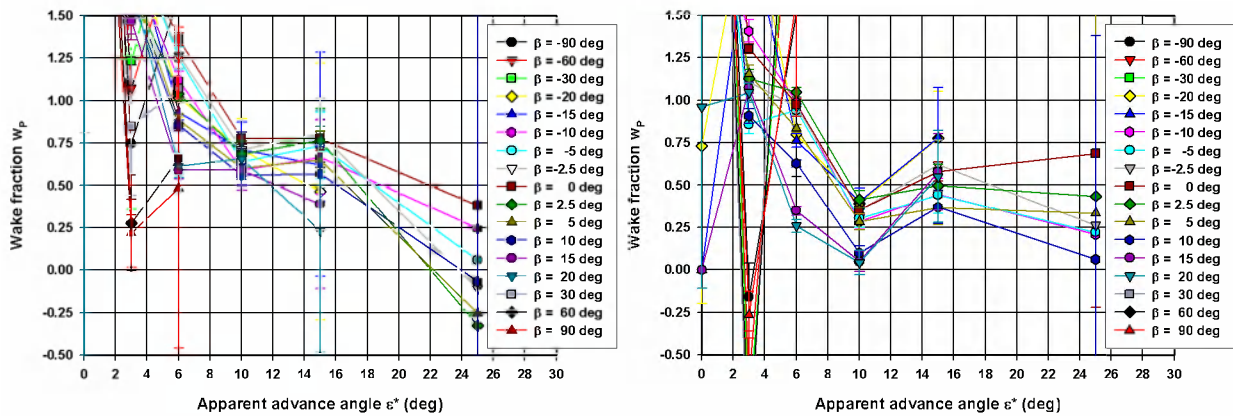
Figure 5.35 Model E, *global model*, tabular model for wake factor w_P (quadrant 1, 20% UKC left and 50% UKC right)
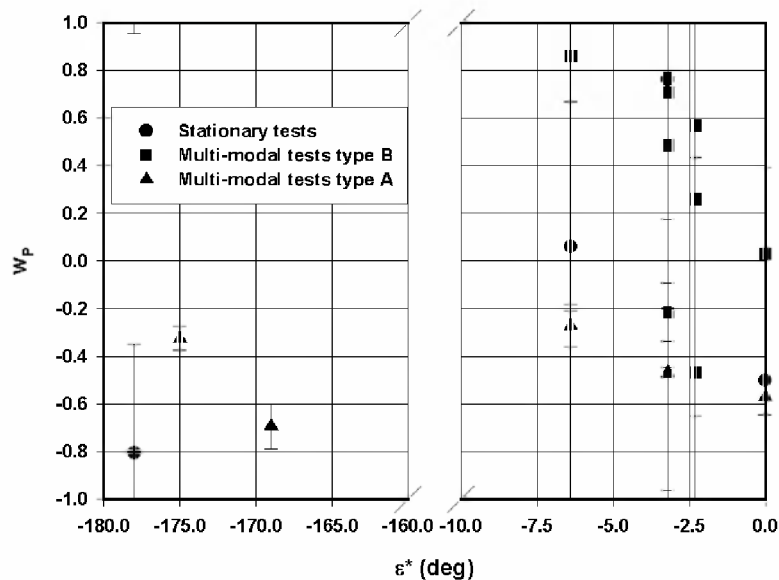
Figure 5.36 Model D, *global model*, comparison of wake factor w_P for a straight astern motion and different test types (quadrant 3 and 4)
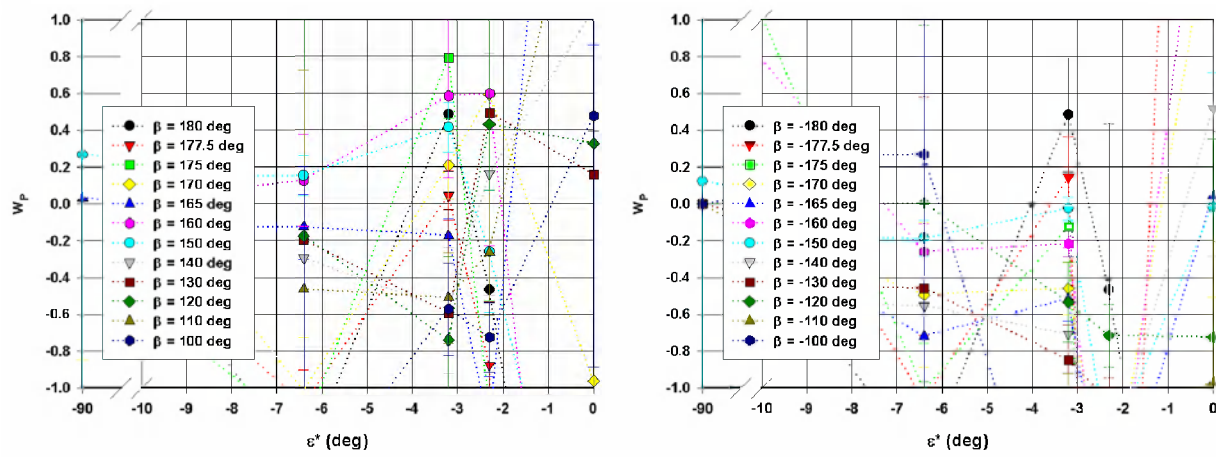
Figure 5.37 Model D, *global model*, tabular model for wake factor w_P (multi-modal tests type B, quadrant 4, increasing propeller rate)
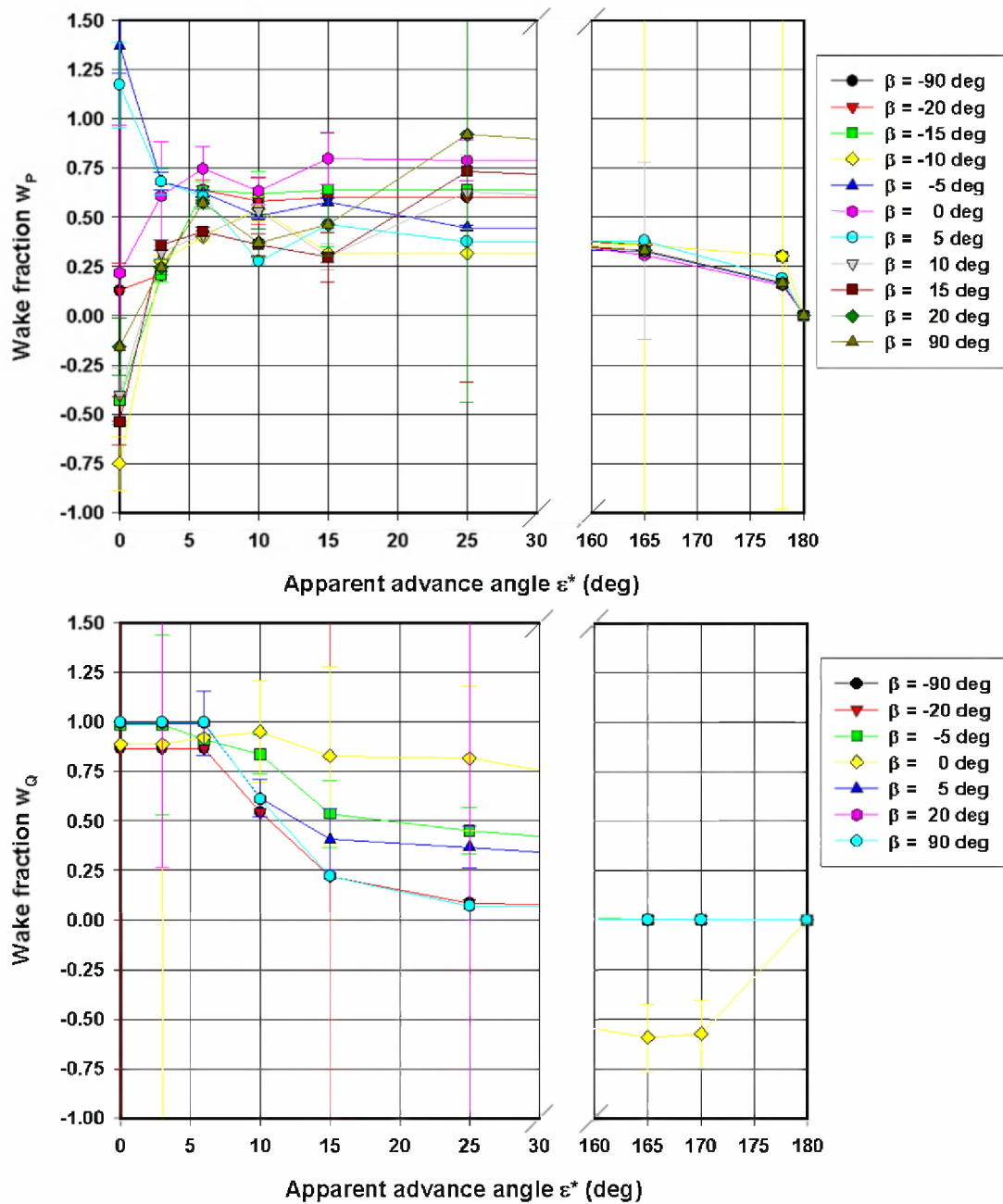
Figure 5.38 Model D, selected tabular model for wake factor w_P and w_Q for quadrant 1 and 2
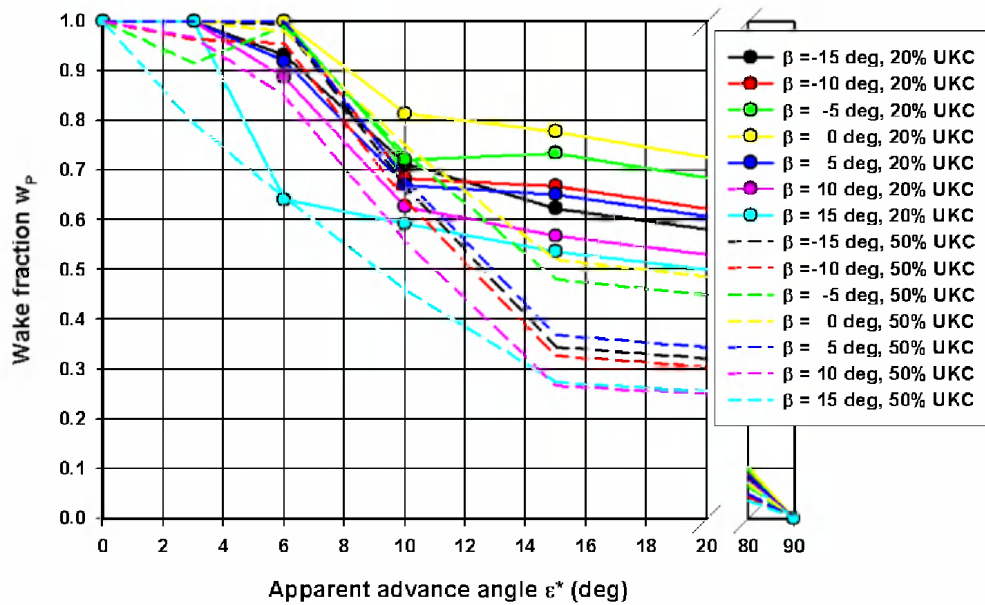
Figure 5.39 Model E, comparison of wake factor w_P at 50% and 20% UKC for different drift angles β
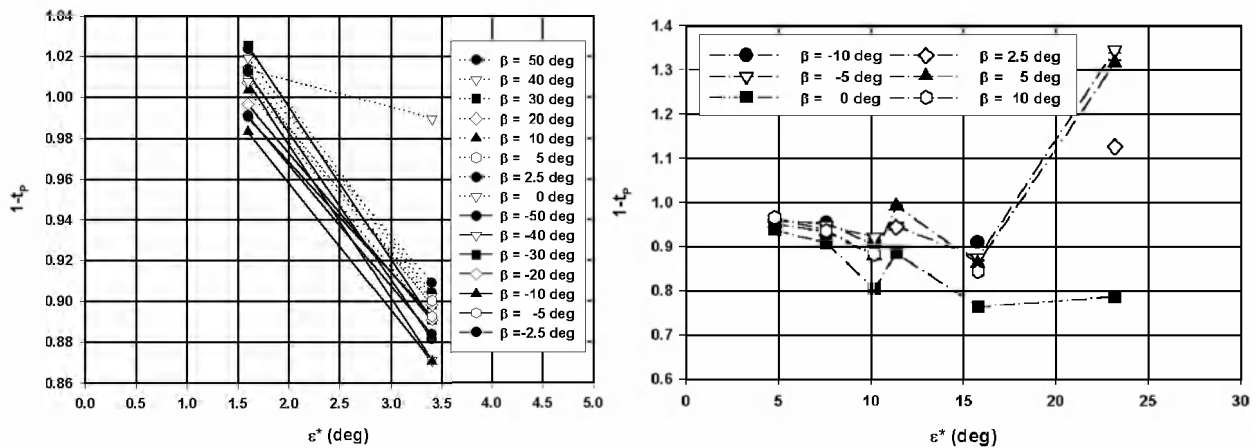
Figure 5.40 Model D, *model per Froude number*, tabular model for thrust deduction $1\text{-}t_P$ (stationary tests, low speed F_n=0.016 left and ordinary speed F_n≥0.049 right)
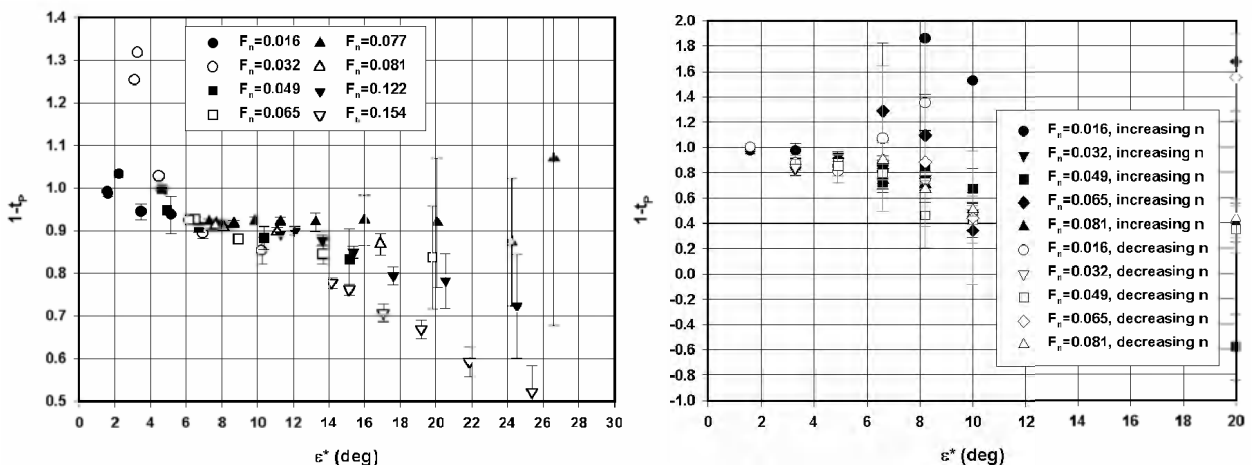
Figure 5.41 Model D, *model per Froude number*, calculated individual thrust deduction values $1\text{-}t_P$ for multi-modal tests type A and tabular models for thrust deduction $1\text{-}t_P$ for multi-modal tests type B during straight-line tests.
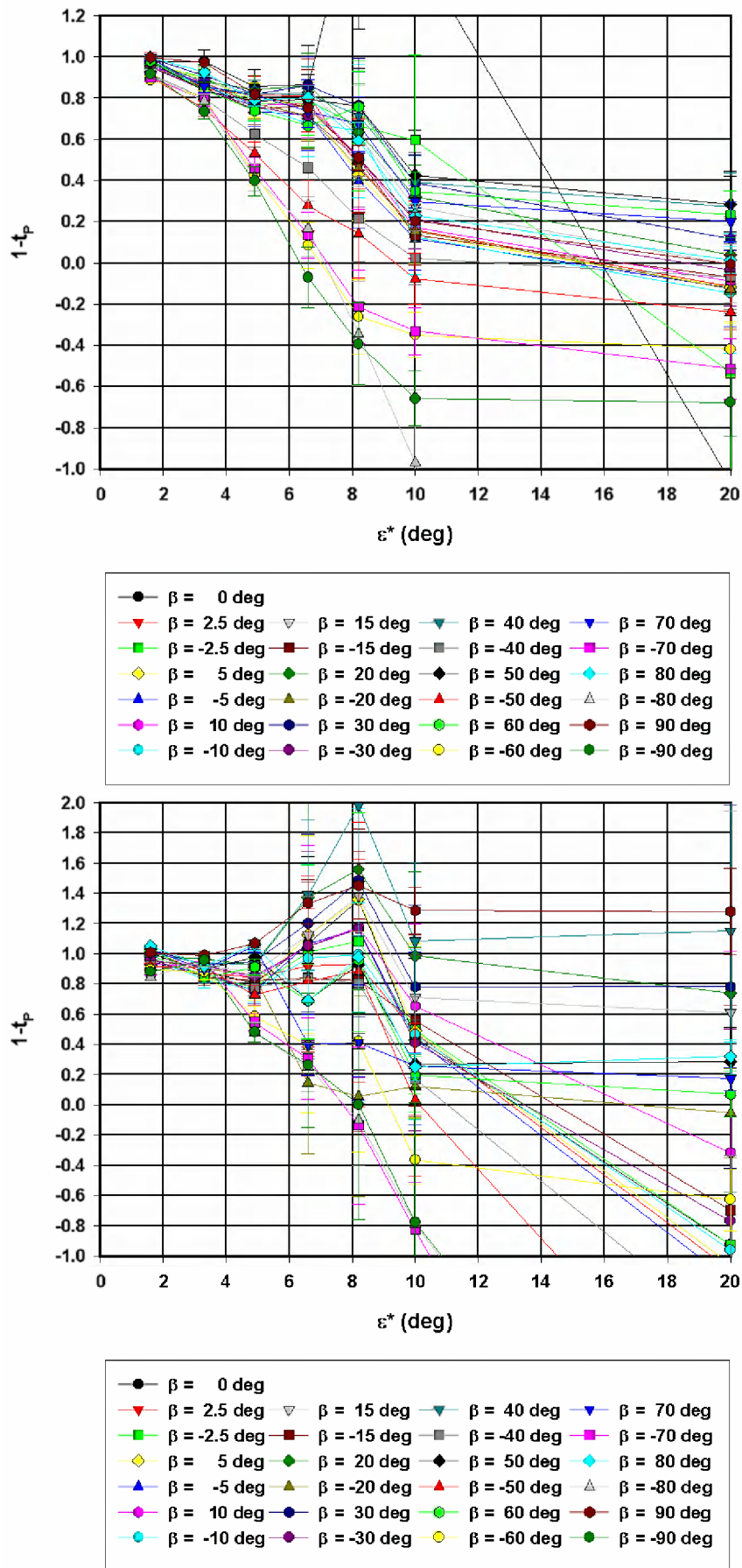
Figure 5.42 Model D, *model per Froude number*, tabular model for thrust deduction 1-t_P (multi-modal tests type B, F_n=0.016, increasing propeller rate at top and decreasing propeller rate at bottom)
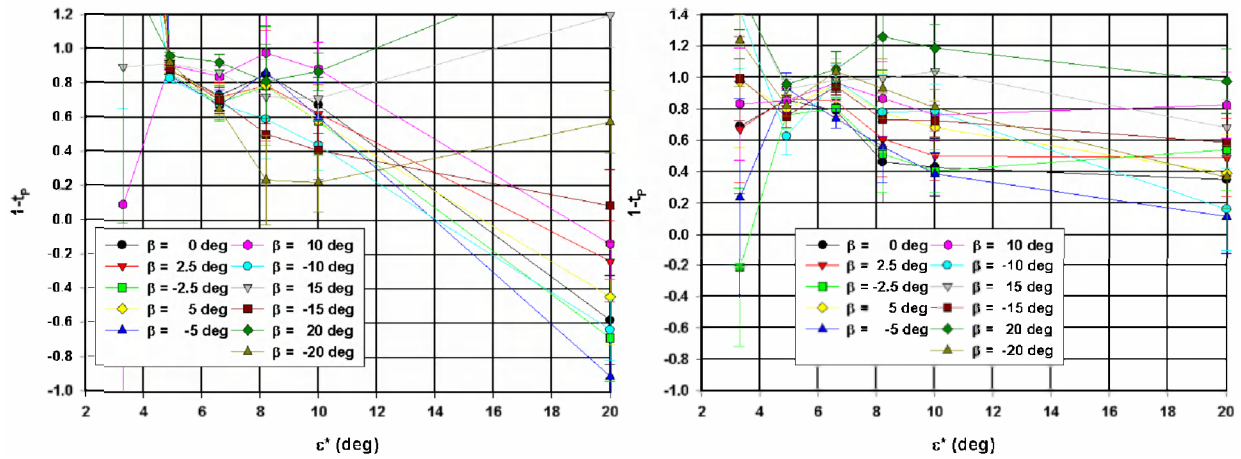
Figure 5.43 Model D, *model per Froude number*, tabular model for thrust deduction 1-t_P (multi-modal tests type B, F_n=0.049, increasing propeller rate left and decreasing propeller rate right)
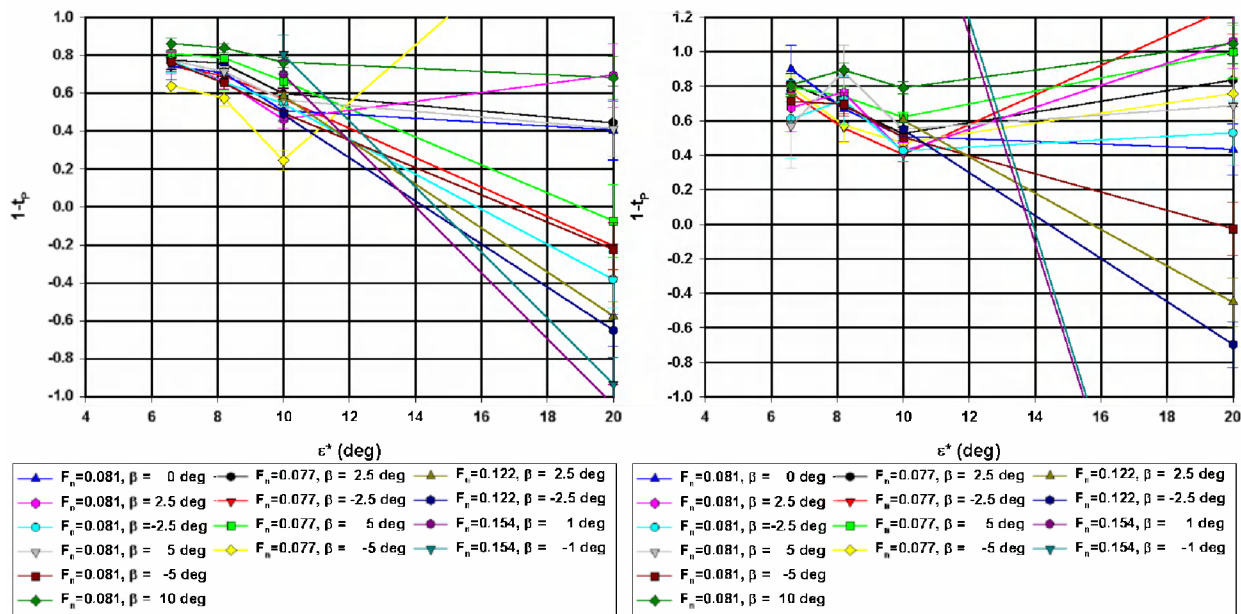
Figure 5.44 Model D, *model per Froude number*, tabular model for thrust deduction 1-t_P (multi-modal tests type B, $F_n \geq 0.077$, increasing propeller rate left and decreasing propeller rate right)
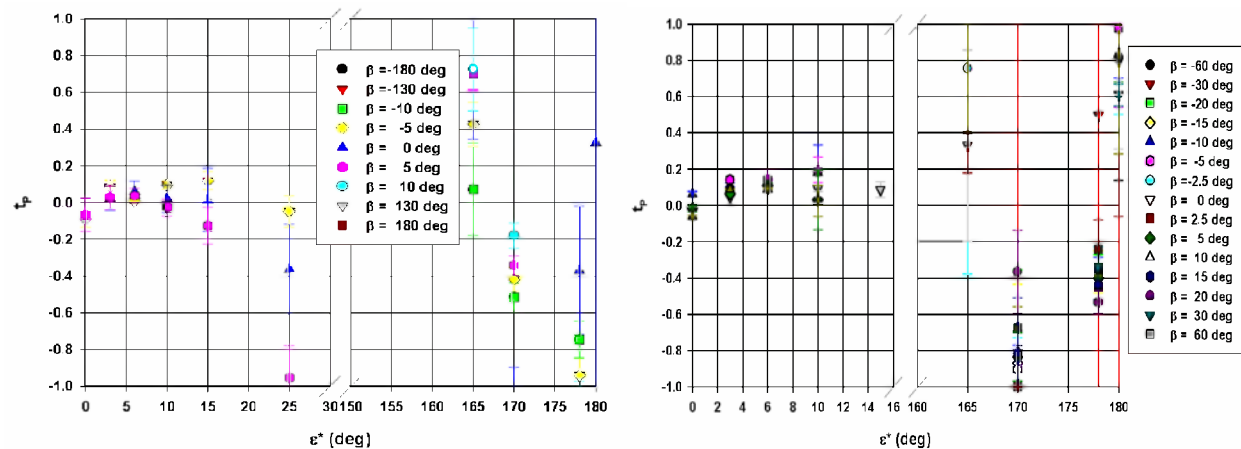
Figure 5.45 Model D, *global model*, tabular model for thrust deduction t_P for stationary tests with series D1 (left, measured propeller thrust) and series DA (right, modelled propeller thrust) (quadrant 1 and 2)
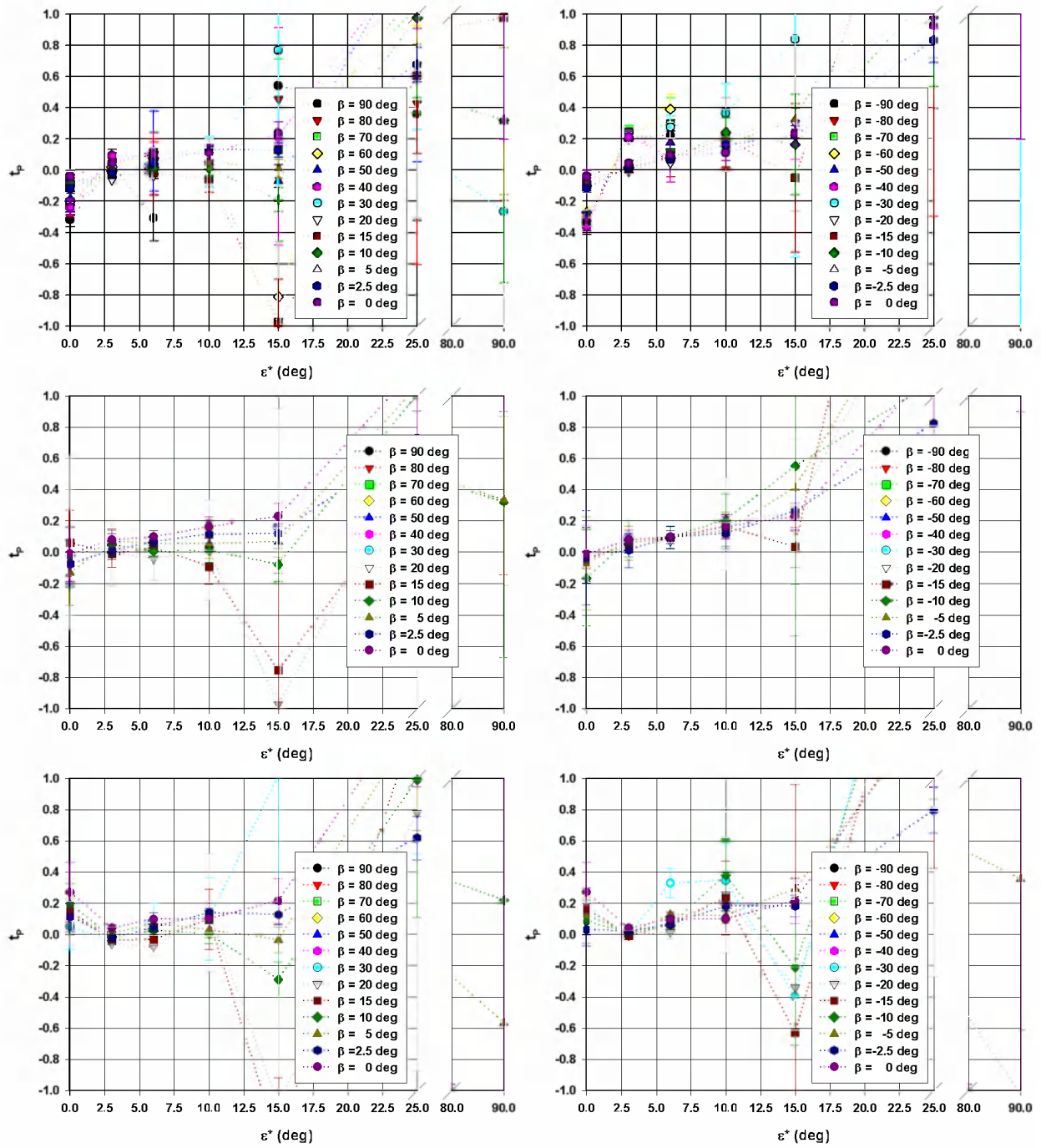
Figure 5.46 Model D, *global model*, tabular model for thrust deduction t_P for multi-modal tests of type B (all propeller rates, top, increasing propeller phase, middle, decreasing propeller phase, bottom) (quadrant 1)
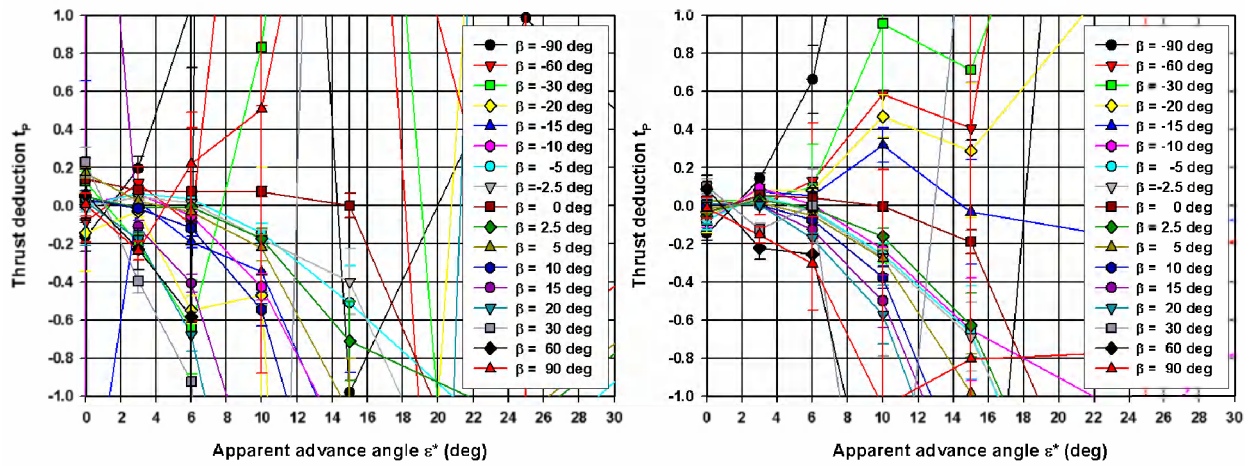
Figure 5.47 Model E, *global model*, tabular model for thrust deduction t_P (quadrant 1, all propeller rates, 20% UKC left and 50% UKC right)
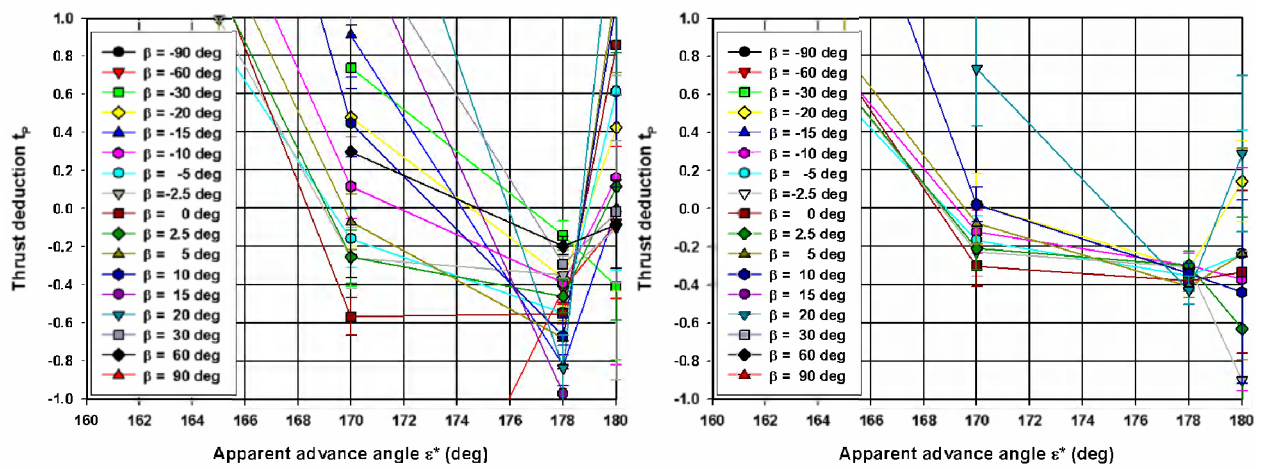
Figure 5.48 Model E, *global model*, tabular model for thrust deduction t_P (quadrant 2, all propeller rates, 20% UKC left and 50% UKC right)
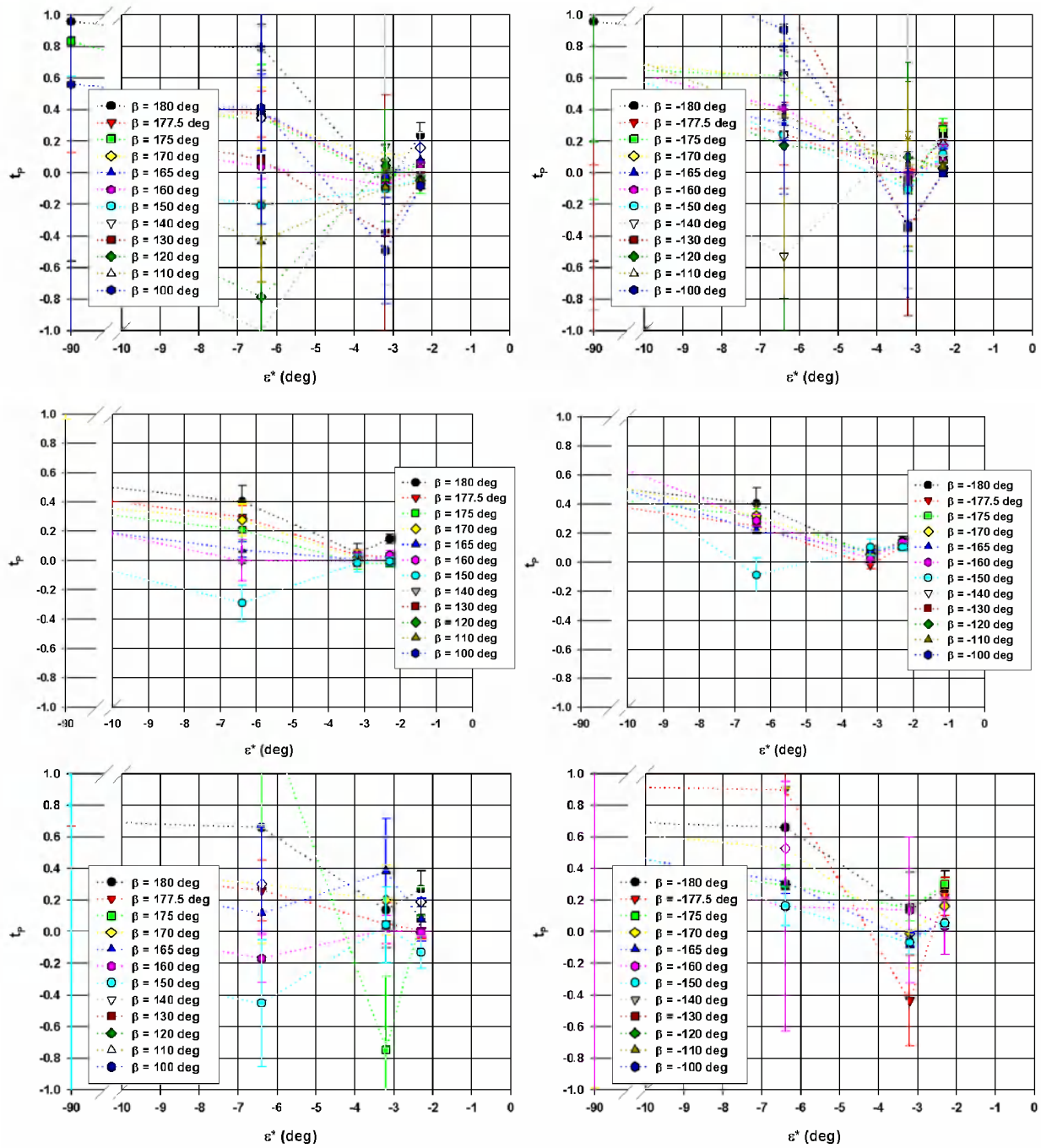
Figure 5.49 Model D, *global model*, tabular model for thrust deduction t_P for multi-modal tests of type B (all propeller rates, top, increasing, middle, and decreasing propeller phase, bottom) (quadrant 4)
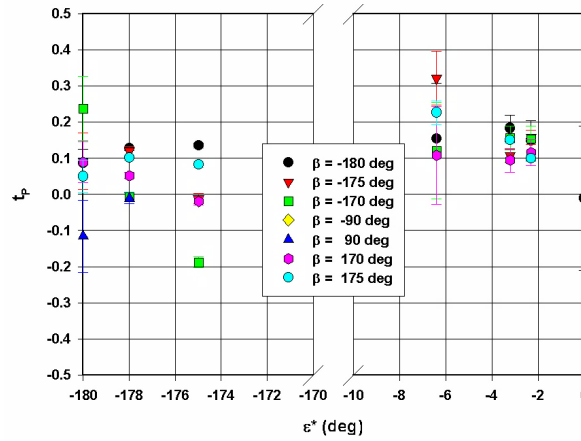
Figure 5.50 Model D, *global model*, tabular model for thrust deduction t_P for stationary tests with series DA (modelled propeller thrust) (quadrant 3 and 4)
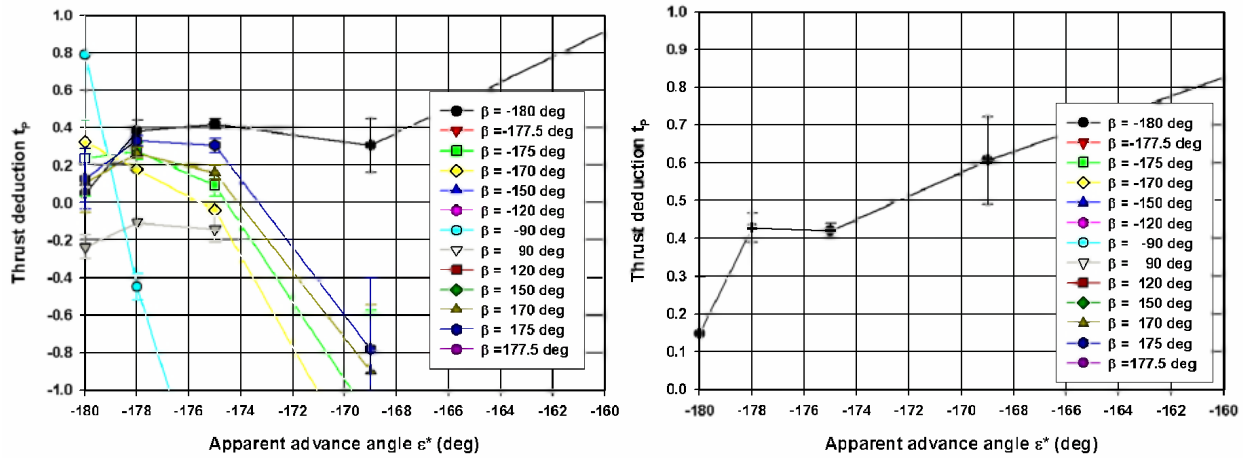
Figure 5.51 Model E, *global model*, tabular model for thrust deduction t_P (quadrant 3, all propeller rates, 20% UKC left and 50% UKC right)
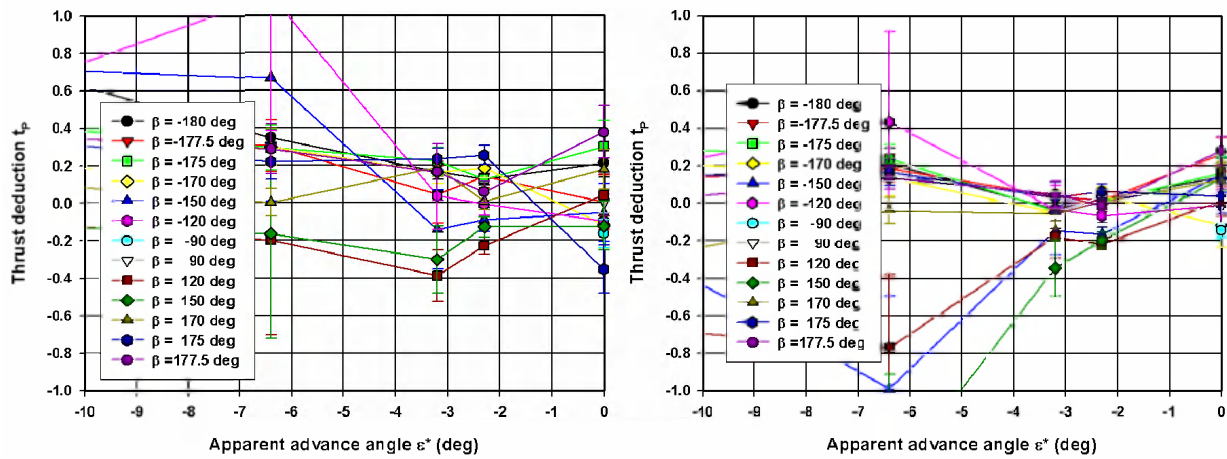
Figure 5.52 Model E, *global model*, tabular model for thrust deduction t_P (quadrant 4, all propeller rates, 20% UKC left and 50% UKC right)
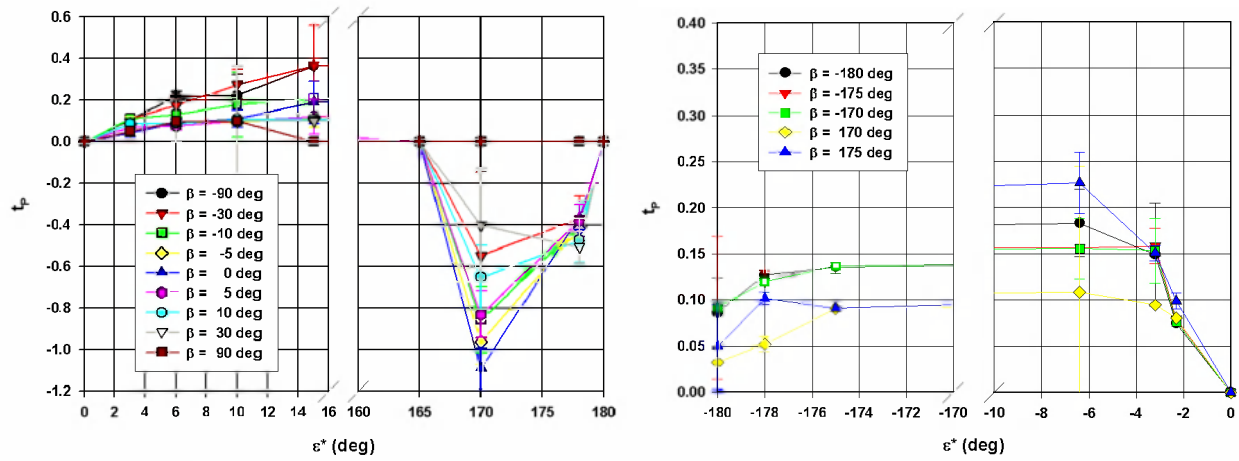
Figure 5.53 Model D, selected tabular model for thrust deduction t_P for quadrant 1 and 2 at left side and quadrant 3 and 4 at right side
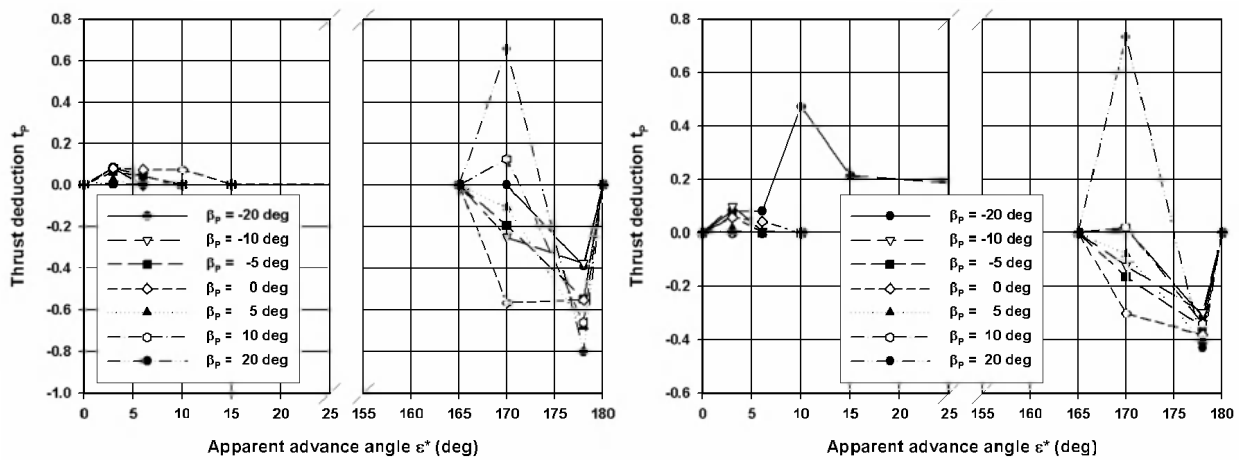
Figure 5.54 Model E, selected tabular model for thrust deduction t_P for quadrant 1 and 2 (20% UKC left and 50% UKC right)
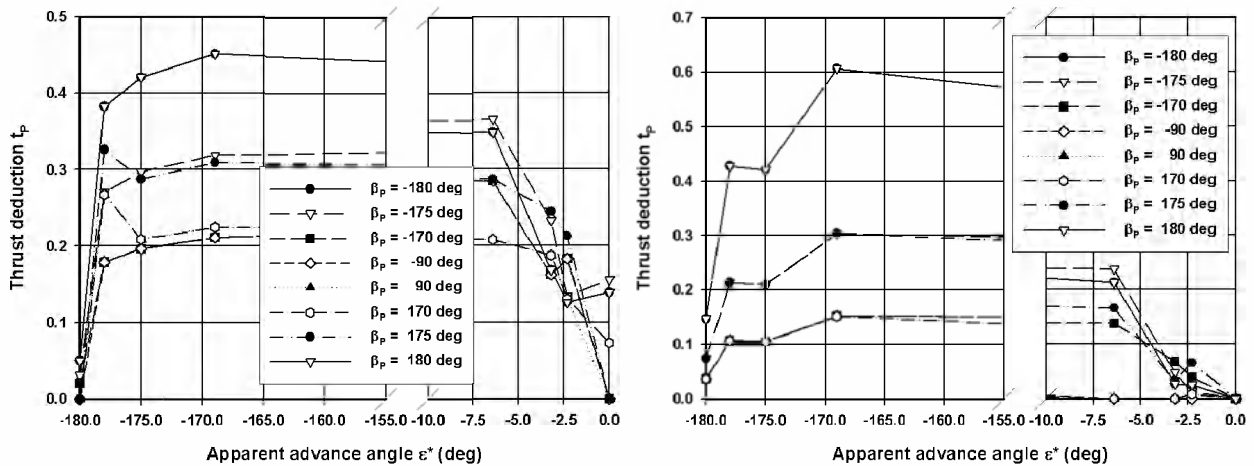
Figure 5.55 Model E, selected tabular model for thrust deduction t_P for quadrant 3 and 4 (20% UKC left and 50% UKC right)
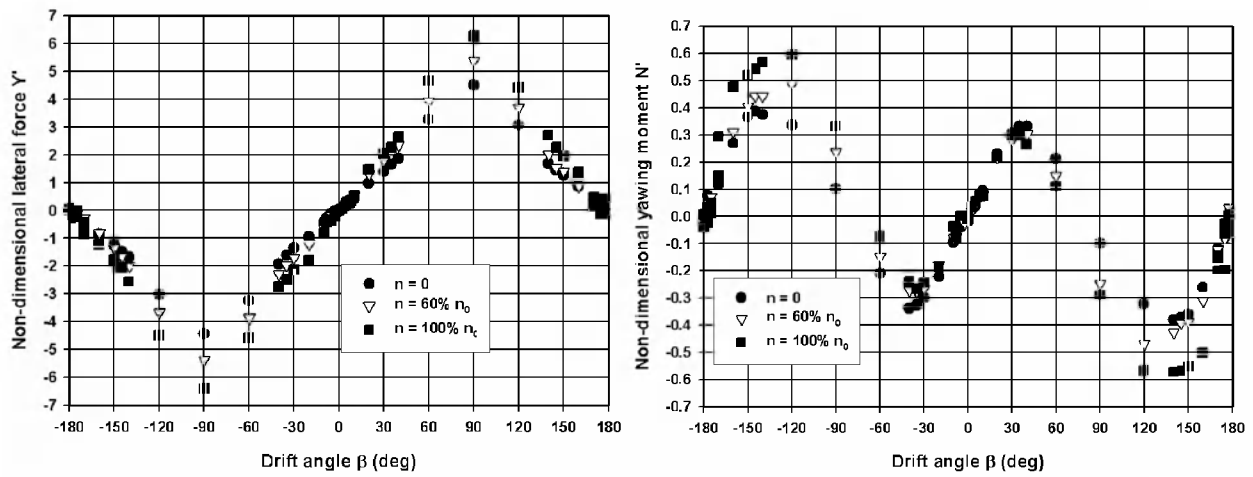
Figure 5.56 Model E at 20% UKC, *quadrant 1 and 4*, influence of a positive propeller action on lateral force and yawing moment during stationary oblique towing tests
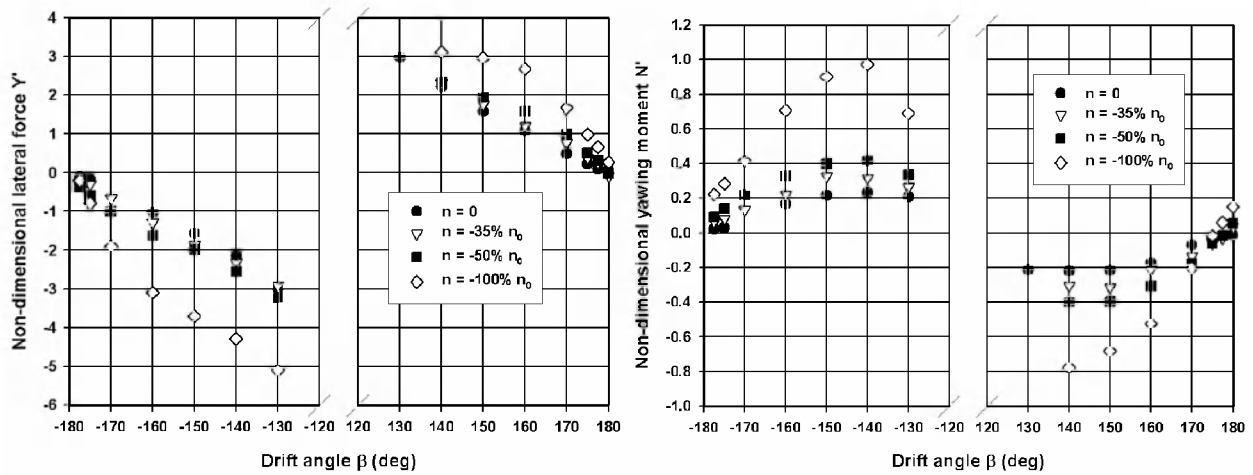
Figure 5.57 Model D at 20% UKC, *quadrant 3*, influence of a negative propeller action on lateral force and yawing moment during stationary oblique towing tests
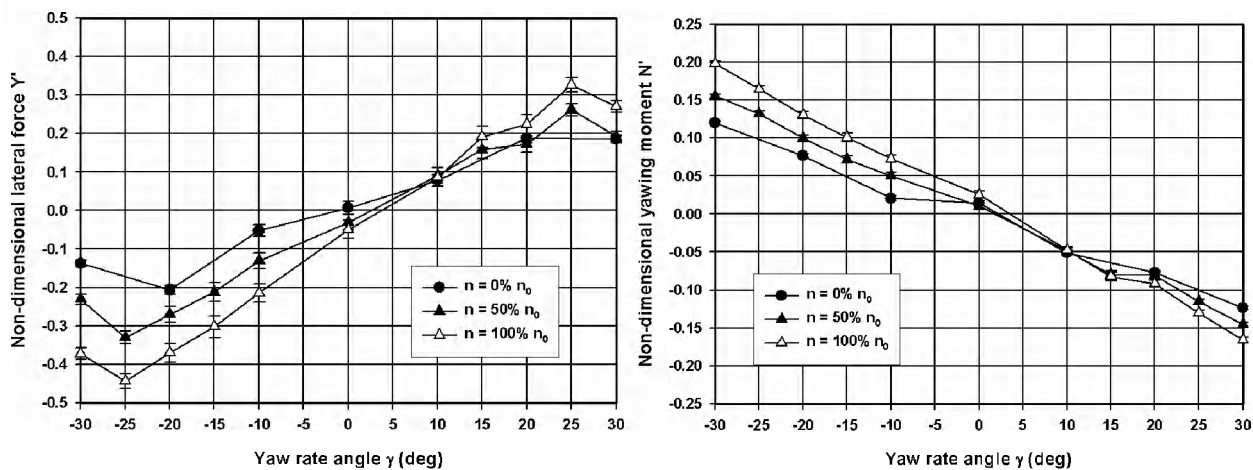
Figure 5.58 Model E at 20% UKC, *quadrant 1*, influence of a positive propeller action on lateral force and yawing moment during PMM yaw tests (F_n=0.033, ψ_A=15 deg, T=27s)
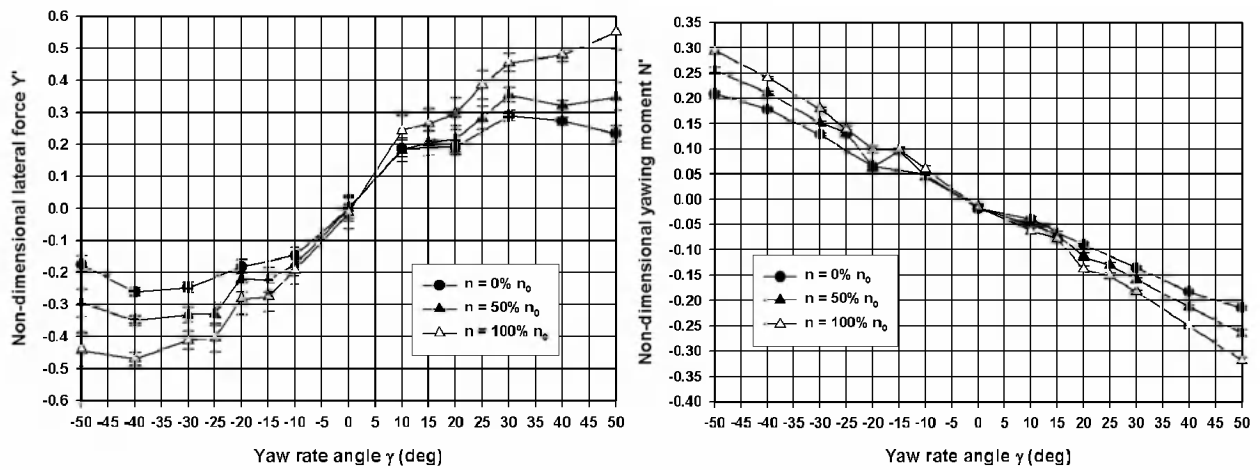
Figure 5.59 Model E at 20% UKC, *quadrant 1*, influence of a positive propeller action on lateral force and yawing moment during PMM yaw tests (F_n=0.033, ψ_A=25 deg, T=27s)
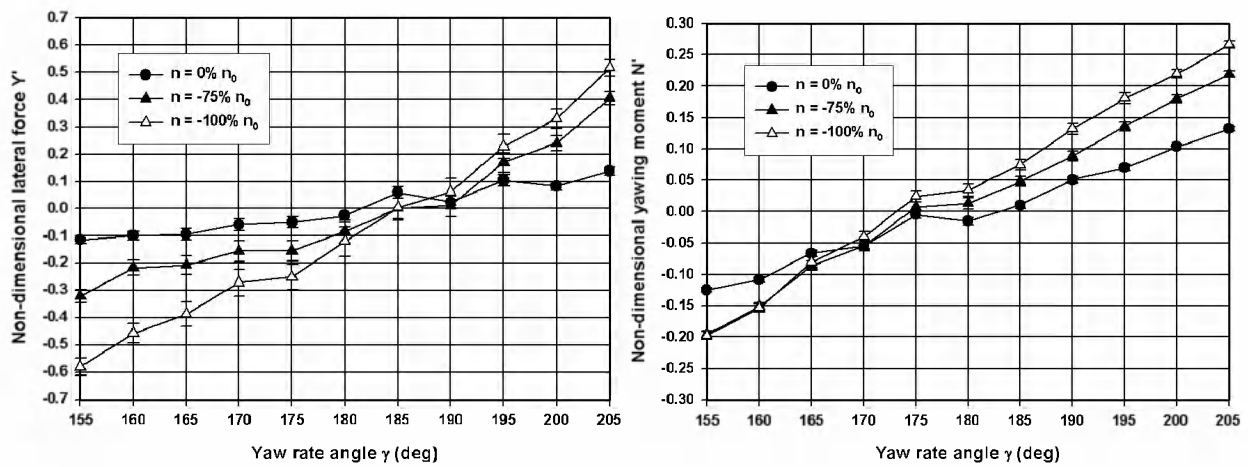
Figure 5.60 Model D at 20% UKC, *quadrant 3*, influence of a negative propeller action on lateral force and yawing moment during PMM yaw tests (F_n=-0.032, ψ_A=25 deg, T=54s)
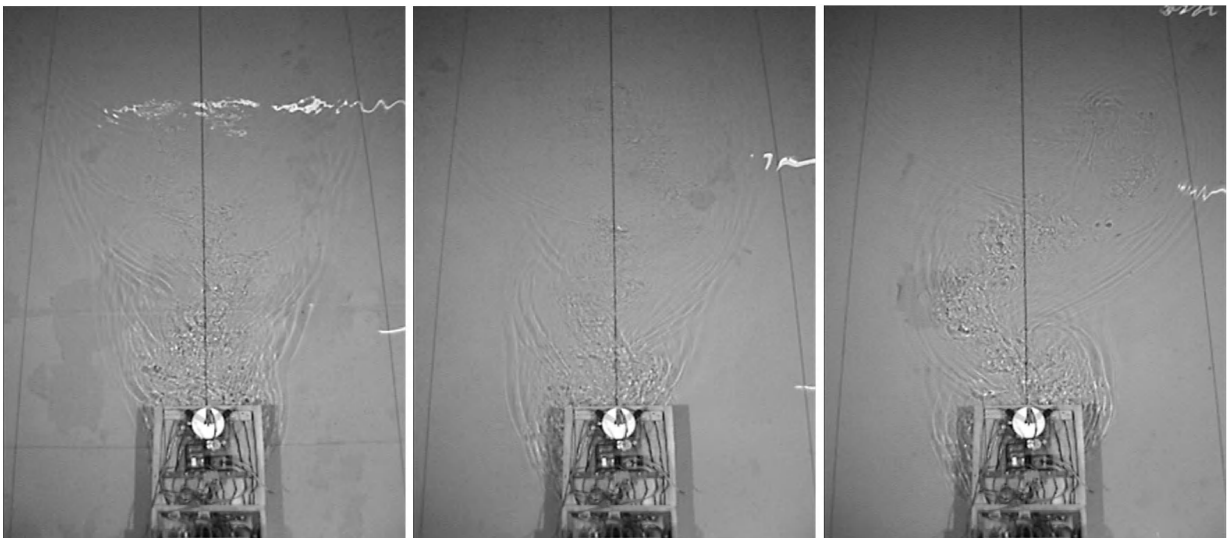
(a) Forward motion with a velocity of 8 knots full scale and a reversed propeller rate of -50% n_0 (the interval of time is 20 seconds on model scale)
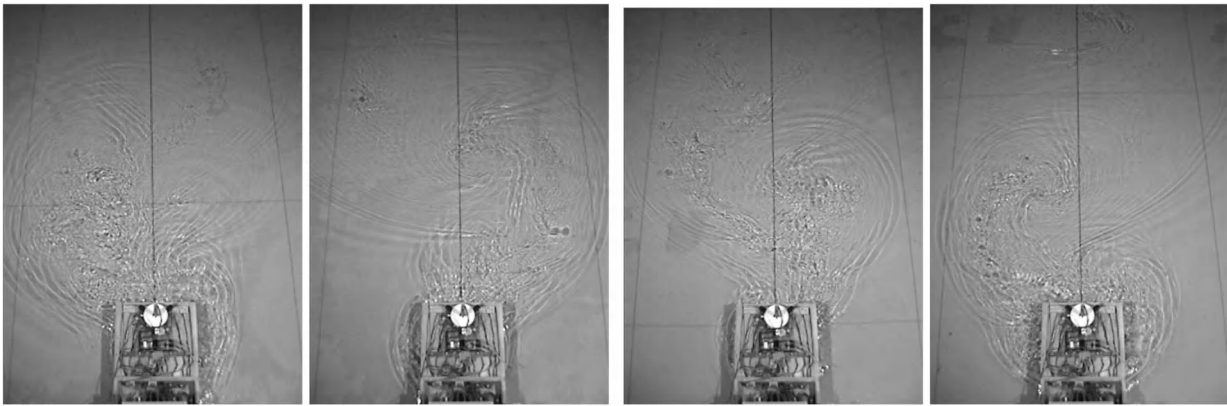
(b) Forward motion with a velocity of 8 knots full scale and a reversed propeller rate of -80% n_0 (for each combination of two photographs at left side or right side the interval of time is 4 seconds on model scale)

Figure 5.61 Model U, quadrant 2, development of an oscillating flow at the stern during a captive model test with a forward speed of 8 knots full scale and reversed propeller, condition UO (T = 12.0 m, 10% UKC)
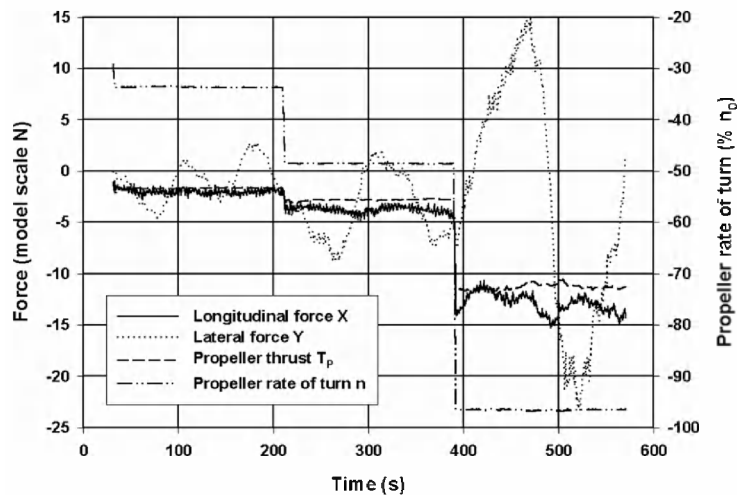
Figure 5.62 Model D, *quadrant 2*, series D1, oscillating lateral force measured at three combinations of reversed propeller rate of turn during one test run (F_n=0.016)
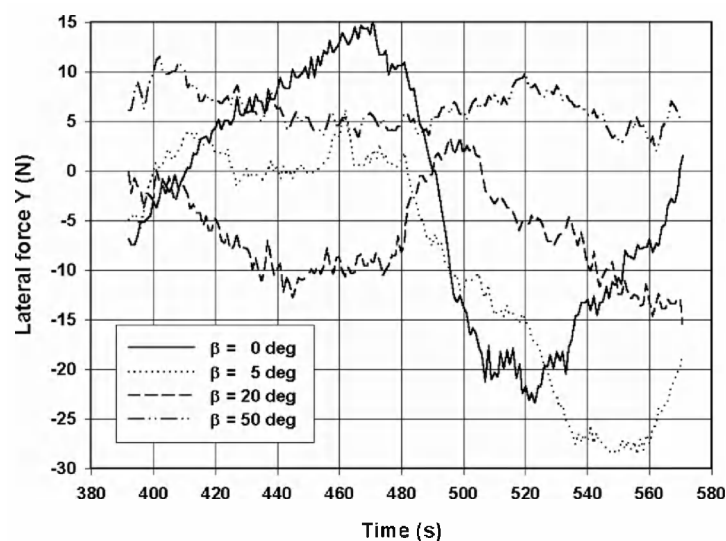
Figure 5.63 Model D, *quadrant 2*, series D1, influence of drift angle on measured oscillating lateral force during a stopping manoeuvre (F_n=0.016, n=-100%n_0)
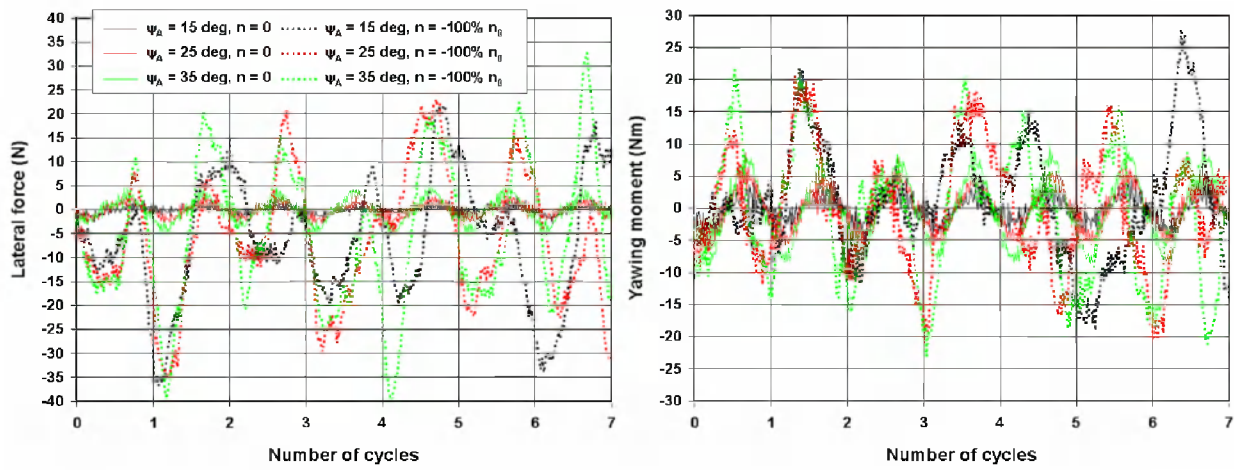
Figure 5.64 Model D, *quadrant 2*, series DA, influence of yaw amplitude on measured oscillating lateral force and yawing moment during a stopping manoeuvre (F_n=0.016)
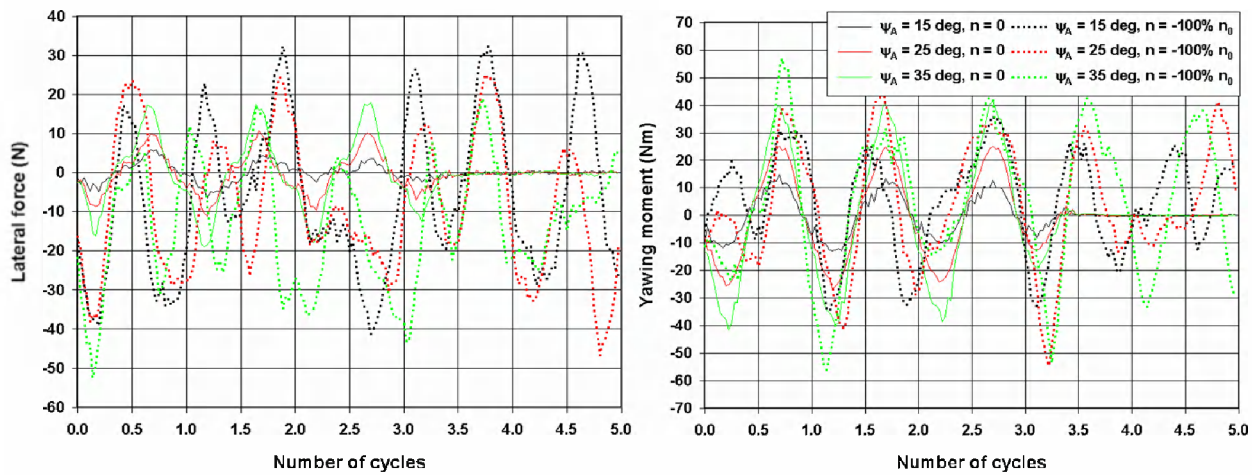
Figure 5.65 Model D, *quadrant 2*, series DA, influence of yaw amplitude on measured oscillating lateral force and yawing moment during a stopping manoeuvre (F_n=0.049, n=-100%n_0)
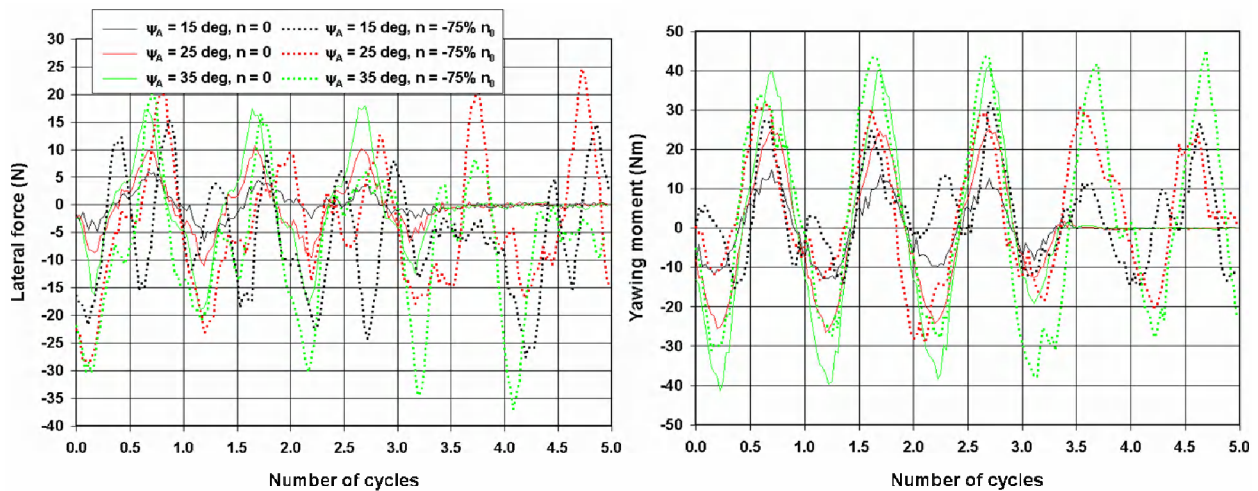
Figure 5.66 Model D, *quadrant 2*, series DA, influence of yaw amplitude on measured oscillating lateral force and yawing moment during a stopping manoeuvre (F_n=0.049, n=-75%n_0)
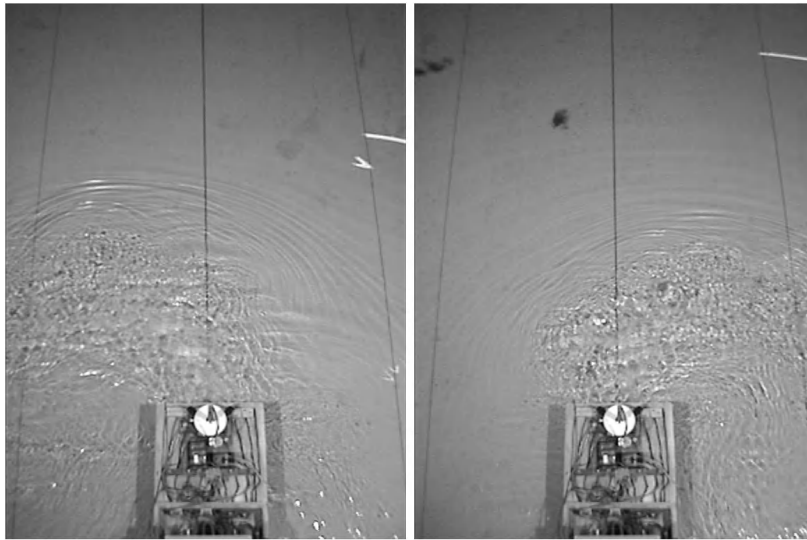
Figure 5.67 Model U, quadrant 4, development of an oscillating flow at the stern during a captive model test with a backward velocity of -4 knots full scale and an ahead propeller rate of 80% n_0 for condition UO (T = 12.0 m, 10% UKC). The pictures have been taken with an approximate interval of time of 12 seconds model scale.
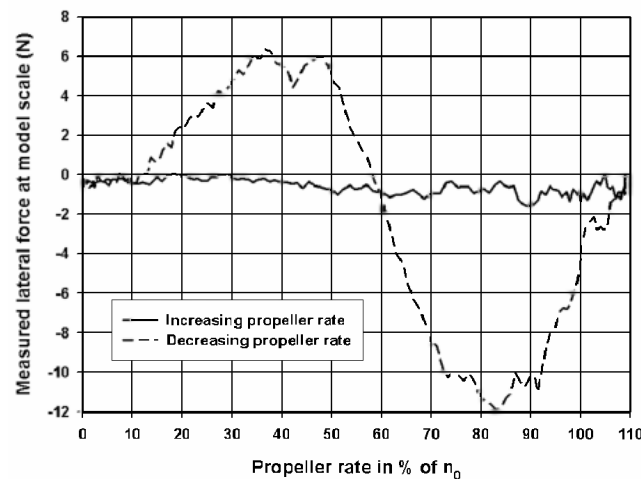
Figure 5.68 Model E at 20% UKC, *quadrant 4*, a stable flow during the increasing phase and occurrence of oscillations during the decreasing phase of a multi-modal test of type B (β = -177.5 deg)
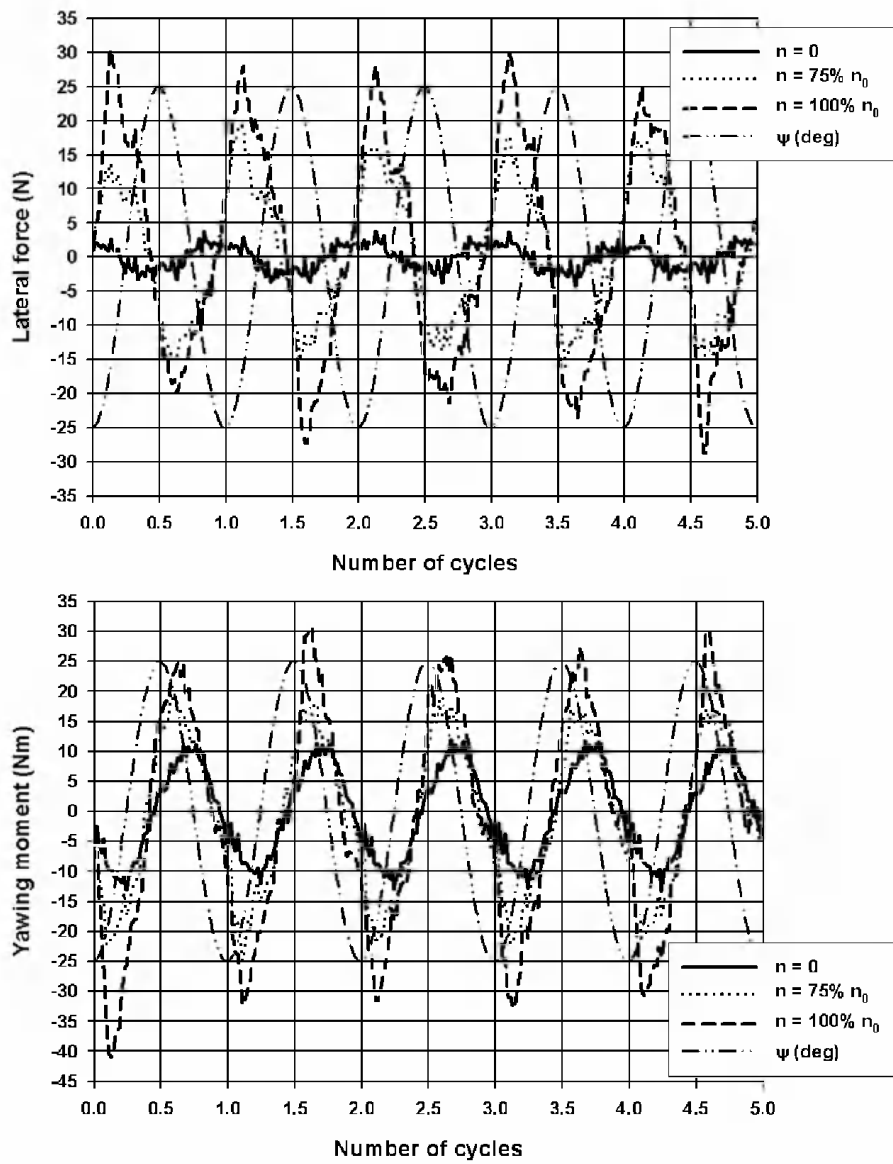
Figure 5.69 Model D, *quadrant 4*, series DA, influence of positive propeller action on measured oscillating lateral force and yawing moment during a stopping manoeuvre from sternway (F_n=-0.032)
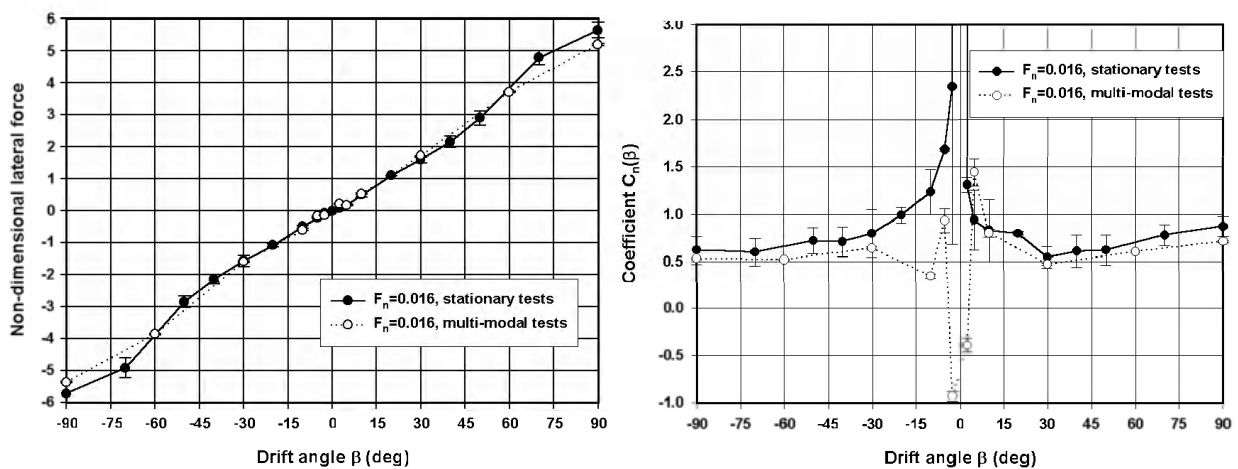
Figure 5.70 Model D, *quadrant 1*, comparison of non-dimensional lateral force and coefficient C_n on fully appended hull for stationary and multi-modal tests type B <u>without rudder deflection</u> (F_n=0.016 or low speed)
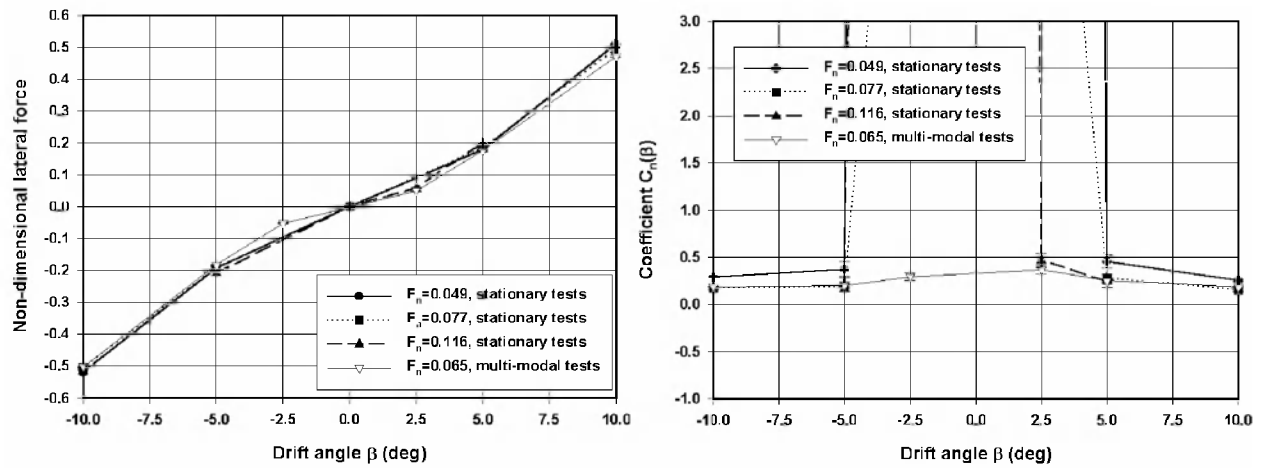
Figure 5.71 Model D, quadrant 1, comparison of non-dimensional lateral force and coefficient C_n on fully appended hull for stationary and multi-modal tests type B <u>without rudder deflection</u> (ordinary speed)
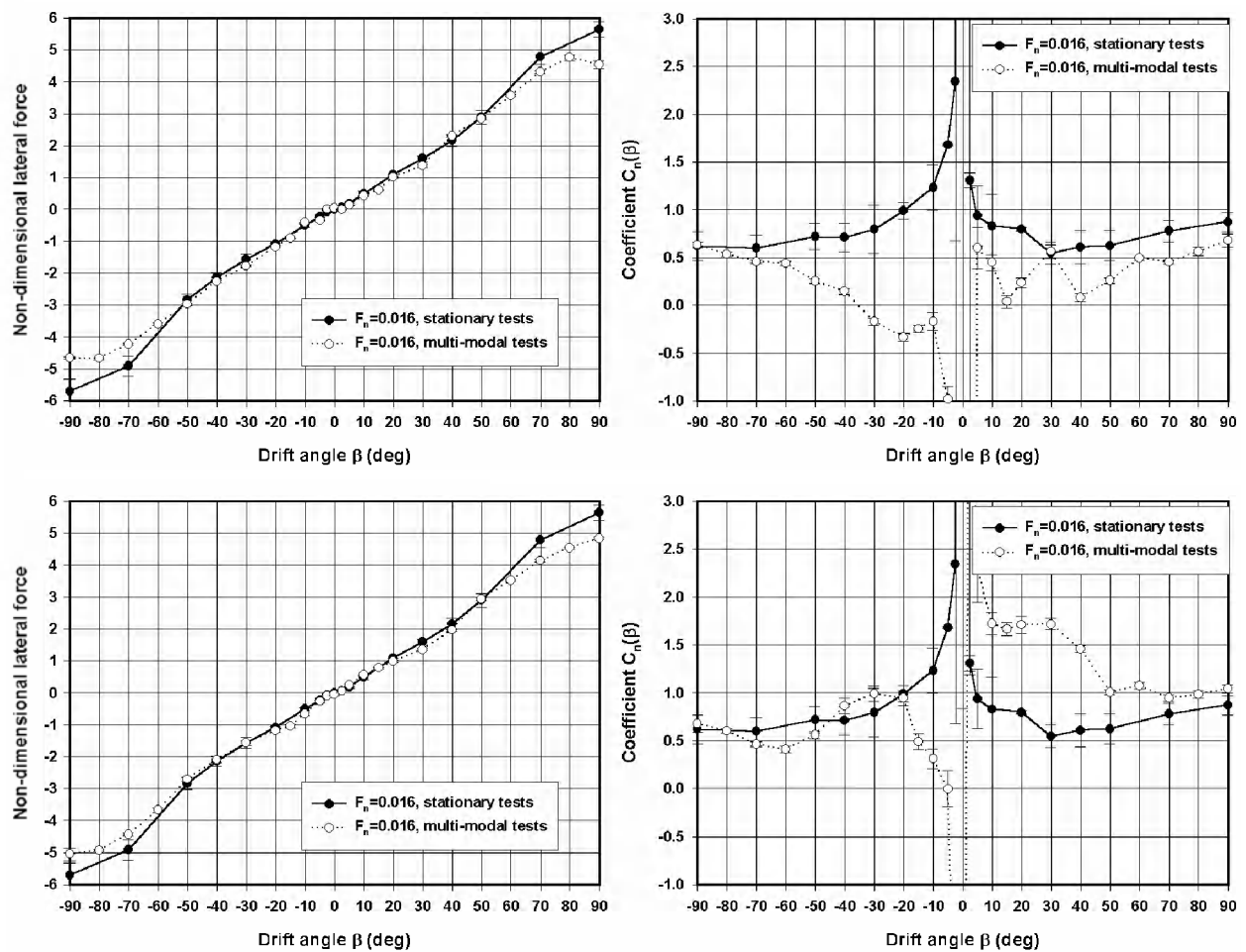
Figure 5.72 Model D, *quadrant 1*, comparison of non-dimensional lateral force and coefficient C_n on fully appended hull for stationary and multi-modal tests type B <u>with rudder deflection</u> (F_n=0.016 or low speed, increasing phase for n at the top, decreasing phase for n at the bottom)

305
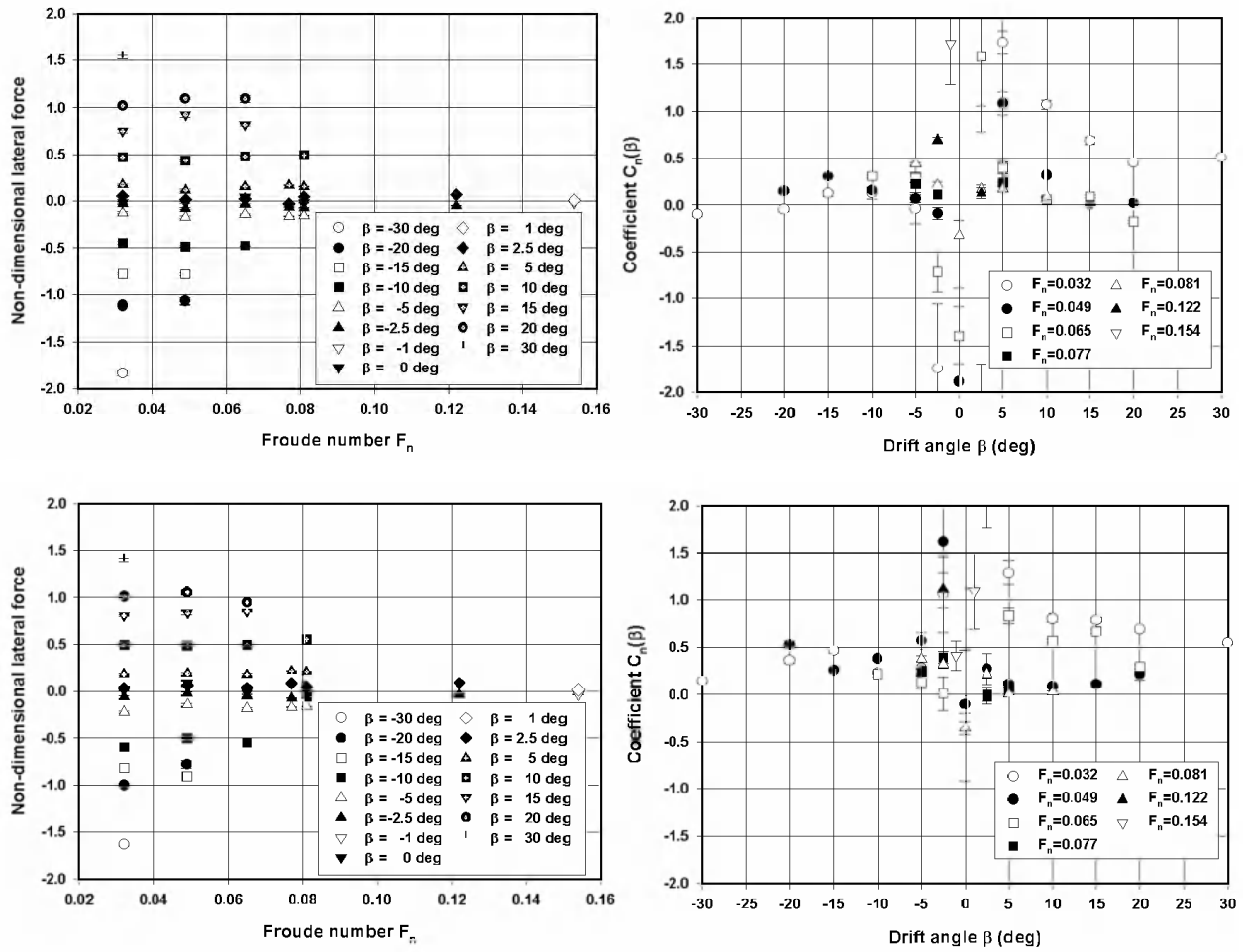
Figure 5.73 Model D, *quadrant 1*, non-dimensional lateral force and coefficient C_n on fully appended hull for stationary and multi-modal tests type B <u>with rudder deflection</u> (ordinary speed, increasing phase for n at the top, decreasing phase for n at the bottom)
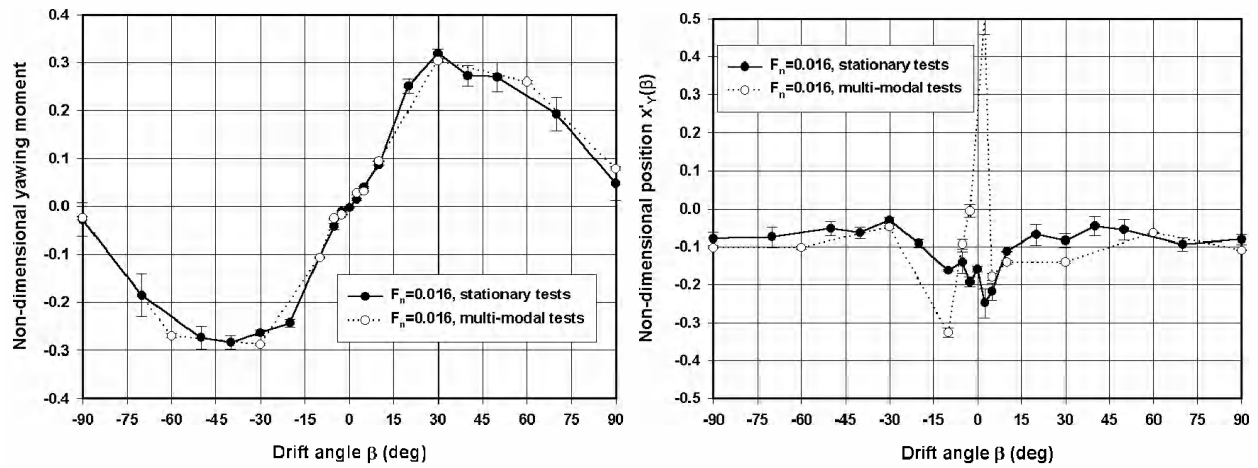
Figure 5.74 Model D, *quadrant 1*, comparison of non-dimensional yawing moment and application point x'_Y on fully appended hull for stationary and multi-modal tests type B <u>without rudder deflection</u> (F_n=0.016 or low speed)
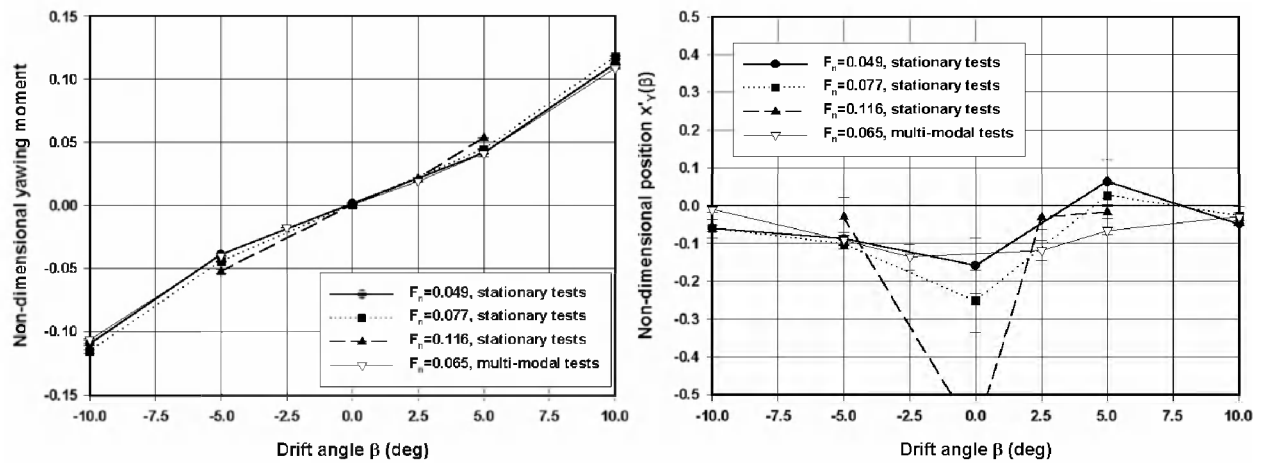
Figure 5.75 Model D, quadrant 1, comparison of non-dimensional yawing moment and application point x'$_Y$ on fully appended hull for stationary and multi-modal tests type B without rudder deflection (ordinary speed)
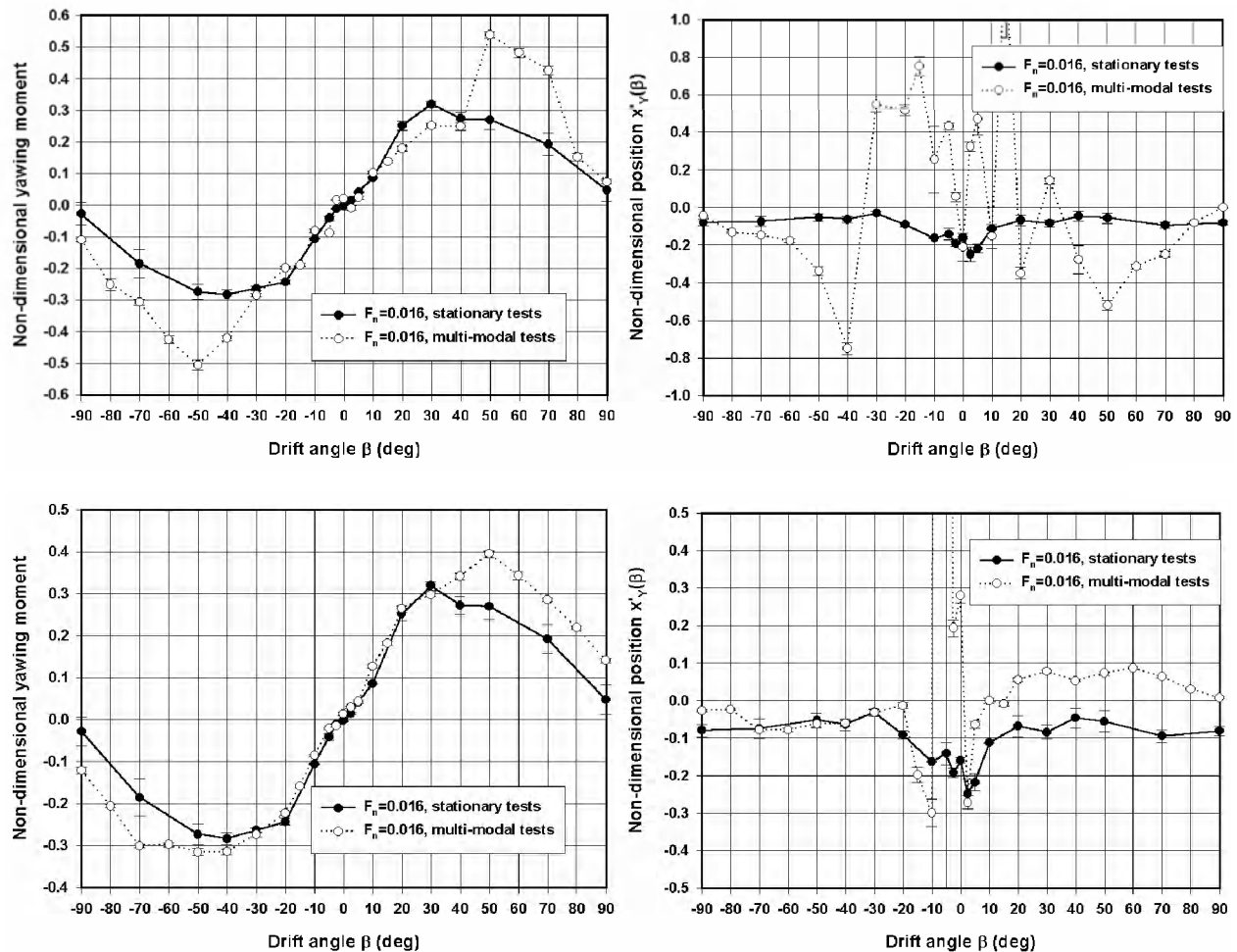
Figure 5.76 Model D, *quadrant 1*, comparison of non-dimensional yawing moment and application point x'$_Y$ on fully appended hull for stationary and multi-modal tests type B with rudder deflection (F$_n$=0.016 or low speed, increasing phase for n at the top, decreasing phase for n at the bottom)
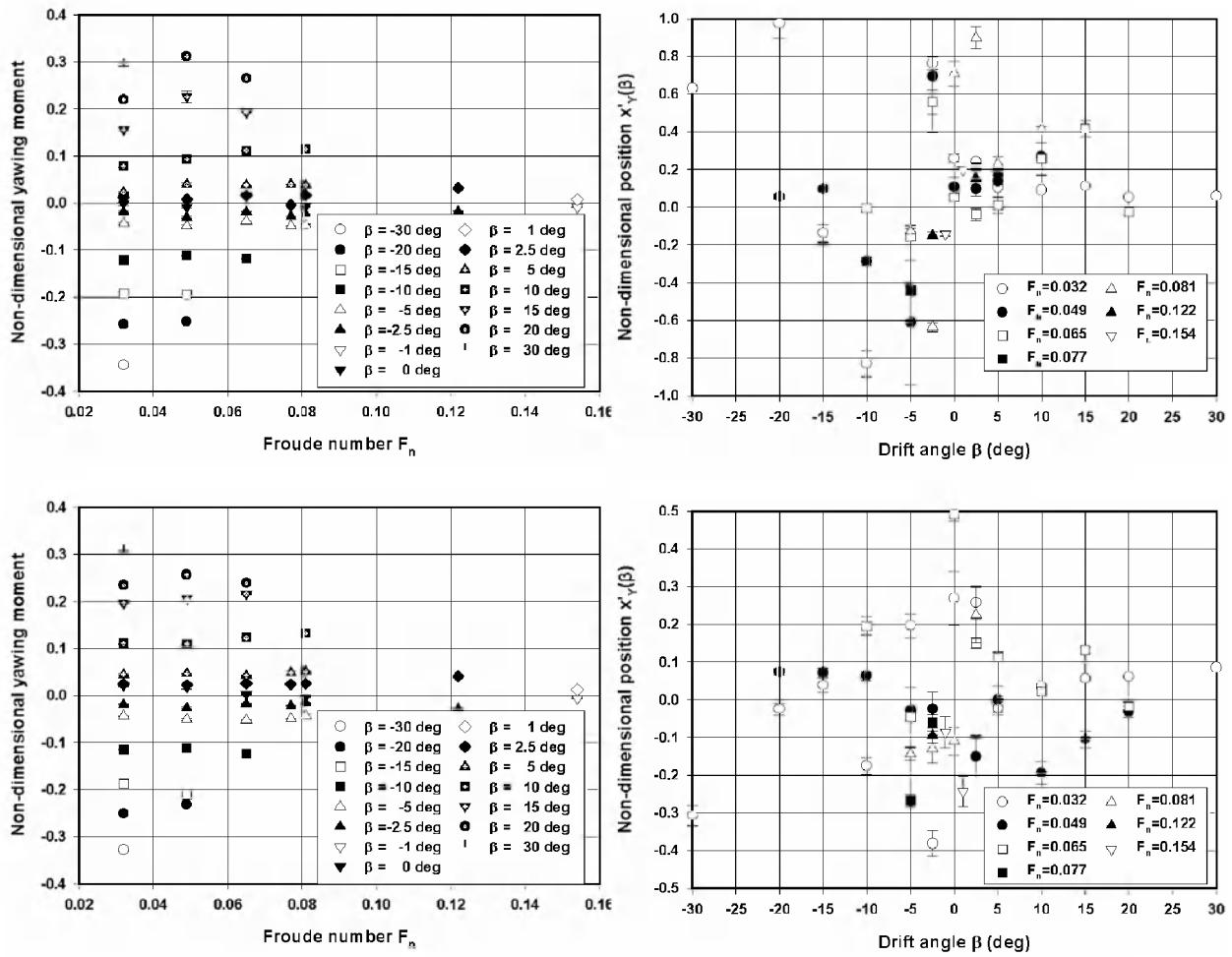
Figure 5.77 Model D, *quadrant 1*, non-dimensional yawing moment and application point x'$_Y$ on fully appended hull for stationary and multi-modal tests type B <u>with rudder deflection</u> (ordinary speed, increasing phase for n at the top, decreasing phase for n at the bottom)
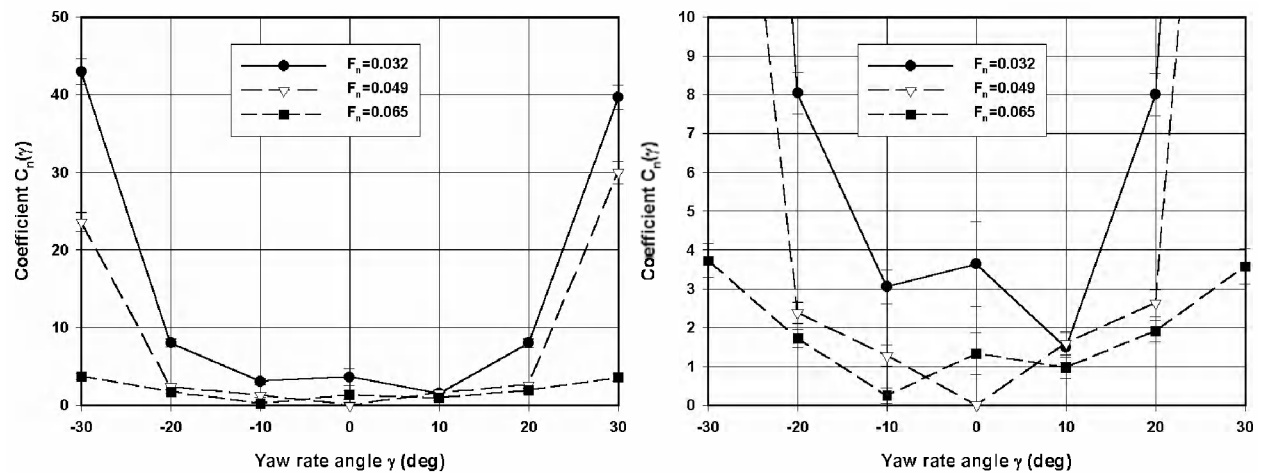
Figure 5.78 Model D, *quadrant 1*, influence of Froude number on coefficient C$_n$ for harmonic yawing tests <u>without rudder deflection</u> (right, detail)
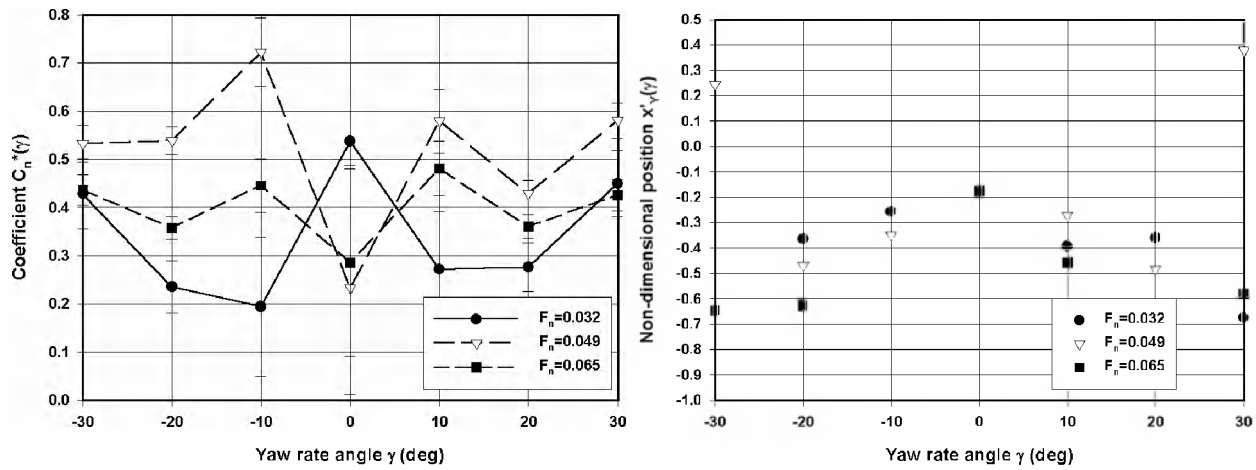
Figure 5.79 Model D, *quadrant 1*, influence of Froude number on coefficient C_n^* or application point x'_γ for harmonic yawing tests <u>without rudder deflection</u>
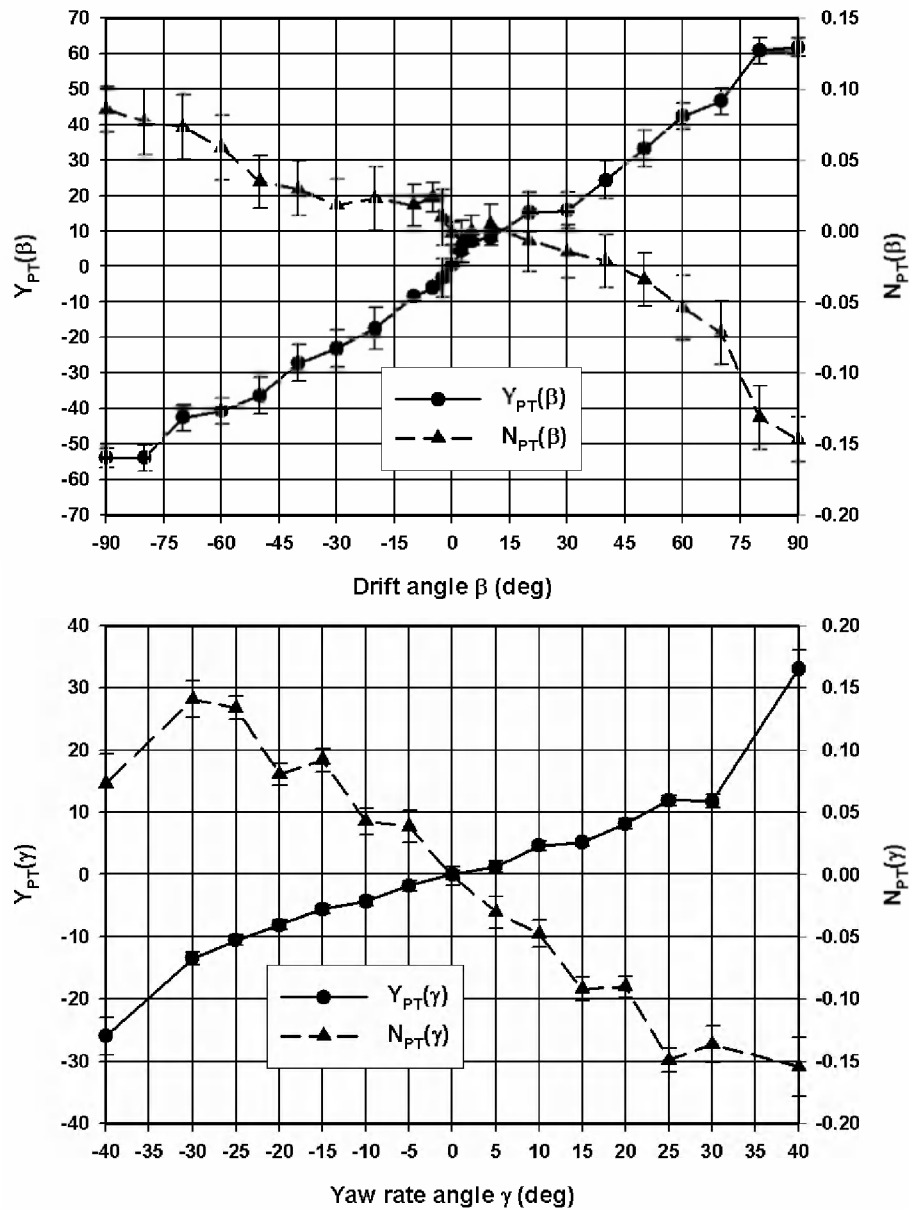
Figure 5.80 Model D, *quadrant 1*, propeller induced lateral force and yawing moment due to sway and yaw according to (5.19) and (5.20)
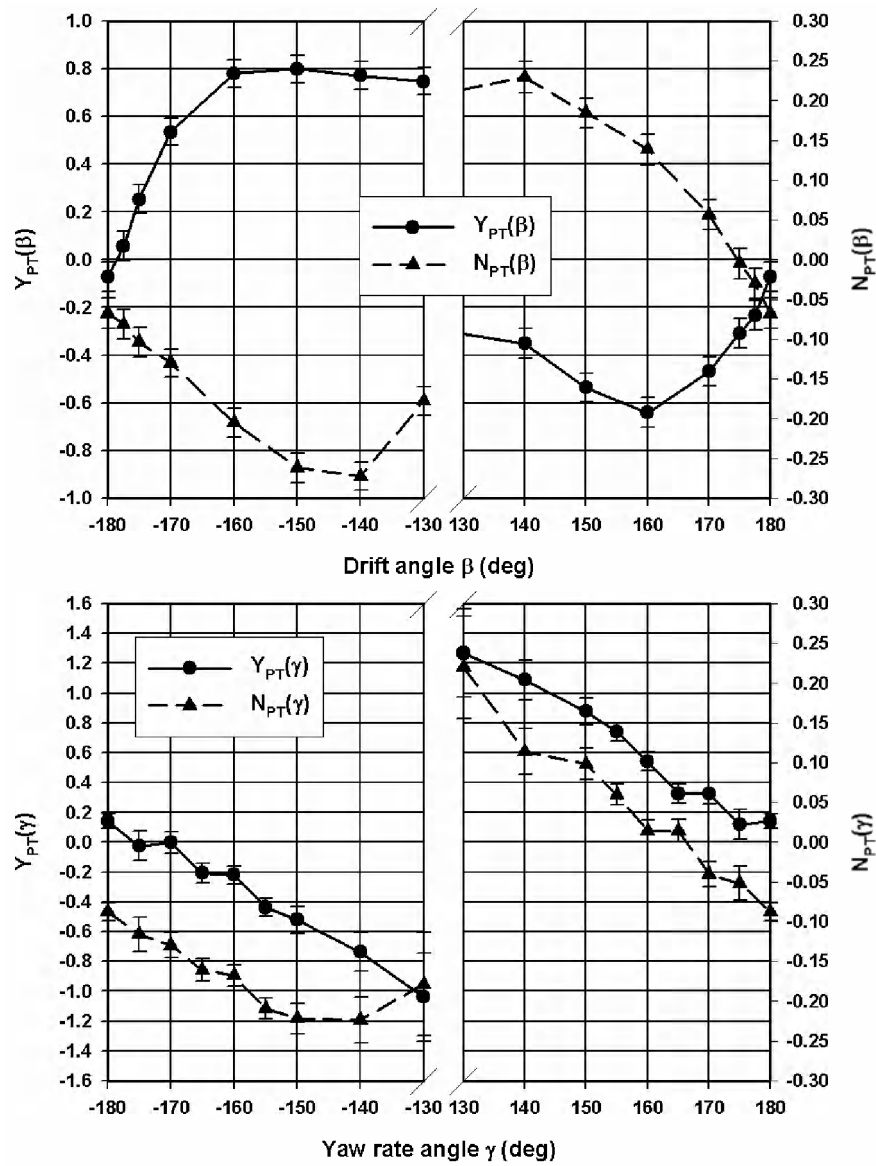
Figure 5.81 Model D, *quadrant 3*, propeller induced lateral force and yawing moment due to sway and yaw according to (5.19) and (5.20)
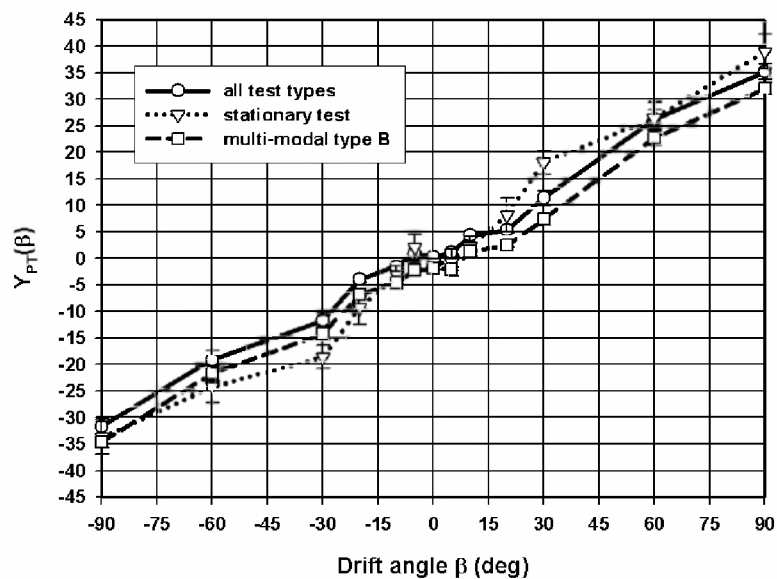
Figure 5.82 Model E at 50% UKC, *quadrant 1*, influence of test type on propeller induced lateral force and yawing moment due to sway

310
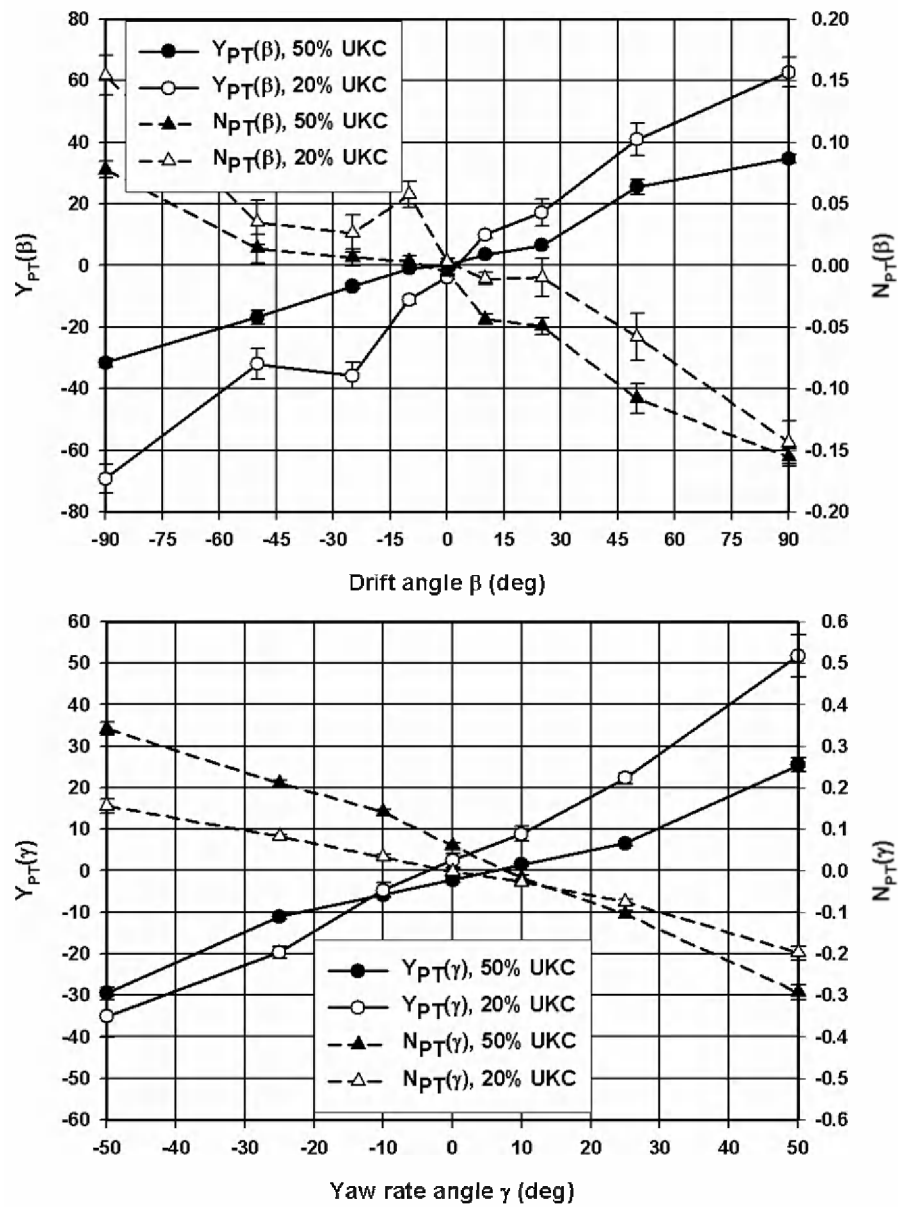
Figure 5.83 Model E, comparison of propeller induced lateral forces and yawing moment for 50% and 20% UKC according to (5.19) and (5.20)
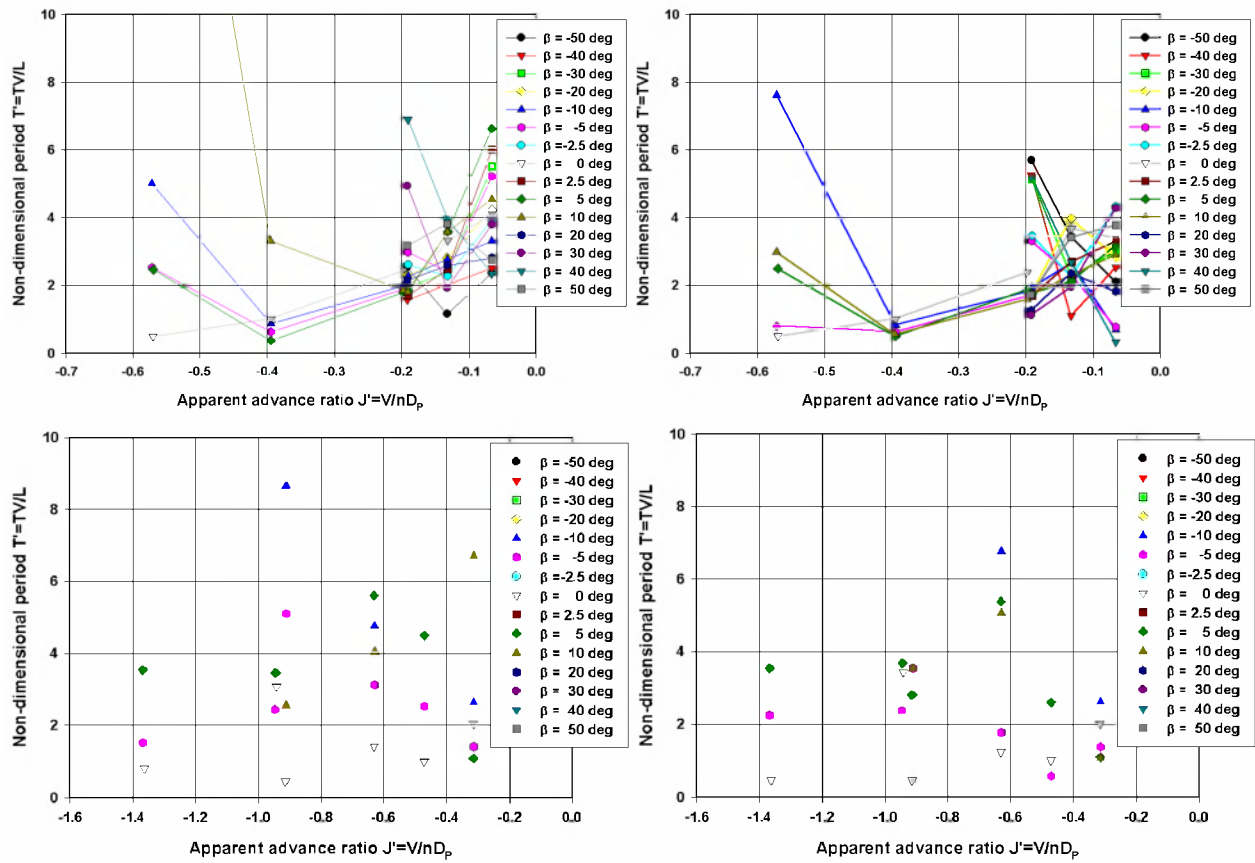
Figure 5.84 Model D, *quadrant 2*, non-dimensional period T' of oscillating lateral force (left) and oscillating yawing moment (right) as function of the apparent advance ratio J', series D1 ($F_n \leq 0.049$, top, and $F_n \geq 0.077$, bottom)
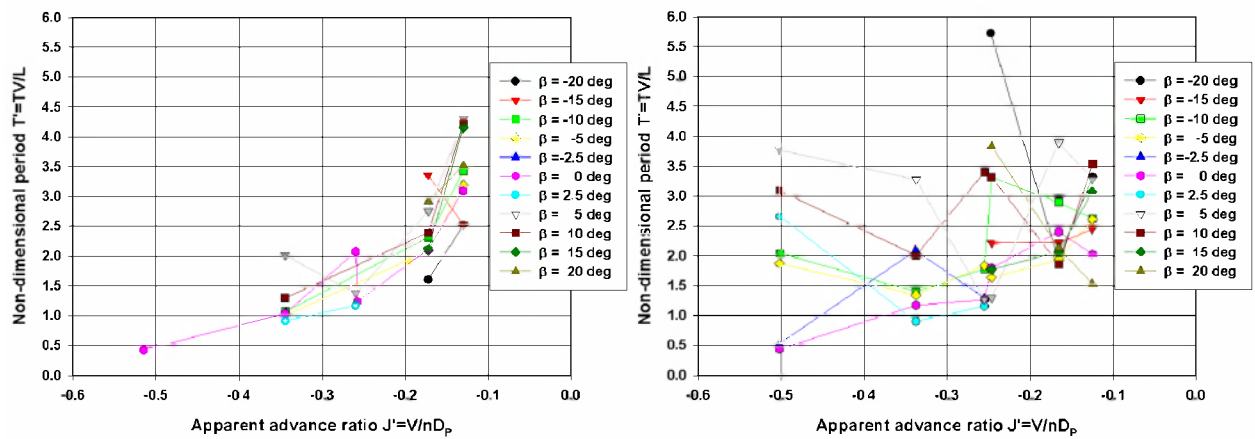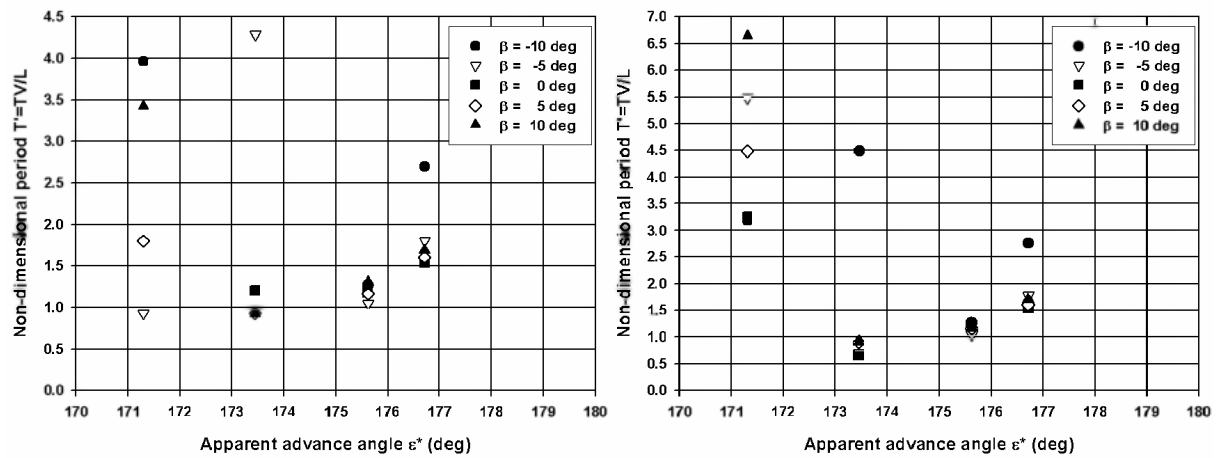

Figure 5.85 Model D, *quadrant 2*, non-dimensional period T' of oscillating lateral force as function of the apparent advance ratio J', series DA ($F_n \leq 0.065$, one value of propeller rate of turn n during each test run, left, and combination of three values of propeller rate of turn n during each test run, right)
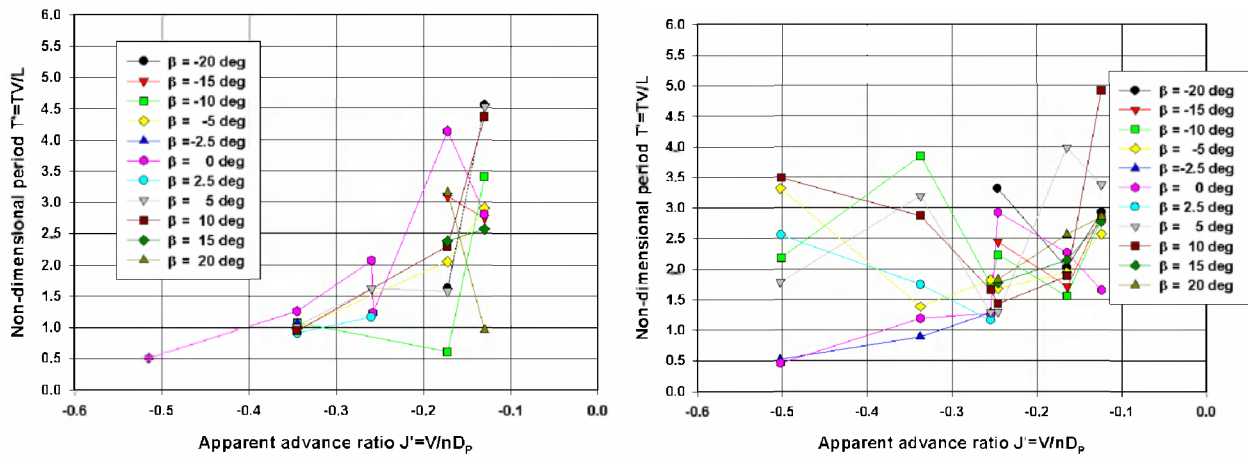
Figure 5.86 Model D, *quadrant 2*, non-dimensional period T' of oscillating yawing moment as function of the apparent advance ratio J', series DA ($F_n \leq 0.065$, one value of propeller rate of turn n during each test run, left, and combination of three values of propeller rate of turn n during each test run, right)
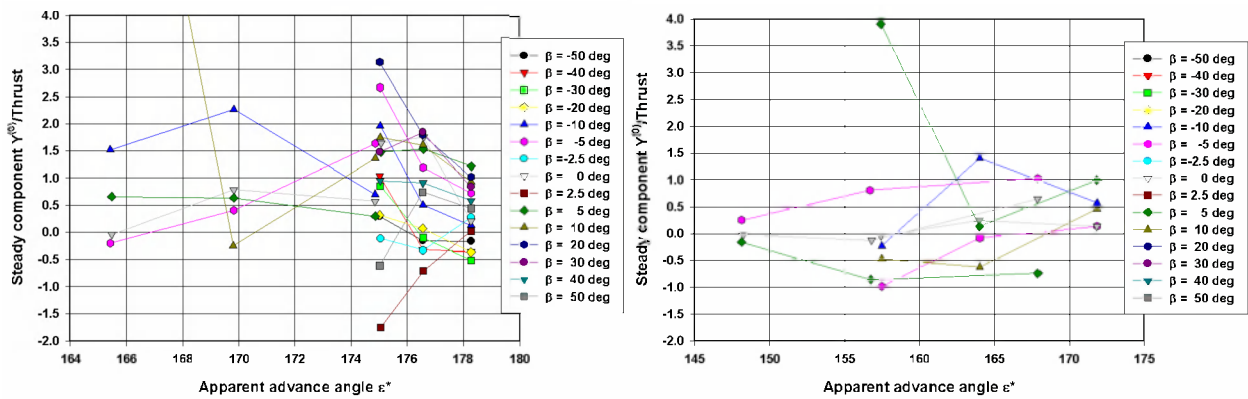
Figure 5.87 Model D, *quadrant 2*, ratio of steady component $Y^{(0)}$ to propeller thrust as function of the apparent advance angle ε^* (deg), series D1 ($F_n \leq 0.049$, left, and $F_n \geq 0.077$, right)
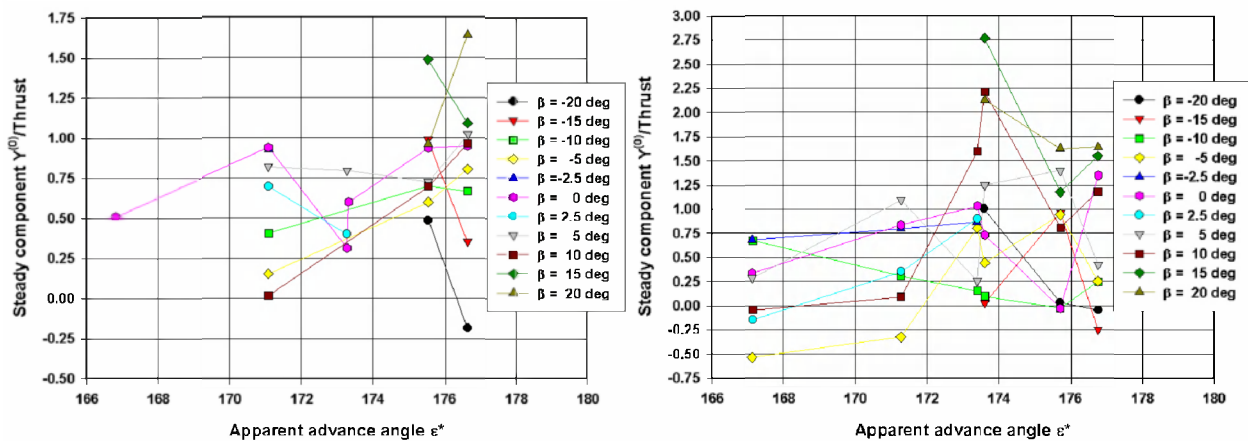
Figure 5.88 Model D, *quadrant 2*, ratio of steady component $Y^{(0)}$ to propeller thrust as function of the apparent advance angle ε^* (deg), series DA ($F_n \leq 0.065$, one value of propeller rate of turn n during each test run, left, and combination of three values of propeller rate of turn n during each test run, right)
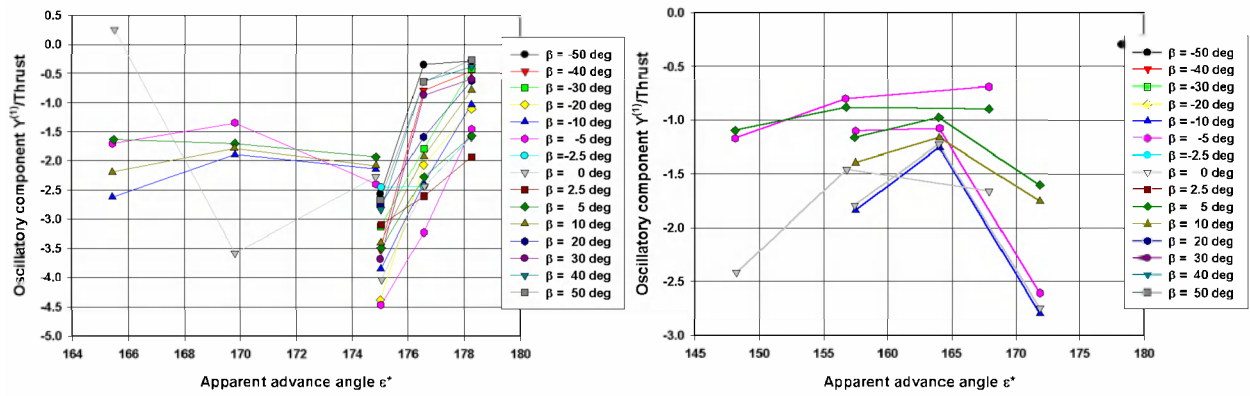
Figure 5.89 Model D, *quadrant 2*, ratio of oscillatory component $Y^{(1)}$ to propeller thrust as function of the apparent advance angle ε^* (deg), series D1 ($F_n \leq 0.049$, left, and $F_n \geq 0.077$, right)
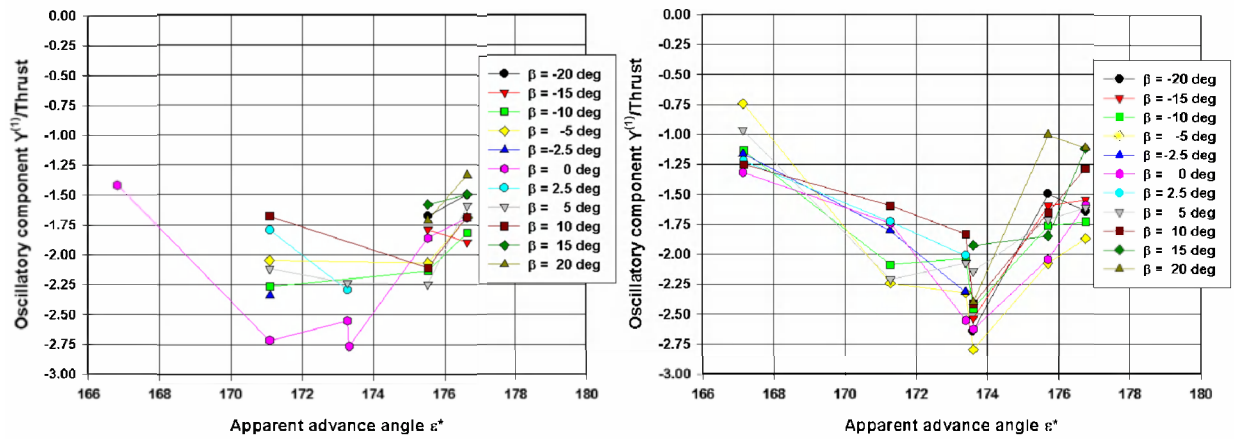
Figure 5.90 Model D, *quadrant 2*, ratio of oscillatory component $Y^{(1)}$ to propeller thrust as function of the apparent advance angle ε^* (deg), series DA ($F_n \leq 0.065$, one value of propeller rate of turn n during each test run, left, and combination of three values of propeller rate of turn n during each test run, right)
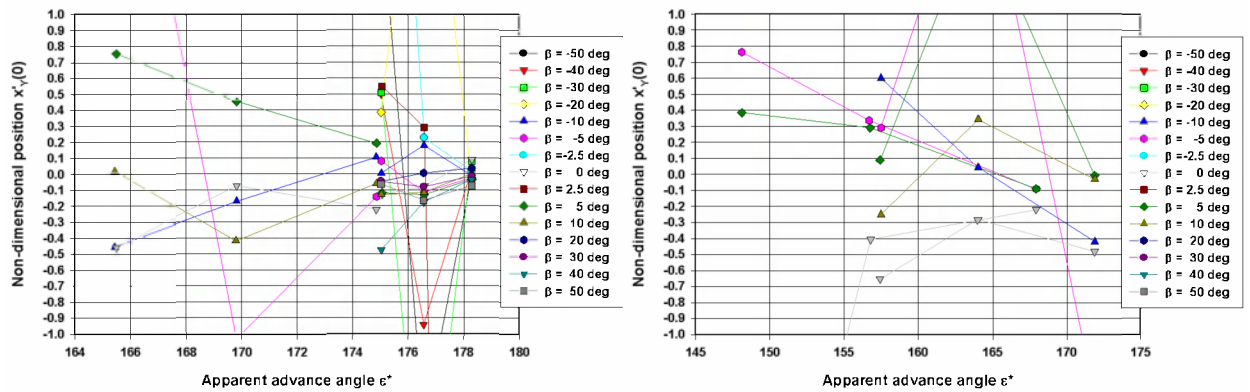
Figure 5.91 Model D, *quadrant 2*, non-dimensional position $x'_Y(0)$ as function of apparent advance angle ε^* (deg), series D1 ($F_n \leq 0.049$, left, and $F_n \geq 0.077$, right)
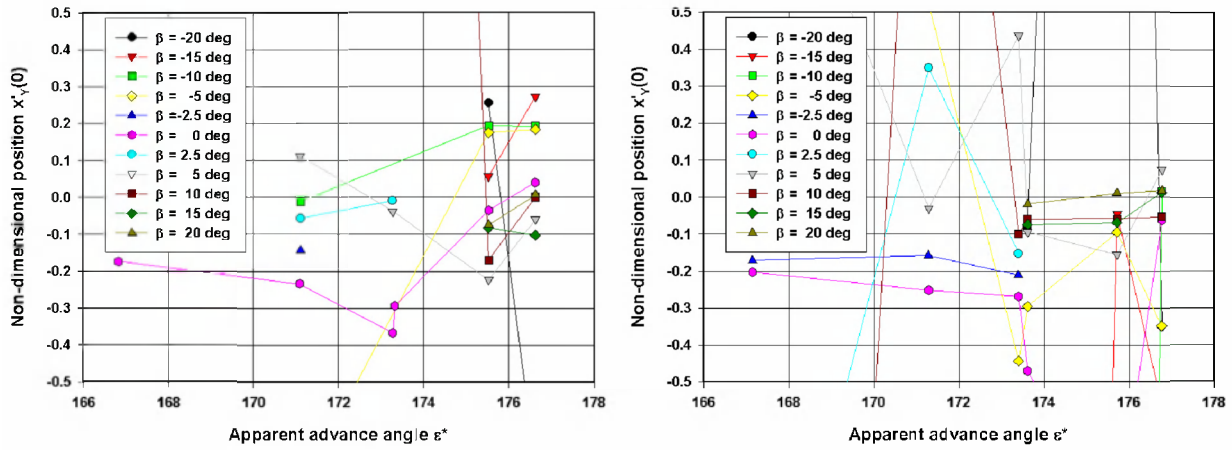
Figure 5.92 Model D, *quadrant 2*, non-dimensional position x'$_Y$(0) as function of apparent advance angle ε* (deg), series DA (F$_n$ ≤ 0.065, one value of propeller rate of turn n during each test run, left, and combination of three values of propeller rate of turn n during each test run, right)
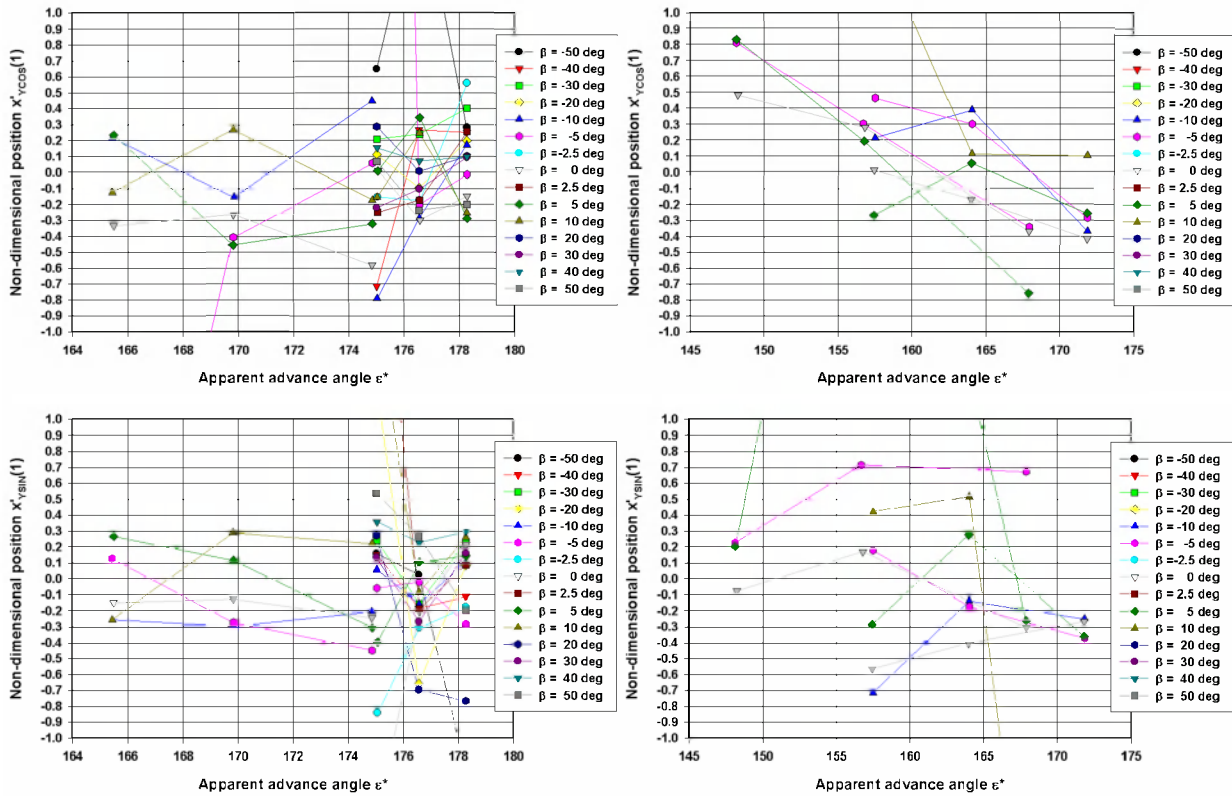
Figure 5.93 Model D, *quadrant 2*, non-dimensional position x'$_{YCOS}$(1) (top) and x'$_{YSIN}$(1) (bottom) as function of apparent advance angle ε* (deg), series D1 (F$_n$ ≤ 0.049, left, and F$_n$ ≥ 0.077, right)
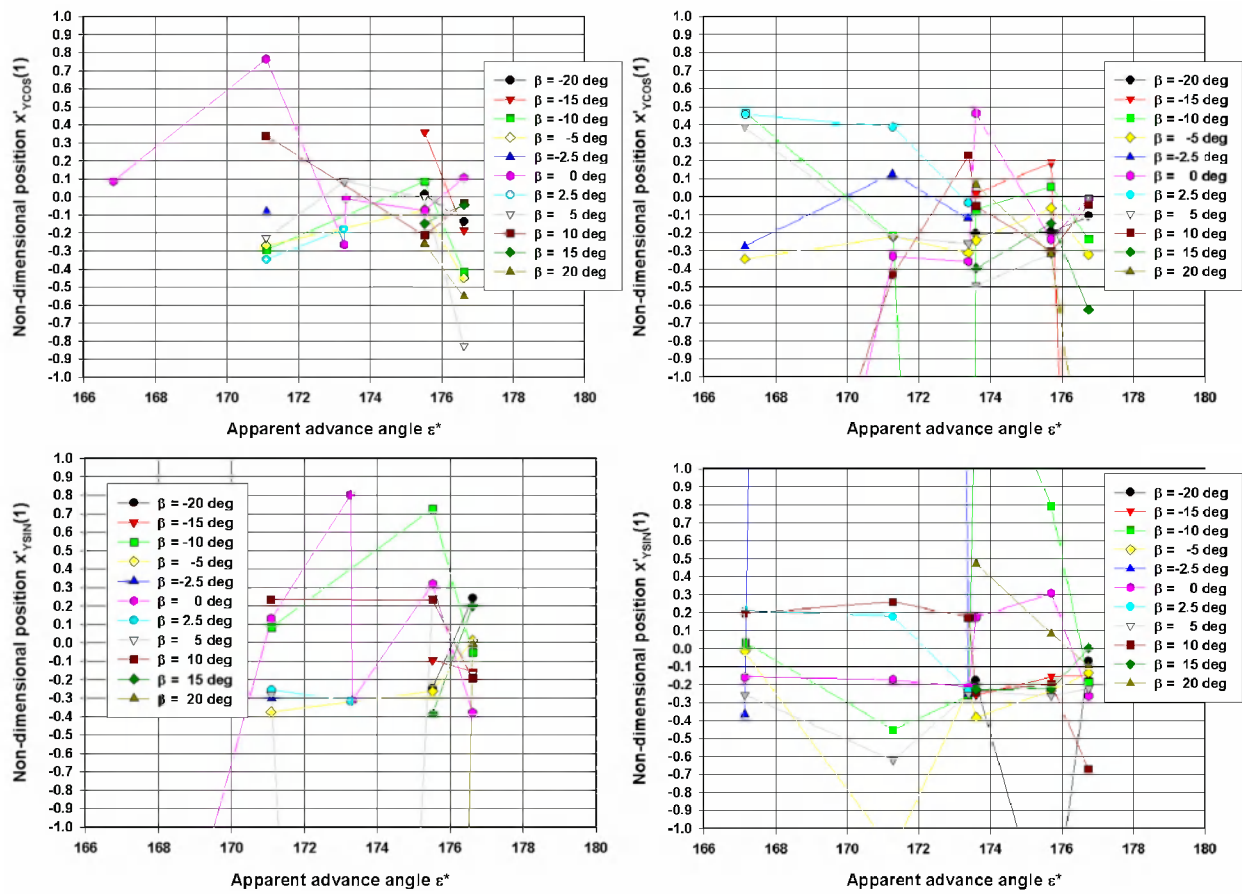
Figure 5.94 Model D, *quadrant 2*, non-dimensional position x'$_{YCOS}$(1) (top) and x'$_{YSIN}$(1) (bottom) as function of apparent advance angle ε* (deg), series DA (F$_n$ ≤ 0.065, one value of propeller rate of turn n during each test run, left, and combination of three values of propeller rate of turn n during each test run, right)

(a) reference photograph   (b) photograph 5 seconds later than (a)

(c) photograph 13 seconds later than (a)   (c) photograph 1 min. 8 seconds later than (a)
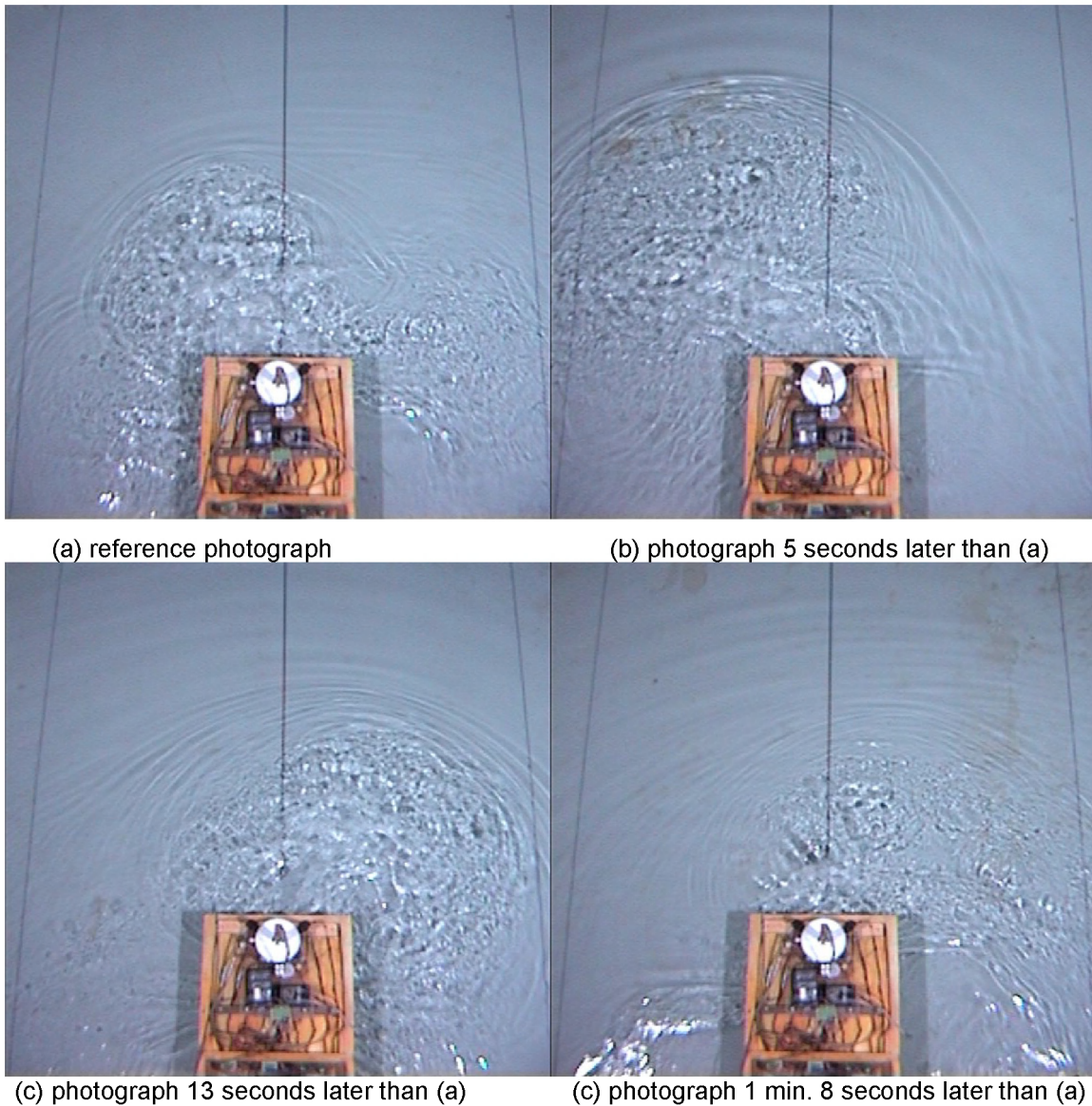
Figure 5.95 Observation of eddies which are shed from the stern of the model due to a backward velocity and a positive propeller rate resulting into fluctuating lateral forces and yawing moments. Ship model U (at a full scale draught of 13.5 m and an UKC of 10%)
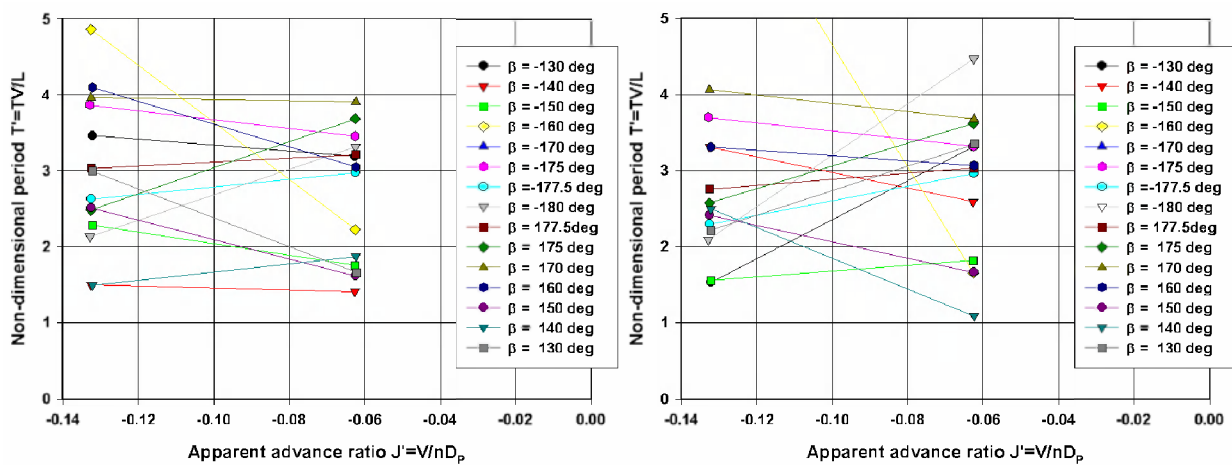
Figure 5.96 Model D, *quadrant 4*, non-dimensional period T' of oscillating lateral force (left) and yawing moment (right) as function of the apparent advance ratio J', series D1 (F_n = -0.016, no rudder deflection)
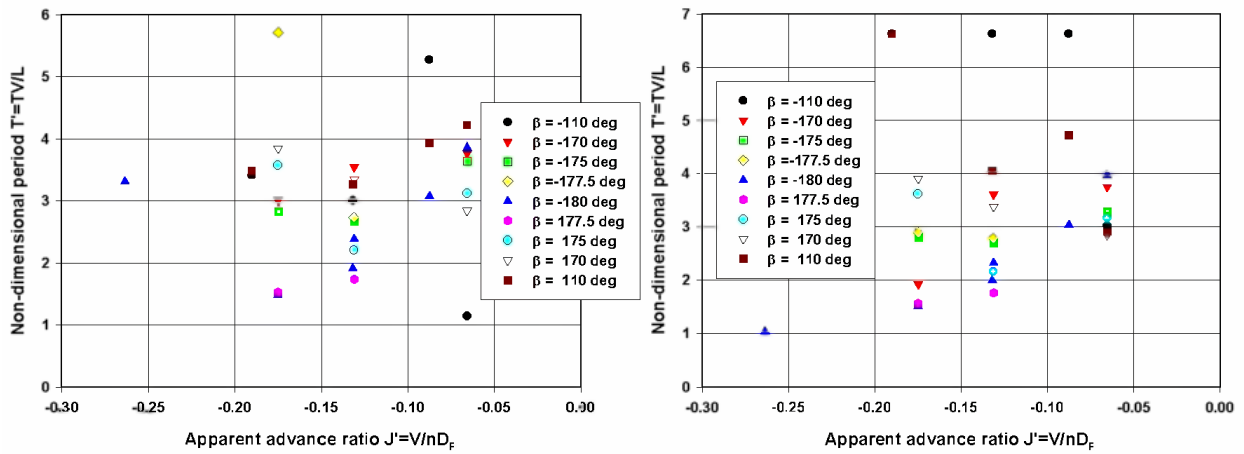
Figure 5.97 Model D, *quadrant 4*, non-dimensional period T' of oscillating lateral force (left) and yawing moment (right) as function of the apparent advance ratio J', series DA (F_n = -0.016 and −0.032, no rudder deflection)
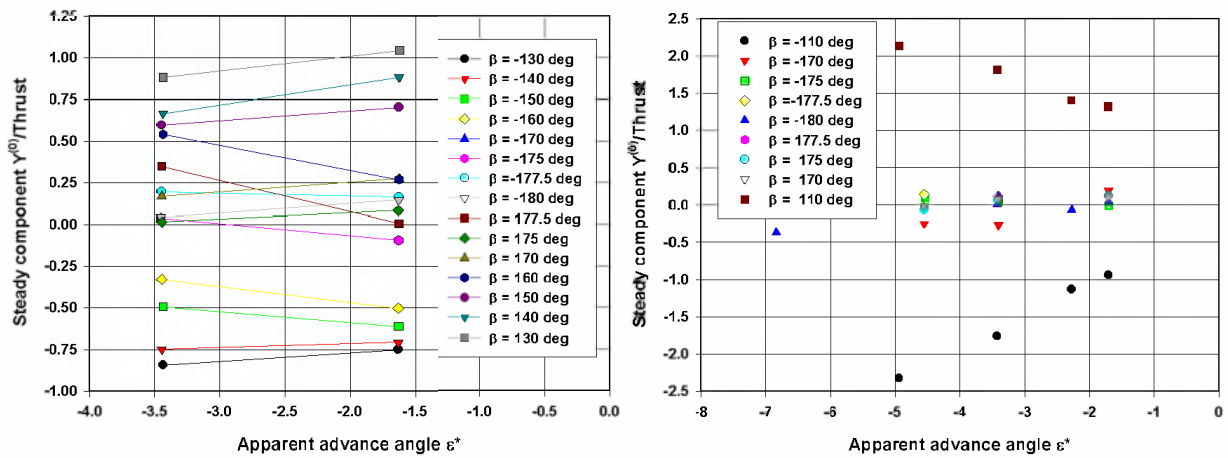
Figure 5.98 Model D, *quadrant 4*, ratio of steady component $Y^{(0)}$ to propeller thrust as function of the apparent advance angle ε* (deg) (series D1, left, F_n = -0.016, and series DA, right, F_n = -0.016 and −0.032 no rudder deflection)
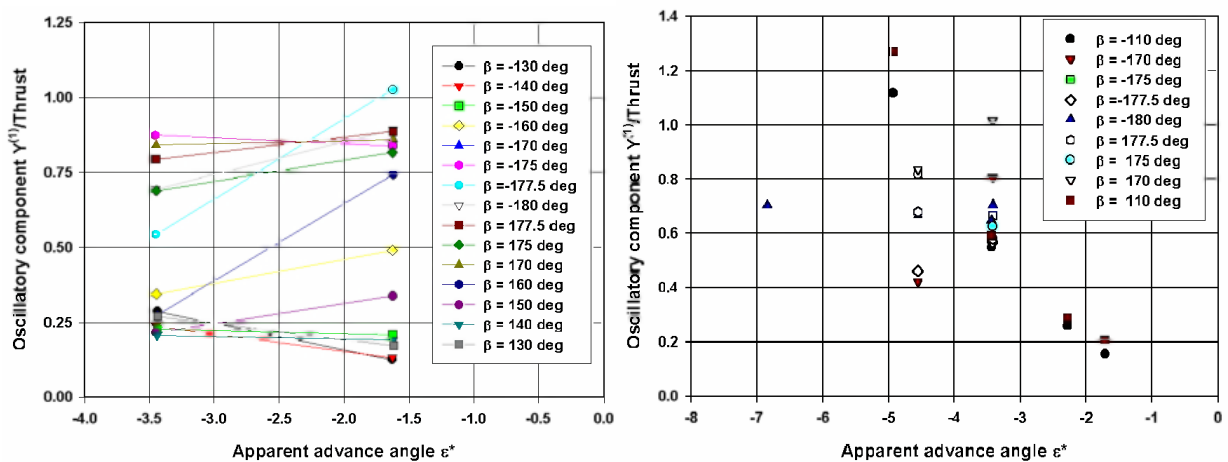
Figure 5.99 Model D, *quadrant 4*, ratio of oscillatory component $Y^{(1)}$ to propeller thrust as function of the apparent advance angle ε* (deg) (series D1, left, F_n = -0.016, and series DA, right, F_n = -0.016 and −0.032 no rudder deflection)

318
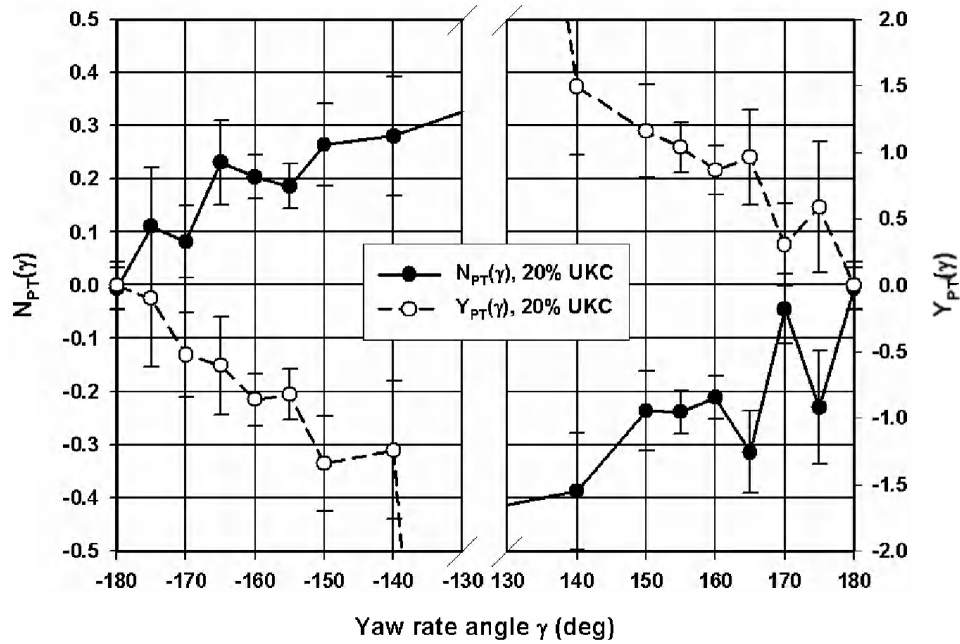
Figure 5.100 Model E at 20% UKC, *quadrant 4*, influence of yaw rate angle on steady components for lateral force and yawing moment
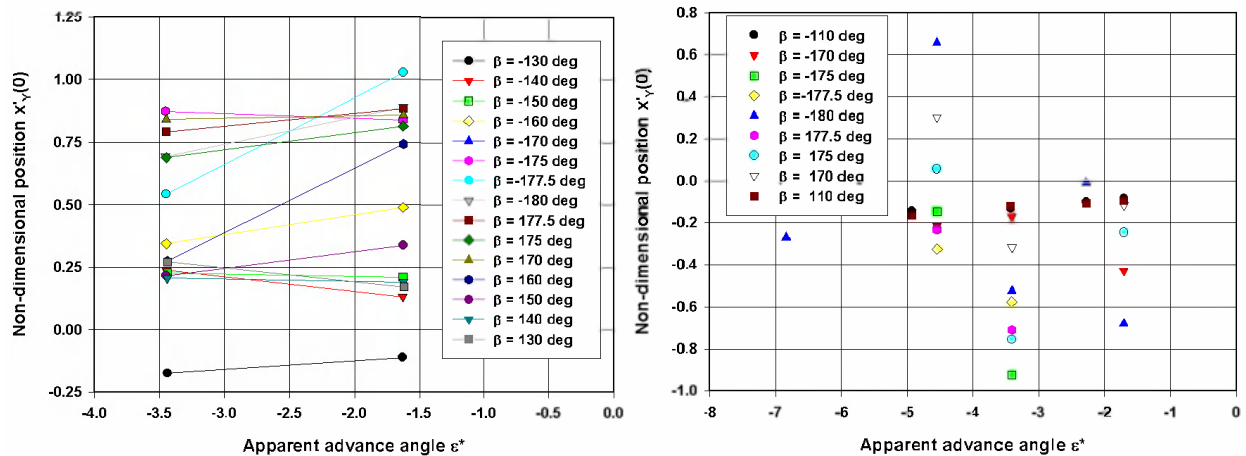
Figure 5.101 Model D, *quadrant* 4, non-dimensional position $x'_Y(0)$ as function of the apparent advance angle ε^* (deg) (series D1, left, F_n = -0.016, and series DA, right, F_n = -0.016 and −0.032 no rudder deflection)
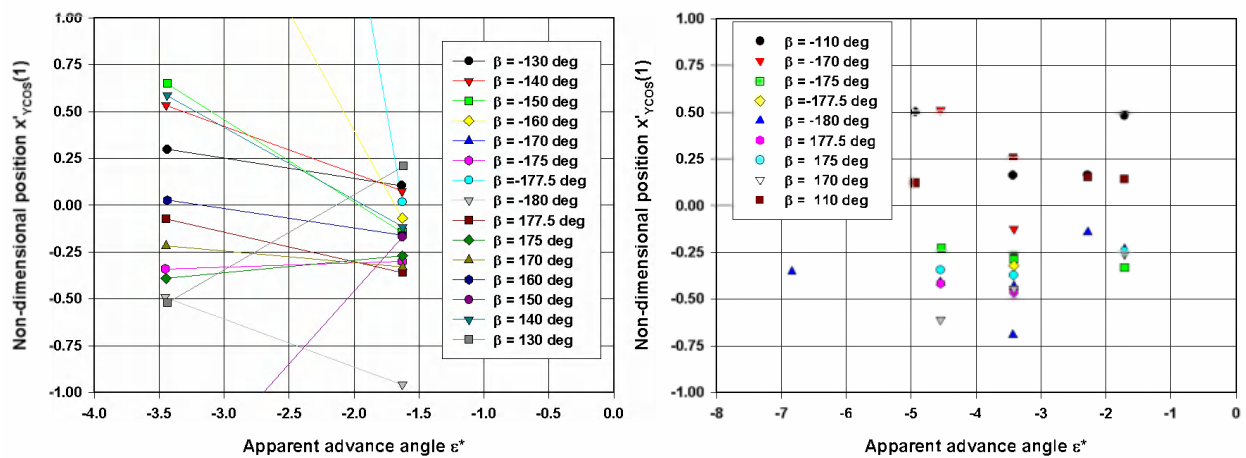
Figure 5.102 Model D, *quadrant* 4, non-dimensional position $x'_{YCOS}(1)$ as function of the apparent advance angle ε^* (deg) (series D1, left, F_n = -0.016, and series DA, right, F_n = -0.016 and −0.032 no rudder deflection)
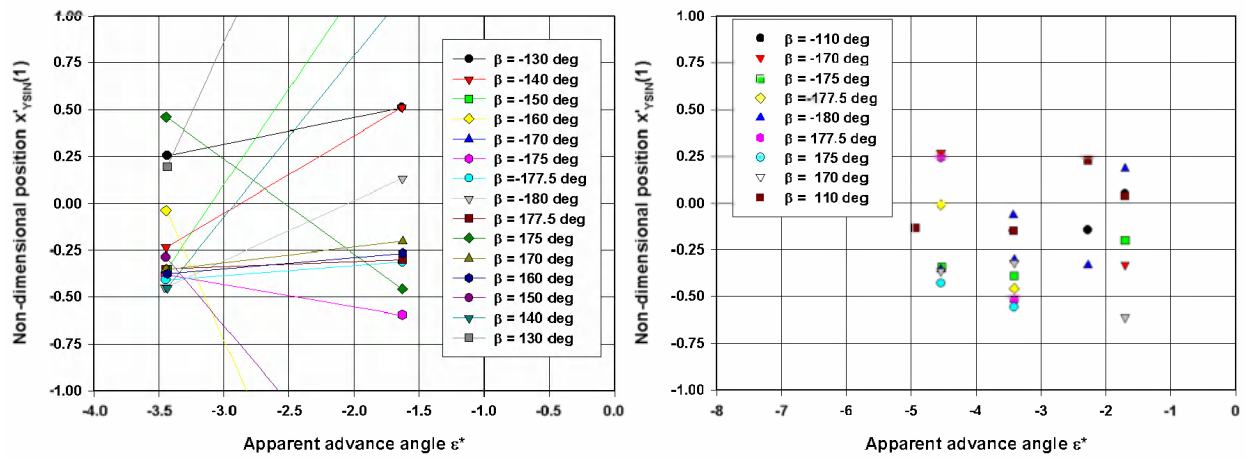
Figure 5.103 Model D, *quadrant 4*, non-dimensional position x'$_{YSIN}$(1) as function of the apparent advance angle ε* (deg) (series D1, left, F$_n$ = -0.016, and series DA, right, F$_n$ = -0.016 and −0.032 no rudder deflection)

Figure 5.104 Model E at 20% UKC, *quadrant 2*, non-dimensional period T' of oscillating lateral force (left) or oscillating yawing moment (right) as function of the apparent advance angle ε*
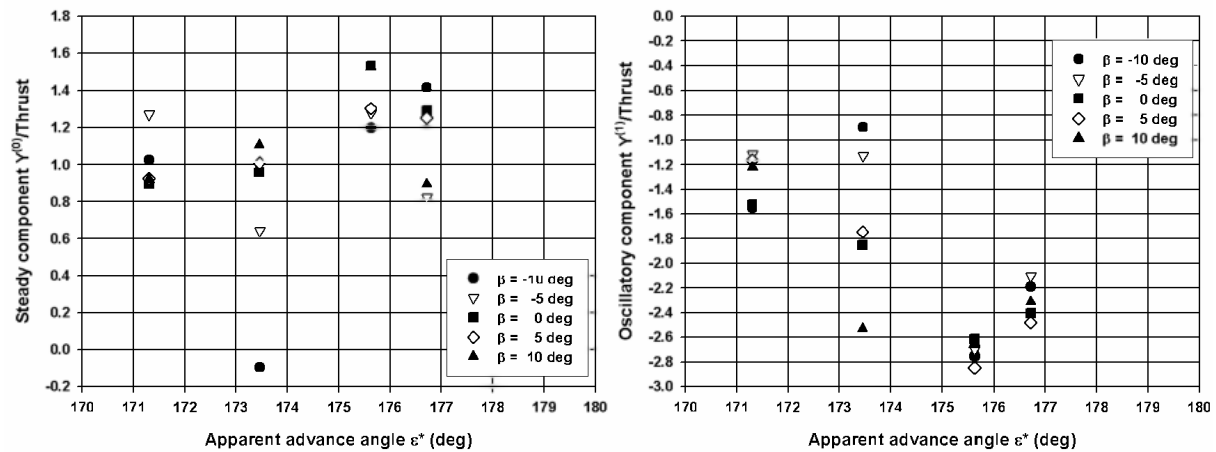
Figure 5.105 Model E at 20% UKC, *quadrant 2*, steady and oscillatory component as function of apparent advance angle ε*
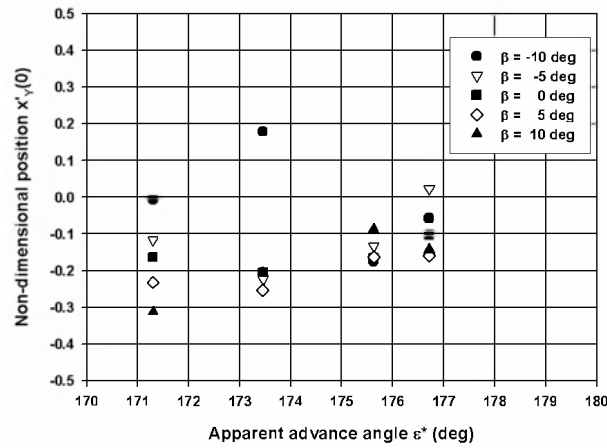
Figure 5.106 Model E at 20% UKC, *quadrant 2*, non-dimensional position $x'_Y(0)$ as function of the apparent advance angle ε^*
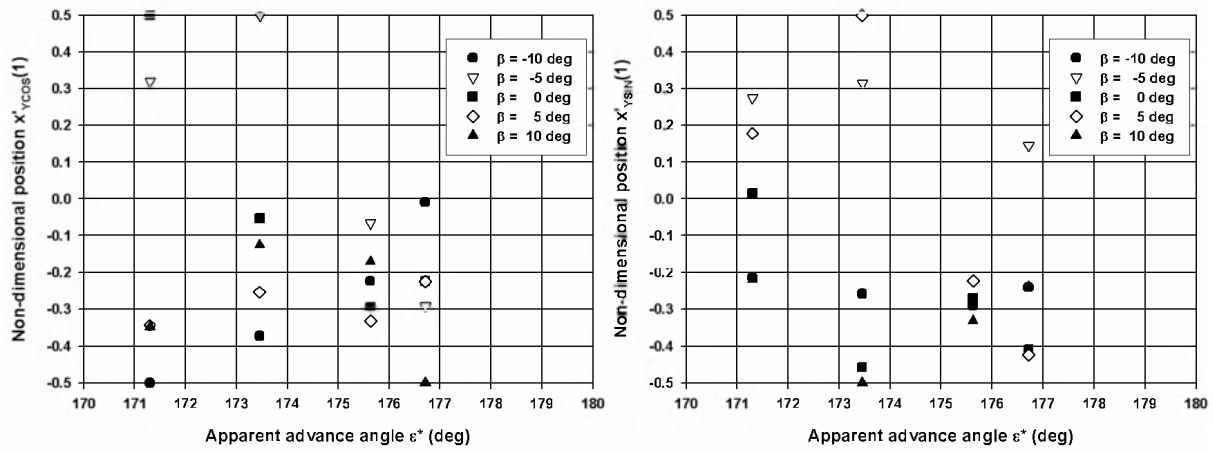
Figure 5.107 Model E at 20% UKC, *quadrant 2*, non-dimensional position $x'_{YCOS}(1)$ and $x'_{YSIN}(1)$ as function of the apparent advance angle ε^*
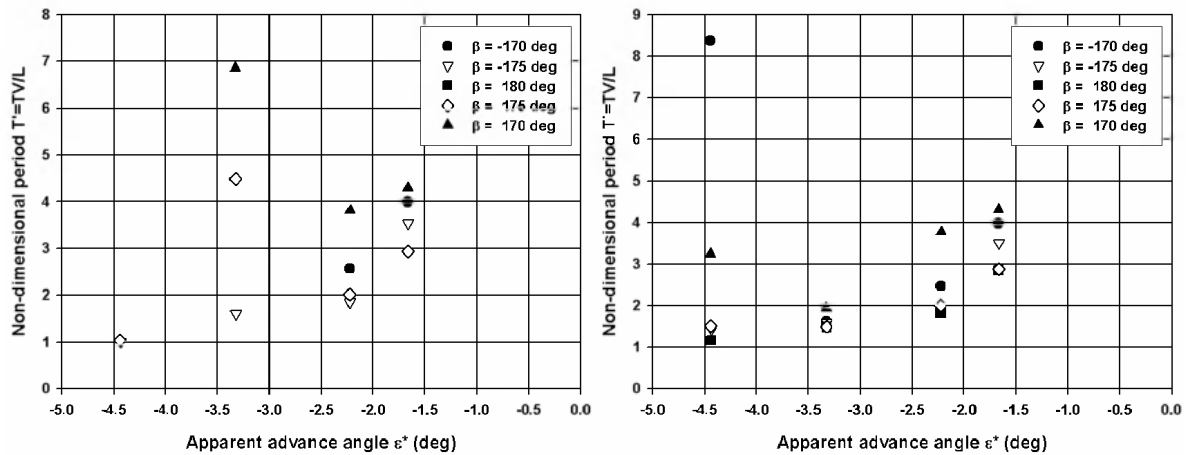
Figure 5.108 Model E at 20% UKC, *quadrant 4*, non-dimensional period T' of oscillating lateral force (left) or oscillating yawing moment (right) as function of the apparent advance angle ε^*
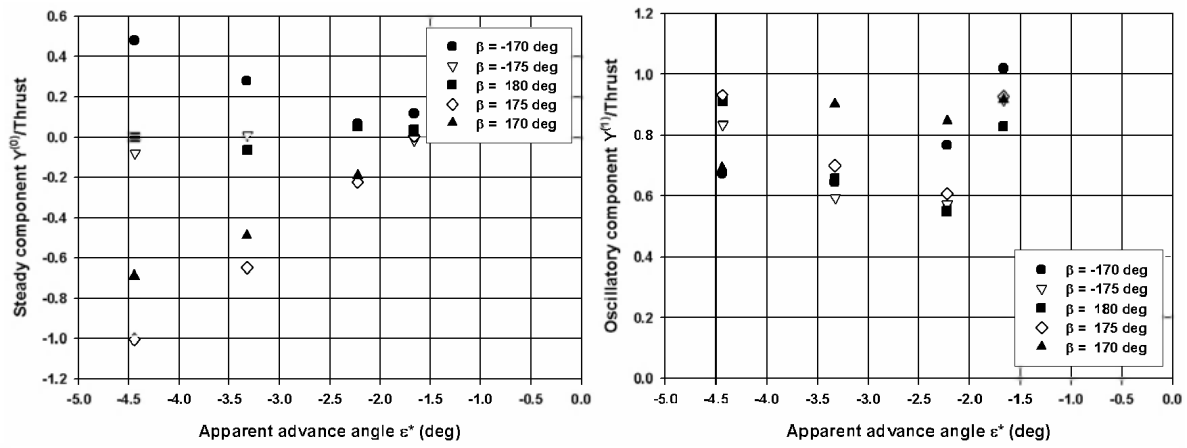
Figure 5.109 Model E at 20% UKC, *quadrant 4*, steady and oscillatory component as function of apparent advance angle ε^*
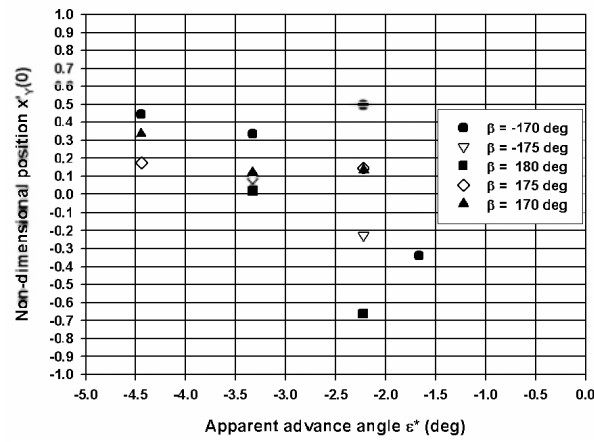
Figure 5.110 Model E at 20% UKC, *quadrant 4*, non-dimensional position $x'_Y(0)$ as function of the apparent advance angle ε^*
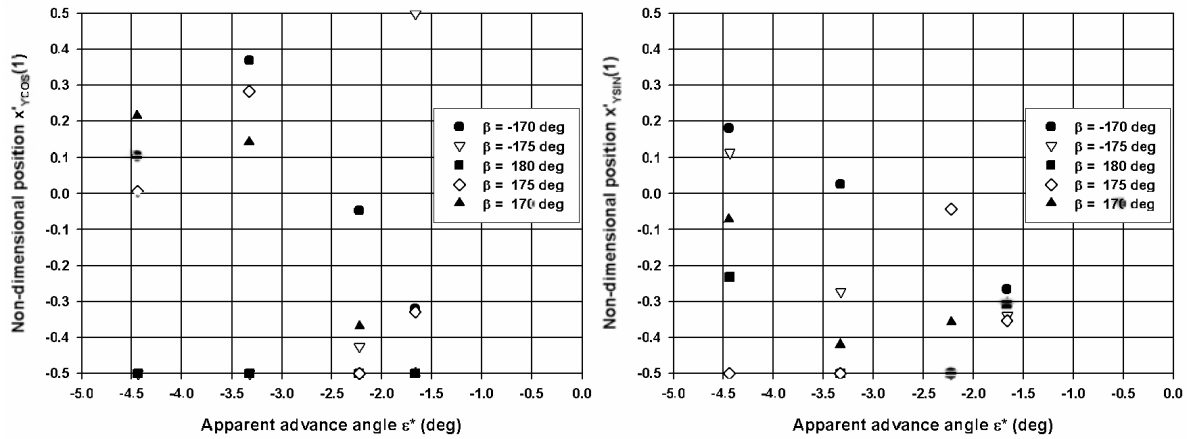
Figure 5.111 Model E at 20% UKC, *quadrant 4*, non-dimensional position $x'_{YCOS}(1)$ and $x'_{YSIN}(1)$ as function of the apparent advance angle ε^*

322
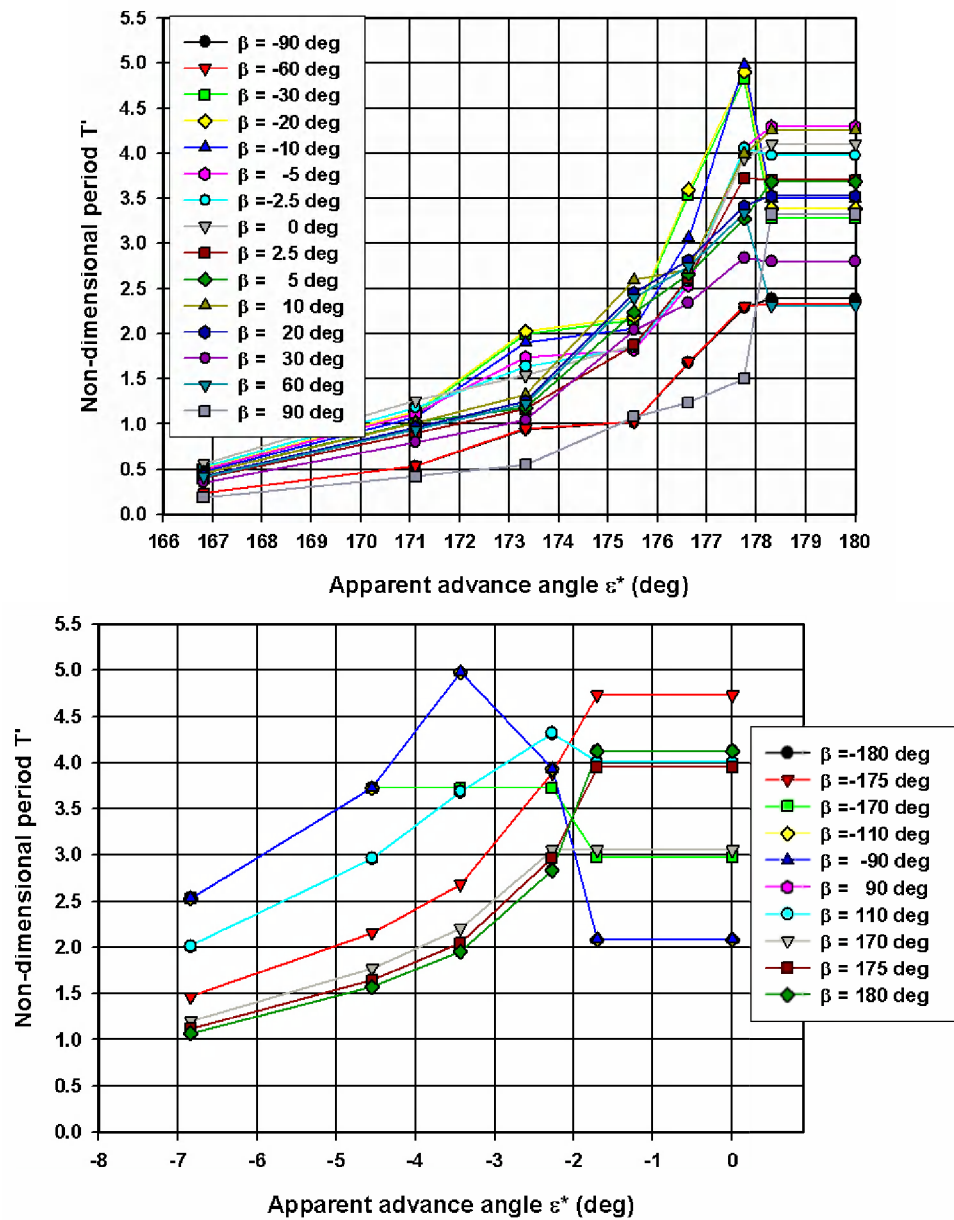
Figure 5.112 Model D, modelled values for non-dimensional period T', *quadrant 2* at the top and *quadrant 4* at the bottom
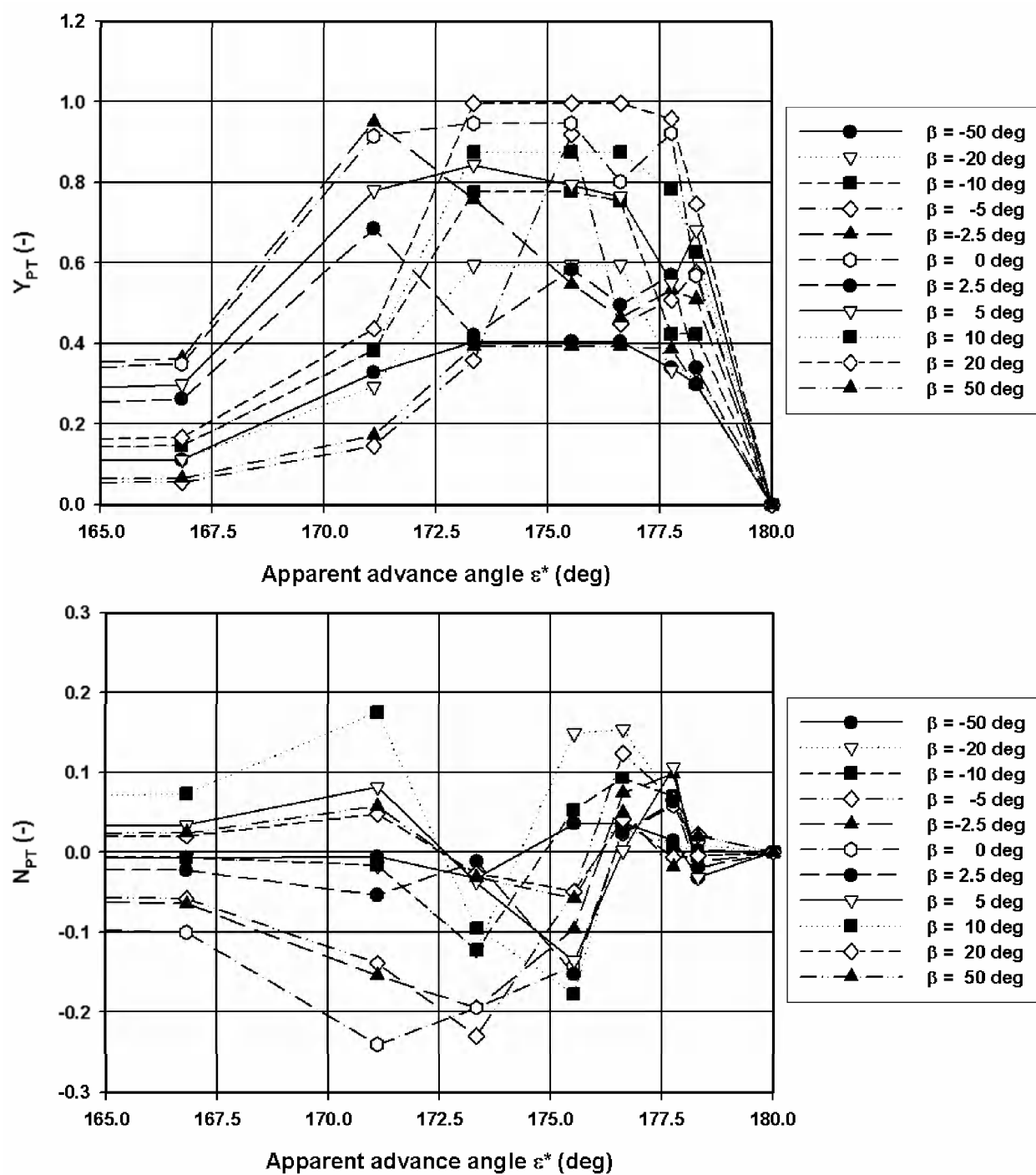
Figure 5.113 Model D, *quadrant 2*, selected tabular models for steady component of lateral force and yawing moment
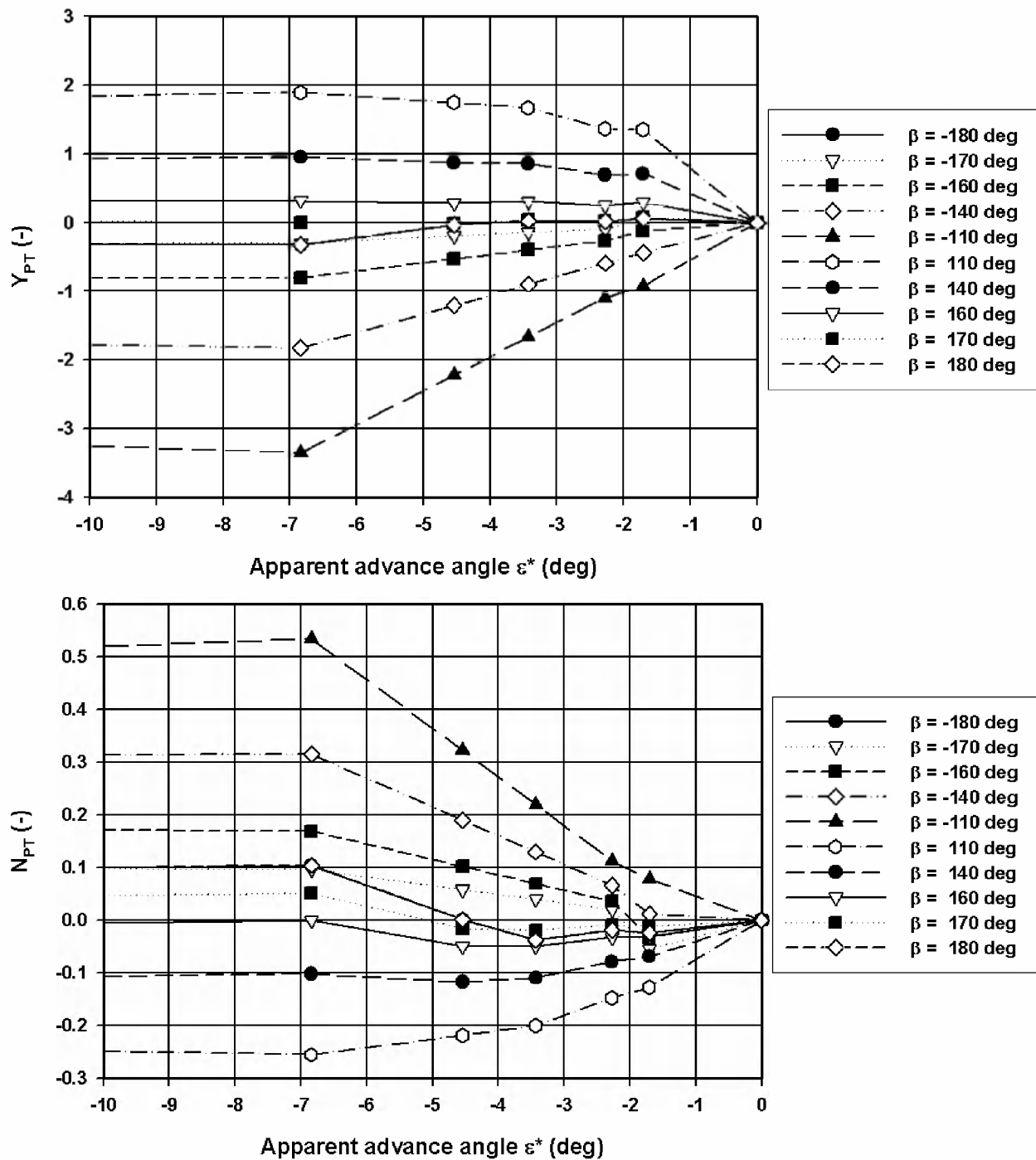
Figure 5.114 Model D, *quadrant 4*, selected tabular models for steady component of lateral force and yawing moment
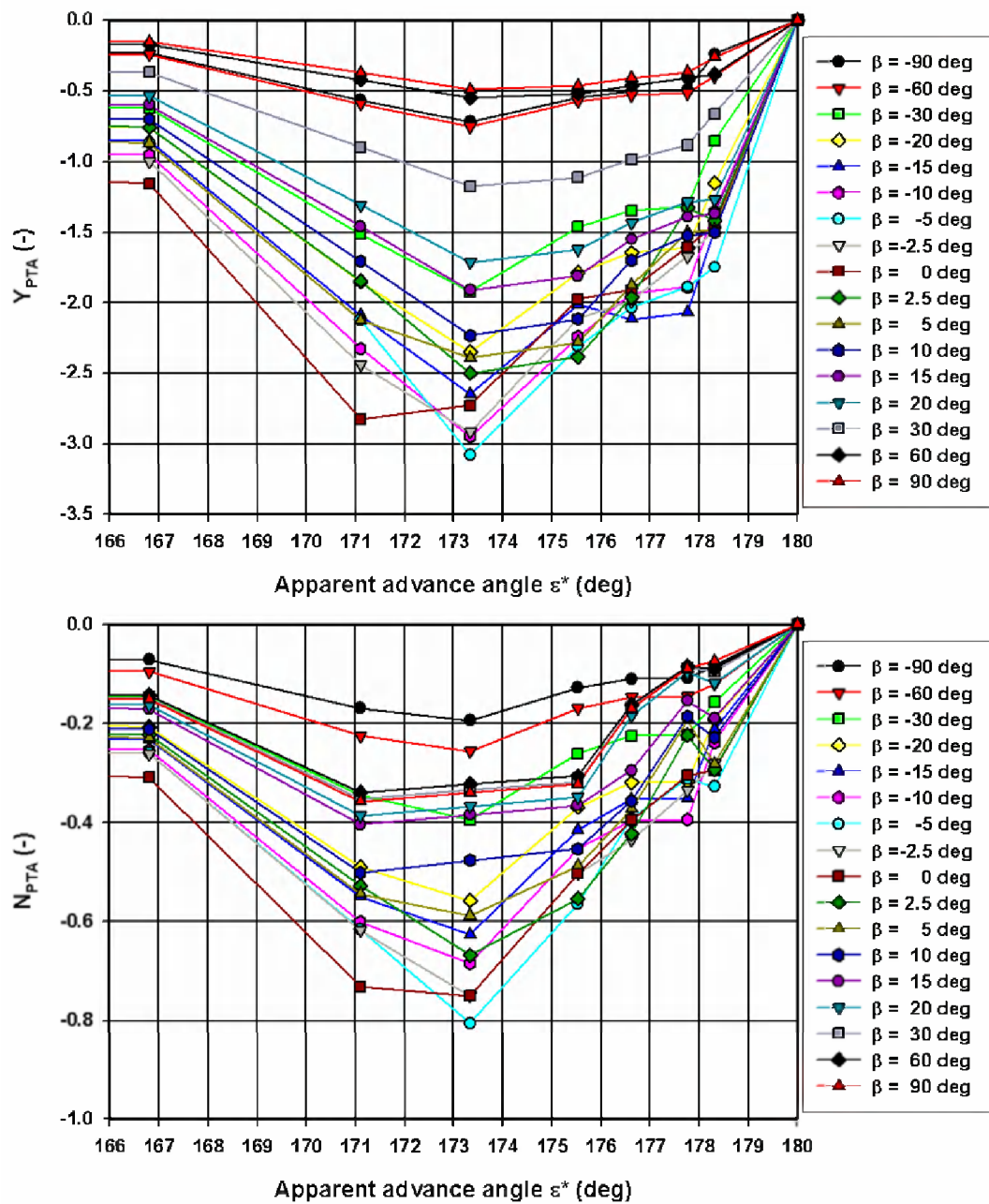
Figure 5.115 Model D, *quadrant 2*, selected tabular models for the amplitude of oscillatory components Y_{PTA} and N_{PTA}
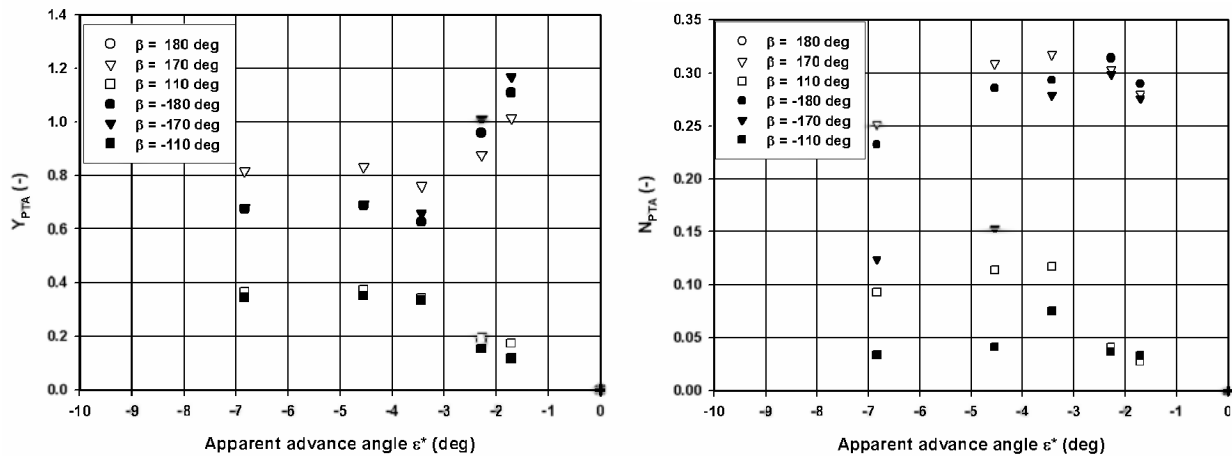
Figure 5.116 Model D, *quadrant 4*, selected tabular models for the amplitude of oscillatory components Y_{PTA} and N_{PTA}

326
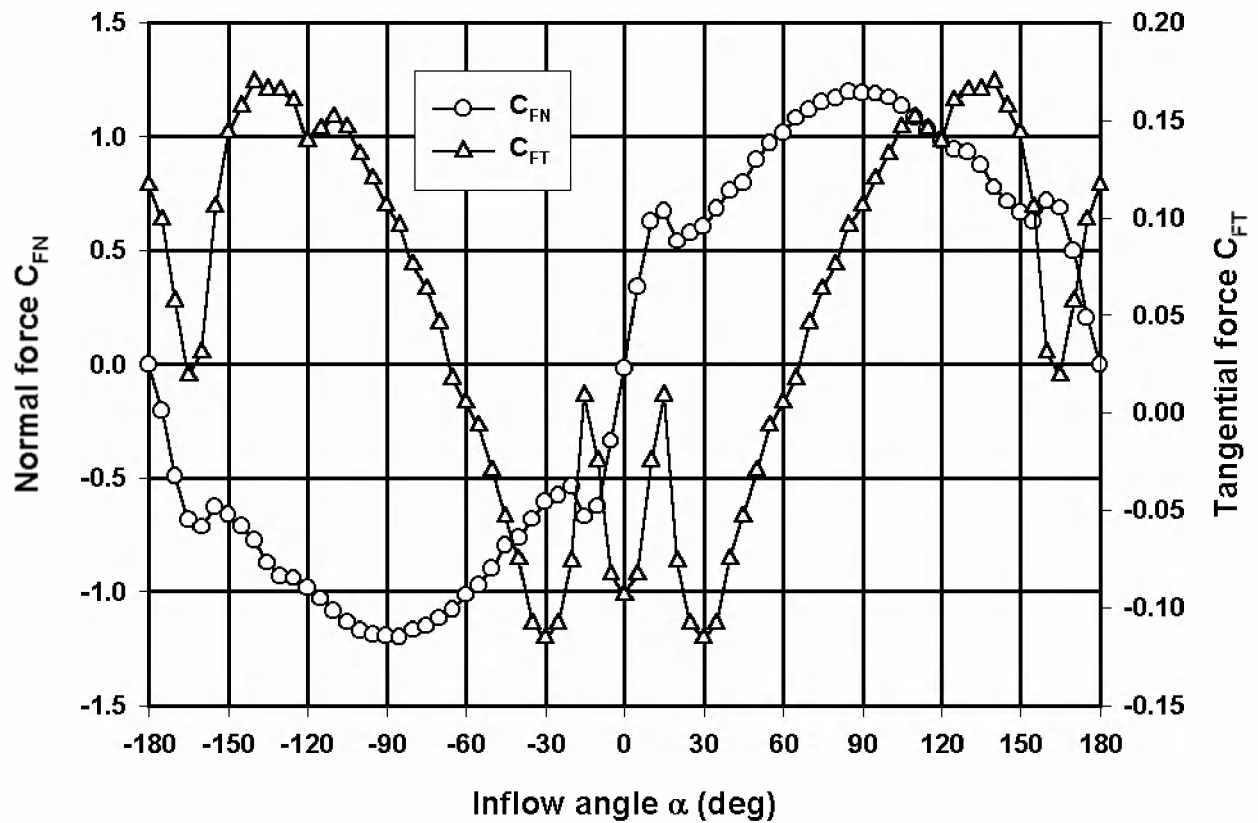
Figure 6.1 Open water characteristics C_{FT} and C_{FN} for the rudder profile of model D
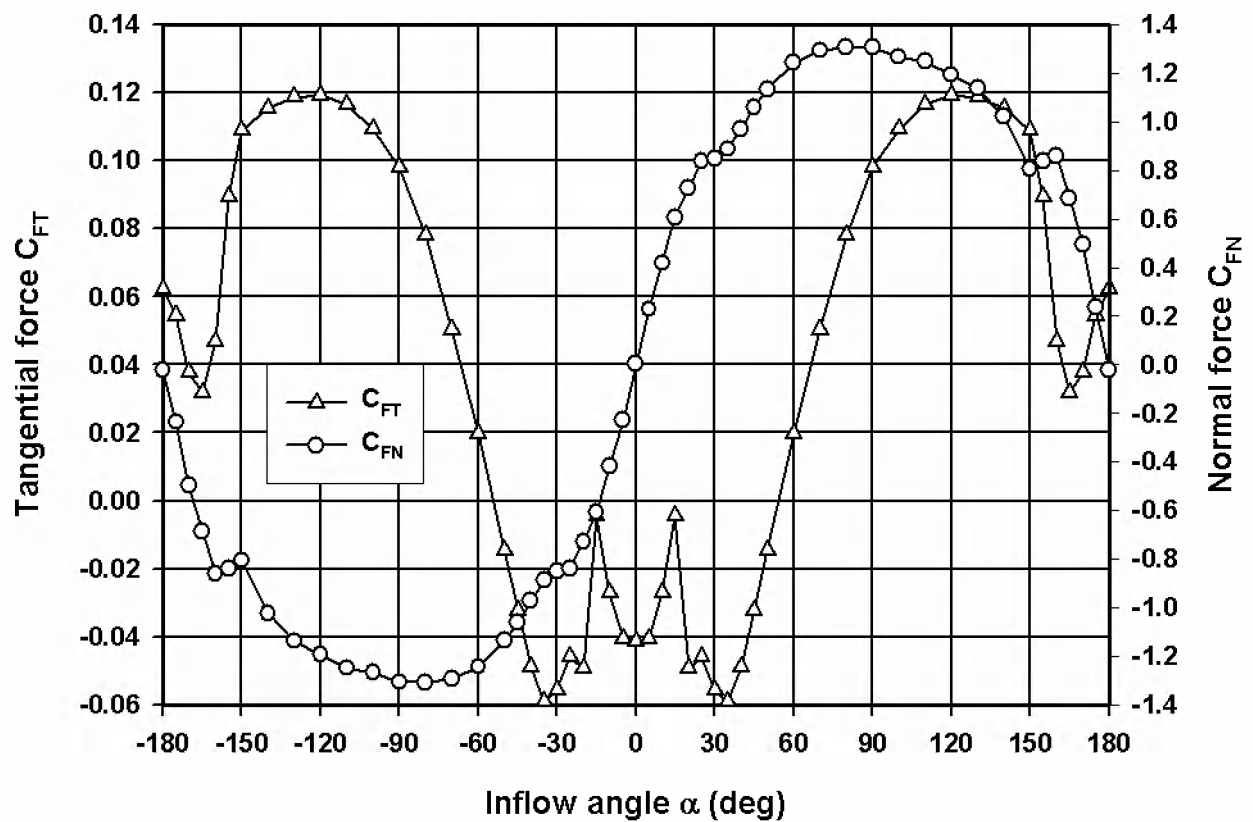
Figure 6.2 Open water characteristics C_{FT} and C_{FN} for the rudder profile of model E
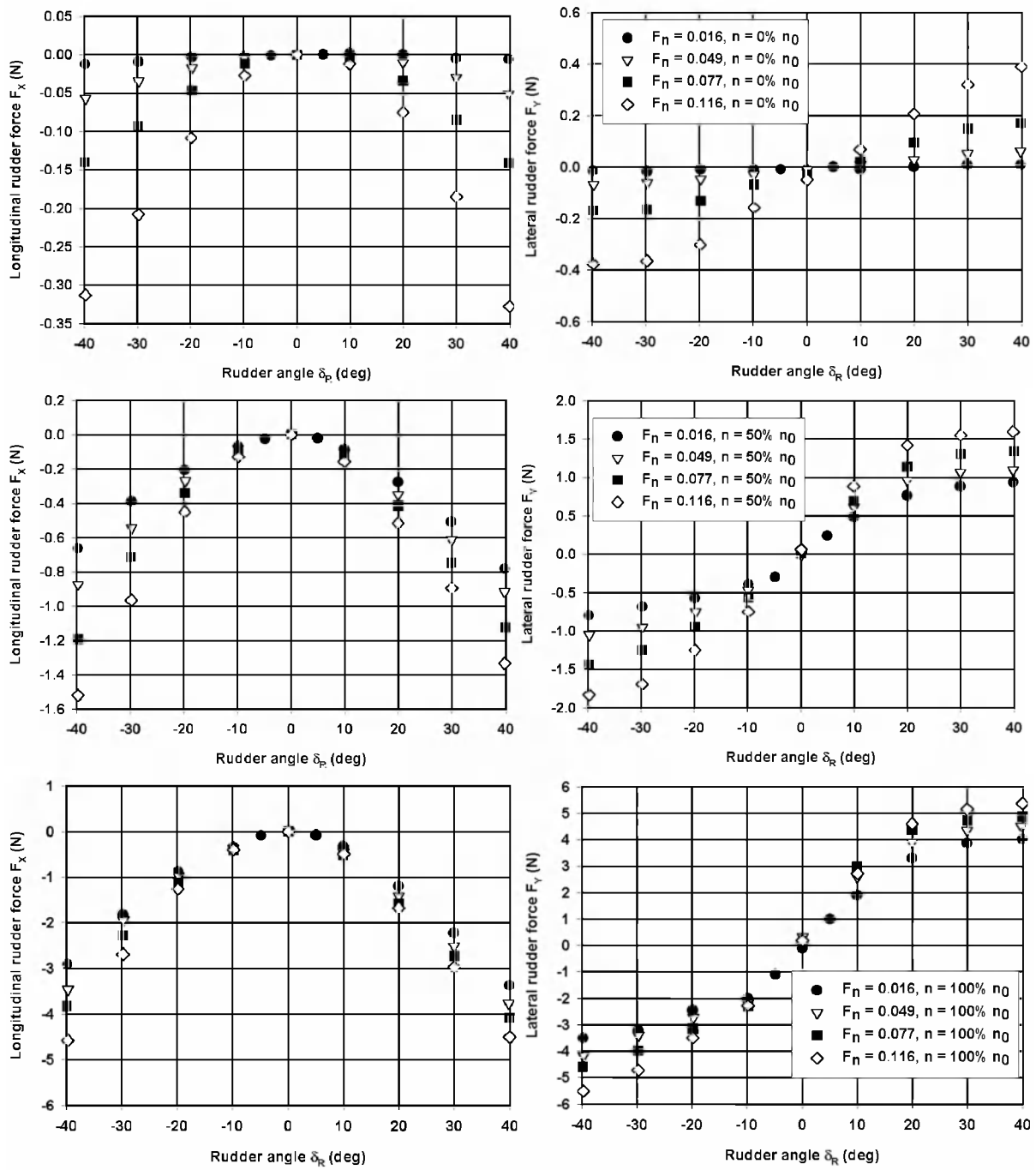
Figure 6.3 Model D, *quadrant 1*, longitudinal and lateral rudder force based on F_{RN}, stationary tests with varying Froude number and propeller rate
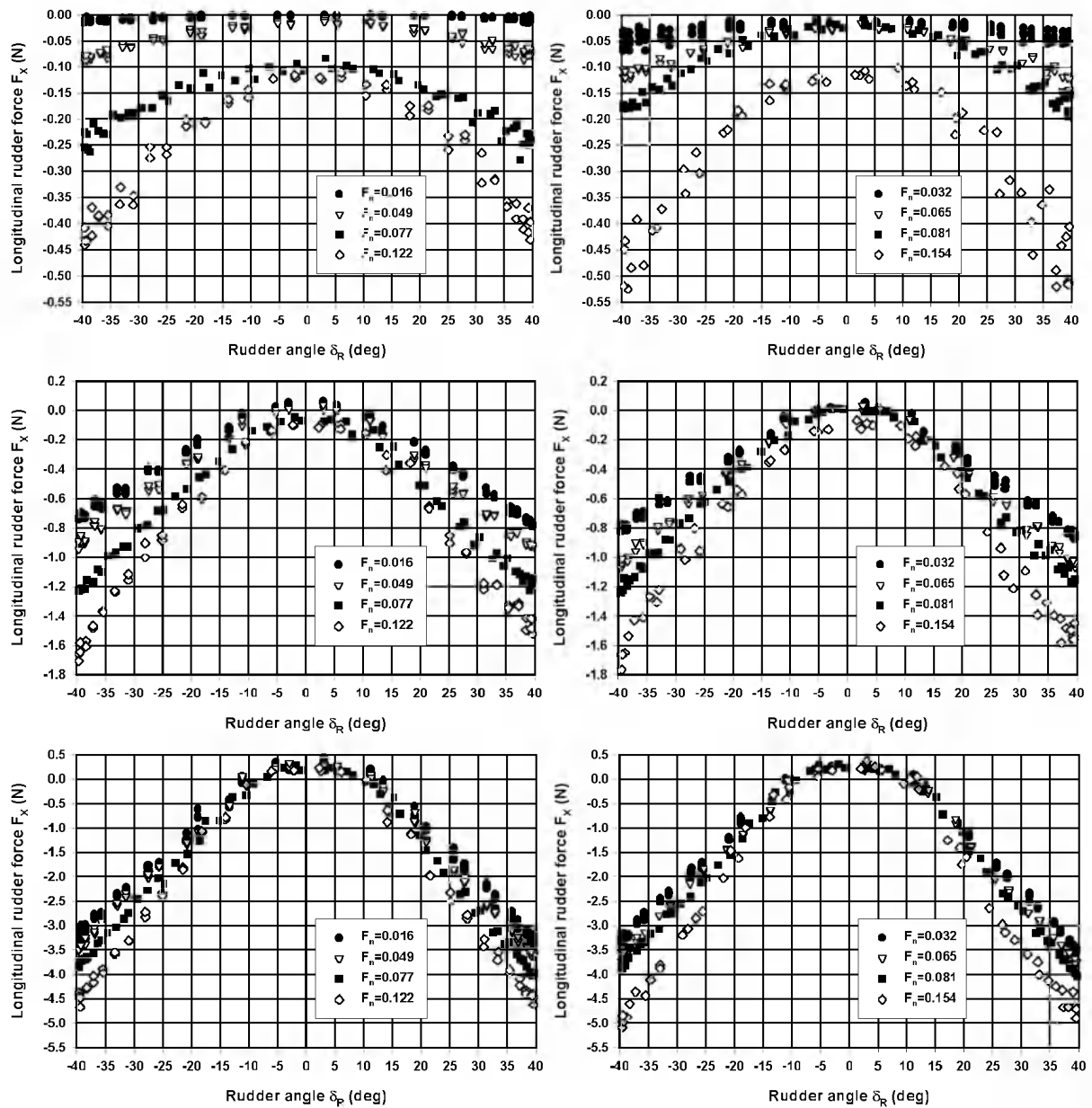
Figure 6.4 Model D, *quadrant 1*, longitudinal rudder force based on F_{RT} and F_{RN}, multi-modal tests of type A with varying Froude number and propeller rate (0% top, 50% middle, 100% bottom)
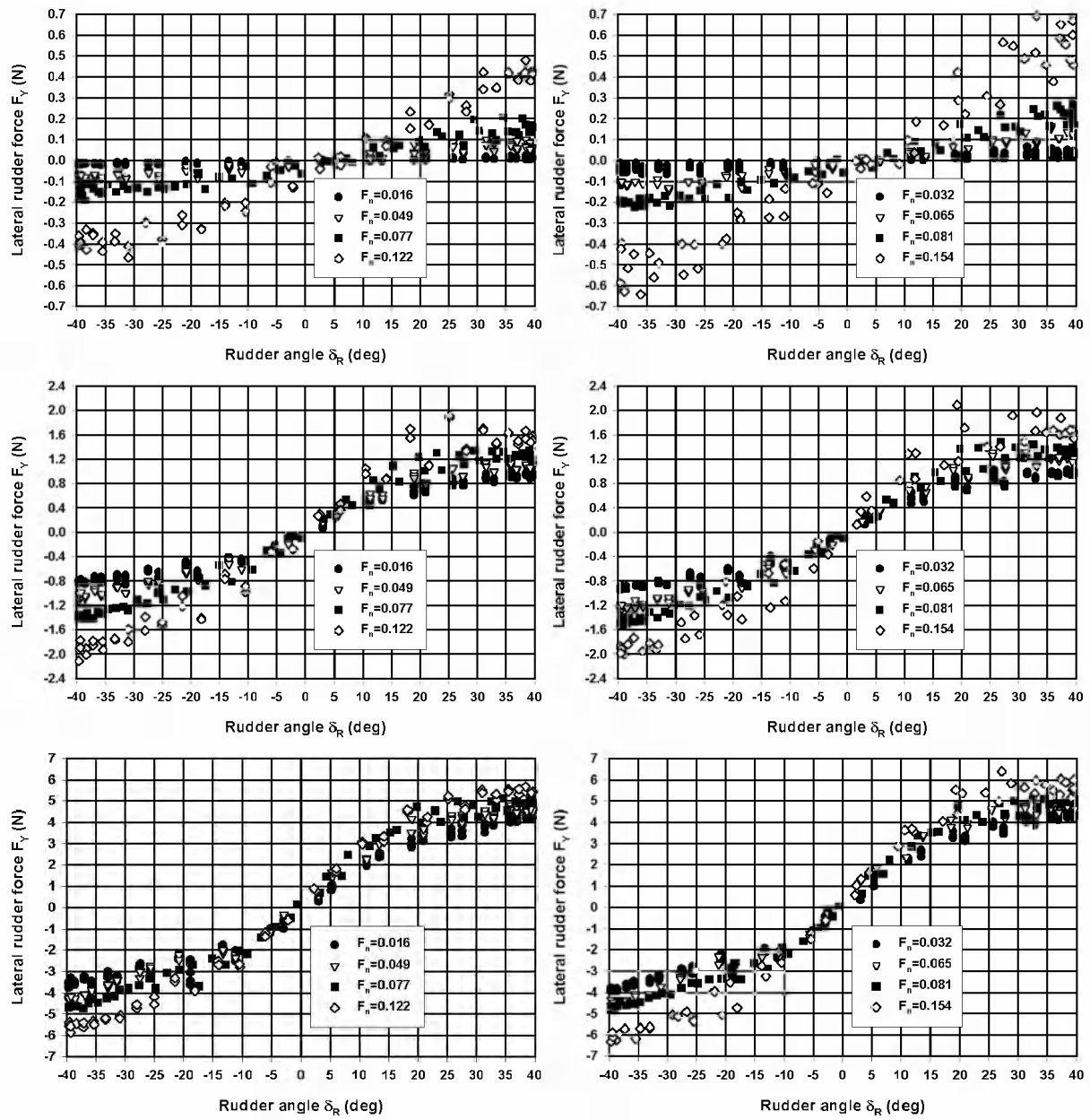
Figure 6.5 Model D, *quadrant 1*, lateral rudder force based on F_{RT} and F_{RN}, multi-modal tests of type A with varying Froude number and propeller rate (0% top, 50% middle, 100% bottom)

330
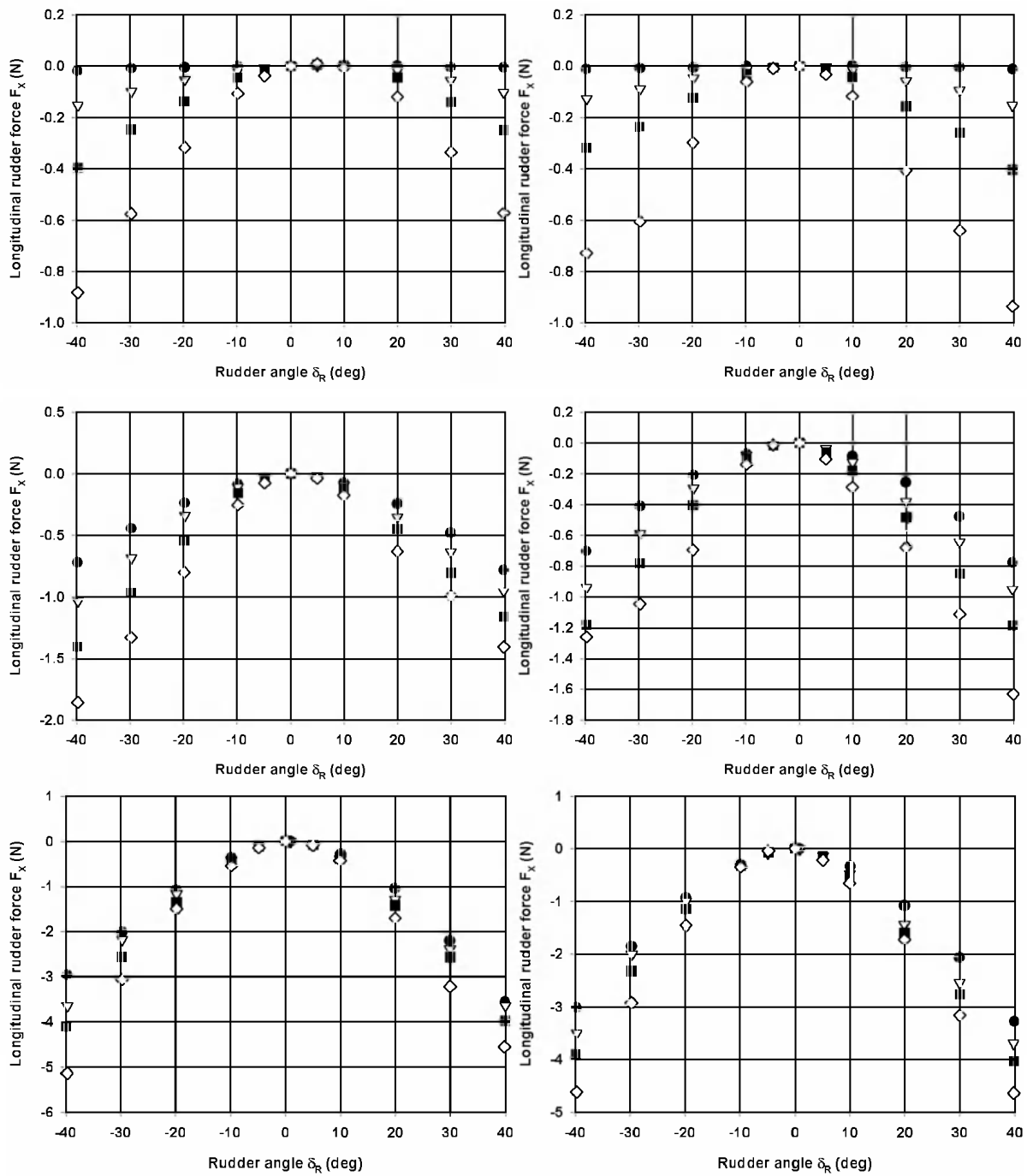
Figure 6.6 Model D, *quadrant 1*, longitudinal rudder force based on F_{RN}, stationary tests, β=-5 deg left and β=+5 deg right (legend see Figure 6.7, 0% top, 50% middle, 100% bottom)
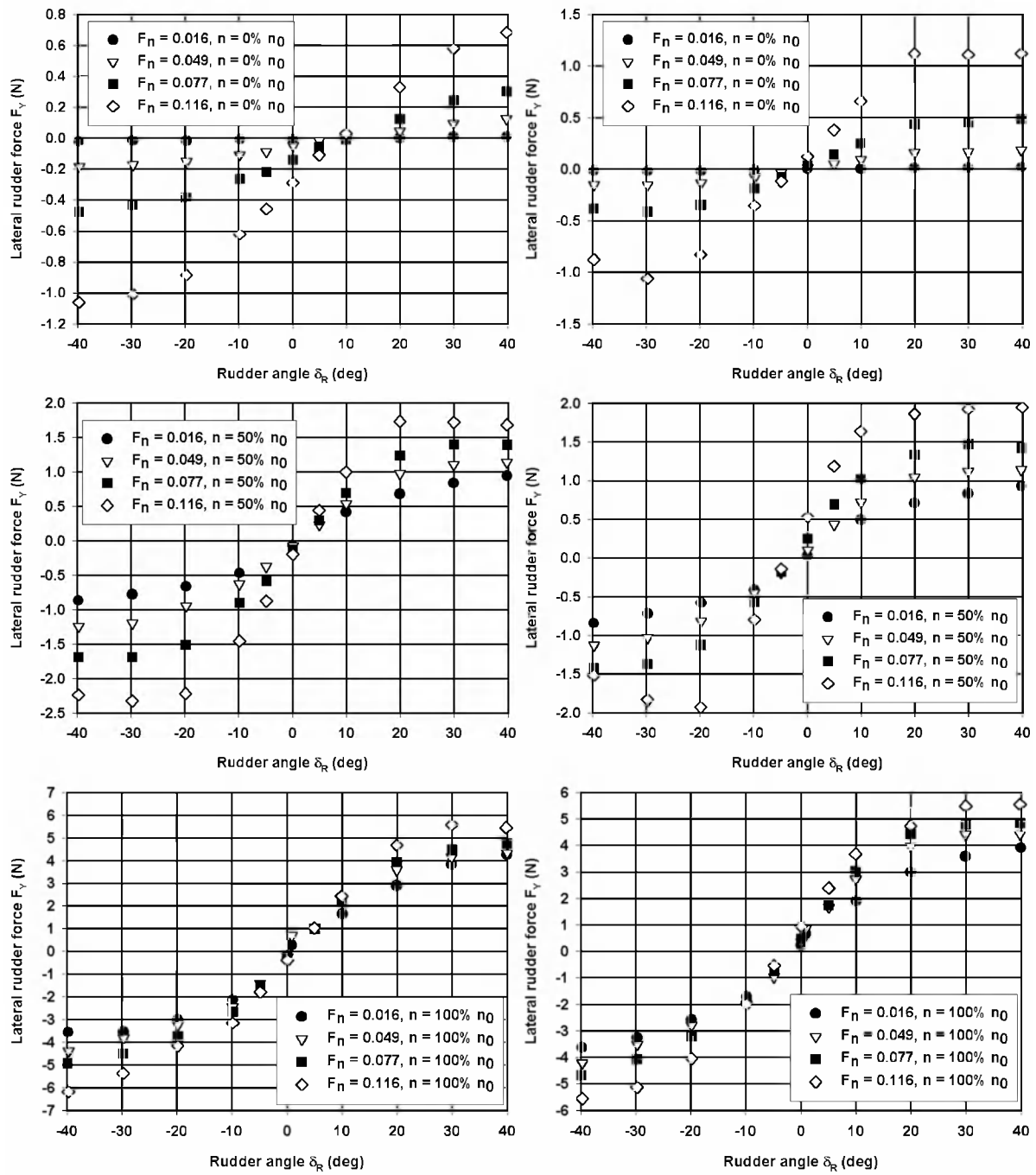
Figure 6.7 Model D, *quadrant 1*, lateral rudder force based on F_{RN}, stationary tests, β=-5 deg left and β=+5 deg right
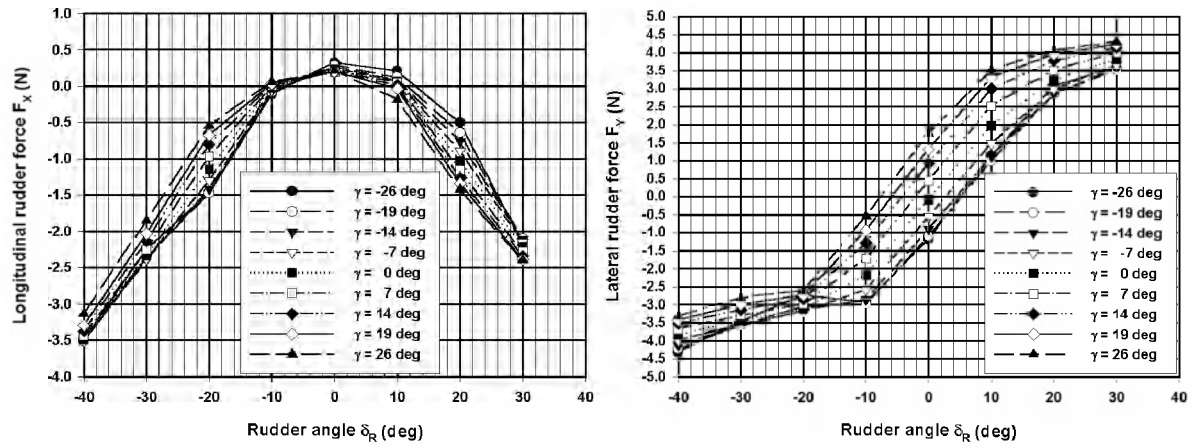
Figure 6.8 Model D, *quadrant 1*, longitudinal and lateral rudder force based on F_{RT} and F_{RN}, n=100% n_0, F_n=0.032 and β=0 deg
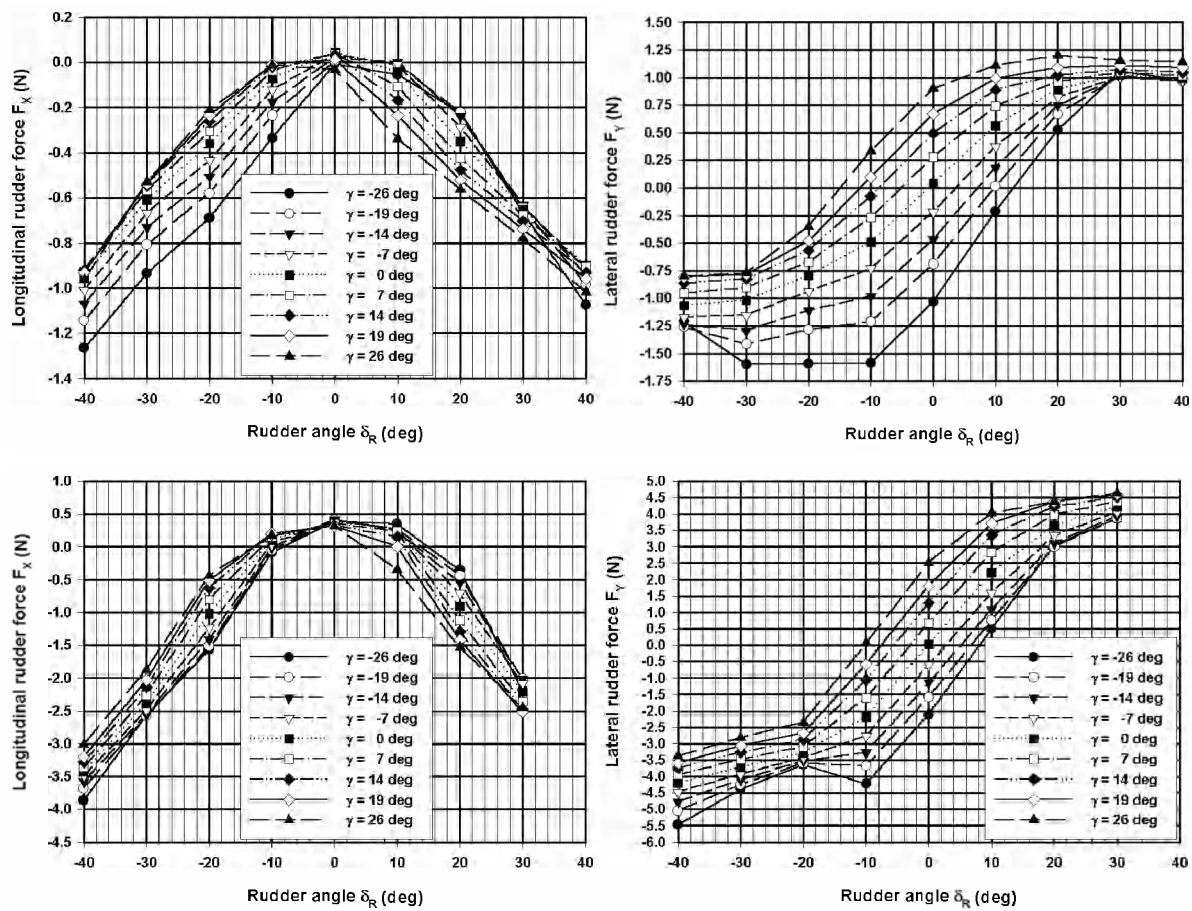
Figure 6.9 Model D, *quadrant 1*, longitudinal and lateral rudder force based on F_{RT} and F_{RN}, F_n=0.049 and β=0 deg (n=50% n_0 top, n=100% n_0 bottom)

333
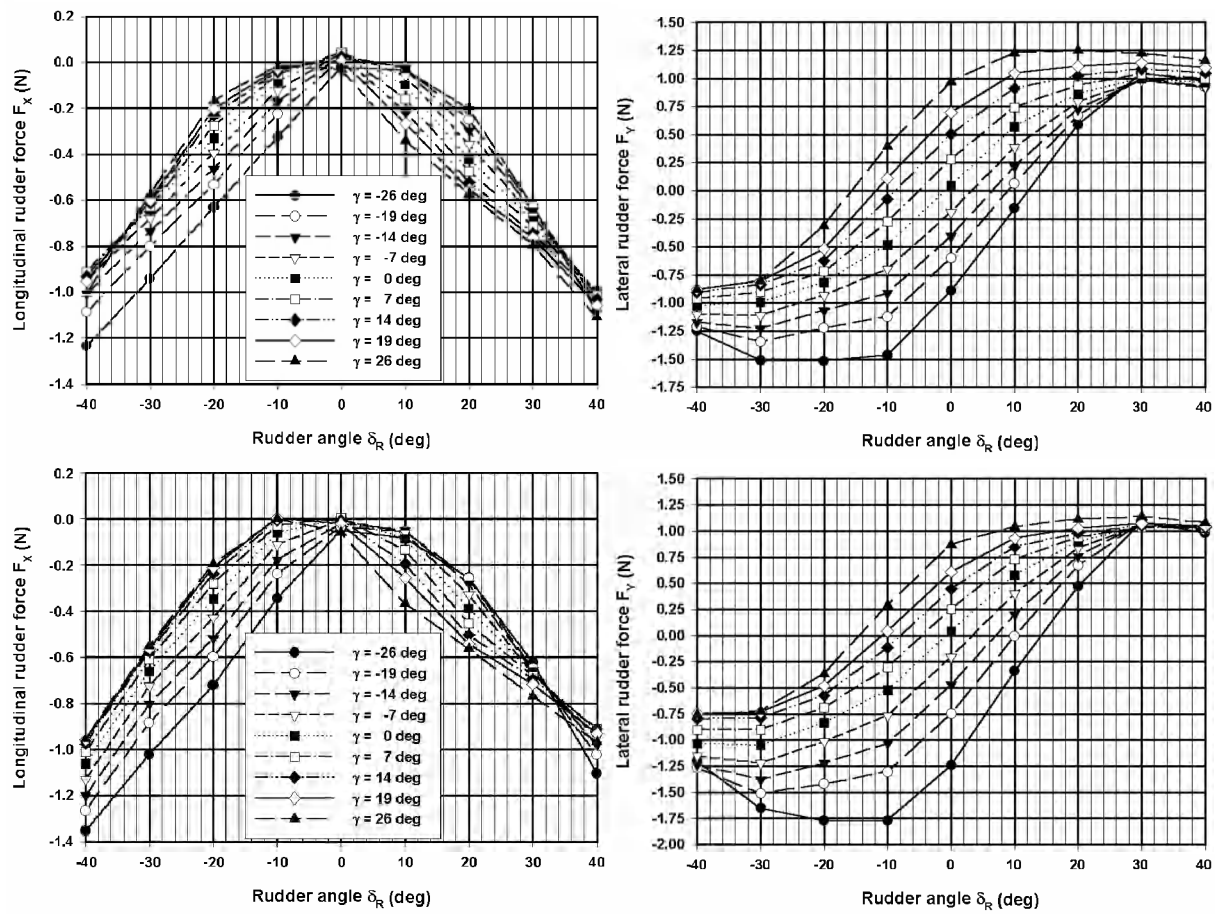
Figure 6.10 Model D, *quadrant 1*, longitudinal and lateral rudder force based on F_{RT} and F_{RN}, F_n=0.049 and n=50% n_0, (β=+2.5 deg top and β=-2.5 deg bottom)
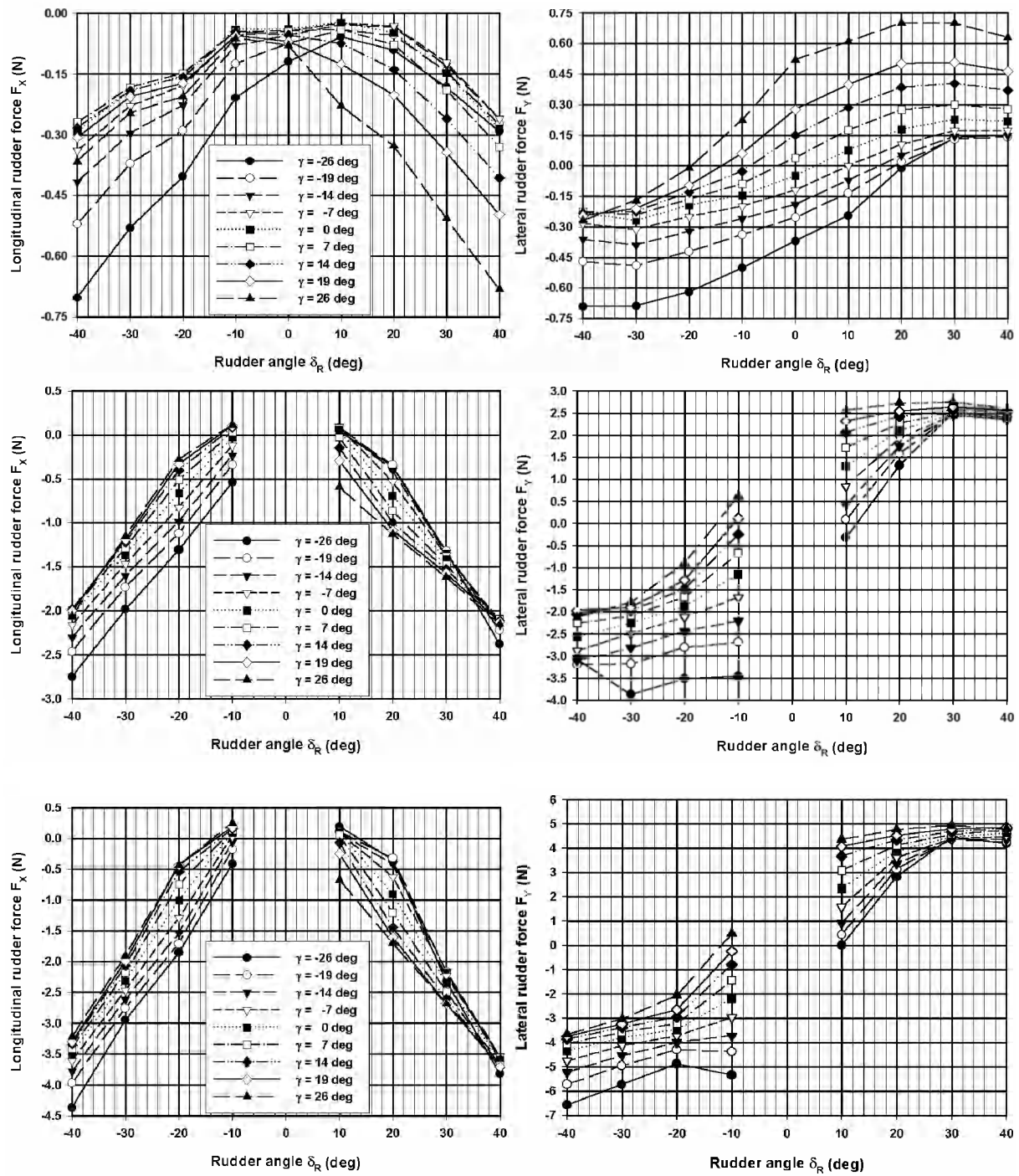
Figure 6.11 Model D, *quadrant 1*, longitudinal and lateral rudder force based on F_{RT} and F_{RN}, F_n=0.065 and β=0 deg (n=0% n_0 top, n=75% n_0 middle, n=100% n_0 bottom)
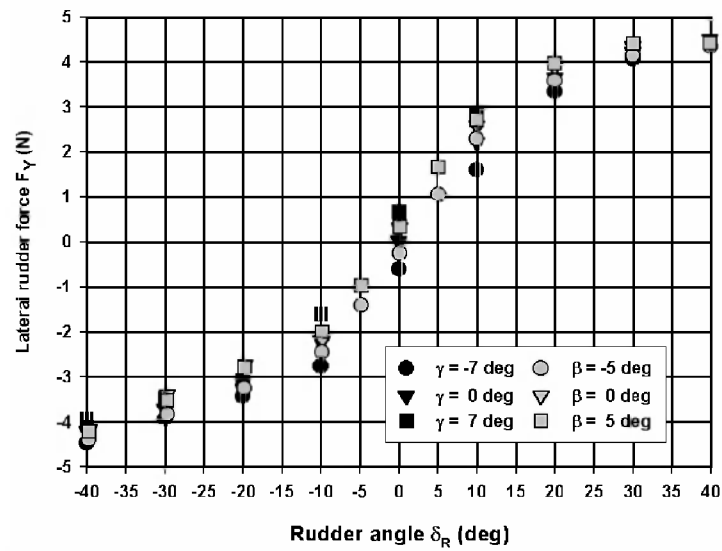
Figure 6.12 Model D, *quadrant 1*, comparison of lateral rudder force F_Y for stationary and PMM yaw tests (F_n=0.049, n=100% n_0)
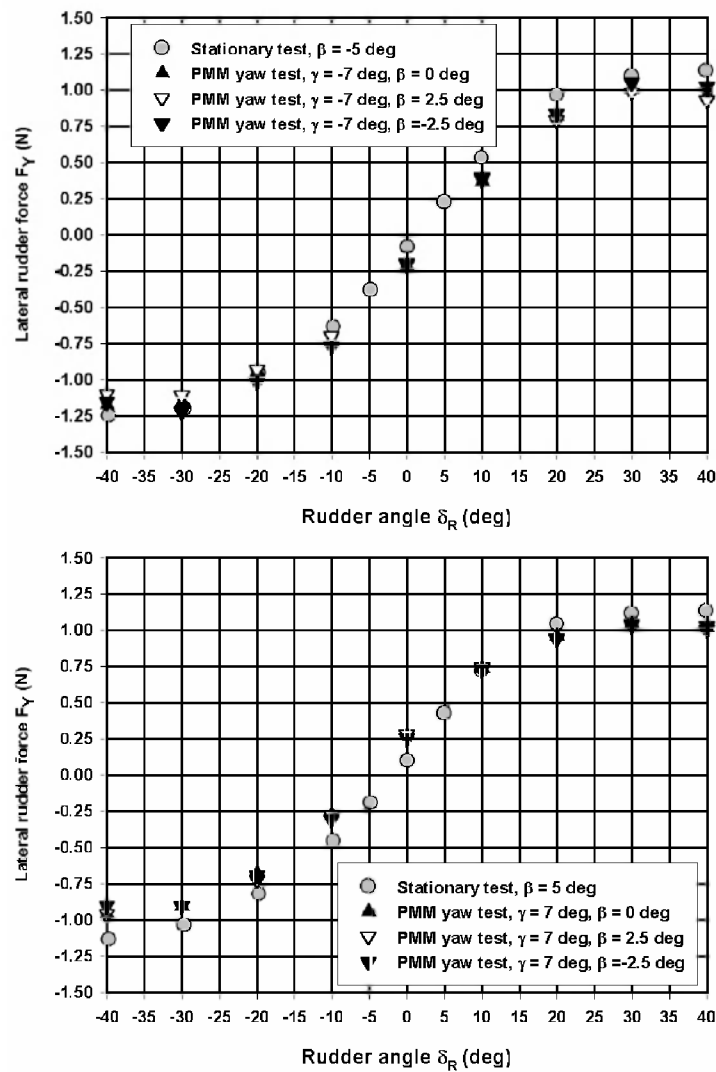
Figure 6.13 Model D, *quadrant 1*, comparison of lateral rudder force F_Y for stationary and PMM yaw tests (F_n=0.049, n=50% n_0)
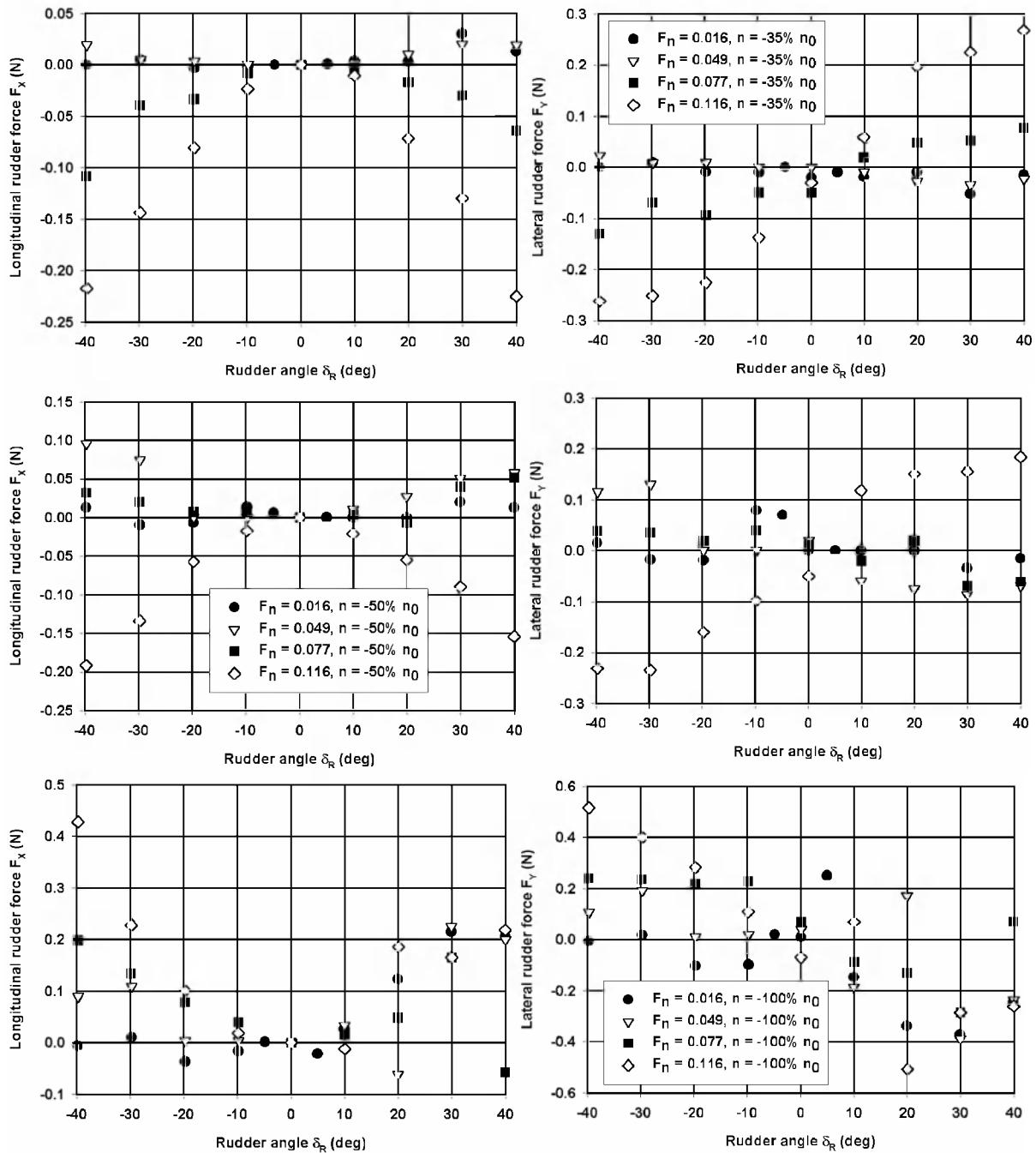
Figure 6.14 Model D, *quadrant 2*, longitudinal and lateral rudder force based on F_{RN}, stationary tests with varying Froude number and propeller rate
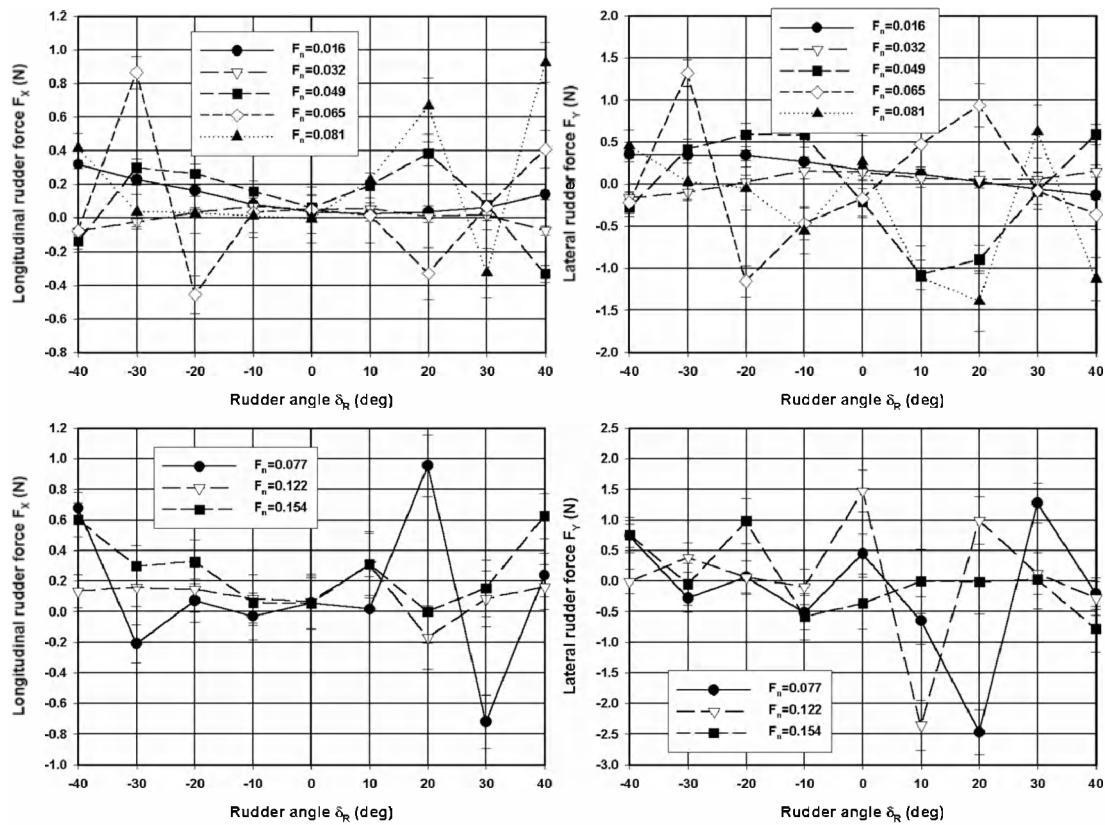
Figure 6.15 Model D, *quadrant 2*, tabular model for measured longitudinal and lateral rudder force based on F_{RT} and F_{RN}, -100% of n_0, multi-modal tests type A with varying Froude number
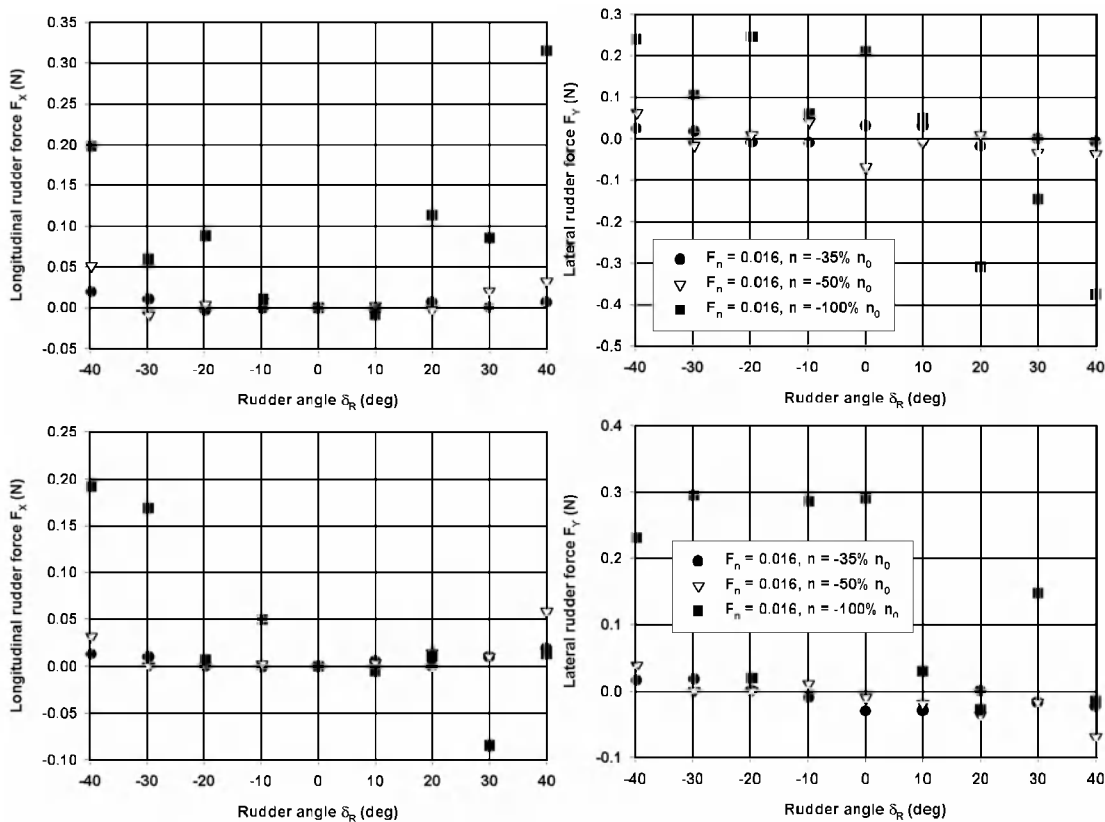
Figure 6.16 Model D, *quadrant 2*, influence of propeller loading on longitudinal and lateral rudder force based on F_{RN}, stationary tests, β=-5 deg top, β=+5 deg bottom
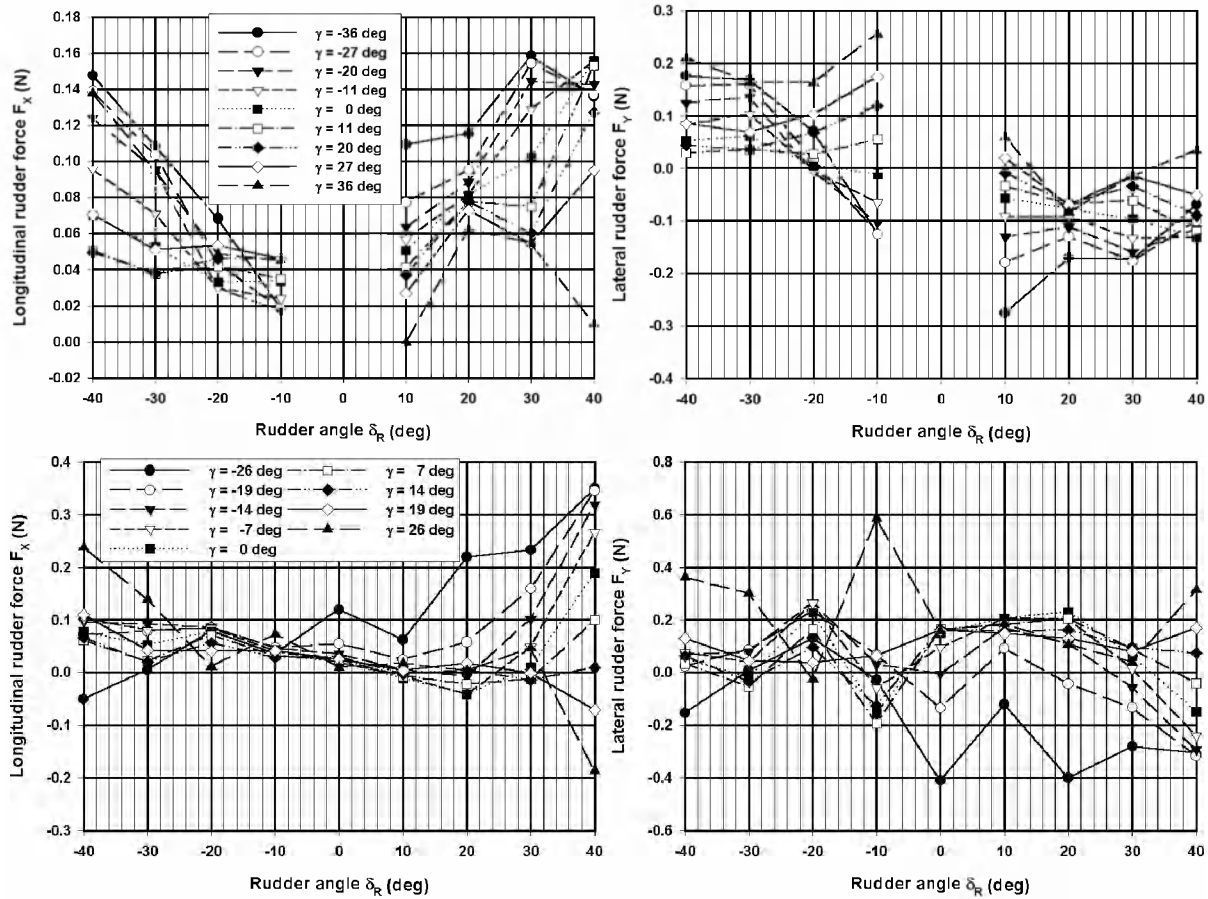
Figure 6.17 Model D, *quadrant 2*, longitudinal and lateral rudder force during PMM yaw tests (F_n=0.016, n=-100%n_0, top and F_n=0.049, n=-100%n_0, bottom)
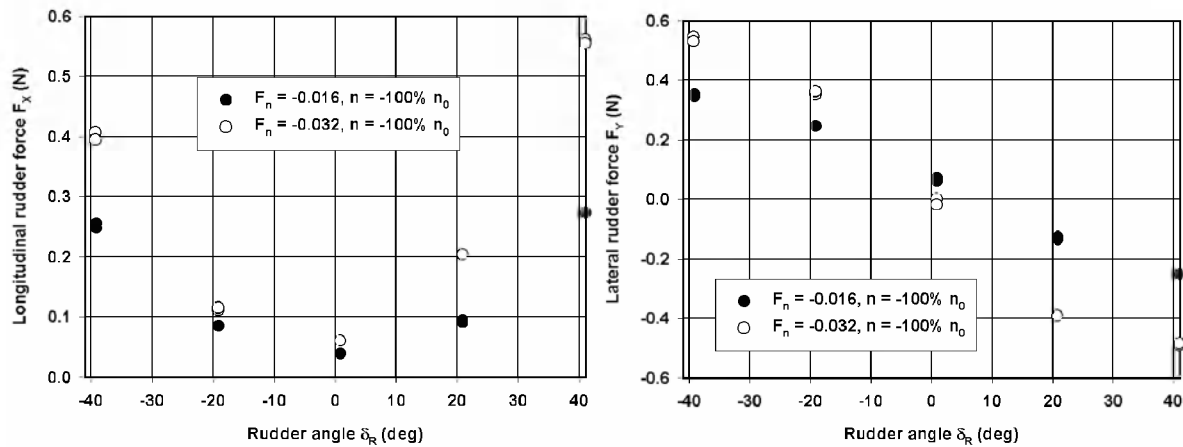
Figure 6.18 Model D, *quadrant 3*, influence of backward velocity on longitudinal and lateral rudder force based on F_{RT} and F_{RN}, stationary tests
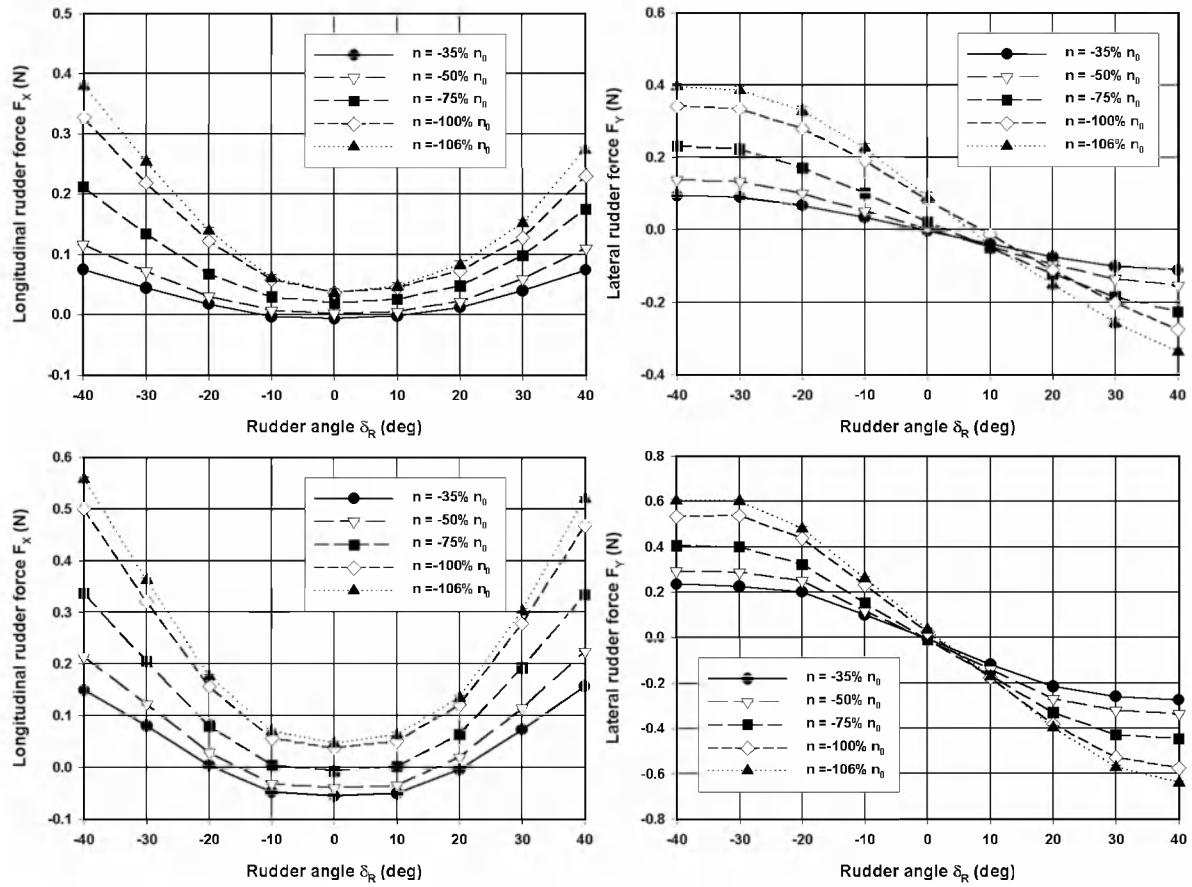
Figure 6.19 Model D, *quadrant 3*, tabular model for measured longitudinal and lateral rudder force based on F_{RT} and F_{RN}, multi-modal tests type A with varying propeller rate n (F_n=-0.016, top and F_n=-0.032, bottom)
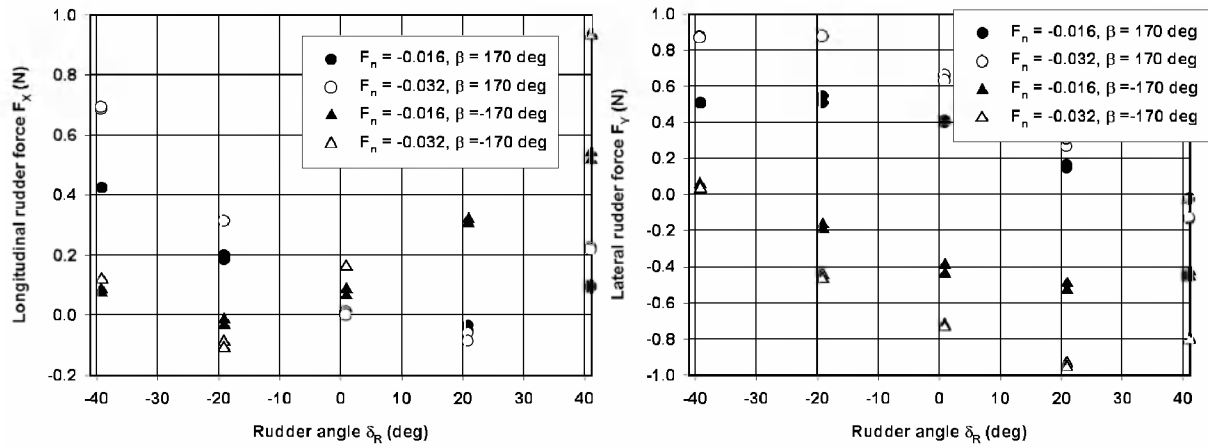

Figure 6.20 Model D, *quadrant 3*, influence of backward velocity and drift angle on longitudinal and lateral rudder force based on F_{RT} and F_{RN}, stationary tests, n=-100%n_0
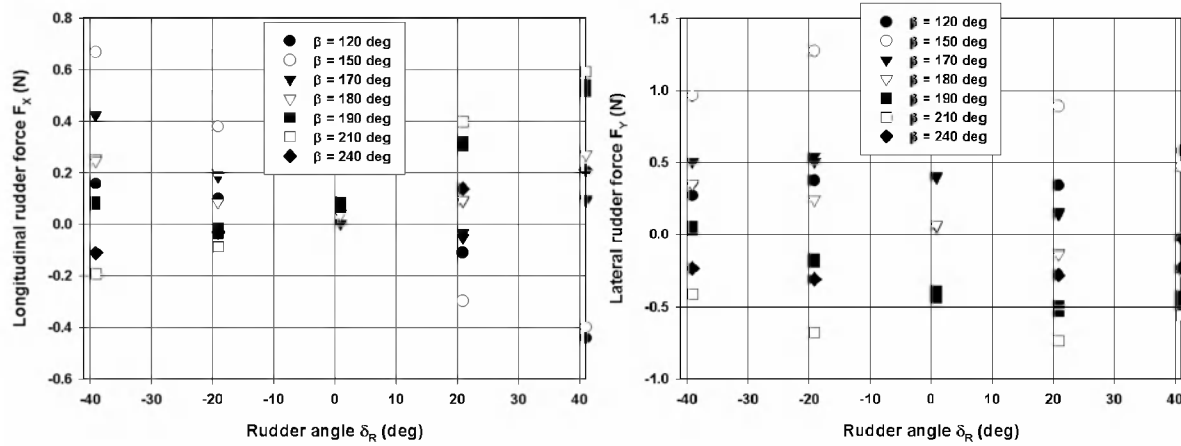
Figure 6.21 Model D, *quadrant 3*, influence of drift angle on longitudinal and lateral rudder force based on F_{RT} and F_{RN}, stationary tests, F_n=-0.016 and n=-100%n_0
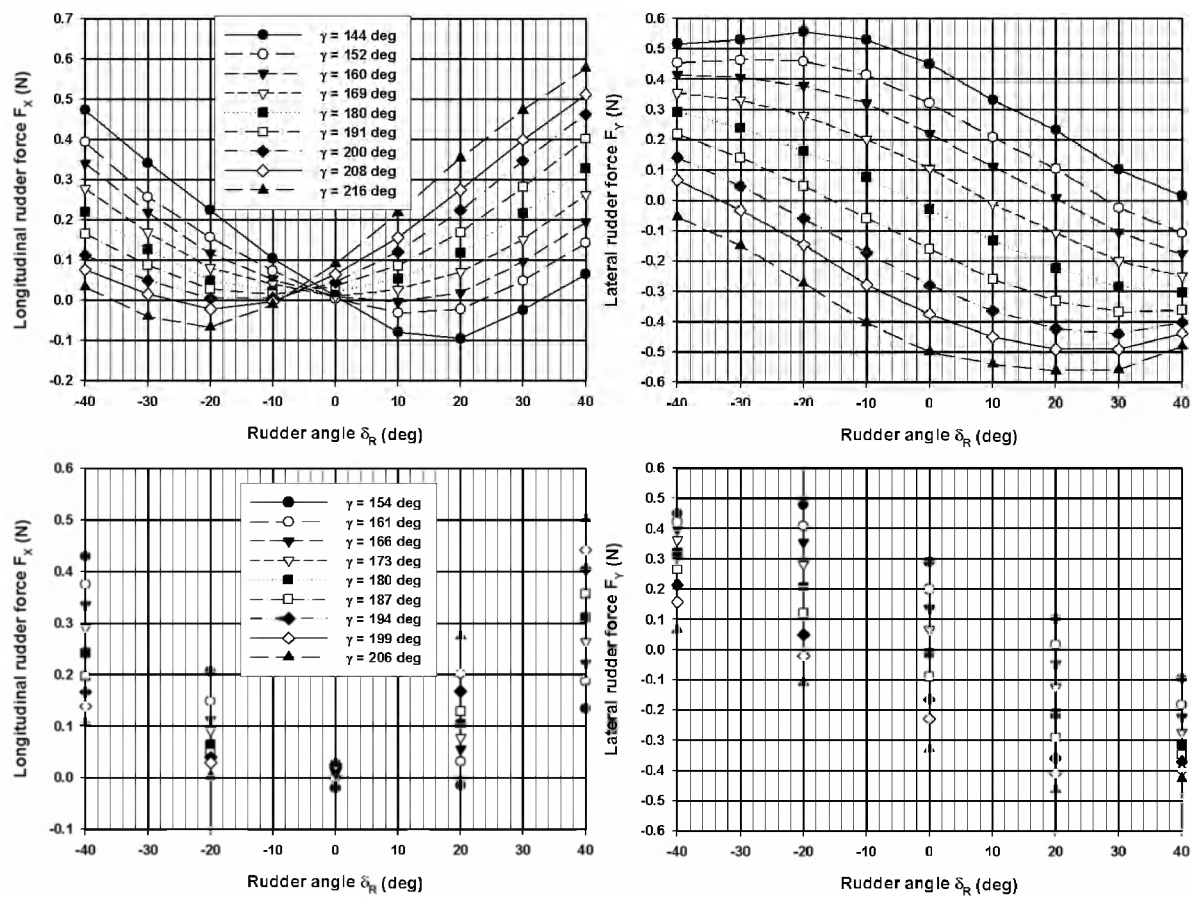

Figure 6.22 Model D, *quadrant 3*, longitudinal and lateral rudder force based on F_{RT} and F_{RN}, PMM yaw tests, F_n=-0.016 and n=-100%n_0 (period=72s, top, and period=108s, bottom)
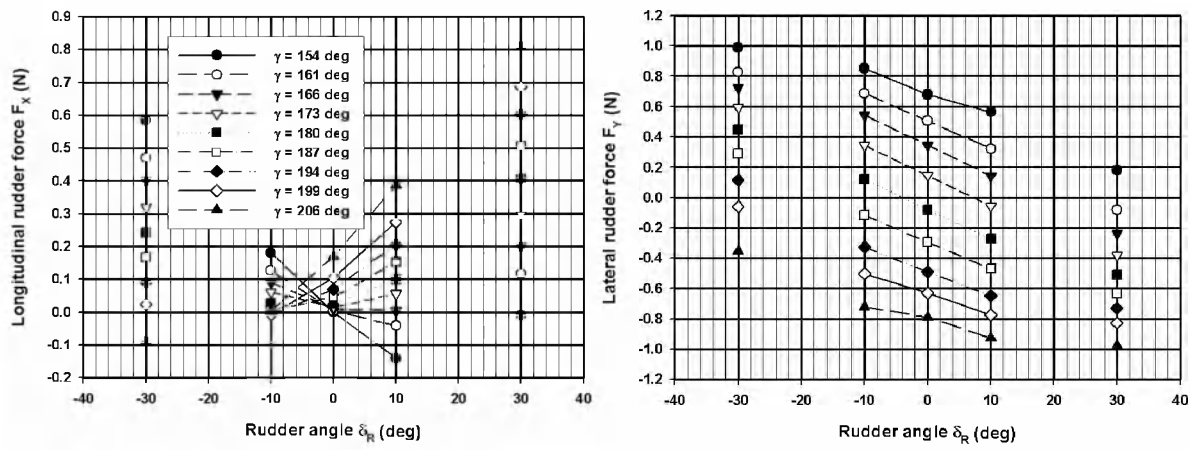
Figure 6.23 Model D, *quadrant 3*, longitudinal and lateral rudder force based on F_{RT} and F_{RN}, PMM yaw tests, F_n=-0.032 and n=-100%n_0 (period=54s)
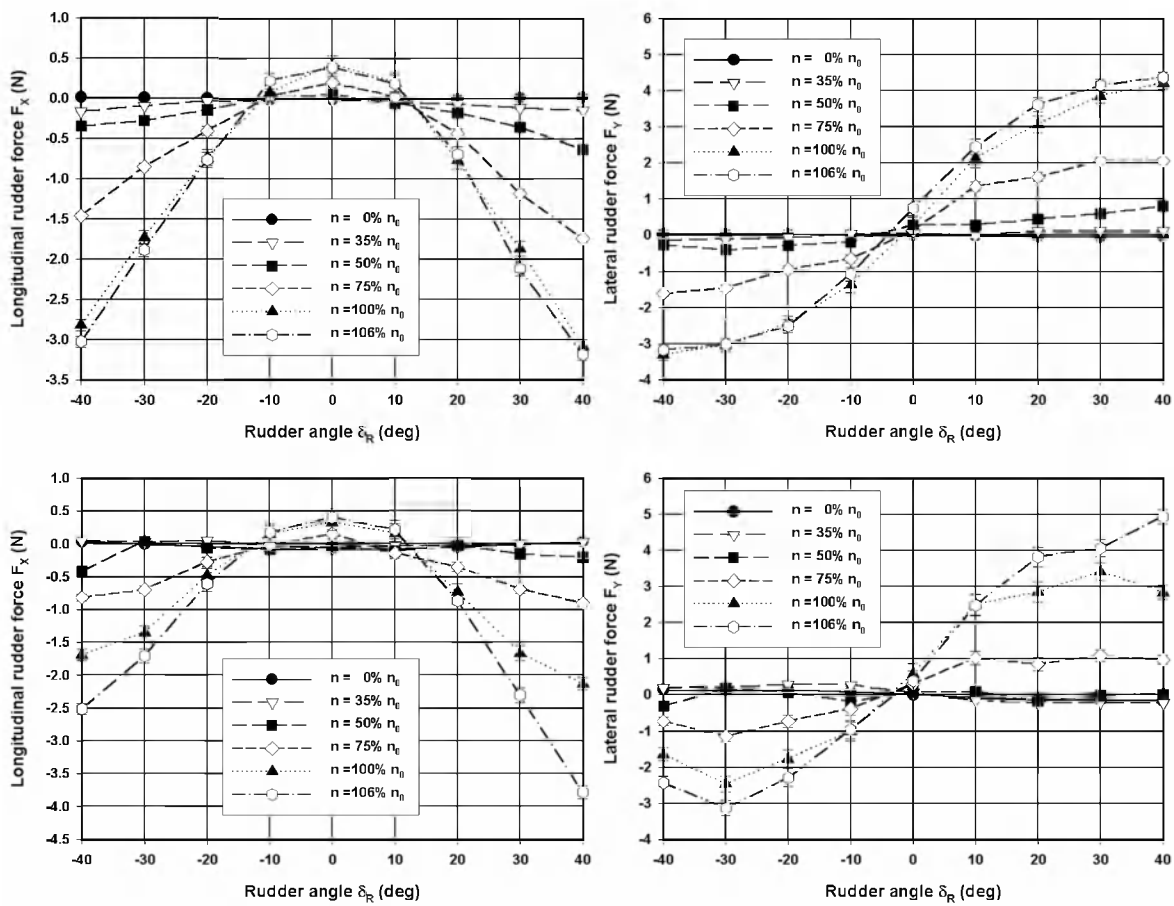

Figure 6.24 Model D, *quadrant 4*, tabular model of measured longitudinal and lateral rudder force based on F_{RT} and F_{RN}, multi-modal tests type A with varying propeller rate n (F_n=-0.016, top and F_n=-0.032, bottom)
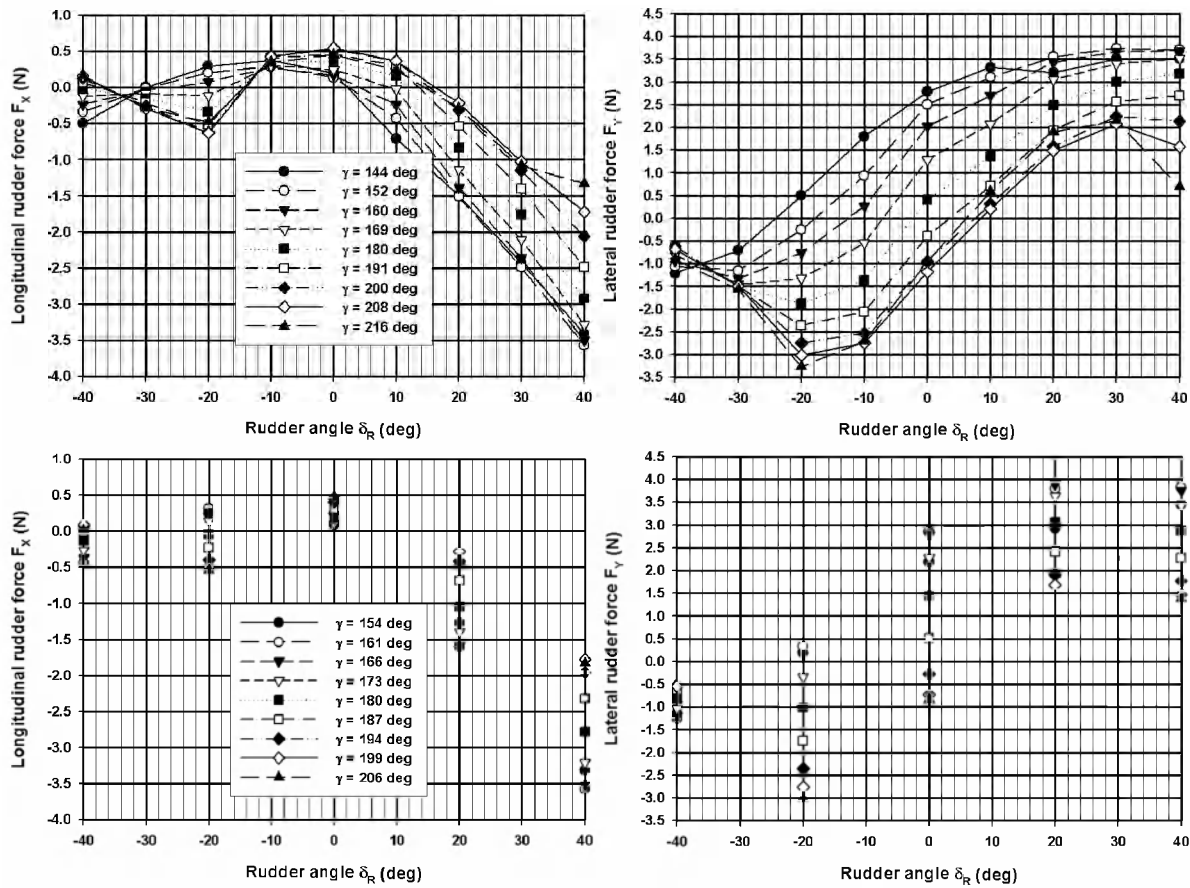
Figure 6.25 Model D, *quadrant 4*, longitudinal and lateral rudder force based on F_{RT} and F_{RN}, PMM yaw tests, F_n=-0.016 and n=100%n_0 (period=72s, top, and period=108s, bottom)
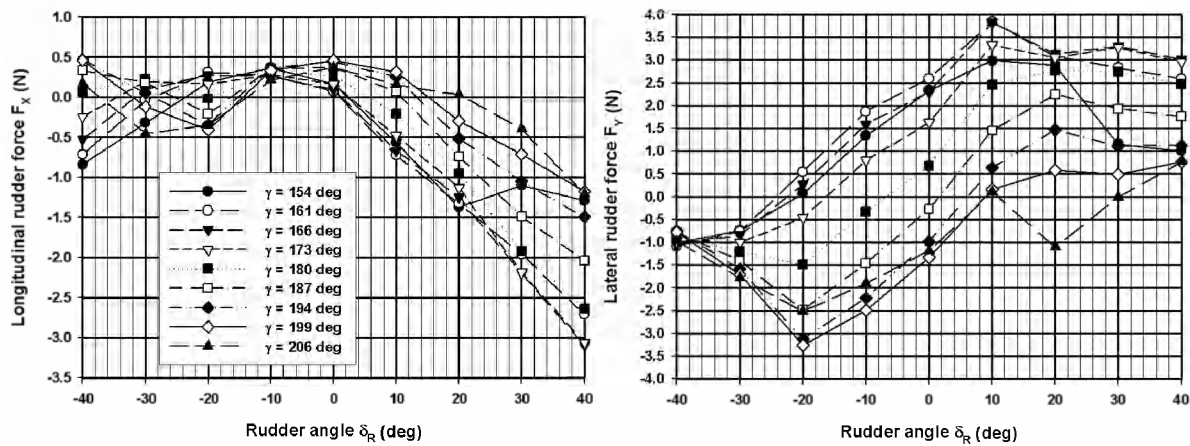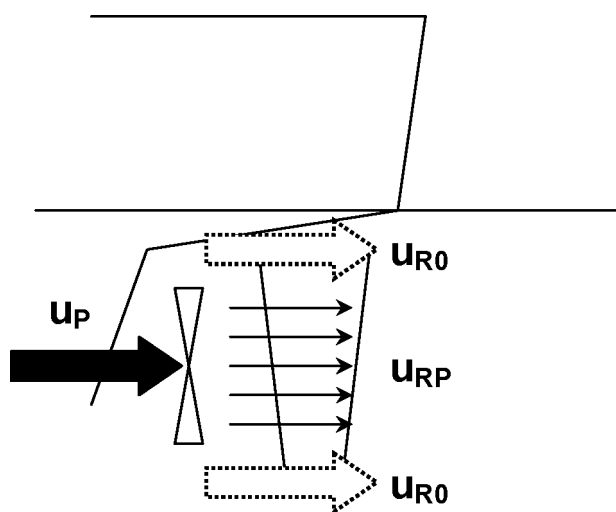

Figure 6.26 Model D, *quadrant 4*, longitudinal and lateral rudder force based on F_{RT} and F_{RN}, PMM yaw tests, F_n=-0.032 and n=100%n_0 (period=54s)

343

Group-MMG	$u_{RP} = u_{R0} + K_m u_{A\infty}$ with $u_{A\infty}$ function of u_P
HSVA model	$u_{RP} = u_P + K_m u_{A\infty}$ ahead (u>0) $u_{RP} = u_P + (1 - K_m)u_{A\infty}$ astern (u<0) with $u_{A\infty}$ function of u_P
Mod582 model	$u_{RP} = u_{R0} + K_m u_{A\infty}$ with $u_{A\infty}$ function of u_{R0}

Figure 6.27 Schematic representation of the inflow velocity u_{RP} into the rudder due to the propeller slipstream
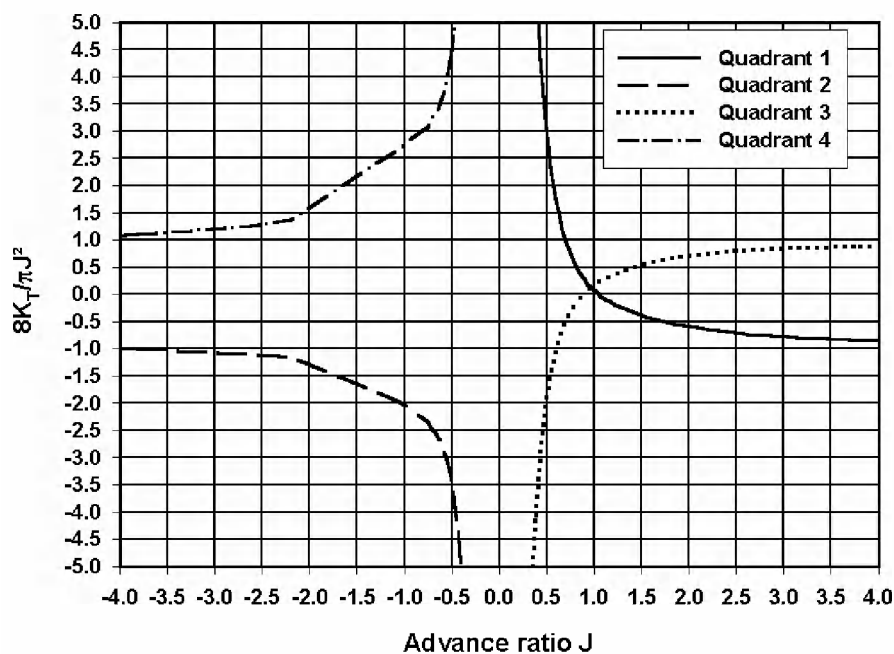
Figure 6.28 Model D, propeller loading value $8K_T/\pi J^2$ based on the open water K_T curve
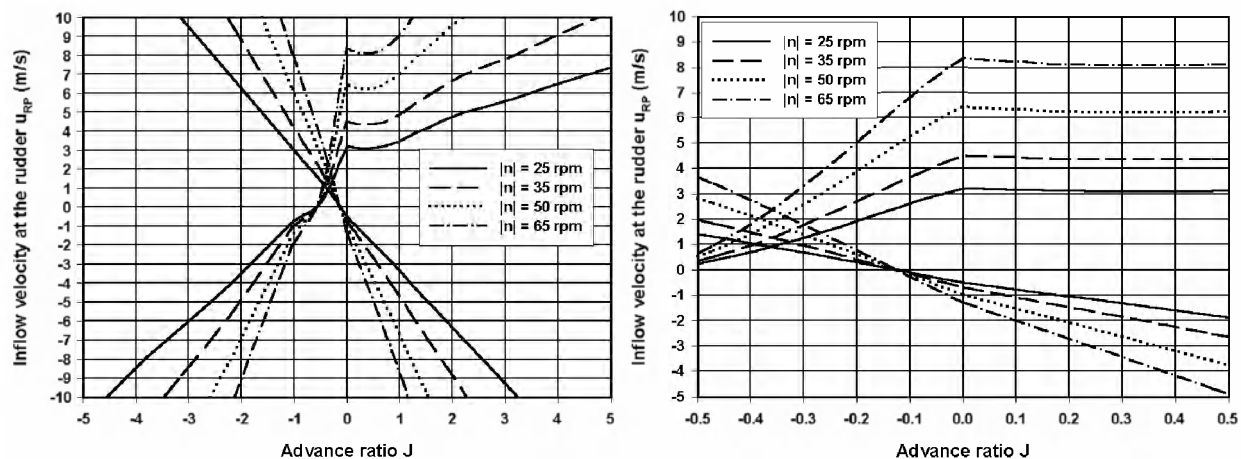
Figure 6.29 A theoretical calculation of the inflow velocity at the rudder due to the slipstream (containership D, K_m=0.85, D_P=8.145 m full scale, detail at right figure)

344
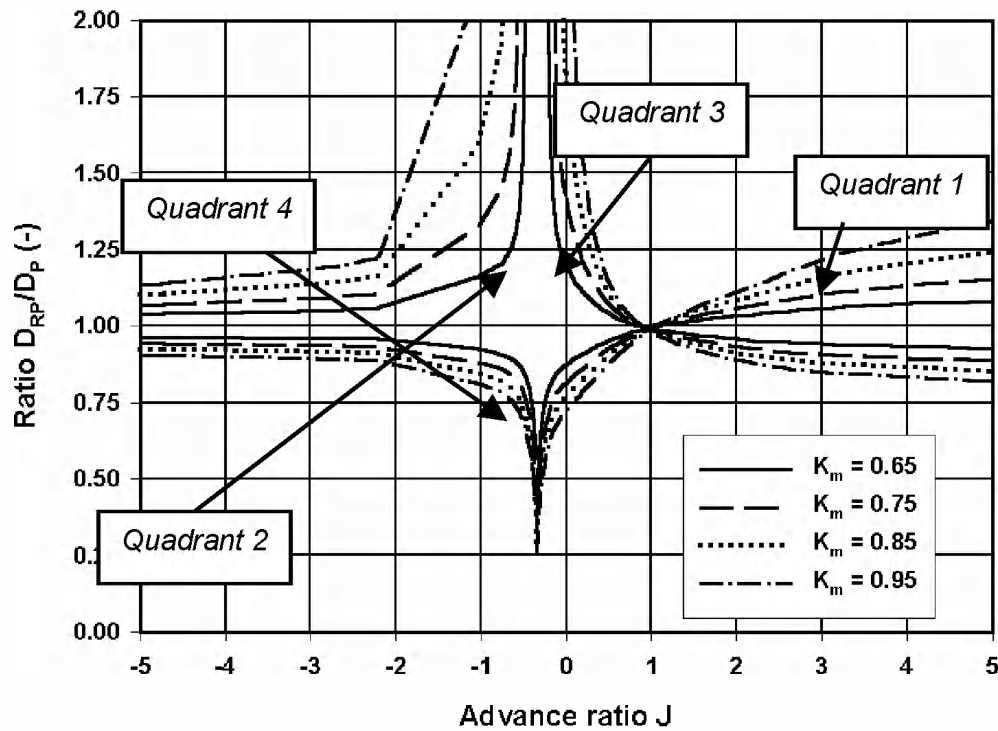
Figure 6.30 A theoretical calculation of ratio D_{RP}/D_P for varying value K_m (containership D, D_P=8.145 m full scale)
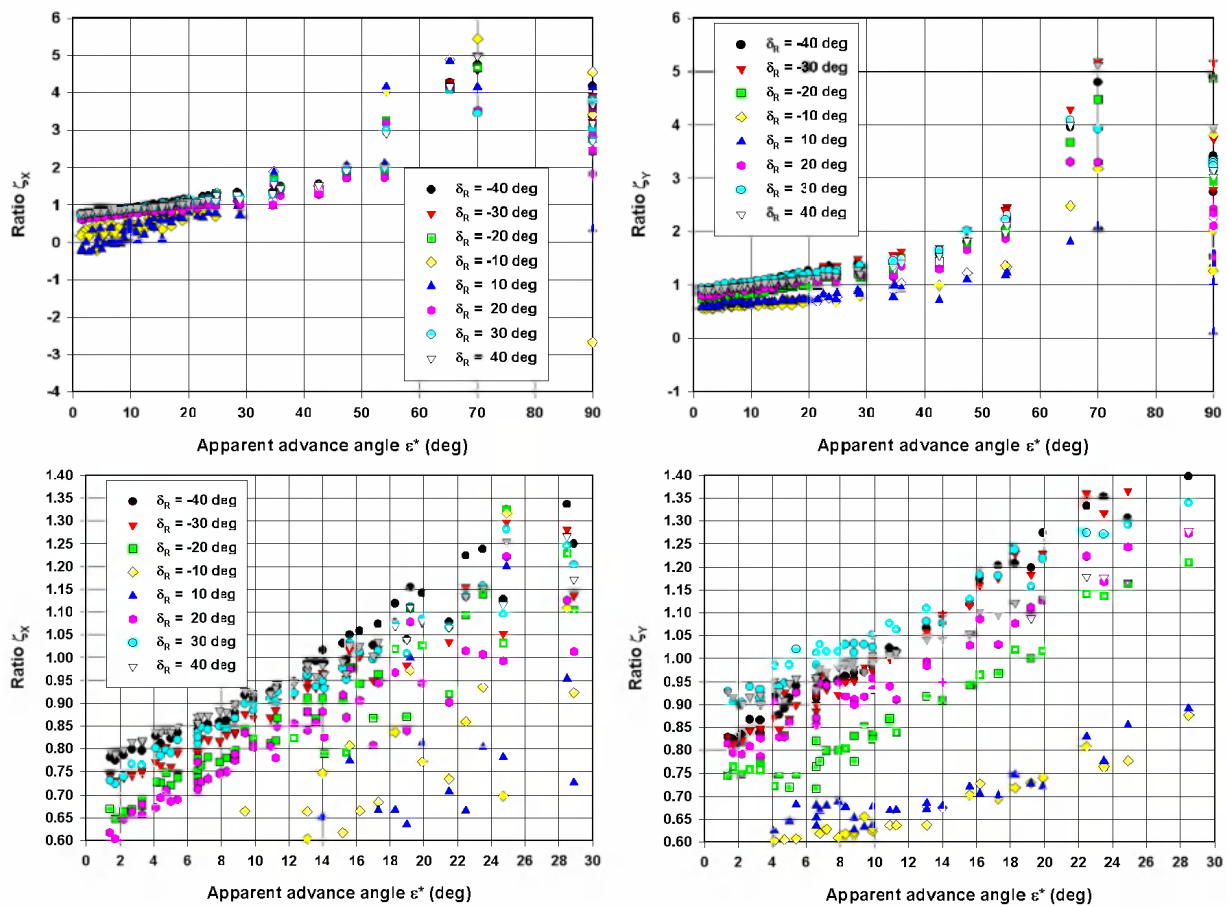
Figure 6.31 Model D, *quadrant* 1, calculated ratios ζ_X and ζ_Y for ship model D and equation (6.35) (figures at the bottom are a detail of the figures at the top)
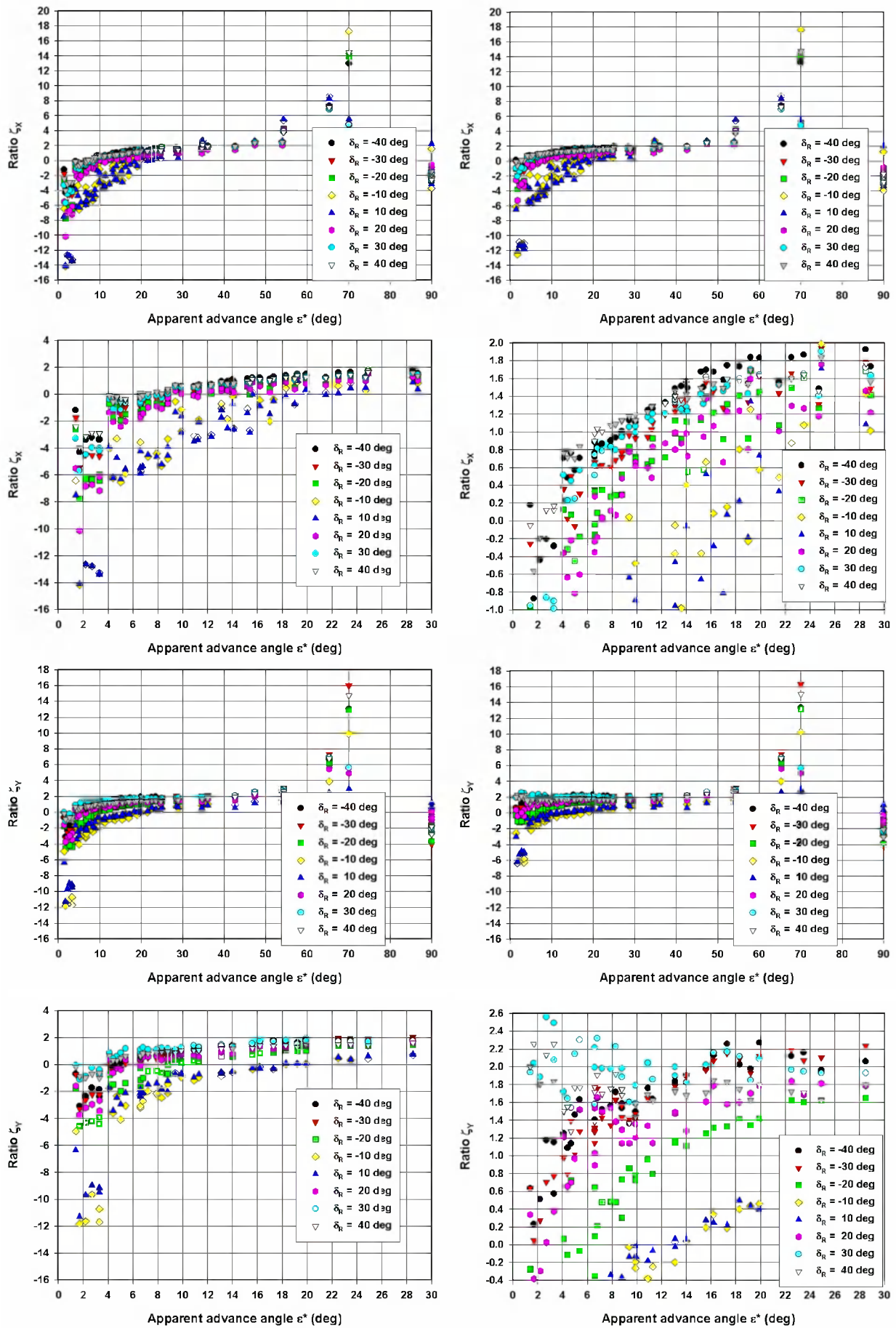
Figure 6.32 Model D, *quadrant* 1, calculated ratios ζ_X and ζ_Y for ship model D and equation (6.36) (K_m=0.94 left and K_m=0.80 right)
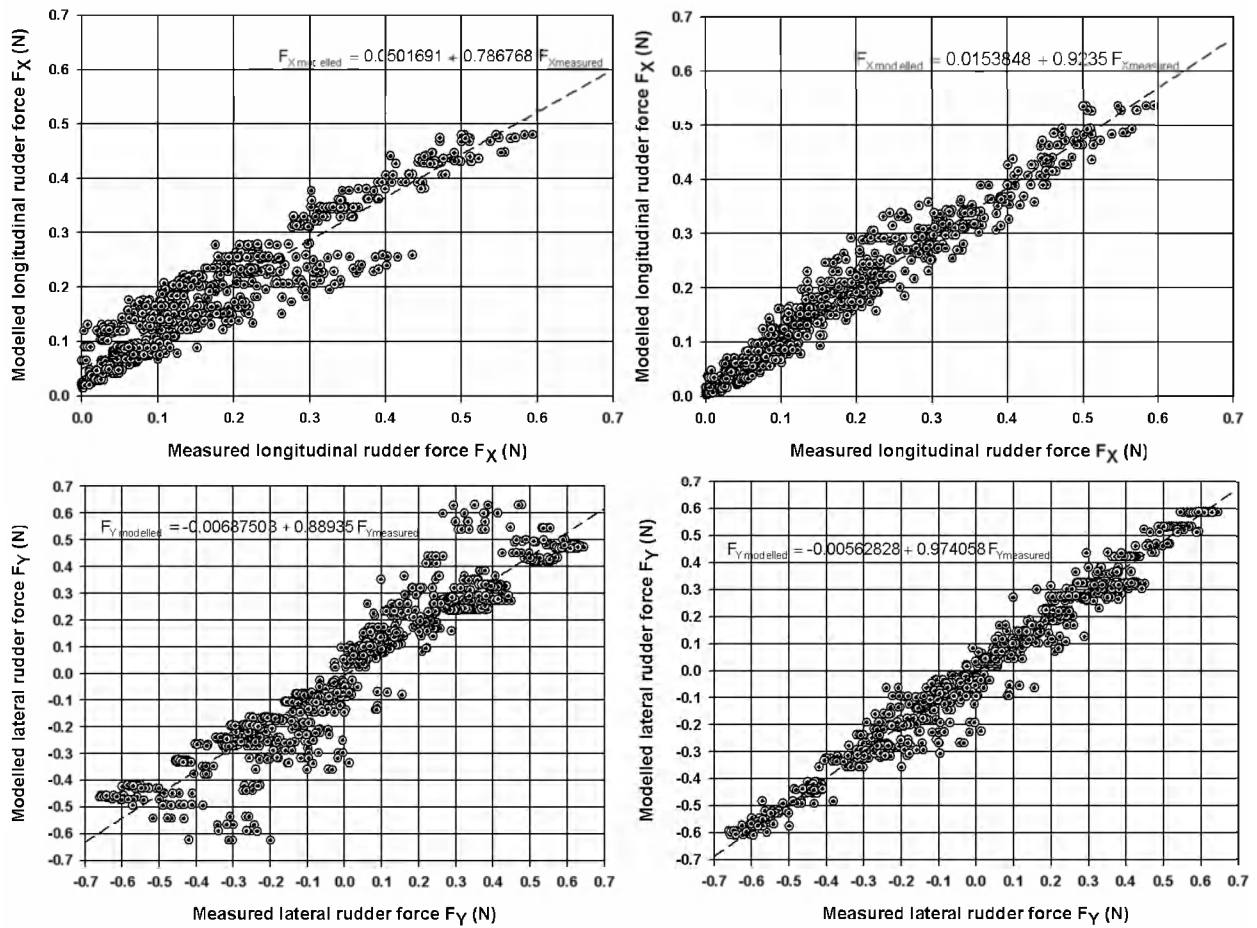
Figure 6.33 Model D, *quadrant 3*, comparison of modelled and measured rudder forces (equation (6.22) left and (6.32) right)
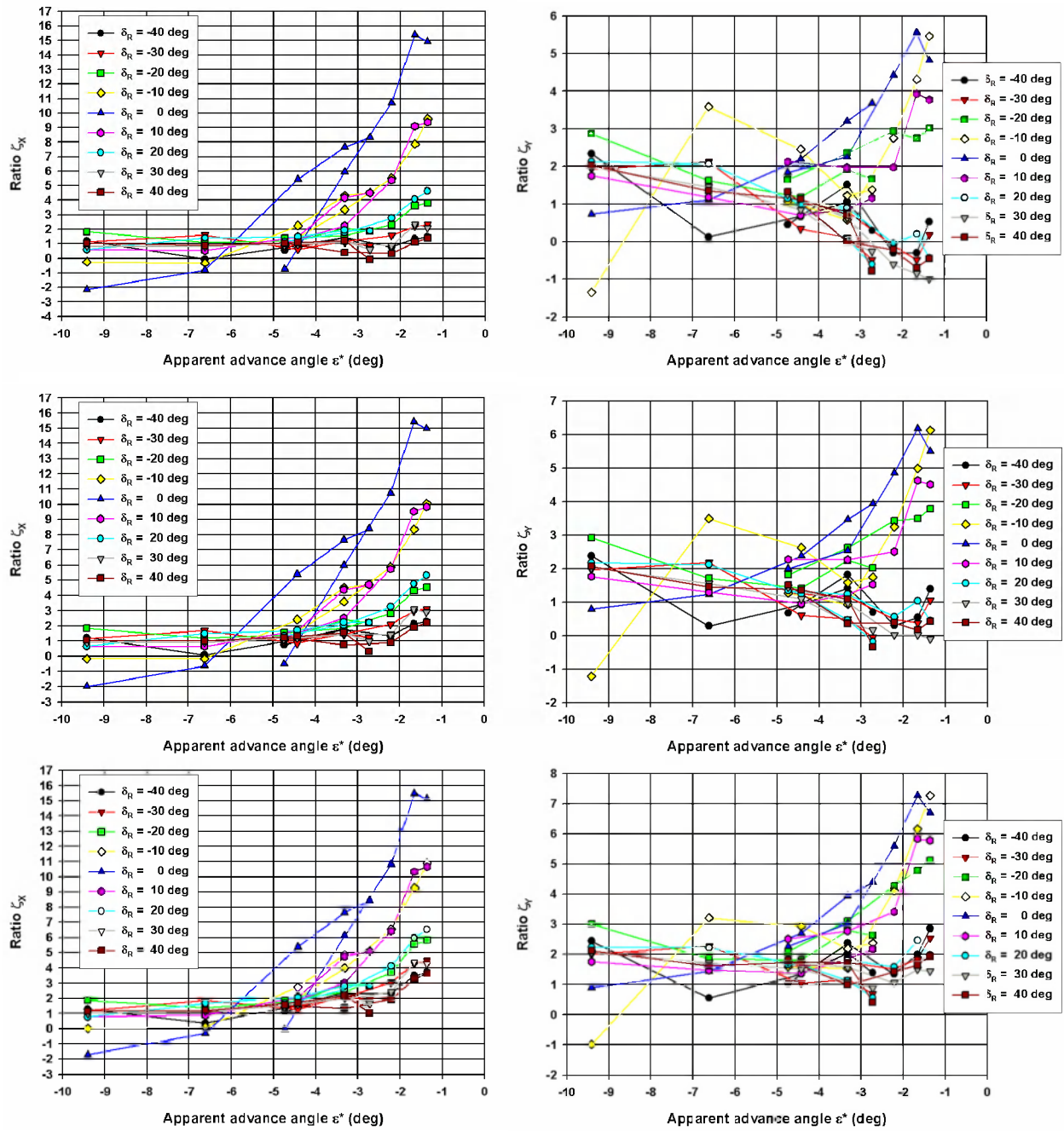
Figure 6.34 Model D, *quadrant 4*, calculated ratios ζ_X and ζ_Y based on equations (6.33) and (6.34) (K_m=0.94 top, K_m=0.85 middle and K_m=0.80 bottom)
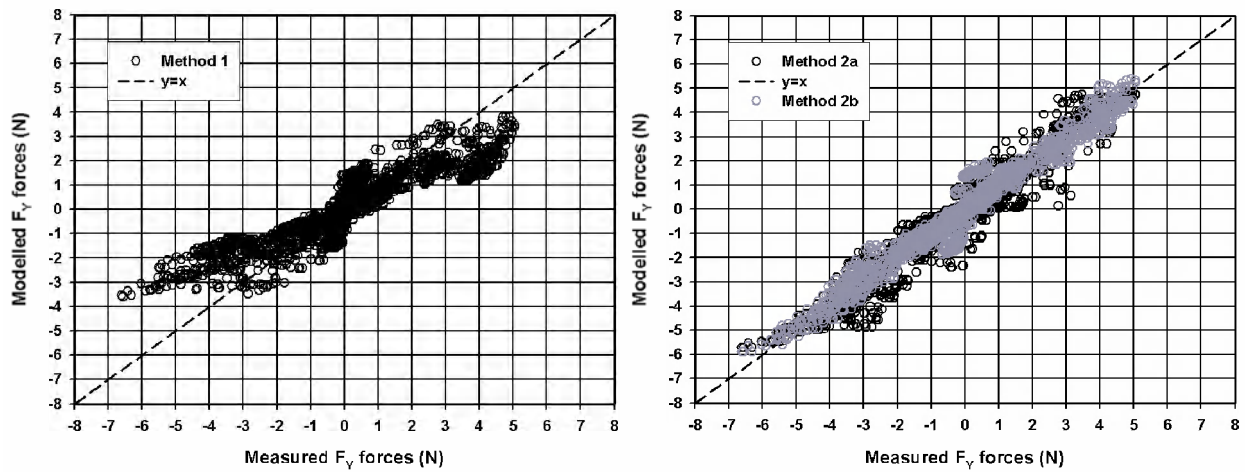
Figure 6.35 Model D, data set of PMM yaw tests, comparison of measured and modelled values for lateral rudder force F_Y according to the prediction methods 1, 2a and 2b.
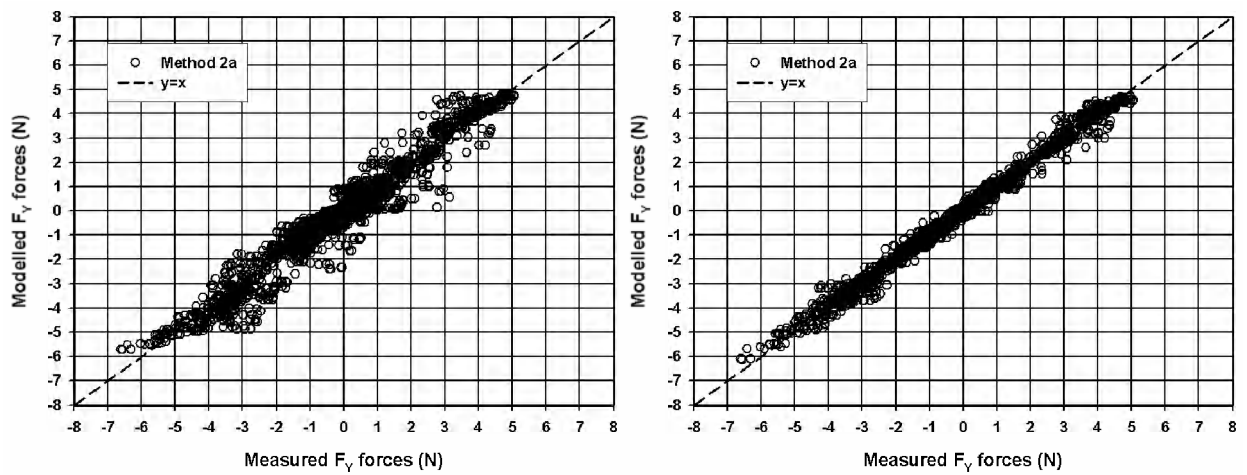
Figure 6.36 Model D, data set of PMM yaw tests, comparison of measured and modelled values for lateral rudder force F_Y according to method 2a without (left) and with (right) a distinction for the advance angle ε^*
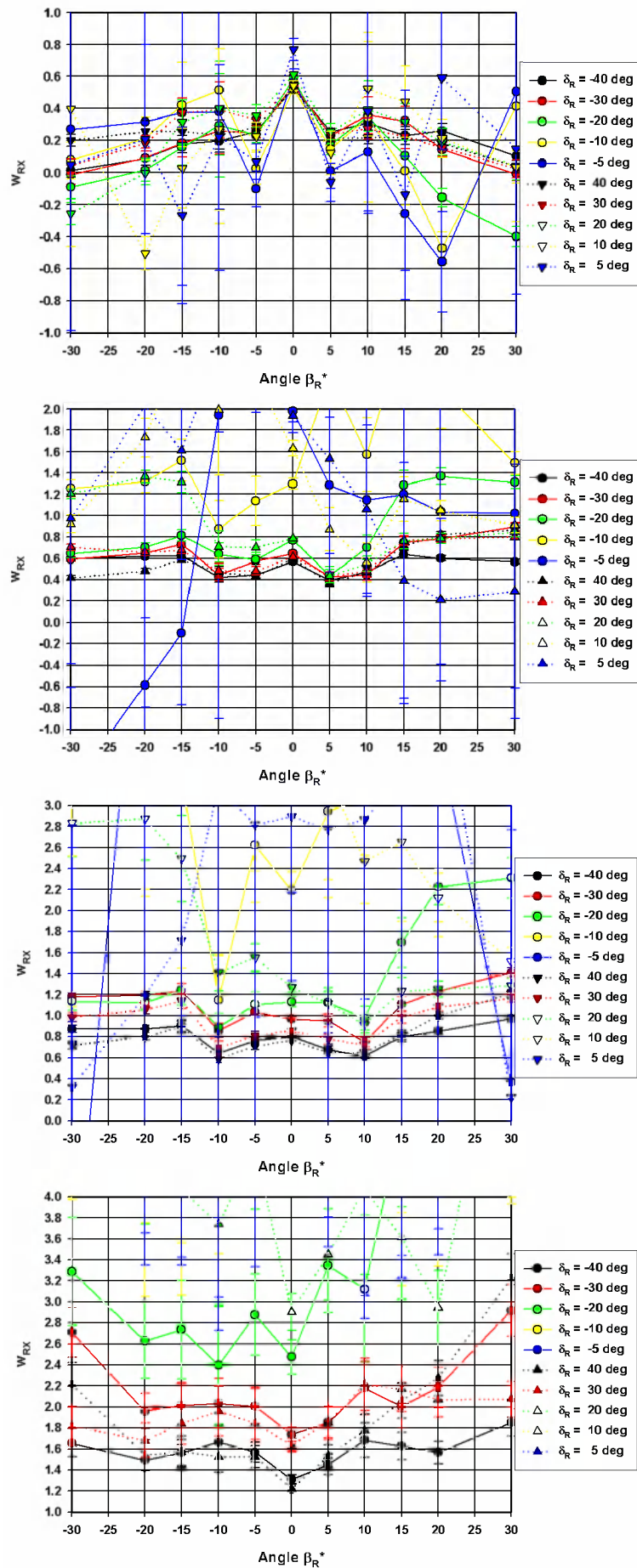
Figure 6.37 Model D, *quadrant 1*, wake factor $w_{R,X}$ as function of rudder angle δ_R and inflow angle β_R^* according to rudder model 1 (from top to bottom, $\varepsilon^* = 90$ deg, 22 deg, 6.65 deg and 2.75 deg)

Figure 6.38 Model D, *quadrant 1*, wake factor $w_{R,Y}$ as function of rudder angle δ_R and inflow angle β_R^* according to rudder model 1 (from top to bottom, $\varepsilon^* = 90$ deg, 22 deg, 6.65 deg and 2.75 deg)

Figure 6.39 Model D, *quadrant 1*, wake factors $w_{R,X}$ and $w_{R,Y}$ and coefficients $K_{m,X}$ and $K_{m,Y}$ as function of rudder angle δ_R and inflow angle $\beta_R{}^*$ according to rudder model 2
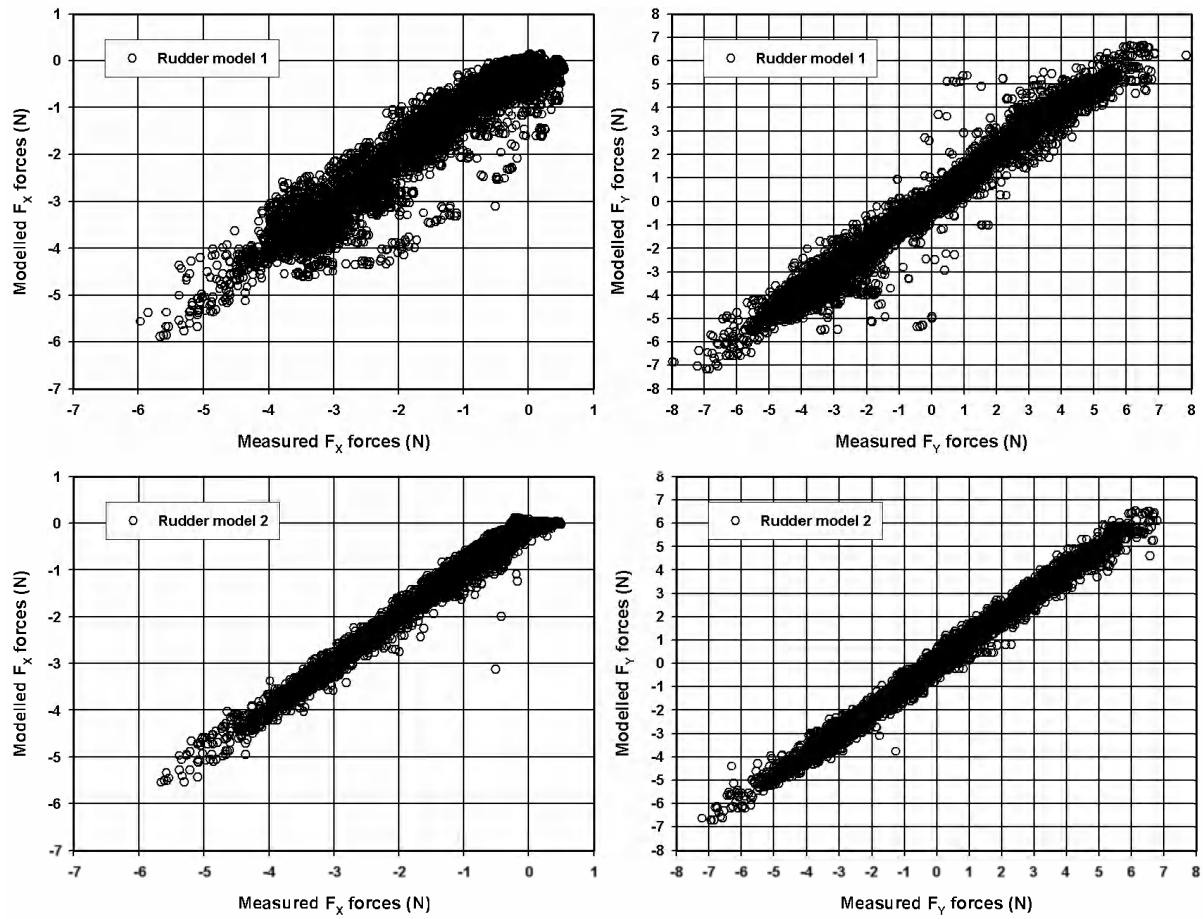
Figure 6.40 Model D, *quadrant 1*, comparison of rudder models for longitudinal and lateral rudder forces F_X and F_Y
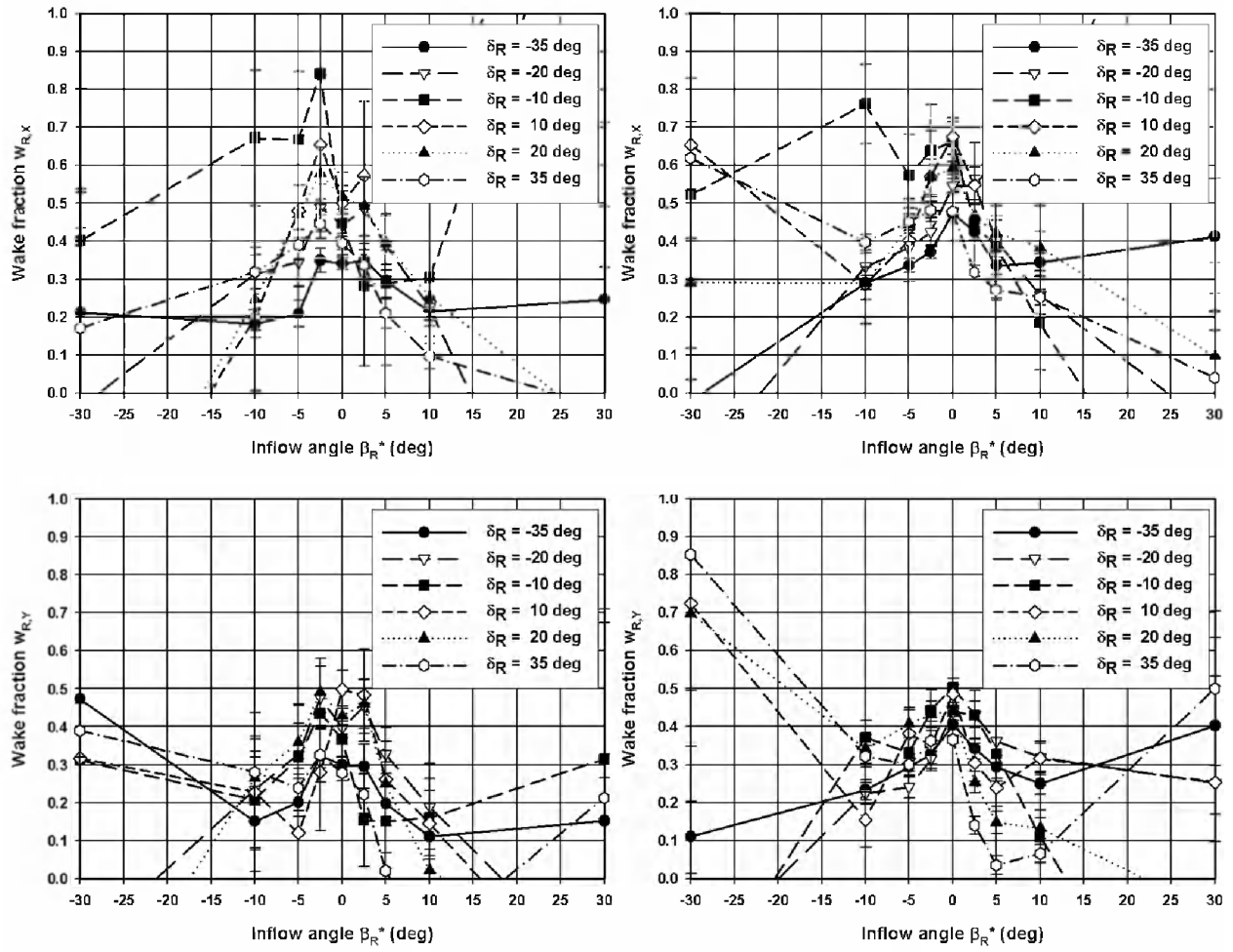
Figure 6.41 Model E, *quadrant 1*, comparison of wake factor at the rudder $w_{R,X}$ and $w_{R,Y}$ for the calculation of rudder force F_X respectively F_Y for 50% UKC (left) and 20% UKC (right)
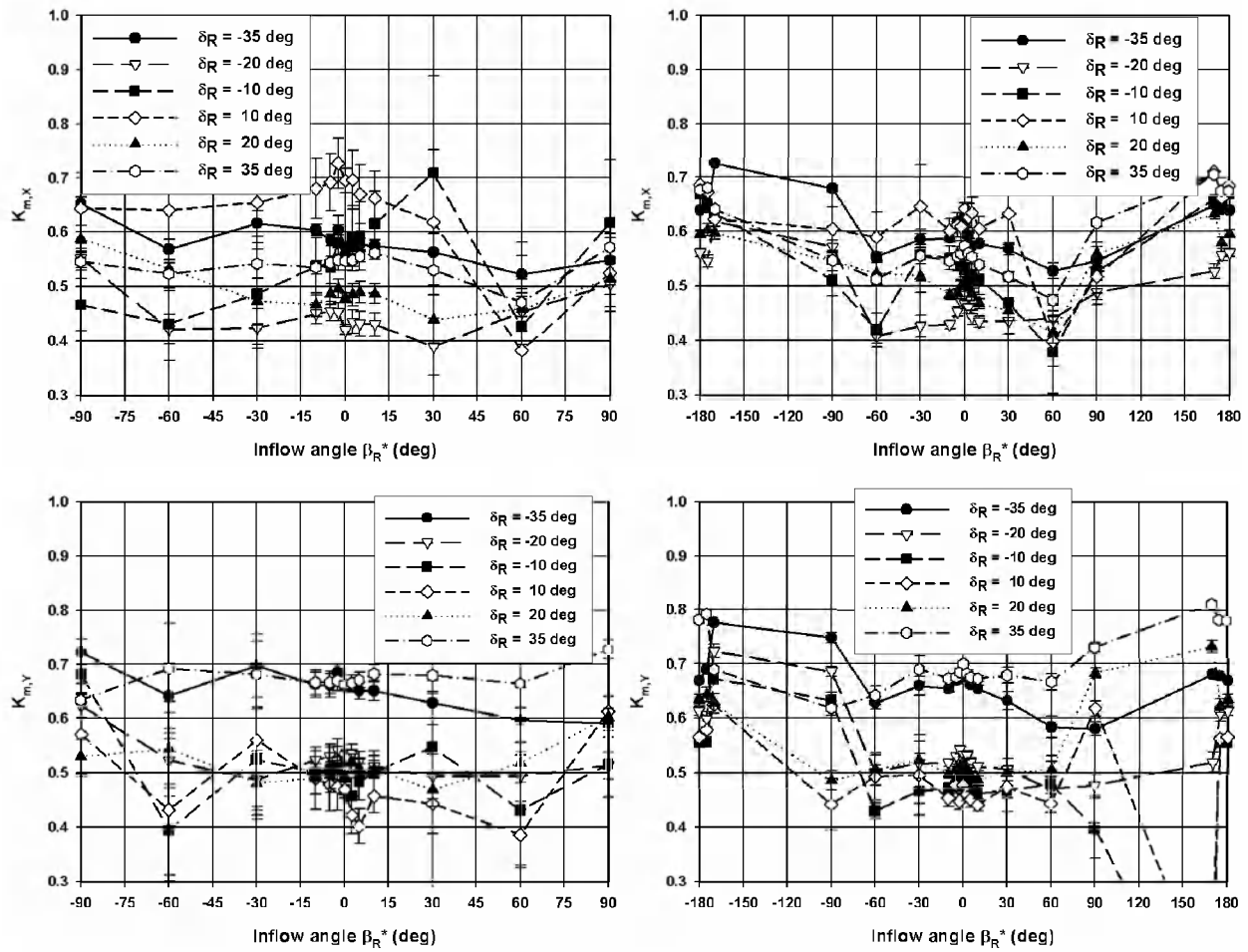
Figure 6.42 Model E, *quadrants 1 and 4*, comparison of coefficient $K_{m,X}$ and $K_{m,Y}$ for the calculation of rudder force F_X respectively F_Y for 50% UKC (left) and 20% UKC (right)
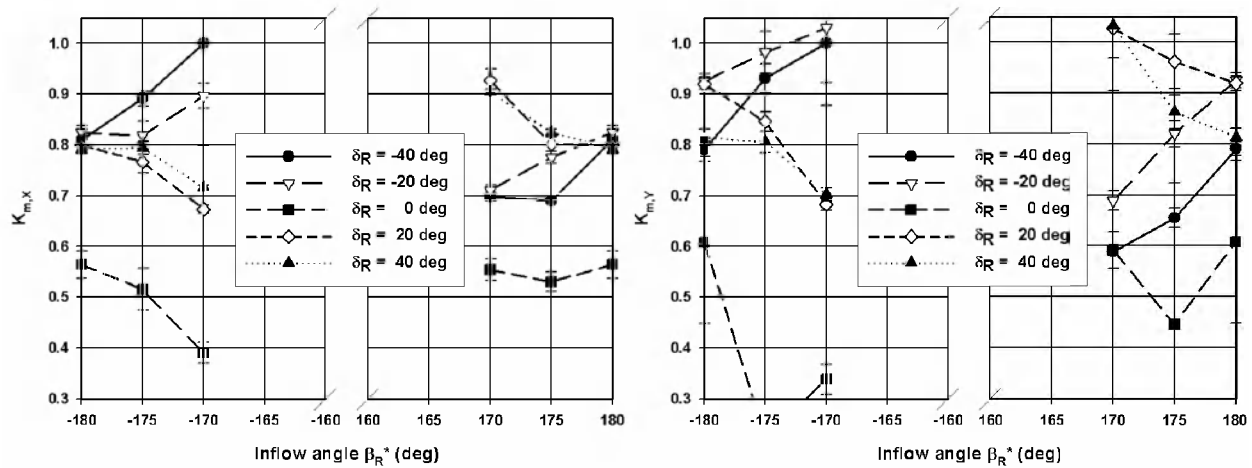
Figure 6.43 Model E, *quadrant 3*, coefficient $K_{m,X}$ and $K_{m,Y}$ for the calculation of rudder force F_X respectively F_Y for 20% UKC
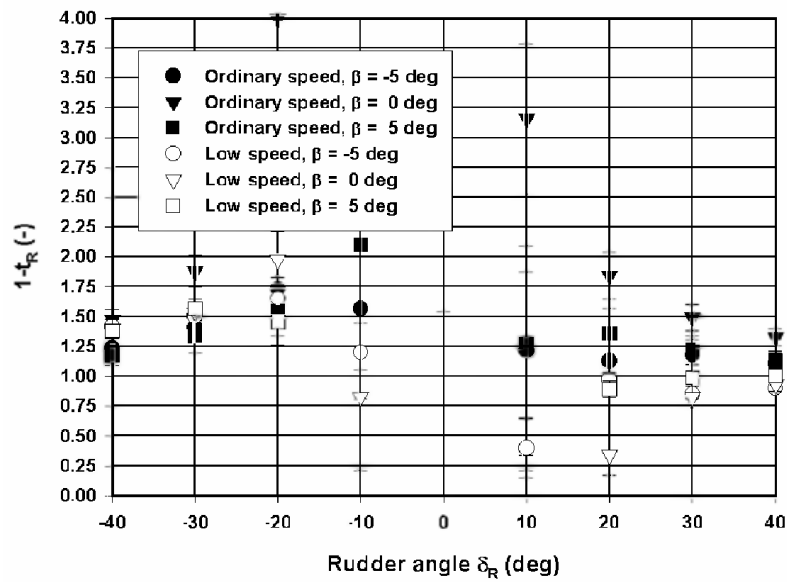
Figure 6.44 Model D, *quadrant 1*, coefficient 1-t_R from stationary tests (F_x based on F_{RN})
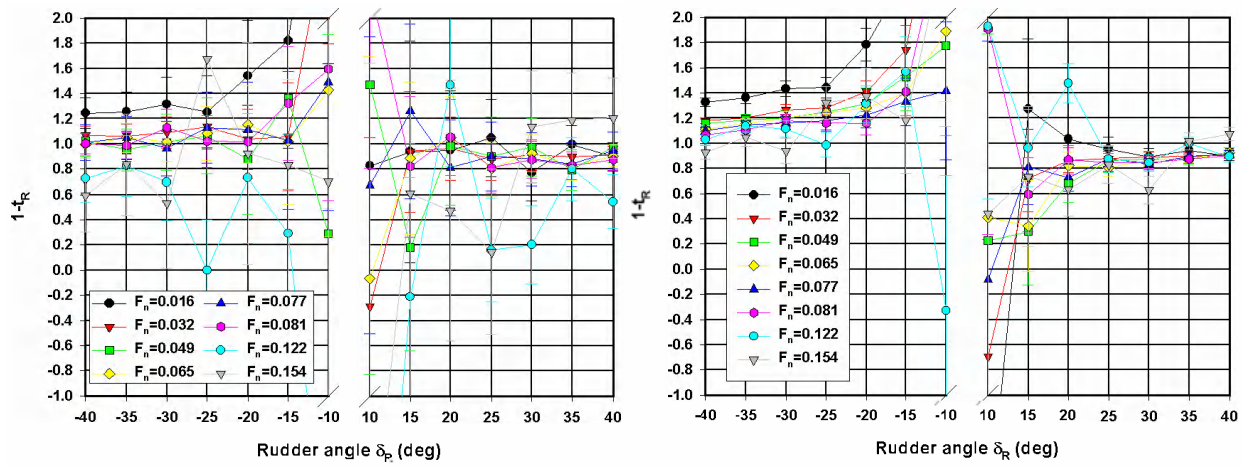
Figure 6.45 Model D, *quadrant 1*, coefficient 1-t_R from multi-modal tests type A, influence of Froude number at a propeller loading of 50%n_0 (left) or 100%n_0 (right) (F_x based on F_{RN} and F_{RT})
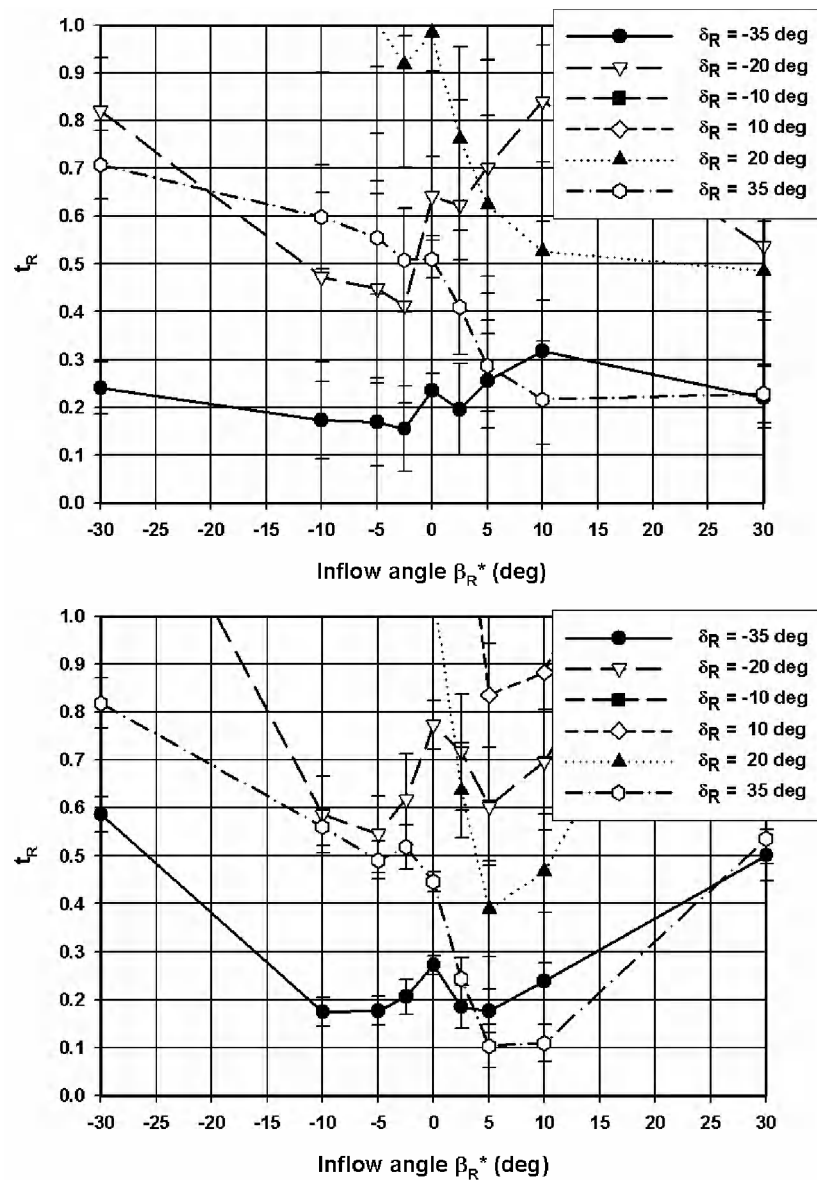
Figure 6.46 Model E, *quadrant 1*, coefficient t_R from different test types as function of rudder angle and inflow angle for 50% UKC (top) and 20% UKC (bottom)
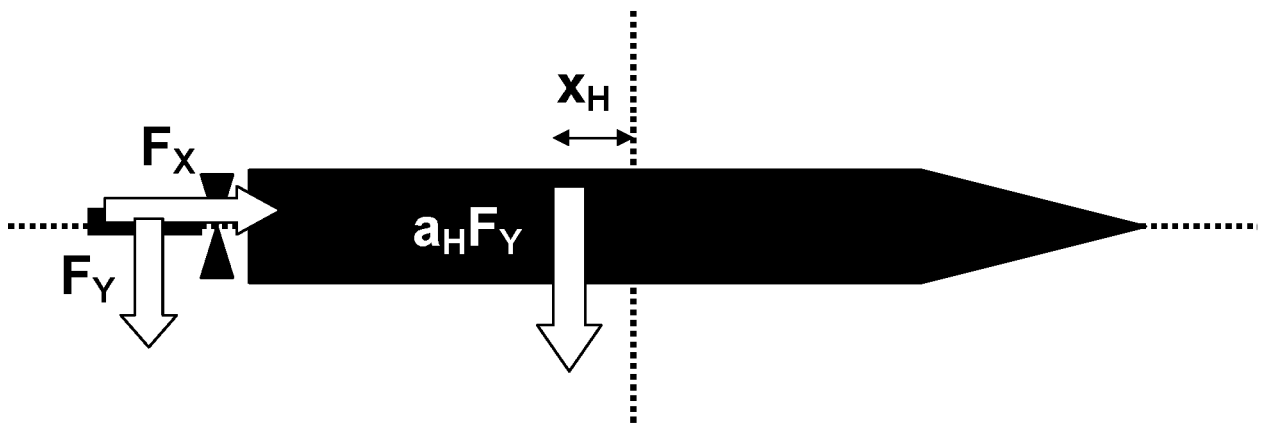
Figure 6.47 Schematic view of correlation parameters a_H and x'_H for the rudder induced lateral force on ship hull $a_H F_Y$ with an application point at a distance x_H from the midhip position
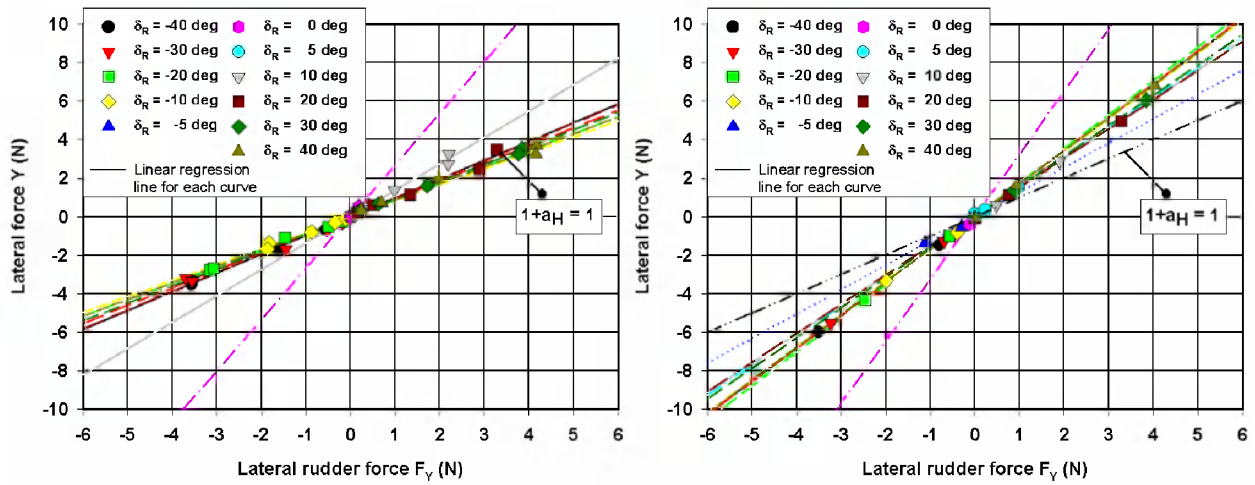
Figure 6.48 Model D, *quadrant 1*, measured values and linear regression lines for coefficient 1+a$_H$ based on stationary straight-line tests (low speed manoeuvring, F$_n$=0, left and F$_n$=0.016, right)
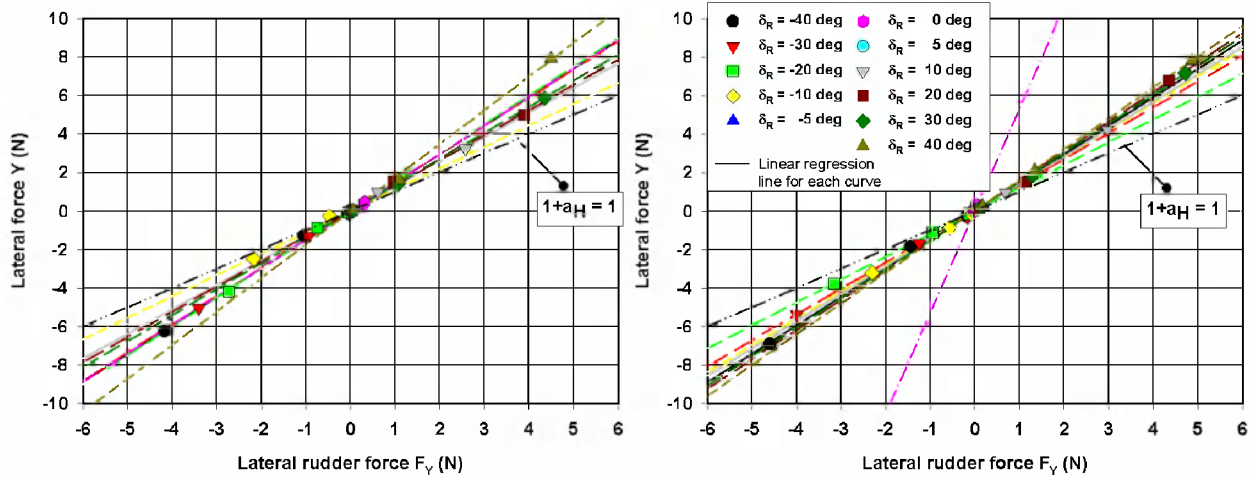
Figure 6.49 Model D, *quadrant 1*, measured values and linear regression lines for coefficient 1+a$_H$ based on stationary straight-line tests (ordinary speed manoeuvring, F$_n$=0.049, left and F$_n$=0.077)
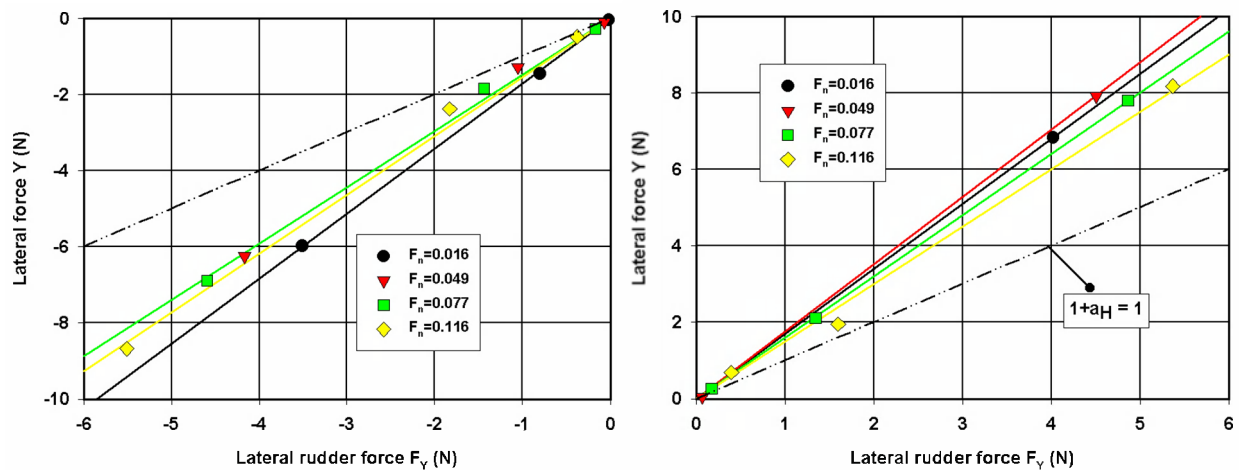
Figure 6.50 Model D, *quadrant 1*, measured values and linear regression lines for coefficient 1+a$_H$ based on stationary straight-line tests with -40deg (left) and 40deg rudder angle (right)

358
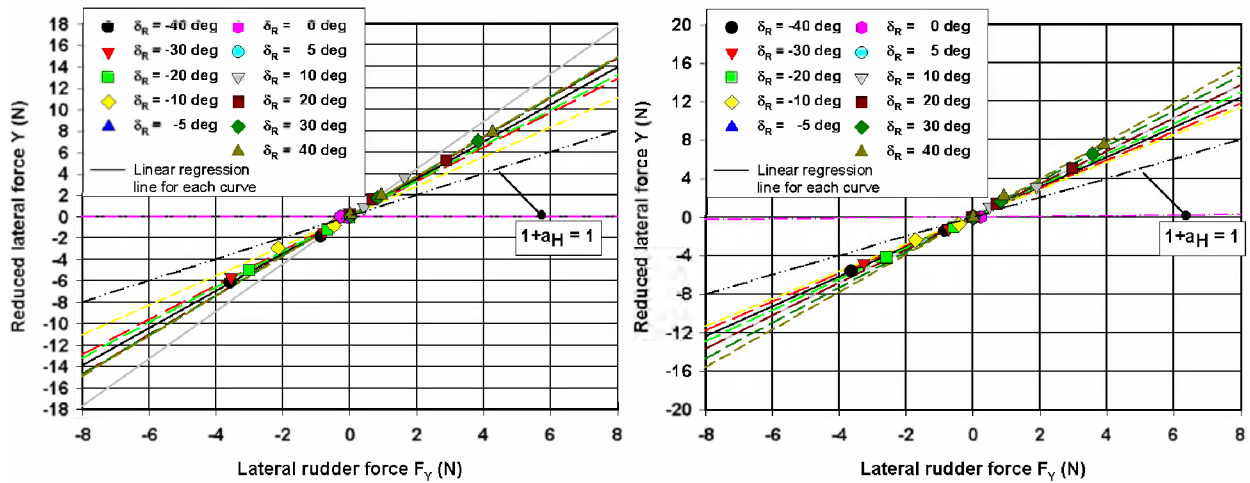
Figure 6.51 Model D, *quadrant 1*, measured values and linear regression lines for coefficient $1+a_H$ based on stationary oblique towing tests (F_n=0.016, β=-5deg, left and β=5deg, right)
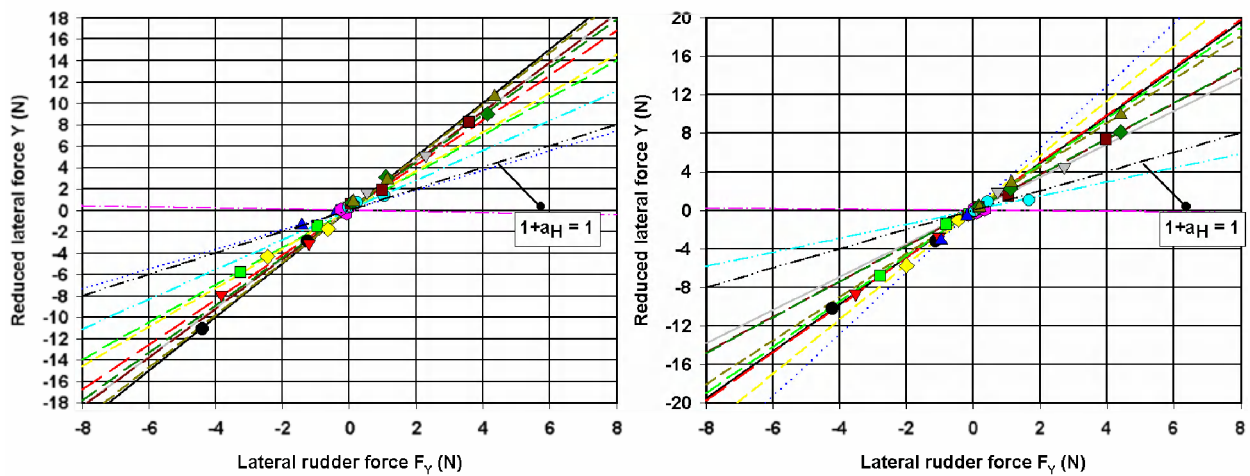
Figure 6.52 Model D, *quadrant 1*, measured values and linear regression lines for coefficient $1+a_H$ based on stationary oblique towing tests (F_n=0.049, β=-5deg, left and β=5deg, right)
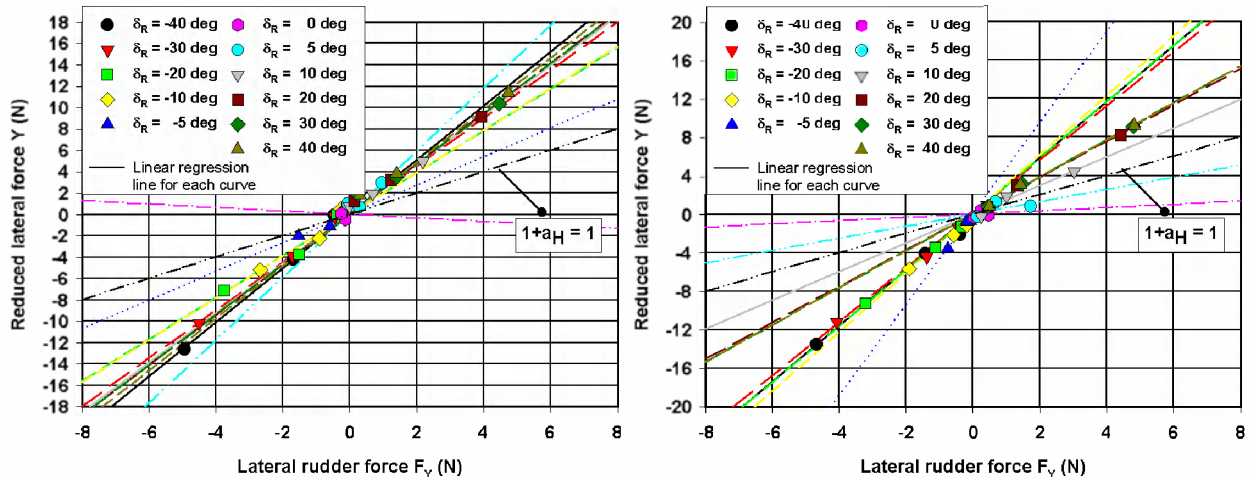
Figure 6.53 Model D, *quadrant 1*, measured values and linear regression lines for coefficient $1+a_H$ based on stationary oblique towing tests (F_n=0.077, β=-5deg, left and β=5deg, right)
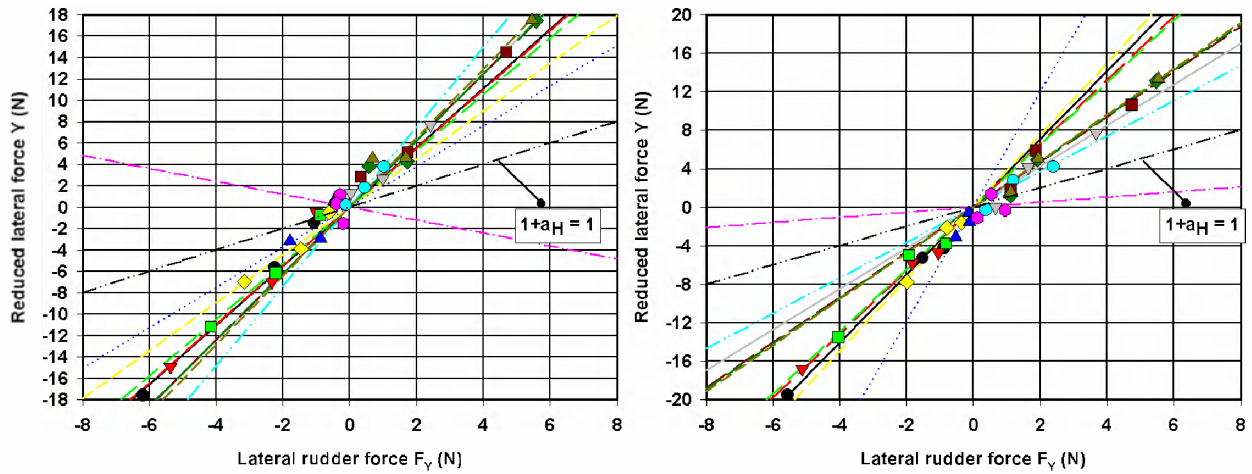
Figure 6.54 Model D, *quadrant 1*, measured values and linear regression lines for coefficient $1+a_H$ based on stationary oblique towing tests (F_n=0.116, β=-5deg, left and β=5deg, right)
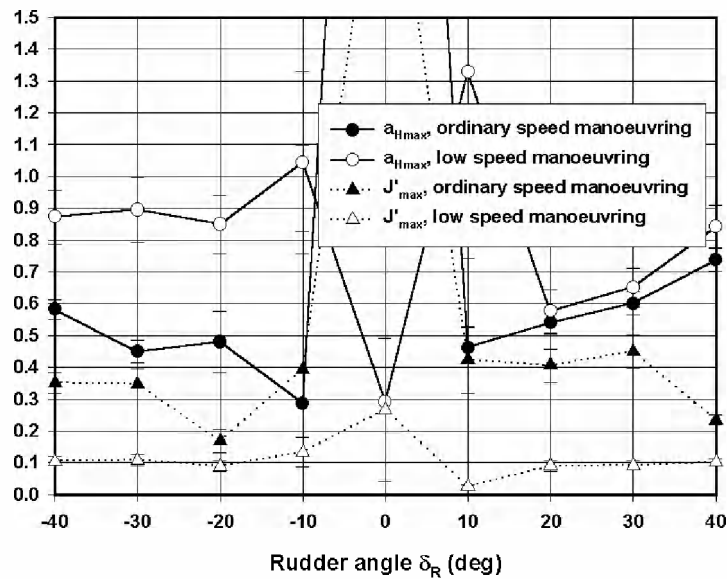
Figure 6.55 Model D, *quadrant 1*, tabular models for J'_{max} and a_{Hmax} based on stationary straight-line tests (low and ordinary speed manoeuvring)
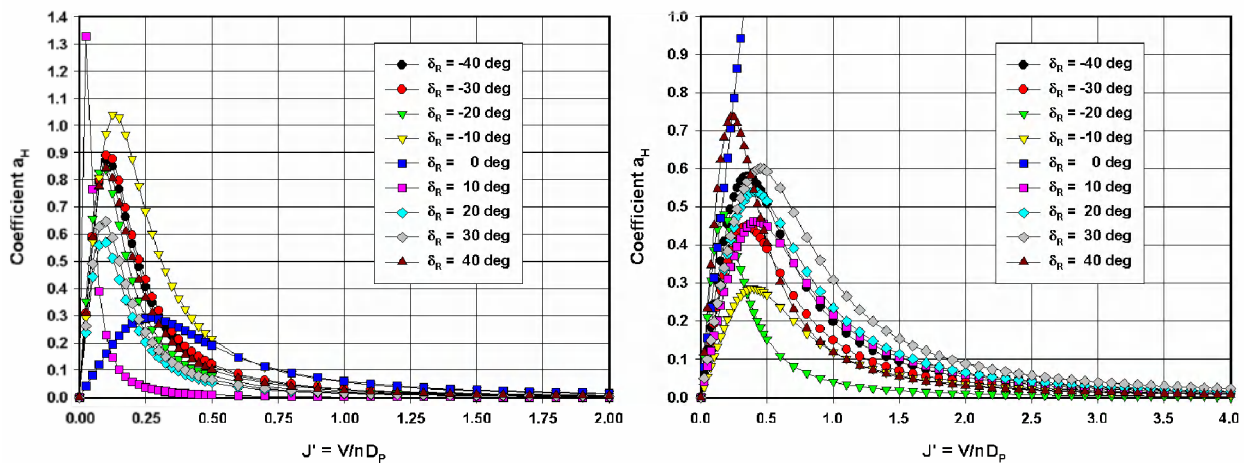
Figure 6.56 Model D, *quadrant 1*, mathematical models for coefficient a_H as function of apparent advance coefficient J' for low speed manoeuvring (F_n=0.016, β=0, left) and ordinary speed manoeuvring ($F_n \geq 0.049$, β=0, right)

360
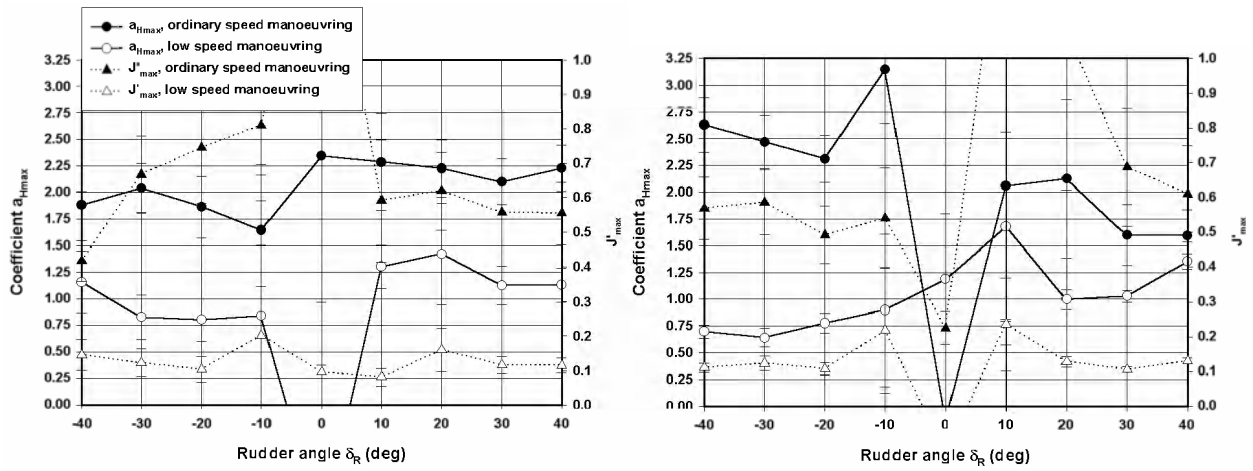
Figure 6.57 Model D, *quadrant 1*, tabular models for J'$_{max}$ and a$_{Hmax}$ based on oblique towing tests (low and ordinary speed manoeuvring, β=-5deg, left and β=5deg, right)
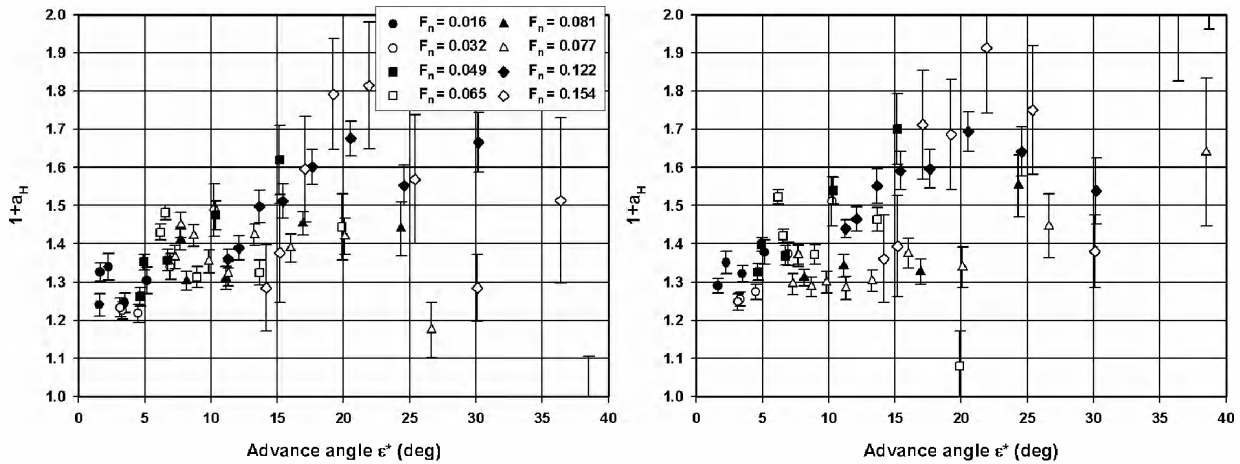
Figure 6.58 Model D, *quadrant 1*, hull coefficient 1+a$_H$ for multi-modal straight-line tests of type A (δ_R=-40deg, left, and δ_R=40deg, right)
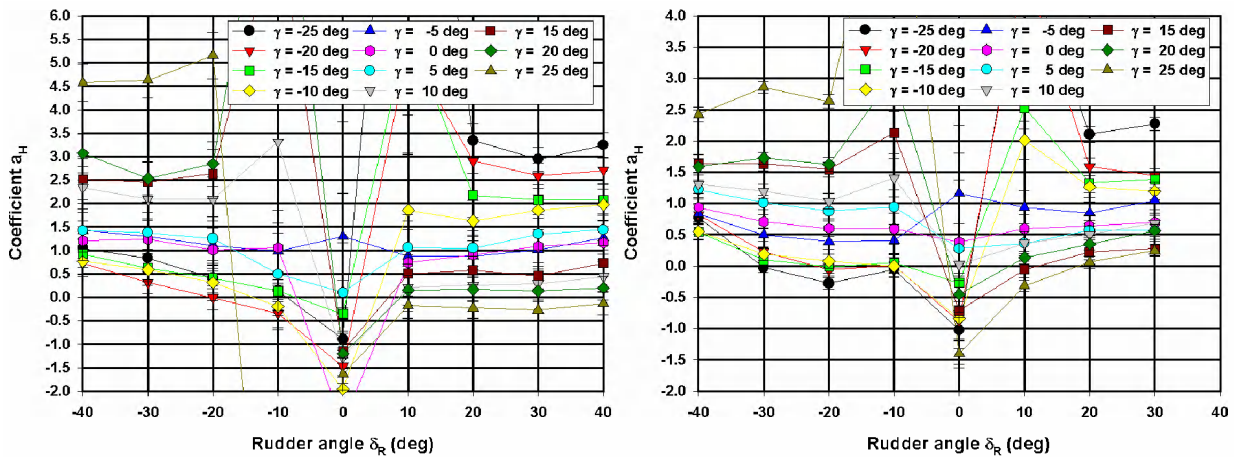
Figure 6.59 Model D, *quadrant 1*, coefficient a$_H$ for harmonic yawing tests with Froude number F$_n$=0.032 and propeller rate n=50% n$_0$, left, n=100% n$_0$, right
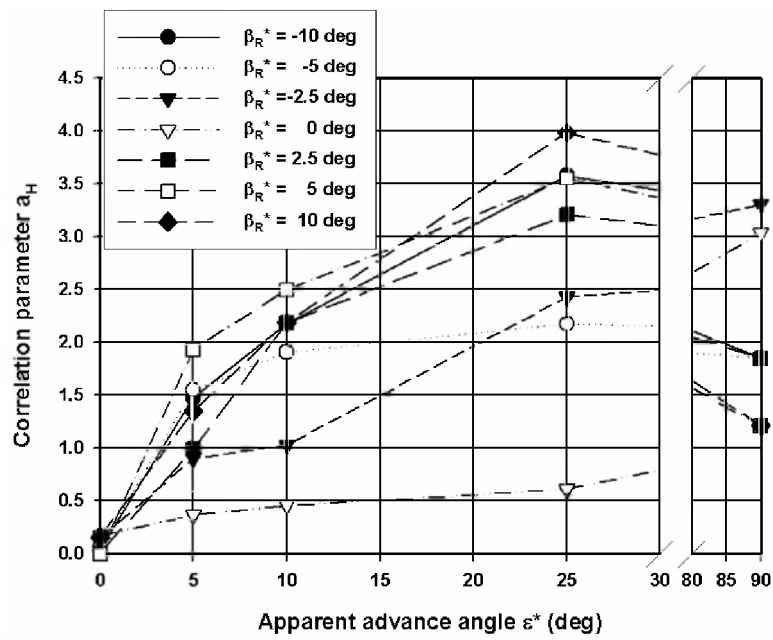
Figure 6.60 Model D, *quadrant 1*, two dimensional tabular model for correlation parameter a_H based on maximum values obtained for positive and/or negative rudder angles
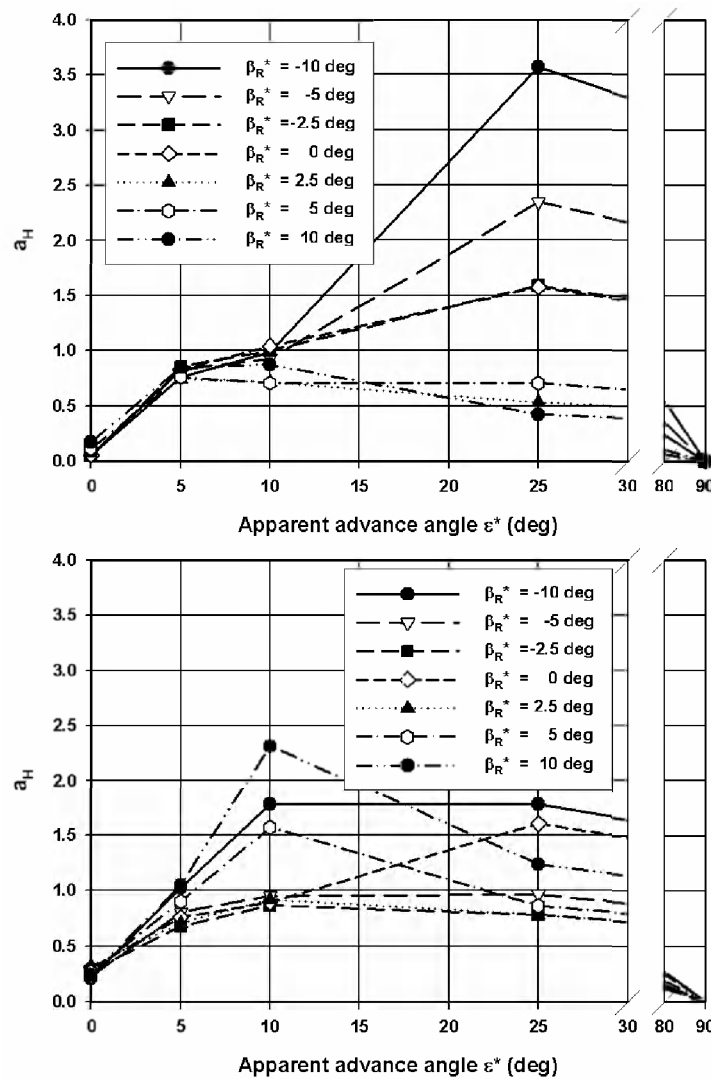
Figure 6.61 Model E, *quadrant 1*, two dimensional tabular models for correlation parameter a_H as function of inflow angle and apparent advance angle for 50% UKC (top) and 20% UKC (bottom)
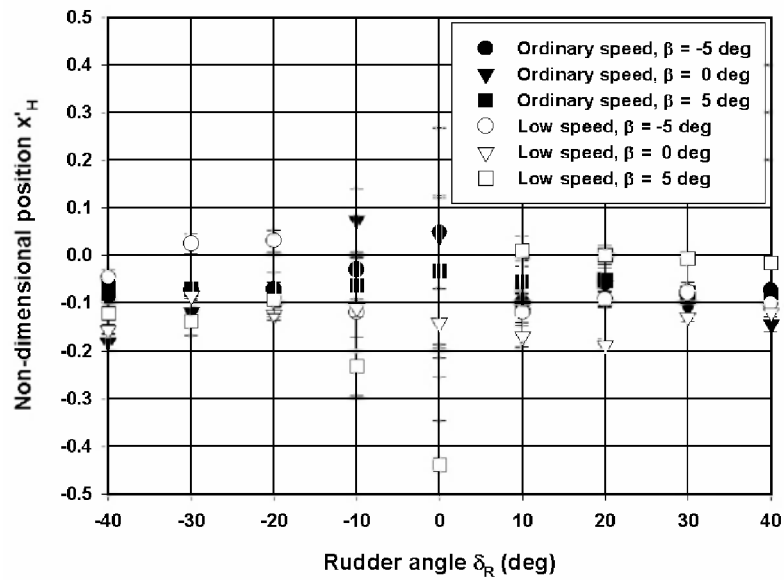
Figure 6.62 Model D, *quadrant 1*, non-dimensional position x'$_H$ based on stationary straight-line and oblique towing tests (low and ordinary speed manoeuvring)
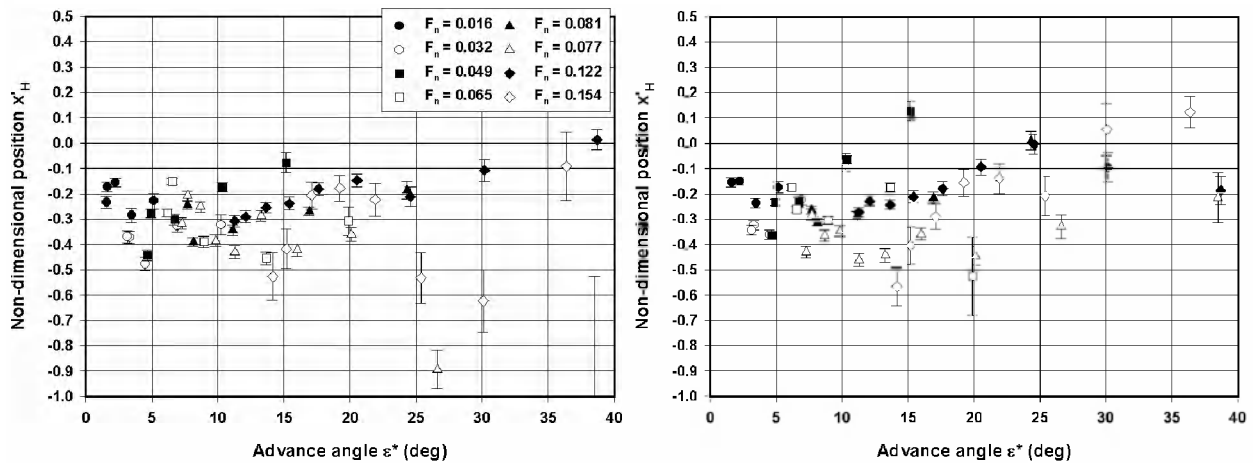
Figure 6.63 Model D, *quadrant 1*, non-dimensional position x'$_H$ based on multi-modal straight-line tests type A (δ_R=-40deg, left, and δ_R=40deg, right)
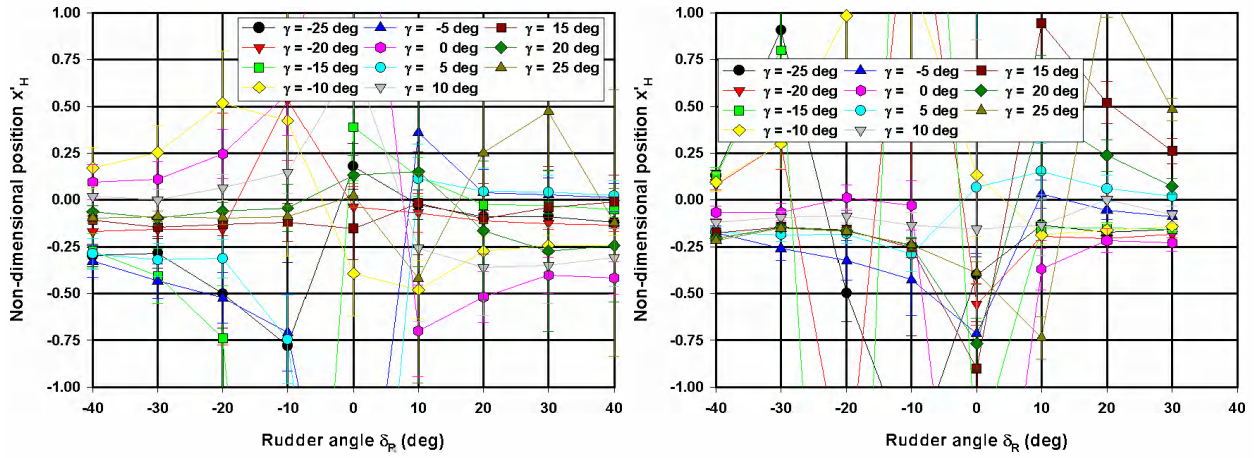
Figure 6.64 Model D, *quadrant 1*, non-dimensional position x'$_H$ based on harmonic yawing tests with Froude number F$_n$=0.032 and propeller rate n=50% n$_0$, left, n=100% n$_0$, right
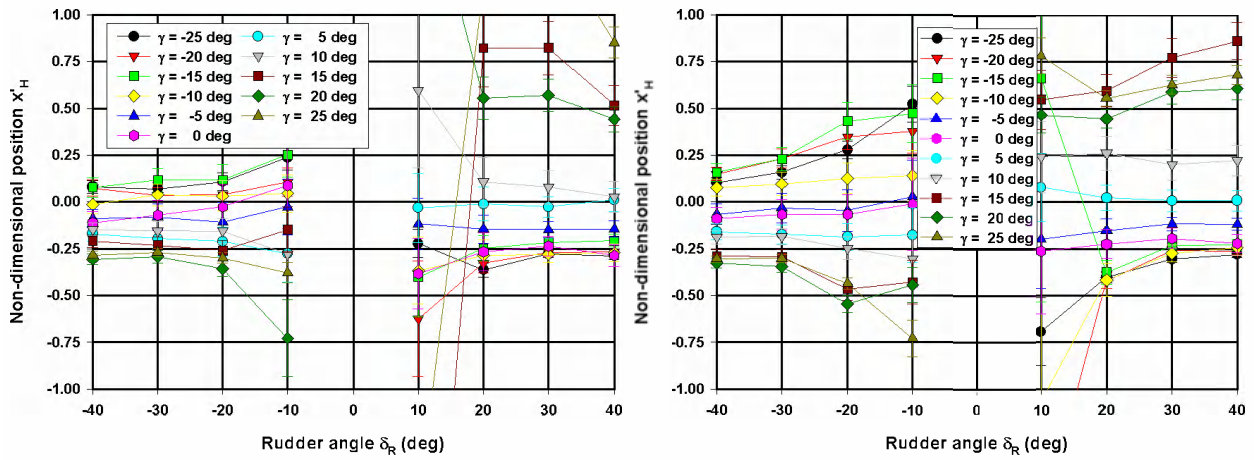
Figure 6.65 Model D, *quadrant 1*, non-dimensional position x'$_H$ based on harmonic yawing tests with Froude number F$_n$=0.065 and propeller rate n=75% n$_0$, left, n=100% n$_0$, right
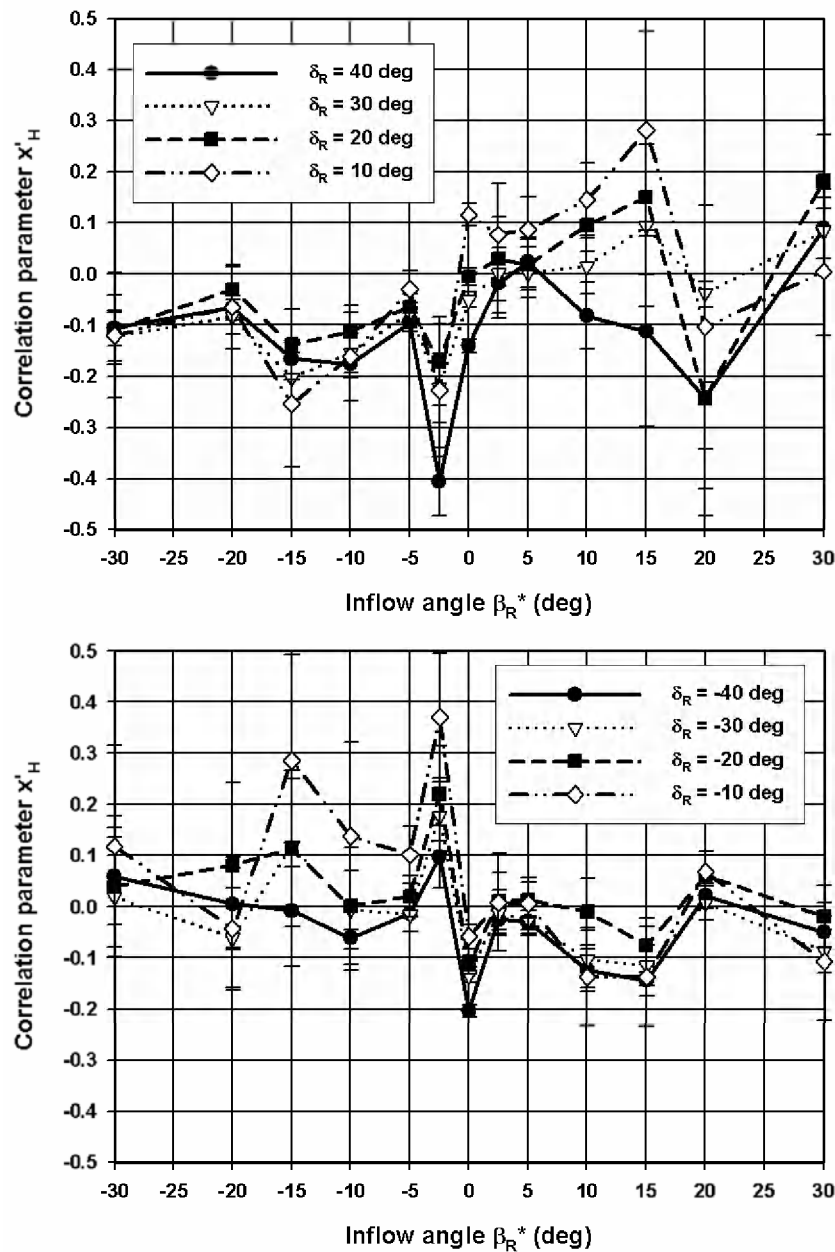
Figure 6.66 Model D, *quadrant 1*, tabular models for non-dimensional position x'_H based on all available ship types for rudder angles to port (top) and to starboard (bottom)
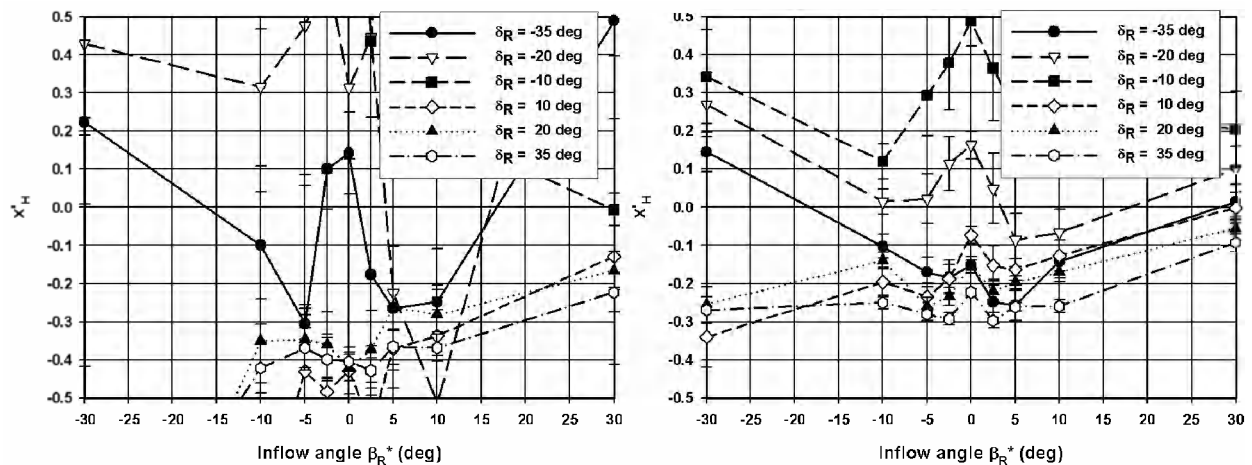
Figure 6.67 Model E, quadrant 1, comparison of rudder induced non-dimensional application point x'_H for 50% UKC (left) and 20% UKC (right)

365

ADVANCE AT 45° HEADING CHANGE
(Coasting Turn Only)

45°

MAX. SWEPT TACTICAL DIAMETER

TACTICAL DIAMETER

TRANSFER

ADVANCE

MAX. SWEPT ADVANCE
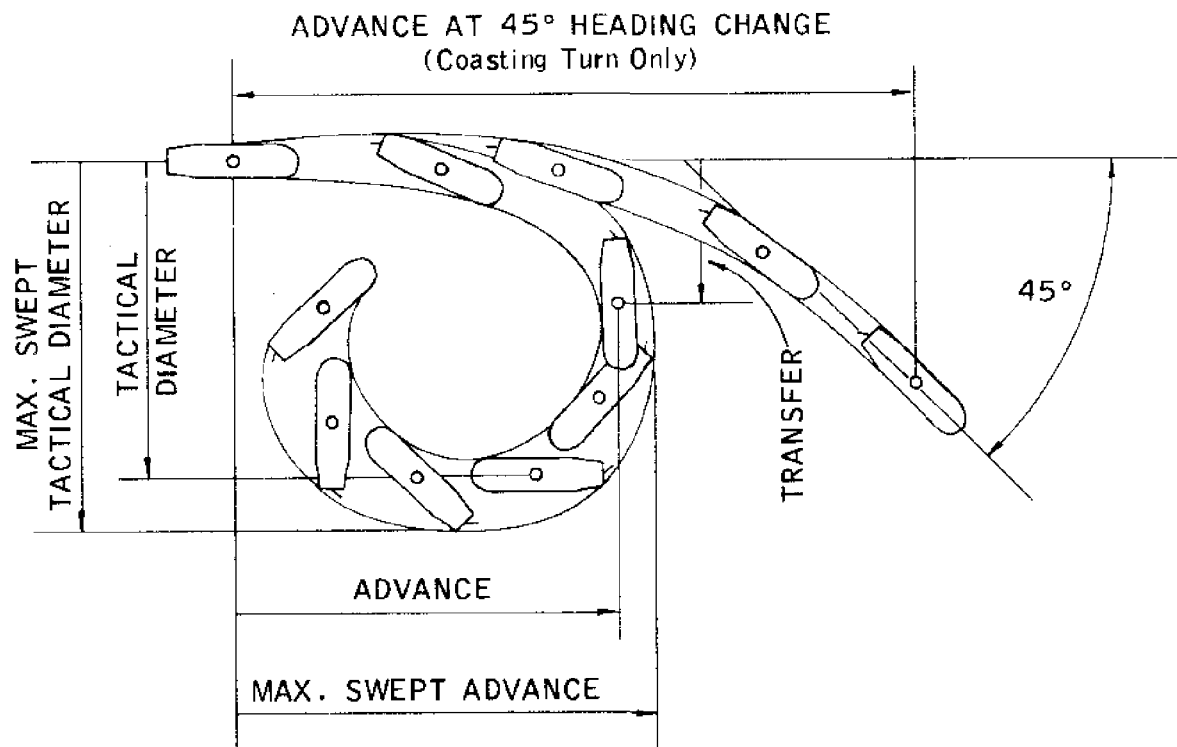
Figure 7.1 Characteristics of a turning circle manoeuvre and a coasting turn [73]

DISTANCE, METERS

ADVANCE AT MAXIMUM
LATERAL DEVIATION, METERS

MAXIMUM LATERAL
DEVIATION, METERS

SWEPT PATH

ANGLE, DEGREES

RUDDER ANGLE

HEADING
CHANGE

TIME

1st YAW ANGLE OVERSHOOT
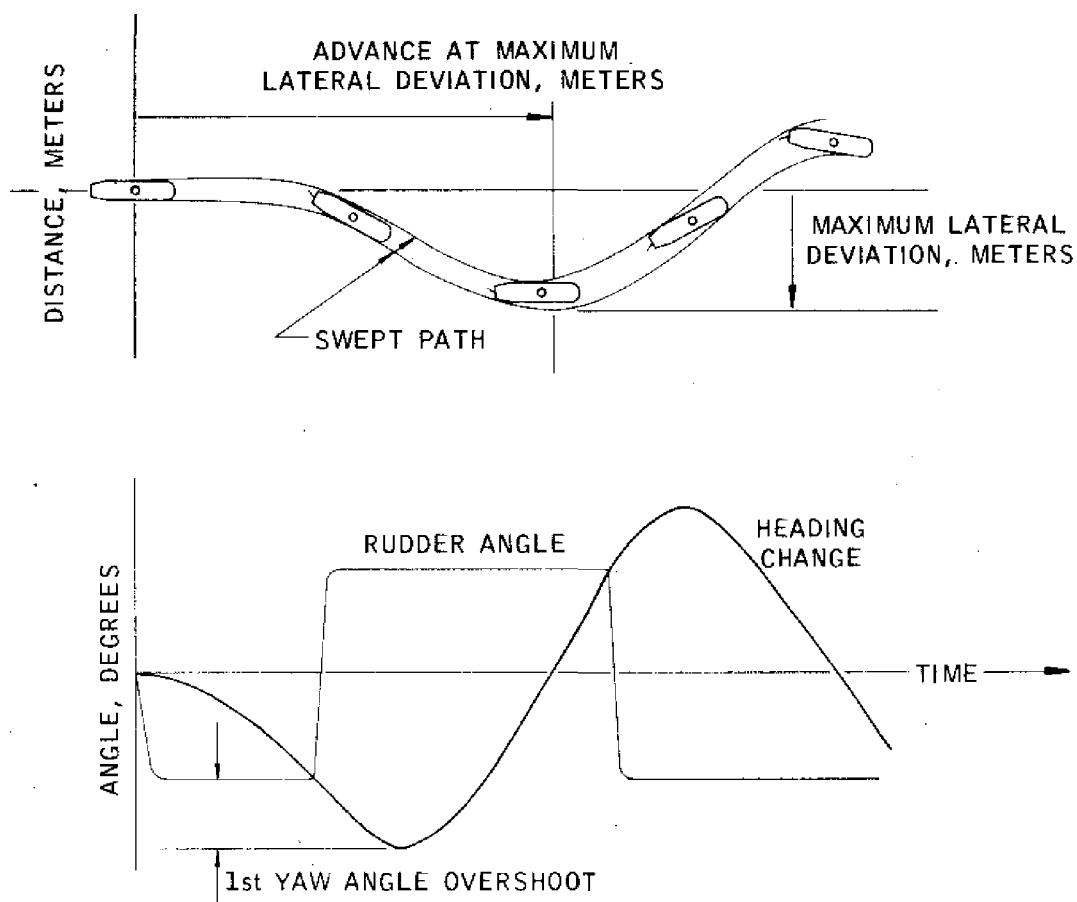
Figure 7.2 Characteristics of a zigzag manoeuvre [73]
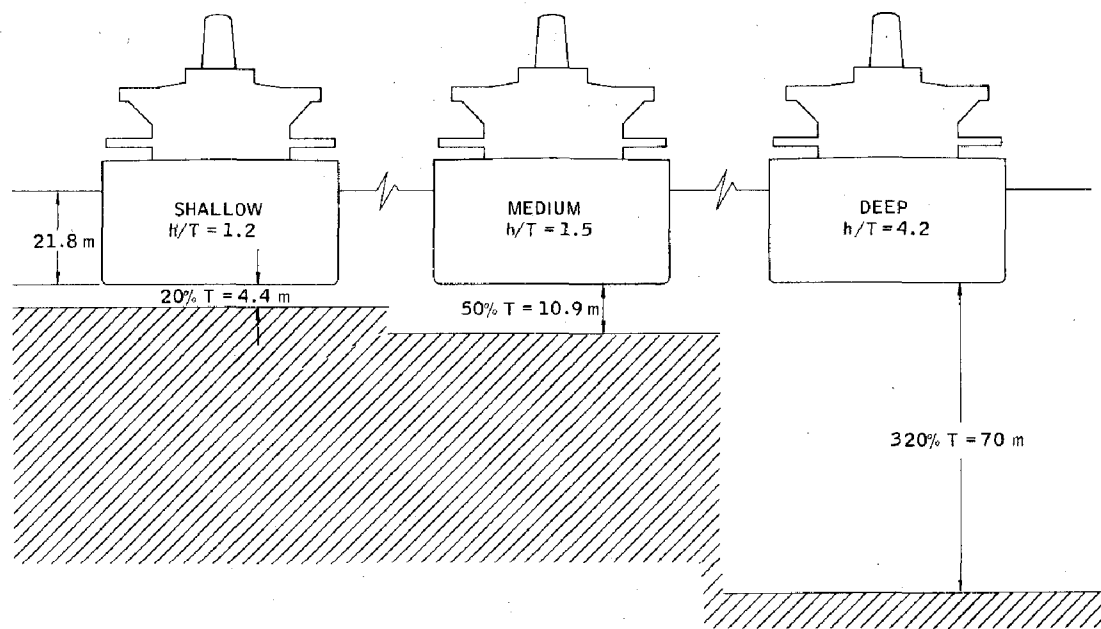
Figure 7.3 Schematic view of the reduction of water depth and the keel clearance for the Esso Osaka [73]
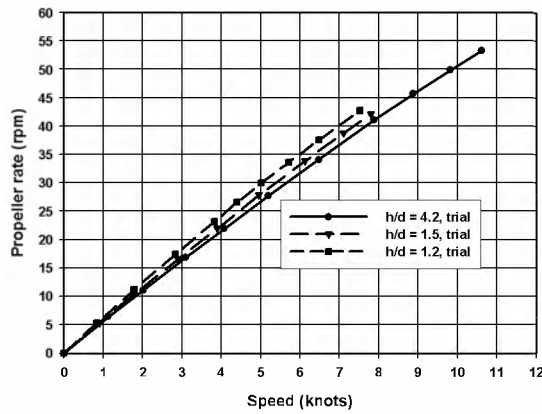
(a) calibration runs
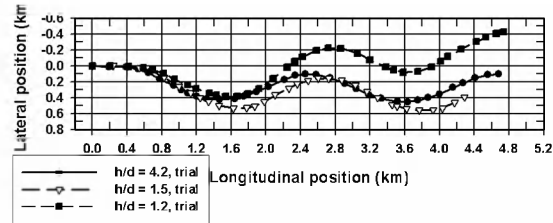
(b) conventional zigzag manoeuvres
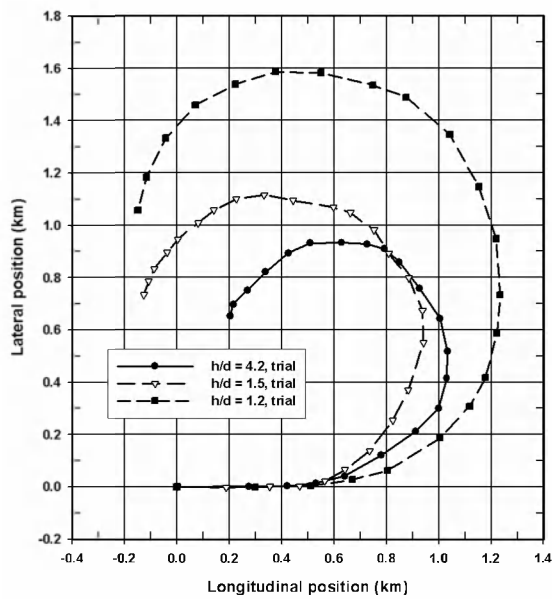
(c1) conventional turning circle to port (35 deg) (c2) conventional turning circle to starboard (-35 deg)
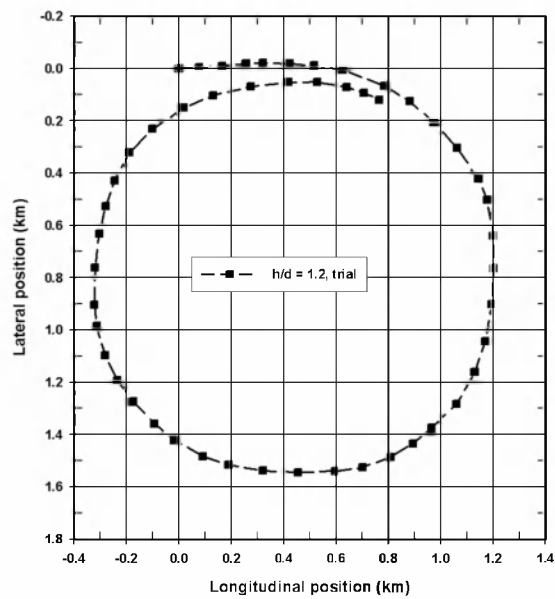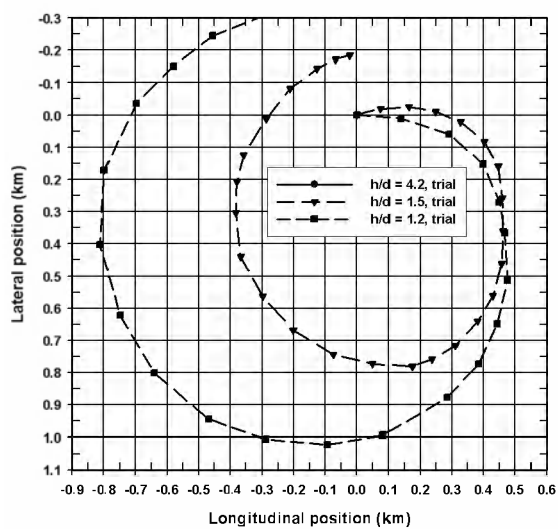
(d) accelerating turn to starboard (-35 deg)
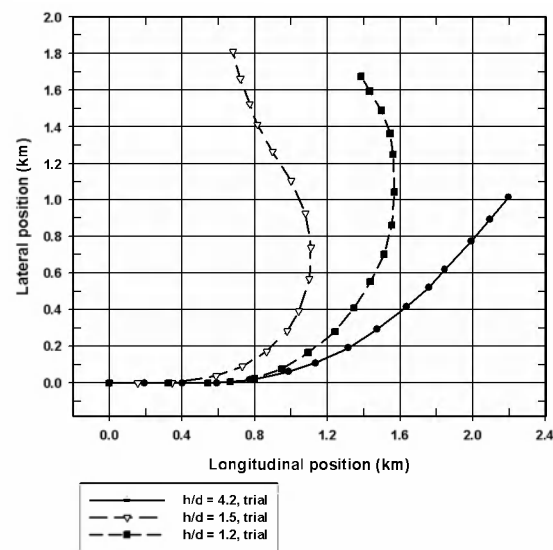
(e) coasting turn to port (35 deg)

Figure 7.4 Overview of the trajectories of some conventional and non-conventional low speed manoeuvres with the Esso Osaka at three water depths, based on the report in [73]
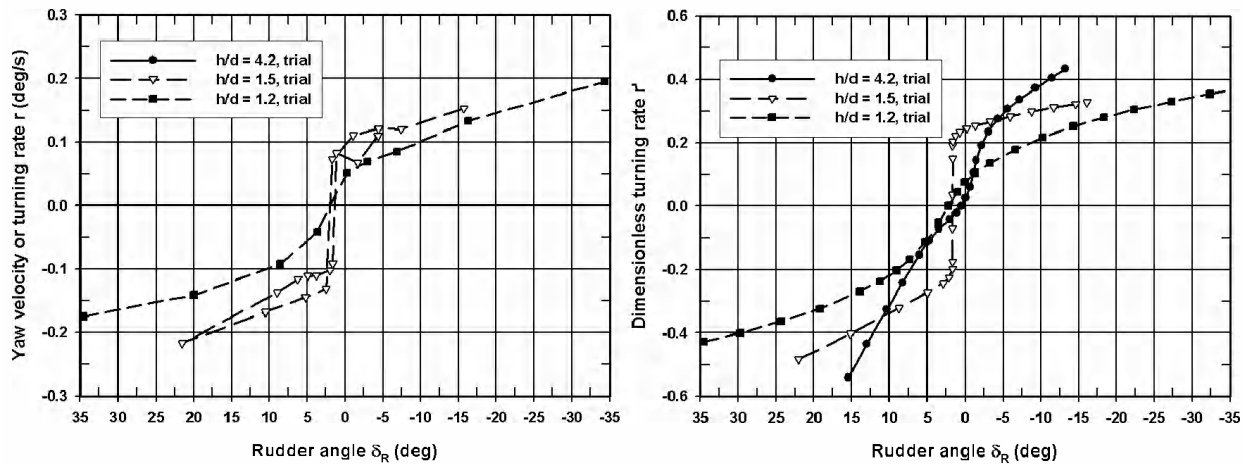
Figure 7.5 Esso Osaka, measured turning rate in deg/s during spiral tests (left) and smoothed spiral test curves with non-dimensional turning rate r'=rL/V based on r (deg/s) and velocity V (m/s, approach speed or final speed?) (right)
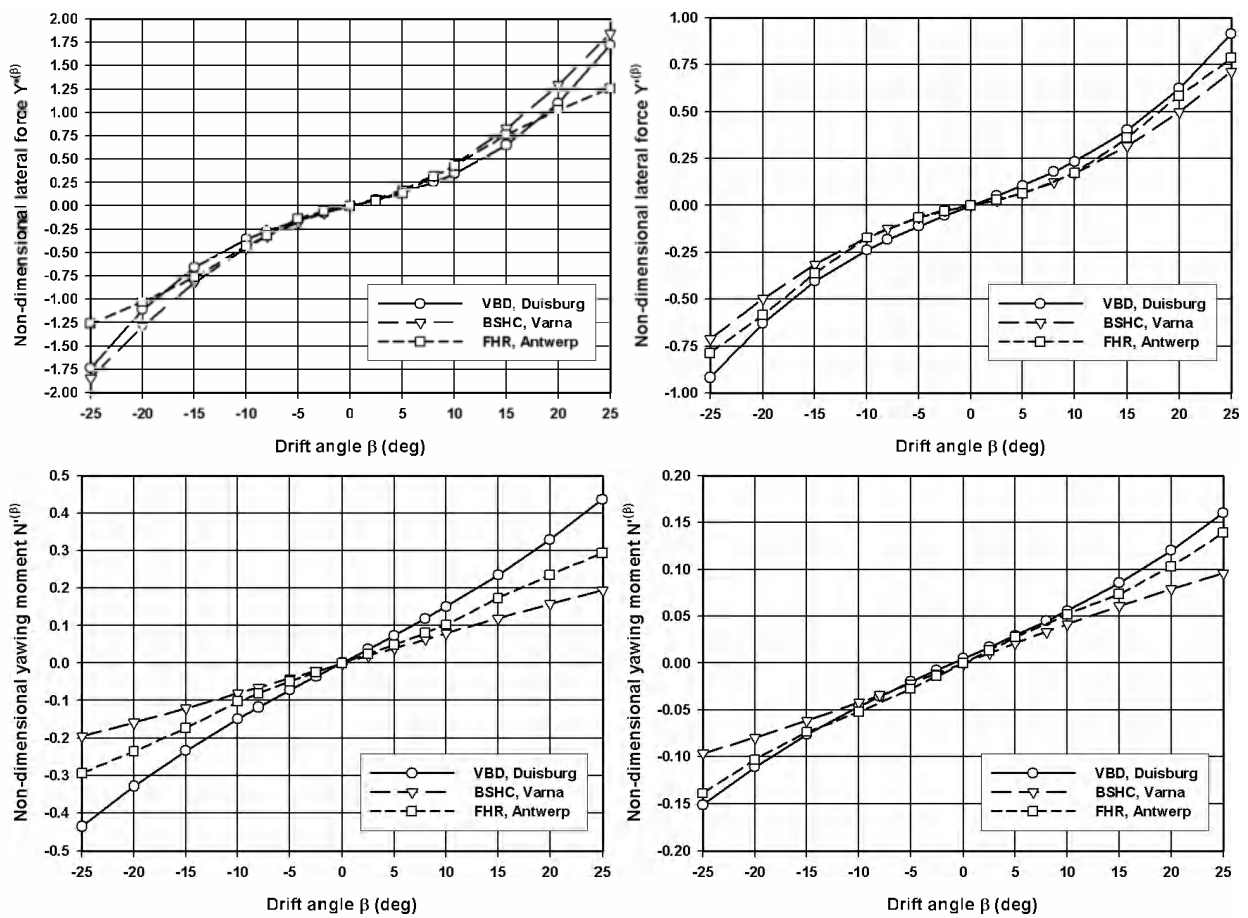
Figure 7.6 Esso Osaka, comparison of velocity dependent hull forces for pure drift based on captive model tests from different institutes (20% UKC, left, and 50% UKC, right)

370
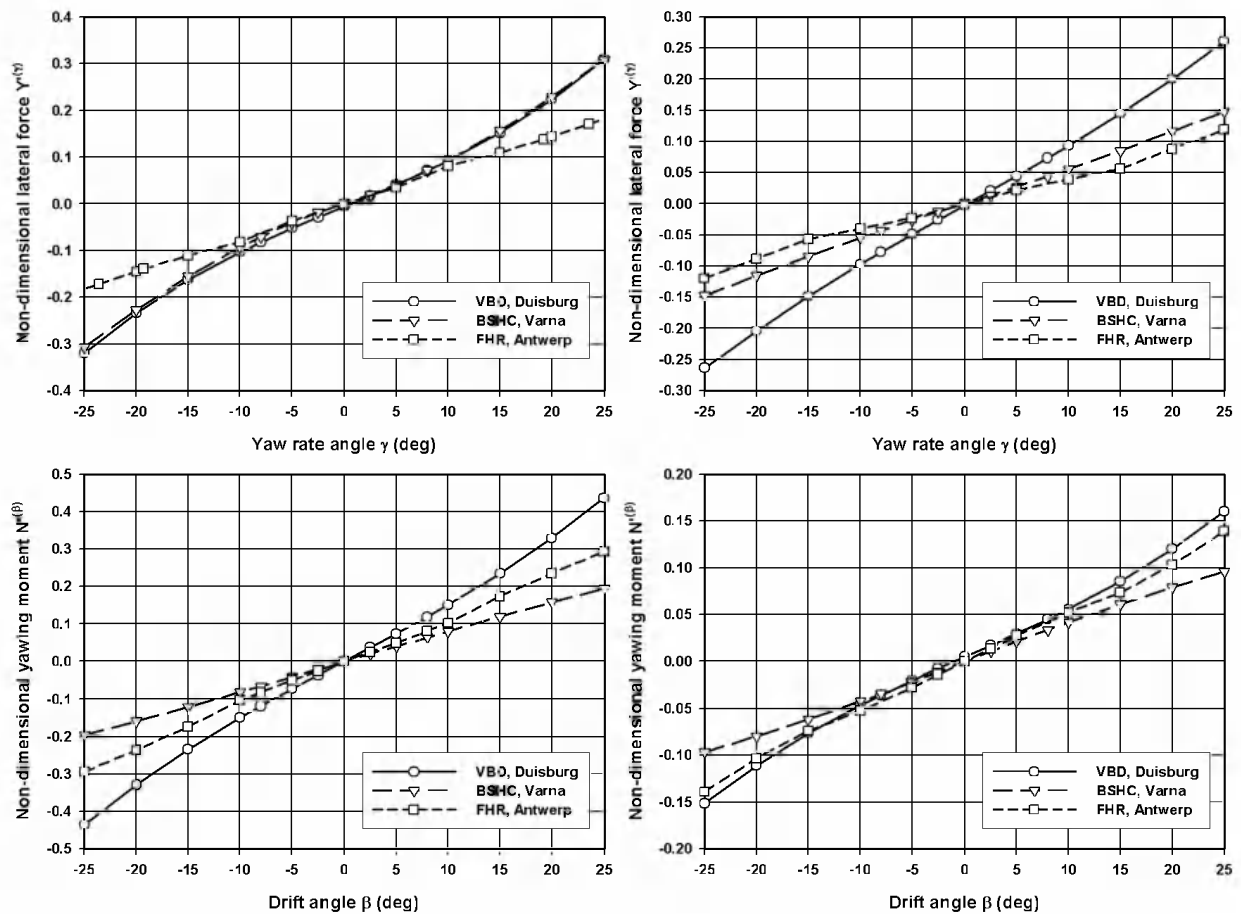
Figure 7.7 Esso Osaka, comparison of velocity dependent hull forces for pure yaw based on captive model tests from different institutes (20% UKC, left, and 50% UKC, right)
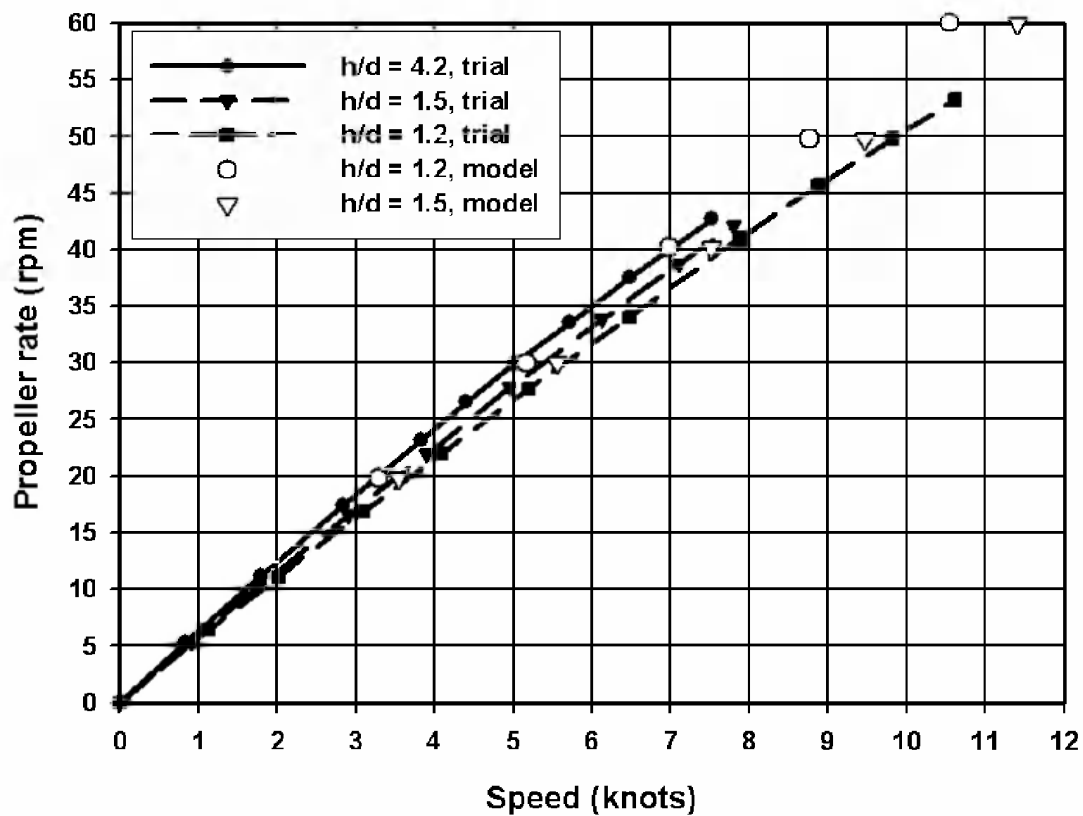
Figure 7.8 Esso Osaka, comparison of calibration tests for going ahead
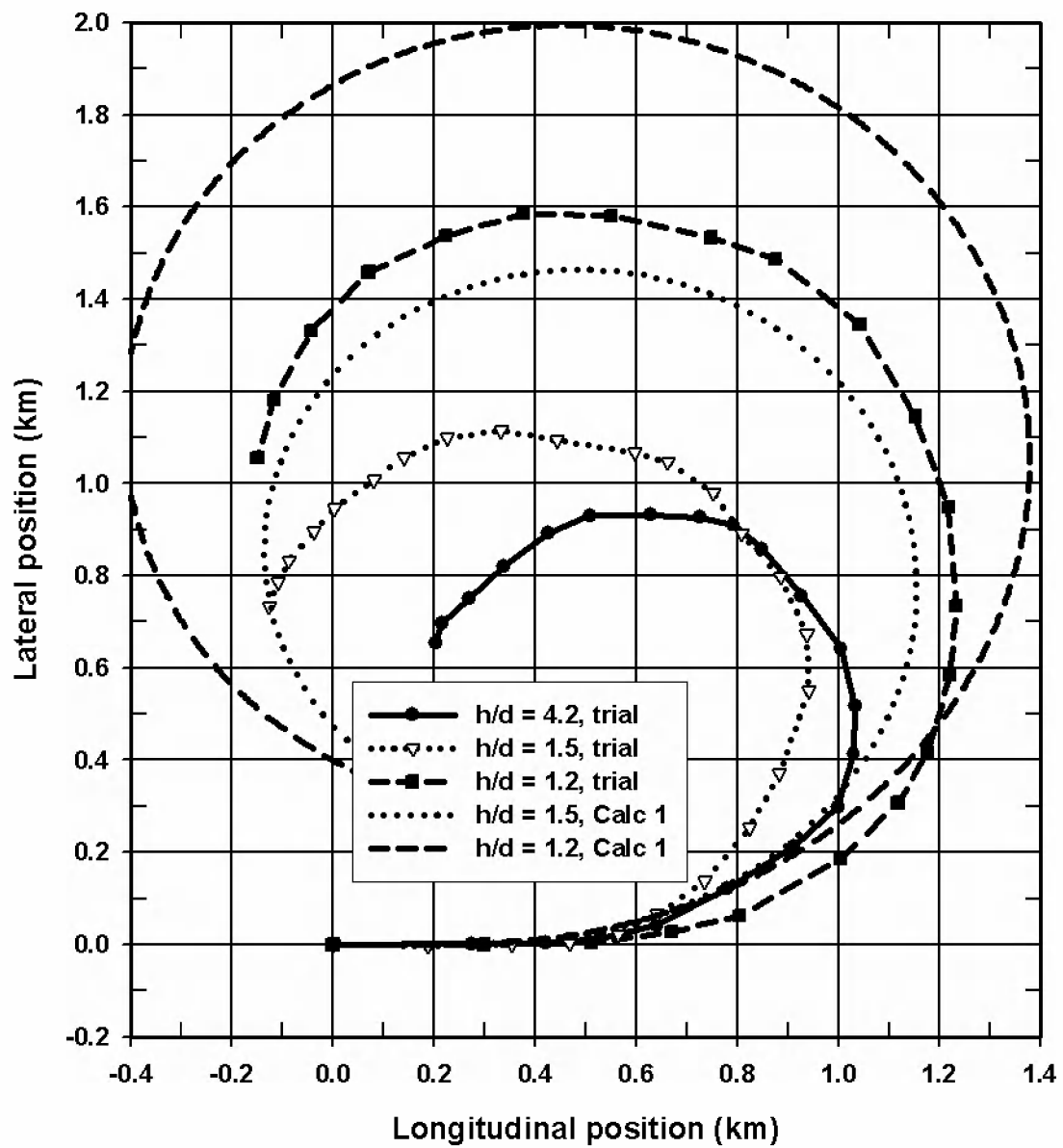
Figure 7.9 Esso Osaka, comparison of trial and model for a conventional turn to port
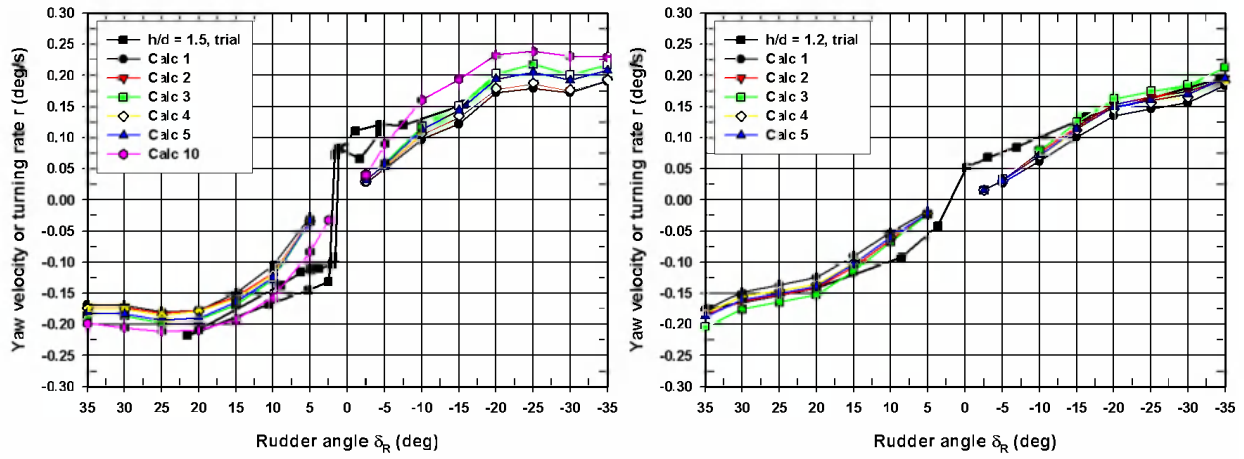
Figure 7.10 Esso Osaka, comparison of turning rate measured during spiral tests at full scale and modelled during turning circles with different rudder angles: variation of the velocity dependent hull lateral force and yawing moment according to Table 7.14 (50% UKC left and 20% UKC right)
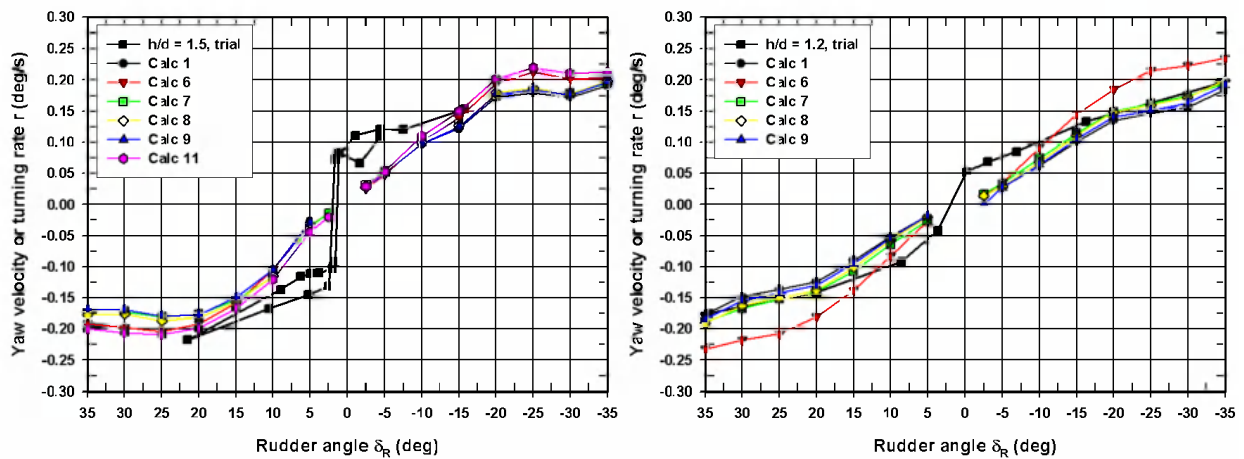
Figure 7.11 Esso Osaka, comparison of turning rate measured during spiral tests at full scale and modelled during turning circles with different rudder angles: variation of the rudder dependent coefficients according to Table 7.14 (50% UKC left and 20% UKC right)
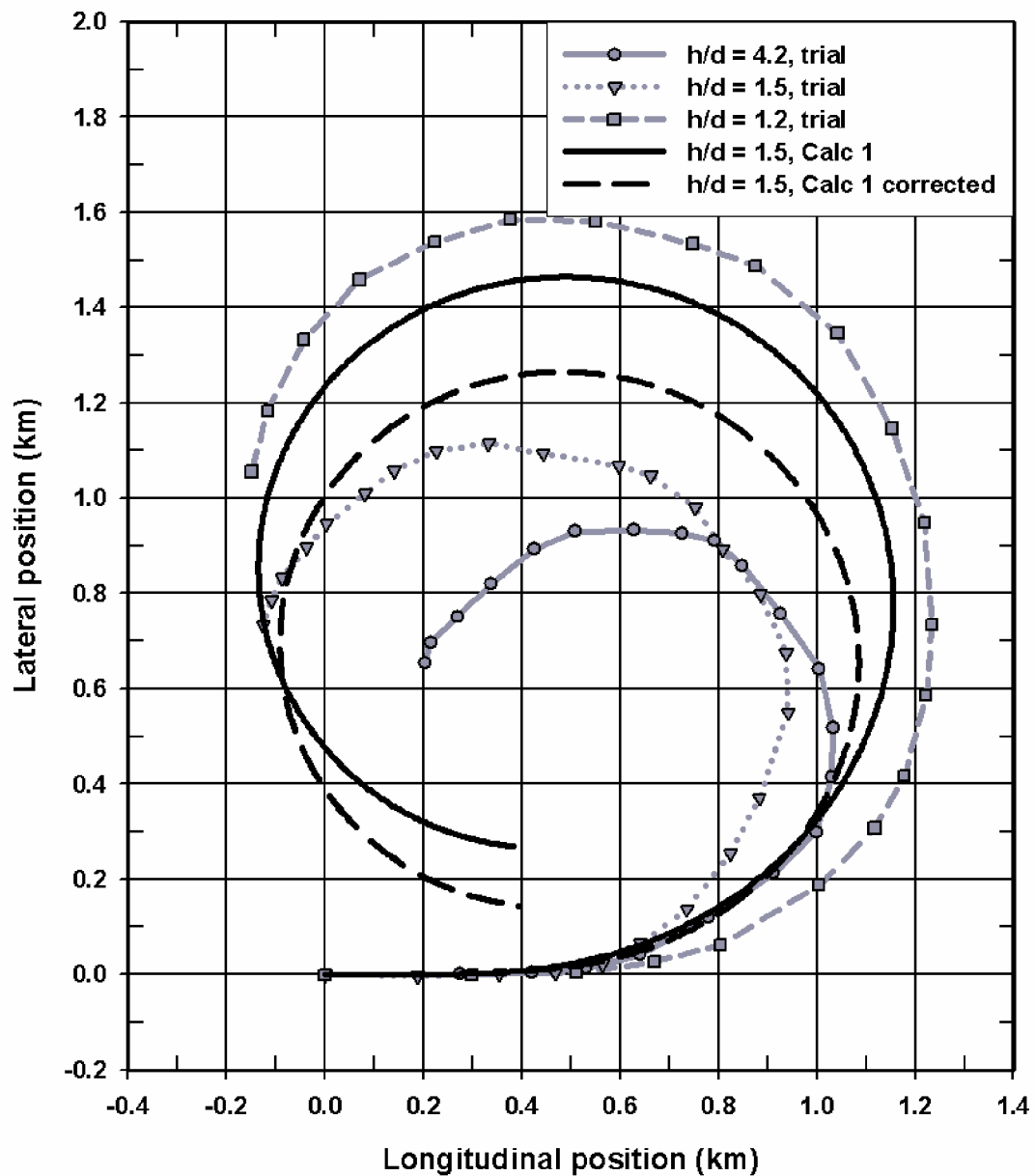
Figure 7.12 Esso Osaka, at 50% UKC, influence of correction for wake factor w_{RX} and w_{RY} on the manoeuvring characteristics of a conventional turn to port: comparison calc 1 and calc 1 corrected
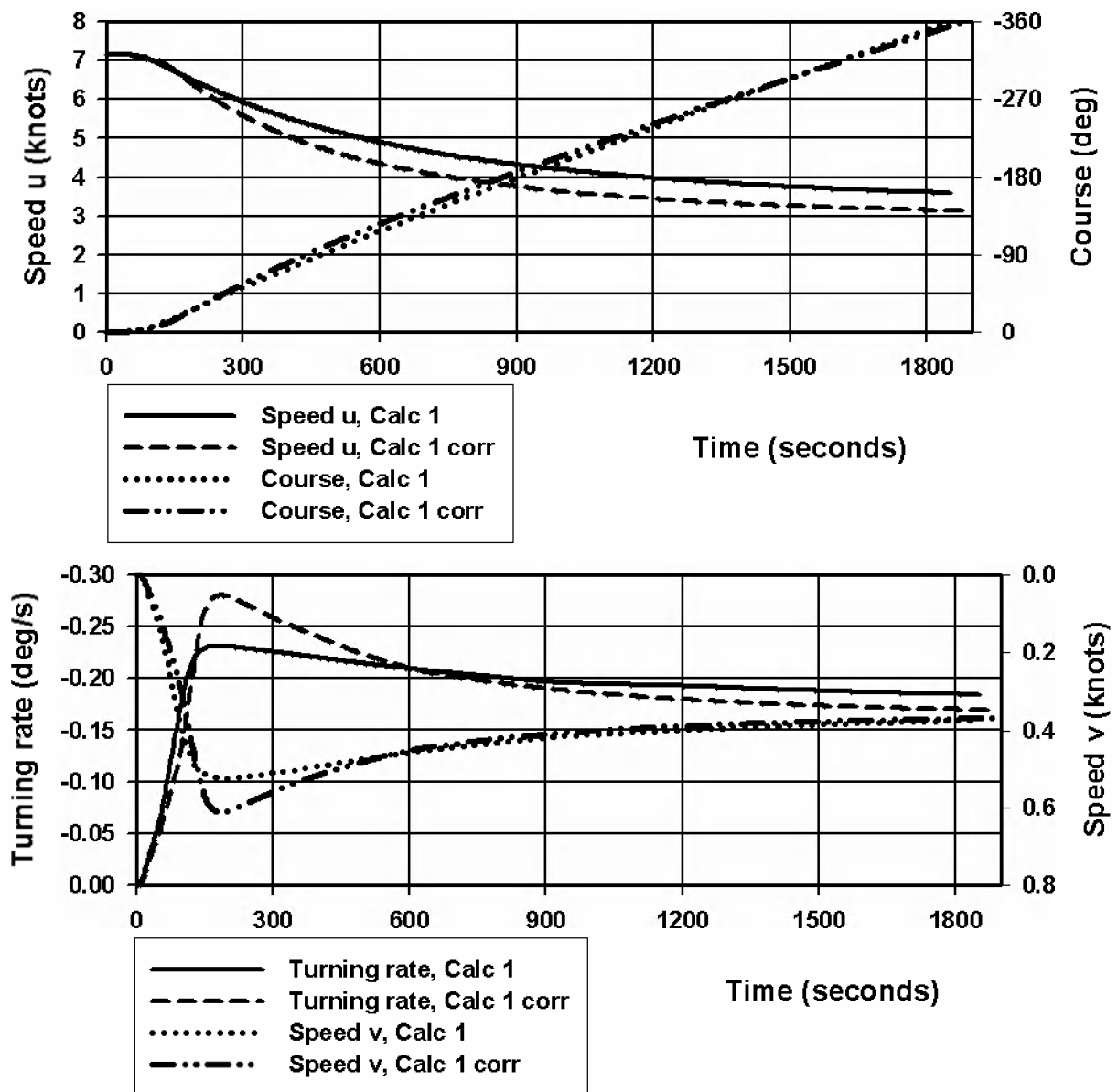
Figure 7.13 Esso Osaka, at 50% UKC, comparison of speed components, turning rate and course change as function of time for calculation 1 and the corrected version of calculation 1
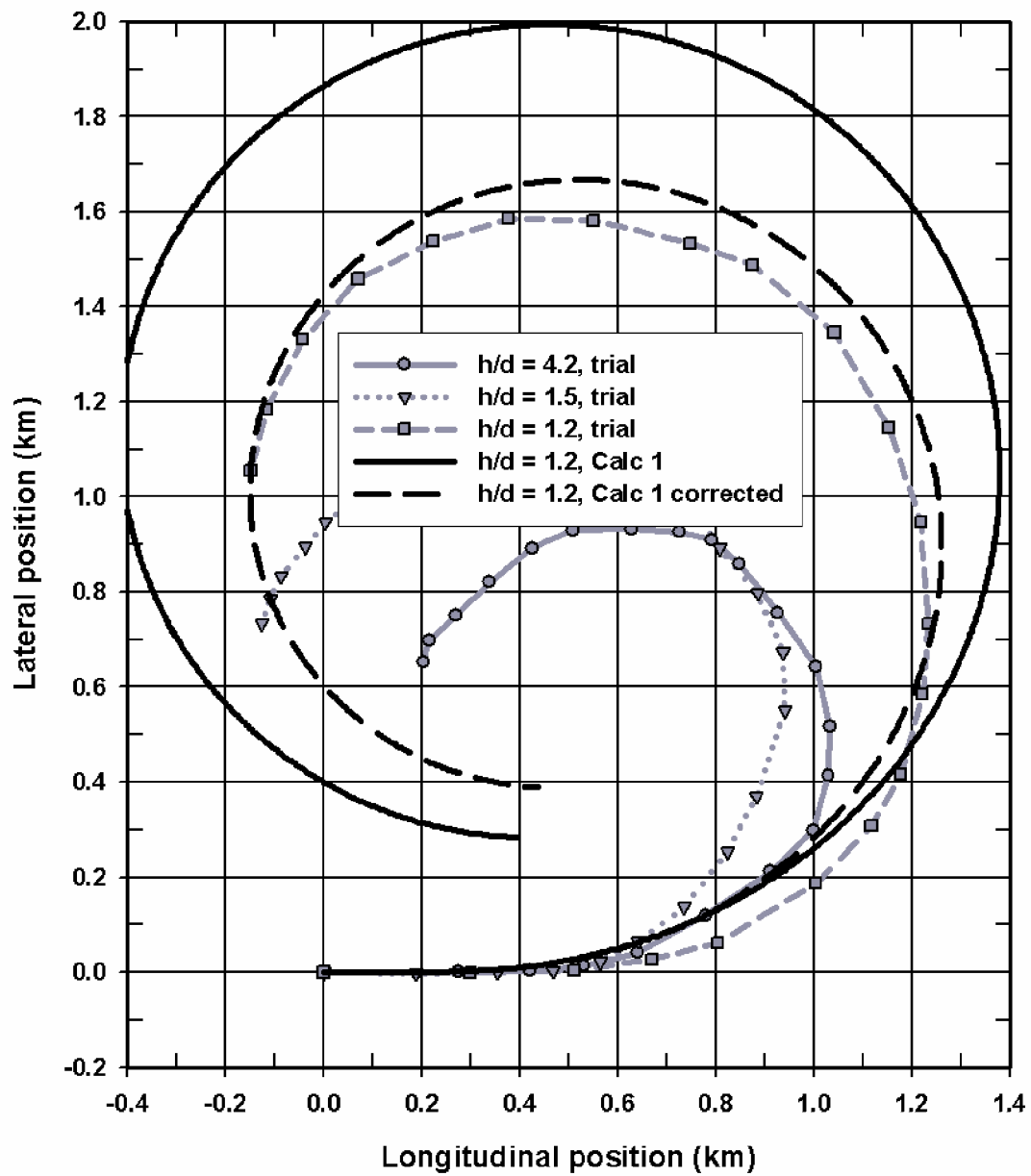
Figure 7.14 Esso Osaka, at 20% UKC, influence of correction for wake factor $w_{R,X}$ and $w_{R,Y}$ on the manoeuvring characteristics of a conventional turn to port: comparison calc 1 and calc 1 corrected
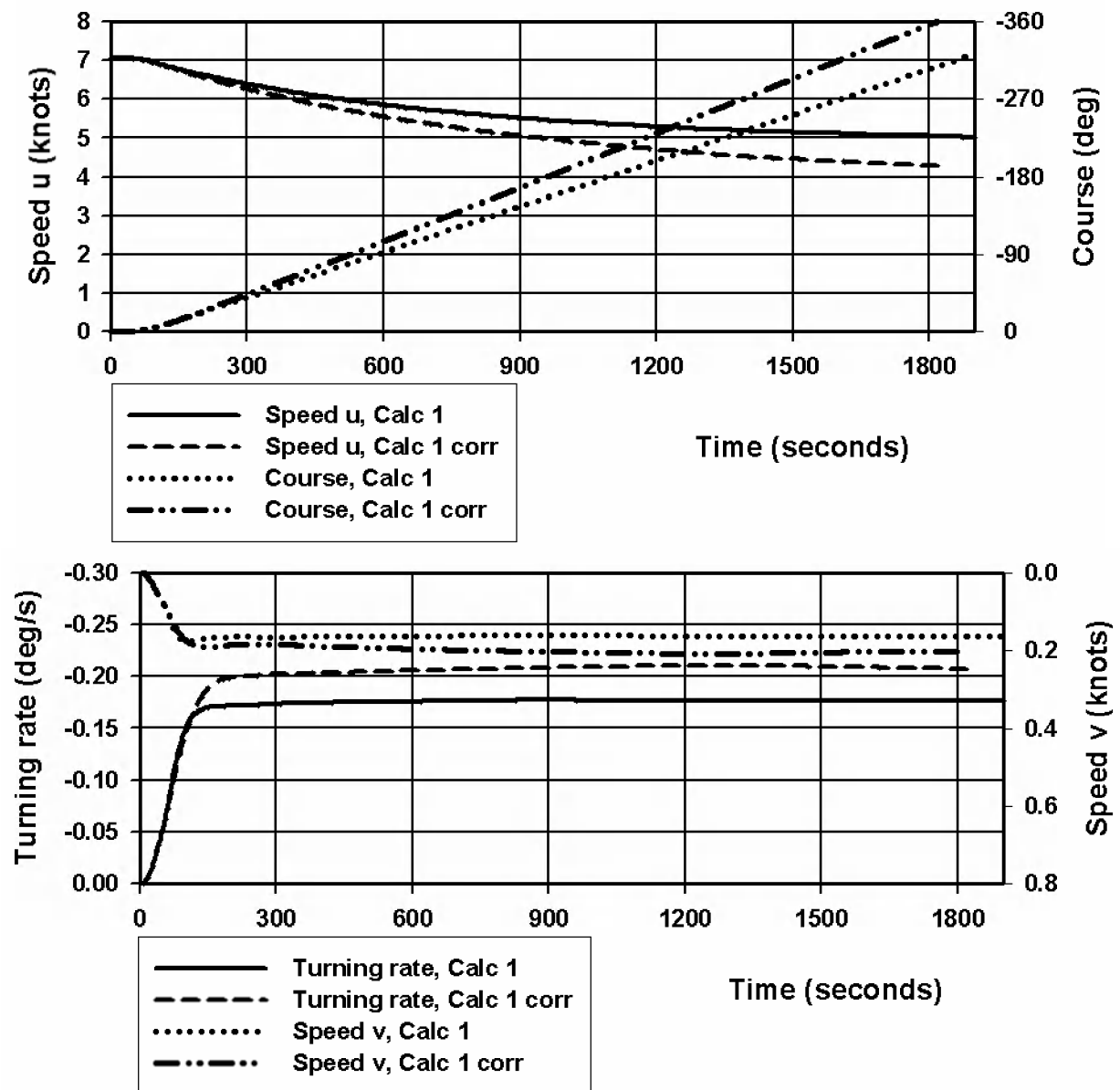
Figure 7.15 Esso Osaka, at 20% UKC, comparison of speed components, turning rate and course change as function of time for calculation 1 and the corrected version of calculation 1
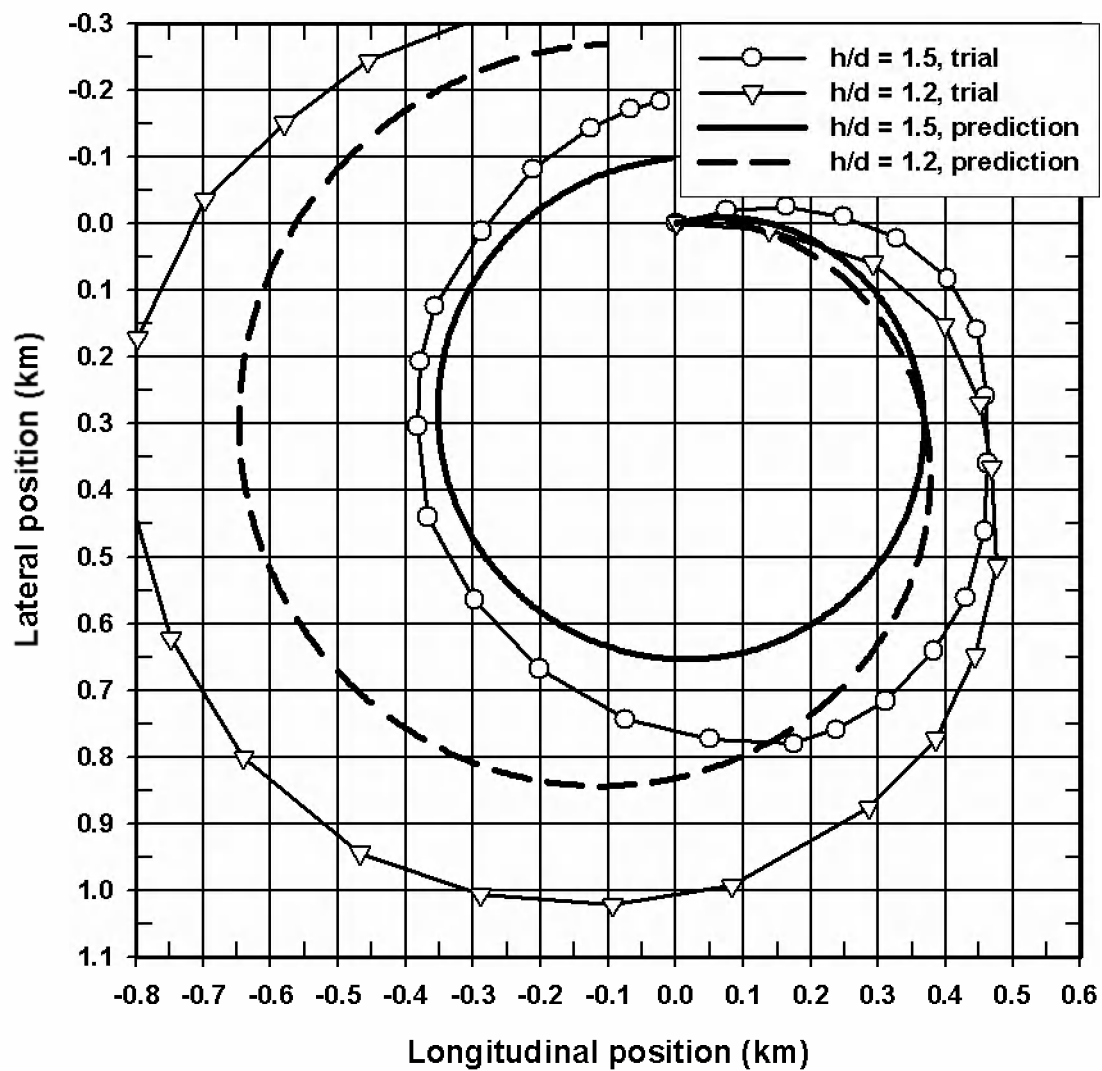
Figure 7.16 Esso Osaka, comparison of trial and model for an accelerating turn
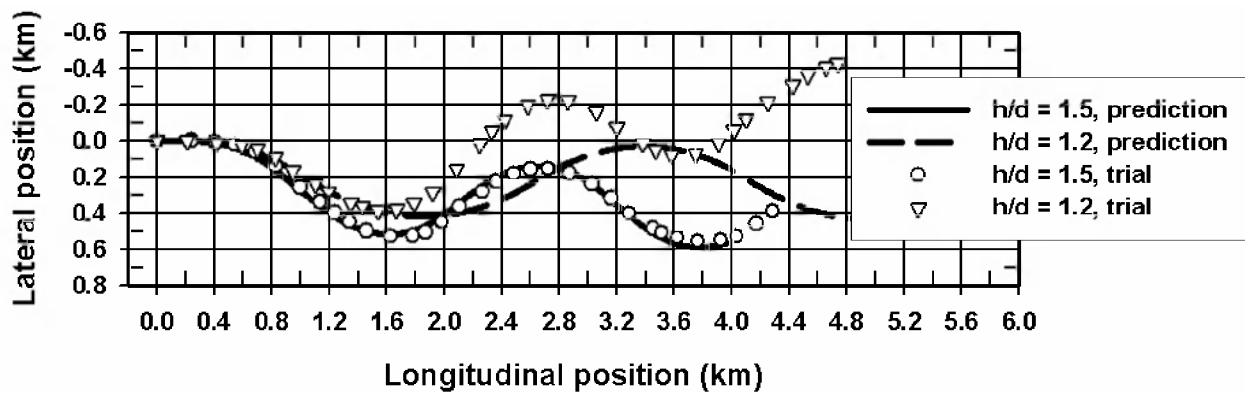
Figure 7.17 Esso Osaka, comparison of trial and model for a conventional zigzag manoeuvre
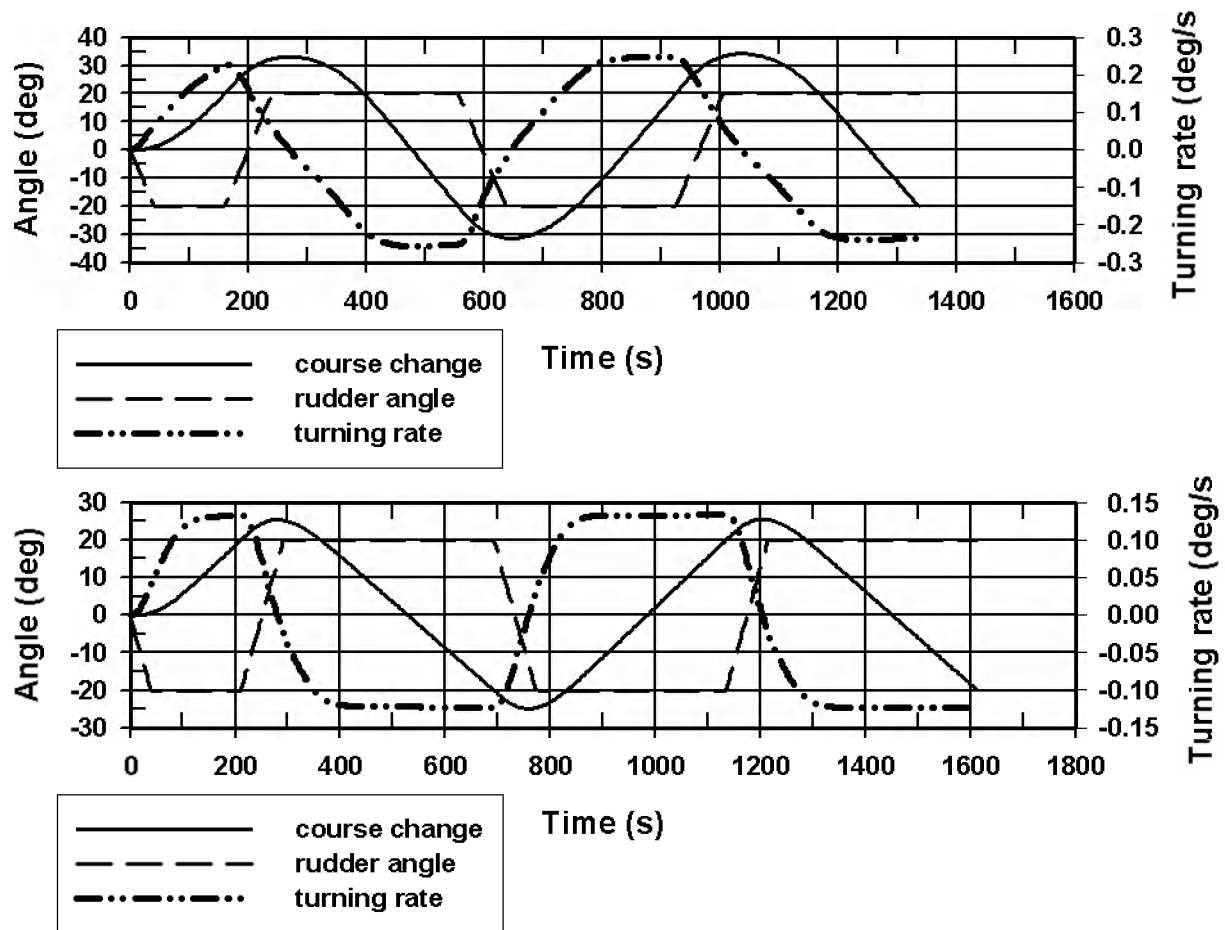
Figure 7.18 Esso Osaka, time dependence of course change, turning rate and rudder angle for a conventional zigzag (50% UKC, top, and 20% UKC, bottom)
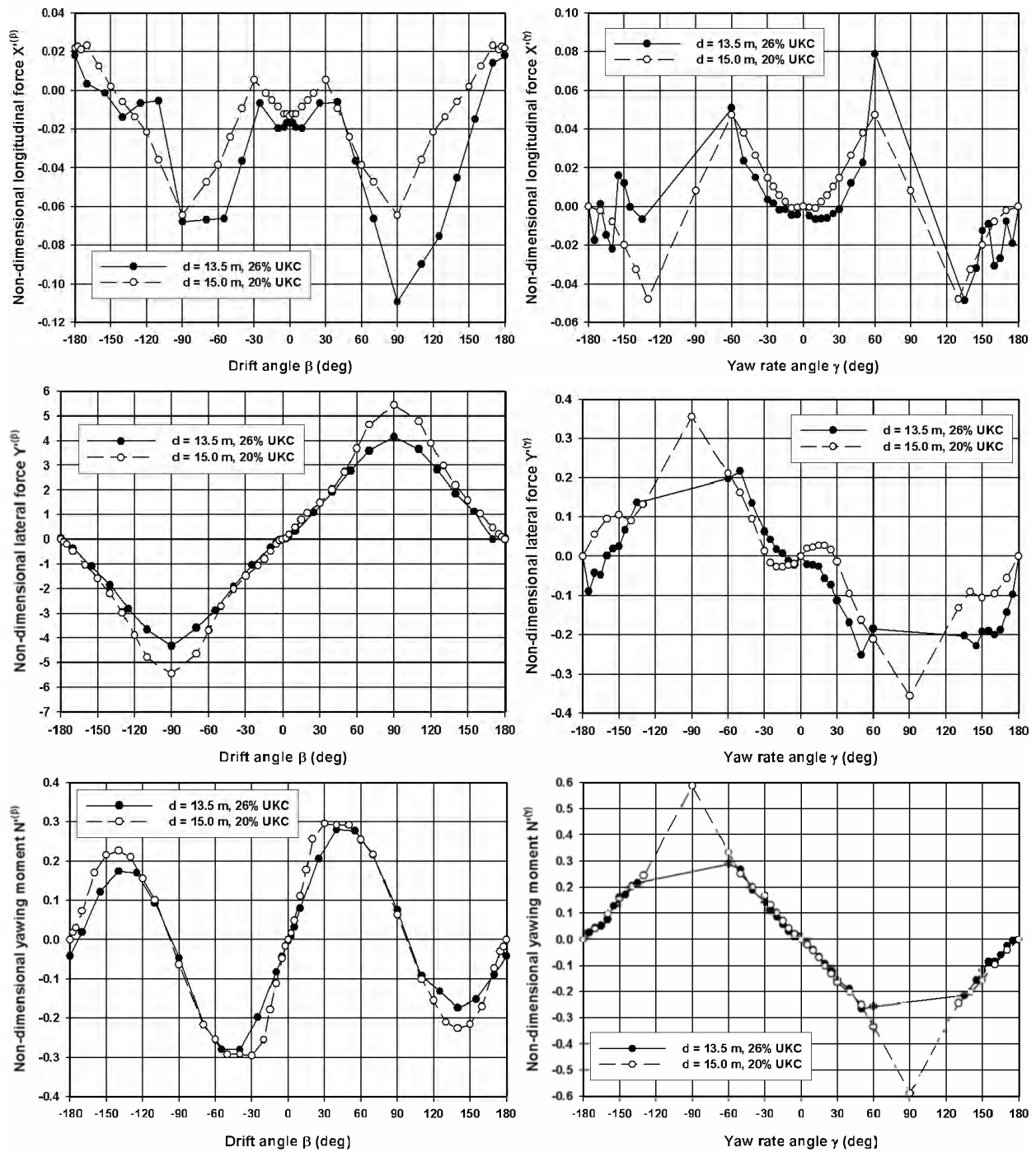
Figure 7.19 Containership D, comparison of sway and yaw dependent hull forces for a combination (draught = 13.5 m, 26% UKC) and (draught = 15.0 m, 20% UKC)
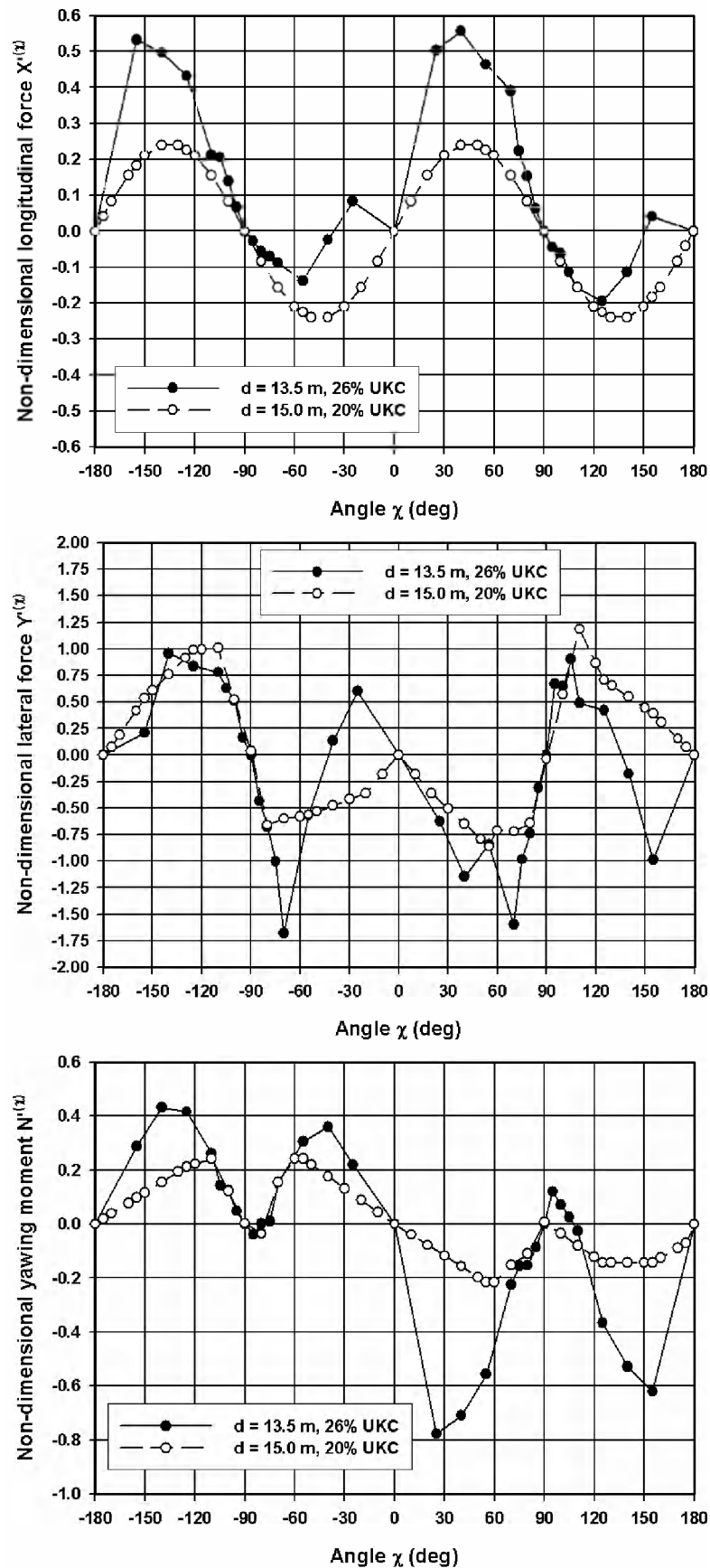
Figure 7.20 Containership D, comparison of hull forces due to cross-coupling sway-yaw for a combination (draught = 13.5 m, 26% UKC) and (draught = 15.0 m, 20% UKC)
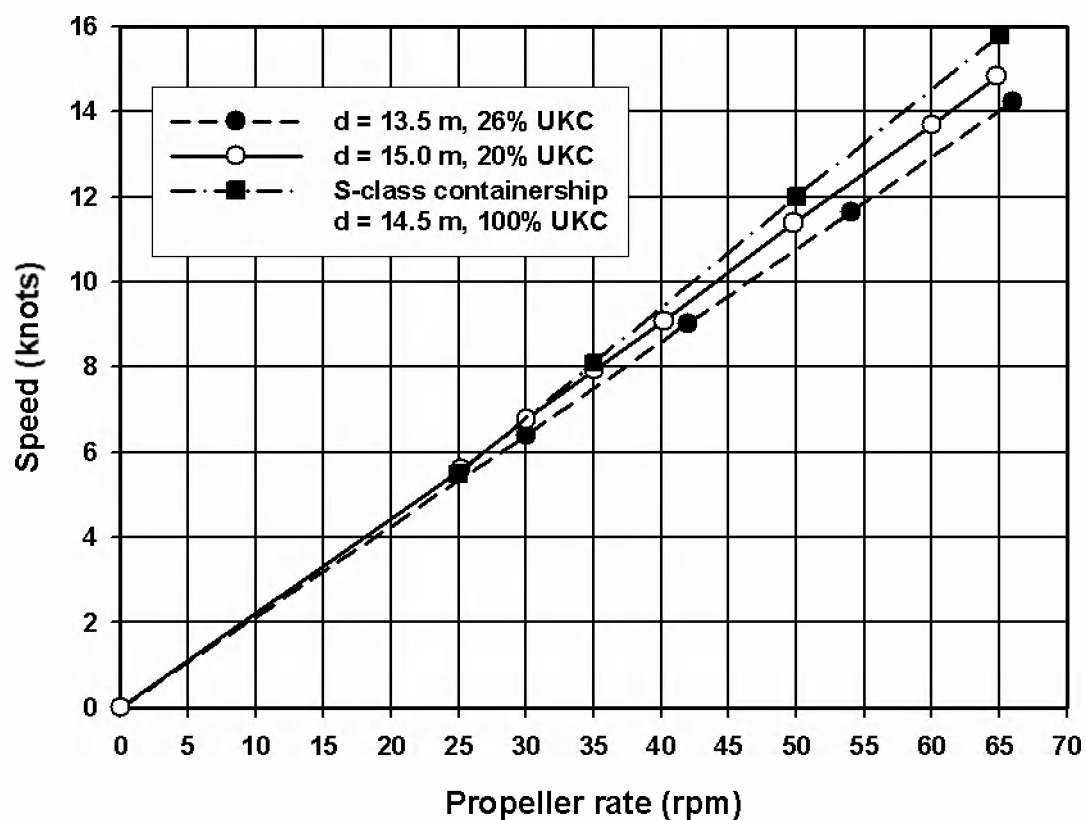
Figure 7.21 Containership D, comparison speed-rpm table for model D at 13.5 m and 15 m draught in shallow water and a S-class containership in deep water
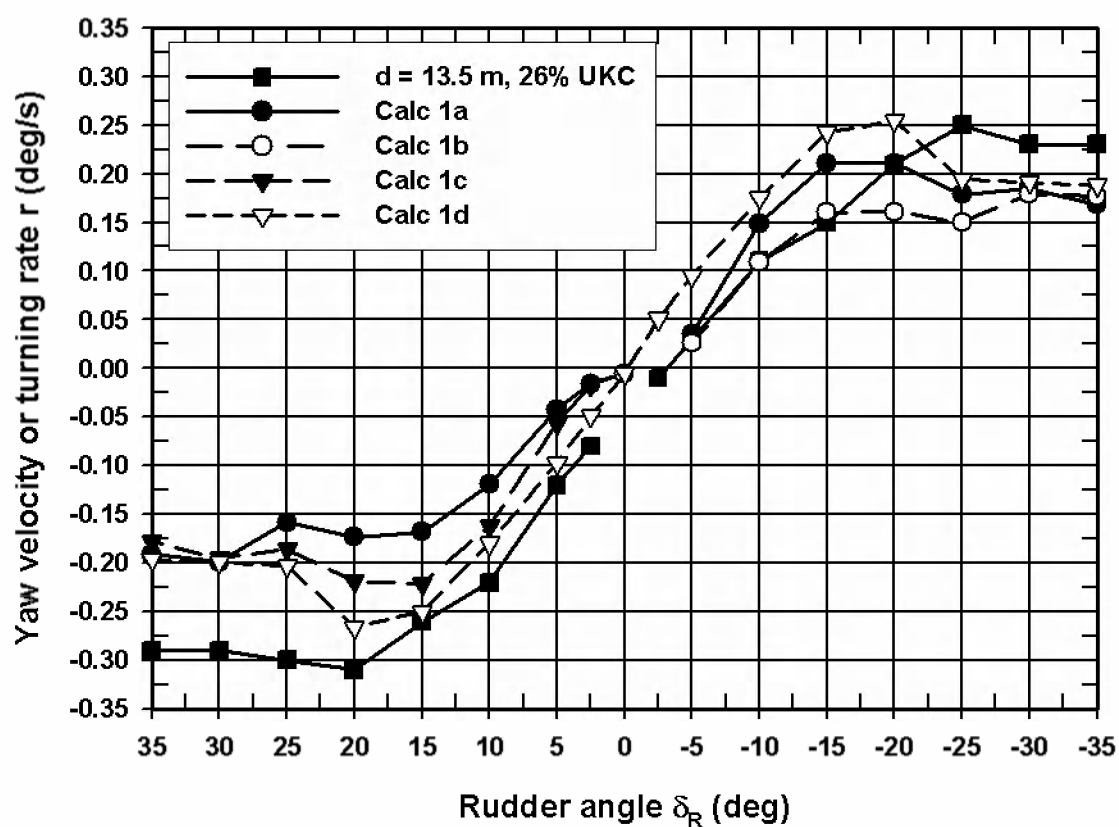
Figure 7.22 Containership D, turning circle manoeuvres, examination of the asymmetry induced by the rudder
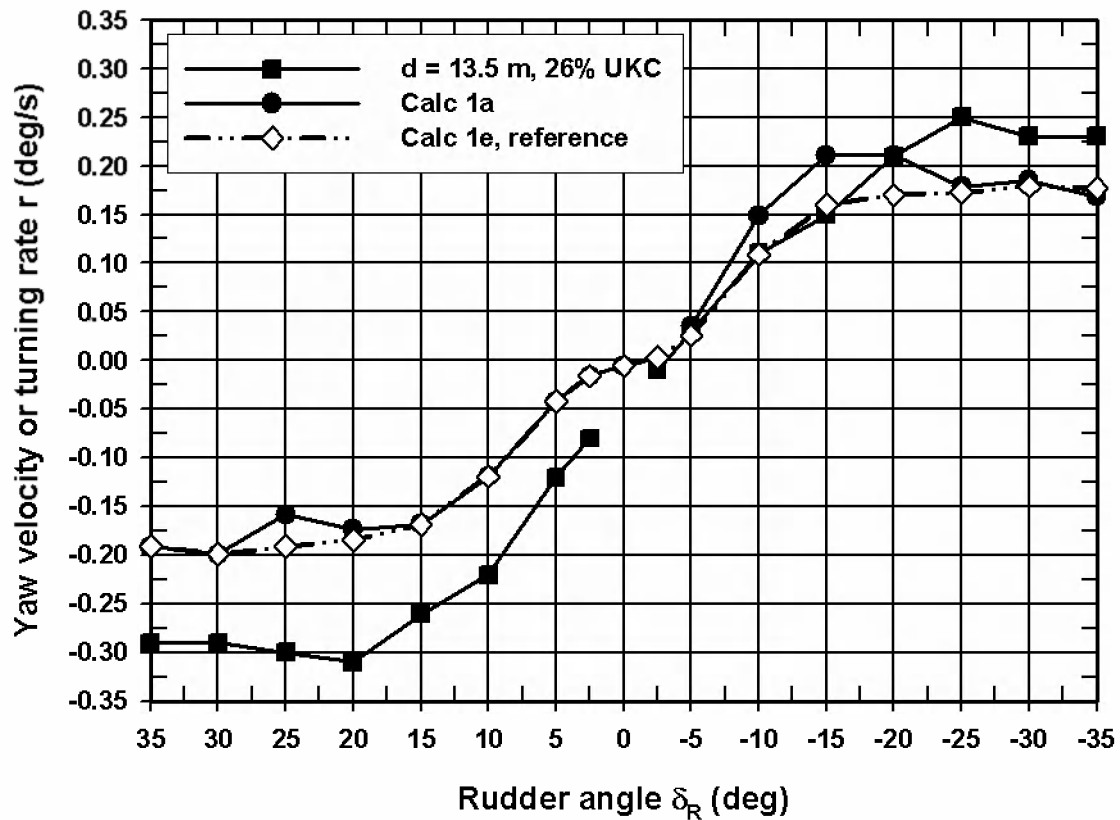
Figure 7.23 Containership D, determination of a reference condition for the sensitivity analysis
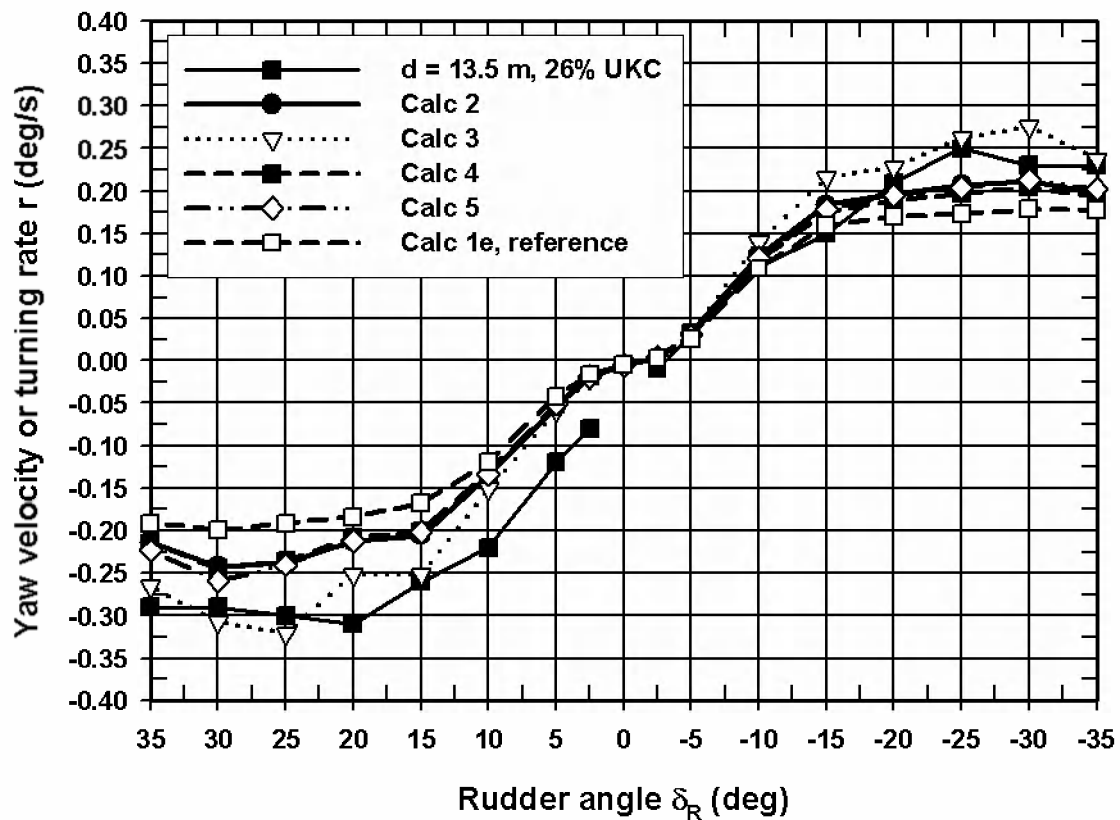
Figure 7.24 Containership D, variation of turning rate during a sensitivity analysis of velocity dependent hull forces
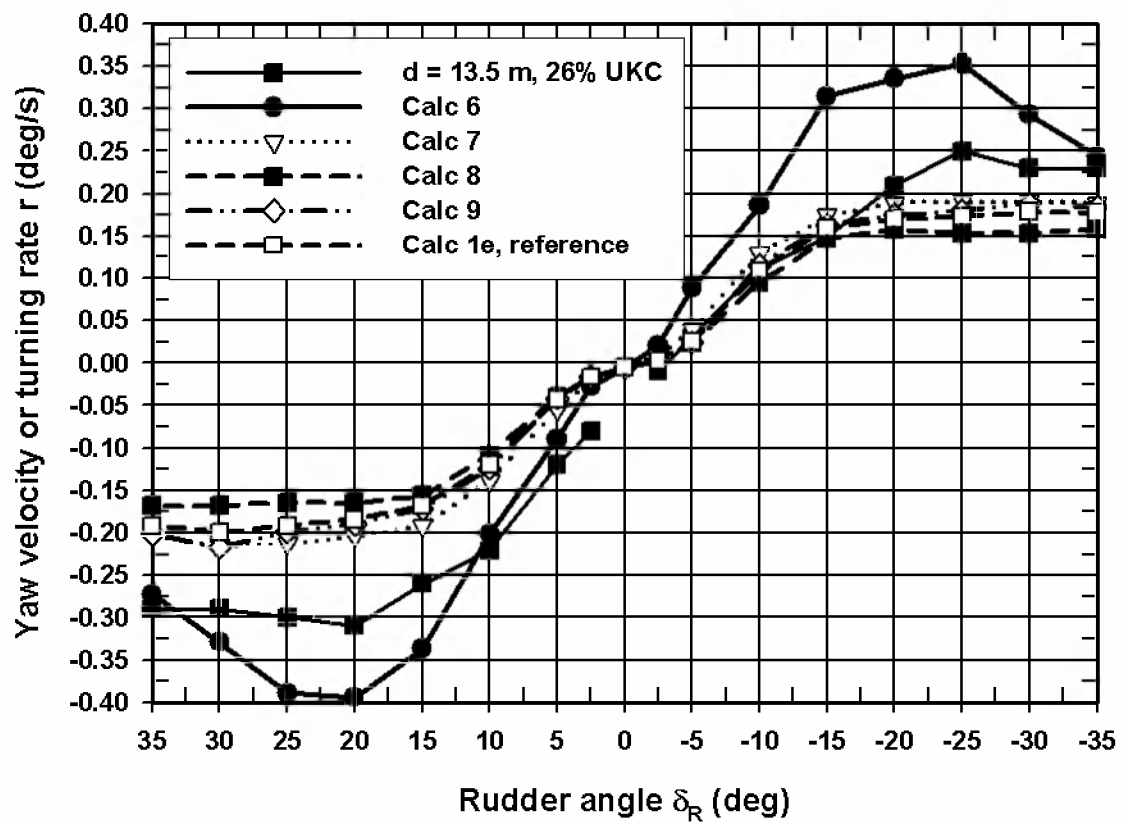
Figure 7.25 Containership D, variation of turning rate during a sensitivity analysis of rudder induced coefficients

IMO Standards for ship manoeuvrability

In november 1993 the IMO "Interim Standards for Ship Manoeuvrability" were adopted by resolution A.751(18) to ensure that ships are designed to a uniform standard. Involved with safe navigation the Maritime Safety Committee (MSC) of the IMO hoped to improve the ship performance at the design stage by offering standards for the ship designer and regulatory authorities. After collecting data during almost a decade the interim standards where evaluated and turned into the "Standards for ship manoeuvrability" by resolution MSC.137(76) in december 2002 [97].

Table 1 The IMO Criteria applied to the Standards for ship manoeuvrability

Turning ability	Advance $\leq$ 4.5 L Tactical Diameter $\leq$ 5 L
Initial turning ability	With 10 deg rudder angle to port or starboard, the ship should not have travelled more than 2.5 L by the time the heading has changed by 10 deg from its initial value.
Yaw checking and Course keeping qualities	The value of the first overshoot angle in the 10/10 Z-manoeuvre should not exceed: 10 deg if L/V < 10 seconds 20 deg if L/V $\geq$ 30 seconds $\left(5 + \frac{1}{2}\left(L/V\right)\right)$ deg for 10 $\leq$ L/V $\leq$ 30 seconds The value of the second overshoot angle in the 10/10 Z-manoeuvre should not exceed the above criterion values for the overshoot by more than 15 deg. The value of the first overshoot angle in the 20/20 Z-manoeuvre should not exceed 25 deg.
Stopping ability	The track reach in the full astern stopping test should not exceed 15 to 20 L.
Dieudonné spiral	Depending on the behaviour of the vessel in relation to the above criteria, a Dieudonné spiral test can be performed and the width and height of any hysteresis loop determined.

(Note: V = vessel's normal service speed in m/s)

The IMO Criteria, summarized in [97], judge some manoeuvring characteristics like (initial) turning ability, yaw checking, course keeping and stopping ability. They comprise four main and one optional criteria (Table 1) that are to be satisfied at the vessel's normal service speed V in calm weather, in winds less than 10 knots and in the absence of currents (or have to be corrected for current influences). These criteria only describe manoeuvres at the fully loaded or design condition in quadrant 1 and the transition between quadrant 1 and 2 during a stopping manoeuvre. In Table 2 a quadrant distribution for some manoeuvres is given. These manoeuvres are not only restricted to the Standards but are extended to manoeuvres at low speed in deep or shallow water.

Table 2 Quadrant distribution of the IMO Criteria according to [23]

Category	Characteristics	Manoeuvre(s)	Quadrant(s)
Manoeuvring In deep water	Course change	Initial turning	Quad. 1
		Course change	Quad. 1
	Turning circle	Max. rudder turning circle from Full Sea	Quad. 1
	Accelerating turn	Max. rudder accelerating turn from rest	Quad. 1
	Yaw checking	Zigzag	Quad. 1
		Pull-out	Quad. 1
	Man-overboard & Parallel course	Man-overboard	Quad. 1
		Parallel course	Quad. 1
	Lateral thruster	Turning at zero speed	Quad. 1
		Turning with forward speeds	Quad. 1
Stopping & speed control in deep water	Stopping	Full astern from Full Sea AHD	Quad. 1 $\rightarrow$ 2
		Full astern from Full AHD	Quad. 1 $\rightarrow$ 2
		Full astern from Half AHD	Quad. 1 $\rightarrow$ 2

Category	Characteristics	Manoeuvre(s)	Quadrant(s)
		Full astern from Slow AHD	Quad. 1 → 2
	Coasting stop	Stop engine from Full Sea AHD	Quad. 1
		Stop engine from Full AHD	Quad. 1
		Stop engine from Half AHD	Quad. 1
		Stop engine from Slow AHD	Quad. 1
	Deceleration	Full Sea to standby engine	Quad. 1
		Full AHD to Half AHD	Quad. 1
		Half AHD to Slow AHD	Quad. 1
		Slow AHD to Dead Slow AHD	Quad. 1
	Acceleration	From rest to Full Sea	Quad. 1
Manoeuvring in shallow water	Turning circle	Max. rudder turning circle from Half	Quad. 1
	Squat	Desired information specified, but no specific manoeuvre described	Quad. 1
Manoeuvring at low speed		Desired information specified, but no specific manoeuvre described	Quad. 1

A short description is given of:
❑ the test program in deep water: Table 1
❑ the number of tests for the deep water program: Table 2
❑ the test program in shallow water: Table 3
❑ the number of tests for the shallow water program: Table 4

Table 1 Test program in deep water

(a)   Bollard pull tests at zero speed

Bollard pull tests (type PAAL)

Propeller rate	Rudder angle (°)
-0.8 n_0	0
-0.5 n_0	0
0.4 n_0	*-40, -30, -20, -10, 0, 10, 20, 30, 40*
0.6 n_0	*-40, -30, -20, -10, 0, 10, 20, 30, 40*
1.0 n_0	*-40, -30, -20, -10, 0, 10, 20, 30, 40*

Multi-modal tests (type MULTI0)

Speed (kn)	Propeller rate	ψ (°)	Time (s) of regime	Rudder angle (model scale)			
				mean (°)	amplitude (°)	period (s)	phase (°)
0	$0.4n_0$	0	50	0	40	25	0
0	$0.6n_0$	0	50	0	40	25	0
0	$1.0n_0$	0	50	0	40	25	0

(b)   Stationary tests (type STATX)

Quadrant	Speed (kn)	Propeller rate	Rudder angle (°)	Sense	ψ (°)
1	2	$0.4n_0$, $0.6n_0$, $0.8n_0$	0	+	0
	4	$0.4n_0$, $0.6n_0$, $0.8n_0$	-40	+	0
		$0.4n_0$, $0.6n_0$, $0.8n_0$	-2.5	+	0
		$0.4n_0$, $0.6n_0$, $0.8n_0$	0	+	0
		$0.4n_0$, $0.6n_0$, $0.8n_0$	2.5	+	0
		$0.4n_0$, $0.6n_0$, $0.8n_0$	40	+	0
		$0.4n_0$, $0.6n_0$, $0.8n_0$	-40	+	+/-10
		$0.4n_0$, $0.6n_0$, $0.8n_0$	40	+	+/-10
		$0.4n_0$, $0.6n_0$, $0.8n_0$	-40	+	+/-25
		$0.4n_0$, $0.6n_0$, $0.8n_0$	40	+	+/-25
	6	$0.4n_0$, $0.6n_0$, $0.8n_0$	0	+	0
	8	$0.4n_0$, $0.6n_0$, $0.8n_0$	-40	+	0
		$0.4n_0$, $0.6n_0$, $0.8n_0$	0	+	0
		$0.4n_0$, $0.6n_0$, $0.8n_0$	40	+	0
		$0.4n_0$, $0.6n_0$, $0.8n_0$	-40	+	+/-10
		$0.4n_0$, $0.6n_0$, $0.8n_0$	40	+	+/-10
		$0.4n_0$, $0.6n_0$, $0.8n_0$	-40	+	+/-15
		$0.4n_0$, $0.6n_0$, $0.8n_0$	40	+	+/-15
	10	$0.4n_0$, $0.6n_0$, $0.8n_0$	0	+	0
	16	$0.4n_0$, $0.6n_0$, $0.8n_0$	-2.5	+	0
		$0.4n_0$, $0.6n_0$, $0.8n_0$	0	+	0
		$0.4n_0$, $0.6n_0$, $0.8n_0$	2.5	+	0
2	2	$-0.5 n_0$; $-0.8n_0$	0	+	0
		$-0.5 n_0$; $-0.8n_0$	0	+	2.5
		$-0.5 n_0$; $-0.8n_0$	0	+	5
		$-0.5 n_0$; $-0.8n_0$	0	+	10
		$-0.5 n_0$; $-0.8n_0$	0	+	25
		$-0.5 n_0$; $-0.8n_0$	0	+	40
		$-0.5 n_0$; $-0.8n_0$	0	+	55

Quadrant	Speed (kn)	Propeller rate	Rudder angle (°)	Sense	ψ (°)
		$-0.5\,n_0$; $-0.8n_0$	0	+	70
		$-0.5\,n_0$; $-0.8n_0$	0	+	90
	4	$-0.5\,n_0$; $-0.8n_0$	0	+	0
		$-0.5\,n_0$; $-0.8n_0$	0	+	5
		$-0.5\,n_0$; $-0.8n_0$	0	+	-5
		$-0.5\,n_0$; $-0.8n_0$	0	+	10
		$-0.5\,n_0$; $-0.8n_0$	0	+	-10
	8	$-0.5\,n_0$; $-0.8n_0$	0	+	0
		$-0.5\,n_0$; $-0.8n_0$	0	+	5
		$-0.5\,n_0$; $-0.8n_0$	0	+	10
3	2	$-0.35n_0$; $-0.5\,n_0$; $-0.8n_0$	-40	-	0
		$-0.35n_0$; $-0.5\,n_0$; $-0.8n_0$	-20	-	0
		$-0.35n_0$; $-0.5\,n_0$; $-0.8n_0$	0	-	0
		$-0.35n_0$; $-0.5\,n_0$; $-0.8n_0$	20	-	0
		$-0.35n_0$; $-0.5\,n_0$; $-0.8n_0$	40	-	0
	4	$-0.35n_0$; $-0.5\,n_0$; $-0.8n_0$	-40	-	0
		$-0.35n_0$; $-0.5\,n_0$; $-0.8n_0$	-20	-	0
		$-0.35n_0$; $-0.5\,n_0$; $-0.8n_0$	0	-	0
		$-0.35n_0$; $-0.5\,n_0$; $-0.8n_0$	20	-	0
		$-0.35n_0$; $-0.5\,n_0$; $-0.8n_0$	40	-	0
	2	$-0.35n_0$; $-0.5\,n_0$; $-0.8n_0$	-40	-	+/-10
		$-0.35n_0$; $-0.5\,n_0$; $-0.8n_0$	40	-	+/-10
	4	$-0.35n_0$; $-0.5\,n_0$; $-0.8n_0$	-40	-	+/-10
		$-0.35n_0$; $-0.5\,n_0$; $-0.8n_0$	40	-	+/-10
	2	$-0.35n_0$; $-0.5\,n_0$; $-0.8n_0$	-40	-	+/-25
		$-0.35n_0$; $-0.5\,n_0$; $-0.8n_0$	40	-	+/-25
	4	$-0.35n_0$; $-0.5\,n_0$; $-0.8n_0$	-40	-	+/-25
		$-0.35n_0$; $-0.5\,n_0$; $-0.8n_0$	40	-	+/-25
4	2	$0.6n_0$; $0.8n_0$	-40	-	0
			0	-	0
			40	-	0
		$0.6n_0$; $0.8n_0$	-40	-	+/-10
			0	-	+/-10
			40	-	+/-10
		$0.6n_0$; $0.8n_0$	-40	-	+/-25
			0	-	+/-25
			40	-	+/-25
	4	$0.6n_0$; $0.8n_0$	-40	-	0
			0	-	0
			40	-	0
		$0.6n_0$; $0.8n_0$	-40	-	+/-10
			0	-	+/-10
			40	-	+/-10
		$0.6n_0$; $0.8n_0$	-40	-	+/-25
			0	-	+/-25
			40	-	+/-25

(c)   Harmonic PMM sway tests (type PMMY2)

Speed (kn)	Propeller rate	Sway motion (model scale)		
		amplitude y_{OA} (m)	period T_y (s)	$|\beta_{MAX}|$ (°)
-2	0	0.2	100	174
2	0	0.2	40	15
6	0	0.2	27	8
12	0	0.2	24	4

(d) **Harmonic PMM yaw tests (type PMMPSI2)**

Qu.	Speed (kn)	Propeller rate	Rudder angle (°)	Sense	ψ (model scale)			
					mean (°)	amplitude (°)	period (s)	$\lvert \gamma_{MAX} \rvert$ (°)
1	4	0	0	+	+/-25, 0	10	50	11
		0	0	+	0	15, 25, 35	50	16, 26, 34
		0	0	+	0	15, 25, 35	34	23, 35, 45
		0	0	+	+/-10, +/-5	25	50	26
		$0.4n_0$	-40, -30, -20, -10, 0, 10, 20, 30, 40	+	0	25	50	26
		$0.8n_0$	-40, -30, -20, -10, 0, 10, 20, 30, 40	+	0	25	50	26
	<u>12</u>	0	0	+	0	15, 25, 35	25	11, 18, 24
		0	0	+	0	15, 25, 35	17	16, 25, 34
		0	0	+	+/-10, +/-5	25	25	18
		$0.4n_0$	-40, -30, -20, -10, 0, 10, 20, 30, 40	+	0	25	25	18
		$0.8n_0$	-40, -30, -20, -10, 0, 10, 20, 30, 40	+	0	25	25	18
3	4	0	0	-	0	15, 25, 35	34	156, 144, 134
		0	0	-	+/-10, +/-5	25	34	144
		$-0.5n_0$	-40, -20, 0, 20, 40	-	0	25	34	144
		$-0.8n_0$	-40, -20, 0, 20, 40	-	0	25	34	144
4	4	$0.6n_0$	-40, -30, -20, -10, 0, 10, 20, 30, 40	-	0	25	34	144
		$0.8n_0$	-40, -30, -20, -10, 0, 10, 20, 30, 40	-	0	25	34	144
		$0.8n_0$	0	-	0	5	34	172

(e) **Oscillatory tests at zero speed (type OSCPSI)**

Speed (kn)	ψ_A (°)	Period (s)	Phase (°)	# cycli
0	25	54	90	3

(f) **Multi-modal tests (type MULTI0 and MULTI1)**
type B

Speed (kn)	Sense	ψ (°)	Propeller rate (model scale)			
			mean	amplitude	period (s)	phase (°)
2	+	0, 2.5, 5, 10, 25, 40, 55, 70, 90	$0.4n_0$	$0.4n_0$	400	-90
2	+	*-2.5, -5, -10, -25, -40, -55, -70, -90*	*$0.4n_0$*	*$0.4n_0$*	*400*	*-90*
4	+	0, 2.5, 5, 10, 25	$0.4n_0$	$0.4n_0$	200	-90
4	+	*-2.5, -5, -10, -25*	*$0.4n_0$*	*$0.4n_0$*	*200*	*-90*
8	+	0, 2.5, 5, 10, 15	$0.4n_0$	$0.4n_0$	100	-90
8	+	*-2.5, -5, -10, -15*	*$0.4n_0$*	*$0.4n_0$*	*100*	*-90*
<u>16</u>	+	0, 5	$0.4n_0$	$0.4n_0$	<u>50</u>	-90
<u>16</u>	+	*-5*	*$0.4n_0$*	*$0.4n_0$*	*<u>50</u>*	*-90*
-2	-	0, 5, 10, 25, 40, 55, 70	$0.4n_0$	$0.4n_0$	400	-90
-2	-	*-5, -10, -25, -40, -55, -70*	*$0.4n_0$*	*$0.4n_0$*	*400*	*-90*

type A – quadrant 1

Speed (kn)	Propeller rate	ψ (°)	Rudder angle (model scale)			
			mean (°)	amplitude (°)	period (s)	phase (°)
2	$0.4n_0$	0	0	40	200	0
	$0.6n_0$	0, 5, 10, 25, 40, 55, 70, 90	0	40	200	0
	$0.6n_0$	*-5, -10,-25,-40,-55,-70, -90*	*0*	*40*	*200*	*0*
	$0.8n_0$	0	0	40	200	0
4	$0.4n_0$	0	0	40	100	0

Speed (kn)	Propeller rate	ψ (°)	Rudder angle (model scale)			
			mean (°)	amplitude (°)	period (s)	phase (°)
	$0.6n_0$	0, 5, 10, 25	0	40	100	0
	$0.6n_0$	-5, -10, -25	0	40	100	0
	$0.8n_0$	0	0	40	100	0
8	$0.4n_0$	0	0	40	50	0
	$0.6n_0$	0, 5, 10, 15	0	40	50	0
	$0.6n_0$	-5, -10, -15	0	40	50	0
	$0.8n_0$	0	0	40	50	0
<u>16</u>	$0.4n_0$	0	0	40	<u>25</u>	0
	$0.6n_0$	0, 5	0	40	<u>25</u>	0
	$0.6n_0$	-5	0	40	<u>25</u>	0
	$0.8n_0$	0	0	40	<u>25</u>	0

type A – quadrant 3

Speed (kn)	Propeller rate	ψ (°)	Rudder angle (model scale)			
			mean (°)	amplitude (°)	period (s)	phase (°)
-2	$-0.5n_0$	0, 5, 10, 25, 40, 55, 70	0	40	200	0
	$-0.5n_0$	-5, -10, -25, -40, -55, -70	0	40	200	0
	$-0.8n_0$	0	0	40	200	0
-4	$-0.5n_0$	0, 5, 10, 25	0	40	100	0
	$-0.5n_0$	-5, -10, -25	0	40	100	0
	$-0.8n_0$	0	0	40	100	0

type A – quadrant 4

Speed (kn)	Propeller rate	ψ (°)	Rudder angle (model scale)			
			mean (°)	amplitude (°)	period (s)	phase (°)
-2	$0.6n_0$	0, 5, 10, 25, 40, 55, 70	0	40	200	0
	$0.6n_0$	-5, -10, -25, -40, -55, -70	0	40	200	0
	$0.8n_0$	0	0	40	200	0
-4	$0.6n_0$	0, 5, 10, 25	0	40	100	0
	$0.6n_0$	-5, -10, -25	0	40	100	0
	$0.8n_0$	0	0	40	100	0

type C: transition between quadrants 1-2 en 3-4

Speed			
mean (kn)	amplitude (kn)	period (s) (model scale)	phase (°)
-2	2	200	90
<u>8</u>	<u>8</u>	100	-90

type D: validation runs

Run	Parameter				Parameter				Parameter				Parameter			
	f_m	f_A	T_f(s)	ϕ_f (°)	f_m	f_A	T_f(s)	ϕ_f (°)	f_m	f_A	T_f(s)	ϕ_f (°)	f_m	f_A	T_f(s)	ϕ_f (°)
1	Propeller rate				Rudder angle (°)				Speed u_0 (kn)							
	$0.5n_0$	$0.5n_0$	30	-90	0	40	40	0	<u>8</u>	<u>8</u>	100	-90				
2	Propeller rate				Rudder angle (°)				Speed u_0 (kn)				ψ (°)			
	$0.4n_0$	$0.4n_0$	30	-90	0	40	40	0	4	4	100	-90	10	0	10	0
3	Propeller rate				Rudder angle (°)				Speed u_0 (kn)				ψ (°)			
	$0.4n_0$	$0.4n_0$	30	-90	0	40	40	0	4	4	100	-90	-10	0	10	0
4	Propeller rate				Speed u_0 (kn)				ψ (°)							
	$0.4n_0$	0	30	90	4	4	50	-90	0	20	100	-90				
5	Propeller rate				Yaw velocity r (°/s)				Rudder angle (°)				Speed u_0 (kn)			
	$0.4n_0$	$0.4n_0$	280	180	0	2.25	70	90	0	40	45	0	2	0	720	0
6	Propeller rate				Yaw velocity r (°/s)				Rudder angle (°)				Speed u_0 (kn)			
	$0.4n_0$	$0.4n_0$	28	180	0	2.25	70	90	0	40	45	0	2	2	140	90

Table 2 Test program in deep water: number of tests

TYPE	Speed	RPM	Rudder	Qu.		Base	Optio nal	Total (base)	Total (optional)
PAAL	0	< 0	0	Q2-Q3	UXAA	2		2	
	0	> 0	0	Q1-Q4	UXAA		3		3
STATX	> 0	> 0	0	Q1	UXCB1	1		101	
					UXCC1	1			
					UXCE1	1			
					UXCI	1			
	> 0	> 0	<> 0	Q1	UXCC1	12			
					UXCE1	10			
					UXCI	2			
	> 0	< 0	0	Q2	UXCB2	9			
					UXCC2	5			
					UXCE2	3			
	< 0	< 0	0	Q3	UXCJ3	1			
					UXCK3	1			
	< 0	< 0	<> 0	Q3	UXCJ3	12			
					UXCK3	12			
	< 0	> 0	0	Q4	UXCJ4	5			
					UXCK4	5			
	< 0	> 0	<> 0	Q4	UXCJ4	10			
					UXCK4	10			
PMMY2	> 0	0	0		UXFB	1		4	
					UXFD	1			
					UXFG	1			
	< 0	0	0		UXFJ	1			
PMMPS2	> 0	0	0	Q1	UXGC	13		95	
					UXGE	10			
	> 0	> 0	0	Q1	UXGC	2			
					UXGE	2			
	> 0	> 0	<> 0	Q1	UXGC	16			
					UXGE	16			
	< 0	0	0	Q3	UXGK	7			
	< 0	< 0	0	Q3	UXGK	2			
	< 0	< 0	<> 0	Q3	UXGK	8			
	< 0	> 0	0	Q4	UXGK	3			
	< 0	> 0	<> 0	Q4	UXGK	16			
OSCPSI	0	0	0		UXOP	1		1	
MULTI0 A	0	> 0	<> 0	Q1-Q4	UXMA	3		91	55
	> 0	> 0	<> 0	Q1	UXMB	10	7		
					UXMC	6	3		
					UXME	6	3		
					UXMI	4	1		
	< 0	< 0	<> 0	Q3	UXMJ	8	6		
					UXMK	5	3		

TYPE	Speed	RPM	Rudder	Qu.		Base	Optional	Total (base)	Total (optional)
	< 0	> 0	<> 0	Q4	UXMJ	8	6		
					UXMK	5	3		
MULTI0 B	> 0	> 0	0	Q1	UXMB	9	8		
					UXMC	5	4		
					UXME	5	4		
					UXMI	2	1		
	< 0	> 0	0	Q4	UXMJ	7	6		
MULTI1	< 0	0	0		UXML	1			
	> 0	0	0		UXMN	1			
	> 0	> 0	<> 0		UXMV(*)	4			
					UXMV1(*)	2			
TOTAL								294	58

(*) validation runs

Table 3 Test program in shallow water

(a) **Bollard pull tests at zero speed**

Bollard pull tests (type PAAL)

Propeller rate	Rudder angle (°)
-0.8 n_0	0
-0.5 n_0	0
0.4 n_0	*-40, -30, -20, -10, 0, 10, 20, 30, 40*
0.6 n_0	*-40, -30, -20, -10, 0, 10, 20, 30, 40*
1.0 n_0	*-40, -30, -20, -10, 0, 10, 20, 30, 40*

Multi-modal tests (type MULTI0)

Speed (kn)	Propeller rate	ψ (°)	Rudder angle (model scale)			
			mean (°)	amplitude (°)	period (s)	phase (°)
0	0.4n_0	0	0	40	25	0
0	0.6n_0	0	0	40	25	0
0	0.8n_0	0	0	40	25	0

(b) **Stationary tests (type STATX)**

Quadrant	Speed (kn)	Propeller rate	Rudder angle (°)	Sense	ψ (°)
1	2	0.4n_0, 0.6n_0, 0.8n_0	0	+	0
	4	0.4n_0, 0.6n_0, 0.8n_0	-40	+	0
		0.4n_0, 0.6n_0, 0.8n_0	-2.5	+	0
		0.4n_0, 0.6n_0, 0.8n_0	0	+	0
		0.4n_0, 0.6n_0, 0.8n_0	2.5	+	0
		0.4n_0, 0.6n_0, 0.8n_0	40	+	0
		0.4n_0, 0.6n_0, 0.8n_0	-40	+	+/-10
		0.4n_0, 0.6n_0, 0.8n_0	40	+	+/-10
		0.4n_0, 0.6n_0, 0.8n_0	-40	+	+/-25
		0.4n_0, 0.6n_0, 0.8n_0	40	+	+/-25
	6	0.4n_0, 0.6n_0, 0.8n_0	0	+	0
	8	0.4n_0, 0.6n_0, 0.8n_0	-40	+	0
		0.4n_0, 0.6n_0, 0.8n_0	0	+	0
		0.4n_0, 0.6n_0, 0.8n_0	40	+	0
		0.4n_0, 0.6n_0, 0.8n_0	-40	±	+/-5
		0.4n_0, 0.6n_0, 0.8n_0	40	±	+/-5
		0.4n_0, 0.6n_0, 0.8n_0	-40	+	+/-10

Quadrant	Speed (kn)	Propeller rate	Rudder angle (°)	Sense	ψ (°)
		$0.4n_0$, $0.6n_0$, $0.8n_0$	40	+	+/-10
		$0.4n_0$, $0.6n_0$, $0.8n_0$	-40	+	+/-25
		$0.4n_0$, $0.6n_0$, $0.8n_0$	40	+	+/-25
	10	$0.4n_0$, $0.6n_0$, $0.8n_0$	-2.5	+	0
		$0.4n_0$, $0.6n_0$, $0.8n_0$	0	+	0
		$0.4n_0$, $0.6n_0$, $0.8n_0$	2.5	+	0
	12	$0.4n_0$, $0.6n_0$, $0.8n_0$	-2.5	+	0
		$0.4n_0$, $0.6n_0$, $0.8n_0$	0	+	0
		$0.4n_0$, $0.6n_0$, $0.8n_0$	2.5	+	0
2	2	$-0.8n_0$	0	+	0
		$-0.8n_0$	0	+	2.5
		$-0.8n_0$	0	+	5
		$-0.5\,n_0$; $-0.8n_0$	0	+	10
		$-0.5\,n_0$; $-0.8n_0$	0	+	25
		$-0.5\,n_0$; $-0.8n_0$	0	+	40
		$-0.5\,n_0$; $-0.8n_0$	0	+	55
		$-0.8n_0$	0	+	70
		$-0.8n_0$	0	+	90
		$-0.5n_0$	0	+	0
		$-0.5n_0$	0	+	2.5
		$-0.5n_0$	0	+	5
		$-0.5n_0$	0	+	70
		$-0.5n_0$	0	+	90
	4	$-0.5\,n_0$; $-0.8n_0$	0	+	0
		$-0.5\,n_0$; $-0.8n_0$	0	+	5
		$-0.5\,n_0$; $-0.8n_0$	0	+	-5
		$-0.5\,n_0$; $-0.8n_0$	0	+	10
		$-0.5\,n_0$; $-0.8n_0$	0	+	-10
	8	$-0.5\,n_0$; $-0.8n_0$	0	+	0
		$-0.5\,n_0$; $-0.8n_0$	0	+	5
		$-0.5\,n_0$; $-0.8n_0$	0	+	10
3	2	$-0.35n_0$; $-0.5\,n_0$; $-0.8n_0$	-40	-	0
		$-0.35n_0$; $-0.5\,n_0$; $-0.8n_0$	-20	-	0
		$-0.35n_0$; $-0.5\,n_0$; $-0.8n_0$	0	-	0
		$-0.35n_0$; $-0.5\,n_0$; $-0.8n_0$	20	-	0
		$-0.35n_0$; $-0.5\,n_0$; $-0.8n_0$	40	-	0
		$-0.35n_0$; $-0.5\,n_0$; $-0.8n_0$	-40	-	+/-10
		$-0.35n_0$; $-0.5\,n_0$; $-0.8n_0$	40	-	+/-10
		$-0.35n_0$; $-0.5\,n_0$; $-0.8n_0$	-40	-	+/-25
		$-0.35n_0$; $-0.5\,n_0$; $-0.8n_0$	40	-	+/-25
	4	$-0.35n_0$; $-0.5\,n_0$; $-0.8n_0$	-40	-	0
		$-0.35n_0$; $-0.5\,n_0$; $-0.8n_0$	-20	-	0
		$-0.35n_0$; $-0.5\,n_0$; $-0.8n_0$	0	-	0
		$-0.35n_0$; $-0.5\,n_0$; $-0.8n_0$	20	-	0
		$-0.35n_0$; $-0.5\,n_0$; $-0.8n_0$	40	-	0
		$-0.35n_0$; $-0.5\,n_0$; $-0.8n_0$	-40	-	+/-10
		$-0.35n_0$; $-0.5\,n_0$; $-0.8n_0$	40	-	+/-10
		$-0.35n_0$; $-0.5\,n_0$; $-0.8n_0$	-40	-	+/-25
		$-0.35n_0$; $-0.5\,n_0$; $-0.8n_0$	40	-	+/-25
4	2	$0.6n_0$; $0.8n_0$	-40	-	0
		$0.6n_0$; $0.8n_0$	0	-	0
		$0.6n_0$; $0.8n_0$	40	-	0
		$0.6n_0$; $0.8n_0$	-40	-	+/-10
		$0.6n_0$; $0.8n_0$	0	-	+/-10
		$0.6n_0$; $0.8n_0$	40	-	+/-10
		$0.6n_0$; $0.8n_0$	-40	-	+/-25
		$0.6n_0$; $0.8n_0$	0	-	+/-25
		$0.6n_0$; $0.8n_0$	40	-	+/-25
	4	$0.6n_0$; $0.8n_0$	-40	-	0
		$0.6n_0$; $0.8n_0$	0	-	0

Quadrant	Speed (kn)	Propeller rate	Rudder angle (°)	Sense	ψ (°)
		$0.6n_0$; $0.8n_0$	40	-	0
		$0.6n_0$; $0.8n_0$	-40	-	+/-10
		$0.6n_0$; $0.8n_0$	0	-	+/-10
		$0.6n_0$; $0.8n_0$	40	-	+/-10
		$0.6n_0$; $0.8n_0$	-40	-	+/-25
		$0.6n_0$; $0.8n_0$	0	-	+/-25
		$0.6n_0$; $0.8n_0$	40	-	+/-25

(c)   Harmonic PMM sway tests (type PMMY2)

Speed (kn)	Propeller rate	Sway motion (model scale)		
		amplitude y_{OA} (m)	period T_y (s)	$\lvert\beta_{MAX}\rvert$ (°)
-2	0	0.2	70, 100	171, 174
2	0	0.2	40, 60, 80, 100	15, 10, 8, 6
6	0	0.2	27, 60	8, 3
12	0	0.2	24	4

(d)   Harmonic PMM yaw tests (type PMMPS2)

Qu	Speed (kn)	Propeller rate	Rudder angle (°)	Sense	ψ (model scale)			
					mean (°)	amplitude (°)	period (s)	$\lvert\gamma_{MAX}\rvert$ (°)
1	4	0	0	+	+/-25, 0	10	50	11
		0	0	+	0	15, 25, 35	50	16, 26, 34
		0	0	+	0	15, 25, 35	34	23, 35, 45
		0	0	+	+/-10, +/-5	25	50	26
		$0.4n_0$	-40,-30,-20,-10, 0,10,20,30,40	+	0	25	50	26
		$0.8n_0$	-40,-30,-20,-10 ,0,10,20,30,40	+	0	25	50	26
	8	0	0	+	0	15, 25, 35	25	16, 26, 34
		0	0	+	0	<u>5, 10,</u> 15, 25, 35	17	<u>8, 16,</u> 23, 35, 45
		0	0	+	+/-10, +/-5	<u>15,</u> 25	25	<u>16,</u> 26
		$0.4n_0$	-40,-30,-20,-10 ,0,10,20,30,40	+	0	<u>15,</u> 25	25	<u>16,</u> 26
		$0.8n_0$	-40,-30,-20,-10 ,0,10,20,30,40	+	0	<u>15,</u> 25	25	<u>16,</u> 26
3	4	0	0	-	0	15, 25, 35	34	156, 144, 134
		0	0	-	+/-10, +/-5	25	34	144
		$-0.5n_0$	-40,-20 ,0,20,40	-	0	25	34	144
		$-0.8n_0$	-40,-20 ,0,20,40	-	0	25	34	144
4	4	$0.6n_0$	-40,-30,-20,-10, 0,10,20,30,40	-	0	25	34	144
		$0.8n_0$	-40,-30,-20,-10, 0,10,20,30,40	-	0	25	34	144
		$0.8n_0$	0	-	0	5	34	172

(e)   Oscillatory tests at zero speed (type OSCPSI)

Speed (kn)	ψ_A (°)	Period (s)	Phase (°)	# cycli
0	25	54	90	3

(f)   Multi-modal tests (type MULTI0)

type B

Speed (kn)	Sense	ψ (°)	Propeller rate (model scale)			
			mean	amplitude	period (s)	phase (°)
2	+	0, 2.5, 5, 10, 25, 40, 55, 70, 90	$0.4n_0$	$0.4n_0$	400	-90
		-2.5,-5,-10,-25,-40,-55,-70,-90	$0.4n_0$	$0.4n_0$	400	-90
4	+	0, 2.5, 5, 10, 25	$0.4n_0$	$0.4n_0$	200	-90
		-2.5, -5, -10, -25	$0.4n_0$	$0.4n_0$	200	-90
8	+	0, 2.5, 5, 10, 15	$0.4n_0$	$0.4n_0$	100	-90
		-2.5, -5, -10, -15	$0.4n_0$	$0.4n_0$	100	-90
10	±	0, 5	$0.4n_0$	$0.4n_0$	70	-90
		-5	$0.4n_0$	$0.4n_0$	70	-90
12	+	0, 5	$0.4n_0$	$0.4n_0$	70	-90
-2	-	0, 5, 10, 25, 40, 55, 70	$0.4n_0$	$0.4n_0$	400	-90
		-5, -10, -25, -40, -55, -70	$0.4n_0$	$0.4n_0$	400	-90

type A – quadrant 1

Speed (kn)	Propeller rate	ψ (°)	Rudder angle (model scale)			
			mean (°)	amplitude (°)	period (s)	phase (°)
2	$0.4n_0$	0	0	40	200	0
	$0.6n_0$	0, 5, 10, 25, 40, 55, 70, 90	0	40	200	0
	$0.6n_0$	-5,-10,-25,-40,-55,-70,-90	0	40	200	0
	$0.8n_0$	0	0	40	200	0
4	$0.4n_0$	0	0	40	100	0
	$0.6n_0$	0, 5, 10, 25	0	40	100	0
	$0.6n_0$	-5, -10, -25	0	40	100	0
	$0.8n_0$	0	0	40	100	0
8	$0.4n_0$	0	0	40	50	0
	$0.6n_0$	0, 5, 10, 15	0	40	50	0
	$0.6n_0$	-5, -10, -15	0	40	50	0
	$0.8n_0$	0	0	40	50	0
10	$0.4n_0$	0	0	40	35	0
	$0.6n_0$	0, 5	0	40	35	0
	$0.6n_0$	-5	0	40	35	0
	$0.8n_0$	0	0	40	35	0
12	$0.4n_0$	0	0	40	35	0
	$0.6n_0$	0, 5	0	40	35	0
	$0.8n_0$	0	0	40	35	0

type A – quadrant 3

Speed (kn)	Propeller rate	ψ (°)	Rudder angle (model scale)			
			mean (°)	amplitude (°)	period (s)	phase (°)
-2	$-0.5n_0$	0, 5, 10, 25, 40, 55, 70	0	40	200	0
	$-0.5n_0$	-5, -10, -25, -40, -55, -70	0	40	200	0
	$-0.8n_0$	0	0	40	200	0
-4	$-0.5n_0$	0, 5, 10, 25	0	40	100	0
	$-0.5n_0$	-5, -10, -25	0	40	100	0
	$-0.8n_0$	0	0	40	100	0

type A – quadrant 4

Speed (kn)	Propeller rate	ψ (°)	Rudder angle (model scale)			
			mean (°)	amplitude (°)	period (s)	phase (°)
-2	$0.6n_0$	0, 5, 10, 25, 40, 55, 70	0	40	200	0
	$0.6n_0$	-5,-10,-25,-40,-55,-70	0	40	200	0
	$0.8n_0$	0	0	40	200	0
-4	$0.6n_0$	0, 5, 10, 25	0	40	100	0
	$0.6n_0$	-5, -10, -25	0	40	100	0
	$0.8n_0$	0	0	40	100	0

type C: transition between quadrants 1-2 en 3-4

Speed			
mean (kn)	amplitude (kn)	period (s) (model scale)	phase (°)
-2	2	200	90
4	4	100	-90
5	5	100	-90
6	6	100	-90

type D: validation runs

Run	Parameter				Parameter				Parameter				Parameter			
	f_m	f_A	$T_f(s)$	$\phi_f(°)$	f_m	f_A	$T_f(s)$	$\phi_f(°)$	f_m	f_A	$T_f(s)$	$\phi_f(°)$	f_m	f_A	$T_f(s)$	$\phi_f(°)$
1	Propeller rate				Rudder angle (°)				Speed u_0 (kn)							
	$0.4n_0$	$0.4n_0$	30	-90	0	40	40	0	6	6	100	-90				
2	Propeller rate				Rudder angle (°)				Speed u_0 (kn)				$\psi(°)$			
	$0.4n_0$	$0.4n_0$	30	-90	0	40	40	0	4	4	100	-90	10	0	10	0
3	Propeller rate				Rudder angle (°)				Speed u_0 (kn)				$\psi(°)$			
	$0.4n_0$	$0.4n_0$	30	-90	0	40	40	0	4	4	100	-90	-10	0	10	0
4	Propeller rate				Speed u_0 (kn)				$\psi(°)$							
	$0.4n_0$	0	30	90	4	4	50	-90	0	20	100	-90				
5	Propeller rate				Yaw velocity r (°/s)				Rudder angle (°)				Speed u_0 (kn)			
	$0.4n_0$	$0.4n_0$	280	180	0	2.25	70	90	0	40	45	0	2	0	720	0
6	Propeller rate				Yaw velocity r (°/s)				Rudder angle (°)				Speed u_0 (kn)			
	$0.4n_0$	$0.4n_0$	280	180	0	2.25	70	90	0	40	45	0	2	2	140	90

Table 4 Test program in shallow water: number of tests

TYPE	Speed	RPM	Rudder	Qu.		Base	Optio nal	Total (base)	Total (optional)
PAAL	0	< 0	0	Q2-Q3	UXAA	2		2	
	0	> 0	0	Q1-Q4	UXAA		3		3
STATX	> 0	> 0	0	Q1	UXCB1	1		106	
					UXCC1	1			
					UXCE1	1			
					UXCF	1			
	> 0	> 0	<> 0	Q1	UXCC1	12			
					UXCE1	10			
					UXCF	2			
	> 0	< 0	0	Q2	UXCB2A	10			
					UXCB2B	4			
					UXCC2	5			
					UXCE2	3			
	< 0	< 0	0	Q3	UXCJ3	1			
					UXCK3	1			
	< 0	< 0	<> 0	Q3	UXCJ3	12			
					UXCK3	12			
	< 0	> 0	0	Q4	UXCJ4	5			
					UXCK4	5			
	< 0	> 0	<> 0	Q4	UXCJ4	10			
					UXCK4	10			
PMMY2	> 0	0	0		UXFB	4		8	
					UXFD	2			
	< 0	0	0		UXFJ	2			
PMMPS2	> 0	0	0	Q1	UXGC	13		103	
					UXGE	9			
	> 0	> 0	0	Q1	UXGC	2			
					UXGE	3			
	> 0	> 0	<> 0	Q1	UXGC	16			
					UXGE	24			
	< 0	0	0	Q3	UXGK	7			
	< 0	< 0	0	Q3	UXGK	2			
	< 0	< 0	<> 0	Q3	UXGK	8			
	< 0	> 0	0	Q4	UXGK	3			
	< 0	> 0	<> 0	Q4	UXGK	16			
OSCPSI	0	0	0		UXOP	1		1	
MULTI0 A	0	> 0	<> 0	Q1-Q4	UXMA	3		92	53
	> 0	> 0	<> 0	Q1	UXMB	10	7		
					UXMC	6	3		
					UXME	6	3		
					UXMF	4			
	< 0	< 0	<> 0	Q3	UXMJ	8	6		

TYPE	Speed	RPM	Rudder	Qu.		Base	Optio nal	Total (base)	Total (optional)
					UXMK	5	3		
	< 0	> 0	<> 0	Q4	UXMJ	8	6		
					UXMK	5	3		
MULTI0 B	> 0	> 0	0	Q1	UXMB	9	8		
					UXMC	5	4		
					UXME	5	4		
					UXMF	2			
	< 0	> 0	0	Q4	UXMJ	7	6		
MULTI1	< 0	0	0		UXML	1			
	> 0	0	0		UXMM	2			
	> 0	> 0	<> 0		UXMV(*)	4			
					UXMV1(*)	2			
TOTAL								**312**	**56**

(*) validation runs

398